

**MICROWAVE AND MILLIMETER WAVE  
TECHNOLOGIES: FROM PHOTONIC BANDGAP  
DEVICES TO ANTENNA AND APPLICATIONS**



**MICROWAVE AND MILLIMETER WAVE  
TECHNOLOGIES: FROM PHOTONIC BANDGAP  
DEVICES TO ANTENNA AND APPLICATIONS**

Edited by  
**PROF. IGOR MININ**

***In-Tech***  
*intechweb.org*

Published by In-Teh

**In-Teh**

Olajnica 19/2, 32000 Vukovar, Croatia

Abstracting and non-profit use of the material is permitted with credit to the source. Statements and opinions expressed in the chapters are those of the individual contributors and not necessarily those of the editors or publisher. No responsibility is accepted for the accuracy of information contained in the published articles. Publisher assumes no responsibility liability for any damage or injury to persons or property arising out of the use of any materials, instructions, methods or ideas contained inside. After this work has been published by the In-Teh, authors have the right to republish it, in whole or part, in any publication of which they are an author or editor, and the make other personal use of the work.

© 2010 In-teh

[www.intechweb.org](http://www.intechweb.org)

Additional copies can be obtained from:

[publication@intechweb.org](mailto:publication@intechweb.org)

First published March 2010

Printed in India

Technical Editor: Sonja Mujacic

Cover designed by Dino Smrekar

Microwave and Millimeter Wave Technologies: from Photonic  
Bandgap Devices to Antenna and Applications,

Edited by Prof. Igor Minin

p. cm.

ISBN 978-953-7619-66-4

## Preface

This book deal with the modern developing of microwave and millimeter wave technologies. The first chapter is aimed at describing the evolution of technological processes for the design of passive functions in millimetre-wave frequency range. From the results HR SOI seems to be a good candidate in the coming year to address both low cost and low power mass market CMOS digital and RF/ MMW applications.

Materials that exhibit negative index (NI) of refraction have several potential applications in microwave technology. Examples include enhanced transmission line capability, power enhancement/size reduction in antenna applications and, in the field of nondestructive testing, improved sensitivity of patch sensors and detection of sub-wavelength defects in dielectrics by utilizing a NI superlens. The next two chapters explains the physics underlying the design of purely dielectric NI metamaterials and will discuss some ways in which these materials may be used to enhance various microwave technologies.

There are two main reasons to want to have information for the actual anisotropy of a substrate – to control the technology (necessary for the manufacturers) and to conduct more realistic simulations of the structures, containing anisotropic materials (necessary for the users). The 3rd chapter represented the increasing importance of the material's anisotropy in the modern design and the possibilities for accurate determination of this characteristic by waveguide and resonance methods.

Wave propagation in suppositional material was first analyzed by Victor Vesalago in 1968. Suppositional material is characterised by negative permittivity and negative permeability material properties. Under these conditions, phase velocity propagates in opposite direction to group velocity. Since then, these electrical structures have been studied extensively and are referred to as meta-material structures. In the 4th chapter the authors analyze meta-material concepts using transmission line theory proposed by Caloz and Itho and propose effective materials for realising these concepts. They propose a novel NPLH (Near Pure Left Handed) transmission line concept to reduce RH (Right Handed) characteristics and realize compact small antenna designs using meta-material concepts and the possibility of realising negative permittivity using EM shielding of concrete block is considered.

The basic theory of microwave filters, to describe how to design practical microwave filters, and to investigate ways of implementing high performance filters for modern communication systems are given in the 5th chapter.

And the 6th chapter covered filters made using different technologies including active devices, MEMS, ferroelectric and ferromagnetic materials. Filters involving combined technologies

were covered; and also the traditional tuning using mechanically adjustable screws was discussed.

The 7th chapter present several key points in materials optimization, capacitor structure, and device designs that Georgia Institute of Technology and nGimat have focused on in the last few years.

In the 8th chapter summarizes the current status of the MOSFET's for very high frequency applications.

The potential of high permittivity dielectric materials for local capacitive loading of microstrip components has been demonstrated in the 9th Chapter. The designs of miniature microstrip resonators, filters, and antennas with local high-permittivity dielectric loading have been developed, and the prototypes have been fabricated by using the LTCC technology that allowed for coprocessing different ceramic materials in multilayer and planar architecture.

Three types of microstrip-to-waveguide transitions are presented in the 10th chapter. One is a transition with a short-circuited waveguide which is quite broadband such that bandwidth of reflection below  $-20$  dB is 24.9 GHz (32.5 %). Others two are a planar transition in multi-layer and single-layer substrate substrates.

The original reflector antenna design with the cylindrical monopole antenna as a sub-reflector for application in radio monitoring for information protection has been presented in 11 chapter.

In the 12 chapter present a brief coverage of both established and emerging techniques in materials characterization.

The 802.11 a/b/g FEM with PAM was composed of a SPDT switch, a Rx diplexer, two Rx BPFs, a Tx diplexer, two Tx LPFs, two matching circuits, and a dual-band PAM and discussed in the 13 chapter.

In simple terms, a millimeter-wave imaging sensor is a camera that uses millimeter waves. The authors in the 14th chapter reviewed imaging sensors using the millimeter-wave band. But to my regret the authors searched publications mainly on International Microwave Symposium and did not survey papers on SPIE and others sources. So the good review is not full, for example, Table 2 could be added by the results from [1] and so on.

The authors in the chapter 15 describe and exemplify from many fractals applications one possible use, fractal antenna for terrestrial vehicles.

In order to protect the antenna from various environments, dielectric radome is usually covered in front of the antenna. The authors in the chapter 16 mainly focus on the analysis and optimal design of the radome in millimeter wave band. But it could be noted that in some of case with help of 3D diffractive optics it is possible to design a millimeter-wave antenna without special radome [2].

Additional, in the chapter 17 the authors described the design scheme for multibeam dielectric lens antennas that well balances the conflicting aims of high gain and low sidelobe level. The scheme is based on pareto-GA and lens shape is associated with GA chromosomes.

In the chapter 18 investigated several structures in order to find the main geometrical parameters able to improve performances of a PBG based particle accelerator. All the

simulations reveal good performances for a structure based on dielectric rods and a suitable number of grating periods.

In the last chapter, specific millimeter-wave features of the Fabry-Perot resonator are discussed.

It is expected the book will attract more interest in microwave and millimeter wave technologies and simulate new ideas on this fascinating subject.

References:

1. O.V.Minin and I.V.Minin. Diffractive optics of millimeter waves. IOP Publisher, Bristol and Philadelphia, 2004, 396p. ISBN 0-7503-0907-5
2. I.V.Minin and O.V.Minin. Three Dimensional Fresnel Antennas. In: Advances on Antennas, Reflectors and Beam Control, Research Signpost, Kerala, INDIA, 2005, pp. 113-148. ISBN 81-308-0067-5

Prof. Igor Minin

*Novosibirsk State Technical University*

*Russia*

Prof.minin@gmail.com





## Contents

Preface	V
1. Trend on Silicon Technologies for Millimetre-Wave Applications up to 220 GHz Gaëtan Prigent, Thanh Mai Vu, Eric Rius and Robert Plana	001
2. Integrated Silicon Microwave and Millimeterwave Passive Components and Functions Philippe Benech, Jean-Marc Duchamp, Philippe Ferrari, Darine Kaddour, Emmanuel Pistono, Tan Phu Vuong, Pascal Xavier and Christophe Hoarau and Jean-Daniel Arnould	031
3. Negative Refractive Index Composite Metamaterials for Microwave Technology Nicola Bowler	055
4. Dielectric Anisotropy of Modern Microwave Substrates Plamen I. Dankov	075
5. Application of meta-material concepts Ho-Yong Kim and Hong-Min Lee	103
6. Microwave Filters Jiafeng Zhou	133
7. Reconfigurable Microwave Filters Ignacio Llamas-Garro and Zabdiel Brito-Brito	159
8. Electronically Tunable Ferroelectric Devices for Microwave Applications Stanis Courrèges <sup>1</sup> , Zhiyong Zhao <sup>2</sup> , Kwang Choi <sup>2</sup> , Andrew Hunt <sup>2</sup> and John Papapolymerou <sup>1</sup>	185
9. Advanced RF MOSFET's for microwave and millimeter wave applications: RF characterization issues Julio C. Tinoco and Jean-Pierre Raskin	205
10. Development of Miniature Microwave Components by Using High Contrast Dielectrics Elena Semouchkina	231
11. Broadband and Planar Microstrip-to-waveguide Transitions Kunio Sakakibara	257

12. Microwave and Millimeter Wave Technologies A New X-Band Mobile Direction Finder Sergey Radionov, Igor Ivanchenko, Maksym Khruslov, Aleksey Korolev and Nina Popenko	273
13. Characterization techniques for materials' properties measurement Hussein KASSEM, Valérie VIGNERAS and Guillaume LUNET	289
14. Implementation of the Front-End-Module with a Power Amplifier for Wireless LAN Jong-In Ryu, Dongsu Kim and Jun-Chul Kim	315
15. Millimeter-wave Imaging Sensor Masaru Sato and Koji Mizuno	331
16. Fractal Antenna Applications Mircea V. Rusu and Roman Baican	351
17. Analysis and Design of Radome in Millimeter Wave Band Hongfu Meng and Wenbin Dou	383
18. Design of dielectric lens antennas by multi-objective optimization Yoshihiko Kuwahara and Takashi Maruyama	405
19. Modelling and Design of Photonic Bandgap Devices: a Microwave Accelerating Cavity for Cancer Hadrontherapy Roberto Marani and Anna Gina Perri	431
20. Specific Millimeter-Wave Features of Fabry-Perot Resonator for Spectroscopic Measurements Petr Piksa, Stanislav Zvánovec and, Petr Černý	451

# Trend on Silicon Technologies for Millimetre-Wave Applications up to 220 GHz

Gaëtan Prigent <sup>1</sup>, Thanh Mai Vu <sup>2</sup>, Eric Rius <sup>3</sup>, Robert Plana <sup>2</sup>

<sup>1</sup> *Université de Toulouse; INPT, UPS ; CNRS LAPLACE ; France*

<sup>2</sup> *Université de Toulouse ; UPS, INSA, INPT, ISAE ; CNRS LAAS ; France*

<sup>3</sup> *Université Européenne de Bretagne ; Université de Brest ; CNRS Lab-STICC ; France*

## 1. Introduction

Largely reserved for military applications at the origin, the field of transmissions by electromagnetic waves is strongly prevalent in recent years with the emergence of new applications. Recent evolutions in modern civilian millimetre-wave applications, such as collision-avoidance radar sensor, inter-satellite communications, pico-cell networks, and microwave imaging have led to hardened constraints in terms of selectivity, performances, and bulk reduction. In this frequency range, a high level technological resolution is needed at low wavelength. This means that millimetre-wave monolithic integrated circuits (MWMICs) are generally preferred to hybrid technology.

Moreover, with the constant evolution of systems in millimetre wave frequency range, the ever growing mass market forced the technological to reduce their costs of production. Thereby, technologies usually reserved to millimetre-wave applications, such as III-V technologies (InP or GaAs), have reduced their use for the benefit of silicon clusters. Indeed, III-V technologies have been for a long time the unique ones able to address millimetre-wave applications. One of the major advantages of III-V technologies is their low loss level; nevertheless their cost is prohibitive for general public applications and limited to a small series production. Conversely, silicon technologies which are more economics, present level of losses too high to meet drastic specifications of actual systems, especially for passive functions. Thereby, recently many studies were led to take advantage of silicon technology for the integration of passive functions on active chip. The trend was reversed since Si-based technologies now offer competing performances. Si-based technologies are indeed cheaper, which is reinforced by their high integration capabilities. Then increasing efforts have been carried out during the past years to evaluate the potential of silicon technologies to address millimetre-wave applications. For instance, the 7 GHz unlicensed bandwidth around 60 GHz and 77 GHz for automotive radar applications has focussed many attention since large volumes can be expected for those applications. Due to its cost advantage, improved millimetre-wave transistor characteristics, and ease of integration of high performance digital and high speed analog/RF circuits, silicon has emerged as the favourite solution satisfying the needs of rapidly growing communications market, and is now a competitive

alternative to classical III-V technologies to address millimetre-wave applications. Moreover, next-generation silicon-based RF CMOS and BiCMOS technologies, which offer NMOS and SiGe HBT devices with cutoff frequencies beyond 277 GHz (Kuhn et al., 2004) and 300 GHz (Rieh et al., 2004) respectively, will enable the implementation of millimetre-wave system-on-chip (SoC) such as 60 GHz WLAN (Floyd et al., 2006),(Doan et al., 2004), 40/80/160 Gb/s optic-fiber transceivers (Perndl et al., 2004) or 24/77 GHz collision avoidance radars, which were reserved until recently to III-V compound semiconductors application domain.

However, integration of high performances passive components remains a key issue in silicon technologies. Some of the available solutions consists in the use of silicon as a support for active function development, passive functions being implemented on silicon using specific technologies such as membrane technologies (Vu et al., 2008) or thin film microstrip (TFMS) based technologies developed on Si-BCB substrate (Six et al., 2006), (Prigent et al., 2004), (Wolf et al., 2005). Nevertheless, if such technologies have already proved their efficacy for sub-millimeter wave functions, their implementation remains difficult since they need complex technological process. Recent work (Gianesello et al., 2006) have demonstrated that silicon technologies are able to address higher frequencies applications up to G-band (140-220 GHz) if high resistivity (HR) silicon-on-insulator (SOI) technology is used. Moreover, feasibility of integrated antenna made on advanced CMOS standard technology has been demonstrated (Montusclat et al., 2005) and HR SOI technology has proved its efficacy to improve the overall performances of integrated antennas. However, in millimeter frequency range, the design of narrow-band planar filters appears as one of the most critical point. Hence, in view of the required selectivity levels, designers are, indeed, faced with problems in relation to control design, i.e. modelling accuracy, as well as the high insertion loss levels inherent in such devices. Moreover, due to low electrical lengths involved in millimetre-wave, the technological dispersion has to be as low as possible.

This chapter is aimed at describing the evolution of technological processes for the design of passive functions in millimetre-wave frequency range. III-V technologies that are behind the development of millimetre-microwave functions in W-band are first described. Performances obtained in III-V technology for wide- and narrow-band filters reported here will be the reference for comparison with other technologies. Several technological process dedicated to silicon technologies were then studied: membrane and thin film microstrip technologies. Finally, millimetre-wave electrical performances of devices were reported for passive components and active circuits achieved in ST-Microelectronics advanced CMOS HR SOI technology, so as to investigate the suitability of that technology to address millimetre-wave Systems on Chip (SOC) up to 220 GHz and beyond. Classical stub-based broadband filters implemented in coplanar waveguide technology were first designed so as to prove the technological process accuracy as well as its performances which are fully competitive with III-V technologies. Then, the design of coupled-lines narrowband filters was investigated in the V-band, at 60 GHz. These concepts were validated through comparison with experiments performed up to 220 GHz.

## 2. III-V Technology Application

### 2.1 Technological process

The first technology cluster that we present is the III-V (either GaAs or InP) technological process developed in the IEMN laboratory of Lille, France. The use of semi-conductor substrate allows taking advantage of transport properties of charge inherent in this material for active functions implementation (transistor for instance) (Dambrine et al., 1999). Thus, such a technology offers the possibility to realize millimetre-wave monolithic integrated circuits (MWMICs) for which passive and active components are made on the same medium. Thereby, the losses induced by the surface mounting and the wiring of the components are reduced, as well as the cost of production.

This technology is based on the deposit of successive metal layers. Due to its good conductivity ( $\rho \approx 4.1 \cdot 10^7$ ) as well as its high resistance to oxidation, metal widely used for III-V technologies is gold. In millimetre frequency range, gold thickness is an important parameter, generally 3- $\mu\text{m}$ -thick, so as to reduce propagation losses. Several techniques are possible to achieve this metallic deposit. The usual plating techniques such as vacuum evaporation or spraying are costly when the metal thickness exceeds the micron. That is why, in order to minimize costs, the filing of metallization is by electroplating. We will briefly describe the steps needed to implement components in III-V technology, namely technology of electroplating and lithography combined, as well as the masks topology.

The basic principle of the technology studied hereafter is the deposit of successive layers of sacrificial photoresist layers. The sacrificial layer parts that are subject to insulation are etched and eliminated after dilution onto remover. Therefore, patterns are defined through optical masks used in the phases of the sacrificial layer insulation. In the described technology, two optical masks were used: the first whose dimensions are higher (3  $\mu\text{m}$ ) than the actual pattern dimensions, the second having the exact dimensions. The use of such a process allows, if there is no overlap between the two sacrificial layers, to avoid bulges forming on the edge of the patterns during the metallization. Moreover, this process allows an extra margin for alignment of optical masks, preciseness in alignment being of the order of micron.

So as to perform electroplating, it is necessary to make conductor the pattern to be metallic. So a thin metal layer (few hundred angstroms) is deposited either by vacuum evaporation or by cathode spraying. This last technique is preferred to the first one since it avoids tearing of the sacrificial layers, and therefore the protected patterns. Moreover, it allows a greater rigidity of the metallic layer. In conventional III-V technologies, this thin metal layer is composed of a 200- $\text{\AA}$ -thick titanium layer to ensure a good adhesion followed by a 300- $\text{\AA}$ -thick gold deposit that allows metal growth. Indeed, because of the strong oxidation of titanium in air, it is virtually impossible to achieve electrolysis directly on the titanium.

Once electroplating performed the adhesion layer is chemically etched. Nevertheless, during the etching of the device, both adhesion layer and gold deposit are etched. Moreover, for patterns of low dimensions, it is necessary to insist in the etching process, this has the effect of reducing the metal thickness and size of the pattern, but also to increase the roughness of the deposit. One should also remark that, most of the time, during the etching process, there is a slight film of gold to prevent the titanium etching which creates short-circuits between patterns. For this reasons, the proposed technology uses a nickel deposit that satisfies all the requirements: a good substrate adhesion, a good gold-growth and ease in etching process.

The third step consists in electroplating itself, once achieved patterns definition and thin metal layer deposit phases. An electric current flow in an electrolyte solution (solution of double cyanide of gold and potassium ( $\text{KAu}(\text{CN})_2$ )) creates a chemical reaction near electrodes. Gold ions being positive, the sample foil is attached to the cathode. It follows a phenomenon of transfer of charges called electroplating. This basic principle is relatively simple; however this operation must still be undertaken with some caution. Indeed, ohmic losses of a transmission line depend not only on the resistivity of the metal, but also to its surface state. But the roughness of the metallic layer increases with the current density. It is therefore necessary to apply a current density relatively low. However, if very low current density yields a very low roughness, it also increases the time of filing causing problems of mechanical strength of the sacrificial layer. We must therefore find a compromise between roughness and mechanical strength.

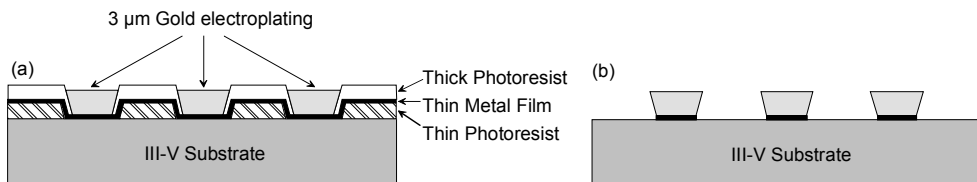


Fig. 1. Transmission line realization: a- Lithography process, b- Transmission lines after sacrificial layer removing and thin metal layer etching.

In the millimetre and sub-millimetre frequency range coplanar waveguides are more commonly used in the design of circuits (Argarwal et al., 1998), (Haydl et al, 1999), (Hirose et al., 1998), (Papapolymerou et al., 1999). Many studies have, indeed, shown that coplanar waveguides can be considered as a good alternative to microstrip lines in this frequency range (Houdard, 1976), (Hirota & Ogawa, 1987), (Ogawa & Minagawa, 1987), (Brauchler et al., 1996), (Kulke & Wolff, 1996), (Herrick et al., 1998). Because all conductors are located on the same plane, the ground connections through via-holes are eliminated and no reverse side processing is needed, which significantly reduces cost. Because of the large decoupling between the different elements of a coplanar system, global size reduction may be obtained as well. Another advantage of the coplanar technology is flexibility in the design of the passive circuits. Indeed, a large number of geometrical parameters can be chosen to design a transmission line with given impedance.

Electrical characteristics can then be improved by correctly defining the ratio between the strip width and the slot width. However, designers are faced with two major drawbacks when they deal with coplanar technology. The first one is the lack of mature equivalent-circuit models like those available for microstrip lines. The second one concerns the suppression of the fundamental, but parasitic, slot line mode that may be excited by non symmetrical coplanar waveguide discontinuities such as, for example, bends or T-junctions. The suppression of such perturbing modes is achieved by inserting bridges over the centre conductor, so that the potentials on either side of the lateral ground planes are identical (Koster et al., 1989), (Beilenhoff et al., 1991). Consequently, additional steps in the production process are needed for the fabrication of the bridges.

There are two types of air-bridges: classical inter-ground and inter-conductor bridges, their role is to force a similar voltage on either side of the central conductor. Whatever the bridge

topology, the technological process for bridge realization is identical and similar to the technological process described above (Fig. 2). Besides the good definition for devices due to the high-resolution technology, one of the advantages of this technological process is the control of the shape of the air-bridge. Indeed in hybrid technology, air-bridges are generally implemented by using wire-bonding connected manually to the ground plane. By such a process the shape of the bridge is difficult to control involving a problem of reproducibility first and in the other hand problems with bridge modelling. Here, however, the technology used allows good control of the fixture of these bridges as illustrate in Fig. 2.

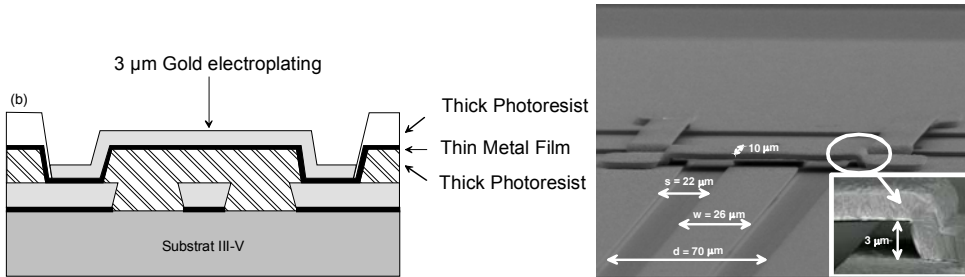


Fig. 2. Air-bridge realization: (a)- Lithography process, (b)- Airbridges realized with IEMN technological process.

In order to minimize the parasitic influence of the bridge on the electrical characteristic of the lines and provide mechanical stability, the dimensions of the air bridge used are: 3  $\mu\text{m}$  height, 10  $\mu\text{m}$  width, 80  $\mu\text{m}$  length ( $d=70 \mu\text{m} + 10 \mu\text{m}$  minimum spacing between slot border and bridge), and 3- $\mu\text{m}$  metal thickness. Moreover, to give it a good mechanical stability, a maximum length must be defined for a given width: for example, 10  $\mu\text{m}$  and 20  $\mu\text{m}$  widths allow maximum lengths of 100 and 180  $\mu\text{m}$ , respectively. Although the bridge introduces an excess capacitance, this does not constitute a problem for the bridge widths here as long as the strip widths of the coplanar line are all kept small. Under a configuration with these dimensions, no compensation techniques, such as using sections of high-impedance line, are required (Rius et al., 2000-a), (Weller et al., 1999).

## 2.2 Optimal dimensions for coplanar transmission lines

So as to determine the optimum sizing of coplanar transmission lines, we rely on the work of W. Heinrich (Heinrich, 1993). The proposed quasi-TEM description ensued from a quasi-static approach. The *RLCG* equivalent circuit components are determined from approximate analytical equations derived from a global analysis. These values depend for electrical and geometrical parameter of the transmission lines as well as the frequency. *C* and *G* elements are considered invariant with frequency. However, as the skin effect modifies the current distribution in conductors depending on frequency, the *R* and *L* elements are highly dependant on frequency. For instance, let us consider a 50  $\Omega$  coplanar transmission line implemented in GaAs technology ( $h=400 \mu\text{m}$ ,  $t=3 \mu\text{m}$ ,  $\epsilon_r=11.9$ ,  $\tan\delta=2\times 10^{-4}$ ,  $\sigma=4.1\times 10^7 \text{ S.m}$ ) with line- and slot-width of  $W=26 \mu\text{m}$ ,  $S=22\mu\text{m}$ , respectively. Fig. 3 illustrates the evolution of the *R* and *L* parameter for transmission line model as a function of the frequency.

With knowledge of *RLCG* parameters, one can easily determine the parameters of propagation, attenuation, impedance and effective permittivity and, therefore optimal rules for transmission line sizing as a function of its geometrical parameters: line- and slot-widths as well as ground-to-ground distance. The inter-ground distance ( $d=W+2 \cdot S$ ) is an important parameter for wave propagation. Indeed, so as to avoid propagation of parasitic modes, this distance  $d$  has to be low compared to the wavelength; the commonly used constraint is  $d \leq \lambda_g/10$ . An increase of this constraint ( $d \leq \lambda_g/20 = d_{max}$ ) allows neglecting the radiation losses. Moreover, it limits extend of radiating waves, and therefore the problems relied to packaging. However, according to Fig. 4-(a), the attenuation also depends on the ground-to-ground distance. It is, in fact, inversely proportional to the distance  $d$ . It follows that inter-ground distance  $d$  must be the closest to  $d_{max}$ .

Once the inter-ground distance chosen, we are interested in the relation between the dimensions of the line-width and inter-ground distance. This ration  $W/d$  is predominant in the choice of the achievable characteristic impedances. According to Fig. 4-(b) so as to limit the attenuation, it is preferable to set  $W$  in the interval between  $0.3 \times d$  and  $0.6 \times d$ . Moreover, the ground plane width ( $W_g$ ) and the substrate thickness ( $h_s$ ) are chosen to make a trade-off between losses and low dispersion up to the W-frequency band. To summarize, the following conditions are then chosen to realize our devices:

$$d = (W + 2 \cdot S) \leq \frac{\lambda_g}{20} = d_{max} \quad (1)$$

$$0.3 \cdot d \leq W \leq 0.6 \cdot d \quad (2)$$

$$W_g \geq W + 2 \cdot S \quad (3)$$

$$h_s \geq 2 \cdot (W + 2 \cdot S) \quad (4)$$

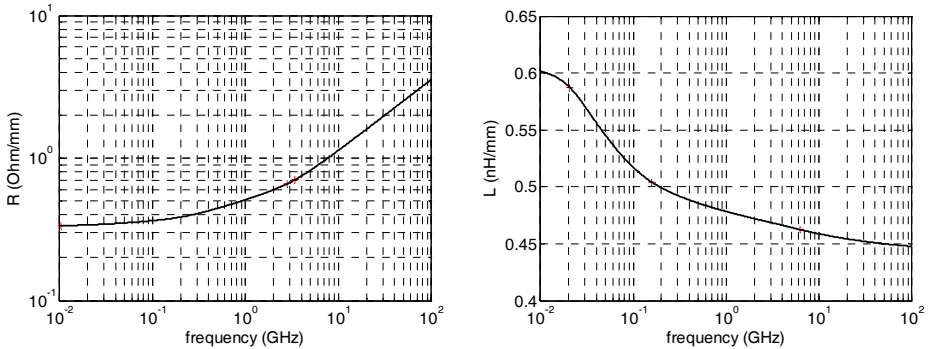


Fig. 3. Evolution of  $R$  and  $L$  parameters as a function of the frequency.



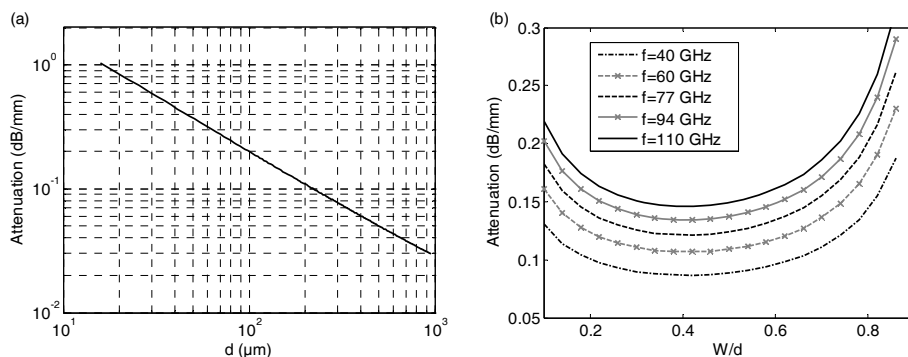


Fig. 4. Evolution of the attenuation as a function of : (a) ground-to-ground distance. (b) Line width ( $W$ ) to ground-to-ground ( $d$ ) ration.

### 2.3 Wide-band bandpass filter design

We first investigated on the design of quarter-wavelength shunt-stub filters. Such topology includes shorted stubs as resonators separated by quarter-wavelength transmission lines as inverters. The synthesis developed by Matthaei (Matthaei et al., 1980) indicates that the bandwidth is in close relation with the impedance level of the resonators. In the present case, so as to respect optimal sizing described above the impedance range extends from  $30 \Omega$  to  $70 \Omega$ . Thus, the available 3-dB bandwidth will be approximately bounded by 100% and 36%. For bandwidths below 36%, very low impedance levels are needed. Thus, shape factors become too large for correct performance from the device with regard to both the parasitic influences of the discontinuities and modelling difficulties. So, other topologies such as coupled-line filters are preferred.

The first results presented here deal with 58% and 36%, 3-dB-bandwidth, 3<sup>rd</sup>-order filters centred on 82.7 GHz. According to synthesis, the first example with 58% 3-dB-bandwidth results in a  $25 \Omega$  impedance for the resonators when inverters are kept to  $51 \Omega$ . Twenty-five is chosen so as to introduce double  $50 \Omega$  stubs for the resonator (Fig. 5-(a)). According to the low level of insertion losses, the standard geometry was chosen as follows:  $26 \mu\text{m}$  for the strip widths and  $22 \mu\text{m}$  for the slot widths. The 36% bandwidth was reached by selecting impedances of  $56 \Omega$  and  $15 \Omega$  for inverters and resonators, respectively. As before,  $15 \Omega$  was obtained with two double  $30 \Omega$  stubs. It corresponds to the lowest bandwidth that can be reached with an impedance range bounded by  $30 \Omega$  and  $70 \Omega$ . For the inverters, strips and slots were  $20 \mu\text{m}$  and  $25 \mu\text{m}$ , respectively, and  $54 \mu\text{m}$  and  $8 \mu\text{m}$  for the resonators. The layout and frequency response are displayed in Fig. 5-(b). As for the first prototype, experimental and simulated results agree over a broad-band frequency.

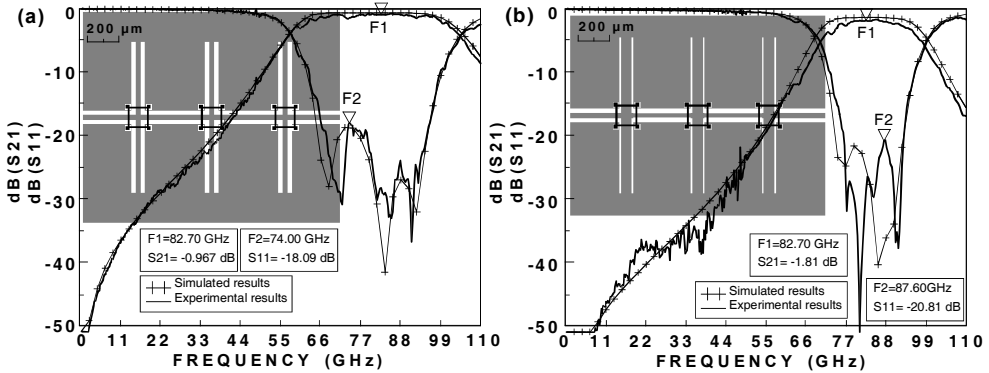


Fig. 5. Layout, simulated, and experimental associated magnitude responses of the 82.7-GHz central-frequency, (a) 58% 3-dB-bandwidth and (b) 36% 3-dB-bandwidth filters.

As shown in Fig. 5, insertion losses increase with filter selectivity: 0.96, and 1.81 dB are obtained for 58%, and 36% bandwidth filters, respectively. These values are in complete agreement with the following expression (Matthaei et al., 1980), (Cohn, 1959):

$$I.L. = \frac{4.343 \cdot n}{Q_u \cdot w} \tag{5}$$

with  $I.L.$  the insertion loss in decibels,  $n$  the filter order,  $w$  its relative bandwidth, and  $Q_u$  the unloaded quality factor, which is close to 25 for the standard 50 Ω transmission line used here.

### 2.5 Narrow-band bandpass filter design

Two major problems are related to narrow-band bandpass coupled-lines filters. First, insertion losses become important when the selectivity of the filter is increased. The second problem deals with accuracy which is directly in relation to the level of selectivity.

In order to illustrate this, we present the results obtained with two classical coupled-lines third-order bandpass filters. The first one is at a center frequency of 65 GHz, 22% 3-dB bandwidth whereas the second one is at 94 GHz, 5% 3-dB bandwidth. Figs. 6 and 7 show the layouts of these filters. For such topologies, according to well-known synthesis (Matthaei et al., 1980), the bandwidth and the coupling coefficient level of the coupled-lines sections are in close relation. Indeed, narrow selective bandwidths are obtained with low coupling levels on the central sections of the filter. A convenient solution consists of using a separating ground plane between the coupled strips. This leads to low coupling levels on a reduced bulk and this separate ground plane acts as a good parasitic mode filter (Fig. 7). According to the finite conductivity of the metal ( $4.1 \times 10^7$  S.m for gold metallization) and to the dissipation factor of the GaAs substrate ( $\tan\delta=2 \times 10^{-4}$ ), very high insertion losses are expected when designing such narrow-band filters. These insertion losses can be predicted roughly from (5). For instance, for a third-order, 22% 3-dB-bandwidth coupled-line filter designed with 26-μm strip widths, insertion losses between 1.95 dB and 2.95 dB are obtained. However, if the bandwidth is decreased to 5%, insertion losses reach a critical

level between 8.7 and 13 dB. These values were calculated with the unloaded quality factor of 20 and 30. One way of improving this critical point is to increase the strip widths, but this gives rise to several problems. The first problem concerns the bridge topology: a large ground-to-ground spacing is, indeed, forbidden because of mechanical stability constraints. A good way to solve this problem is to fabricate an inter-strip bridge as shown in Figs. 6 and 7. By doing so, the ground connections used for filtering the coupled-slotline modes are made directly with a tiny strip on the first metallization layer.

The second one concerns modelling. Obviously, as the strips are wider, the conditions of low dispersion given in Section 2.2 are not necessarily still valid. Moreover, the validity conditions of the analytical quasi-TEM models used are not always met. Finally, the dimensions of the discontinuities increase with the strip widths and, consequently, strong parasitic effects appear. Modelling them accurately is quite difficult and it allows only an approximation. Nevertheless, as an optimization procedure is needed to adjust all the characteristics of the filter response correctly, it requires the use of a very fast modelling technique (Prigent, et al., 2004-b). As shown in Fig. 6 for the 22% 3-dB-bandwidth prototype a good agreement is observed between simulated and experimental results. This agreement is valid over a wide frequency band from 500 MHz to 110 GHz and, as expected, correct insertion loss levels of about 1.4 dB are observed in the bandwidth.

Since the bandwidth is very selective, the measurements were only made on a frequency range from 66 to 110 GHz for the second prototype. The experimental results are presented in Fig. 7 and give a 4-dB insertion loss and 10-dB return loss for a centre frequency of 91.5 GHz. Compared to the expected results, one should also note a significant bandwidth broadening. In this case, this problem is only due to the reverse side of the substrate. Indeed, as the ground-to-ground spacing is very large, the electromagnetic fields are strongly modified by the electrical condition on the reverse side of the dielectric substrate: open or grounded. Impedance and coupling levels are subject to changes that significantly modify the frequency response. Post-simulation was carried out to check the bandwidth broadening by taking into account correct conditions on the substrate backside. This post-simulation is presented in Fig. 7. As this problem masks the errors due to the modelling method, it is difficult to form any conclusions regarding its accuracy in this frequency range. Although the insertion loss appears to be correct, new experiments on filters with a correct bandwidth and return loss are necessary to assess the insertion loss accurately. Nevertheless, when designing future very high-selectivity filters for which the confinement of the electromagnetic field is a problem, the designer must keep in mind the packaging aspect. As grounded CPW lines are not a very convenient solution, three-dimensional technological solutions using, for instance, thin- or thick-film microstrip transmission lines appear to be equally well suited (Rius et al., 2000-b), (Six et al., 2001), (Aftanasar et al., 2001), (Warns et al., 1998), (Schneider & Heinrich, 2001).

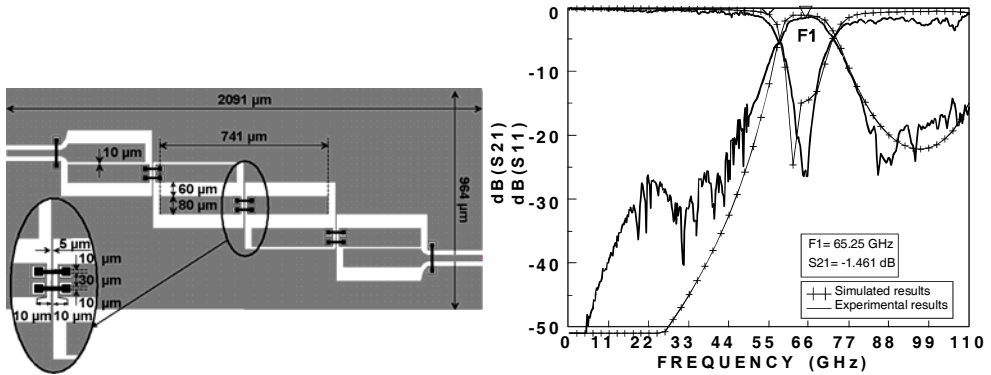


Fig. 6. Layout, Simulated and experimental results of a 65-GHz central-frequency, 22% 3-dB-bandwidth, coupled-line filter.

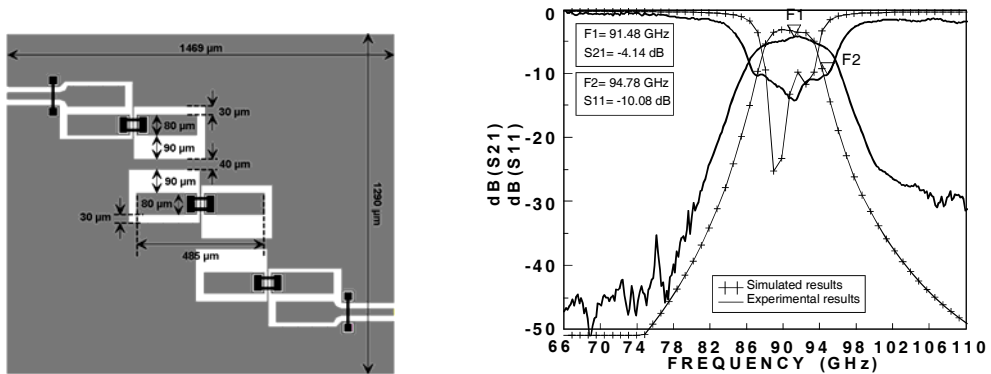


Fig. 7. Layout, Simulated and experimental results of a 65-GHz central-frequency, 5% 3-dB-bandwidth, coupled-line filter.

### 3. Membrane Technologies

#### 3.1 Technological process

Contrary to the previously described III-V technologies which production cost limits their use to little series, technologies on silicon offer an interest with respect to cost reduction while retaining their interest in the integration of active functions. Nevertheless their major drawback is that levels of dielectric losses are not compatible with the specifications required for the passive functions. An alternative consists in the use of silicon membrane technology whose primary function is to mechanically support circuits while remaining transparent for functions in microwave. Thus, the electrical characteristics of this support match with those of vacuum, the ideal dielectric. On the other hand, membrane technology permits to minimize phenomena of dispersion, as well as the removal of cavity modes.

The technological process developed here is nearly the same as the one developed in III-V technology. The major difference is the membrane realization and the backside etching of the silicon. The membrane technology developed at the LAAS laboratory (Toulouse, France)

is realized on a 400- $\mu\text{m}$ -thick silicon substrate ( $\epsilon_r = 11.9$ ,  $\tan\delta = 0.018$ ). The technological process is composed of five main steps as depicted in Fig. 8.

The first step consists in a deposition of two layers  $\text{SiO}_2$  (0.8  $\mu\text{m}$ ,  $\epsilon_r = 4$ ) and  $\text{Si}_{3.4}\text{N}_4$  (0.6  $\mu\text{m}$ ,  $\epsilon_r = 8$ ) realized on both size of silicon wafer. Then,  $\text{SiO}_{0.7}\text{N}_{0.7}$  layer (5  $\mu\text{m}$ ,  $\epsilon_r = 5.5$ ) is deposited on the front side. Next, the elaboration of metal level is performed by first the evaporation of a Ti/Au seed layer and then a 3  $\mu\text{m}$  gold electroplating into a photoresist mould. After the suppression of photoresist mould, the seed layer is suppressed in the slots. The third step is to realize air bridges. A photoresist mould is used to fill up coplanar slots. A sacrificial layer with the same type of photoresist mould is then deposited to form air bridges. A gold seed layer is evaporated and then 3- $\mu\text{m}$ -thick gold is electroplated. The plating is followed by gold etching. The next step consists in realisation membrane by removing silicon substrate in the back side. Silicon etching is realized by dry way using Deep Reactive Ion Etching (DRIE) technique through a thick photoresist mould. Moreover, to protect air bridges and to avoid the membrane breaking during DRIE process, the wafer is bonded to a support one in the front side. Finally, the structures are released from the support substrate using acetone bath followed by  $\text{CO}_2$  drying process. With these three layers of dielectric, the membrane possesses a mechanical stiffness strong enough to absorb the stresses induced by various technological processes while retaining effective permittivity of 1.8 which is close to 1.

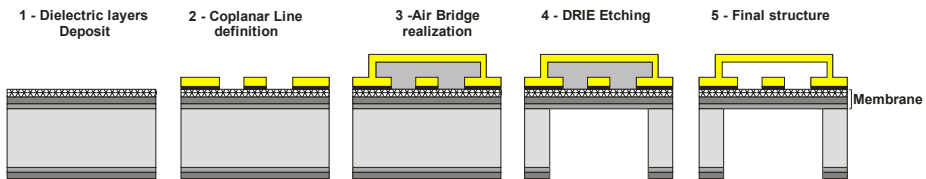


Fig. 8. Membrane technological process

### 3.2 Wide-band bandpass filter Design

The use of such technology has already been the subject of many studies and has demonstrated its effectiveness for circuits in millimetre band and for low frequencies operating (C-band). Nevertheless, its use in W-band is reported to be more sensitive concerning the required level of technological accuracy. While membrane technologies offer an interest in the reduction of dielectric losses, a permittivity close to 1 severely limits their use in terms of achievable impedances. Indeed, when meeting the conditions described by Heinrich (Section 2.2) so as to limit both the dispersion of the transmission lines and losses, for a relative permittivity of 1.8, the ground-to-ground dimension ( $d$ ) is about 230  $\mu\text{m}$  @ 94 GHz. Within these conditions, the strip width should be set in an interval between 65  $\mu\text{m}$  and 140  $\mu\text{m}$ , which makes the achievement of 50  $\Omega$  transmission line impossible. However, as the membrane technology is less dispersive than the III-V technology, the constraints can be relaxed to release limits in the impedance range. Thereby,  $W$  was chosen to be in an interval between 33  $\mu\text{m}$  and 199  $\mu\text{m}$ , this lead to achievable characteristic impedances from 50  $\Omega$  to 138  $\Omega$  at 94 GHz.

The filter presented here a classical 4<sup>th</sup>-order shunt-stubs filter with centre frequency of 94 GHz. Despite the degree of freedom is available in the synthesis (Matthaei et al., 1980) which permits to adjust impedance values, the limitation of the achievable impedance range for

membrane technologies does not allow us to reach bandwidth less than 55%. Nevertheless, the use of topology with dual stubs allows us to achieve narrower bandwidth. The layout of a 4<sup>th</sup>-order filter with dual short-ended stubs at 94 GHz is displayed in Fig. 9-(a). An insertion loss of 2 dB for a relative bandwidth of 45% is obtained by electromagnetic simulation HFSS (Fig. 9-(b)). Experimental results were made from 60 GHz to 110 GHz.

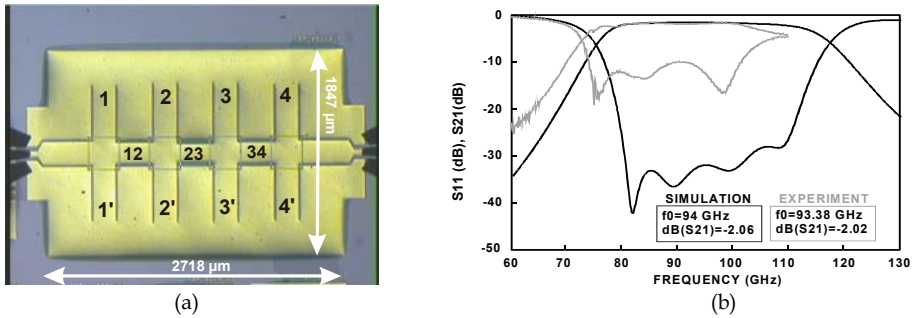


Fig. 9. 4<sup>th</sup>-ordre classical shunt-stubs bandpass filter. Photograph (a), Simulated and experimental magnitude responses (b)

Based on the previous filter topology, we have developed a 4<sup>th</sup>-order filter with folded stubs in short-circuit termination. The benefit of such a structure is to promote a coupling between non-adjacent resonators. Thus, it creates a transmission zero whose frequency depends on the nature of the coupling created. For electrical coupling (capacitive) it creates a zero in a high frequency, while magnetic coupling (inductive) will create a zero in a low frequency. In the case of study, stubs were in short-ended termination, so we promoted a generation of magnetic coupling between stubs 1'-3 and 2'-4 (Fig. 10-(a)). The response of such a filter (Fig. 10-(b)) has a bandwidth of 37.6% and an insertion loss of 1.685 dB. An apparent reduction in the band is due to the presence of a transmission zero at low frequency. Thus, it is possible to relax constraints on the nominal filter bandwidth consequently resulting in a slightly reduced insertion loss. In comparison with experimental results, we can notice that there is a 4 GHz frequency shift. In regards to the complexity of such a topology, the results are however satisfactory.

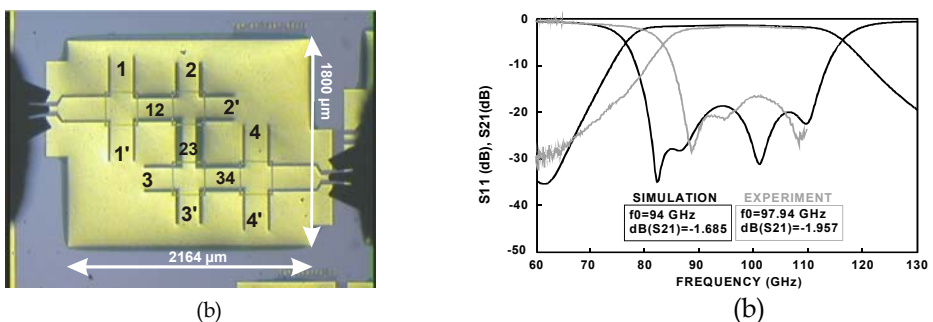


Fig. 10. Filter with folded stubs. Photograph (a), Simulated and experimental magnitude responses (b)

### 3.3 Narrow-band bandpass filter Design

The proposed technology has proven to be appropriate for achieving broadband filters. However, the difficulties met in the design of bandpass filters are tougher for achieving a filter with narrow bandwidth (5% 3-dB bandwidth). With the use of classical coupled-line filters, when designing a filter at 94 GHz we are facing technological impossibilities. Technological constraints impose line- and slot-widths to be greater than  $10\ \mu\text{m}$ . Inter-ground distances of coupled lines are large, which yields a difficulty to ensure the continuity of ground, and on the other hand, problems of mechanical stability of inter-ground bridges. Moreover, in considering the low permittivity and electrical lengths at 94 GHz, we are faced with coupled lines whose width to length ratio is too large (Vu et al., 2008). Therefore, the topology we developed is a pseudo-elliptic filter with ring resonator. Such a filter is characterized by the presence of two separate propagating modes, which create transmission zeros. The separation of the two modes of propagation is usually ensured by the introduction of discontinuities in the ring. In our case we used a topology with lateral coupled-lines access which synthesis was developed by M.K. Mohd Salleh (Mohd Salleh et al., 2008). This 2<sup>nd</sup>-order ring-based filter at 94 GHz has a relative bandwidth of 5%. It consists of two quarter wavelength lines excited by two identical quarter wavelength coupled-lines. The joint use of such a simplified topology and synthesis made the design ease and strongly limited the tuning steps. The electromagnetic simulations (Fig. 11) show a 5.3% bandwidth for an insertion loss of 3.57 dB and a return loss of 19 dB at 94 GHz. Experimental and simulated results are in good agreement. An insertion loss of 6.46 dB at 94.69 GHz and a return loss better than 20 dB are obtained for experimental results.

However, despite quite good results for the proposed filter, the membrane technology suffer from major drawbacks that limit its use for the filter design: the first one concerns the limited achievable impedance range; the second concerns the low permittivity which, while interesting to limit the dispersion of the line, limits its use to relatively low frequency range; the last one concerns technological aspect, since Silicon etching shape which is realized by dry way using Deep Reactive Ion Etching is difficult to control. Therefore, one has to develop new technologies to implement passive functions in millimeter frequency range.

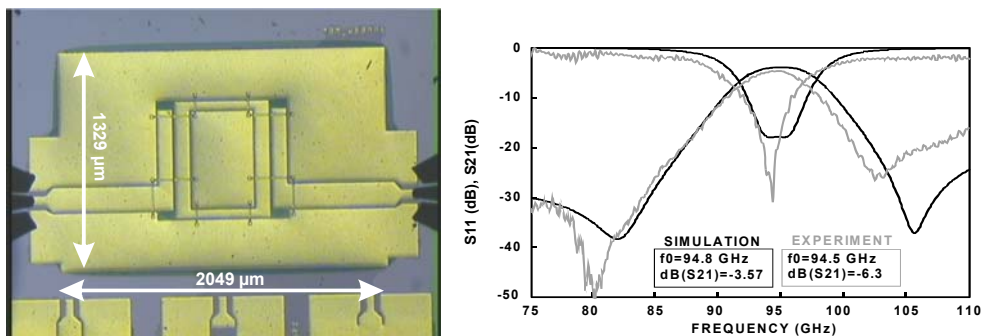


Fig. 11. 2nd-order ring resonator filter. (a) Photograph. (b) Simulated and experimental results.

## 4. Thin Film Microstrip (TFMS) Technologies

### 4.1 Technological process

The TFMS technology presented hereafter can be either implemented on III-V or silicon substrate. However, it is particularly well suited for silicon based technology. Indeed, benefits of silicon technology are undisputable in the design of active devices. Nevertheless, according to the silicon low resistivity ( $\rho \approx 10 \Omega \cdot \text{cm}$ ), implementation of passive devices is difficult because of the high insertion-loss levels. As our purpose was to keep the silicon substrate for implementation of active functions, an alternative consisted in the use of silicon as mother board. Passive functions are then transferred to a dielectric layer [Benzocyclobutene (BCB)] deposited on the motherboard, the dielectric layer and silicon being insulated via a ground plane. The presence of this ground plane allows avoiding dielectric-loss effects related to the silicon low-resistivity. Moreover, well-supplied libraries with various models are available for such a technology, microstrip by nature.

The first step of the technological process (Fig. 12.) is ground plane achievement through the deposition of a 3- $\mu\text{m}$ -thick layer of electroplated gold. So as to ensure the metal growth, thin-tungsten and gold-based adhesion films (200 Å/ 300 Å) were first deposited by evaporation. Due to poor adhesion between BCB and gold, a 300-Å-thin film of titanium was evaporated on the ground plane.

The dielectric we used was the photosensitive BCB 4026-26 from Dow Chemical, Midland, MI, ( $\epsilon_r=2.65$ ,  $\tan\delta=2.10^{-3}$ ). It allows a 10- $\mu\text{m}$ -thick layer deposition. The first photosensitive BCB film was then spin coated onto the Ti film. The BCB film thickness is a function of subsequent processing steps, including pre-baked conditions, spin coating speed, exposure dose and development. After these processing operations, BCB pads of 10  $\mu\text{m}$  thickness were obtained. A soft baking (up to 210° C) of this first dielectric was made to ensure resistance to subsequent processing operations. The second 10- $\mu\text{m}$ -thick BCB film polymer film was then spin coated and patterned (photolithography: UV light exposure and DS2100 developer) in the same way as the first layer. Then a final hard baking for polymerization was performed from in-stage annealing up to 230 °C. The signal transmission lines as well as the coplanar accesses were fabricated at the same time. The coplanar accesses on the top of BCB were connected to the ground plane through the sides of the dielectric. In order to obtain metallization using gold electroplating, a bi-layer photoresist was used. The first photoresist layer is used to protect other devices. After the spin coating of the photoresist and the photolithography process (pre-baking, exposure and development), transmission lines and coplanar accesses with wider dimensions (3  $\mu\text{m}$ ) were made. A thin conductor film (Ti/Au, 300 Å/200 Å) for electroplating was then evaporated, and the second thick photoresist layer (greater than the envisaged metallization thickness) is spin coated and photoprocessed to define the exact dimensions of the transmission line and coplanar access. After electroplating of 3  $\mu\text{m}$  of gold, the upper photoresist was removed using a photoresist developer stage. The thin conductor film was removed with wet-etching, and the lower photoresist was finally diluted with a remover. The transmission line structure obtained is illustrated in Fig. 13.



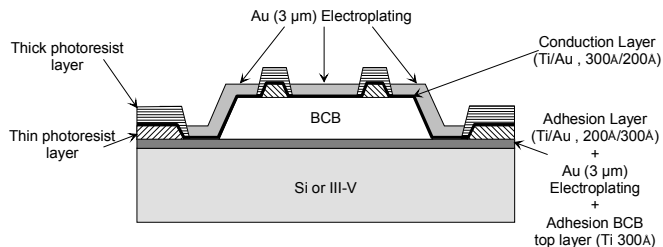


Fig. 12. Technological process for BCB-based transmission line.

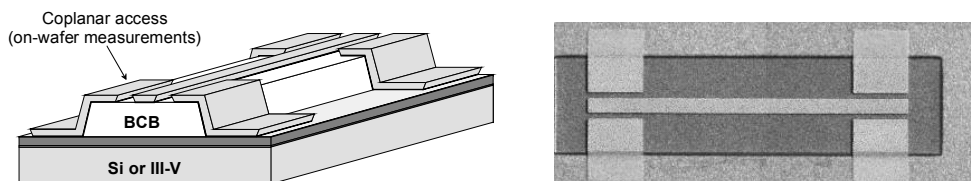


Fig. 13. Topology and microphotograph of a 50- $\Omega$  transmission line in TFMS.

Previous works have shown that the BCB layer thickness is a parameter that most influences the losses (Six et al., 2005), (Leung et al., 2002), (Prigent et al., 2004-a). Investigations were carried out so as to reduce these insertion losses. As shown in Fig. 14, the transmission line attenuation decreases with the BCB thickness increase. It was shown that a 20- $\mu\text{m}$ -thick BCB layer can be considered as the optimum dielectric thickness. Beyond 20- $\mu\text{m}$ -thick, no significant attenuation improvement was obtained. Within such a topology, measurements were performed through a broad frequency range from 0.5 GHz to 220 GHz.

Transmission line with 50- $\Omega$  impedance was calibrated out. This was achieved by means of thru-reflection line calibration method (TRL). The calibration standards and transmission line were fabricated on the same wafer. HP 8510 XF and Anritsu 37147C network analyzers were used in the (45 MHz-120 GHz) and (140 GHz-220 GHz) frequency range, respectively. Simulated results and experiments are in a good agreement in a wide frequency range. Attenuation measured for a 50- $\Omega$  transmission line at 220 GHz is of the order of 0.6 dB/mm (Fig. 15).

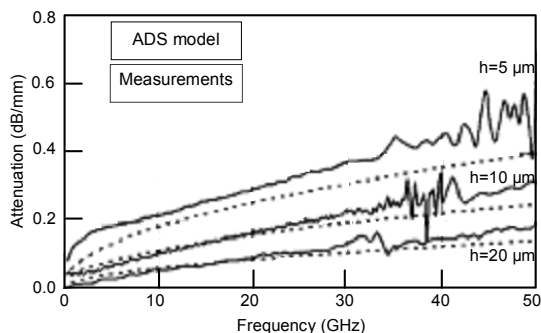


Fig. 14. Attenuation of 50- $\Omega$  TFMS-lines for different BCB thickness. Comparison between simulation and experimental results

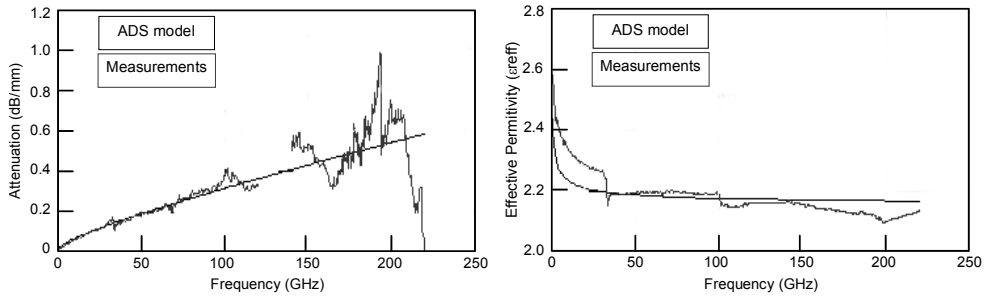


Fig. 15. Comparison between simulation (ADS) and measurement results of a 50- $\Omega$  TFMS-line with 20- $\mu\text{m}$  BCB thickness up to 220 GHz.

#### 4.2 Bandpass filter Design

So as to illustrate the Si-BCB based thin film microstrip technology, the filter to be designed roughly corresponds to a U-band filter, the 3-dB passband is 49–51 GHz, the rejection level in the 41.15–46.15-GHz frequency band is 35 dB, and no specification for the upper band beyond 51 GHz is required.

Coupled-line topologies are basically well suited for narrow bandpass filters. Nevertheless, in view of the desired insertion losses and rejection levels, such topologies become unsuitable with the above filter specifications. Indeed, the closeness of the passband and lower reject band imposes high rejection levels. Hence, the filter order has to be increased, which significantly degrades global insertion losses. These considerations have led us to choose a new filter topology based on dual behavior resonators (DBRs), which means both stopband and passband (Rizzi, 1988). Such a resonator results from two different open-ended stubs set in parallel. Each stub brings a transmission zero on either side of the passband. Development of a global synthesis enabled us to independently control the bandwidth, the upper and lower frequency bands, as well as the different transmission-zero frequencies of an  $n^{\text{th}}$ -order filter, *i.e.*, composed of DBRs (Quendo et al., 2003). Let us apply an alike development to the design of a 4<sup>th</sup>-order filter that meets the desired specifications. It results in a filter with four transmission zeros on both sides of the passband. These transmission zeros being independent, their frequencies are either separated or joined. This depends on the electrical length of the four resonators: they can differ or be identical (Fig. 16). For the sake of simplicity, the electrical characteristics of the upper frequency stubs, *i.e.*, (L1a, Z1a), (L2a, Z2a), (L3a, Z3a) and (L4a, Z4a), were chosen equal, which meant that the upper transmission zeros were joined. Similarly, the lower frequency stubs were of equal length, *i.e.*, (L1b, L2b, L3b, and L4b), and the associated transmission zeros were joined. The filter was designed based on the joint use of the synthesis (Quendo et al., 2003) and the DOE based design method that allows simple and rapid correction process (Prigent et al., 2003-a), (Prigent et al., 2003-b), (Tagushi, 1987), (Prigent et al., 2002). As depicted in Fig. 17, the filter electrical response obtained with this design method was in a very good agreement with the simulations results (ADS-Momentum).

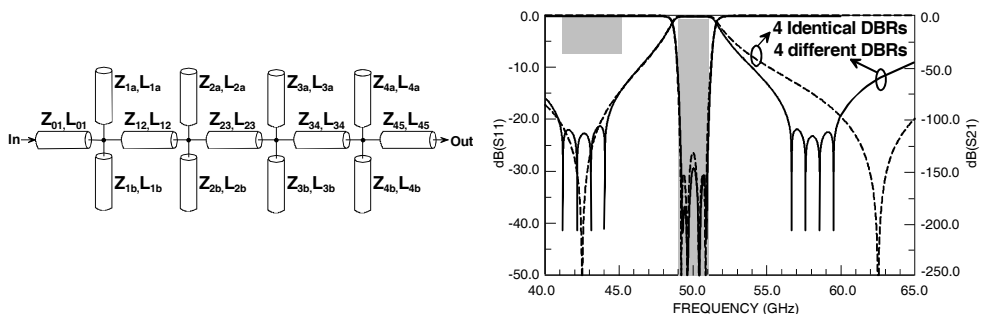


Fig. 16. 4<sup>th</sup>-order ideal DBR topology and response : with different resonator type (impedance and length) or with four identical resonators.

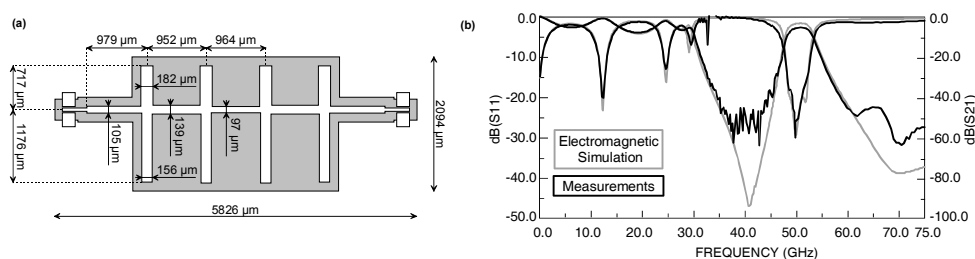


Fig. 17. (a) Layout of the 4<sup>th</sup>-order DBR filter in U-band. (b) comparison of electromagnetic simulation with experiment, in wide frequency range up to 75 GHz (c).

### 4.3 Application in the G-band (140 GHz-220 GHz)

According to the quality of the experimental results observed at 94 GHz, one has attempted to transpose our concepts to upper frequency domain in G-band (140-220 GHz). In this frequency range, the problems due to sensitivity and design accuracy are all the more important since the electrical lengths that are involved are very small.

Let us consider the design of a 4<sup>th</sup>-order classical shunt-stubs filter with 10% 3-dB-bandwidth. According to classical synthesis (Matthaei et al., 1980), while designing filter with such specifications, we are faced to technical impossibilities. Indeed, at this frequency level, transmission lines are wider than long. Hence, the electromagnetic simulation results are strongly debased. Moreover, the filter dimensions made the electrical response correction difficult, indeed impossible. So as to overcome such a difficulty, the solution we have developed (Prigent et al., 2005) consists in considering the first harmonic as the frequency of interest, not the fundamental frequency. Thus, the filter to be designed is a 4<sup>th</sup>-order filter with 60 GHz central frequency. In this way, one can reach the filter specifications while keeping a correct shape factor for the stubs (Fig. 18). Measurement results were made in 0-110 GHz and 140-220 GHz bands. Despite a slight insertion losses improvement, the measurement results are in a complete accordance with the desired specifications.

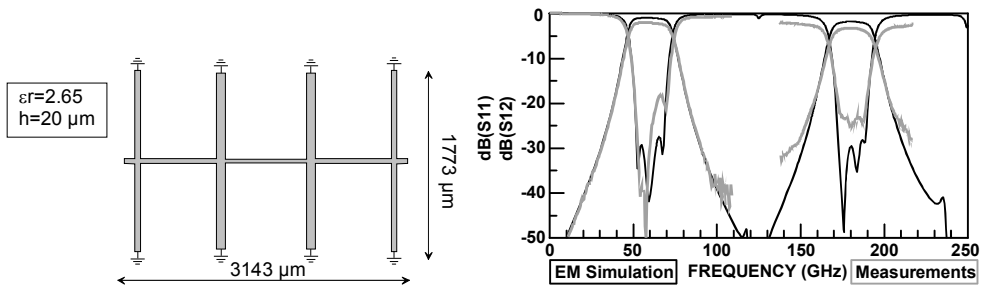


Fig. 18. Electromagnetic simulation results (Momentum) of the 4<sup>th</sup>-order shunt-stub filter with 60 GHz central frequency. Comparison with experimental results in 0-220 GHz band.

Within these conditions, there still remains the fundamental frequency which could be harmful in a global system insertion perspective. As a consequence, the fundamental harmonic has to be suppressed using insertion of filtering functions, such as high- or band-pass filters, in the nominal band-pass device.

Considering the filter electrical response (Fig. 18) the solution we advocated is the insertion of high-pass filter. The filter to be designed is a 2<sup>nd</sup>-order high-pass filter with 130 GHz cutoff frequency. The BCB technology contributes to realize the series capacitance which is usually difficult to achieve in 2D planar technologies. Indeed, it was possible to take advantage of the Si-BCB topology to realize multi-layer capacitance. It consists of a CPW to TFMS transition based upon the use of capacitive coupling between the main conductor of the TFMS-line and the coplanar guide, through the thin dielectric layer. The final high-pass filter topology is described in Fig. 19.

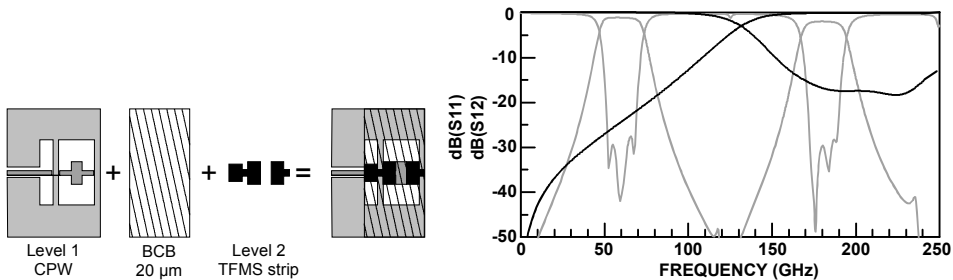


Fig. 19. Layout and simulation results (Ansoft - HFSS) of the 2<sup>nd</sup>-order high-pass filter with 130 GHz central frequency. Comparison with the bandpass filter electrical response.

One just has to insert this high-pass cells at the in/out access lines level. The electromagnetic simulation results of the resulting band-pass filter topology (Fig. 20) attest from this design method contribution toward the design of band-pass filter in very high frequency range. Indeed, the fundamental harmonic was suppressed while keeping the filter bandwidth as well as correct return losses.

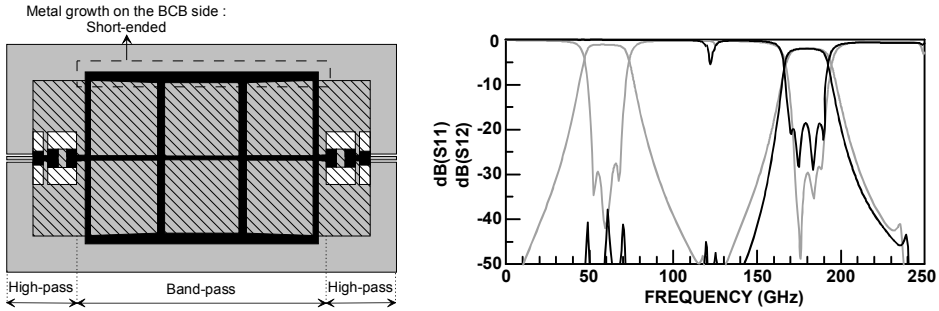


Fig. 20. Layout and electromagnetic simulation results (HFSS) of the final bandpass filter at 180 GHz with 10% 3-dB-bandwidth. Comparison with the initial bandpass filter response.

According to the previous results, one has attempted to apply the design method for a narrower band-pass filter. The filter to be designed is a 3<sup>rd</sup>-order DBR filter at 180 GHz with 5% 3-dB-bandwidth. If the design of previous filter was limited to reduction of the first harmonic, it is not the same for DBR filters. Indeed, by order of the resonators nature, the electrical response of DBR filters presents spurious resonances on either side of the pass-band. Moreover, as the filter was designed with 60 GHz central frequency, the frequency of interest being 180 GHz, spurious response level is very important compared with the filter bandwidth (Fig. 21). Therefore, sizeable modifications had to be brought to the filter design. The first step of the design consisted in spurious resonance attenuation. This was achieved using integration of the DBR filter in the previous shunt-stub band-pass-filter. In this way, as the shunt-stub filter bandwidth is twice the DBR ones, both fundamental and first harmonics of the DBR filter were preserved while taking advantage of the shunt-stub filter rejection level for out-of-band improvement (Fig. 22). Finally, it only remained to suppress the fundamental frequency using the high-pass filter previously designed (Fig. 23).

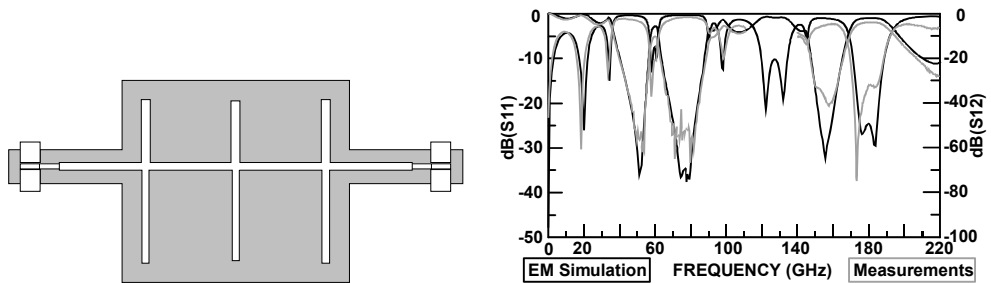


Fig. 21. Layout and simulation results (Momentum) of a 3<sup>rd</sup>-order DBR filter at 180 GHz with 5% 3-dB-bandwidth. Comparison with experimental results in 0-220 GHz band.

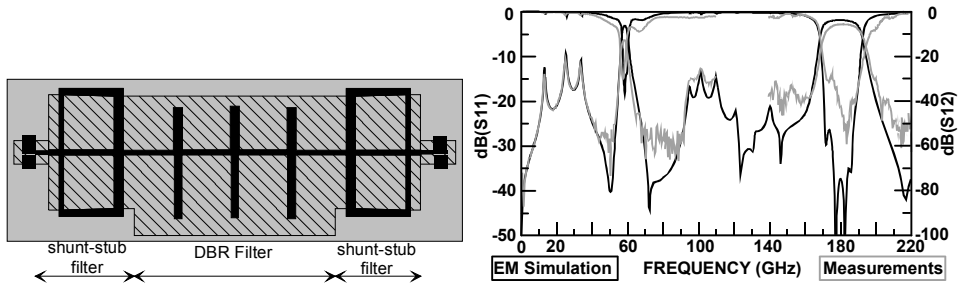


Fig. 22. Layout and electromagnetic simulation results of DBR filter integration in classical shunt-stub filter. Comparison with experimental results in 0-220 GHz frequency band.

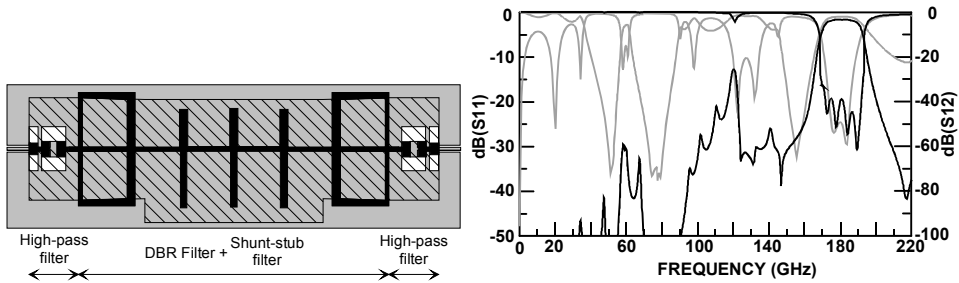


Fig. 23. Layout and electromagnetic simulation results of the final bandpass filter at 180 GHz with 5% 3-dB-bandwidth. Comparison with the initial DBR filter response.

Comparison made between theoretical and measurement results over a wide frequency range up to 220 GHz evidenced the efficiency of the design method we developed as well as the accuracy of BCB technology for the design of passive function for very high frequencies. These concepts were demonstrated, not only for filters, but also for other passive functions such as couplers or balanced matching networks (Prigent et al., 2006a), (Prigent et al., 2006b).

## 5. Advanced CMOS SOI technology on High Resistivity substrate

### 5.1 65 nm MOSFET Performances

Through careful optimization and modelling rules for active and passive components, a standard 0.13  $\mu\text{m}$  CMOS process was proved to be capable of 60 GHz operation despite the related low  $F_t/F_{\text{max}}$  which was in the order of 100 GHz (Doan et al., 2004). Measurements of 65-nm CMOS technology (Dambrine et al., 2005) demonstrate  $F_t$  of 220 GHz and  $F_{\text{max}}$  of 240 GHz (Fig. 24), which are clearly comparable to advanced commercially available 100 nm III-V HEMT or state-of-the-art SiGe HBT (Chevalier et al., 2004). Moreover, HF noise figure is in the order of 2 dB at 40 GHz. As a consequence, from active devices point of view there is no reason to prevent the integration of millimetre-wave applications in CMOS technology.

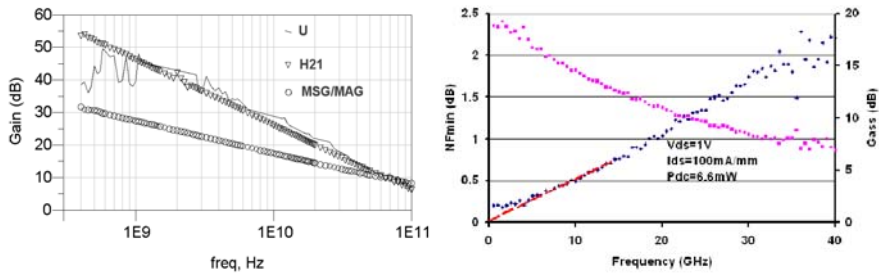


Fig. 24. Measured gains for 64x1/0.06 NMOS in 65nm bulk technology ( $I_{DS}/W=439 \mu\text{A}/\mu\text{m}$ ,  $V_{DS}=1.2\text{V}$ ).  $NF_{\min}$  and  $G_{\text{ass}}$  vs frequency for  $50 \times 2 \times 0.055 \mu\text{m}^2$  n-MOSFET ( $V_{DS}=0.7\text{V}$ ,  $I_{DS}=100 \text{ mA}/\text{mm}$ ).

### 5.2 65nm On-Chip Transmission line performances up to 220 GHz

The integration of high quality passive components in standard silicon technology is not obvious. It is well known that passive components integrated in standard silicon technologies suffer from high substrate losses. This point is clearly the fundamental limitation for conventional bulk technologies (either CMOS or BiCMOS) to address millimetre-wave applications. But recently (Gianesello et al., 2006-a), high quality passive components (Coplanar Waveguide with less than 1 dB/mm of losses @ 100 GHz) integrated in advanced 130 nm HR SOI CMOS technology have demonstrated performances comparable to state of the art III-V technologies up to W band (75-100 GHz).

At millimetre-wave frequency range, the use of transmission lines is generally preferred to integrate passive components since implementation of spiral inductors is feasible but suffers from accuracy issues. Two kinds of structures can be considered, transmission lines which are sensitive to substrate effects (CPW presented in Fig. 25) and transmission lines which do not (microstrip with ground plane as shield not presented here). Since microstrip transmission lines have demonstrated electrical performances worse than CPW ones in advanced standard digital silicon Back-End-Of-Line (BEOL) with HR substrate (Gianesello, et al., 2007) we have focused our attention on coplanar transmission lines achieved on HR SOI.

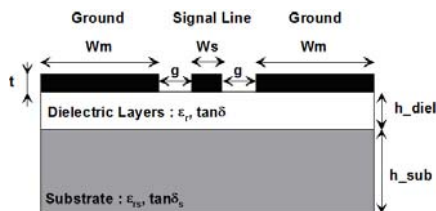


Fig. 25. Coplanar transmission line structure.

Since it has been demonstrated that in HR SOI substrate losses are drastically reduced, we propose here the use of a new stacked coplanar transmission line dedicated to HR SOI technology. By doing so, we can reduce the metallic losses which occur in the transmission line. Moreover, this kind of coplanar transmission line is very similar to the one integrated

in III-V since it lies directly on the silicon substrate. Hence, one can use similar dimension rules than in III-V. For example, in this work a ground-to-ground dimension of  $35\mu\text{m}$  was used which is the typical dimension used in III-V at G-band.

On chip transmission lines reported in this work were fabricated in advanced SOI CMOS technology with Cu damascene back-end-of-line (BEOL). The BEOL layers configuration depicted in Fig. 26 is composed of six levels of copper: M1-M5 Layers are  $0.35\mu\text{m}$ -thick whereas M6 is  $0.9\mu\text{m}$ -thick. Additional aluminium layer is deposited as top level. Each coppers level are separated by  $0.4\mu\text{m}$ -thick dielectric layer ( $\text{SiO}_2$ ) and connected with vias-holes.

On-wafer measurements have been performed up to 110 GHz using an Agilent HP8510XF Vector Network Analyzer, and from 140 to 220 GHz using Anritsu 37147C VNA and Oleson test heads. Phase velocity of this stacked CPW transmission line is fully linear up to 220 GHz (Fig. 26) which ensures a quasi-TEM propagation mode. State-of-the-art attenuation, in the order of  $1\text{ dB/mm}$  @ 100GHz and  $1.5\text{ dB/mm}$  @200 GHz, has been measured (Gianesello, Gloria et al., 2007).

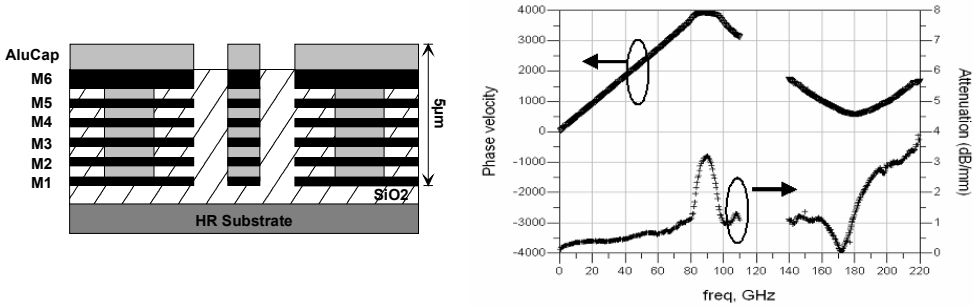


Fig. 26. Stacked Coplanar transmission line architecture dedicated to HR SOI technologies. Measured phase velocity and attenuation of a  $50\Omega$  stacked coplanar transmission line ( $W_s=11\mu\text{m}$ ,  $g=12\mu\text{m}$ ,  $W_M=105\mu\text{m}$ ).

### 5.3 Bandpass filter application

To illustrate the performance of the CPW Transmission lines realized in HR SOI technologies, a CPW stub-based filter has been realized on bulk (65nm and 130 nm) and HR SOI substrate. Photography of the filter is depicted in Fig. 27. The filter was designed to have its fundamental response between 60 and 80 GHz. This filter was measured up to 220 GHz (Fig. 27) to investigate CPW transmission line performance at millimetre-wave range. The insertion loss of the filter realized in 65 nm is close to that of the same filter realized in 130 nm bulk (but shows 1 dB higher loss). This is due to the fact that we have to work closer from the substrate in 65-nm bulk technology because of BEOL structure and so substrate losses are more important. Beyond 100 GHz, no bulk filter is workable because of the bad performance achieved with bulk CPW at this frequency range. On the contrary, the filter implemented in HR SOI technology is fully workable up to 200 GHz. It demonstrates 6 dB less losses in the 60-80 GHz band, and even at 200 GHz it has only around 4.5 dB losses, which is better than the performance achieved by bulk filters at 80 GHz.

The electrical performances were compared with equivalent topology developed in GaAs technology (Fig. 5) (Rius et al., 2003), (Wolf et al., 2005). Table 1 evidences that performances



were comparable to state of art III-V technologies. Indeed, even if central frequencies were not identical, but of the same order (70-GHz for HR SOI, 82-GHz for GaAs), the relative bandwidth being identical, the filter developed in HR SOI technology exhibits an insertion losses level of 2.01 dB which is very close to the one obtained in GaAs technology (1.8 dB).

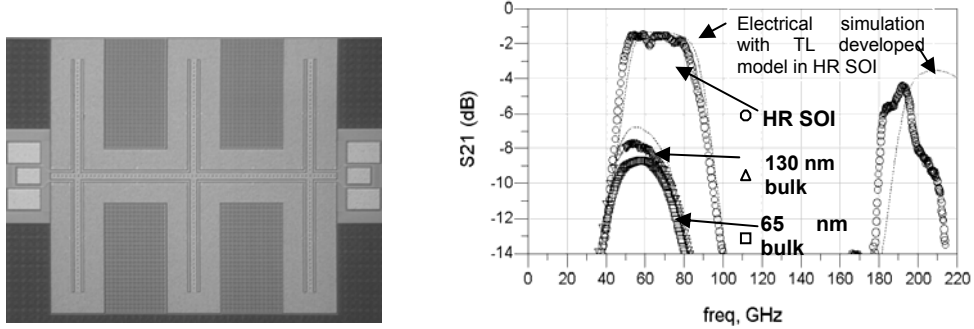


Fig. 27. Simulated and measured results for classical 3<sup>rd</sup>-order shunt stub bandpass filter. Electrical performances comparisons for filters implemented in different technologies.

	65nm Bulk	130nm Bulk	HR SOI	GaAs
dB(S <sub>21</sub> ) @ f=f <sub>0</sub>	9.1	7.9	2.01	1.8

Table 1. Comparison of the 3<sup>rd</sup>-order CPW filter performances for 3<sup>rd</sup>-order bandpass filter

One should note that the proposed technology (HR-SOI) provides solutions towards coplanar transmission lines. Indeed, generally odd-mode filters are realized with air-bridges which suffer from mechanical stability. In the present technological process, as the metallization consists of 7 metal layers, all layers being stacked on HR-SOI so as to reduce metallic losses, the bridge realization lies in three steps: Transmission lines and bridge definition on the first layer, transmission line aperture in layers 2-6, transmission line definition in top level metal (Fig. 28).

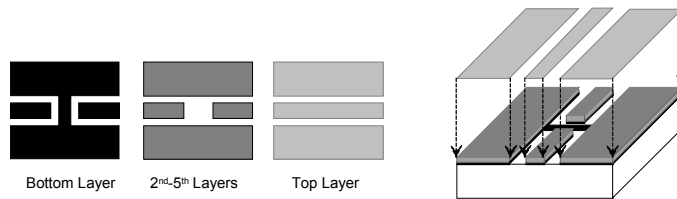


Fig. 28. Metal layers definition for bridge realization.

For narrowbandpass filter, the filter that we have developed has a topology with direct tapped-line access. The choice of this topology was dictated by problems of realization and minimizing losses (Prigent et al., 2003). Indeed, according to the filter synthesis, a degree of freedom is available that allows to modify the even- and odd-modes impedances of

constitutive coupled-lines. Thus, the transmission lines quality factor can be improved. Nevertheless, this parameter has a poor influence on the input/output coupled lines, which significantly limits the insertion losses improvement. Moreover, these coupled lines are very difficult to achieve in considering the technological constraints. Finally, the input/output lines do not participate in the definition of the filter order but adjust the level of return loss. Thus, a very convenient way to overcome this limitation consists in replacing the in/out coupled lines by tapped-line feedings as depicted in Fig. 29 (Dishal, 1965), (Cristal, 1975), (Cohn, 1974) which allows for a reduction in size as well as an extra transmission zero.

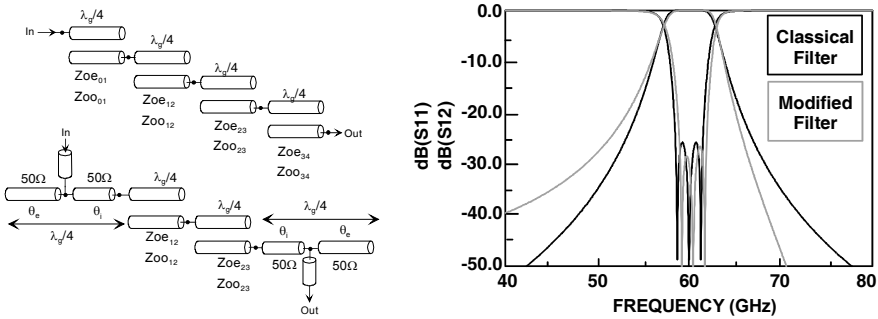


Fig. 29. Comparison between response of classical and modified 3<sup>rd</sup>-order coupled-lines filter.

The modified filter topology was designed in coplanar technology implemented in HR SOI CMOS. Measurement results depicted in Fig. 30 show a frequency shift of the order of 5%, as well as return loss degradation. Nevertheless, with regard to the filter geometry complexity, those results are encouraging since insertion loss obtained are 6.6 dB in spite of the poor matching level, it should be enhanced while improving the return loss. For instance, equivalent bandpass filter implemented on massive silicon substrate would have led to more than 10-dB insertion losses.

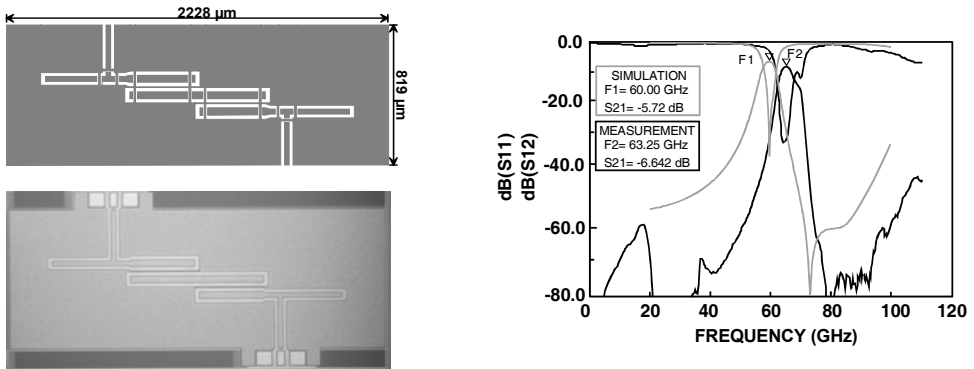


Fig. 30. Bottom metal layer, photography and measurement results of the 3<sup>rd</sup>-order bandpass filter @ 60 GHz.

## 6. Conclusion

The design of bandpass filters were investigated, using III-V, Silicon Membrane Technology, TFMS technology on Si-BCB and CMOS HR-SOI. If advantages of III-V technologies are undisputable toward electrical performances for passive function, silicon technologies are becoming more competitive and achieve the performance level of the state of the art of III-V. Up to now, the exploitation of V, W and G bands has been minimal because of the high cost of III-V technology needed to process the millimetre-wave signals. Use of advanced HR SOI CMOS technology, according to 65 nm MOSFET performances and HR SOI filters presented in this chapter, makes now feasible the offer of CMOS low cost MMW mass market applications up to G band. Thus, HR SOI seems to be a good candidate in the coming year to address both low cost and low power mass market CMOS digital and RF/ MMW applications. Moreover, as HR SOI benchmark is multilayer by nature, implementation of filters in multilevel technologies could afford interesting properties.

## 7. References

- Aftanasar, M. S.; Young, P. R.; Robertson, I. D.; Minalgene, J. & Lucyszyn, S. (2001). Photoimageable thick-film millimeter-wave metal-pipe rectangular waveguides, *Electronic Letters*, vol 37, no 18, pp 1122-1123, August 2001, ISSN : 0013-5194.
- Argarwal, B.; Schmitz, A. E.; Brown, J. J.; Matloubian, M.; Case, M. G.; Le, M.; Lui, M. & Rodwell, M. J. W. (1998). 112-GHz, 157-GHz, and 180-GHz InP HEMT traveling-wave amplifiers, *IEEE Transactions on Microwave Theory and Techniques*, vol. 46, no 12, pp 2553-2559, December 2005, ISSN : 0018-9480
- Beilenhoff, K.; Heinrich, W. & Hartnagel, H. L. (1991). The scattering behaviour of air bridges in coplanar MMICs, *Proceedings of European Microwave Conference*, Roma, Italy, October 1976, vol. 2, pp. 1131-1135. Artech House, Boston London, UK.
- Brauchler, F.; Robertson, S.; East, J. & Katehi, L. P. B. (1996). W band FGC line circuit elements, *Proceedings of IEEE Microwave Theory and Techniques International Symposium*, San Francisco, CA, 1996, pp 1845-1848, ISBN : 0-7803-3246-6, San Francisco CA, USA, June 1996, IEEE, Picataway NJ, USA.
- Chevalier P.; Fellous C.; Rubaldo L.; Dutartre D.; Laurens M.; Jagueneau T.; Leverd F.; Bord S.; Richard C.; Lenoble D. ; Bonnouvrier J.; Marty M.; Perrotin A.; Gloria D.; Saguin F.; Barbalat B.; Beerkens R.; Zerounian N.; ANniel F. & Chantre A. (2004). 230 GHz self-aligned SiGeC HBT for 90 nm BiCMOS technology, *Proceeding of the IEEE Bipolar/BiCMOS Circuits and Technology Meetings*, pp 225-228, ISBN : 0-7803-8618-3, Montreal PQ, Canada, September 2004, IEEE, Picataway NJ, USA.
- Cohn, S. B. (1959). Dissipation loss in multiple-coupled-resonator filters, *Proceedings of IRE*, vol. 47, no 8, pp 1342-1348, August 1959, ISSN : 0096-8390.
- Cohn, S. B. (1974). Generalized design of bandpass and other filters by computer optimization, *Proceedings of IEEE Transactions on Microwave Theory and Techniques International Symposium*, Atlanta, USA, 1974, pp 272-274, ISBN : 0-7803-3246-6, Atlanta, USA, December 1974, IEEE, Picataway NJ, USA.

- Cristal, E. D. (1975). Tapped-line coupled transmission lines with application to interdigital and combline filters, *IEEE Transactions on Microwave Theory and Techniques*, vol. 23, no 12, pp 1007-1012, December 1975, ISSN : 0018-9480
- Dambrine, G.; Hoel, V.; Boret, S.; Grimbert, B.; Aperce, G.; Bollaert, S.; Happy, H.; Wallart, X.; Lepillet, S. & Cappy, A. (1999). 94 GHz low noise amplifier on InP in coplanar technology. *Proceedings of GigaHertz Devices and Systems Conference*, pp. 32-37, ISBN: 0-8194-3454-X, September 1999, Boston MA, USA, SPIE, Bellingham WA, USA
- Dambrine, G.; Gloria, D.; Scheer, P.; Raynaud, C.; Danneville, F.; Lepilliet, S.; Siligaris, A.; Pailloncy, G.; Martineau, B.; Bouhana, E. & Valentin, R. (2005). High frequency low noise potentialities of down to 65nm technology nodes MOSFETs. *Proceedings of IEEE European Gallium Arsenide and other Semiconductor Application Symposium*, pp. 97-100, ISBN: 88-902012-0-7, October 2005, Paris, France, IEEE, Piscataway NJ, USA.
- Dishal, M. (1965). A simple design procedure for small percentage bandwidth round-rod interdigital filters, *IEEE Transactions on Microwave Theory and Techniques*, vol. 13, no 5, pp 696-698, May 1965, ISSN : 0018-9480
- Doan, C. H.; Emami, S.; Sobel, D.; Niknejad, A. M. & Brodersen, R. W. (2004). 60 GHz CMOS radio for Gb/s wireless LAN, *Proceedings of IEEE Radio Frequency Integrated Circuits (RFIC) Symposium*, pp. 225-228, ISBN : 0-7803-8333-8, Fort Worth TX, USA, June 2004, IEEE, Piscataway NJ, USA.
- Floyd, B.; Reynolds, S.; Pfeiffer, U.; Beukema, T.; Grzyb, J. & Haymes, C. (2006). A Silicon 60GHz Receiver and Transmitter Chipset for Broadband Communications, *Proceedings of IEEE International Solid State Circuits Conference*, pp. 184-185, ISBN : 1-4244-0079-1, San Francisco CA, USA, February 2006, IEEE, Piscataway NJ, USA.
- Gianesello, F.; Gloria, D.; Montusclat, S.; Raynaud, C.; Boret, S.; Clement, C.; Dambrine, G.; Lepilliet, S.; Saguin, F.; Scheer, P.; Benech, P. & Fournier, J.M. (2006a). 65 nm RFCMOS technologies with bulk and HR SOI substrate for millimeter wave passives and circuits characterized up to 220 GHz, *Proceedings of IEEE Microwave Theory and Techniques International Symposium*, pp 1927-1930, ISBN : 0-7803-9541-7, San Francisco CA, USA, June 2006, IEEE, Piscataway NJ, USA.
- Gianesello, F.; Gloria, D.; Raynaud, C.; Montusclat, S.; Boret, S.; Benech, P.; Fournier, J. M. & Dambrine, G. (2006b). State of the art integrated MMW passive components and circuits in advanced thin SOI CMOS on high resistivity substrate. *Proceedings of IEEE International Silicon On Insulator Conference*, pp 121-122, ISBN : 1-4244-0289-1, Niagara Falls NY, USA, October 2006, IEEE, Piscataway NJ, USA.
- Gianesello, F.; Gloria, D.; Montusclat, S.; Raynaud, C.; Boret, S.; Dambrine, G.; Lepilliet, S.; Martineau, B. & Pilard, R. (2007). 1.8 dB insertion loss 200 GHz CPW band pass filter integrated in HR SOI CMOS Technology, *Proceedings of IEEE International Microwave Symposium*, pp 453-456, ISBN : 1-4244-0688-9, Honolulu HI, USA, June 2007, IEEE, Piscataway NJ, USA.
- Haydl, W. H.; Neumann, M.; Erveyen, L.; Bangert, A.; Kudzus, S.; Schlechtweg, M.; Hülsmann, A.; Tessmann, A.; Reinert & Krems, T. (1999). Single-chip coplanar 94-GHz FMCW radar sensors, *IEEE Microwave and Guided Wave Letters*, vol. 9, no 2, pp 73-75, February 1999, ISSN : 1051-8207.

- Heinrich, W. (1993). Uniplanar Quasi-TEM description of MMIC coplanar lines including conductor-loss effects, *IEEE Transactions on Microwave Theory and Techniques*, vol. 41, no 1, pp. 45-52, January 1993, ISSN : 0018-9480.
- Herrick, K. J.; Schwarz, T. & Katehi, L. P. B. (1998). Si-Micromachined coplanar waveguide for use in high-frequency circuit, *IEEE Transactions on Microwave Theory and Techniques*, vol. 46, no 6, pp 762-768, June 1998, ISSN : 0018-9480
- Hirose, T.; Makiyama, K.; Ono, K.; Shimura, T. M.; Aoki, S.; Ohashi, Y.; Tokokawa, S. & Watanabe, Y. (1998). A flip-chip MMIC design with coplanar waveguide transmission line in the W-band, *IEEE Transactions on Microwave Theory and Techniques*, vol. 46, no 2, pp. 2276-2282, December 1998, ISSN : 0018-9480.
- Hirota, T. & Ogawa, H. (1987). Uniplanar MMIC hybrids—A proposed new MIC structures, *IEEE Transactions on Microwave Theory and Techniques*, vol 35, no 6, pp. 576-581, June 1987, ISSN : 0018-9480.
- Houdard, M. (1976). Coplanar lines: Application to broadband microwave integrated circuits, *Proceedings of European Microwave Conference*, Roma, Italy, October 1976, pp. 49-53. Artech House, Boston London, UK.
- Koster, N. H. L.; Koslowski, S.; Bertenburg, R.; Heinen, S. & Wolff, I. (1989) Investigation on airbridges used for MMIC's in CPW technique, *Proceedings of European Microwave Conference*, London, UK, October 1989, pp. 666-671. Artech House, Boston London, UK
- Kuhn, K.; Basco, R.; Betcher, D.; Hattendorf, M.; Packan, M.; Post, P.; Vandervoom, L. & Young, P. (2004). A comparison of state-of-the-art NMOS and SiGe HBT devices for analog/mixed-signal/RF circuit applications, *Proceedings of VLSI Technology Symposium*, pp. 224-225, ISBN : 0-7803-8289-7, Honolulu HI, USA, June 2004, IEEE, Picataway NJ, USA.
- Kulke, R. & Wolff, I. (1996). Design of passive coplanar filters in V band, *Proceedings of IEEE Microwave Theory and Techniques International Symposium*, San Francisco, CA, 1996, pp 1647-1659, ISBN : 0-7803-3246-6, San Francisco CA, USA, June 1996, IEEE, Picataway NJ, USA.
- Leung, L. L. W.; Chen, K. J.; Huo, X. & Chan P. C. H. (2002). On chip filters on standard silicon substrate incorporating a low-K BCB dielectric layer. *Proceedings of European Conference on Wireless Technology*, pp 37-40, Milan, Italy, October 2002.
- Matthaei, G. ; Young, L. & Jones, E. M. T. (1980). *Microwave Filters, Impedance-Matching Networks and Coupling Structure*, Artech House, ISBN: 978-0890060995, Dedham, USA
- Mohd Salleh, M. K.; Prigent, G. ; Pigaglio, O. & Carampaigne, R. (2008). Quarter wavelength side-coupled ring resonator for bandpass filter, *IEEE Transactions on Microwave Theory and Techniques*, vol. 56, no 1, pp 156-162, January 2008, ISSN : 0018-9480
- Montusclat, S.; Giancesello, F.; Gloria, D. & Tedjini, S. (2005). Silicon integrated antenna developments up to 80GHz for millimeter waves wireless links. *Proceedings of European Conference on Wireless Technology*, pp 237-240, ISBN : 2-9600551-1-X, Paris, France, October 2005, Artech House, Boston London, UK.
- Ogawa, H. & Minagawa, A. (1987). Uniplanar MIC balanced multiplier -- A proposed new structure for MIC's, *IEEE Transactions on Microwave Theory and Techniques*, vol. 35, no 12, pp 1363-1368, December 1987, ISSN : 0018-9480

- Papapolymerou, J.; Brauchler, F.; East, J. & Katehi, L. P. B. (1999). W-band finite ground coplanar monolithic multipliers, *IEEE Transactions on Microwave Theory and Techniques*, vol. 47, no 5, pp. 614–619, May 1999, ISSN : 0018-9480.
- Perndl, W.; Knapp, H.; Wurzer, M.; Aufinger, K.; Meister, T. F.; Bock, T.F.; Simburger, W. & Scholtz, A.L. (2004). A low-noise, and high-gain double-balanced mixer for 77 GHz automotive radar front-ends in SiGe bipolar technology, *Proceedings of IEEE Radio Frequency Integrated Circuits (RFIC) Symposium*, pp. 47-50, ISBN : 0-7803-8333-8, Fort Worth TX, USA, June 2004, IEEE, Picataway NJ, USA.
- Prigent, G.; Rius, E.; Le Pennec, F. ; Le Maguer, S. ; Ney, M. & Le Floch, M. (2002). DOE based design method for coupled-lines narrow bandpass filter improvement, *Proceedings of IEEE European Microwave Conference*, vol 3, pp 1129-1132, Milan, Italy, October 2002.
- Prigent, G. ; Rius, E. ; Le Pennec, F. & Le Maguer, S. (2003-a). A design method for improvement of  $\lambda g/4$  coupled-line narrow bandpass filter response, *Microwave and Optical Technology Letter*, Wiley, vol. 39, no 2, pp 121-125, August 2003, ISSN : 0895-2477
- Prigent, G.; Rius, E.; Le Pennec, F. ; Le Maguer, S. & Quendo, C. (2003-b). A novel design method for narrow band-pass filter response improvement, *Proceedings of IEEE Microwave Theory and Techniques International Symposium*, pp 519-522, ISBN : 0-7803-7695-1, Philadelphia NJ, USA, June 2003, IEEE, Picataway NJ, USA.
- Prigent, G. ; Rius, E. ; Le Pennec, F.; Le Maguer, S.; Quendo, C.; Six, G. & Happy, H. (2004-a). Design of narrow-band DBR planar filters in Si-BCB technology for millimeter-wave applications, *IEEE Transactions on Microwave Theory and Techniques*, vol. 52, no 3, pp 1045-1051, March 2004, ISSN : 0018-9480
- Prigent, G. ; Rius, E. ; Le Pennec, F. ; Le Maguer, S. & Quendo, C. (2004-b). A novel design method for improvement of narrow bandpass planar filter response, *Microwave and Optical Technology Letter*, Wiley, vol. 41, no 2, pp 98-104, April 2004, ISSN : 0895-2477
- Prigent, G.; Rius, E.; Blarry, K. ; Happy, H.; Lepilliet, S.; Dambrine, G. & Cappy, A. (2005). Design of Narrow Band-pass Planar Filters for Millimeter-Wave Applications up to 220 GHz, *Proceedings of IEEE Microwave Theory and Techniques International Symposium*, ISBN : 0-7803-8845-3, Long Beach CA, USA, June 2005, IEEE, Picataway NJ, USA.
- Prigent, G.; Rius, Happy, H.; E.; Blary, K. & Lepilliet, S. (2006a). Design of Wide-Band Branch-Line Coupler in the G-Frequency Band, *Proceedings of IEEE Microwave Theory and Techniques International Symposium*, pp 986-989, ISBN : 0-7803-9541-7, San Francisco CA, USA, June 2006, IEEE, Picataway NJ, USA.
- Prigent, G.; Rius, E.; Happy, H. ; Blary, K. & Lepilliet, S. (2006b). Design of branch-line couplers in the G-frequency band, *Proceedings of IEEE European Microwave Conference*, pp 1296-1299, ISBN : 2-9600551-6-0, Manchester, UK, September 2006, IEEE, Picataway NJ, USA.

- Rieh, J. S.; Greenberg, D.; Khater, M.; Schonenberg, K. T.; Jeng, J. S.; Pagette, F.; Adam, T.; Chinthakindi, A.; Florhey, J.; Jagannathan, B.; Johnson, J.; Krishnasamy, R.; Sanderson, D.; Schnabel, C.; Smith, P.; Stricker, A.; Sweedney, S.; Vaed, K.; Yanagisawa, T.; Ahlgren, D.; Stein, K. & Freeman, G. (2004). SiGe HBTs for millimeter-wave applications with simultaneously optimized  $f_{T\max}$  of 300 GHz, *Proceedings of IEEE Radio Frequency Integrated Circuits (RFIC) Symposium*, pp. 395-398, ISBN : 0-7803-8333-8, Fort Worth TX, USA, June 2004, IEEE, Piscataway NJ, USA.
- Rius, E.; Coupez, J. P.; Toutain, S.; Person, C. & Legaud, P. (2000-a). Theoretical and experimental study of various dielectric bridges for millimeter-wave coplanar application, *IEEE Transactions on Microwave Theory and Techniques*, vol. 48, no 1, pp 152-156, January 2000, ISSN : 0018-9480
- Rius, E.; Person, C.; Le Nadan, T.; Quendo, C. & Coupez, J. P. (2000-b). 3D integrated narrowband filters for millimeter-wave wireless applications, *Proceedings of IEEE Microwave Theory and Techniques International Symposium*, pp 323-326, ISBN : 0-7803-5787-X, Boston MA, USA, June 2000, IEEE, Piscataway NJ, USA.
- Rius, E.; Prigent G.; Happy, H.; Dambrine, G. & Cappy, A. (2003). Wide- and narrow-band bandpass coplanar filters in the W-frequency band, *IEEE Transactions on Microwave Theory and Techniques*, vol. 51, no 3, pp 784-791, March 2003, ISSN : 0018-9480
- Quendo, C.; Rius, E. & Person, C. (2003). Narrow Bandpass filters using Dual-Behavior Resonators, *IEEE Transactions on Microwave Theory and Techniques*, vol. 51, no 3, pp 734-743, March 2003, ISSN : 0018-9480
- Rizzi, P. (1988). *Microwave Engineering, Passive Circuits*, pp 466-468, ISBN: 978-01358670209, Englewood Cliffs, NJ : Prentice Hall,
- Schnieder, F. & Heinrich, W. (2001). Model of thin-film microstrip line for circuit design, *IEEE Transactions on Microwave Theory and Techniques*, vol. 49, no 1, pp 104-110, January 2001, ISSN : 0018-9480
- Six, G.; Vanmackelberg, M.; Happy, H.; Dambrine, G.; Boret, S. & Gloria, D. (2001). Transmission lines on low resistivity silicon substrate for MMIC's application. *Proceedings of European Conference on Wireless Technology*, pp 193-196, ISBN : 2-9600551-1-X, London, UK, October 2001, Artech House, Boston London, UK.
- Six, G.; Prigent, G.; Rius, E.; Dambrine, G. & Happy, H. (2005). Fabrication and characterization of low-loss TFMS on silicon substrate up to 220 GHz, *IEEE Transactions on Microwave Theory and Techniques*, vol. 53, no 1, pp 301-305, January 2005, ISSN : 0018-9480
- Tagushi, G. (1987). *System of experimental design*, Kraus, ISBN: 978-0527916213, White Plains, NY, USA
- Vu, T. M.; Prigent, G.; Mazenq, L.; Bary, L.; Rumeau, A. & Plana, R. (2008). Design of bandpass filter in W-band on a Silicon membrane, *Proceedings of IEEE Asia Pacific Microwave Conference*, ISBN : 978-1-4244-2641-6, Hong Kong, China, December 2008, IEEE, Piscataway NJ, USA.
- Warns, C.; Menzel, W. & Schumacher, H. (1998). Transmission lines and passive elements for multilayer coplanar circuits on silicon, *IEEE Transactions on Microwave Theory and Techniques*, vol. 46, no 5, pp 616-622, May 1998, ISSN : 0018-9480

- Weller, T. M.; Henderson, R. M.; Herrick, K. J.; Robertson, S. V.; Kihm, R. T. & Katehi, L. P. B. (1999). Three-dimensional High-frequency distribution network – Part I: Optimization of CPW discontinuities, *IEEE Transactions on Microwave Theory and Techniques*, vol. 47, no 5, pp 614-619, May 1999, ISSN : 0018-9480
- Wen, C. P. (1969). Coplanar waveguide: A surface strip transmission line suitable for non reciprocal gyromagnetic devices applications, *IEEE Transactions on Microwave Theory and Techniques*, vol. 17, no 12, pp 1087-1090, December 1969, ISSN : 0018-9480
- Wolf, G.; Prigent, G.; Rius, E.; Demichel, S.; Leblanc, R.; Dambrine, G. & Happy, H. (2005). Band-pass coplanar filters in the G-frequency band, *IEEE Microwave and Wireless Components Letters*, vol 15, no 11, pp 799-801, November 2005, ISSN : 1531-1309.



# Integrated Silicon Microwave and Millimeter-wave Passive Components and Functions

Philippe Benech, Jean-Marc Duchamp, Philippe Ferrari,  
Darine Kaddour, Emmanuel Pistono, Tan Phu Vuong,  
Pascal Xavier and Christophe Hoarau and Jean-Daniel Arnould  
*IMEP-LAHC UMR 5130 Grenoble INP, University Joseph Fourier, CNRS  
France*

## 1. Introduction

The continuous scaling down of device size makes high-speed circuits achievable as a result of the inverse relationship between gate length and transition time. In the same time, passive components like capacitors, inductors, antennas or interconnect transmission lines become a limiting factor to the global integration particularly for functions like filters. For example Wireless communications have increased in a spectacular way over recent years due to the quest of complete transceiver integration (RF/digital/analog blocks) on a same chip in order to meet cost effective. In this context, the reduction of off-chip components is necessary. This trend has gradually led to a greater integration of passive components in the back end of line (BEOL) of silicon technologies. Integrated in BEOL (Figure 1) metallization of CMOS or BiCMOS technologies, these devices have to meet requirements in terms of high RF performances, low area and compatibility with silicon substrate such as bulk silicon or SOI (Silicon On Insulator).

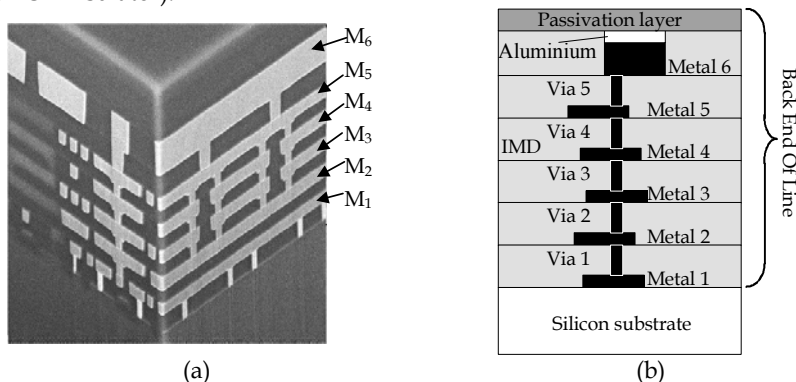


Fig. 1. BEOL with 6 interconnect levels: (a) 3D view, (b) schematic view (IMD=Inter-Metallization Dielectric)

The BEOL is at the origin dedicated to the interconnections of the digital circuits and then the analog circuits. In this context, it was advantageous to use interconnect levels to design passive components.

The difficulty of realizing integrated passive components having strong performance and weak surface in the BEOL, resides in the technological change of the levels of interconnections tightening with a reduction increasingly more important of metals thicknesses and dependent on the increasing integration of the active devices. To overcome this limitation, the use of one or two thick metal layers, which thickness can reach 3  $\mu\text{m}$ , is now implemented in different technologies.

Another important point for BEOL, is the damascene process introduced with copper metallization. Copper is for most of passive components the best conductive material mainly because of its low conductivity; but damascene architecture imposes a copper density usually between 20 % and 80 % due to chemical and mechanical polishing (CMP). To comply with this rule, it is necessary to include small cube of copper typically of 1  $\mu\text{m}^3$  and called dummies. From an electromagnetic point of view, particularly in millimeter range, dummies can have a strong impact on passive components as function of the design.

## 2. Capacitors and inductors for RF applications

The recent progress of CMOS technologies makes possible to consider today, an increasingly thorough integration of RF and millimeter waves analog circuits. These circuits require at the same time powerful passive components, and a weak occupied surface. These components are indissociable of the functions like the amplifiers, the mixers, the filters...

Today one of the problems, to answer the need for massive integration and low cost on silicon of a complete electronic system, lies in the number and the performance of the passive L and C components compared to the number of transistors, which these functions require. From microelectronics point of view, they are studied since a long time (Burghartz et al., 1997) taking into account technological evolution and the frequency of operation.

### 2.1 Capacitors

A capacitor is constituted of a dielectric surrounded by two metal electrodes. Classically the value of the capacitor can be obtained by the well-known relation:  $C = \epsilon S / t$ , where  $\epsilon$  is the permittivity of the dielectric material,  $S$  is the surface of the electrodes and  $t$  is the thickness of the dielectric material.

The main parameters that are used to characterize the quality of a capacitor are the quality factor, the resonant frequency and the capacity per unit surface. This last parameter is of great importance for silicon integration as the cost of an integrated circuit is directly dependent on its surface.

Taking into account the basic equation of the capacitor, there are three possibilities to change the capacitor value and particularly to increase its value when necessary. The first one is to change the surface; this can be done easily but will increase the cost of the circuit for big values and consequently large area. The second possibility is to reduce the thickness of the dielectric, but this is more difficult if the thickness reaches few nanometers. Moreover, reducing the thickness can lead to a degradation of the performance of dielectric material and the break down voltage of the material is strongly dependent on its thickness.

Another possibility to increase capacitor value is to use various dielectric materials as those of Table 1 (Mondon & Blonkowskic, 2003 ; Allers et al., 2003; Berthelot et al., 2006; Defay et al., 2006). The last column of Table 1 gives an indication about the capacitor density, but the proposed typical values are dependent of the possible thickness of the dielectric used and the type of capacitor. An attention must be paid to the possible use in high frequency and particularly losses, because some of these materials are not well known in mm range. A last possibility is to occupy the whole thickness of the BEOL. For that purpose, different structures of capacitors are studied as presented in the next section.

Dielectric	Permittivity	Breakdown field (V/nm)	Typical density value (fF/ $\mu\text{m}^2$ )
SiO <sub>2</sub>	4.2	0.1	1
Si <sub>3</sub> N <sub>4</sub>	7	0.07	2
Al <sub>2</sub> O <sub>3</sub>	9	0.08	3.5
HfO <sub>2</sub>	18	0.06	14
Ta <sub>2</sub> O <sub>5</sub>	25	0.05	5
ZrO <sub>2</sub>	45	0.04	35
SrTiO <sub>3</sub>	150	0.01	10

Table 1. Main dielectrics used to realize capacitors and typical density value of planar MIM capacitors.

When a capacitor will be chosen an important parameter is its value. The more its value is bigger, the more the resonance frequency presents a low value. In an other words, it is quasi impossible to obtain large capacitor values working in frequency above few GHz. This is due to losses and to inductive behavior of metallic part of the capacitor which limit its performance. Thus for mm-wave application, low capacitor values are required and can be obtained with one of the most used shape described in the next section.

### 2.1.1 Different capacitors type

#### A. MIM capacitors

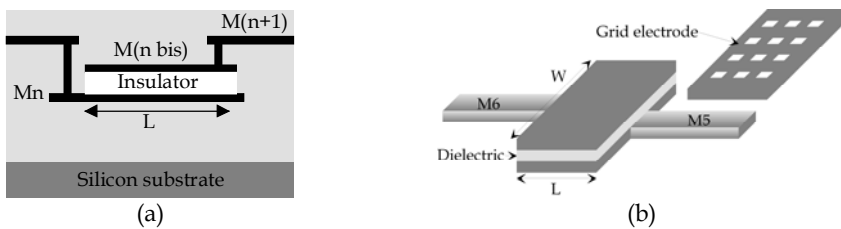


Fig. 2. Schematic view of a MIM capacitor: (a) cross-section, (b) 3D view

The Metal Insulator Metal (MIM) capacitor is a planar capacitor as shown in Figure 2. The advantage of this capacitor is its simplicity to design and to realize, but it requires an intermediate metal level Mn<sub>bis</sub> as shown in Figure 2(a). To respect metal density rules different kind of electrodes can be used (Figure 2(b)). This will reduce the capacitance per unit area. To increase the capacitor value, it is possible to design one capacitor in the last level and another in the next to last level (Chen et al., 2002) of the BEOL.

### B. Finger capacitors

Finger capacitors are derived from MIM capacitor and use all metallic levels of the BEOL. The main advantage is to increase the capacitance density. This kind of structure allows to increase capacitance density of about 30% as compared to MIM capacitor (Subramaniam et al., 2005 and 2007). They are constituted of interdigital or crossed metal fingers. They need a lot of via to connect all fingers. They are more difficult to check and a large attention is required to the position of the access points.

### C. 3D and Trench capacitors

Trench capacitors were developed to increase the capacitance per unit area. The basic principle of this capacitor is to realize a vertical MIM capacitor as shown in Figure 3 with 4 metal levels (Jeannot et al., 2007). The obtained result gives a capacitance approximately 10 times higher than for planar MIM, but with a more complex process. An interesting structure is given by (Büyüktas et al., 2009) where they have design and realized trench capacitor in the front-end part (near active component). They have tested they capacitor up to 10 GHz.

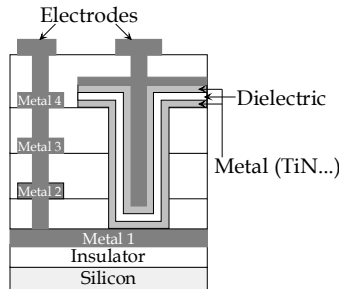


Fig. 3. Principle of 3D capacitor

### 2.1.2 Modeling and performances

The model of a capacitor is easier to develop if the context is not taken into account. From a perfect capacitor, it is necessary to complete the model by first taking into account dielectric losses. This can be done usually by adding a conductance in parallel with the inductance. In RF and millimeter waves, the influence of electrodes must be included in the model. At high frequencies, electrodes act like a lossy inductor. In fine, for an integrated capacitor it is necessary to take into account at minimum, coupling phenomenon with the substrate. Whatever the shape of the capacitor, the substrate under the lower electrode has a great importance on the behavior of the capacitor. Coupling between the lower electrode and the substrate can change all the parameters of the capacitor. (Arnould et al. 2004).

This lumped model of Figure 4 is the more commonly used. In this model, the series branch comprises the nominal capacitance of the dielectric ( $C_p$ ), the losses in the dielectric ( $R_p$ ), the resistance ( $R_s$ ) and inductive behavior ( $L_s$ ) of the metal electrodes.  $C_{ox}$ ,  $C_{si}$  and  $R_{si}$  represent the complex capacitance to the substrate due to electrodes.  $C_{ox}$  is the substrate to top and bottom electrode capacitance.  $R_{sub}$  and  $C_{sub}$  are the frequency dependent substrate resistance and capacitance, respectively.

This model refers first to planar MIM capacitors. In fact, for the other structures of capacitors it can be change and some components of this model can be removed in accordance with the physical design of the capacitor. For example, if the first metallic layer

of the BEOL is a ground plane, the part taking into account the substrate can be removed. Distributed models has been studied (Cai et al., 2004; Lee et al., 2006-1) and give interesting results, but are more complicated and not used in microelectronic design kit.

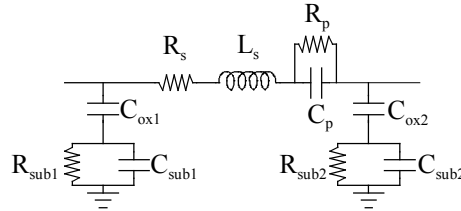


Fig. 4. The more commonly used electric model of capacitor

The factor of merit traditionally used is the quality factor. For a measured component, it is calculated after parameters extraction from the model. The quality factor depends mainly on the value of the capacitor and on losses. But the inductive effect of the electrodes limits its maximum frequency of use. Figure 5 shows a typical Q factor with the main parameters influence.

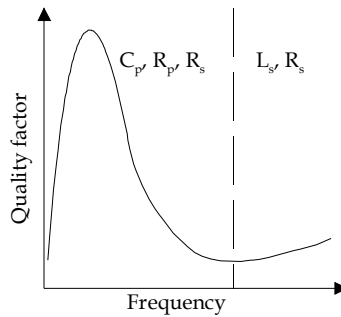


Fig. 5. Typical quality factor versus frequency and parameters influence

An important parameter to take into account when a capacitor is designed, is the position of the access lines with regard to electrodes. This is of great importance to reduce the electrodes resistance and to increase quality factor. To give an example, for a MIM capacitor realized in a 120 nm CMOS technology (Figure 2(a)), Table 2 summarize the value of the extracted parameters of the model (Lemoigne et al., 2006) for different shapes of electrodes. The biggest width gives the minimum resistance. This result can be extended to any kind of capacitor.

	W (μm)	L (μm)	C (pF)	R(Ω)	G (S)	L (pH)
C <sub>0</sub>	66	66	3.5	4.2	4.16 10 <sup>-4</sup>	85
C <sub>1</sub>	120	66	8	0.7	4.16 10 <sup>-4</sup>	85
C <sub>2</sub>	174	66	11.5	0.1	4.16 10 <sup>-4</sup>	85

Table 2. Losses comparison for different shapes of capacitor

Finally, the choice of a capacitor having the highest capacitance density while preserving the other capacitor properties (leakage, stability, and reliability) depends on the technological parameters, but also on the frequency. For millimeter wave, capacitors of low value can be achieved with good performances.

## 2.2. Inductors

As for capacitors, inductors have been studied since a long time. Their performances are always a problem for designers. Integrated inductors can have mainly three forms:

### A. Above IC Inductors

Inductors are added on the passivation layer at the end of the process. This technique of manufacture allows a greater freedom on the choice of materials, thicknesses and the shape of the components (Sun et al., 2006). But it is still at a stage of advanced research and not of industrialization for technological constraints.

### B. Inductors of the type MEMS

It is an extension of the previous type with more complex structures using Micro Electro-Mechanical Systems (MEMS) and using micro-machining process (Jiang et al., 2000). The obtained components can be suspended in air. However, this type of structure suffers for the moment, of a low mechanical resistance and a perfectible reproducibility

### C. BEOL inductors

The last possibility is to design inductors in the BEOL like capacitors. For this component the goals are more or less the same than for capacitors: the best inductor for the minimum occupied surface. They don't need modification of fabrication process and this is the best advantage. But they suffer from a poor quality factor and usually a great occupied surface as compared to the rest of electronic RF-circuit. This kind of inductor will be more detailed.

Advanced microelectronic technologies offer less thick metal layers. This induces an increase of limiting factors like skin effect. A second problem is the low resistivity of silicon substrates, required for latch-up of MOS transistors, which induces resistive losses.

### 2.2.1. Various inductors shapes

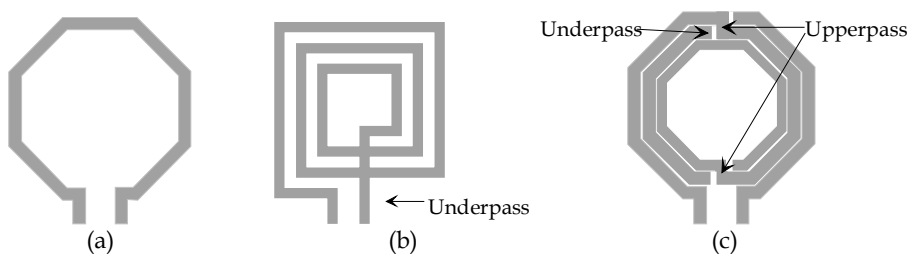


Fig. 6. (a) octagonal one turn inductor, (b) square inductor with one underpass, (c) symmetric octagonal inductor with several underpass and upperpass.

The more common shapes are square or hexagon (Figure 6). Usually hexagon is preferred to remove the right angles that are not favorable to operation with high frequencies. If the inductor value is low, a one-turn inductor can be designed. But for others values a multi-turn inductor is required. It can be designed using all metal layers of the BEOL. An

important parameter when using copper BEOL is the presence of dummies. Some rules must be respected as suggested by (Pastore et al., 2008-1). An important point when designing inductance is to take care to underpass and upperpass, because they can generate more losses due to via. As shown in example of Figure 6, only one turn inductors don't need to use two metal levels and consequently don't need via and upper or underpass.

**2.2.2. Modeling and performances**

The first integrated planar inductor on silicon was developed in 1990 by (Nguyen et al., 1990). In the same time they have proposed a basic model of Figure 7(a). In 2000, a modified model (Figure 7(b)), more close to fabrication process and geometry of inductor, was proposed by (Yue & Wong, 2000). An other model (Figure 7(c)), taking into account electromagnetic coupling with silicon substrate were developed by (Melendy et al., 2002). But, a wide band model was proposed by (Lee et al., 2006-2), where intrinsic and extrinsic refer respectively to the inductor and to the environment (Figure 7(d)). The choice of a model is greatly dependent of the technology and the shape of the inductor.

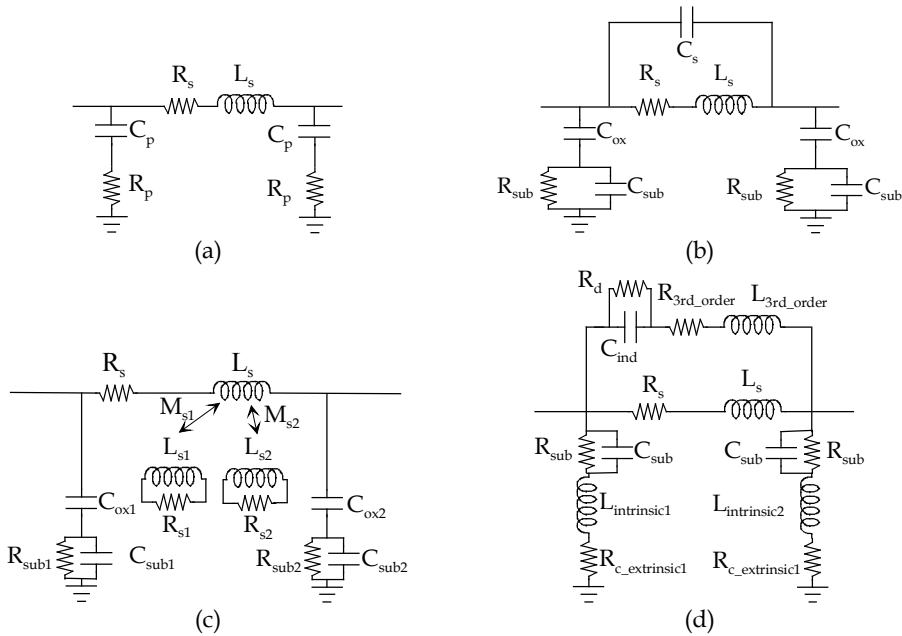


Fig. 7. Models of planar inductors, (a) (Nguyen & Meyer 90), (b) (Yue & Wong, 2000), (c) (Melendy et al.,2002), (d) (Lee et al., 2006-2)

These more or less complex models, must take into account various physical phenomena and geometrical parameters, coming from the design or which can have an influence on the design. The geometrical parameters are: the thickness and the dielectric constant of insulator used in the BEOL, the width of conductors, the spacing between two conductors for a spiral inductor, the inner diameter of the coil, the turns number for spiral shape, vias ensuring the passage from one metal level to an other for inductors using several metal levels. The

physical phenomena are: magnetic coupling between conductors, metallic losses (DC and skin effect in RF), Eddy current effects between conductors and silicon substrate.

If the models of Figure 7 are considered, it is possible to identify with more or less accuracy, the parameters listed below. For example, the components of Figure 7(b) represent:  $L_s$  the inductance,  $R_s$  ohmic losses in metal,  $C_s$  the capacitor between turns and between access points,  $C_{ox}$  the capacitor between metal layers and the silicon substrate,  $C_{sub}$  the capacitance of the substrate which is often negligible in the field of the radio frequencies as compared to the value of associated resistance  $R_{sub}$ .

As for the capacitors, the factor of merit traditionally used is the quality factor. For a measured component, it is calculated after components extraction from the chosen model. The quality factor depends mainly on the value of the inductor and on losses. Figure 8 shows a typical Q factor with the main parameters influence for the model of Figure 7(c).

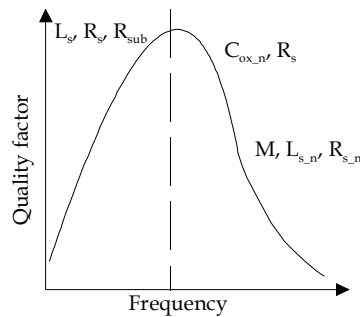


Fig. 8. Typical quality factor versus frequency and parameters influence

### 2.2.3. High performances inductors

To overcome the limitations induced by traditional BEOL, two possibilities were developed. The first is to use thick copper layers at the last level of BEOL and the second is to use SOI or porous silicon. Several works were done using porous silicon (Royet et al., 2003, Contopanagos & Nassiopoulou, 2007). They have obtained a Q factor of 32 with porous silicon at 3.8 GHz. But one of the best results was obtained by (Pastore et al., 2008-2). They have designed an octagonal symmetric inductors integrated in the hole six levels of BEOL. A high resistivity SOI substrate was chosen and an excellent Q factor of 34 at 4.5 GHz for a current capability of 57 mA/ $\mu$ m at 125°C was obtained.

## 3. High-Q slow-wave compact transmission lines and potential applications

### 3.1. State of the art

Conventional transmission lines such as microstrip, coplanar waveguides (CPW) and grounded coplanar waveguides (G-CPW), realized in industrial CMOS processes typically suffer from significant losses and poor quality factors in the RF and millimeter-wave ranges. Actually, thin-film microstrip transmission lines are suitable for most circuits because of their compact layout. However, due to technology evolution and continuous decrease of the  $\text{SiO}_2$  layer thickness, the signal line of the microstrip transmission lines has to be reduced in order to address 50 $\Omega$  transmission lines, leading to an increase of the metallic losses. In



(Gianesello et al., 2006), integrated transmission lines showing attenuation losses of 0.9 dB/mm at 10 GHz, and 3 dB/mm at 60 GHz have been demonstrated. However, high-impedance transmission lines can not be realized due to a drastic increase of the attenuation loss, and no efficient miniaturization way has been identified.

Coplanar CPW transmission lines could be a good candidate for high-impedance integrated transmission lines. More flexibility in the design of the CPW transmissions lines is obtained by adjusting the gap to the signal line width. However, high losses occur, due to the dielectric loss in the low-resistivity silicon substrate. Attenuation loss of 2 dB/mm have been reported on conventional CPW transmission lines on silicon substrates fabricated through commercial CMOS foundries (Milanovic et al., 1998). Lower losses can be achieved (0.2 dB/mm and 0.6 dB/mm at 20 GHz and 60 GHz, respectively) by the use of a high-cost SOI CMOS technology using a high resistivity substrate (Gianesello et al., 2006). Besides, CPW quarter-wave transmission lines will result in relatively large occupying areas, depending of the working frequency on silicon substrates. Such areas, of course, are not compatible with the miniaturization concept of monolithic integrated circuits.

To reduce dielectric losses, a solution could be to use the grounded G-CPW configuration. Nevertheless, inserting a solid metal shield is not an optimum solution due to the eddy current's losses (Klevend et al., 2001). Moreover, inserting such continuous metal shield significantly reduces the characteristic impedance, thus making it more difficult to achieve transmission line characteristic impedances in the order of 50  $\Omega$ .

In order to overpass the limitations of microstrip, CPW and G-CPW technologies, in terms of quality factor and miniaturization, new topologies of coplanar transmission lines with improved performances were investigated. The slow-wave concept has been employed to shorten the wavelength and improve the quality factors of the transmission lines. A new topology of coplanar waveguides with floating strips has been introduced for the design of low-loss compact microwave on-chip systems.

The first coplanar waveguides with floating strips, firstly introduced by Hasegawa in 1977, were realized on GaAs substrates (Hasegawa & Okizaki, 1977). These transmission lines exhibit a slow-wave propagation phenomenon but suffer from high insertion losses. A few years later, the floating strips were placed above the CPW and the structure was named "crosstie overlay CPW" (Wang & Itoh, 1987). However, a large attenuation, mainly due to the large floating strips pattern geometry, was reported in (Hasegawa & Okizaki, 1977-Wang & Itoh, 1987). Indeed, these structures were realized using non-standard processes where the resolution was high enough to show the merits of the structure.

Afterwards, the same shielded coplanar waveguides (S-CPW) topology implemented in a BiCMOS technology has shown very interesting results with better performances (Cheung & Long, 2006).

Moreover, the reported benefits of shielded coplanar transmission lines have been supported by several equivalent circuit models in the literature. The first RLCC equivalent model was proposed in (Wang et al, 2004) to describe the line performance below the resonant frequencies. Later, nonphysical RLCC models for lossy transmission lines developed for simulating the extracted characteristic impedance and propagation constant showed good correlation with TDR measurements (Kim & Swaminathan, 2005). Unlike physical models where the transmission line parameters are correlated with the physical structure, the nonphysical models are extracted directly from the frequency response and, therefore, do not relate to the physical structure of the transmission line. Afterward, efforts

have been put into developing analytical expressions for the shielded transmission lines inductances to describe key performance figures with a good accuracy (Tiemeijer et al, 2007; Masuda et al, 2008). In (Wang et al, 2008), the authors tried to go further by calculating the inductance and the resistance of the shielded coplanar waveguides using the partial element equivalent circuits (PEEC) method. After all, the simplest RLGC model taking advantage of the well established models of grounded and standard coplanar waveguides was described in (Sayag et al, 2008).

### 3.2. Shielded coplanar waveguides transmission lines description

Figure 9(a) shows the 3D geometric view of the shielded coplanar waveguide transmission lines realized in (Kaddour et al, 2008). The four Copper metal layer 0.35- $\mu\text{m}$  CMOS low-cost technology, as described in Figure 9(b), is used. The S-CPW geometric design parameters are the following:  $W$ ,  $G$ , and  $W_g$  are the CPW central conductor, gap, and ground strip widths, respectively.  $SL$  and  $SS$  are the floating strip length and spacing, respectively. In order to reduce the transmission line conductive losses, a thick top metal layer is realised. The CPW is made on the 2.8  $\mu\text{m}$ -thick top metal layer (M4) while the floating strips are patterned on the second highest metal layer (M3) with a thickness of 0.64  $\mu\text{m}$ . The distance between the top metal (M4) and the bottom patterned shield (M3) is 1  $\mu\text{m}$ .

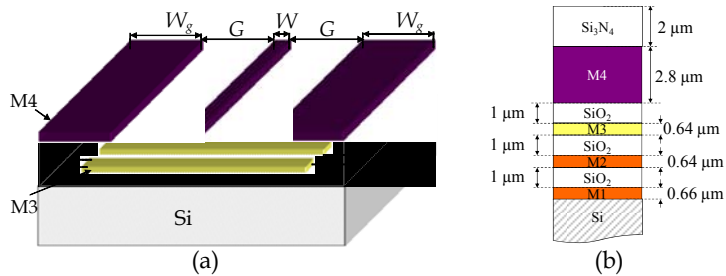


Fig. 9. (a) 3D geometric view of the slow-wave coplanar transmission line with floating metal strips. (b) Four copper metal layers 0.35- $\mu\text{m}$  CMOS technology schematic description.

The patterned ground shield underneath the CPW transmission line acts as a perfect conductor for the electric fields, due to the small strip spacing  $SS$  (0.6  $\mu\text{m}$  in the realized devices) compared to the silicon oxide thickness (1  $\mu\text{m}$ ). The magnetic field passes through the patterned ground. So, the capacitance per unit length is greatly enhanced, whereas the inductance remains quite unchanged. Therefore the phase velocity is reduced, predicting the slow-wave propagation behaviour. Thanks to the increase of the propagation constant, lower losses per wavelength are measured in S-CPW transmission lines leading thus to improved transmission lines quality factor defined as  $Q = \beta / 2\alpha$ , where  $\alpha$  is the attenuation constant, and  $\beta$  is the phase propagation constant.

In (Kaddour et al, 2008), a comprehensive study on the geometric factors affecting the S-CPW key performance figures was provided. Following the design guidelines published in (Kaddour et al, 2008), three sets of S-CPW transmission lines with different geometries were fabricated using the 0.35  $\mu\text{m}$  CMOS technology. Figure 10 is a micrograph of the fabricated S-CPW transmission lines. Geometric specifications of the fabricated transmission lines are shown in Table 3.

The CPW dimensions ( $W$  and  $G$ ) are chosen to reach a characteristic impedance near to  $50 \Omega$  with a high slow-wave factor. In order to reduce the conductive losses, the minimal central conductor width  $W$  is limited to  $10 \mu\text{m}$ . Moreover, it has been demonstrated in (Kaddour et al, 2008) that narrow ground planes could be used to improve the high frequency electrical performances of the S-CPW transmission lines. Therefore, the ground plane width is set to  $60 \mu\text{m}$ , limiting thus the footprint for all the fabricated S-CPW transmission lines. The metal shield is designed using minimized design rules, i.e. minimum allowed metal strip length ( $SL = 0.6 \mu\text{m}$ ) and spacing ( $SS = 0.6 \mu\text{m}$ ) in the  $0.35\text{-}\mu\text{m}$  CMOS technology. Indeed, simulations carried out in (kaddour et al, 2008) have shown that insertion losses are reduced with the use of a finer ground shield pattern. Thus, the strip spacing should be kept to a minimum to boost the shield effect from the lossy silicon substrate while narrow metal strips should be used to minimize eddy currents.

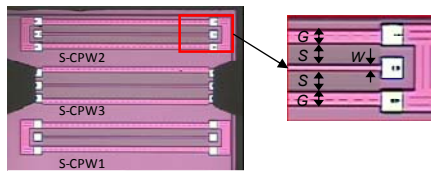


Fig. 10. Micrograph of the fabricated S-CPW transmission lines.

	$W$ ( $\mu\text{m}$ )	$G$ ( $\mu\text{m}$ )	$W_g$ ( $\mu\text{m}$ )	$SL$ ( $\mu\text{m}$ )	$SS$ ( $\mu\text{m}$ )
S-CPW1	10	100	60	0.6	0.6
S-CPW2	18	100	60	0.6	0.6
S-CPW3	18	150	60	0.6	0.6

Table 3. S-CPW transmission lines geometrical dimensions.

### 3.3. Shielded coplanar waveguides transmission lines simulations and measurements

Figure 11-a compares the simulated (dashed lines) and the measured (solid lines) effective relative permittivity for the three fabricated S-CPW transmission lines, all simulations being carried out with the 3D Full-wave electromagnetic simulator: HFSS<sup>TM</sup>. A good agreement is obtained between the measurements and the simulations of the S-CPW lines, except for the widest dimensions ( $G = 150 \mu\text{m}$ ). The slow-wave phenomenon exhibited by the S-CPW transmission lines is highlighted by very high values of the measured effective relative permittivity ( $36 < \epsilon_{r\text{-eff}} < 48$ ). The higher slow-wave factor is obtained for the wider CPW dimensions (S-CPW3). The measured value is about eight times larger than that of a conventional CPW transmission line on a silicon substrate. This significant increase in the effective dielectric permittivity is very promising for the miniaturization of the overall size of RF components based on transmission lines.

Figure 11-b illustrates the comparison between the simulations (dashed lines) and the measurements (solid lines) of the attenuation constant  $\alpha$  expressed in dB per millimeter. The attenuation constant is very low, comparable to state-of-the-art results obtained with conventional MMIC transmission lines on silicon.

The quality factor is then derived in Figure 12. It increases with the frequency, and reaches 40 near to 30 GHz for the best case. With these values, the S-CPW quality factor is more than 3 times greater than that of the state-of-the-art conventional CPW transmission lines.

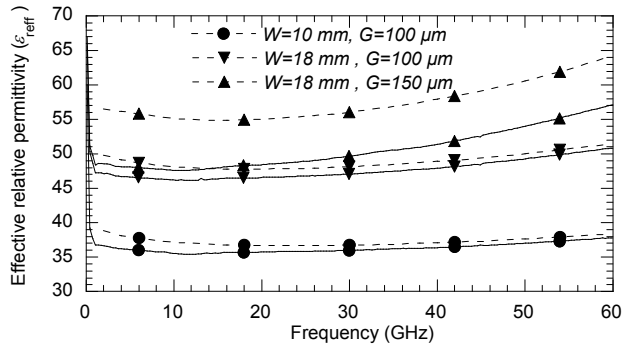


Fig. 10. Comparison of the EM simulated (dashed lines) and measured (solid lines) relative permittivity of the realized S-CPW transmission lines.

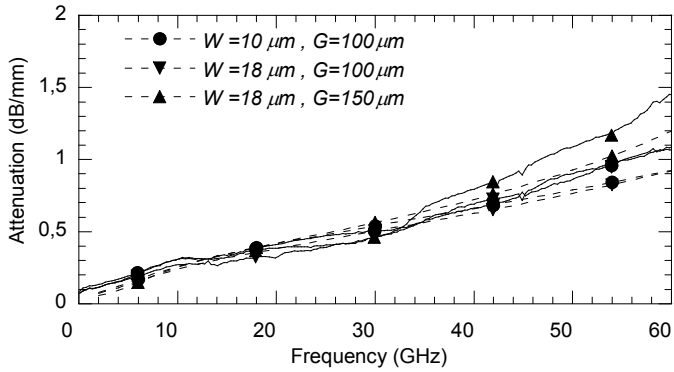


Fig. 11. Comparison of the EM simulated (dashed lines) and measured (solid lines) attenuation of the realized S-CPW transmission lines.

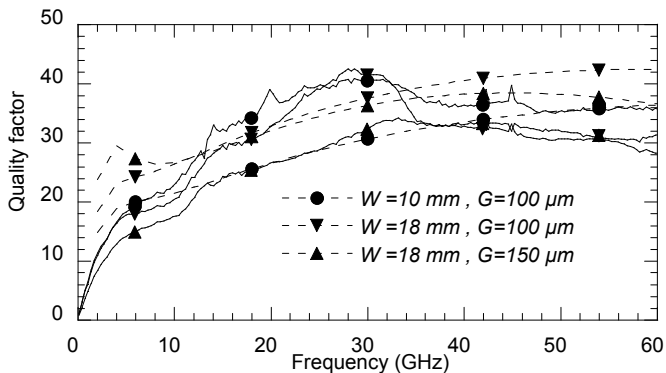


Fig. 12. Comparison of the EM simulated (dashed lines) and measured (solid lines) quality factor of the S-CPW transmission lines.

### 3.4. Shielded coplanar waveguides transmission lines applications

The measured results clearly show the interest of S-CPW transmission lines for achieving high quality factor and miniaturized transmission lines at millimetre-wave frequencies. Potential applications include several RF passive circuits in the millimetre-wave bands, such as filters, phase shifters, power dividers, and matching networks (Sayag et al., 2008). A simple and general approach for the design of narrow-band bandstop filters is based on an open-circuited stub. Based on S-CPW, two open-circuited stubs with the geometric dimensions  $W = 10 \mu\text{m}$ ,  $G = 100 \mu\text{m}$  and  $W_g = 60 \mu\text{m}$ , were fabricated on a CMOS  $0.35 \mu\text{m}$  technology. The micrograph of the S-CPW stubs is shown in Figure 13, with two open-circuited stubs showing lengths of 1.6 mm and 2.7 mm, respectively. The measured  $|S_{21}|$  of both stubs is given in Figure 13. The ripples observed in the frequency response are due to the appearance of parasitic propagation modes near to the T-junction. Resonant frequencies occur at 4.4 and 7.5 GHz, respectively, for the long and the short stubs. With these measured resonant frequencies, an effective dielectric permittivity of 40 can be extracted. This value is in good agreement with the measured value in Figure 11. It is important to note, that the same resonant frequencies would be obtained with longer lines realized in a CPW classical technology. Thanks to the slow-wave factor, the length is reduced by a factor near to 3.

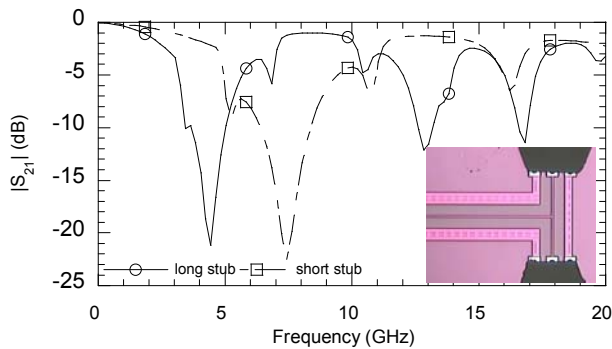


Fig. 13. Measurements of the transmission coefficient modulus  $|S_{21}|$  of two stubs realized with S-CPW lines.

## 4. Integrated antennas and RF mm-wave interconnects

Two main problems can be identified concerning communications inside integrated circuits on one hand and on the other hand concerning 3D integration and communications systems that requires integrated antennas. The main objective is to demonstrate the feasibility of such components and to take into account the specific problem linked to the mm-Wave domain.

The continuous scaling down of transistor size makes high-speed digital and analog RF circuits achievable. In the same time, conventional global interconnect lines become a limiting factor due to their RC signal delay (ITRS 2003). As example, clock distribution networks are going to suffer from skew, jitter, power dissipation and area consumption for future generations of integrated circuits (Mehrotra & Boning, 2001). Alternative interconnect systems such as optical (Miller, 2002), 3D (Souri et al., 2000) or RF interconnects (Kim et al.,

2000) are required to overcome the limits of conventional interconnects. Among the possible solutions wireless interconnects has a great interest because they can be developed without modifying the technological steps. In particular antennas can be designed using metal layers of integrated circuit of metal layer used 3D (SOC-SIP) integration.

#### 4.1. Intra chip interconnect

Among possible planar antennas (patch, zig-zag, spiral...(Kim, 2000)), the dipole is chosen for its best compromise between performances and occupied surface.

Figure 14 represents a simplified schema of a pair of copper on-chip dipole antennas. We may distinguish the dielectric layer ( $\epsilon_r = 4.2$ ) necessary to isolate the copper lines, the silicon substrate ( $\epsilon_r = 11.7$ ) and finally the backside metallization of integrated circuits. The antennas are designed to operate at frequencies around 30 GHz and are characterized by a length of 1.98 mm, a width of 10  $\mu\text{m}$  and a spacing of 20  $\mu\text{m}$  between the two branches. The distance between face to face antennas is 2.5 mm.

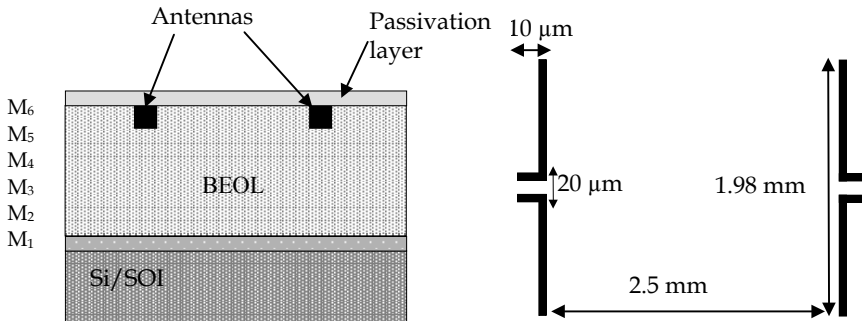


Fig. 14. Schematic view of antennas

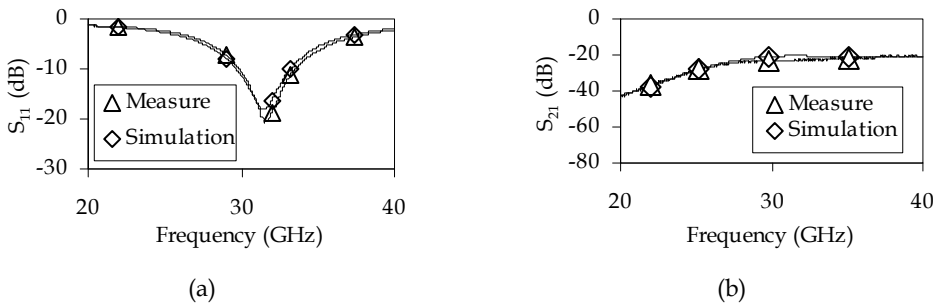


Fig. 15. Comparison between measure and simulation of  $S_{11}$  (a) and  $S_{21}$  (b) for a silicon bulk substrate of thickness 725  $\mu\text{m}$  and resistivity of 20 Ohm.cm.

Understanding the propagation of electromagnetic waves generated by such an antenna pair requires the comprehension of the propagation paths. When electromagnetic waves are travelling through one medium, phase velocity estimation can show through which medium the wave is travelling. However the case of on-chip antennas is quite different, as there are more than one medium involved in the waves propagation (air, dielectric, silicon) and

consequently multiple propagation paths. Actually there is no electromagnetic model describing with precision the propagation characteristics of waves generated by on-chip antennas. Consequently the modeling and simulation were done using a 3D electromagnetic solver with finite element method. The used model is based on the Greens functions resolution and it seems to be acceptable for any value of the substrate permittivity and thickness. It suggests that the surface wave number generated by the dipoles in a given frequency is a function of the substrate permittivity and thickness as the maximum energy involve in this transmission propagates inside the substrate. Figure 15 presents a comparison between simulation and measurement. A good agreement is observed for correct simulation conditions and for measurement with set up as discussed later.

The possible transmission of energy between two antennas disposed in the same plane is obtained by the wave propagation into the silicon substrate. Then, the substrate is important in the proposed configuration.

As the back end of line is about 6  $\mu\text{m}$  thick, the most important is the silicon of which thickness can vary according to technological facilities from 1 mm to few hundred micrometers, if the substrate is thinned. The propagation path can be in a first approach considered as dielectric medium with ground shield on the bottom face. In this system the propagation of TE and TM modes is possible.

The cut-off frequency of these modes depends on the properties of the substrate: thickness and dielectric constant. These cut-off frequencies can be evaluate using the following equations (Pozar, 1998):

$$f_{cm} = \frac{m \cdot c}{2 \cdot h \cdot \sqrt{\epsilon_r - 1}} \quad m = 0,1,2 \quad \text{for } TM_m \text{ waves} \quad (1)$$

$$f_{cm} = \frac{(2 \cdot m - 1) \cdot c}{4 \cdot h \cdot \sqrt{\epsilon_r - 1}} \quad m = 1,2 \quad \text{for } TE_m \text{ waves} \quad (2)$$

From previous equations, for every propagation structure, there is always one mode that propagates, the  $TM_0$ . This mode is prevailing with a zero cut-off frequency.

In Table 4, the propagation modes cut-off frequencies are reported as function of the silicon substrate thickness. For the thickness of 975  $\mu\text{m}$ , the  $TM_1$ ,  $TE_1$  and  $TE_2$  occurs at different frequencies in the frequency band of the analysis. Consequently, the emitted energy by the excited antenna will be distributed on these modes with the increase of frequency. At higher frequency each mode will contribute to the propagation, but the attenuation will not be the same for each of them. The measurement results will give information about the transmitting energy and the effect of the multi-mode propagation at high frequency far from the mono-mode frequency excitation.

Thickness ( $\mu\text{m}$ )	$f_c$ - $TM_1$ (GHz)	$f_c$ - $TE_1$ (GHz)	$f_c$ - $TE_2$ (GHz)
375	121	61	182
525	86	43	130
650	70	36	105
975	47	23	70
1300	35	17	52
1625	28	14	41

Table 4. Propagation Modes

For this kind of component the characterization method is of great importance. The resonance frequency and the frequency band change significantly next to a GS or to GSG excitation related to probes. This may be related to many effects like the difference in the excited propagated modes, or the difference in the antenna effective length for the two kinds of probes. This effect is very marked for low thickness substrates like the one used for the results of Figure 16 of which thickness is of  $375\mu\text{m}$ , moreover this effect is dependent on the frequency of excitation and consequently on the wavelength of generated waves as compared to thickness.

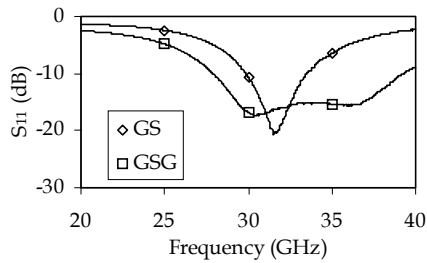


Fig. 16. Influence of probe type on reflection coefficient

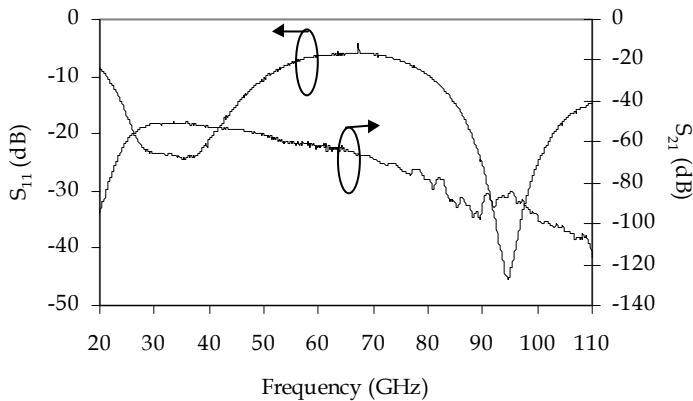


Fig. 17. Reflection and transmission coefficients of a pair of antennas up to 110 GHz

The previous antennas were also tested up to 110 GHz in order to verify their behavior at higher frequencies and the possible use of interconnects in millimeter range.

Figure 17 shows the reflection coefficient  $S_{11}$ . The first resonance of the antenna occurs at 31 GHz. The antenna was designed to operate around this frequency. The second resonance occurs at 95 GHz. This corresponds to a three half-wavelength resonance, as it can be predicted by antenna theory. From this observation and taking into account the value of the reflection coefficient, it is possible to generate electromagnetic waves at 95 GHz with these antennas. This sharp resonance indicates a good matching with the  $50\ \Omega$  source at this frequency, but this is not sufficient to ensure a good transmission.

A transmission gain of  $-25\ \text{dB}$  is achieved in the band 30 to 45 GHz and the band pass at  $-3\ \text{dB}$  is of  $28\ \text{dB}$  from 25 GHz to 50 GHz. For the second promising band around the second



resonance of 95 GHz, the transmission gain is -45 dB. This value is relatively low and therefore the transmission is possible but not so efficient as in the 25 GHz to 50 GHz range. If we compare this result with the propagation mode analysis, we can conclude that the multi-mode propagation frequency is not as good as a mono-mode transmission. The consequence is that, if it is possible to propagate waves at sub-millimeters frequencies, the efficiency can be improved by designing antennas in accordance with substrate thickness and frequency.

To conclude for intrachip interconnect, the best result was obtained at 30 GHz for antennas on high resistivity SOI substrates. The transmission gain was -15 dB and in comparison for low resistivity silicon bulk substrate, without ground shield under the antennas, the maximum transmission gain was at -30 dB. Moreover this kind of interconnect are not different from usual ones in term of coupling (Triantafyllou et al. 2005; Rashid et al 2003).

#### 4.2. Communications antennas for mm-waves

The increasing of wireless network needs demands the use of the broadband multimedia components to satisfy this performance. A new era, of future commercial communication devices in mm-wave range based on the 60 GHz unlicensed frequency band offers worldwide wideband operation (Nesic et al., 2001).

In particular, for dense local communications, the 60 GHz band for wireless personal area network (WPAN) applications (Figure 18) is of special interest for short-range communications, due to the RF attenuation of the atmospheric oxygen by 16dB/km, in a bandwidth of approximately 7GHz, centered around 60 GHz. Due to the spectrum availability (5-7 GHz) a variety of the short range high data rate applications may be targeted, in the scope from analog wideband transmission, up to digital GBit/s system solutions.

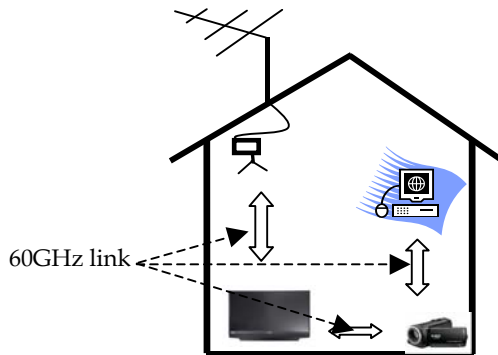


Fig. 18. Possible in-door home application scenario for both analog and digital application.

However, the interference due to attenuation of the atmospheric oxygen at 60GHz is very high link density (16dB/km) then the link distance is limited to 2 km at this frequency. A 60 GHz signal can only be intercepted in the tiny wedge and will only interfere with another 60 GHz link in that wedge (Guo et al., 2008).

To overcome the effects of atmospheric absorption and maintain reliability, radio links in millimeter wave region must use highly focused, or higher-gain, antennas in order to focus

as much as possible of the transmitted signal onto the receiving antenna. As RF frequency increases, signal wavelength becomes shorter, making it possible for smaller antennas to produce the required gain (Volakis, 2007).

In this frequency range and for that kind of transmission, antenna will not be integrated on silicon, but will be integrated by System on Chip (SOC) or System in Package (SIP) process. Some examples of millimeter waves antennas which offer the needed performances are presented: the patch antenna (Figure 19), the patch slot antenna (Figure 20), the Yagi antenna (Figure 21), the dipole (Figure 22). S-parameter are obtained by simulation with CST Microwave Studio. The resonance frequency of each antenna can be adjusted and the band width is lied to the type and geometry of the antenna. To obtain high gain an array can be build with these typical antennas (Volakis, 2007; Huang & Edwards 2006). These antennas can be realized by photolithographic process, with a roger 4003 substrate of  $\epsilon_r=3.38$ ,  $h=0.305\text{mm}$ ,  $\tan\delta=0.0027$  and with a  $17\mu\text{m}$  metallization layer. Table 5 shows measured antenna gains for 64 and 256 antenna elements.

Type	Size (8x8)	Gain (dBi)
Patch antenna	11mmx11mmx0.61mm	24.87
Slot Patch Antenna	11mmx11mmx0.61mm	24.08
Yagi Antenna	11mmx6mmx11mm	26.54

Table 5. Gain of the different arrays antennas.

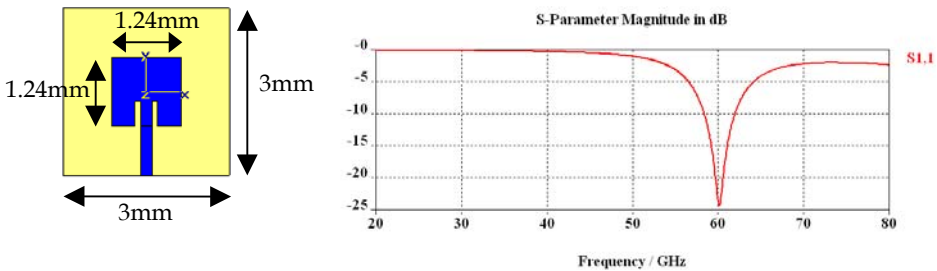


Fig. 19. Patch antenna millimeter wave and his  $S_{11}$

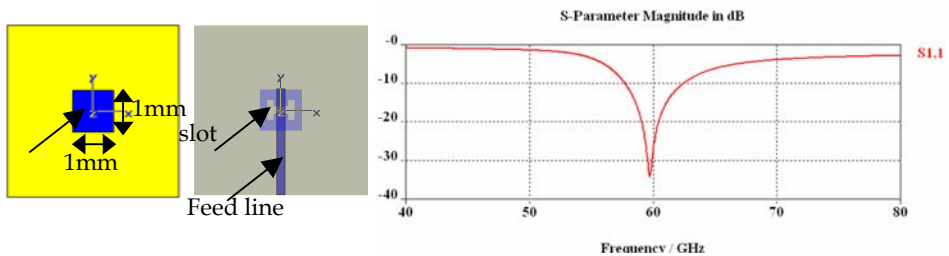


Fig. 20. Patch slot antenna millimeter wave and his  $S_{11}$

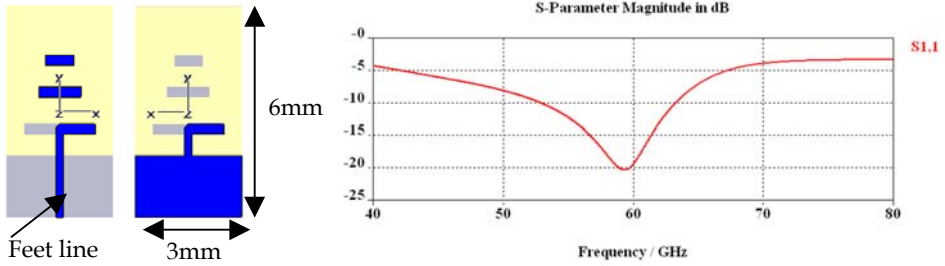


Fig. 21. Patch slot antenna millimeter wave and his  $S_{11}$

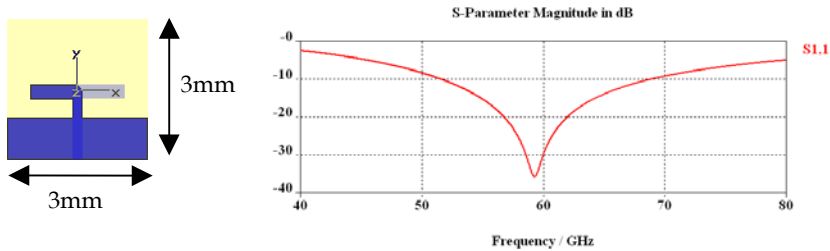


Fig. 22. Dipole antenna millimeter wave and his  $S_{11}$

### 5. Impedance matching in RF domain

Microwave impedance matching is used to maximize the power transmission between two devices. This function is classically implemented in integrated front-end RF applications with antennas, power amplifiers (Figure 23), mixers or in noise figure systems (Abrie, 1985).

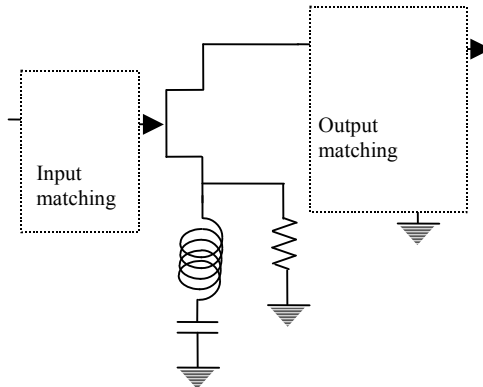


Fig. 23. Typical stand-alone MMIC amplifier with matching networks

The principal characteristics of matching networks that have to be carefully designed are the insertion losses, the reflection coefficient, the frequency band, the noise figure and the power consumption. The topology of the matching network has a great importance for the

overall behaviour and performances of the function. As it is shown, one can distinguish between lumped elements structures (Figure 24) or distributed elements ones (Figure 25).

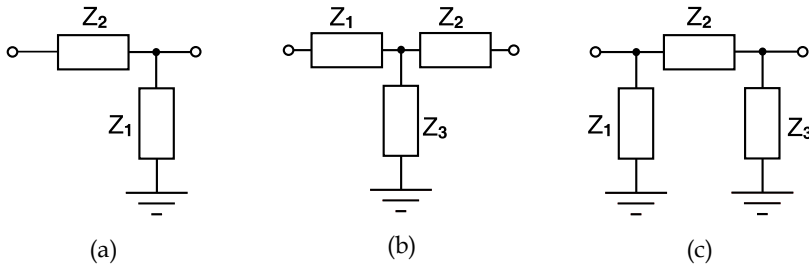


Fig. 24. Lumped topologies of matching networks, (a) two components, (b) T structure, (c)  $\Pi$  structure

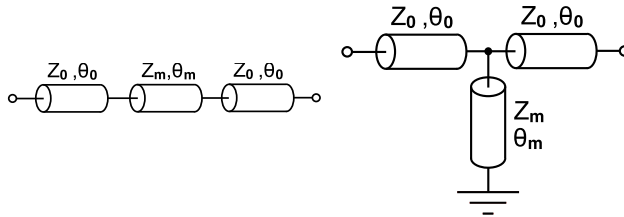


Fig. 25. Distributed topologies of matching networks with characteristic impedance  $Z$  and electric length  $\theta$

The design of the function is strictly equivalent in hybrid or integrated circuit (IC) technology but the size of the circuit is noticeably different since it is typically  $1 \text{ cm}^2$  for the first technology and  $1 \text{ mm}^2$  for the second one. Furthermore, the reachable operating frequencies are higher in IC technology than in hybrid one (typically 25 GHz against 2,5 GHz) but, on the contrary, the insertion losses are typically better in hybrid technology (0,2 dB against 3,5 dB). This last problem is due to the IC substrate RF behaviour and to low quality factors of IC transmission lines.

One of the main advantages of the IC technology for industrial matching networks is its very high reliability rate. Nevertheless, it has to be said that IC structures suffer from non-linearity behaviour at high power, even if some PIN diodes or transistors structures claim to operate up to 40 dBm. In the literature, very few data are reported on noise behaviour of IC matching networks although it shall not be a good point for that kind of structure.

Of course, due to the recent development of multiband and multistandard communications, some tuneable matching networks were realized and the flexibility of IC technology and the control of diodes or transistors brings some advantages in that frame (Sinsky & Westgate, 1997). In fact, the integrated circuit (IC) technology drastically reduces dimension of lumped components so of the devices, the order of magnitude becoming the millimetre. For a classical CMOS IC, such impedance tuning device is quite large but it is usual in RF front-end applications. The tunability is obtained as in hybrid technology, with the ability of switching transistors. For RF distributed components, typical IC substrates, like SOI or float-zone Si substrates are not convenient since the losses are too strong, with sometimes

insertion loss near 10dB. The quality factor of lines is poor because of conductors and dielectric losses. In (McIntosh et al, 1999; De Lima et al, 2000) devices were found from 1GHz to 20GHz. Higher frequency devices are difficult to design because of the dielectrics and conductors losses. Nevertheless, the main advantage of this technology is that the fabrication process is standard, and research prototype can be easily transferred to industry. Recently (Hoarau et al, 2008), have designed an integrated  $\Pi$  structure with a CMOS AMS 0.35 $\mu\text{m}$  technology of varactors and spiral inductors (Figure 26). Simulated results obtained with ADS show that only a quarter of the smith chart is covered on a 1 GHz band around the center frequency of 2 GHz. L structures could also be used to reduce the total number of components and the losses.

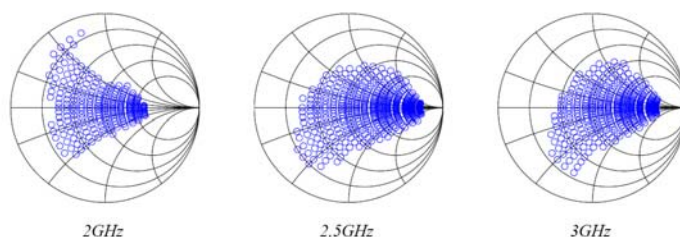


Fig. 26. Smith chart of simulated results of a CMOS AMS 0.35 $\mu\text{m}$  device for 3 frequencies

## 6. References

- Abrie, P. L. D. (1985). The design of impedance-matching networks for radio-frequency and microwave amplifiers, Artech House
- Allers, K.-H., Brenner, P. & Schrenk, M. (2003). Dielectric reliability and material properties of  $\text{Al}_2\text{O}_3$  in metal insulator metal capacitors (MIMCAP) for RF bipolar technologies in comparison to  $\text{SiO}_2$ ,  $\text{SiN}$  and  $\text{Ta}_2\text{O}_5$ , *Proc. of BCTM 2003*, pp. 35-38, Toulouse (France), October 2003
- Arnould, J.-D.; Benech, Ph.; Cremer, S.; Torres, J. & Farcy, A. (2004). RF MIM capacitors using  $\text{Si}_3\text{N}_4$  dielectric in standard industrial BiCMOS technology, *Proc. of IEEE ISIE 04*, pp. 27-30, Ajaccio (France), May 2004
- Berthelot, A. ; Caillat, C. ; Huard, V. ; Barnola, S. ; Boeck, B. ; Del-Puppo, H.; Emonet, N. & Lalanne, F. (2006). Highly Reliable  $\text{TiN}/\text{ZrO}_2/\text{TiN}$  3D Stacked Capacitors for 45 nm Embedded DRAM Technologies, *Proc. of ESSDERC 2006*, pp. 343-346, Montreux, Switzerland, Sept. 2006
- Burghartz, J.N.; Soyuer, M.; Jenkins, K.A.; Kies, M.; Dolan, M.; Stein, K.J.; Malinowski, J. & Haramé, D.L. (1997). Integrated RF components in a SiGe bipolar technology. *IEEE Journal of Solid-State Circuits*, vol. 32, n° 9 (Sept. 1997), pp. 1440-1445
- Büyüktas, K.; Geiselbrechtinger, A.; Decker S. & Koller K. (2009). Simulation and modelling of a high-performance trench capacitor for RF applications. *Semicond. Sci. Technol.* vol. 24, n° 7, (July 2009), 10 p
- Cai, W.Z.; Shastri, S.C.; Azam, M.; Hoggatt, C.; Loechelt, G.H.; Grivna, G.M.; Wen, Y. & Dow, S. (2004). Development and extraction of high-frequency SPICE models for Metal-Insulator-Metal capacitors, *Proc. of ICMTS '04*, pp. 231-234, Hyogo (Japan), March 2004

- Chen Z.; Guo L.; Yu M. & Zhang Y. (2002). A study of MIMIM on-chip capacitor using Cu/SiO<sub>2</sub> interconnect technology. *IEEE Microwave and Wireless Components Letters*, vol. 12, n° 7, July 2002, pp. 246-248
- Cheung, T.S.D. & Long, J.R. (2006). Shielded passive devices for silicon-based monolithic microwave and millimeter-wave integrated circuits, *IEEE Journal of Solid-state circuits*, vol. 41, n° 5, May 2006, pp. 1183-1200.
- Contopanagos, H. & Nassiopoulou, A.G. (2007). Integrated inductors on porous silicon. *Physica status solidi (a)*, vol. 204, n° 5 (Apr. 2007), pp. 1454 - 1458
- Defay, E.; Wolozan, D.; Garrec, P.; Andre, B.; Ulmer, L.; Aid, M.; Blanc, J.-P.; Serret, E.; Delpech, P.; Giraudin, J.-C. ; Guilan, J. ; Pellissier, D. & Ancey, P. (2006). Above IC integrated SrTiO high K MIM capacitors, *Proc. of ESSDERC*, pp. 186-189, Montreux, Switzerland, Sept. 2006
- De Lima, R. N.; Huyart, B.; Bergeault, E. & Jallet, L. (2000). MMIC impedance matching system, *Electronics Letters*, vol. 36 (Aug 2000), pp. 1393-1394
- Gianesello, F.; Gloria, D.; Montusclat, S.; Raynaud, C.; Boret, S.; Clement, C.; Dambrine, G.; Lepilliet, S.; Saguin, F.; Scheer, P.; Benech, P. & Fournier, J.M. (2006). 65 nm RFCMOS technologies with bulk and HR SOI substrate for millimeter wave passives and circuits characterized up to 220 GHz, *Proceedings of Microwave Symposium Digest, 2006. IEEE MTT-S International*, pp. 1927-1930, San Francisco, CA, June 2006.
- Guo P.J. & Chuang H.R. (2008). A 60-GHz Millimeter-wave CMOS RFIC-on-chip Meanderline Planar Inverted-F Antenna for WPAN Applications, *IEEE Trans. Antennas Propagation*, July 2008.
- Hasegawa, H. & Okizaki, H. (1977). MIS and Schottky slow-wave coplanar striplines on GaAs substrates. *IEEE Electronics Letters*, Vol. 13, No. 22, Oct. 1977, pp. 663-664.
- Hoarau, C.; Corrao, N.; Arnould, J.-D. ; Ferrari, P. & Xavier, P. (2008). Complete Design And Measurement Methodology For A RF Tunable Impedance Matching Network", *IEEE Trans. on MTT*, vol. 56, n° 11 (Nov. 2008), pp. 2620-2627
- Huang, K. C. & Edwards, D. J. (2006). 60 GHz multibeam antenna array for gigabit wireless communication networks. *IEEE Trans. Antennas Propagation*, vol. 54, no. 12, pp. 3912-3914, Dec. 2006.
- International technology roadmap for semiconductors (2003).
- Jeannot, S.; Bajolet, A.; Manceau, J.-P.; Cremer, S.; Deloffre, E.; Oddou, J.-P.; Perrot, C.; Benoit, D.; Richard, C.; Bouillon, P. & Bruyere, S. (2007). Toward next high performances MIM generation: up to 30fF/μm<sup>2</sup> with 3D architecture and high-k materials, *Proc. of IEEE IEDM 2007*, pp. 997-1000, Dec. 2007, Washington DC (USA)
- Jiang, H.; Wang, Y.; Yeh, J.-L.A. & Tien, N.C. (2000). Fabrication of high-performance on-chip suspended spiral inductors by micromachining and electroless copper plating. *Proc. of IEEE MTT-S IMS*, pp. 279-282, Boston MA (USA), June 2000
- Kaddour, D.; Issa H.; Abdelaziz, M.; Podevin, F.; Pistono, E.; Duchamp, J.-M. & Ferrari P. (2008). Design guidelines for low-loss slow-wave coplanar transmission lines in RF-CMOS technology, *M. and Opt. Tech. Lett.*, vol. 50, n° 12, Dec. 2008, pp. 3029-3036.
- Kim, K. (2000). Design and Characterisation of Components for Inter and Intra-Chip Wireless Communications. *Dissertation*, University of Florida, Gainesville, 2000.
- Kim, K; Yoon, H. & O. K.K. (2000). On-chip wireless interconnection with integrated antennas, *IEDM Technical Digest*, San Francisco CA (USA), Dec. 2000, pp. 485-488.

- Kim, W. & Swaminathan, M. (2005). Simulation of lossy package transmission lines using extracted data from one-port TDR measurements and nonphysical RLGC model. *IEEE Trans. on Advanced Packaging*, vol. 28, n° 4, Nov. 2005, pp. 736-744.
- Lee, K.Y.; Mohammadi, S.; Bhattacharya, P.K. & Katehi, L.P.B. (2006-1). Compact Models Based on Transmission-Line Concept for Integrated Capacitors and Inductors. *IEEE Trans. on MTT*, vol. 54, n° 12 (Dec. 2006), pp. 4141-4148
- Lee, K.-Y.; Mohammadi, S.; Bhattacharya, P.K. & Katehi, L.P.B. (2006-2). A Wideband Compact Model for Integrated Inductors. *IEEE Microwave and Wireless Components Letters*, vol. 16, n° 9 (Sept. 2006), pp. 490-492
- Lemoigne, P.; Arnould, J.-D.; Bailly, P.-E.; Corrao, N.; Benech, P.; Thomas, M.; Farcy, A. & Torres, J. (2006). Extraction of equivalent electrical models for damascene MIM capacitors in a standard 120 nm CMOS technology for ultra wide band applications, *Proc. of IEEE IECON 2006*, pp. 3036-3039, Paris (France), Nov. 2006
- Masuda, T.; Shiramizu, N.; Nakamura, T. & Washio, K. (2008). Characterization and modelling of microstrip transmission lines with slow-wave effect. *Proceedings of SiRF*, pp. 155-158, Orlando, USA, January 2008.
- McIntosh, C. E.; Pollard, R. D. & Miles, R. E. (1999). Novel MMIC source-impedance tuners for on-wafer microwave noise-parameter measurements. *IEEE Trans. on MTT*, vol. 47, n° 2 (Feb. 1999), pp. 125-131
- Mehrotra V. & Boning D. (2001). Technology scaling impact of variation on clock skew and interconnect, *Proc. of the IEEE 2001 IITC*, San Francisco, CA
- Melendy, D.; Francis, P.; Pichler, C.; Kyuwoon, H.; Srinivasan, G. & Weisshaar, A. (2002). Wide-band Compact Modeling of Spiral Inductors in RFICs, *Digest of Microwave Symposium*, Seattle (USA), pp.717-720, June 2002.
- Milanovic, V.; Ozgur, M.; Degroot, D.C.; Jargon, J.A.; Gaitan, M. & Zaghloul, M.E. (1998). Characterization of Broad-Band Transmission for Coplanar Waveguides on CMOS Silicon Substrates. *IEEE Trans. on MTT*, vol. 46, n° 5, May 1998, pp. 632-640.
- Miller D.A.B. (2002). Optical interconnects to silicon. *IEEE J. Sel. Top. Quantum Electron.*, vol. 6, issue 6 (Nov./Dec. 2002), pp. 1312-1317
- Mondon F. & Blonkowskic S. (2003). Electrical characterisation and reliability of HfO<sub>2</sub> and Al<sub>2</sub>O<sub>3</sub>-HfO<sub>2</sub> MIM capacitors. *Microelectronics Reliability*, vol. 43, n° 8 (August 2003), pp. 1259-1266
- Nesic A.; Nesic, D.; Brankovic, V.; Sasaki, K. & Kawasaki, K. (2001). Antenna Solution for Future Communication Devices in mm-Wave Range. *Microwave Review*, Dec. 2001.
- Nguyen, N.M. & Meyer, R.G. (1990). Si IC-Compatible Inductors and LC Passive Filters. *IEEE Journal of Solid-State Circuits*, vol. 25, n°4 (Aug. 1990), pp. 1028-1031
- Pastore, C.; Giancesello F.; Gloria, D.; Serret, E. & Benech, Ph. (2008-1). Impact of dummy metal filling strategy dedicated to inductors integrated in advanced thick copper RF BEOL. *Microelectronic Engineering*, vol. 85, n° 10 (October 2008), pp. 1962-1966
- Pastore, C.; Giancesello F.; Gloria, D.; Serret, E.; Bouillon, E.; Rauber, P. & Benech, Ph. (2008-2). Double thick copper BEOL in advanced HR SOI RF CMOS technology: Integration of high performance inductors for RF front end module, *Proc. of IEEE International 2008 SOI Conference*, pp. 137-138, Oct. 2008, New York (USA)
- Pozar, D. M. (1998). *Microwave Engineering*, 2nd ed. John Wiley and Sons, Inc. 1998

- Rashid, A.B.M.H.; Watanabe, S.; Kikkawa, T. (2003). Crosstalk isolation of monopole integrated antenna on Si for ULSI wireless interconnect, *Proc. of the IEEE 2003 IITC*, pp. 156-158, San Francisco CA (USA), June 2003.
- Royet, A.-S.; Cuchet, R.; Pellissier, D. & Ancey, P. (2003). On the investigation of spiral inductors processed on Si substrates with thick porous Si layers, *Proc. of ESSDERC*, pp. 111-113, Sept. 2003, Estoril (P)
- Sayag, A.; Levin, S.; Regev, D.; Zfira, D.; Shapira, S.; Goren, D. & Ritter, D. (2008). One stage 24 GHz LNA with 6.4 dB gain and 2.8 dB NF using 0.18  $\mu\text{m}$  CMOS technology and slow wave transmission lines. *Proc. of the 1st Conf. on Microwaves, Communications, Antennas and Electronic Systems (COMCAS)*, pp.1-10, Israel, May 2008.
- Sinsky J. H. & Westgate C. R. (1997). Design of an electronically tunable microwave impedance transformer. *Int. Micro. Symp. Digest*, pp. 647-650, Denver, June 1997
- Souri, S.J.; Banerjee, K.; Mehrotra, A. & Saraswat, K.C. (2000). Multiple Si Layer ICs: Motivation, performance analysis and design implications, *Proc. of the 37th Annual Design Automation Conf.*, pp. 213-220, 2000 Los Angeles CA (USA), June 2000
- Subramaniam, K.; Kordesch, A.V. & Esa, M. (2005). Design and modeling of metal finger capacitors for RF applications. *Proc. APACE 2005*, pp. 293-296, Dec. 2005, Johor (Malaysia)
- Subramaniam, K.; Kordesch, A.V. & Esa, M. (2007). Low and High Frequency Characterization of Metal Finger Capacitors for RFICs, *Proc. of ISSSE '07*, pp. 567-570, Montreal (Canada), July-August 2007
- Sun, X.; Carchon, G.; Kita, Y.; Tani, T. & De Raedt, W. (2006). Experimental Analysis of Above IC Inductor Performance with Different Patterned Ground Shield Configurations and Dummy Metals, *Proc. of the 36th EUMC*, pp. 40-43, Manchester (UK), Sept. 2006
- Tiemeijer, L.; Pijper, R.; Havens, R. & Hubert, O. (2007). Low-loss patterned ground shield interconnect transmission lines in advanced IC processes. *IEEE Trans. on Microwave Theory and Techniques*, vol. 55, n<sup>o</sup>. 3, March 2007, pp. 561-570.
- Triantafyllou, A.; Farcy, A.; Benech, Ph.; Ndagijimana, F., Exshaw, O.; Tinella, C.; Richard, O.; Raynaud, C. & Torres, J. (2005). Intra chip wireless interconnections based on high performances integrated antennas. *Solid State Electronics*, vol. 49, issue 9 (Sept. 2005), pp. 1477-1483
- Volakis J.L. (2007). *Antenna Engineering Handbook*, 4th ed., McGraw Hill Professional, 2007.
- Wang, P. & Kan, E. (2004). High-speed interconnects with underlayer orthogonal metal grids. *IEEE Trans. on advanced packaging*, vol. 27, n<sup>o</sup>. 3, Aug. 2004, pp. 497-507.
- Wang, T.-H. & Itoh, T. (1987). Compact grating structure for application to filters and resonators in monolithic microwave integrated circuits. *IEEE Trans. on Microwave Theory and Techniques*, vol. 35, n<sup>o</sup>. 12, Dec. 1987, pp. 1176-1182.
- Wang, X.; Yin, W.-Y. & Mao, J.-F. (2008). Parameter Characterization of Silicon-Based Patterned Shield and Patterned Ground Shield Coplanar Waveguides, *Proceedings of GSMM08*, pp. 142-145, Nanjing, China, April 2008.
- Yue, C. P. & Wong, S. S. (2000). Physical Modelling of Spiral Inductors on Silicon. *IEEE Trans. on Electron Devices*, vol. 47, n<sup>o</sup> 3 (March 2000.), pp. 560-568



# Negative Refractive Index Composite Metamaterials for Microwave Technology

Nicola Bowler  
*Iowa State University*  
USA

## 1. Introduction

Materials that exhibit negative index (NI) of refraction have several potential applications in microwave technology. Examples include enhanced transmission line capability, power enhancement/size reduction in antenna applications and, in the field of nondestructive testing, improved sensitivity of patch sensors and detection of sub-wavelength defects in dielectrics by utilizing a NI superlens.

Since NI materials do not occur naturally, several approaches exist for creating NI behaviour artificially, by combinations of elements with certain properties that together yield negative refractive index over a certain frequency band. Present realizations of NI materials often employ metallic elements operating below the plasma frequency to provide negative permittivity ( $\epsilon < 0$ ), in combination with a resonator (e.g. a split-ring resonator) that provides negative permeability ( $\mu < 0$ ) near resonance. The high dielectric loss exhibited by metals can severely dampen the desired NI effect. Metallic metamaterials also commonly rely on periodic arrays of the elements, posing a challenge in fabrication. A different approach is to employ purely dielectric materials to obtain NI behaviour by, for example, relying on resonant modes in dielectric resonators to provide  $\epsilon < 0$  and  $\mu < 0$  near resonance. Then, the challenge is to design a metamaterial such that the frequency bands in which both  $\epsilon$  and  $\mu$  are negative overlap, giving NI behaviour in that band. Two potential advantages to this approach compared with NI materials based on metallic elements are i) decreased losses and ii) simplified fabrication processes since the NI effect does not necessarily rely on periodic arrangement of the elements.

This chapter explains the physics underlying the design of purely dielectric NI metamaterials and will discuss some ways in which these materials may be used to enhance various microwave technologies.

## 2. Basic Theory of Left-Handed Light

### 2.1 Effective permittivity and permeability of a composite material

In this chapter, the design of materials with negative refractive index,  $n < 0$ , will proceed on the basis of achieving negative real parts of effective permittivity,  $\epsilon$ , and permeability,  $\mu$ , in a

composite material. Such a material is termed ‘double-negative’ or ‘DNG’. First, let’s discuss what is meant by *effective* parameters  $\varepsilon$  and  $\mu$ .

Adopting notation in which the vector fields are denoted by bold font and second-order tensors by a double overline, the constitutive relations can be written as

$$\mathbf{D} = \bar{\bar{\varepsilon}} \cdot \mathbf{E} \quad \text{and} \quad \mathbf{B} = \bar{\bar{\mu}} \cdot \mathbf{H}, \quad (1)$$

in which  $\mathbf{D}$  is electric displacement,  $\mathbf{E}$  is the electric field,  $\mathbf{B}$  is the magnetic induction field and  $\mathbf{H}$  is the magnetic field. In the following development, however, it will be assumed that the materials are isotropic so that  $\varepsilon$  and  $\mu$  are scalar. Then,

$$\mathbf{D} = \varepsilon \mathbf{E} \quad \text{and} \quad \mathbf{B} = \mu \mathbf{H}. \quad (2)$$

The assumption of isotropic properties holds for cubic lattices and entirely random structures of spherical particles embedded in a matrix, for example.

It is often convenient to work in terms of dimensionless relative permittivity and permeability,  $\varepsilon_r$  and  $\mu_r$ , respectively, which are related to  $\varepsilon$  and  $\mu$  by the free-space values  $\varepsilon_0 = 8.854 \times 10^{-12}$  F/m and  $\mu_0 = 4\pi \times 10^{-7}$  H/m as follows;

$$\varepsilon = \varepsilon_r \varepsilon_0 \quad \text{and} \quad \mu = \mu_r \mu_0. \quad (3)$$

## 2.2 Double-negative means negative refractive index

Considering the following familiar definition of the refractive index,

$$n = \sqrt{\varepsilon_r \mu_r}, \quad (4)$$

it is not immediately obvious why, in the case of a double-negative (DNG) medium, with  $\text{Re}\{\varepsilon\} < 0$  and  $\text{Re}\{\mu\} < 0$  that  $n < 0$  as well. The answer lies in the fact that  $\varepsilon_r$ ,  $\mu_r$  and  $n$  are, in general, complex quantities. Practically speaking,  $\varepsilon_r$  and  $\mu_r$  exhibit complex behaviour at frequencies close to a resonance or relaxation. These kinds of processes exist at microwave frequencies in many materials and some of them will be discussed in following sections of this chapter. So, given that  $\varepsilon_r$  and  $\mu_r$  may be complex, write

$$\varepsilon_r = |\varepsilon_r| e^{-j\theta} \quad \text{and} \quad \mu_r = |\mu_r| e^{-j\phi}, \quad (5)$$

where it is assumed that fields are varying time-harmonically as  $\text{Re}\{e^{j\omega t}\}$  with  $\omega = 2\pi f$  the angular frequency and  $f$  the frequency in Hz. Then, from (4),

$$n = \sqrt{|\varepsilon_r| |\mu_r|} e^{\pm j(\theta+\phi)/2}. \quad (6)$$

From (6) it is clear that in order to determine the sign of  $n$  when  $\text{Re}\{\varepsilon\} < 0$  and  $\text{Re}\{\mu\} < 0$ , the phase angles  $\theta$  and  $\phi$  must be considered.

Notice, first, that if  $\text{Re}\{\varepsilon\} < 0$  and  $\text{Re}\{\mu\} < 0$  then both  $\theta$  and  $\phi$  lie between the limits  $\pi/2$  and  $3\pi/2$ . [This can be shown by employing Euler’s theorem  $e^{-j\psi} = \cos\psi - j \sin\psi$  and considering the properties of the cosine function.] This also means that

$$\frac{\pi}{2} < \frac{\theta + \phi}{2} < \frac{3\pi}{2}. \quad (7)$$

Secondly, the condition that is required for the medium to be passive, or non-absorbing, will be applied. This has the effect of further restricting the range of  $(\theta + \phi)/2$ . In the case of a

passive medium,  $\text{Im}\{n\} < 0$ . Again from Euler's theorem but now considering the properties of the sine function, the restriction that the imaginary part of  $n$  is negative and taking the appropriate root from (6) leads to the condition

$$0 < \frac{\theta + \phi}{2} < \pi. \quad (8)$$

Finally it can be seen that satisfaction of both (7) and (8) requires

$$\frac{\pi}{2} < \frac{\theta + \phi}{2} < \pi \quad (9)$$

and, due to the fact that  $\cos[(\theta + \phi)/2] < 0$  when (9) applies, it follows that

$$\text{Re}\{n\} = \sqrt{|\varepsilon_r||\mu_r|} \cos[(\theta + \phi)/2] < 0 \quad (10)$$

for a passive medium in which  $\text{Re}\{\varepsilon\} < 0$  and  $\text{Re}\{\mu\} < 0$ .

In contrast with the refractive index, the impedance of a medium, defined

$$Z = \sqrt{\frac{\mu_r \mu_0}{\varepsilon_r \varepsilon_0}}, \quad (11)$$

retains its positive sign in a DNG medium (Caloz et al., 2001; Ziolkowski & Heyman, 2001).

### 2.3 Wave propagation in a negative-refractive-index medium

We have shown that a double-negative medium has a negative index of refraction. What consequences follow for the propagation of an electromagnetic wave in such a medium?

A negative-refractive-index medium supports *backward wave propagation* described by a left-handed vector triad of the electric field  $\mathbf{E}$ , magnetic field  $\mathbf{H}$ , and wave vector  $\mathbf{k}$  (Veselago, 1968; Caloz et al., 2001). Both  $\mathbf{k}$  and the phase velocity vector  $\mathbf{v}_p$  exhibit a sign opposite to that which they possess in a conventional right-handed medium (RHM). This has led to such materials also being known as left-handed materials (LHMs), but it should be noted that left-handedness is not a necessary nor sufficient condition for negative refraction (Zhang & Mascarenhas, 2007). Regarding the Poynting vector  $\mathbf{S}$  and the group velocity  $\mathbf{v}_g$  in an LHM,  $\mathbf{E}$ ,  $\mathbf{H}$  and  $\mathbf{S}$  form a right-handed triad and  $\mathbf{S}$  still points in the same direction as the propagation of energy, as in an RHM. Thus, in an LHM,  $\mathbf{v}_p$  and  $\mathbf{v}_g$  are of opposite sign and the wave fronts propagate towards the source.

Now let's consider how Snell's law of refraction applies in the case of a NI medium. Recalling that the ratio of the sine functions of the angles of incidence and refraction (to the surface normal) of a wave crossing an interface between two media is equivalent to the ratio of the velocities of the wave in the two media, Snell's Law can be expressed as

$$\frac{\sin \theta_1}{\sin \theta_2} = \frac{v_1}{v_2} = \frac{n_2}{n_1} \quad (12)$$

or, equivalently, as  $n_1 \sin \theta_1 = n_2 \sin \theta_2$ . A conventional case in which  $n_2 > n_1 > 0$  is illustrated in Fig. 1a). In the case of one of the media having negative refractive index, then the refracted wave propagates on the same side of the surface normal as the incident wave. This is illustrated in Fig. 1b) for the case  $n_2 = -n_1$ , for which  $\sin \theta_2 = -\sin \theta_1$  and  $\theta_2 = -\theta_1$  due to the odd nature of the sine function. In the next section it will be shown how a planar

slab of NI material can form a focusing device for electromagnetic waves (Veselago, 1968). Not only that, but we will see how a planar slab of negative index material with the property  $n_2 = -n_1$  forms a so-called 'perfect' lens in the sense that it overcomes the limitations of conventional optics by focusing all Fourier components of an incident wave including evanescent components that are usually lost to damping (Pendry, 2000).

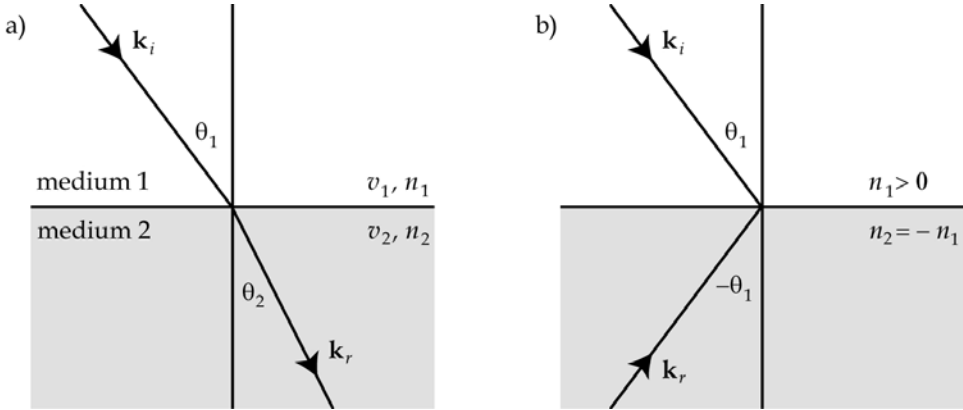


Fig. 1. Snell's Law of Refraction illustrated for a) a conventional case in which  $n_2 > n_1 > 0$  and b) the case in which medium 2 has negative refractive index,  $n_2 = -n_1$ .

#### 2.4 Negative-refractive-index medium as a planar lens

According to classical optics, the resolving power of a conventional optical lens is fundamentally limited in a manner that is related to the wavelength of the light passing through it. This limitation cannot be overcome by improving the quality of the lens. Consider a  $z$ -directed electromagnetic wave incident on a conventional lens whose axis is parallel to the  $z$ -direction. From Maxwell's equations it can be shown that the wavenumber in the direction of propagation,  $k_z$ , is given by

$$k_z = \sqrt{(\omega/c)^2 - k_x^2 - k_y^2}, \quad (\omega/c)^2 > k_x^2 + k_y^2, \quad (13)$$

for relatively small values of the transverse wavevector  $k_x^2 + k_y^2$ . In (13),  $\omega$  is the angular frequency,  $c$  the speed, and  $k_x$  and  $k_y$  are  $x$ - and  $y$ -directed Fourier components of the electromagnetic wave. The lens operates by correcting the phase of each of the Fourier components of the wave so that they are brought to a focus some distance beyond the lens, producing an image of the source. The condition  $(\omega/c)^2 > k_x^2 + k_y^2$  given in (13) provides the restriction on the resolving power of the lens because the transverse wavevector may not exceed a certain maximum magnitude;  $k_{\max} = \omega/c$ . This means that the best resolution of the lens,  $\Delta$ , is limited to (cannot be smaller than)

$$\Delta \approx \frac{2\pi}{k_{\max}} = \frac{2\pi c}{\omega} = \lambda \quad (14)$$

where  $\lambda$  is the wavelength.

Some time ago it was shown that a planar slab of NI material has the ability to behave as a lens, bringing propagating light to a focus both within and beyond the slab (Veselago, 1968). This can be shown easily by applying Snell's Law in the manner of Fig. 1b) to two parallel surfaces. As illustrated in Fig. 2, light originating in a medium with refractive index  $n_1 > 0$ , and from a source located at distance  $d_1$  from the first face of a NI slab with thickness  $d_2$  and negative index  $n_2 = -n_1$ , is refracted to a focus both *within* the slab (at distance  $d_1$  from the first face) and again on emerging from the slab, at distance  $d_2 - d_1$  from the second face.

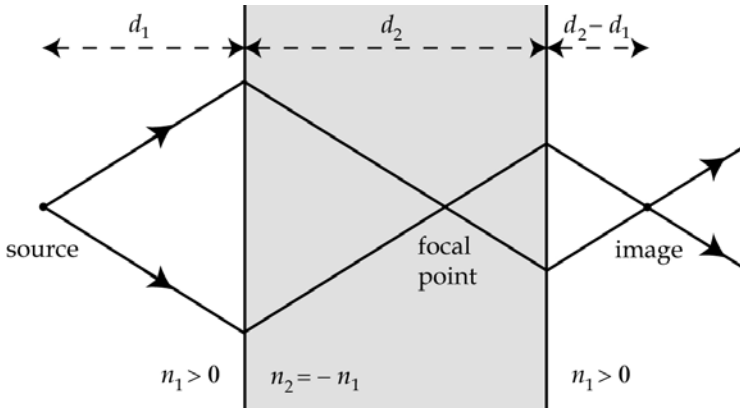


Fig. 2. Light focusing by a planar lens formed from a slab of NI material. The z-direction is from left to right.

More recently, it was pointed out that not only are the propagating components of the light represented by (13) brought to a focus by the lens illustrated in Fig. 2, but so are the evanescent components that are lost to damping in a conventional optical lens (Pendry, 2000). This has led to adoption of the term 'perfect lens' to describe the lens of Fig. 2. The real wavenumber expressed in (13) represents only propagating waves. Evanescent waves are described by the other inequality  $(\omega/c)^2 < k_x^2 + k_y^2$ , in other words for relatively large values of  $k_x^2 + k_y^2$ . Rather than as in (13),  $k_z$  is now imaginary, written as

$$k_z = -j \sqrt{k_x^2 + k_y^2 - (\omega/c)^2}, \quad (\omega/c)^2 < k_x^2 + k_y^2, \quad (15)$$

and the wave is evanescent, decaying exponentially with  $z$ . The phase corrective behaviour of a conventional lens works only for the propagating components of the wave represented in (13) because it cannot restore the reduced amplitude of the evanescent components. The focusing mechanism of the planar NI lens is, however, able to cancel the decay of evanescent waves. Surprisingly, evanescent waves emerge from the second face of the lens enhanced in amplitude (Pendry, 2000).

Another important practical feature is exhibited by the perfect lens. Since the condition  $n_2 = -n_1$  derives from the relations  $\epsilon_2 = -\epsilon_1$  and  $\mu_2 = -\mu_1$  between the material parameters of the two media, their impedances are perfectly matched;  $Z = \sqrt{\mu_1/\epsilon_1} = \sqrt{\mu_2/\epsilon_2}$ . In other words, there is no reflection loss at the faces of an ideal perfect lens - it is a perfect transmitter. Obviously this is a result of tremendous practical significance.

Now that we have considered some of the fundamental behaviours of an NI material, we move to consider how such a material might be constructed.

### 3. Dielectric Resonator Composites

#### 3.1 Dielectric resonators for NI metamaterials

Materials composed of especially engineered components that together exhibit properties and behaviours not shown by the individual constituents are often termed metamaterials (Sihvola, 2002). As mentioned in the introduction to this chapter, many experimental demonstrations of NI materials to date have relied upon metallic elements to achieve  $\epsilon < 0$  below the plasma frequency of the metal, and other specially shaped metallic elements to achieve negative permeability  $\mu < 0$  due to resonance that is created in or between them in a certain frequency band (Smith et al., 2000; Zhou et al., 2006). In a contrasting approach, the possibility of forming an isotropic DNG metamaterial by collecting together a three-dimensional array of non-conductive, magneto-dielectric spheres has also been proposed (Holloway et al., 2003). In that case, a simple-cubic array of spheres was analyzed and DNG behaviour predicted at frequencies just above those of the Mie resonances for TE and TM mode polarizations, which were made to occur at similar frequencies in order to give  $\text{Re}\{\epsilon\} < 0$  and  $\text{Re}\{\mu\} < 0$  in overlapping frequency bands.

Of greatest relevance to this discussion, it has been shown that an array of purely dielectric spheres can be made to exhibit isotropic  $\text{Re}\{\mu\} < 0$  (Wheeler et al., 2005). Further, two complementary approaches have been reported, showing that isotropic DNG behaviour can be achieved in a system composed of two interpenetrating lattices of dielectric spheres. In the first design, TE and TM resonances were excited at similar frequencies in spheres with different radius but equal permittivity (Vendik et al., 2006; Jylhä et al., 2006). In the second case, two sets of spheres with the same radius but different permittivity were employed to achieve the same effect (Ahmadi & Mosallaei, 2008). These two schemes were adopted because the fundamental electric resonance in a dielectric sphere naturally occurs at higher frequency than the fundamental magnetic resonance (Bohren & Huffman, 1983). In order to achieve overlapping bands of  $\text{Re}\{\epsilon\} < 0$  and  $\text{Re}\{\mu\} < 0$ , the resonance frequencies  $\omega_r$  of the two sphere types must be made to be similar. From the analysis of Mie theory it is found that  $\omega_r \propto 1/(a\sqrt{\epsilon_{r1}})$ , where  $a$  is the sphere radius and  $\epsilon_{r1}$  its relative permittivity. This allows tuning of  $\omega_r$  by adjusting  $a$  and/or  $\epsilon_{r1}$ .

#### 3.2 Dielectric resonators

Not only are spherical resonators good candidates for dielectric NI metamaterials, but other shapes, in particular cylinders, have been studied and employed in various microwave applications for some time. A general discussion of the properties of dielectric resonators of various kinds may be found in the text edited by Kajfez & Guillon (1986). A specific example of the use of cylindrical dielectric resonators to provide  $\text{Re}\{\mu\} < 0$  in a NI prism was demonstrated recently (Ueda et al., 2007).

#### 3.3 Plane wave scattering by a dielectric sphere

A dielectric sphere in the path of an incident plane electromagnetic wave gives rise to a scattered wave that exhibits an infinite number of resonances due to resonant modes excited

in the sphere. The frequencies at which these resonances occur depend on the permittivity and radius of the sphere, and the wavelength of the incident wave. As mentioned above, these resonances in  $\epsilon$  and  $\mu$  can be exploited to achieve DNG behaviour in a composite metamaterial. In order to design a composite that exhibits DNG behaviour, it is useful to understand the theory of plane wave scattering by a dielectric sphere.

First solved by Gustav Mie (Mie, 1908), a modern description of the theory of plane wave scattering by a sphere has been given by Bohren & Huffman (1983). In the context of designing NI metamaterials by collecting together an array of dielectric spheres, Mie's theory provides a foundation for understanding how the material parameters of the constituents, the particle radius and permittivity and the matrix permittivity, affect the frequencies and bandwidths of the electric and magnetic resonances that lead to  $\epsilon < 0$  and  $\mu < 0$ . For this reason it is instructive to study the theory, although it should be kept in mind that the development is for an isolated sphere. In the case of a composite in which the spherical inclusions are quite disperse (i.e. the volume fraction is low, around 0.3 or smaller, and the particles are well-separated), predictions of the frequencies of the resonant modes according to Mie theory can be expected to be quite numerically accurate. If the system is not dilute, however, the predictions of Mie theory can provide qualitative guidelines for DNG metamaterials design, but inter-particle interaction effects should be taken into account to achieve numerical accuracy. Here, the main features of Mie theory are outlined. For full details the reader is referred to Bohren & Huffman (1983).

### 3.3.1 Governing equations and general solution

We begin with the equations that govern a time-harmonic electromagnetic field in a linear, isotropic, homogeneous medium. Both the sphere and the surrounding medium are assumed to have these properties. From Maxwell's equations, the electric and magnetic fields must satisfy the wave equation;

$$(\nabla^2 + k^2)\mathbf{E} = 0, \quad (\nabla^2 + k^2)\mathbf{H} = 0, \quad (16)$$

in which  $k^2 = \omega^2\epsilon\mu$ . They must also be divergence-free;

$$\nabla \cdot \mathbf{E} = 0, \quad \nabla \cdot \mathbf{H} = 0 \quad (17)$$

and are related to each other as follows;

$$\nabla \times \mathbf{E} = -j\omega\mu\mathbf{H}, \quad \nabla \times \mathbf{H} = j\omega\epsilon\mathbf{E}. \quad (18)$$

The solution proceeds by constructing two vector functions,  $\mathbf{M}$  and  $\mathbf{N}$ , that both satisfy the vector wave equation and are defined in terms of the same *scalar* function  $\psi$  and an arbitrary constant vector  $\mathbf{c}$ . Through these constructions, the problem of finding solutions to the vector field equations (16), (17) and (18) reduces to the simpler problem of solving the scalar wave equation  $(\nabla^2 + k^2)\psi = 0$ . Later, the vector functions  $\mathbf{M}$  and  $\mathbf{N}$  will be employed to express an incident plane wave in terms of an infinite sum of vector spherical harmonics. This facilitates the application of interface conditions at the surface of the scattering sphere and allows the solution to be determined.

Construct the vector function  $\mathbf{M} = \nabla \times (\mathbf{c}\psi)$  for which, by identity,  $\nabla \cdot \mathbf{M} = 0$ . Employing vector identity relations it can be shown that

$$(\nabla^2 + k^2)\mathbf{M} = \nabla \times [\mathbf{c}(\nabla^2 + k^2)\psi]. \quad (19)$$

This means that  $\mathbf{M}$  satisfies the vector wave equation if  $\psi$  is a solution of the scalar wave equation. Now construct a second vector function  $\mathbf{N} = \frac{1}{k}\nabla \times \mathbf{M}$ , that also satisfies the vector wave equation

$$(\nabla^2 + k^2)\mathbf{N} = 0 \quad (20)$$

and is also related to  $\mathbf{M}$  by  $\nabla \times \mathbf{N} = k\mathbf{M}$ . Through these definitions it is seen that  $\mathbf{M}$  and  $\mathbf{N}$  exhibit all the required properties of an electromagnetic field;

- Both  $\mathbf{M}$  and  $\mathbf{N}$  satisfy the vector wave equation.
- They are divergence free.
- The curl of  $\mathbf{M}$  is proportional to  $\mathbf{N}$ .
- The curl of  $\mathbf{N}$  is proportional to  $\mathbf{M}$ .

The solution for plane wave scattering by a sphere will now be obtained by solving the scalar wave equation for  $\psi$ , from which the electromagnetic field represented by  $\mathbf{M}$  and  $\mathbf{N}$  can be obtained via their definitions in terms of  $\psi$ , given above.

Before continuing, note that  $\psi$  is often termed a *generating function* for the *vector harmonics*  $\mathbf{M}$  and  $\mathbf{N}$ , whereas  $\mathbf{c}$  is termed the *guiding* or *pilot* vector. It is also useful to note that  $\mathbf{M} = -\mathbf{c} \times \nabla\psi$ , which implies that  $\mathbf{M}$  is directed perpendicular to the pilot vector.

The specific choice of pilot vector is guided by the geometry of the particular problem at hand. In the case of plane wave scattering by a sphere centered at the origin of a spherical coordinate system, a natural choice for the pilot vector is the radial vector  $\mathbf{r}$ . Then,

$$\mathbf{M} = \nabla \times (\mathbf{r}\psi) \quad (21)$$

is everywhere tangential to a spherical surface defined by  $|\mathbf{r}| = \text{constant}$ , and  $\psi$  is selected to be a solution of the scalar wave equation in spherical polar coordinates. Assuming a particular solution  $\psi(r, \theta, \varphi) = R(r)\Theta(\theta)\Phi(\varphi)$ , the scalar wave equation in spherical polar coordinates can be separated into three equations;

$$\begin{aligned} \frac{d^2\Phi}{d\varphi^2} + m^2\Phi &= 0 \\ \frac{1}{\sin\theta} \frac{d}{d\theta} \left( \sin\theta \frac{d\Theta}{d\theta} \right) + \left[ n(n+1) - \frac{m^2}{\sin^2\theta} \right] \Theta &= 0 \\ \frac{d}{dr} \left( r^2 \frac{dR}{dr} \right) + [k^2r^2 - n(n+1)]R &= 0 \end{aligned} \quad (22)$$

where the constants of separation  $m$  and  $n$  are to be determined by other conditions that  $\psi$  must satisfy. The linearly independent solutions for  $\Phi$  are

$$\Phi_e = \cos m\varphi \quad \text{and} \quad \Phi_o = \sin m\varphi \quad (23)$$

in which the subscripts e and o denote even and odd functions of  $\varphi$ , respectively. Solutions for  $\Theta$  that are finite at  $\theta = 0$  and  $\pi$  are associated Legendre functions of the first kind;  $P_n^m(\cos\theta)$  of degree  $n$  and order  $m$  where  $n = m, m+1, \dots$ . When  $m = 0$  the  $P_n(\cos\theta)$  are the Legendre polynomials. For the dependence on the radial variable  $r$ , the solution is obtained by introducing the dimensionless variable  $\rho = kr$  and the function  $R' = R\sqrt{\rho}$ . Then the third of the group of equations (22) becomes



$$\rho \frac{d}{d\rho} \left( \rho \frac{dR'}{d\rho} \right) + \left[ \rho^2 - \left( n + \frac{1}{2} \right)^2 \right] R' = 0 \quad (24)$$

with solutions being the Bessel functions of the first and second kinds,  $J_\nu$  and  $Y_\nu$ , with half-integer order  $\nu = n + 1/2$ . The fact that the order is half-integer indicates that the linearly independent solutions of (24) are the *spherical* Bessel functions

$$j_n(\rho) = \sqrt{\frac{\pi}{2\rho}} J_{n+1/2}(\rho) \quad \text{and} \quad y_n(\rho) = \sqrt{\frac{\pi}{2\rho}} Y_{n+1/2}(\rho). \quad (25)$$

The  $j_n(\rho)$  are finite as  $\rho \rightarrow 0$  whereas the  $y_n(\rho)$  are singular as  $\rho \rightarrow 0$ . For example,

$$j_0(\rho) = \frac{\sin \rho}{\rho}, \quad j_1(\rho) = \frac{\sin \rho}{\rho^2} - \frac{\cos \rho}{\rho}, \quad (26)$$

$$y_0(\rho) = -\frac{\cos \rho}{\rho} \quad \text{and} \quad y_1(\rho) = -\frac{\cos \rho}{\rho^2} - \frac{\sin \rho}{\rho}. \quad (27)$$

From these first two orders of the spherical Bessel functions, the higher-order functions can be generated by means of recurrence relations. At this point it is useful to define the spherical Bessel functions of the third kind, also known as spherical Hankel functions, that shall be useful in later developments;

$$h_n^{(1)}(\rho) = j_n(\rho) + jy_n(\rho) \quad \text{and} \quad h_n^{(2)}(\rho) = j_n(\rho) - jy_n(\rho). \quad (28)$$

For the reader who is not familiar with the properties of these functions, an excellent resource is the handbook edited by Abramowitz & Stegun (1972).

Having obtained linearly independent solutions to the set of equations (22), we can write down two linearly independent functions that satisfy the scalar wave equation in spherical polar coordinates;

$$\psi_{emn} = z_n(kr) P_n^m(\cos \theta) \cos m\phi \quad \text{and} \quad \psi_{omn} = z_n(kr) P_n^m(\cos \theta) \sin m\phi. \quad (29)$$

In (29),  $z_n(kr)$  represents any of the four spherical Bessel functions given in (25) and (28). Any function that satisfies the scalar wave equation in spherical polar coordinates may be expanded as an infinite series in the functions (29), because these functions form a complete set. Write the vector spherical harmonics generated by  $\psi_{emn}$  and  $\psi_{omn}$  as

$$\mathbf{M}_{emn} = \nabla \times (\mathbf{r}\psi_{emn}), \quad \mathbf{M}_{omn} = \nabla \times (\mathbf{r}\psi_{omn}), \quad (30)$$

$$\mathbf{N}_{emn} = \frac{1}{k} \nabla \times \mathbf{M}_{emn} \quad \text{and} \quad \mathbf{N}_{omn} = \frac{1}{k} \nabla \times \mathbf{M}_{omn}. \quad (31)$$

Now, any solution of the field equations can be expanded in an infinite series of the functions  $\mathbf{M}_{emn}$ ,  $\mathbf{M}_{omn}$ ,  $\mathbf{N}_{emn}$  and  $\mathbf{N}_{omn}$ . This is how the problem of plane wave scattering by a sphere can be solved. Note again that, as a consequence of choosing  $\mathbf{r}$  as the pilot vector,  $\mathbf{M}_{emn}$  and  $\mathbf{M}_{omn}$  are transverse to the radial direction, with only  $\hat{\theta}$ - and  $\hat{\phi}$ -components, whereas  $\mathbf{N}_{emn}$  and  $\mathbf{N}_{omn}$  exhibit a radial component as well.

### 3.3.2 Expansion of a plane wave in vector spherical harmonics

Forming the relationship between an incident plane wave, that is most easily described in a Cartesian coordinate system, and a scatterer whose boundary is a sphere, that is obviously

best described in a spherical coordinate system, is the central issue in the solution of plane wave scattering by a sphere. The development of the previous section, in which it was shown that the vector spherical harmonics  $\mathbf{M}_{emn}$ ,  $\mathbf{M}_{omn}$ ,  $\mathbf{N}_{emn}$  and  $\mathbf{N}_{omn}$  form a complete set that can represent any function that satisfies the scalar wave equation in spherical polar coordinates, will now be employed to represent the plane wave incident on the sphere. In this way, application of the interface conditions at the sphere boundary becomes straightforward.

Consider a plane,  $x$ -polarized wave propagating in the  $z$ -direction and incident on an arbitrary sphere;

$$\mathbf{E}^i = E_0 e^{-jkz} \hat{x} = E_0 e^{-jkr \cos \theta} \hat{x}. \quad (32)$$

Expand (32) in vector spherical harmonics. In general,

$$\mathbf{E}^i = \sum_{m=0}^{\infty} \sum_{n=m}^{\infty} (B_{emn} \mathbf{M}_{emn} + B_{omn} \mathbf{M}_{omn} + A_{emn} \mathbf{N}_{emn} + A_{omn} \mathbf{N}_{omn}), \quad (33)$$

but various orthogonality relationships imply that many of these terms are identically zero (Bohren & Huffman, 1983). In fact, the only terms that are non-zero are those with coefficients  $B_{o1n}$  and  $A_{e1n}$ . Further, the incident field is finite at the origin of the spherical coordinate system, which means that the appropriate spherical Bessel function in the generating functions  $\psi_{o1n}$  and  $\psi_{e1n}$  is  $j_n(kr)$ . Indicating the presence of  $j_n(kr)$  in the generating functions by superscript (1),  $\mathbf{E}^i$  can be written

$$\mathbf{E}^i = \sum_{n=1}^{\infty} (B_{o1n} \mathbf{M}_{o1n}^{(1)} + A_{e1n} \mathbf{N}_{e1n}^{(1)}). \quad (34)$$

To complete the expression of  $\mathbf{E}^i$  in terms of vector spherical harmonics, it remains to evaluate the coefficients  $B_{o1n}$  and  $A_{e1n}$ . Evaluation of the appropriate integrals (Bohren & Huffman, 1983) shows that  $B_{o1n}$  and  $A_{e1n}$  differ only by the factor  $j$ . Finally, the desired expansion of the plane wave is found as

$$\mathbf{E}^i = \sum_{n=1}^{\infty} E_n (\mathbf{M}_{o1n}^{(1)} + j \mathbf{N}_{e1n}^{(1)}) \quad (35)$$

and

$$\mathbf{H}^i = -\frac{k}{\omega \mu} \sum_{n=1}^{\infty} E_n (\mathbf{M}_{e1n}^{(1)} - j \mathbf{N}_{o1n}^{(1)}) \quad (36)$$

with

$$E_n = E_0 (-j)^n \frac{2n+1}{n(n+1)}. \quad (37)$$

$\mathbf{H}^i$ , (36), was obtained by taking the curl of  $\mathbf{E}^i$ , (35), according to (18).

### 3.3.3 The scattered field and scattering coefficients

Assume the scatterer to be a homogeneous, isotropic sphere with radius  $a$ , permittivity  $\epsilon_1$  and permeability  $\mu_1$ . In order to apply interface conditions at the surface of the sphere, it is

necessary to express the electromagnetic field internal to the sphere, and the electromagnetic field scattered by it, in terms of vector spherical harmonics.

As in the case of the incident field, the field internal to the sphere is finite at the origin of the spherical coordinate system and, therefore,  $j_n(kr)$  is the appropriate spherical Bessel function in the generating functions  $\psi_{o1n}$  and  $\psi_{e1n}$ . Denoting the fields internal to the sphere by the superscript *int*,

$$\mathbf{E}^{int} = \sum_{n=1}^{\infty} E_n \left( c_n \mathbf{M}_{o1n}^{(1)} + j d_n \mathbf{N}_{e1n}^{(1)} \right) \quad (38)$$

and

$$\mathbf{H}^{int} = -\frac{k_1}{\omega \mu_1} \sum_{n=1}^{\infty} E_n \left( d_n \mathbf{M}_{e1n}^{(1)} - j c_n \mathbf{N}_{o1n}^{(1)} \right) \quad (39)$$

where the wavenumber inside the sphere is given by  $k_1^2 = \omega^2 \epsilon_1 \mu_1$ .

The scattered field external to the sphere, denoted by the superscript *s*, is appropriately expressed in terms of the spherical Hankel functions of the first kind  $h_n^{(1)}$ . This is the correct choice because both  $j_n$  and  $y_n$  are well-behaved outside the sphere, and at large distances  $h_n^{(1)}$  represents an outgoing spherical wave according to

$$h_n^{(1)}(kr) \sim -j^n \frac{e^{-jkr}}{jkr}, \quad kr \gg n^2. \quad (40)$$

Then,

$$\mathbf{E}^s = -\sum_{n=1}^{\infty} E_n \left( b_n \mathbf{M}_{o1n}^{(3)} + j a_n \mathbf{N}_{e1n}^{(3)} \right) \quad (41)$$

and

$$\mathbf{H}^s = \frac{k}{\omega \mu} \sum_{n=1}^{\infty} E_n \left( a_n \mathbf{M}_{e1n}^{(3)} - j b_n \mathbf{N}_{o1n}^{(3)} \right) \quad (42)$$

in which the superscript (3) indicates that the radial dependence of the generating functions is specified by  $h_n^{(1)}$ . With the incident, internal and scattered fields now all expressed in terms of vector spherical harmonics, in (35) through (42), it is now possible to apply interface conditions and determine the coefficients  $a_n$ ,  $b_n$ ,  $c_n$  and  $d_n$ .

Continuity of the tangential components of  $\mathbf{E}$  and  $\mathbf{H}$  at the sphere boundary may be expressed

$$(\mathbf{E}^i + \mathbf{E}^s - \mathbf{E}^{int}) \times \hat{r} = (\mathbf{H}^i + \mathbf{H}^s - \mathbf{H}^{int}) \times \hat{r} = 0. \quad (43)$$

Applying these conditions to the field expansions leads to a system of linear equations that may be solved readily for the coefficients  $a_n$ ,  $b_n$ ,  $c_n$  and  $d_n$ . Here, only  $a_n$  and  $b_n$  are given explicitly since they are important for the application of interest in this chapter; determining the bulk response of a composite material formed from a mixture of spherical scatterers embedded in a supporting matrix. Similar expressions exist for  $c_n$  and  $d_n$  (Bohren & Huffman, 1983). To express the coefficients  $a_n$  and  $b_n$  compactly it is convenient to

introduce i) the dimensionless size parameter  $\alpha = ka = 2\pi na/\lambda$ , in which  $n$  is the refractive index of the medium external to the sphere and ii) the relative refractive index defined as the ratio of that in the sphere to that external to the sphere;  $N = n_1/n$ . After some manipulation,

$$a_n = \frac{\mu N^2 j_n(N\alpha) [\alpha j_n(\alpha)]' - \mu_1 j_n(\alpha) [N\alpha j_n(N\alpha)]'}{\mu N^2 j_n(N\alpha) [\alpha h_n^{(1)}(\alpha)]' - \mu_1 h_n^{(1)}(\alpha) [N\alpha j_n(N\alpha)]'} \quad (44)$$

and

$$b_n = \frac{\mu_1 j_n(N\alpha) [\alpha j_n(\alpha)]' - \mu j_n(\alpha) [N\alpha j_n(N\alpha)]'}{\mu_1 j_n(N\alpha) [\alpha h_n^{(1)}(\alpha)]' - \mu h_n^{(1)}(\alpha) [N\alpha j_n(N\alpha)]'}. \quad (45)$$

In (44) and (45) the prime denotes that the derivative with respect to the argument of the Bessel function should be taken. This pair of equations is also commonly written in terms of the Riccati-Bessel functions,  $\rho z_n(\rho)$ , where  $z_n(\rho)$  represents any of the four spherical Bessel functions given in (25) and (28).

In general, the scattered field is a superposition of normal modes. Due to the forms of (44) and (45), however, there are conditions under which one particular mode may dominate, when the denominator of either (44) or (45) is very small. These are the conditions that lead to resonance in either the bulk permittivity or permeability of a composite filled with identical dielectric spheres and, therefore, to negative bulk permittivity and permeability in a band above the resonant frequency.

The  $a_n$  mode dominates for a particular  $n$  when the frequency or particle radius is such that

$$\frac{[\alpha h_n^{(1)}(\alpha)]'}{h_n^{(1)}(\alpha)} = \frac{\mu_1 [N\alpha j_n(N\alpha)]'}{\mu N^2 j_n(N\alpha)} = \frac{\varepsilon [N\alpha j_n(N\alpha)]'}{\varepsilon_1 j_n(N\alpha)}. \quad (46)$$

Likewise, the  $b_n$  mode dominates for

$$\frac{[\alpha h_n^{(1)}(\alpha)]'}{h_n^{(1)}(\alpha)} = \frac{\mu [N\alpha j_n(N\alpha)]'}{\mu_1 j_n(N\alpha)}. \quad (47)$$

Note that these two expressions differ only in the ratios  $\varepsilon/\varepsilon_1$  and  $\mu/\mu_1$ . Dominance of  $a_n$  implies that  $\mathbf{E}^s \propto \mathbf{N}_{e1n}^{(3)}$  and  $\mathbf{H}^s \propto \mathbf{M}_{e1n}^{(3)}$ . These are transverse magnetic (TM) modes in which there is no radial component of  $\mathbf{H}^s$  since the  $\mathbf{M}_{e1n}$  and  $\mathbf{M}_{o1n}$  have only  $\hat{\theta}$ - and  $\hat{\phi}$ -components. Similarly, dominance of  $b_n$  implies that  $\mathbf{E}^s \propto \mathbf{M}_{o1n}^{(3)}$  and  $\mathbf{H}^s \propto \mathbf{N}_{o1n}^{(3)}$ . When  $b_n$  dominates, the modes are transverse electric (TE), for which there is no radial component of  $\mathbf{E}^s$ . Several texts (Stratton, 1941; Bohren & Huffman, 1983) reproduce Mie's original diagrams (Mie, 1908) showing the electric field distribution on a spherical surface with radius greater than  $a$ , for the first few TM and TE modes. Also note that for any particular order  $n$  of the spherical Bessel functions in (46) and (47) there are an infinite number of resonances as a function of the size parameter  $\alpha$  (Roll & Schweiger, 2000).

### 3.4 Resonators in a composite

One way in which the results of the previous section can be employed to predict the bulk permittivity and permeability of a composite containing dielectric spheres is by treating the composite as an effective medium. In order to treat the composite in this way, the wavelength of the incident field in the effective medium must be significantly larger than

the particle diameter or other significant length scale. For example, effective permittivity and permeability of a simple-cubic lattice of dielectric spheres can be obtained via a modified Maxwell-Garnett relation provided that the wavelength of the incident wave is significantly greater than the lattice constant of the cubic lattice (Lewin, 1947; Holloway et al., 2003).

If the wavelength within the particles is also long, then the response is quasi-static and the electric and magnetic fields are decoupled. The effective permittivity and permeability of the mixture may each be described by the Maxwell-Garnett formula, or by other formulas (Sihvola, 1999). If, on the other hand, the wavelength within the particles is similar to the particle diameter then the dynamic Maxwell equations apply, within the particle, and the electric and magnetic fields are coupled. This is the problem solved by Lewin (1947) for a simple-cubic array of spheres embedded in a host medium. The details of the solution are not repeated here but the result may be summarized as follows.

For an array of homogeneous spheres arranged on the nodes of a simple-cubic lattice and embedded in a matrix with relative permittivity  $\epsilon_r$  and permeability  $\mu_r$  the relative effective permittivity  $\epsilon_{re}$  and permeability  $\mu_{re}$  of the mixture are given by expressions that are *formally* similar to the Maxwell-Garnett mixture formula;

$$\epsilon_{re} = \epsilon_r \left( 1 + \frac{3f}{\frac{\epsilon_{rp} + 2\epsilon_r}{\epsilon_{rp} - \epsilon_r} - f} \right) \quad \text{and} \quad \mu_{re} = \mu_r \left( 1 + \frac{3f}{\frac{\mu_{rp} + 2\mu_r}{\mu_{rp} - \mu_r} - f} \right), \quad (48)$$

where  $f$  is the volume fraction of the spherical inclusions. In the quasi-static regime,  $\epsilon_{rp}$  and  $\mu_{rp}$  are none other than the particle parameters  $\epsilon_{r1}$  and  $\mu_{r1}$ , and equations (48) reduce directly to the Maxwell-Garnett formula. In the case in which the wavelength within the particle,  $\lambda_1$ , is similar to the particle diameter  $2a$ , however, the effective permittivity and permeability of the particles  $\epsilon_{rp}$  and  $\mu_{rp}$  are given by (Lewin, 1947; Holloway et al., 2003)

$$\epsilon_{rp} = F(\vartheta)\epsilon_{r1} \quad \text{and} \quad \mu_{rp} = F(\vartheta)\mu_{r1}. \quad (49)$$

The function  $F(\vartheta)$  that represents the coupling of the electric and magnetic fields is given by

$$F(\vartheta) = \frac{2(\sin \vartheta - \vartheta \cos \vartheta)}{(\vartheta^2 - 1) \sin \vartheta + \vartheta \cos \vartheta}, \quad (50)$$

where  $\vartheta = k_1 a$  and  $k_1$  is the wavenumber inside the sphere, given by  $k_1^2 = \omega^2 \epsilon_1 \mu_1$ . The possibility of resonant behaviour arises through the form of  $F(\vartheta)$  which represents the coupling between the electric and magnetic fields in the system.  $F(\vartheta)$  arises from Mie theory under the approximation that the dielectric spheres act as non-interacting dipole resonators. Under this approximation, higher-order multipole modes are neglected. For this reason, (48) and (49) represent an approximation that is strictly valid only for relatively small values of volume fraction;  $f \leq 0.3$ . When  $f$  increases, inter-particle interaction effects may not be neglected. For example, multipolar inter-particle interaction effects of poles of order up to  $2^7$  among spherical particles arranged on the nodes of a simple-cubic lattice are described by the analytic formula derived by McKenzie et al. (1977). Instead of (48) the inclusion of poles of order up to  $2^7$  gives lengthier expressions (Liu & Bowler, 2009).

Considering (48) it can be seen that  $\epsilon_{re}$  and  $\mu_{re}$  are at resonance when

$$\varepsilon_{rp}^{\text{res}} = -\varepsilon_r \left( \frac{2+f}{1-f} \right) \quad \text{and} \quad \mu_{rp}^{\text{res}} = -\mu_r \left( \frac{2+f}{1-f} \right). \quad (51)$$

These relations define the effective permittivity or permeability of the particle that is needed to achieve resonance in  $\varepsilon_{re}$  and  $\mu_{re}$ . Note that  $\varepsilon_{rp}^{\text{res}}$  and  $\mu_{rp}^{\text{res}}$  are negative. From relations (49) and by consideration of the behaviour of function  $F(\vartheta)$  it is possible to determine how to engineer  $\varepsilon_{rp}$  and  $\mu_{rp}$  to achieve resonance and, therefore, negative bulk permittivity and permeability of the composite;  $\varepsilon_{re} < 0$  and  $\mu_{re} < 0$  for a band of frequencies just above the resonance frequency.

In Fig. 3,  $F(\vartheta)$  is plotted as a function of  $\vartheta$  and a pattern of quasi-periodic singularities is revealed. As described in section 3.3.3, any one of the modes predicted by Mie theory dominates, for a particular order  $n$  of the spherical Bessel functions, when the frequency or particle radius is such that (46) and (47) are satisfied. Also recall that for any particular  $n$  there is an infinite number of resonances whose frequencies depend on the size parameter  $ka$  (Roll & Schweiger, 2000). These resonances give rise to the pattern of singularities (an infinite number) shown in Fig. 3, despite the fact that  $F(\vartheta)$  represents only a dipolar approximation to the full Mie theory. Note that the bandwidth of the resonance decreases as  $\vartheta$  increases.

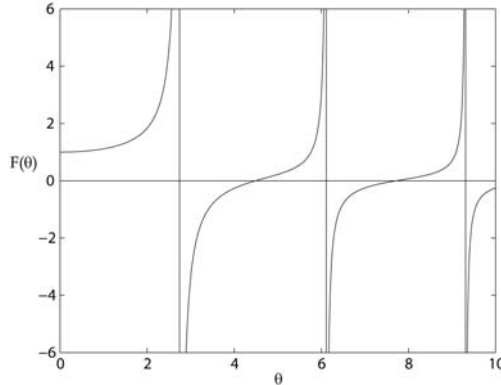


Fig. 3. Functional behaviour of  $F(\vartheta)$ , equation (50).

In example calculations, Holloway et al. (2003) showed that bands of negative  $\varepsilon$  and  $\mu$  can be made to overlap perfectly when  $\varepsilon/\varepsilon_1 = \mu/\mu_1$ . Elsewhere, it has been discussed that composites formed with identical non-magnetic particles with large  $\varepsilon_1$  (i.e.  $\varepsilon/\varepsilon_1 \ll \mu/\mu_1$ ) show a lowest-order resonance in bulk permittivity at a frequency much higher than that in permeability (Jylhä et al., 2006; Vendik et al., 2006; Wheeler et al., 2006; Ahmadi & Mosallaei, 2008). These observations make sense in the light of equations (46) and (47), which embody the full solution to plane wave scattering by a dielectric sphere, and (48) which represents the effective properties of a composite medium based on a dipole approximation of the field scattered by spheres arranged on the nodes of a simple-cubic lattice.

Many experimental demonstrations of NI materials have relied upon metallic elements to achieve negative permittivity  $\text{Re}\{\varepsilon\} < 0$  below the plasma frequency of the metal, and other specially shaped metallic elements to achieve negative permeability  $\text{Re}\{\mu\} < 0$  due to resonance that is created in or between them in a certain frequency band (Smith et al., 2000; Zhou et al., 2006). In other experimental work, dielectric resonators have been used to

achieve  $\text{Re}\{\mu\} < 0$  but not  $\text{Re}\{\varepsilon\} < 0$  (Ueda et al., 2007; Cai et al., 2008). Negative phase velocity was demonstrated in an array of magnetodielectric (YIG) spheres (Baker-Jarvis et al., 2006).

It has also been shown experimentally that both periodic and random arrays of dielectric cylinders can compose a metamaterial with DNG properties (Peng et al., 2007). Most recently a waveguide filter has been constructed using a DNG slab formed from two interpenetrating lattices of dielectric spheres with different radius, one to support  $\text{Re}\{\mu\} < 0$  and the other  $\text{Re}\{\varepsilon\} < 0$  (Siakavara & Damianidis, 2009). This arrangement was analyzed theoretically by Ahmadi & Mosallaei (2008).

## 4. Selected Applications

### 4.1 Transmission lines

The application of left-handedness in transmission lines has been a subject of intense research in recent years. One common configuration is the employment of a periodic, linear array of metallic elements to achieve  $\varepsilon < 0$  and  $\mu < 0$ , although the elements themselves are of a wide variety of shapes and designs. A recent summary of this field is given in the text by Marqués et al. (2008).

### 4.2 Patch antennas

Patch antenna sensors have recently been designed for near-field material property characterization measurements (Zucchelli et al., 2008; Li & Bowler, 2009). Permittivity of a test-piece can be extracted from a measured shift in the resonant frequency of a patch sensor as it is brought near to the test-piece. Or, anomalies in a dielectric material can be detected by the shift in resonant frequency of the sensor. Sensor sensitivity may be defined as the magnitude of the shift in resonant frequency per unit change in test-piece relative permittivity. In both recent works in this area it has been shown that the sensor sensitivity can be improved by reducing the permittivity of the sensor substrate, which forms an insulating layer between the ground plane and resonating patch. Both the permittivity and thickness of the sensor substrate are the primary factors determining the sensor sensitivity but, in order to guarantee the resonant state and penetration depth of the sensor, the substrate thickness is confined to a small range (Bhartia et al., 2001). Employing a negative permittivity substrate, on the other hand, can provide much better sensitivity compared with that of a sensor with a conventional substrate. The sensitivity variation for substrates with various permittivity values is shown in Fig. 4 as a function of the permittivity of the core (second layer) in a three-layer dielectric test-piece, calculated according to an analytic formula (Bernhard & Tousignant, 1999). It can be seen that sensitivity is dramatically enhanced as substrate permittivity becomes negative.

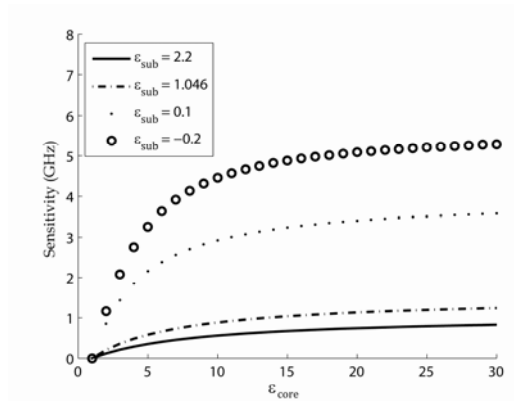


Fig. 4. Change in resonant frequency (sensitivity) of a 10 mm x 10 mm half-wave patch sensor as a function of second-layer (half-space core) permittivity in a coated half-space test-piece, for various values of sensor substrate permittivity. Thickness of the test-piece coating adjacent to the sensor is 0.9 mm and its relative permittivity is 4. Thickness of the sensor substrate is 1.1 mm. Sensitivity values are plotted relative to the resonant frequency for  $\epsilon_{\text{core}} = 1$ .

### 4.3 Superlens

A planar lens fabricated from a metamaterial that exhibits NI behaviour at microwave frequencies can be used to focus the electromagnetic wave emitted by a microwave sensor such as a transmitting monopole or horn antenna. As described in section 2.4 above, this kind of lens can achieve sub-wavelength resolution via the so-called ‘perfect lens’ effect (Veselago, 1968; Pendry, 2000).

Practically speaking, such a lens can be used to combine the advantages of near-field and far-field microwave nondestructive evaluation (NDE) methods by operating at stand-off distances typical for the far-field mode, on the order of tens of centimeters, yet achieving probe size and spatial resolution typical of the near-field mode, on the order of millimeters (Shreiber et al., 2008). For example, the method is not significantly sensitive to changes in the probe standoff distance, when compared to conventional near-field methods in microwave NDE.

A NI-lens-based NDE system operating at 3.65 GHz, with 8.2-cm wavelength, has been shown to detect successfully a 0.037 wavelength (3 mm) cylindrical void in a fiberglass sample at a distance approximating far field (Shreiber et al., 2008). The work employed a NI lens formed from an array of thin metallic wires, to achieve negative permittivity, coupled with an array of metallic split-ring resonators, designed to provide negative permeability. This type of NI lens suffers from significant losses due to the metallic elements employed in fabricating the lens, requiring amplification of the signal and use of a pick-up monopole between the lens and sample for adequate signal detection.

The alternative approach discussed in this chapter, of employing a low-loss, purely dielectric metamaterial lens formed from an array of dielectric resonators embedded in a supporting matrix, offers several advantages over a metallic metamaterial lens. Compared with the lens reported by Shreiber et al. (2008), a purely dielectric lens is expected to exhibit



significantly better transmission properties, enabling sub-wavelength resolution for defect detection without the need for signal amplification or use of an additional pick-up sensor. In this way the measurement system can be simplified, the cost reduced and performance improved.

## 5. Conclusion

To conclude, some key points related to purely dielectric NI metamaterials are emphasized. One advantage of non-metallic DNG materials is improved efficiency due to elimination of metallic loss. In addition, the DNG behaviour does not rely on interparticle interactions, or interactions between unit cells, contrasting with periodic material structures that exhibit DNG behaviour, because the collective response of a metamaterial composed of dielectric resonators arises fundamentally from the properties of each individual resonator. Following from this point, periodic arrangement of the particles is not necessary for DNG behaviour in the dielectric metamaterial system. This suggests that it should be possible to fabricate NI materials using a system of randomly-distributed dielectric particles embedded in a supporting matrix. For microwave applications, smaller particles than those reported by Siakavara & Damianidis (2009) (approximately 1 mm diameter) could be utilized if the particle permittivity is increased, according to  $\omega_r \propto 1/(\alpha\sqrt{\epsilon_{r1}})$ . Such a material would be relatively simple to fabricate compared with NI materials that rely on periodicity in their structure. The DNG bandwidth can be increased by moving the resonating elements closer together, because this increases the coupling between them, reducing the quality-factor of the resonances in  $\epsilon$  and  $\mu$ .

## 6. Acknowledgment

The author thanks Yang Li and Jin Liu for researching some information that appears in this chapter and for assisting with some of the figures.

## 7. References

- Abramowitz, M. & Stegun, I. A. (Eds.), (1972). *Handbook of Mathematical Functions with Formulas, Graphs, and Mathematical Tables*, Dover, ISBN 486612724, New York.
- Ahmadi, A. & Mosallaei, H. (2008). Physical configuration and performance modeling of all-dielectric metamaterials. *Phys. Rev. B*, Vol. 77, Art. No. 045104.
- Baker-Jarvis, J.; Janezic, M. D.; Love, D.; Wallis, T. M.; Holloway, C. L. & Kabos, P. (2006). Phase velocity in resonant structures. *IEEE Trans. Magnetics*. Vol. 42, No. 10, 3344-3346.
- Bernhard, J. T. & Tounsignant, C. J. (1999). Resonant frequencies of rectangular microstrip antennas with flush and spaced dielectric superstrates. *IEEE Trans. Antennas Propagat.*, Vol. 47, No. 2, 302-308.
- Bhartia, P.; Bahl, I.; Garg, R. & Ittibipoon, A. (2001). *Microstrip Antenna Design Handbook*, Artech House, ISBN 0890065136, Boston.
- Bohren, C. F. & Huffman D. R. (1983). *Absorption and Scattering of Light by Small Particles*, Wiley, ISBN 047105772X, New York.

- Cai, X.; Zhu, R. & Hu, G. (2008). Experimental study for metamaterials based on dielectric resonators and wire frame. *Metamaterials*. Vol. 2, 220-226.
- Caloz, C.; Chang, C.-C. & Itoh, T. (2001). Full-wave verification of the fundamental properties of left-handed materials in waveguide configurations. *J. Appl. Phys.*, Vol. 90, No. 11, 5483-5486.
- Holloway, C. L.; Kuester, E. F.; Baker-Jarvis, J. & Kabos, P. (2003). A double negative (DNG) composite medium composed of magnetodielectric spherical particles embedded in a matrix. *IEEE Trans. Antennas Propagat.*, Vol. 51, No. 10, 2596-2603.
- Jylhä, L.; Kolmakov, I.; Maslovski, S. & Tretyakov, S. (2006). Modeling of isotropic backward-wave materials composed of resonant spheres. *J. Appl. Phys.*, Vol. 99, Art. No. 043102.
- Kajfez, D. & Guillon, P. (Eds.), (1986). *Dielectric Resonators*, Artech House, ISBN 0890062013, Boston.
- Lewin, L. (1947). The electrical constants of a material loaded with spherical particles. *Proc. Inst. Elec. Eng.*, Vol. 94, No. 12, 65-68.
- Li, Y. & Bowler, N. (2009). Design of patch sensors for microwave nondestructive evaluation of aircraft radomes. *Proceedings of the 14<sup>th</sup> International Workshop on Electromagnetic Nondestructive Evaluation (ENDE)*, Dayton OH, July 2009, Elsevier, Amsterdam, submitted.
- Liu, J. & Bowler, N. (2009). Analysis of bandwidth and losses in non-metallic double-negative (DNG) metamaterials. *IEEE Trans. Antennas Propag.*, submitted.
- Marqués, R.; Martín, F. & Sorolla, M. (2008). *Metamaterials with Negative Parameters : Theory, Design, and Microwave Applications*, Wiley, ISBN 9780471745822, New York.
- McKenzie, D. R. & McPhedran, R. C. (1977). Exact modeling of cubic lattice permittivity and conductivity. *Nature*, Vol. 265, Issue 5590, 128-129.
- Mie, G. (1908). Contributions on the optics of turbid media, particularly colloidal metal solutions. *Annalen der Physik*, Series IV, Vol. 25, No. 3, 377-445.
- Pendry, J. B. (2000). Negative refraction makes a perfect lens. *Phys. Rev. Lett.*, Vol. 85, No. 18, 3966-3969.
- Peng, L.; Ran, L.; Chen, H.; Zhang, H.; Kong, J. A. & Grzegorzcyk, M. (2007). Experimental observation of left-handed behavior in an array of standard dielectric resonators. *Phys. Rev. Lett.*, Vol. 98, Art. No. 157403.
- Roll, G. & Schweiger, G. (2000). Geometrical optics model of Mie resonances. *J. Opt. Soc. Am. A*, Vol. 17, No. 7, 1301-1311.
- Shreiber, D.; Gupta, M. & Cravey, R. (2008). Microwave nondestructive evaluation of dielectric materials with a metamaterial lens. *Sensors and Actuators A*, Vol. 144, 48-55.
- Siakavara, K. & Damianidis, C. (2009). Microwave filtering in waveguides loaded with artificial single or double negative materials realized with dielectric spherical particles in resonance. *Progress in Electromagnetics Res.*, Vol. 95, 103-120.
- Sihvola, A. (1999). *Electromagnetic Mixing Formulas and Applications*. The Institution of Electrical Engineers, ISBN 0852967721, London.
- Sihvola, A. (2002). Electromagnetic emergence in metamaterials. Deconstruction of terminology of complex media, In: *Advances in Electromagnetics of Complex Media and Metamaterials*, Zouhdi, S. ; Sihvola, A. & Arsalane, M. (Eds.), 3-18, Kluwer, ISBN 1402011016, Boston.

- Smith, D. R.; Padilla, Willie J.; Vier, D. C.; Nemat-Nasser, S. C. & Schultz, S. (2000). Composite medium with simultaneously negative permeability and permittivity. *Phys. Rev. Lett.*, Vol. 84, No. 18, 4184-4187.
- Stratton, J. A. (1941). *Electromagnetic Theory*. McGraw-Hill, New York.
- Ueda, T.; Lai, A. & Itoh, T. (2007). Demonstration of negative refraction in a cutoff parallel-plate waveguide loaded with 2-D square lattice of dielectric resonators. *IEEE Trans. Microwave Theory Tech.* Vol. 55, No. 6, 1280-1287.
- Vendik, I.; Vendik, O.; Kolmakov, I. & Odit, M. (2006). Modelling of isotropic double negative media for microwave applications. *Opto-Electronics Rev.*, Vol. 14, No. 3, 179-186.
- Veselago, V. G. (1968). Electrodynamics of substances with simultaneously negative values of sigma and mu. *Sov. Phys. Usp.*, Vol. 10, 509-514.
- Wheeler, M. S.; Aitchison, J. S. & Mojahedi, M. (2005). Three-dimensional array of dielectric spheres with an isotropic negative permeability at infrared frequencies. *Phys. Rev. B*, Vol. 72, Art. No. 193103.
- Wheeler, M. S.; Aitchison, J. S. & Mojahedi, M. (2006). Coated nonmagnetic spheres with a negative index of refraction at infrared frequencies. *Phys. Rev. B*, Vol. 73, Art. No. 045105.
- Zhang, Y. & Mascarenhas, A. (2007). Negative refraction of electromagnetic and electronic waves in uniform media, In: *Physics of Negative Refraction and Negative Index Materials : Optical and Electronic Aspects and Diversified Approaches*, Krowne, C. M. & Zhang, Y. (Eds.), 1-18, Springer, ISBN 9783540721314, New York.
- Zhou, J.; Koschny, T.; Zhang, L.; Tuttle G. & Soukoulis, C. M. (2006). Experimental demonstration of negative index of refraction. *Appl. Phys. Lett.*, Vol. 88, Art. No. 221103.
- Ziolkowski, R. W. & Heyman, E. (2001). Wave propagation in media having negative permittivity and permeability. *Phys. Rev. E*, Vol. 64, Art. No. 056625.
- Zucchelli, A.; Chimenti, M. & Bozzi, E. (2008). Application of a coaxial-fed patch to microwave non-destructive porosity measurements in low-loss dielectrics. *Progress in Electromagn. Res.*, Vol. 5, 1-14.



# Dielectric Anisotropy of Modern Microwave Substrates

Plamen I. Dankov  
*University of Sofia, Faculty of Physics  
Bulgaria*

## 1. Introduction

The significance of the modern RF substrates in the microwave and millimeter-wave technology has two main aspects. First, there are many new materials with various dielectric characteristics, structures, compositions, sizes, specific thermal, mechanical and chemical properties and, finally, different applications. These, usually reinforced materials, containing woven or unwoven fabrics with appropriate filling, are manufactured by a variety of technological procedures and the resultant dielectric parameters (dielectric constant and dielectric loss tangent) become very informative for a reliable control of the used technology. Therefore, the manufacturers must properly characterize the parameters of their commercial products in order to control the technology and additionally, they have to keep them stable in each technological cycle. Second, the modern RF-design style is based on the utilization of powerful electromagnetic 2D/3D structure and schematic simulators, where the designed devices could be described very realistically in big details. This requirement also means that the RF designers must have accurate enough information for the actual dielectric parameters of each used material (substrate, thin film, multi-layer composite, absorber, etc.) in order to obtain an adequate simulation model of the device.

The RF designers get the needed information for the substrate parameters mainly from the manufacturer's catalogues. These data, obtained by IPC TM-650 2.5.5.5 stripline-resonator test method, include near-to-perpendicular parameters, but this is insufficient in many design cases (design of filters, hybrids, delay lines, matched elements with steps, stubs, gaps, antenna patches, etc.). Several negative facts in the design practice are very suitable to illustrate the problems. Nowadays the RF and antenna designers try to input into the simulators very detailed geometrical models of the structures of interest with extremely big details, but the values of the dielectric parameters are usually introduced rather frivolously. It is known that designers apply an ungrounded, but popular and relatively successful design technique - they usually "tune" the value of the substrate's dielectric constant about the known catalogue value in order to "fit" the simulated and the measured dependencies of a given designed device. Another surprising fact appears, when one device (passive or active) with fixed layout, manufactured on two or more substrates, produced by different manufacturers, but with equal catalogue parameters, demonstrates unequal frequency behaviour of its measured S-parameters. Similar problems appear always, when the used

reinforced substrates or the composite multi-layer materials have a noticeable dielectric anisotropy – different values of the parallel and perpendicular complex dielectric constants, and therefore – unique equivalent dielectric parameters (see section 6). Unfortunately, the dielectric anisotropy of materials is not yet an intrinsic parameter in the RF design.

In this chapter we would like to represent the increasing importance of the material's anisotropy in the modern design and the possibilities for accurate determination of this characteristic by waveguide and resonance methods. Our considerations are based mainly on the author's two-resonator method for characterization of the dielectric anisotropy (Dankov, 2006) and its subsequent variants. The main principles, backgrounds, realization and measurement problems of this method are described. Important information about the practical anisotropy of some popular substrates is presented and compared and the concept of the equivalent dielectric constant is introduced. Finally, the problem how to use the electromagnetic 3D simulators for numerical analysis of structures with anisotropic substrates is discussed and some illustrative examples are presented.

## 2. Characterization of the Substrate Dielectric Parameters and Possibilities to Determine the Dielectric Anisotropy

The modern reinforced PWB (Printed Wire Board) substrates have more or less expressed uniaxial anisotropy – different dielectric constants along the axes 0x, 0y and 0z. Usually, the dielectric constants in the both parallel to the substrate surface directions coincide, and the following diagonal tensor expression for the complex dielectric constant is valid:

$$\hat{\varepsilon}_r = \begin{pmatrix} \varepsilon_{||} & 0 & 0 \\ 0 & \varepsilon_{||} & 0 \\ 0 & 0 & \varepsilon_{\perp} \end{pmatrix}, \text{ where } \varepsilon_{||,\perp} = \varepsilon'_{||,\perp} - j\varepsilon''_{||,\perp} = \varepsilon'_{||,\perp} (1 - j \tan \delta_{\varepsilon_{||,\perp}}). \quad (1)$$

Thus, an anisotropy substrate can be characterized by two pairs of parameters for the dielectric constant and dielectric loss tangent:  $\varepsilon'_{||}$ ,  $\tan \delta_{\varepsilon_{||}}$  – parallel dielectric parameters, and  $\varepsilon'_{\perp}$ ,  $\tan \delta_{\varepsilon_{\perp}}$  – perpendicular dielectric parameters – Fig. 1a. The dielectric anisotropy can be expressed by two ways – as direct ratios  $\alpha_{\varepsilon} = \varepsilon'_{||} / \varepsilon'_{\perp}$  and  $\alpha_{\tan \delta_{\varepsilon}} = \tan \delta_{\varepsilon_{||}} / \tan \delta_{\varepsilon_{\perp}}$  or as normalized ratios  $\Delta A_{\varepsilon} = 2 |\varepsilon'_{||} - \varepsilon'_{\perp}| / (\varepsilon'_{||} + \varepsilon'_{\perp})$  and  $\Delta A_{\tan \delta_{\varepsilon}} = 2 |\tan \delta_{\varepsilon_{||}} - \tan \delta_{\varepsilon_{\perp}}| / (\tan \delta_{\varepsilon_{||}} + \tan \delta_{\varepsilon_{\perp}})$ . In the last case the anisotropy can be presented in percents with positive or negative sign. The parameters  $\alpha_{\varepsilon}$  or  $\Delta A_{\varepsilon}$  represent the dielectric constant anisotropy, while the parameters  $\alpha_{\tan \delta_{\varepsilon}}$  or  $\Delta A_{\tan \delta_{\varepsilon}}$  – the dielectric loss tangent anisotropy.

Three sources of substrate anisotropy can be mentioned. The original concept for the material anisotropy is naturally connected with the magnetic or electric “gyrotropy” of some specific media (ferrites, plasmas, etc.) in external magnetic or electric fields. For example, the asymmetrical-tensor gyrotropy is an important property of the permeability of ferrite substrates or of the permittivity of semiconductor layers both in a biasing magnetic field.

The substrate gyrotropy will not be considered here. Initially the uniaxial anisotropy is connected mainly with the crystallography properties of the optical glasses, microwave ceramics (van Heuven & Vlek, 1972; Fritsch & Wolff, 1992) and liquid crystals (Gaebler et al., 2008). These materials are homogeneous, but anisotropic due to their crystalline anisotropy – different dielectric parameters along to their main crystallographic axes. Contrariwise, the source of the anisotropy of the modern artificial substrate is mainly connected with their

inhomogeneous structure of reinforcing fiber cloths, irregular filling and the miniature air “balloons” technologically inserted in the structures. We can imagine that these chaotic formations act like a great number of series or parallel capacitors depending on the electric field direction. The result is that the dielectric constant along to the glass fibers is bigger (the parallel capacitors are predominant) than the dielectric constant, perpendicular to them (the series capacitors are predominant). Usually the nonwoven substrates have less expressed anisotropy compared to woven substrates (Laverghetta, 2000). The main question is how to measure this resultant anisotropy in the whole substrates with enough accuracy?

There are a lot of measurement methods for characterization of the dielectric parameters of PWB substrates (see the useful comparison of Baker-Jarvis, 1998 and Chen et al., 2004). We will consider here only the resonance methods, because the broad-band non-resonance methods (waveguide, free-space, etc.) could not ensure the accuracy needed for determination of the anisotropy. The most spread resonance method is one of the simplest – the reference IPC TM-650 2.5.5.5 stripline-resonator method, mainly used by the substrate manufacturers – Fig. 1 *b, c*. The substrate under test is placed above a wide stripline conductor of length  $L$  and perturbs the resonance frequencies and the quality factors of the excited in the structure series of the resonance TEM modes. Based on simple analytical expressions this method can give near-to-perpendicular values of the dielectric constant  $\epsilon'_r \sim \epsilon'_{\perp}$  and dielectric loss tangent  $\tan\delta_e \sim \tan\delta_{e\perp}$  in a relatively big frequency range 2-15 GHz. Unfortunately, this wide spread reference method is not convenient for determination of the other pair of dielectric parameters of substrates with uniaxial anisotropy – the parallel ones, when  $\epsilon'_{\parallel} \neq \epsilon'_{\perp}$  and  $\tan\delta_{e\parallel} \neq \tan\delta_{e\perp}$ . In fact, a modified IPC TM-650 method (by Bereskin's patent, 1992) gives an opportunity to separately determine these four parameters by “staking” of several thin unmetallized substrates into a thick bulk sample and measurements in the both directions, but this method is rather inconvenient.

The main principle to determine of the substrate dielectric anisotropy is not new – to use dual- or triple-mode resonators with predominant electric-field distribution parallel or perpendicular to the sample surface. The planar resonators (for example – the microstrip linear or ring resonators; Ivanov & Peshlov, 2002) are not accurate for anisotropy measurements, because their modes have both parallel and normal E fields in an arbitrary mixture, depending on the microstrip width. The cavity (bulk) resonators are more suitable for anisotropy measurements. Several cavity-resonator methods for low-loss dielectric property characterization have been presented in the literature. Most of them are accepted in leading metrology institutions like the National Institute of Standards and Technology (NIST), Boulder, CO, USA, and the National Physics Laboratory (NPL), Middlesex, UK for accurate reference methods for isotropic materials. However, there is no universal solution for the dielectric anisotropy characterization.

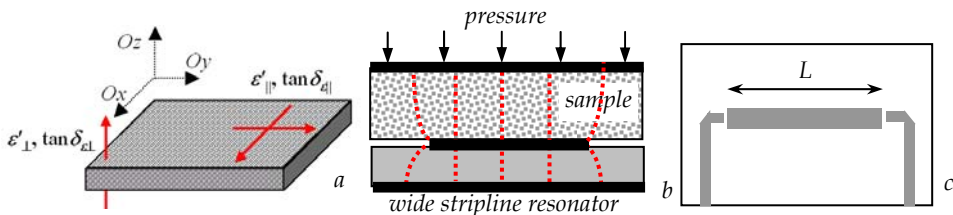


Fig. 1. Anisotropic substrate (a); IPC TM-650 2.5.5.5 test structure: side (a) and top view (b)

The parameters  $\varepsilon'_{||}$  and  $\tan\delta_{\varepsilon||}$  can be measured simply by using popular TE-mode resonance cavities: classical Courtney's method (Courtney 1970), Kent's evanescent-mode tester (Kent 1988), NIST's mode-filtered resonator (Vanzura et al., 1993), split-cylinder resonator (Janezic & Baker-Jarvis, 1999), etc. The parameters  $\varepsilon'_{\perp}$  and  $\tan\delta_{\varepsilon\perp}$  can be estimated using TM-mode resonance cavities (Zhao et al., 1992), low-frequency re-entrant resonators (Baker-Jarvis & Riddle 1996), etc. In fact, only a few publications have been directly dedicated to dielectric-anisotropy measurements. Whispering-gallery modes in single dielectric resonators could be used for accurate anisotropy measurement of extremely low-loss materials (Krupka et al., 1994, 1997). An early split-cavity method for the dielectric-constant anisotropy determination through a long cylindrical cavity with TE<sub>111</sub> and TM<sub>nm0</sub> modes is described by Olyphant, 1979, and data for some reinforced materials are presented. The number of papers dedicated to anisotropy characterization of single and multilayer materials, increases in the last several years (Tobar et al., 2001; Dankov & Ivanov, 2004; Dankov et al., 2005; Egorov et al., 2005; Dankov, 2006; Parka et al., 2007; Gaebler et al., 2008; Momcu et al., 2008, etc.). Some of them will be considered in the next sections. They are dedicated to determination of the dielectric anisotropy in a variety of materials like microwave substrates, high-K ceramics, multilayer radomes, nanocomposite layers, liquid crystals, etc. A useful summary and comparison between the existing methods for dielectric anisotropy measurements is presented by Momcu et al., 2008. Recently, simple planar resonance methods based on coplanar striplines or microstrip lines are proposed for substrate anisotropy determination in low-frequency RF substrate like FR-4 (Rautio, 2009).

### 3. Two-Resonator Method for Determination of the Dielectric Anisotropy

#### 3.1 Measurement principle of the method

The basic idea for determination of the isotropic substrate dielectric parameters by an arbitrary resonance method is simple – to measure the resonance parameters (resonance frequency  $f_{\varepsilon_{meas}}$  and the unloaded quality factor  $Q_{\varepsilon_{meas}}$ ) of the chosen exited mode, which values are perturbed by the sample. The success of this procedure depends on the accuracy of the used model, which ensures the needed relations between the measured resonance parameters ( $f_{\varepsilon_{meas}}$ ,  $Q_{\varepsilon_{meas}}$ ) and the substrate dielectric parameters ( $\varepsilon'_r$ ,  $\tan\delta'_\varepsilon$ ). The principle for determination of the uniaxial dielectric anisotropy is similar, but applied for triple- or dual-mode resonator with electric-field direction orientated strongly along to axes 0x, 0y and 0z – Fig. 1a. An alternative of this method is the idea to use two resonators with different modes, which support “pure” parallel or “pure” perpendicular electric field according to the surface of the sample. The main advantage is that separate resonators could be designed to suppress the parasitic modes and to simplify the measurement process.

The two-resonator method for determination of the dielectric anisotropy in multilayer materials has been proposed by Dankov & Ivanov, 2004 (see also Dankov, 2006). In its original form it is based on two different ordinary cylinder resonators, marked as R1 and R2. They support two suitable for anisotropy measurement modes – TE<sub>011</sub>-mode in R1 (for determination of pure  $\varepsilon'_{||}$ ,  $\tan\delta_{\varepsilon||}$ ) and TM<sub>010</sub>-mode in R2 (for determination of pure  $\varepsilon'_{\perp}$ ,  $\tan\delta_{\varepsilon\perp}$ ) – see Fig. 2 a, b. Each resonator is a cylinder with diameter  $D_{1,2}$  and height  $H_{1,2}$ . A unmetallized disk sample with diameter  $D_s = D_1$  or  $D_s = D_2$ , manufactured from the substrate by cutting with special punch, is placed in the middle of the resonator R1 or on the bottom side of the resonator R2.



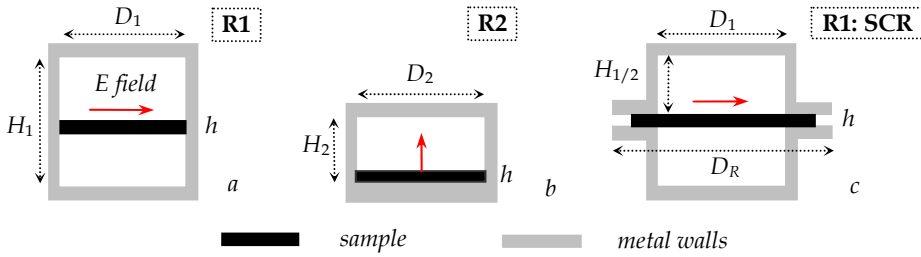


Fig. 2. Ordinary pair of cylindrical resonators: a)  $TE_{011}$ -mode cavity **R1**; b)  $TM_{010}$ -mode cavity **R2**; c)  $TE_{011}$  split-cylinder resonator **SCR** as **R1**; E-field direction is marked by arrow

There are two possibilities to realize the two-resonator method: 1) The measuring resonators have equal diameters  $D_1 = D_2$ , and the measurement of  $\epsilon'_{||}$  and  $\epsilon'_{\perp}$  corresponds to different resonance frequencies denoted as  $f_{\epsilon}^{TE011} > f_{\epsilon}^{TM010}$ . This case is more suitable for materials with a relatively weak frequency dependence on the dielectric constant and loss tangent; 2) The resonators have diameters  $D_1 > D_2$ , for which the values of  $\epsilon'_{||}$  and  $\epsilon'_{\perp}$  are determined at relatively close frequencies  $f_{\epsilon}^{TE011} \sim f_{\epsilon}^{TM010}$ . One unmetallized sample is needed for the first case (the variations in the parameters from sample to sample could be avoided), while two separate samples with differing diameters have to be prepared for the second case. Thus, several pairs of resonators R1/R2 with reasonable diameters 150-15 mm could easily "cover" the frequency range 2.5-25 GHz for characterization of typical substrates with the lowest-order modes (utilization of higher-order modes will increase the upper frequency).

### 3.2 Measurement pairs of resonators

The measuring resonators R1 and R2 could be designed to have special features to increase their selectivity to measure the sample anisotropy. The technical details concerning the ordinary resonator pair R1/R2 are described by Dankov, 2006. The resonator R1 has two movable "contact-less" flanges with absorbing rings in order to suppress the unwanted here TM modes (compression better than -60 dB). In the same time the symmetrical  $TE_{011}$ ,  $TE_{021}$ ,  $TE_{013}, \dots$  modes, suitable for determination of the longitudinal dielectric parameters, can be easily excited in transmission-power regime by two magnetic-type coaxial loops - Fig. 3. The resonator R2 has one movable flange with an improved dc contact and two magnetic-type coaxial loops with axis perpendicular to the resonator axis. A height reduction,  $H_2 < (2-3)D_2$ , is used to ensure single-mode excitation for determination of the transversal dielectric parameters using the lowest-order  $TM_{010}$  mode. Measurements with  $TM_{020}$ ,  $TM_{030}$  modes are also possible, but the near presence of parasitic high-order modes makes the mode identification more difficult. A concrete pair of realized ordinary cylinder resonators is presented on Fig. 6a. The resonator dimensions are designed to be  $D_1 = 30.00$  mm,  $H_1 = 29.82$  mm (denoted as CR1);  $D_2 = 30.00$  mm,  $H_2 = 12.12$  mm (CR2') or  $D_2 = 18.1$  mm,  $H_2 = 12.09$  mm (CR2). The corresponding measured resonance frequencies and unloaded Q-factors of the empty resonators are  $f_0^{CR1} = 13.1519$  GHz,  $Q_0^{CR1} = 14470$  in CR1 and  $f_0^{CR2'} = 7.6385$  GHz,  $Q_0^{CR2'} = 3850$  in CR2' (or  $f_0^{CR2} = 12.6404$  GHz,  $Q_0^{CR2} = 3552$  in CR2). All these parameters are obtained with "daily" variations of  $\pm 0.01\%$  in the resonance frequency and  $\pm 1.5\%$  in the Q-factor (mainly due to room temperature changes, cavity cleanness and influence of tuning elements). We use these resonators for obtaining of the results presented in this chapter.

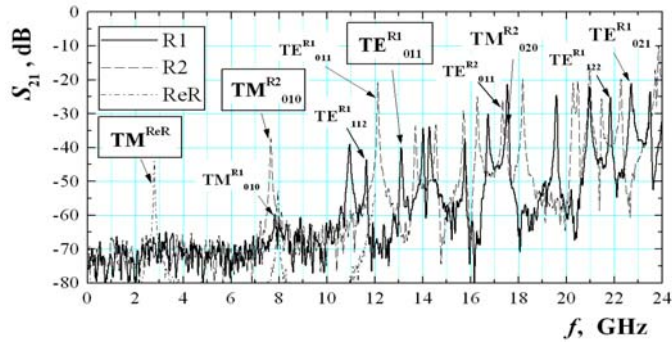


Fig. 3. Frequency responses of the R1, R2 and ReR resonators in transmitted-power regime measured by a network analyzer. The resonance curves of the discussed modes are marked

The ordinary R1 resonator can be successfully replaced with the known type of  $TE_{011}$ -mode split-cylinder resonator (SCR) (Janezic & Baker-Jarvis 1999) – see Fig. 2c. It consists of two equal cylindrical sections with diameter  $D_1$  (as in CR1) and height  $H_{1/2} = 0.5H_1$ . The sample with thickness  $h$  and arbitrary shape is placed into the radial gap between the cylinders. If the sample has disk shape, its diameter  $D_s$  should fit the SCR diameter  $D_1$  with at least 10% in reserve, i. e.  $D_s \geq 1.1D_1$ . The SCR resonator (as R1) is suitable for determination of the longitudinal dielectric parameters –  $\epsilon'_{||}$ ,  $\tan\delta_{\epsilon||}$ . The presented in Fig. 6a SCR has the following dimensions:  $D_1 = 30.00$  mm,  $H_1 = 30.16$  mm, and the  $TE_{011}$ -mode resonance parameters –  $f_0^{SCR} = 13.1574$  GHz,  $Q_0^{SCR} = 8171$ . In spite of the lower Q-factor, the clear advantage of SCR is the easier measurement procedure without preliminary sample cutting. The radial SCR section must have big enough diameter ( $D_R \sim 1.5D_1$ ) in order to minimize the parasitic lateral radiation even for thicker samples (see Dankov & Hadjistamov, 2007).

The considered pair of resonators (CR1&CR2) is not enough convenient for broadband measurements of the anisotropy, even when a set of resonator pairs with different diameters is being used. More suitable for this purpose is the pair of tunable resonators, shown in Fig. 4 and Fig. 6b. The split-coaxial resonator SCoaxR (see Dankov & Hadjistamov, 2007) can successfully replace the ordinary fixed-size resonator R1 (or SCR), while the tunable re-entrant resonator ReR (see Hadjistamov et. al., 2007) – the fixed-size resonator R2. The SCoaxR is a variant of the split-cylinder resonator with a pair of top and bottom cylindrical metal posts with height  $H_r$  and diameter  $D_r$  into the resonator body.

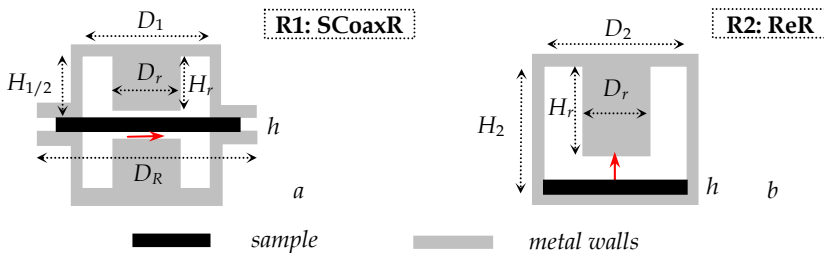


Fig. 4. Pair of tunable resonators: a) split-coaxial cylinder resonator **SCoaxR** as **R1**; b) re-entrant resonator **ReR** as **R2**

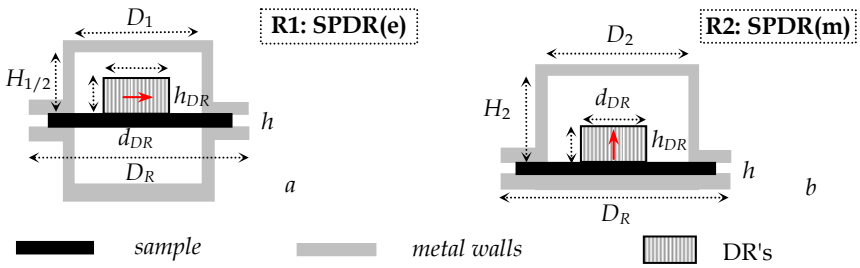


Fig. 5. Pair of split-post dielectric resonator SPDR: a) electrically-split resonator **SPDR(e)** as **R1**; b) magnetically-split resonator **SPDR(m)** as **R2**; both with one DR

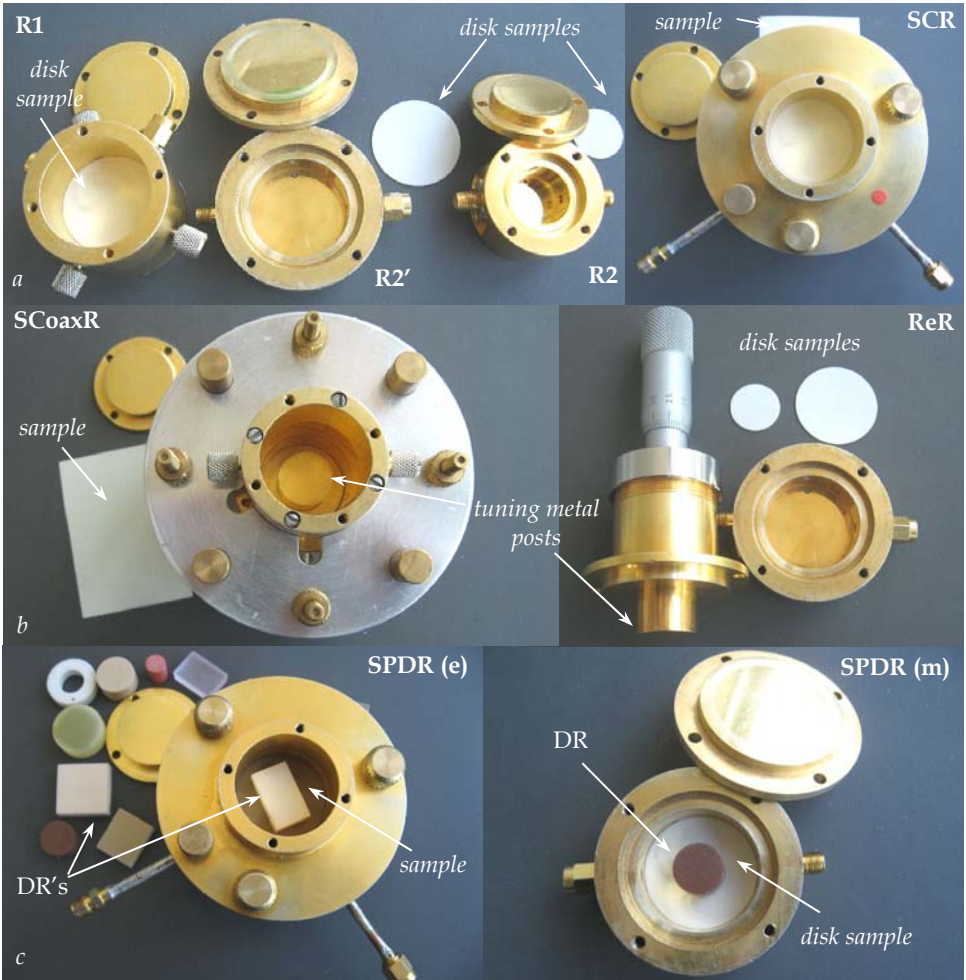


Fig. 6. Resonators' photos of different pairs: a) R1, R2, SCR; b) ReR; SCoaxR; c) SPDR's (e/m)

The adjustment of the resonance frequency is possible by changing of the height  $H_r$ , with more than one octave below the resonance frequency of the hollow split-cylinder resonator. The re-entrant resonator is a known low-frequency measurement structure. It has also an inner metal cylinder with height  $H_r$  and diameter  $D_r$ . A problem of the reentrant and split-coaxial measurement resonators is their lower unloaded Q factors (200-1500) compared to these of the original cylinder resonators (3000-15000). In order to overcome this problem for measurements at low frequency, a new pair of measurement resonators could be used instead of R1 and R2 (see Fig. 5 and Fig. 6c): the split-post dielectric resonators SPDR (e/m) with electric (e) or magnetic (m) type of splitting (e.g., see Baker-Jarvis et al., 1999) (in fact, a non-split version of SPDR (m) is represented in Fig. 6c). The main novelty of this pair is the inserted high-Q dielectric resonators DR's that set different operating frequencies, lower than the resonance frequencies in the ordinary cylinder resonators. The used DR's should be made by high-quality materials (sapphire, alumina, quartz, etc.) and this allows achieving of unloaded Q factors about 5000-20000. A change in the frequency can be obtained by replacement of a given DR with another one. DR's with different shapes can be used: cylinder, rectangular and ring. The DR's dielectric constant should be not very high and not very different from the sample dielectric constant to ensure an acceptable accuracy.

### 3.3 Modeling of the measurement structures

The accuracy of the dielectric anisotropy measurements directly depends upon the applied theoretical model to the considered resonance structure. This model should ensure rigorous relations between the measured resonance parameters ( $f_{gmeas}$ ,  $Q_{gmeas}$ ) and the substrate dielectric parameters ( $\epsilon'_r$ ,  $\tan\delta_\epsilon$ ) along a given direction in dependence of the used resonance mode. The simplest model is based on the perturbation approximation (e.g. Chen et al., 2004), but acceptable results for anisotropy can be obtained only for very thin, low-K or foam materials (Ivanov & Dankov, 2002). If the resonators have simple enough geometry (e.g. CR1, CR2), relatively rigorous analytical models are possible to be constructed. Thus, accurate analytical models of the simplest pair of fixed cylindrical cavity resonators R1&R2 are presented by Dankov, 2006 especially for determination of the dielectric anisotropy of multilayer materials (measurement error less than  $\pm 2-3\%$  for dielectric constant anisotropy, and less than  $\pm 8-10\%$  - for the dielectric loss tangent anisotropy). The relatively strong full-wave analytical models of the split-cylinder resonator (Janezic & Baker-Jarvis, 1999) and split-post dielectric resonator (Krupka et al., 2001) are also suitable for measurement purposes, but our experience shows, that the corresponding models of the re-entrant resonator (Baker-Jarvis & Riddle, 1996) and the split-coaxial resonator are not so accurate for measurement purposes. In order to increase the measurement accuracy, we have developed the common principles for 3D modeling of resonance structures with utilization of commercial 3D electromagnetic simulators as assistance tools for anisotropy measurements (see Dankov et al., 2005, 2006; Dankov & Hadjistamov, 2007). The main principles of this type of 3D modeling especially for measurement purposes with the presented two-resonator method are described in §4. In our investigations we use Ansoft® HFSS simulator.

### 3.4 Measurement procedure and mode identifications

The procedure for dielectric anisotropy measurement of the prepared samples is as follows: First of all, the resonance parameters ( $f_{0meas}$ ,  $Q_{0meas}$ ) of each empty resonator (without sample) from the chosen pair should be accurately measured by Vector Network Analyzer VNA.

This step is very important for determination of the so-called "equivalent parameters" of each resonator (see section 4.3); they should be introduced in the model of the resonator in order to reduce the measurement errors. Then the resonance parameters ( $f_{\text{meas}}$ ,  $Q_{\text{meas}}$ ) of each resonator with sample should be measured (for minimum 3-5 samples from each substrate panel). This ensures well enough reproducibility for reliable determination of the dielectric sample anisotropy with acceptable measurement errors (see section 4.4). The identification of the mode of interest in the corresponding resonator from the pair is also an important procedure. The simplest way is the preliminary simulation of the structure with sample, which parameters are taken from the catalogue. This will give the approximate position of the resonance curve. If the sample parameters are unknown, another way should be used. For example, the mechanical construction of the exciting coaxial probes in the resonators has to ensure rotating motion along the coaxial axis. Because the "pure" TE or TM modes of interest in R1/R2 resonators have electric or magnetic field, strongly orientated along one direction or in one plane (to be able to detect the sample anisotropy), a simple rotation of the coaxial semi-loop orientation allows varying of the resonance curve "height" and this will give the needed information about the excited mode type (TE or TM).

## 4. Measurement of Dielectric Anisotropy, Assisted by 3D Simulators

### 4.1 Main principles

The modern material characterization needs the utilization of powerful numerical tools for obtaining of accurate results after modeling of very sophisticated measuring structures. Such software tools can be the three-dimensional (3D) electromagnetic simulators, which demonstrate serious capabilities in the modern RF design. Considering recent publications in the area of material characterization, it is easy to establish that the 3D simulators have been successfully applied for measurement purposes, too. The possibility to use commercial frequency-domain simulators as assistant tools for accurate measurement of the substrate anisotropy by the two-resonator method has been demonstrated by Dankov et al., 2005. Then, this option is developed for the all types of considered resonators, following few principles – simplicity, accuracy and fast simulations. Illustrative 3D models for some of resonance structures, used in the two-resonator method (R1, R2 and SCR), are drawn in Fig. 7. Three main rules have been accepted to build these models for accurate and time-effective processing of the measured resonance parameters – a stylized drawing of the resonator body with equivalent diameters ( $D_{1e}$  or  $D_{2e}$ ), an optimized number of line segments ( $N = 72-180$ ) for construction of the cylindrical surfaces and a suitable for the operating mode splitting (1/4 or 1/8 from the whole resonator body), accompanied by appropriate boundary conditions at the cut-off planes. Although the real resonators have the necessary coupling elements, the resonator bodies can be introduced into the model as pure closed cylinders and this approach allows applying the eigen-mode solver of the modern 3D simulators (Ming et al., 2008). The utilization of the eigen-mode option for obtaining of the resonance frequency and the unloaded Q-factor (notwithstanding that the modeled resonator is not fully realistic) considerably facilitates the anisotropy measurement procedure assisted by 3D simulators, if additionally equivalent parameters have been introduced (see 4.3) and symmetrical resonator splitting (see 4.2) has been done.

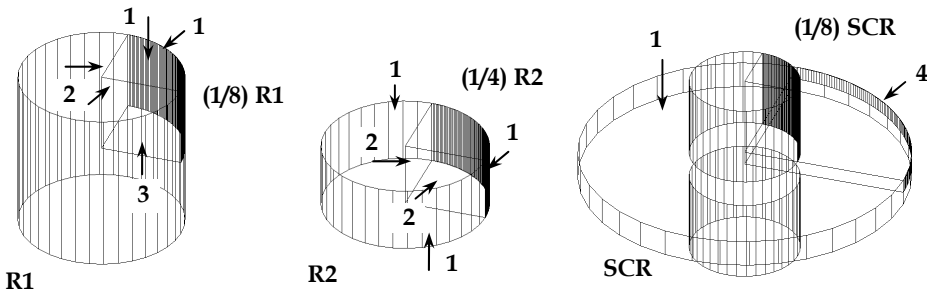


Fig. 7. Equivalent 3D models of three resonators R1, R2 and SCR and boundary conditions BC. BC legend: 1 - finite conductivity; 2 - E-field symmetry; 3 - H-field symmetry; 4 - perfect H-wall (natural BC between two dielectrics); the BC over the all metal surface are 1)

#### 4.2 Resonator splitting

In principle, the used modes in the measurement resonators for realization of the two-resonator method have simple E-field distribution (parallel or perpendicular to the sample surface). This specific circumstance allows accepting an important approach: not to simulate the whole cylindrical cavities; but only just one symmetrical part of them: 1/8 from R1, SPR and 1/4 from R2. Such approach requires suitable symmetrical boundary conditions to be chosen, illustrated in Fig. 7. Two magnetic-wall boundary conditions should be accepted at the split-resonator surfaces – “E-field symmetry” (if the E field is parallel to the surface) or “H-field symmetry” (if the E field is perpendicular to the surface). The simulated resonance parameters of the whole resonator (R1 or R2) and of its (1/8) or (1/4) equivalent practically coincide for equal conditions; the differences are close to the measurement errors for the frequency and the Q-factor (see data in Table 1). The utilization of the symmetrical cutting in the 3D models instead of the whole resonator is a key assumption for the reasonable application of the powerful 3D simulators for measurement purposes. This simple approach solves three important simulation problems: 1) it considerably decreases the computational time (up to 180 times for R1 and 50 times for R2); 2) allows increasing of the computational accuracy and 3) suppresses the possible virtual excitation of non-physical modes during the simulations in the whole resonator near to the modes of interest. The last circumstance is very important. The finite number of surface segments in the full 3D model of the cavity in combination with the finite-element mesh leads to a weak, but unavoidable structure asymmetry and a number of parasitic resonances with close frequencies and different Q-factors appear in the mode spectrum near to the symmetrical TE/TM modes of interest. These parasitic modes fully disappear in the symmetrical (1/4)-R2 and (1/8)-R1 cavity models, which makes the mode identification much easier (see the pictures in Fig. 8).

#### 4.2 Equivalent resonator parameters

Usually, if an empty resonator has been measured and simulated with fixed dimensions, the simulated and measured resonance parameters do not fully coincide,  $f_{0sim} \neq f_{0meas}$ ,  $Q_{0sim} \neq Q_{0meas}$ . There are a lot of reasons for such a result – dimensions uncertainty, influence of the coupling loops, tuning screws, eccentricity, surface cleanness and roughness, temperature variation, etc.). In order to overcome this problem and due to the preliminary decision to

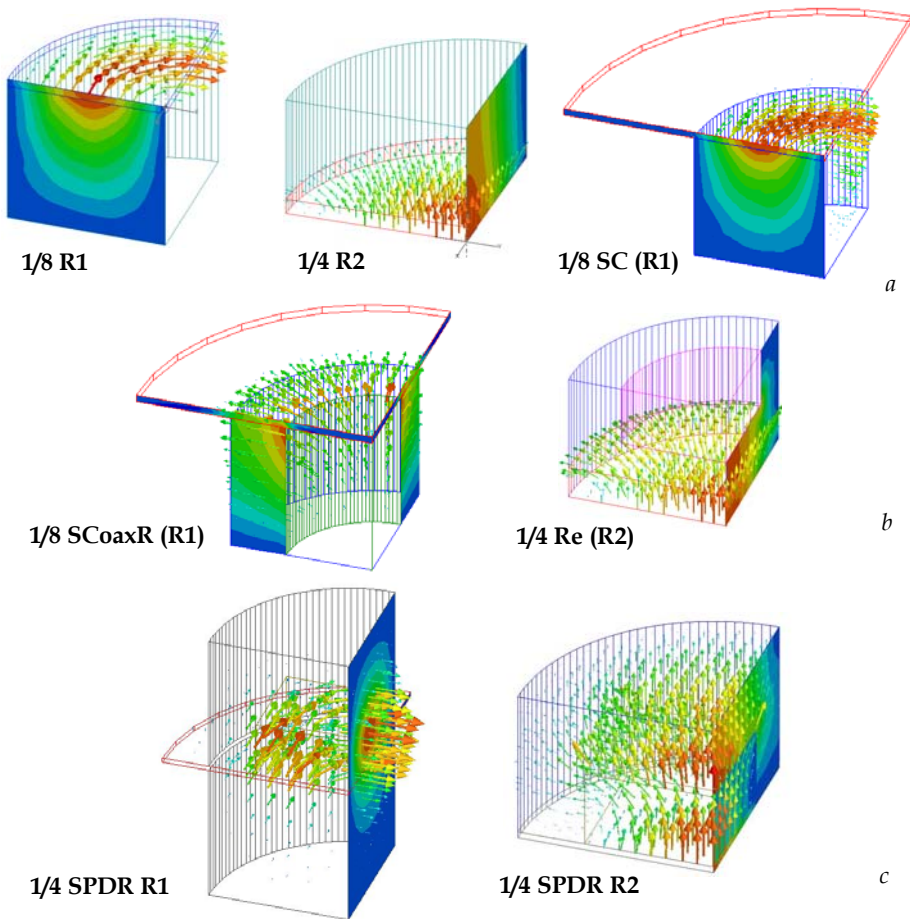


Fig. 8. Simulated electric-field  $E$  distribution (scalar and vector) in the considered pairs of measurement resonators (as R1 or R2): *a*) cylinder resonators; *b*) tunable resonators; *c*) SPDR's. Presence of similar pictures makes the mode identification much easier.

ignore the details and to construct pure stylized resonator model, the approach, based on the introduction of *equivalent parameters* (dimensions and surface conductivity) becomes very important. The idea is clear - the values of these parameters in the model have to be tuned until a coincidence between the calculated and the measured resonance parameters is achieved:  $f_{0sim} \sim f_{0meas}$ ,  $Q_{0sim} \sim Q_{0meas}$  ( $\sim 0.01\%$  coincidence is usually enough). The problem is how to realize this approach? Let's start with the simplest case - the equivalent 3D models of the pair CR1/CR2 (Fig. 7). In this approach each 3D model is drawn as a pure cylinder with *equivalent diameter*  $D_{eq1,2}$  (instead of the geometrical one  $D_{1,2}$ ), actual height  $H_{1,2}$  and *equivalent wall conductivity*  $\sigma_{eq1,2}$  of the empty resonators. The equivalent geometrical parameter ( $D$  instead of  $H$ ) is chosen on the base of simple principle: the variation of which parameter influences most the resonance frequencies of the empty cavities CR1 and CR2?

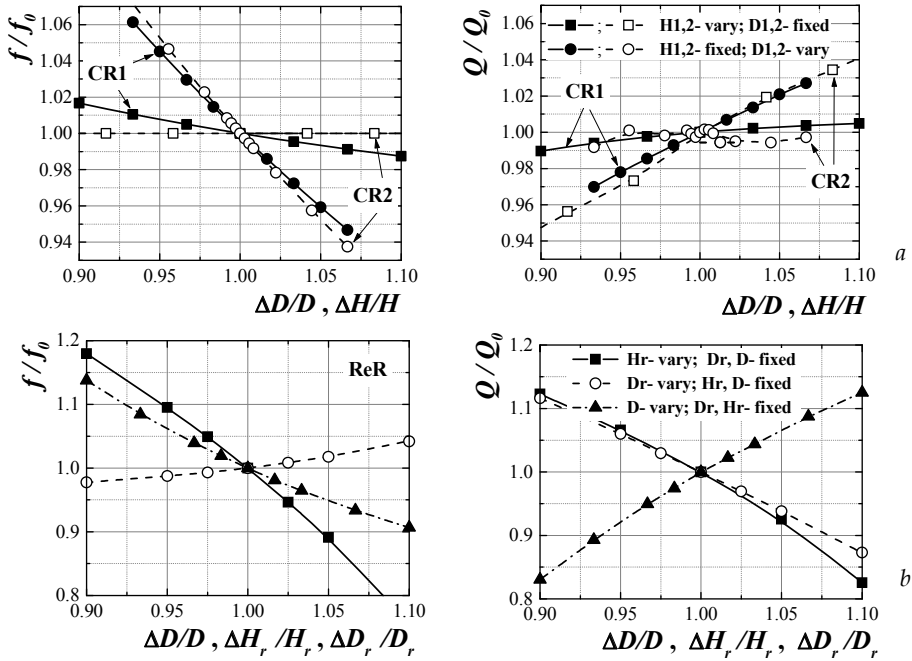


Fig. 8. Dependencies of the normalized resonance frequency and normalized Q-factor of the dominant mode in: a) resonators CR1/CR2; b) re-entrant resonator ReR, when one geometrical parameter varies, while the other ones are fixed

Resonator type	R1	(1/8) R1	R2	(1/4) R2
$f_{0,1,2}$ , GHz	13.1847	13.1846	12.6391	12.6391
$Q_{0,1,2}$	14088	14094	3459	3462
Computational time	177 : 1		47 : 1	

Table 1. Resonance parameters of empty cavities and their equivalents ( $D_1 = 30.0$  mm;  $H_1 = 29.82$  mm,  $D_2 = 18.1$  mm,  $H_2 = 12.09$  mm)

N	72	108	144	180	216	288	Meas.
<b>CR1</b> cavity (TE <sub>011</sub> mode): $D_{eq1} = 30.084$ mm; $\sigma_{eq1} = 1.70 \times 10^7$ S/m							
$f_{01}$ , GHz	13.1578	13.1541	13.1529	13.1527	13.1523	13.1520	13.1528
$Q_{01}$	14086	14106	14115	14111	14108	14109	14117
<b>CR2</b> cavity (TM <sub>010</sub> mode): $D_{eq2} = 18.156$ mm; $\sigma_{eq2} = 0.92 \times 10^7$ S/m							
$f_{02}$ , GHz	12.6460	12.6418	12.6400	12.6392	12.6387	12.6383	12.6391
$Q_{02}$	3552	3475	3487	3533	3545	3571	3526

Table 2. Resonance parameters of empty cavities v/s the line-segment number N



The reason for this assumption is given in Fig. 8, where the dependencies of the normalized resonance frequencies and unloaded Q-factors are presented versus the relative dimension variations. We can see that the diameter variation in both of the cavities affects the resonance frequency stronger compared to the height variation. For example, in the case of CR1 or SCR the increase of  $D_1$  leads to 378 MHz/mm decrease of the resonance frequency  $f_{01}$ , while the increase of  $H_1$  - only 64 MHz/mm decrease of  $f_{01}$ . The effect over the Q-factor in CR1 is similar, but in the case of CR2 the Q-factor changes due to the  $H_2$ -variations are stronger. Nevertheless, we accept the diameter as an equivalent parameter  $D_{eq1,2}$  for the of the cavities - see the concrete values in Table 2. We observe an increase of the equivalent diameters with 0.3% in the both cases ( $D_{eq1} \sim 30.084$  mm;  $D_{eq2} = 18.156$  mm), while for the equivalent conductivity the obtained values are 3-4 times smaller ( $\sigma_{eq1} = 1.70 \times 10^7$  S/m;  $\sigma_{eq2} = 0.92 \times 10^7$  S/m than the value of the bulk gold conductivity  $\sigma_{Au} = 4.1 \times 10^7$  S/m). Thus, the utilization of the equivalent cylindrical 3D models considerably decreases the measuring errors, especially for determination of the loss tangent. Moreover, the equivalent model takes into account the "daily" variations of the empty cavity parameters ( $\pm 0.02\%$  for  $D_{eq1,2}$ ;  $\pm 0.6\%$  for  $\sigma_{eq1,2}$ ) and makes the proposed method for anisotropy measurement independent of the equipment and the simulator used.

It is important to investigate the influence of the number  $N$  of surface segments necessary for a proper approximation of the cylindrical resonator shape over the simulated resonance characteristics. The data in Table 2 show that small numbers  $N < 144$  does not fit well the equivalent circle of the cylinders, while number  $N > 288$  considerably increases the computational time. The optimal values are in the range  $144 < N < 216$  for the both resonators CR1 and CR2. The results show that the resonator CR2 is more sensitive to the  $N$  value. The practical problem is -how to choose the right value  $N$ ? We have found out that the optimal value of  $N$  and the equivalent parameters  $D_{eq}$  and  $\sigma_{eq}$  are closely dependent. Accurate and repeatable results are going to be achieved, if the following rule has been accepted: the values of the equivalent parameters to be chosen from the simple expressions (2, 3), and then to determine the suitable number  $N$  of surface segments in the models. The needed expressions could be deduced from the analytical models (see Dankov, 2006):

$$R_{eq1} = 182.824 H_1 \left( f_{01}^2 H_1^2 - 22468.9 \right)^{1/2}, \quad R_{eq2} = 114.74274 / f_{02}, \quad (2)$$

$$\sigma_{eq1,2} = 3947.842 f_{01,2} / R_{S1,2}^2, \quad (3)$$

where the surface resistance  $R_{S1,2}$  is expressed as

$$R_{S1} = 1.8798 \times 10^{-5} H_1 R_{eq1}^2 f_{01}^3 \frac{1}{Q_{01}} \left[ 0.5 H_1 / R_{eq1} - 1 + 2.9918 \times 10^{-5} (R_{eq1} f_{01})^2 \right]^{-1}, \quad (4)$$

$$R_{S2} = 0.5 H_2 \left( 2.40483 / R_{eq2} \right)^2 \frac{1}{Q_{02}} \left[ 5.56313 \times 10^{-5} f_{02} \left( 1 + H_2 / R_{eq2} \right) \right]^{-1} \quad (5)$$

All the geometrical dimensions  $R_{eq1,2}$  and  $H_{1,2}$  in the expressions (2-5) are in mm,  $f_{01,2}$  - in GHz,  $R_{S1,2}$  - in Ohms and  $\sigma_{eq1,2}$  - in S/m. After the described procedure, the optimal number  $N$  of rectangular segments in CR1/CR2 is  $N \sim 144$ -180. Similar values can be obtained by a simple rule - the line-segment width should be smaller than  $\lambda/16$  ( $\lambda$  - wavelength). This simple rule allows choosing of the right  $N$  value directly, without preliminary calculations.

Let's now to consider the determination of the equivalent parameters in the other types of resonators. In Fig. 8b we demonstrate the influence of the relative shift of each of the dimensions  $D$ ,  $D_r$  and  $H_r$  over the normalized resonance parameters  $f/f_0$  and  $Q/Q_0$  of an empty re-entrant cavity. The results show that the resonance frequency variations are strongest due to the variations of the re-entrant cylinder height  $H_r$  ( $\pm 10\%$  for  $\Delta H_r/H_r \sim \pm 5\%$ ). Therefore, it should be chosen as an equivalent parameter in the 3D model of the re-entrant cavity (*equivalent height*). But the variations due to the outer diameter are also strong ( $\pm 5\%$  for  $\Delta D/D \sim \pm 5\%$ ) (For build-in cylinder diameter the changes are smaller than  $\pm 1\%$  for  $\Delta D_r/D_r \sim \pm 5\%$ ). The variations of the Q-factor of the dominant mode have similar values for all of the considered parameters (note: the effects for  $\Delta H_r/H_r$  and for  $\Delta D/D$  have opposite signs). So, in the re-entrant cavity 3D model we can select *two equivalent geometrical parameters*: 1) equivalent outer cylinder diameter  $D_{eq2}$ , when  $H_r = 0$  (e. g. the re-entrant resonator is a pure cylindrical resonator with TM<sub>010</sub> mode) and 2) equivalent build-in cylinder height  $H_{eq,r}$ , when  $D_{eq2}$  has been already chosen. This approximation allows us a direct comparison between the results from cylindrical and re-entrant resonators, if the last one has a movable inner cylinder. Very similar behaviour has the other tunable cavity SCoaxR – we have to determine an equivalent height  $H_{eq,r}$  of the both coaxial cylinders. The last pair of measurement resonators consists of additional unknown elements – one or two DR's. In this more complicated case, after the determination of the mentioned equivalent parameters of the empty resonance cavity (R1, SCR or R2), an “*equivalent dielectric resonator*” should be introduced. This includes the determination of the actual dielectric parameters ( $\epsilon'_{DR}$ ,  $\tan \delta_{eDR}$ ) of the DR with measured dimensions  $d_{DR}$  and  $h_{DR}$ . The anisotropy of the DR itself is not a problem in our model; in fact, we determine exactly the actual parameters in the corresponding case – parallel ones in SPDR (e) or perpendicular ones in SPDR(m). The actual parameters of the necessary supporting elements (rod, disk) for the DR mounting should also to be determined. The only problem is the “depolarization effect”, which takes place in similar structures with relatively big normal components of the electric field at the interfaces between two dielectrics. In our 3D models the presence of depolarization effects are hidden (more or less) into the parameters of the “equivalent DR”.

#### 4.4 Measurement errors, sensitivity and selectivity

The investigation of the sources of measurement errors during the substrate-anisotropy determination by the two-resonator method is very important for its applicability. The analysis can be done with the help of the 3D equivalent model of a given structure: the value of one parameter has to be varied (e. g. sample height) keeping the values of all other parameters and thus, the particular relative variation of the permittivity and loss tangent values can be calculated. Finally, the total relative measurement error is estimated as a sum of these particular relative variations. A relatively full error analysis was done by Dankov, 2006 for ordinary resonators CR1/CR2. It was shown that the contributions of the separate parameter variations are very different, but the introduction of the equivalent parameters – equivalent  $D_{eq1,2}$ , equivalent height  $H_{eq,r}$  (in ReR and SCoaxR) and equivalent conductivity  $\sigma_{eq1,2}$ , considerably reduce the dielectric anisotropy uncertainty due to the uncertainty of the resonator parameters. Thus, the main benefit of the utilization of equivalent 3D models is that the errors for the measurement of the pairs of values ( $\epsilon'_{||}$ ,  $\tan \delta_{e||}$ ) and ( $\epsilon'_{\perp}$ ,  $\tan \delta_{e\perp}$ ) remain to depend mainly on the uncertainty  $\Delta h/h$  in the sample height (Fig. 9), especially for relative thin sample, and weakly on the sample positioning uncertainty (in CR1).

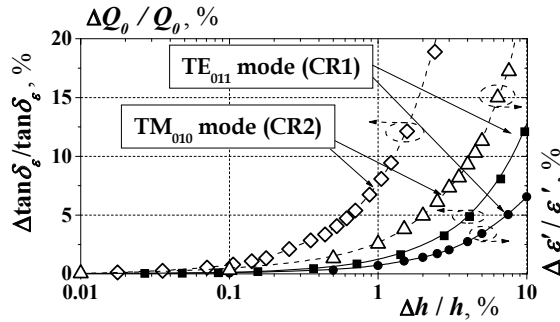


Fig. 9. Calculated relative errors in CR1/CR2:  $\Delta\varepsilon'/\varepsilon'$  v/s  $\Delta h/h$  and  $\Delta\tan\delta_{\varepsilon'}/\tan\delta_{\varepsilon'}$  v/s  $\Delta Q_0/Q_0$

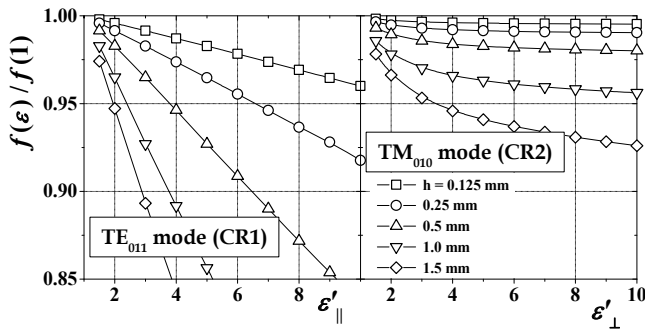


Fig. 10. Calculated sensitivity in CR1/CR2 according to sample dielectric constants  $\varepsilon'_{||}$ ,  $\varepsilon'_{\perp}$

Taking into account the above-discussed issues the measuring errors in the two-resonator method can be estimated as follows:  $< 1.0\text{-}1.5\%$  for  $\varepsilon'_{||}$  and  $< 5\%$  for  $\varepsilon'_{\perp}$  for a relatively thin substrate like RO3203 with thickness  $h = 0.254$  mm measured with errors  $\Delta h/h < 2\%$  (this is the main source of measurement errors for the permittivity). Besides, if the positioning uncertainty reaches a value of 10% for the sample positioning in CR1 (absolute shift up to  $\pm 1.5$  mm), the relative measurement error of  $\varepsilon'_{||}$  does not exceed the value of 2.5%. The measuring errors for the determination of the dielectric loss tangent are estimated as: 5-7% for  $\tan\delta_{\varepsilon'_{||}}$ , but up to 25% for  $\tan\delta_{\varepsilon'_{\perp}}$ , when the measuring error for the unloaded Q-factor is 5% (this is the main additional source for the loss-tangent errors; the other one is the dielectric constant error).

A real problem of the considered method for the determination of the dielectric constant anisotropy  $\Delta A_{\varepsilon}$  is the *measurement sensitivity* of the  $\text{TM}_{010}$  mode in the resonator CR2 (for  $\varepsilon'_{\perp}$ ), which is noticeably smaller compared to the sensitivity of the  $\text{TE}_{011}$  mode in CR1 (for  $\varepsilon'_{||}$ ). We illustrate this effect in Fig. 10, where the curves of the resonance frequency shift versus the dielectric constant have been presented for one-layer samples with height  $h$  from 0.125 up to 4 mm. The shift  $\Delta f/\Delta\varepsilon$  in R1 for a sample with  $h = 0.5$  mm leads to a decrease of 480 MHz for the doubling of  $\varepsilon'_{||}$  (from 2 to 4), while the corresponding shift in CR2 leads only to a decrease of 42.9 MHz for the doubling of  $\varepsilon'_{\perp}$ . Also, the Q-factor of the  $\text{TM}_{010}$  mode in CR2 is smaller compared to the Q-factor of the  $\text{TE}_{011}$  mode in CR1. This leads to an unequal accuracy for the determination of the loss tangent anisotropy  $\Delta A_{\tan\delta_{\varepsilon'}}$ , too.

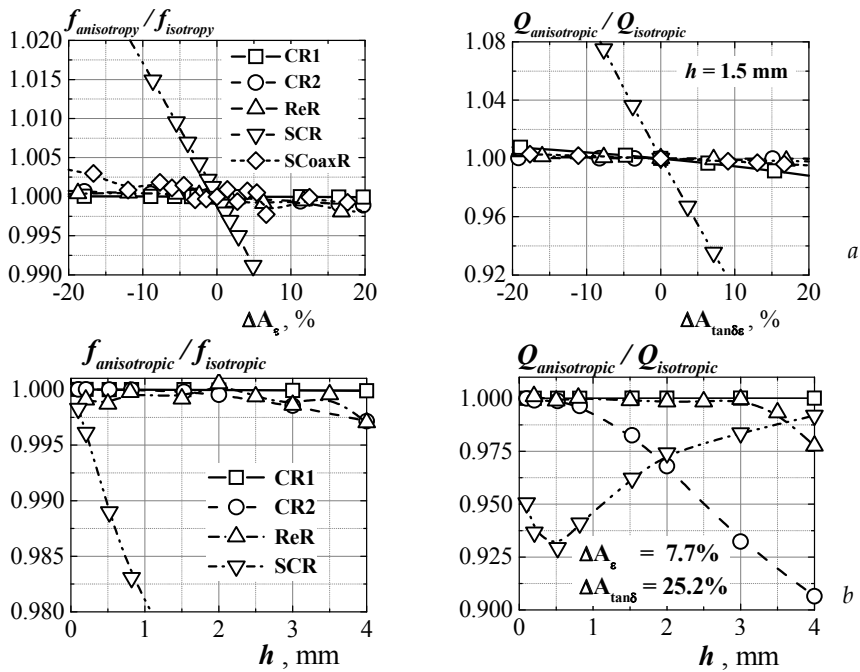


Fig. 11. Dependencies of the normalized resonance frequency and Q-factors of the resonance modes for anisotropic and isotropic samples: *a*) v/s dielectric anisotropy  $\Delta A_\epsilon, \Delta A_{\tan\delta}$ ; *b*) v/s the substrate thickness  $h$

Thus, the measured anisotropy for the dielectric constant  $\Delta A_\epsilon < 2.5\text{-}3\%$  and for the dielectric loss tangent  $\Delta A_{\tan\delta} < 10\text{-}12\%$  can be associated to a *practical isotropy* of the sample ( $\epsilon'_{||} \cong \epsilon'_{\perp}; \tan\delta_{e||} \cong \tan\delta_{e\perp}$ ), because these differences fall into the measurement error margins.

Finally, the problem of the *resonator selectivity* (the ability to measure either pure parallel or pure perpendicular components of the dielectric parameters) is considered. The results for the normalized dependencies of the resonance frequencies and Q-factors for anisotropic and isotropic samples in the separate resonators are presented in Fig. 11. These are two types of dependencies- according to the substrate anisotropy at a fixed thickness and according to the substrate thickness at a fixed anisotropy. How have these data been obtained? Each 3D model of the considered resonators contains sample with fixed dielectric parameters: once isotropic, then - anisotropic. The models in these two cases have been simulated and the obtained resonance frequencies and Q-factors are compared - as ratio  $(f, Q)_{\text{anisotropic}} / (f, Q)_{\text{isotropic}}$ . The presented results unambiguously show that most of the used resonators measure the corresponding "pure" parameters with errors less than  $\pm 0.3\text{-}0.4\%$  for dielectric constant and less than  $\pm 0.5\text{-}1.0\%$  for the dielectric loss tangent in a wide range of anisotropy and substrate thickness. The problems appear mainly in the SCR; so the split-cylinder resonator can be used neither for big dielectric anisotropy, nor for thick samples - its selectivity becomes considerably smaller compared to the good selectivity of the rest of the resonators. A problem appears also for the measurement of the dielectric loss tangent in very thick samples by CR2 resonator (see Fig. 11*b*).

### 5. Data for the Anisotropy of Some Popular Dielectric Substrates

#### 5.1 Isotropic material test

A natural test for the two-resonator method and the proposed equivalent 3D models is the determination of the *dielectric isotropy* of clearly expressed isotropic materials (“isotropic-sample” test). Results for for three types of isotropic materials have been presented in Table 3 with increased values of dielectric constant and loss tangent – PTFE, polyolefine and polycarbonate (averaged for 5 samples). The measured “anisotropy” by the pair of resonators CR1/CR2 is very small ( $< 0.6\%$  for the dielectric constant and  $< 4\%$  for the loss tangent) – i. e. the practical isotropy of these materials is obvious. The next “isotropic-sample” test is for polycarbonate samples with increased thickness (from 0.5 to 3 mm) – Fig. 12. The both resonators give close values for the dielectric constant (measured average value  $\epsilon'_r \sim 2.6525$ ) even for thick samples, nevertheless that the “anisotropy”  $\Delta A_{\epsilon}$  reaches to the value  $\sim 2.5\%$ . The results for the loss tangent are similar – the models give average  $\tan\delta_{\epsilon} \cong 0.005\text{--}0.0055$  and mean “anisotropy”  $\Delta A_{\tan\delta_{\epsilon}} < 4\%$ . All these differences correspond to the practical isotropy of the considered material, especially for small thickness  $h < 1.5$  mm. The final test is for one sample – 0.51-mm thick transparent polycarbonate Lexan® D-sheet ( $\epsilon_r \cong 2.9$ ;  $\tan\delta_{\epsilon} \cong 0.0065$  at 1 MHz), measured by different resonators in wide frequency range 2–18 GHz. The measured “anisotropy” of this material is less than 3% for  $\Delta A_{\epsilon}$  and less than 11% for  $\Delta A_{\tan\delta_{\epsilon}}$ . These values should be considered as an expression of the limited ability of the two-resonator method to detect an ideal isotropy, as well as a possible small anisotropy of microwave materials with relatively small thickness ( $h < 2$  mm).

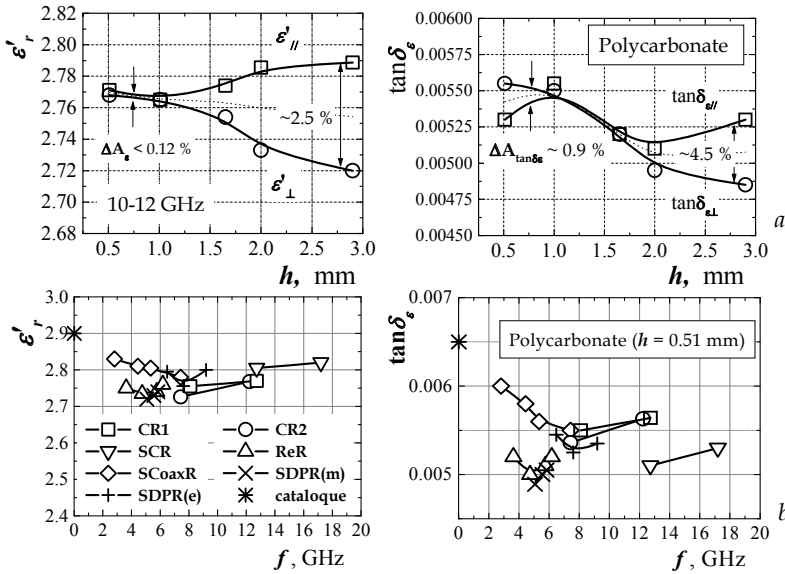


Fig. 12. Isotropy test for polycarbonate sheets: a) v/s the thickness  $h$ ; b) v/s the frequency

Isotropic Sample	$h, \text{ mm}$	CR1:		CR2:		"Anisotropy" $\Delta A_\varepsilon / \Delta A_{\tan\delta_\varepsilon} \%$
		$f_{\varepsilon 1}, \text{ GHz}/Q_{\varepsilon 1}$	$\varepsilon'_{  } / \tan\delta_{\varepsilon  }$	$f_{\varepsilon 2}, \text{ GHz}/Q_{\varepsilon 2}$	$\varepsilon'_{\perp} / \tan\delta_{\varepsilon\perp}$	
PTFE	0.945	12.6945/9596	2.0451/0.00025	12.3499/3160	2.0470/0.00026	-0.1 / -4.0
Polyolefine	0.7725	12.5856/8004	2.3060/0.00415	12.3756/3120	2.3210/0.00400	-0.6 / 3.7
Polycarbonate	1.000	12.3222/775	2.7712/0.00530	12.2325/1767	2.7650/0.00551	0.2 / -4.0

Table 3. "Isotropic-sample test" of the pair CR1/CR2. Cavity parameters: CR1:  $f_{01} = 13.1512$  GHz;  $Q_{01} = 14154$ ;  $D_{eq1} = 30.088$  mm;  $\sigma_{eq1} = 1.71 \times 10^7$  S/m; CR2:  $f_{02} = 12.6394$  GHz;  $Q_{02} = 3465$ ;  $D_{eq2} = 18.156$  mm;  $\sigma_{eq2} = 0.89 \times 10^7$  S/m

## 5.2 Data for some popular PWB substrates

The first example for anisotropic materials includes data for the measured dielectric parameters of several commercial reinforced substrates with practically equal catalogue parameters. These artificial materials contain different numbers of penetrated layers (depending on the substrate thickness) of woven glass with an appropriate filling and therefore, they may have more or less noticeable anisotropy. In fact, the catalogue data do not include an information about the actual values of  $\Delta A_\varepsilon$  and  $\Delta A_{\tan\delta_\varepsilon}$ .

The measured results are presented in Table 4 for several RF substrates with thickness about 0.51 mm (20 mils) with catalogue dielectric constant  $\sim 3.38$  and dielectric loss tangent  $\sim 0.0025$  -  $0.0030$ , obtained by IPC TM-650 2.5.5.5 test method at 10 GHz. The substrates are presented with their authentic designations and with their actual thickness  $h$ . We compare all the measured resonance parameters (resonance frequency and Q-factor) by the pair CR1/CR2 and the forth dielectric parameters. A separate column in Table 4 contains the important information about the measured anisotropy  $\Delta A_\varepsilon$  and  $\Delta A_{\tan\delta_\varepsilon}$ . The dielectric parameters are averaged for minimum 5 samples, extracted from one substrate panel with controlled producer's origin. The measurement errors are:  $(\Delta\varepsilon'/\varepsilon')_{||} \cong 0.3\%$ ;  $(\Delta\varepsilon'/\varepsilon')_{\perp} \cong 0.5\%$ ;  $(\Delta\tan\delta_\varepsilon/\tan\delta_\varepsilon)_{||} \cong 1.2\%$ ;  $(\Delta\tan\delta_\varepsilon/\tan\delta_\varepsilon)_{\perp} \cong 3\%$ ; for  $(\Delta f_\varepsilon/f_\varepsilon) \cong 0.04\%$ ;  $(\Delta Q_\varepsilon/Q_\varepsilon) \cong 1.5\%$ ;  $(\Delta h/h) \cong 0.5\%$ . Nevertheless, that the substrates are offered as similar ones, they demonstrate different measured parameters and anisotropy, which takes places mainly due to the variations in the longitudinal (parallel) values  $\varepsilon'_{||}$  and  $\tan\delta_{\varepsilon||}$ , obtained by CR1 and not included in the catalogues. The measured transversal (normal) values  $\varepsilon'_{\perp}$  and  $\tan\delta_{\varepsilon\perp}$ , obtained by CR2, differ

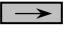

Substrate (20mills thick)	$h, \text{ mm}$	CR1: 		CR2: 		$\Delta A_\varepsilon / \Delta A_{\tan\delta_\varepsilon} \%$	IPC TM 650 2.5.5.5 @ 10 GHz
		$f_{\varepsilon 1}, \text{ GHz}/Q_{\varepsilon 1}$	$\varepsilon'_{  } / \tan\delta_{\varepsilon  }$	$f_{\varepsilon 2}, \text{ GHz}/Q_{\varepsilon 2}$	$\varepsilon'_{\perp} / \tan\delta_{\varepsilon\perp}$		
Rogers Ro4003	0.510	12.5050/1780	3.67/0.0037	12.4235/2834	3.38/0.0028	8.2/27.7	3.38/0.0027
Arlon 25N	0.520	12.5254/1492	3.57/0.0041	12.4243/2671	3.37/0.0033	5.8/21.6	3.38/0.0025
Isola 680	0.525	12.4820/1280	3.71/0.0049	12.4215/1767	3.32/0.0042	11.1/15.4	3.38/0.003
Taconic RF-35	0.512	12.4552/1176	3.90/0.0049	12.4254/2729	3.45/0.0038	12.2/25.3	3.50/0.0033
Neltec NH9338	0.520	12.4062/1171	4.02/0.0051	12.4303/2849	3.14/0.0025	24.6/68.4	3.38/0.0025
GE Getek R54	0.515	12.4544/1163	3.91/0.0050	12.4238/2715	3.50/0.0038	11.1/27.3	3.90/0.0046 by "split-post cavity"

Table 4. Measured dielectric parameters and anisotropy of some commercial substrates, which catalogue parameters are practically equal or very similar




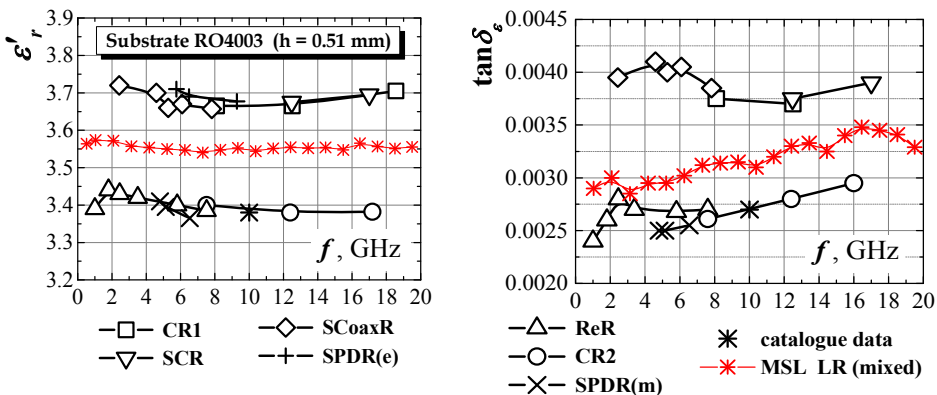
Substrate	$h$ , mm				$\Delta A_\varepsilon / \Delta A_{\tan\delta\theta}$ %	IPC TM 650 2.5.5.5 10 GHz
		$\varepsilon'_{  } / \tan\delta_{\varepsilon  }$	$\varepsilon'_{\perp} / \tan\delta_{\varepsilon\perp}$	$\varepsilon'_{eq} / \tan\delta_{\varepsilon eq}$		
Rogers Ro3003	0.27	3.00/0.0012	2.97/0.0013	2.99/0.0013	1.0/-8.0	3.00/0.0013
Rogers Ro3203	0.26	3.18/0.0027	2.96/0.0021	3.08/0.0025	7.2/25.0	3.02/0.0016
Neltec NH9300	0.27	3.42/0.0038	2.82/0.0023	3.02/0.0023	19.2/49.2	3.00/0.0023
Arlon DiClad880	0.254	2.32/0.0016	2.15/0.00093	2.24/0.0011	7.6/53.0	2.17/0.0009
Rogers Ro4003	0.52	3.66/0.0037	3.37/0.0029	3.53/0.0031	8.3/24.3	3.38/0.0027
Neltec NH9338	0.51	4.02/0.0051	3.14/0.0025	3.51/0.0032	24.6/68.4	3.38/0.0025
Isola FR 4	0.245	4.38/0.015	3.94/0.019	-	10.6/21.6	4.7/0.01 (1MHz)
Corsa Alumina	0.60	9.65/0.0003	10.35/0.0004	-	-6.8/-29	9.8-10.7
3M Epsilam 10	0.635	11.64/0.0022	9.25/0.0045	-	22.9/-69	~9.8
Rogers TMM 10i	0.635	11.04/0.0019	10.35/0.0035	10.45/0.0023	6.5/-59	9.80/0.0020
Rogers Ro3010	0.645	11.74/0.0025	10.13/0.0038	-	14.7/-41	10.2/0.0035

Table 5. Measured parallel, perpendicular and equivalent dielectric parameters of substrates

very slightly from the catalogue data by IPC TM-650 2.5.5.5 test method (the shifts fall into the catalogue tolerances). (An exception is the substrate, measured by a “split-post cavity” technique, which gives its longitudinal parameters). In fact, the bigger differences are observed mainly for the longitudinal parameters, measured along to the woven-glass cloths of the reinforced materials. Therefore, the dielectric constant anisotropy  $\Delta A_\varepsilon$  of these substrates varies in the interval from 5.8 % up to 25%, while the loss tangent anisotropy  $\Delta A_{\tan\delta\theta}$  varies from 15% up to 68 %. All these results for the anisotropy are caused by the specific technologies, used by the manufacturers (see also the additional results in Table 5 for other substrates in the frequency range 11.5-13 GHz). These data show the usefulness of the two-resonator method – it allows detecting of rather fine differences even for substrates, offered in the catalogues as identical.

Fig. 13. Measured dielectric parameters ( $\varepsilon_{||}$ ,  $\varepsilon_{\perp}$ ,  $\tan\delta_{\varepsilon||}$ ,  $\tan\delta_{\varepsilon\perp}$ ) of anisotropic substrate Ro4003 by 3 different pairs of resonators and with planar linear MSL resonator

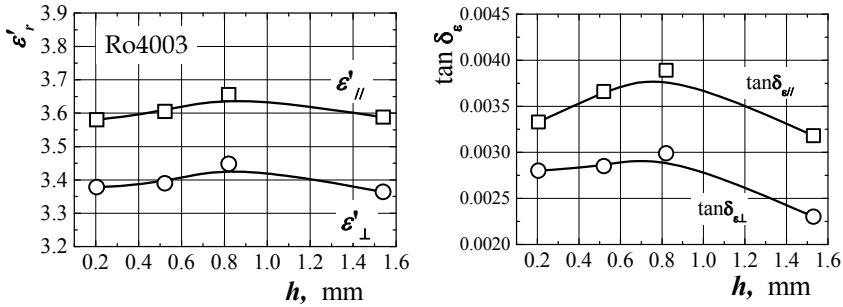


Fig. 14. Dielectric parameters of the anisotropic substrate Ro4003 v/s the thickness

This advantage is demonstrated also in Fig. 13, where the frequency dependencies of the dielectric parameters of one popular microwave non-PTFE reinforced substrate Ro4003 have been presented. The mean measured anisotropy in wide frequency range 2-18 GHz is  $\sim 8.7\%$  for  $\Delta A_{\epsilon}$  and  $\sim 48\%$  for  $\Delta A_{\tan \delta_{\epsilon}}$  (or  $\sim 8.4\%$  for  $\Delta A_{\epsilon}$  and  $\sim 24\%$  for  $\Delta A_{\tan \delta_{\epsilon}}$  at 12 GHz). These data are fully acceptable for design purposes.

### 5.3 Influence of the substrate thickness and substrate inhomogeneity

The mentioned good selectivity of the two-resonator methods allows also investigating of the dielectric anisotropy of the materials versus their standard thickness, offered in the catalogue. Usually the producers do not specify separate data for different thickness, but this is not enough for substrates with great anisotropy. The data in Fig. 14 are for the considered laminate Ro4003 with a relatively weak anisotropy. Our results show that the average anisotropy of this material does not practically change for the offered thickness values,  $\Delta A_{\epsilon} \sim 6-8\%$ ,  $\Delta A_{\tan \delta_{\epsilon}} \sim 20-26\%$ . A maximum for the dielectric constant and the loss tangent is observed for a medium thickness, for which this material has probably biggest density. The explanation is that the thinner samples have smaller number of reinforced cloths, while the thicker samples probably contain more air-filled irregularities between the fibers of the woven fabrics. In the both cases the dielectric parameters slightly decrease.

The users, who are permanently working with great volumes of substrates, often have doubts, whether the parameters of the newly delivered sheets are kept in the frame of the catalogue data, or whether they are equal in the different areas of the whole large-size sheets. We have investigated the local inhomogeneity of the main microstrip parameters of a great number of samples extracted from big sheets of two different substrates and the results for the values of their standard deviations (SD's) in % are presented in Table 6. We can see that the SD's of the dielectric constant and the loss tangent of the 2<sup>nd</sup> substrate are about twice greater than the corresponding values of the 1<sup>st</sup> substrate. This fact could be connected with the bigger deviation of the substrate thickness  $SD/h$  of the substrate 2. The same effect is also the most likely explanation for the bigger SD's of the perpendicular dielectric parameters of the both substrates compared with the SD's of their parallel dielectric parameters.



Substrate	SD $\varepsilon_{  }$	SD $\varepsilon_{\perp}$	SD tan $\delta_{\varepsilon_{  }}$	SD tan $\delta_{\varepsilon_{\perp}}$	SD $h$	Sam ples	SD $Z_c$	SD $\varepsilon_{eff}$	SD $\beta$	SD $\alpha$
Substrate 1	$\pm 0.2$	$\pm 0.5$	$\pm 2.0$	$\pm 9.0$	$\pm 0.2$	32	$\pm 0.22$	$\pm 0.45$	$\pm 0.23$	$\pm 4.4$
Substrate 2	$\pm 0.80$	$\pm 1.00$	$\pm 8.5$	$\pm 13.0$	$\pm 0.7$	90	$\pm 0.52$	$\pm 0.91$	$\pm 0.45$	$\pm 6.1$

Table 6. Measured standard deviations (in %) of the parameters of large-size substrate sheets. The influence of the measured statistical behaviour of the dielectric parameters over the microstrip impedance  $Z_c$  deviations (in Ohms) or over the attenuation  $\alpha$  deviations (in dB/cm) is not so big. In fact, the problems appear for the standard deviations of the effective dielectric constant  $\varepsilon_{eff}$  and the phase shift  $\beta$  (in deg/cm). Nevertheless, that SD's for the 2<sup>nd</sup> substrate are not so big,  $SD\varepsilon_{eff} \cong \pm 0.91$  % and  $SD\beta \cong \pm 0.45$  %, the total phase delay in relatively long feed lines in big antennas (for example  $> 10\lambda_g$ ) can accumulate an additional random phase delay, which can be taken into account in the antenna-array design. For example, two microstrip feeds with equal length 35-40 cm (electrical length 7000-8000 deg) can accumulate a random phase difference about  $\pm 30$ -35 deg, which can easy destroy the beamforming of any planar antenna array.

## 6. Equivalent Dielectric Constant of the Anisotropic Materials

### 6.1 Concept of the equivalent dielectric parameters

Is the dielectric anisotropy of the modern RF substrates a bad or a useful property is a discussible problem. In fact, the application of the anisotropy into the modern simulators is not jet enough popular among the RF designers, despite of the proven fact that the influence of this property might be noticeable in many microwave structures (see Drake et. al., 2000). Some examples for utilization of the anisotropic substrates into the modern simulators have been considered by (Dankov et al., 2003). An interesting example for the benefit of taking into account of the substrate anisotropy in the simulator-based design of ceramic filters has been discussed by (Rautio, 2008). The simulation of 3D structures with anisotropic materials is not an easy task, even impossible in some types of simulators (e.g. method-of-moment based MoM simulators, ordinary schematic simulators, etc.). In the finite-element based FEM or FDTD simulators (HFSS, CST microwave studio, etc.) the introduction of the material isotropy is possible (for example in the eigen-mode option), but the older versions of these products do not allow simultaneously simulations of anisotropic and lossy materials. The latest versions, where the simulations with arbitrary anisotropic materials are possible, have special requirements for the quality of the meshing of the structure 3D model. The utilization of the anisotropy in the simulators should be overcome, if *equivalent dielectric parameters* have been introduced, which transforms the real anisotropic planar structure into an equivalent isotropic one. The concept for the equivalent dielectric constant  $\varepsilon_{eq}$  has been introduced by Ivanov & Peshlov 2003, then the similar concept for the equivalent dielectric loss tangent tan $\delta_{\varepsilon_{eq}}$  has been added by Dankov et al., 2003. We can consider  $\varepsilon_{eq}$  and tan $\delta_{\varepsilon_{eq}}$  as resultant scalar parameters, caused by the influence of the arbitrary mixing of longitudinal and transversal electric fields in a given planar structure. Therefore, the constituent isotropic material should be characterized by the following equivalent parameters:

$$\varepsilon'_{eq} = a \varepsilon'_{||} + b \varepsilon'_{\perp}, \quad \tan \delta_{\varepsilon_{eq}} = c \tan \delta_{\varepsilon_{||}} + d \tan \delta_{\varepsilon_{\perp}} \quad (6)$$

It is easy to predict, that the values of the equivalent dielectric parameters should be dependent on the type of the planar structure under interest. Thus, the usefulness of the equivalent parameters depends on the designed device and it is restricted to transmission lines with non-TEM propagation modes (e. g., coplanar waveguides and coplanar lines), multi-impedance structures and other RF components, which support high-order modes.

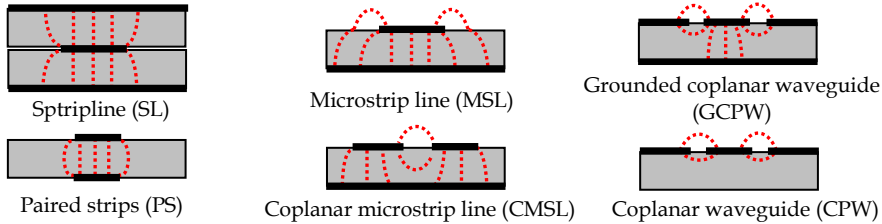


Fig. 15. Investigated planar structures on one substrate – see the results in Fig. 16

### 6.2 Determination of the equivalent dielectric parameters of different planar lines

In this section we will consider the methods for determination of the equivalent parameters  $\epsilon_{eq}$  and  $\tan\delta_{\epsilon,eq}$ . The investigated structures are schematically shown in Fig. 15. The most usable is the ordinary microstrip line, but the other lines also have applications in many RF projects. Considering the E-field curves of the dominant mode in each structure, we can conclude that the substrate anisotropy may disturb the characteristics of these planar lines with different degree. Let's accomplish an experiment – to measure the effective dielectric constant  $\epsilon_{eff}$  and the attenuation  $\alpha$  of the considered structures and then to recalculate the actual (in our case: equivalent) dielectric parameters  $\epsilon_{eq}$  and  $\tan\delta_{\epsilon,eq}$ .

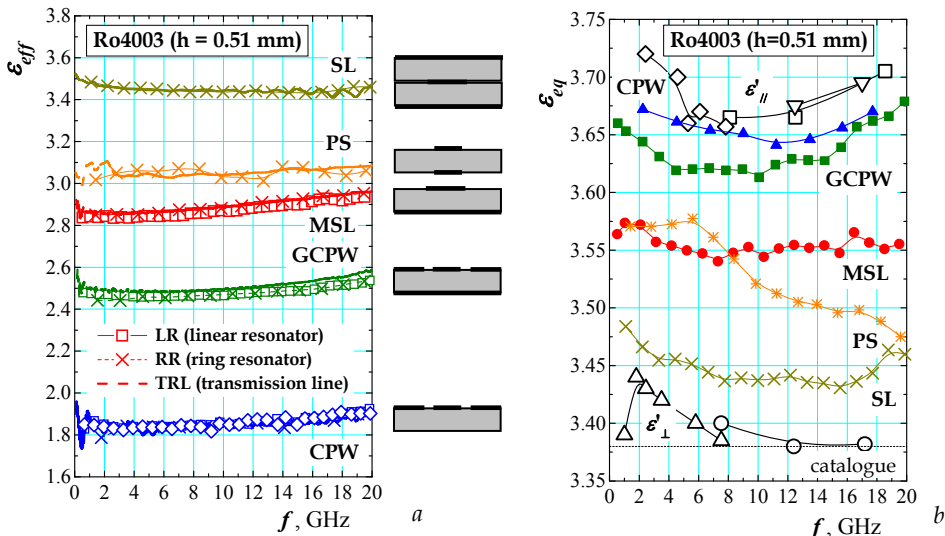


Fig. 16. Unique drawing: the frequency dependencies of the effective (a) and equivalent (b) dielectric constants of several planar structures fabricated on Ro4003 substrate (0.51 mm)

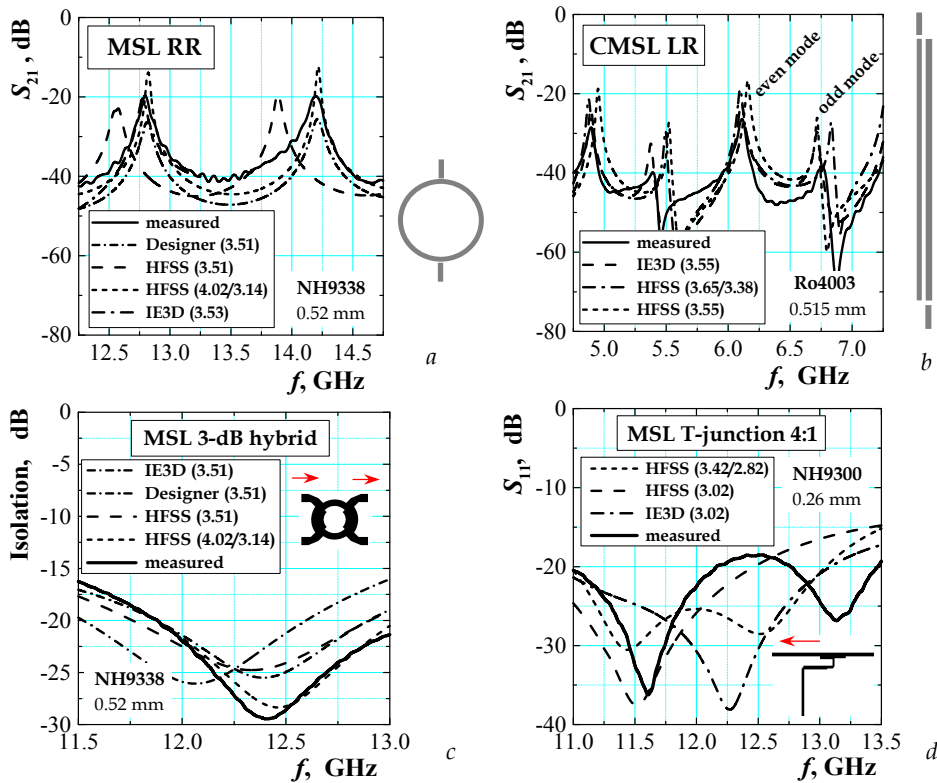


Fig. 17. RF components simulated with anisotropic substrates: *a*) MSL RR (ring diameter 40 mm); *b*) CMSL LR (length 69.6 mm); *c*) 3-dB hybrid; *d*) non-symmetrical T-junction 4:1

The parameters  $\epsilon_{eff}$  and  $\alpha$  (in dB/cm) can be measured by three independent well-known wide-band methods – the ring and linear resonator method (RR, LR) and the transmission-line method (TRL; the “long & short”-line method) (see Chen et. al., 2004). The results for  $\epsilon_{eff}$  are presented in Fig. 16a for 5 planar lines printed on one substrate Ro4003 (data for  $\alpha$  are not given here). We can see the full coincidence between the used 2 or 3 methods for determination of  $\epsilon_{eff}$  -dependencies of each structure. Using the standard methods for converting the parameters:  $\epsilon_{eff} \leftrightarrow \epsilon_{eq}$ ;  $\alpha \leftrightarrow \tan\delta_{\omega,eq}$  (analytical formulas in Wadell, 1991; or standard TRL calculators, which are popular among the RF designers), we can obtain the corresponding equivalent parameters of each planar line (the used method has not been specified, because the presented results are illustrative). The obtained frequency dependencies for  $\epsilon_{eq}$  in wide frequency range 1-20 GHz are drawn in Fig. 16b for each planar line (data for  $\tan\delta_{\omega,eq}$  are presented in Fig. 13 for micro-strip line only). The dependencies are unique; they show how the value of  $\epsilon_{eq}$  is formed for each planar line between the measured values  $\epsilon'_{||}$  and  $\epsilon'_{\perp}$  of Ro4003, depending on the dominant portion of the parallel or perpendicular E fields of the low-order propagation mode. This is also clear evidence why simulations of the planar structures using equivalent parameters are so difficult. In fact, each equivalent parameter depends on the simulated structure and this approach is the

most usable mainly for microstrip lines. Fig. 17 gives 4 illustrative examples for simulations of different planar passive devices with equivalent or with anisotropic parameters. The approach with equivalent parameters gives acceptable results for single-mode, resonance and multi-impedance structures (Fig. 17 *a, c*), while in the case of multi-mode and multi-impedance non-resonance junctions the simulation results with equivalent parameters do not fit the measured characteristics – Fig. 17 *b* (odd mode), *d*.

## 7. Conclusion

The importance of the dielectric anisotropy of the modern RF substrates is the main focus of the investigations in this chapter. There are two main reasons to want to have information for the actual anisotropy of a given substrate – to control the technology (necessary for the manufacturers) and to conduct more realistic simulations of the structures, containing anisotropic materials (necessary for the users). The presented investigations show that the two-resonator method is fully acceptable for determination of the substrate dielectric anisotropy by the help of 3D simulators. The achieved measurement error is less than 3 % for the dielectric constant anisotropy and less than 10 % for the dielectric loss tangent anisotropy in wide frequency range by different pairs of measurement resonators (cylinders, split, coaxial and reentrant cylinders and split-post dielectric resonators) separately for the parallel and for the perpendicular parameters. These parameters can be used in the 3D simulators, when structures with anisotropic materials should be simulated.

## 8. References

- Ansoft HFSS 8 Manual (2001) Eigenmode Problem, [www.ansoft.com/products/hf/hfss/](http://www.ansoft.com/products/hf/hfss/)
- Baker-Jarvis, J. & Riddle B. F. (1996), Dielectric measurement using reentrant cavity, *National Institute of Standards and Technology, Technical Note 1384*, Boulder, CO, USA
- Baker-Jarvis J., Geyer R. G., Grosvenor J. H., Janezic M. D., Jones C. A., Riddle B., Weil C. M. & Krupka J. (1998), Dielectric characterization of low-loss materials. A comparison of techniques, *IEEE Trans. Dielect. Electr. Insul.*, vol. 5, no. 4, pp. 571–577, Aug. 1998.
- Baker-Jarvis, J., Riddle B. & Janezic M. D. (1999), Dielectric and Magnetic Properties of Printed Wiring Boards and Other Substrate Materials, *National Institute of Standards and Technology, Technical Note 1512*, Boulder, CO, USA
- Bereskin, A. B. (1992), Microwave Test Fixture for Determining the Dielectric Properties of the Material, *US Patent 50083088*, Jan. 1992
- Chen, L. F., Ong, C. K., Neo, C. P., Varadan, V. V. & Varadan, V. K. (2004), *Microwave Electronics: Measurement and Materials Characterization*, Wiley, ISBN: 978-0-470-84492-2, Chichester, UK
- Courtney, W. E. (1970), Analysis and evaluation of a method of measuring the complex permittivity and permeability of microwave insulators, *IEEE Trans. Microw. Theory Tech.*, vol. 18, No. 8, Aug. 1970, pp. 476–485, ISSN 0018-9480
- Dankov, P., Kamenopolsky, S. & Boyanov, V. (2003), Anisotropic substrates and utilization of microwave simulators, *Proceedings of 14<sup>th</sup> Microcoll*, pp. 217–220, Budapest Hungary, Sep. 2003

- Dankov, P., Kolev, S. & Ivanov S. (2004), Measurement of dielectric and magnetic properties of thin nano-particle absorbing films, *Proceedings of 17<sup>th</sup> EM Field Mater.*, pp. 89–93, Warsaw, Poland, May 2004
- Dankov, P. I. & Ivanov, S. A. (2004), Two-Resonator Method for Measurement of Dielectric Constant Anisotropy in Multilayer Thin Films, Substrates and Antenna Radomes, *Proceedings of 34<sup>th</sup> European Microwave Conference*, pp. 753-756, ISBN 1-58053-994-7, Amsterdam, The Netherlands, Oct. 2004, Horizon House Publ., London
- Dankov, P. I., Levcheva V. P. & Peshlov, P. N. (2005), Utilization of 3D Simulators for Characterization of Dielectric Properties of Anisotropic Materials, *Proceedings of 35<sup>th</sup> European Microwave Conference*, pp. 517-520, ISBN 1-58053-994-7, Paris, France, Oct. 2005, Horizon House Publ., London
- Dankov, P. I. (2006), Two-Resonator Method for Measurement of Dielectric Anisotropy in Multi-Layer Samples, *IEEE Trans. Microw. Theory Tech.*, vol. 54, No. 4, April 2006, 1534-1544, ISSN 0018-9480
- Dankov, P. I., Hadjistamov, B. N. & Levcheva V. P. (2006), Principles for Utilization of EM 3D Simulators for Measurement Purposes with Resonance Cavities, *Proceedings of IV<sup>th</sup> Mediterranean Microwave Symposium*, pp. 543-546, Genoa, Italy, Sept. 2006
- Dankov, P. I. & Hadjistamov, B. N. (2007), Characterization of Microwave Substrates with Split-Cylinder and Split-Coaxial-Cylinder Resonators, *Proceedings of 37<sup>th</sup> European Microwave Conference*, pp. 933-936, ISBN 1-58053-994-7, Munich, Germany, Oct. 2007, Horizon House Publ., London
- Dankov, P. I. et. all. (2009), Measurement of Dielectric Anisotropy of Microwave Substrates by Two-Resonator Method with Different Pairs of Resonators, Progress in EM Research Symposium *PIERS*, Moscow, Russia, August 2009 (accepted)
- Drake, E., Boix, R. R., Horno, M. & Sarkar, T. K. (2000), Effect of dielectric anisotropy on the frequency behavior of microstrip circuits, *IEEE Trans. Microw. Theory Tech.*, vol. 48, no. 8, Aug. 2000, pp. 1394–1403, ISSN 0018-9480
- EMMA-Club, Nat. Phys. Lab., Middlesex, U.K. (2005), RF and microwave dielectric and magnetic measurements, electro-magnetic material characterization, Online: <http://www.npl.co.uk/electromagnetic/rfmffnewcal/rfmwdielectrics.html>
- Egorov, V. N., Masalov, V. L., Nefyodov, Y. A., Shevchun, A. F., Trunin, M. R., Zhitomirsky, V. E. & McLean, M. (2005), Dielectric constant, loss tangent, and surface resistance of PCB materials at K-band frequencies, *IEEE Trans. Microw. Theory Tech.*, vol. 53, no. 2, Feb. 2005, pp. 627–635, ISSN 0018-9480
- Fritsch U. & Wolff, I. (1992), Characterization of Anisotropic Substrate Materials for Microwave Applications, *IEEE Trans. Microw. Theory Tech.*, MTT-S Digest, No. 12, Dec. 1992, pp. 1131-1134, ISSN 0018-9480
- Gaebler, A., Goelden, F., Mueller, S & Jakoby R. (2008), Triple-Mode Cavity Perturbation Method for the Characterization of Anisotropic Media, *Proceedings of 38<sup>th</sup> European Microwave Conference*, pp. 909-912, ISBN 1-58053-994-7, Amsterdam, The Netherlands, Oct. 2008, Horizon House Publ., London
- Hadjistamov, B., Levcheva V. & Dankov, P. (2007), Dielectric Substrate Characterization with Re-Entrant Resonators, *Proceedings of V<sup>th</sup> Mediterranean Microwave Symposium*, pp. 183-186, Budapest Hungary, May 2007
- IPC TM-650 2.5.5.5 (March 1998) *Test Methods Manual: Stripline Test for Permittivity and Loss Tangent at X-Band*, IPC Northbrook, IL, <http://www.ipc.org/html/fsstandards.htm>

- Ivanov S. A. & Dankov, P. I. (2002), Estimation of microwave substrate materials anisotropy, *J. Elect. Eng. (Slovakia)*, vol. 53, no. 9s, pp. 93–95, ISSN 1335-3632
- Ivanov, S. A. & Peshlov, V. N. (2003), Ring-resonator method—Effective procedure for investigation of microstrip line, *IEEE Microw. Wireless Compon. Lett.*, vol. 13, no. 7, Jul. 2003, pp. 244–246, ISSN 1531-1309
- Janezic, M. D. & Baker-Jarvis, J. (1999), Full-wave analysis of a split-cylinder resonator for nondestructive permittivity measurements, *IEEE Trans. Microw. Theory Tech.*, vol. 47, No. 10, Oct. 1970, pp. 2014–2020, ISSN 0018-9480
- Kent, G. (1988), An evanescent-mode tester for ceramic dielectric substrates, *IEEE Trans. Microw. Theory Tech.*, vol. 36, No. 10, Oct. 1988, pp. 1451–1454, ISSN 0018-9480
- Krupka, J., Cros, D., Aubourg M. & Giullion P. (1994), Study of whispering gallery modes in anisotropic single-crystal dielectric resonators, *IEEE Trans. Microw. Theory Tech.*, vol. 42, no. 1, Jan. 1994, pp. 56–61, ISSN 0018-9480
- Krupka, J., Derzakowski, K., Abramowicz, A., Tobar M. & Gayer, R. G. (1997), Complex permittivity measurement of extremely low-loss dielectric materials using whispering gallery modes, in *IEEE MTT-S Int. Microw. Symp. Dig.*, pp. 1347–1350
- Krupka J., Gregory A.P., Rochard O.C., Clarke R.N., Riddle B., Baker-Jarvis J., (2001) Uncertainty of Complex Permittivity Measurement by Split-Post Dielectric Resonator Techniques, *Journal of the European Ceramic Society*, No. 10, pp. 2673–2676, ISSN 0955-2219
- Laverghetta, T. S. (2000). *Microwave materials and fabrication techniques*, Artech House Publisher, ISBN 1-58053-064-8, Nordwood, MA 02062
- Ming, Y., Panariello, A., Ismail, M. & Zheng J. (2008), 3-D EM Simulators for Passive Devices, *IEEE Microwave Magazine*, vol. 9, no. 6, Dec. 2008, pp.50-61, ISSN 1527-3342
- Mumcu, G., Sertel, K. & Volakis, J. L. (2008), A Measurement Process to Characterize Natural and Engineered Low-Loss Uniaxial Dielectric Materials at Microwave Frequencies, *IEEE Trans. Microw. Theory Tech.*, vol. 56, no. 1, Jan. 2008, pp. 217-223, ISSN 0018-9480
- Olyphant, M. Jr. (1979), Measuring anisotropy in microwave substrates, in *IEEE MTT-S Int. Microw. Symp. Dig.*, 1979, pp. 91–93
- Parka, J., Krupka, J., Dabrowski, R. & Wosik, J. (2007), Measurements of anisotropic complex permittivity of liquid crystals at microwave frequencies, *Journal of the European Ceramic Society*, vol. 27, No. 8-9, 2007, pp. 2903–2905, ISSN 0955-2219
- Rautio, J. C. (2009), A Proposed Uniaxial Anisotropic Dielectric Measurement Technique, *IEEE MTT-S International Microwave Symposium*, Guadalajara, Mexico, Feb. 2009
- Rautio, J. C. (2008), Shortening the Design Cycle, *IEEE Microwave Magazine*, vol. 9, no. 6, Dec. 2008, pp. 86-96, ISSN 1527-3342
- RF Technol. Div., Electron. Elect. Eng. Lab., NIST, Boulder, CO (2005), Electromagnetic properties of materials, Online:<http://www.boulder.nist.gov/div813/emagprop.htm>
- Tobar, M. E., Hartnett, J. G., Ivanov, E. N., Blondy, P. & Cros, D. (2001), Whispering-gallery method of measuring complex permittivity in highly anisotropic materials: Discovery of a new type of mode in anisotropic dielectric resonators, *IEEE Trans. Instrum. Meas.*, vol. 50, no. 4, Apr. 2001, pp. 522–525, ISSN 0018-9456
- van Heuven, J. H. C. & Vlek, T. H. A. M. (1972), "Anisotropy of Alumina Substrates for Microstrip Circuits", *IEEE Trans. Microw. Theory Tech.*, vol. 20, No. 11, Nov. 1972, pp. 775-777, ISSN 0018-9480

- Vanzura, E., Geyer, R. & Janezic, M. (1993), The NIST 60-millimeter diameter cylindrical cavity resonator: Performance for permittivity measurements, NIST, Boulder, CO, *Tech. Note 1354*, Aug. 1993
- Wadell, B. C. (1991). *Transmission Line Design Handbook*, Ch. 3, Artech House Inc. 0-89006-436-9, Norwood, MA, USA
- Zhao, X., Liu, C. & Shen L. C. (1992), Numerical analysis of a TM cavity for dielectric measurements, *IEEE Trans. Microw. Theory Tech.*, vol. 40, No. 10, Oct. 1992, pp. 1951-1958, ISSN 0018-9480





# Application of meta-material concepts

Ho-Yong Kim<sup>1</sup> and Hong-Min Lee<sup>2</sup>

<sup>1</sup>*ACE antenna,*

<sup>2</sup>*Kyonggi University*

*Korea*

## 1. Introduction

Wave propagation in suppositional material was first analyzed by Victor Vesalago in 1968. Suppositional material is characterised by negative permittivity and negative permeability material properties. Under these conditions, phase velocity propagates in opposite direction to group velocity. This phenomenon is referred to as “backward wave” propagation. The realization of backward wave propagation using SRR (Split Ring Resonator) and TW (Thin Wire) was considered by Pendry in 2000. Since then, these electrical structures have been studied extensively and are referred to as meta-material structures. In this chapter we will analyze meta-material concepts using transmission line theory proposed by Caloz and Itho and propose effective materials for realising these concepts. We propose a novel NPLH (Near Pure Left Handed) transmission line concept to reduce RH (Right Handed) characteristics and realize compact small antenna designs using meta-material concepts. In addition we consider enhancing radiation pattern gain of an antenna using FSS (Frequency Selective Surface) and AMC (Artificial Magnetic Conductor). Finally the possibility of realising negative permittivity using EM shielding of concrete block is considered.

## 2. Means of meta-material concepts

The RH and LH transmission lines are shown in Fig. 1.

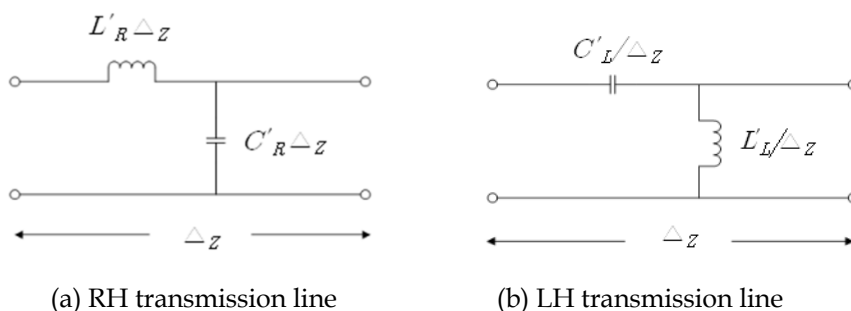


Fig. 1. RH and LH transmission lines

The RH (Right Handed) transmission line consists of serial inductance( $L'_R$ ) and parallel capacitance ( $C'_R$ ). The serial inductance ( $L'_R\Delta z$ ) and parallel capacitance ( $C'_R\Delta z$ ) per unit length are as following equation.

$$C'_R\Delta z = \epsilon_0\epsilon_r \frac{w}{d} \text{ (F/m)} \quad L'_R\Delta z = \mu_0\mu_r \frac{d}{w} \text{ (H/m)} \quad (1)$$

Where, the  $w$  is width of transmission line, the  $d$  is thickness of substrate.

We will consider negative permittivity and negative permeability in transmission line. The serial inductance ( $L'_R\Delta z$ ) and parallel capacitance ( $B_{\text{meta}}$ ) are replaced as negative reactance( $X_{\text{meta}}$ ), which are expressed as following equation.

$$X_{\text{meta}} = -j\omega|L'_R\Delta z| = -j\frac{1}{\omega C_{\text{eff}}} \quad B_{\text{meta}} = -j\omega|C'_R\Delta z| = -j\frac{1}{\omega L_{\text{eff}}} \quad (2)$$

We know that electrical performance of  $L'_R$  and  $C'_R$  are changed into serial capacitance( $C'_L$ ) and parallel inductance( $L'_L$ ) in negative permeability and negative permittivity material.

If we added serial capacitance on normal transmission line, the transmission line with serial capacitance exhibits similar transmission line characteristic using ENG (Epsilon Negative) material. Also, if we use parallel inductance on normal transmission line, the transmission line with parallel inductance express transmission line using MNG (Mu Negative) material. Therefore, we know that the metamaterial concepts can be realized by electrical loading structures, which are gap of microstrip line, via and so on.

The applications of meta-material are shown in Fig. 2. The SNG (Single Negative) materials include ENG material and MNG material. The DNG (Double Negative) material has negative permittivity and negative permeability simultaneously. We will deal with small antenna, CRLH (Composite Right/Left Handed) transmission line, FSS and AMC

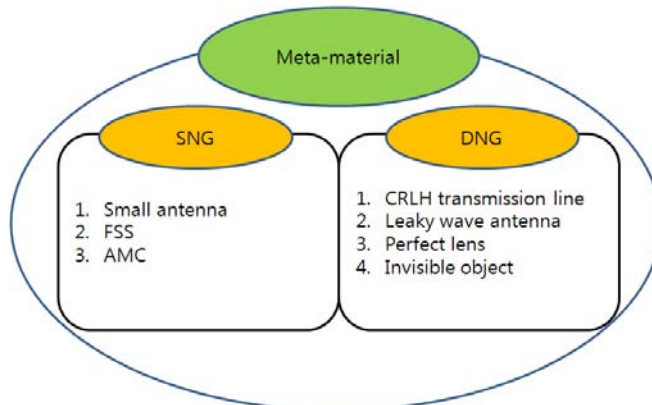


Fig. 2. The applications of meta-material concepts

### 3. NPLH transmission line

#### 3.1 Introduction

Synthesis of meta-material structures has been investigated using various approaches. Amongst these approaches, the transmission line approach has been used to verify backward wave characteristics of LH transmission lines.

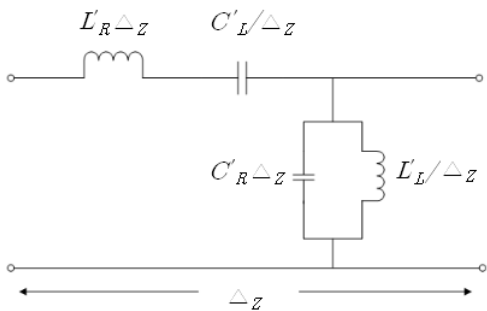
The pure LH (PLH) transmission line can be realized by a unit cell, which is composed of a series capacitor and a parallel inductor and must satisfy effectively homogeneous conditions. However it is difficult to realize an ideal pure LH transmission line, due to generation of parasitic RH (Right Handed) element characteristics of the transmission line which consist of a series inductor and parallel capacitor. A composite Right/ Left Handed (CRLH) transmission line structure concept is therefore used.

A balanced CRLH transmission line structure shows band pass characteristics. The LH dispersion range is below center frequency of pass band and the RH dispersion range is above the center frequency. The LH range is however typically narrow because it is limited by RH parasitic elements.

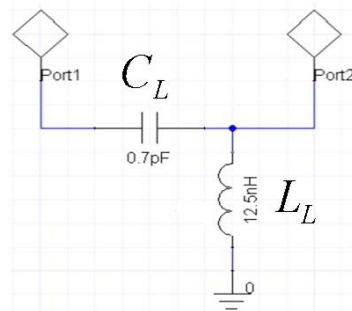
In this section we use a planar parallel plate structure to realise a NPLH transmission line with reduced RH element characteristics. Radiation loss calculations of the LH range is provided and the structure is optimized using CST MWS.

#### 3.2 Analysis of transmission line

The CRLH transmission line and the unit cell of LH transmission line are shown in Fig. 3. The realization of LH transmission line based on microstrip line can't avoid parasitic RH components such as  $C'_R$  and  $L'_R$ . However, if the  $C_R$  and  $L_R$  approximate open state and short state, The Pure LH line can be realized. Consequently, in this paragraph, we replace ground plates as ground lines to reduce  $C'_R$ . Also, the signal line is composed by contiuous capacitive plates for minimization of  $L'_R$ .



(a) CRLH transmission line



(b) PLH transmission line circuit

Fig. 3. The CRLH transmission line and the unit cell of LH transmission line

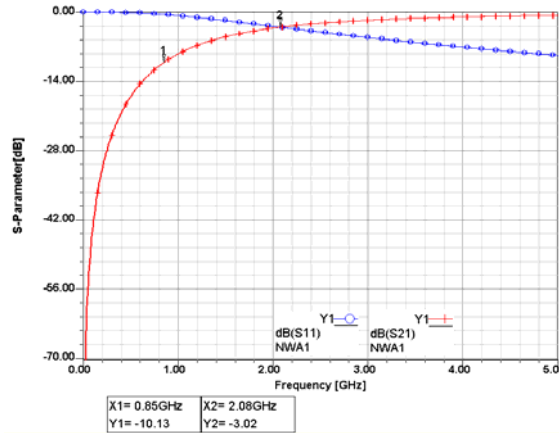


Fig. 4. The S-parameter of PLH transmission line circuit

The PLH transmission line circuit is shown in Fig. 3(b). A large series capacitance of PLH transmission line is needed for applying matched condition in low frequency band, but it is difficult to realize  $C_L$  because it needs very large dimension. To reduce of physical size of PLH transmission line, the equivalent circuit of proposed transmission line is provided in unmatched condition. The S-parameter of PLH transmission line circuit is shown in Fig. 4. The cutoff frequency( $\omega_{CLH}$ ) of PLH transmission line has equation as following

$$\omega_{CLH} = 0.5 \frac{1}{\sqrt{C_L L_L}} \tag{3}$$

The  $\omega_{CLH}$  is about 850MHz. The pass band starts at 2.08GHz. The equivalent circuit of 2 cell-NPLH characteristic is shown in Fig. 5. Near the port 2, the  $C_R$  is added in order to achieve the reciprocal characteristic between 1-port and 2-port. Most CRLH transmission line has a weak point in analysis using circuit simulation. Specially, the important factors of PLH transmission line are phase and radiation loss. The additional components, which are generated by coaxial probe, must be considered for analysis of phase in PLH transmission line. The coaxial feed section, which consists of  $C_f$  and  $L_f$ , is added at equivalent circuit of 2 cells-PLH transmission line.

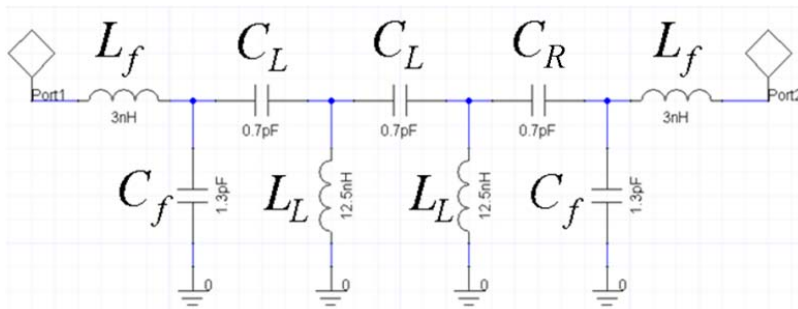


Fig. 5. The equivalent circuit of 2-cells NPLH transmission line

When the coaxial feed section is applied at equivalent circuit, two differences are shown. First is a change of pass band range and second is a start point of phase.

The S-parameter of NPLH transmission line equivalent circuit is shown in Fig. 6. The cutoff frequency is 0.92GHz. The resonance frequencies are 1GHz and 2.05GHz. The transmission bandwidth (over -3dB)of the transmission coefficient is 1.08GHz.

The loci of transmission coefficient of equivalent circuit are shown in Fig. 7. It is important result to realize NPLH transmission line physically, the phases of NPLH transmission line must coincide with the phases of equivalent circuit each frequency.

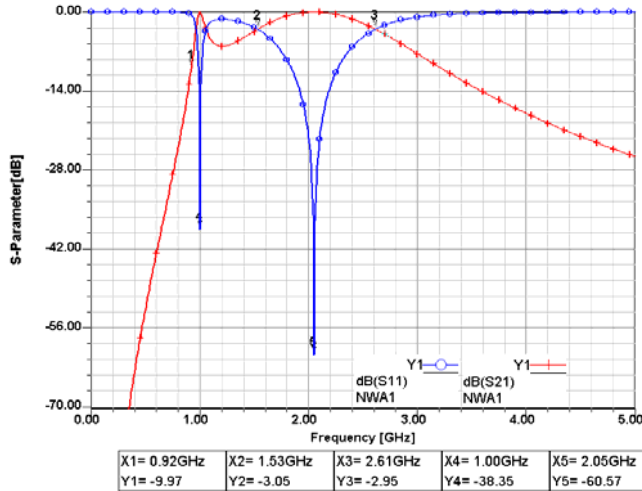


Fig. 6. The S-parameter of NPLH transmission line equivalent circuit

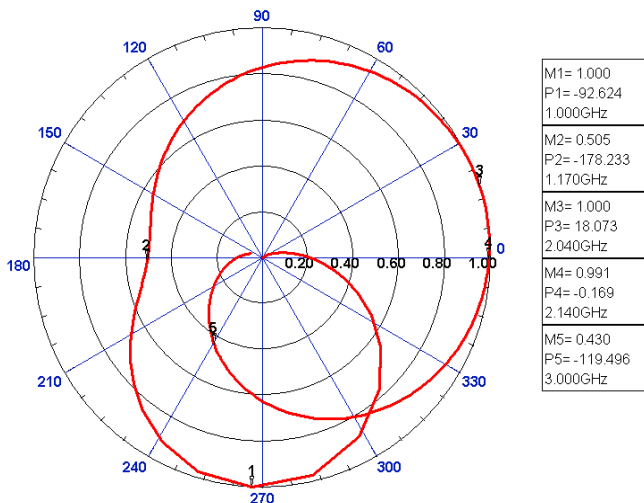


Fig. 7. The loci of transmission coefficient at equivalent circuit

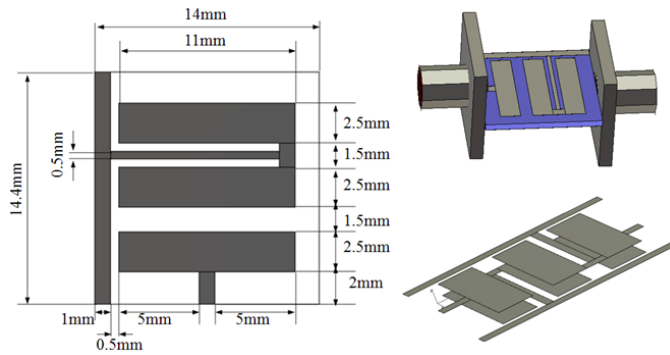


Fig. 8. The geometry of proposed NPLH transmission line

### 3.3 Simulated and experimental results

The geometry of proposed NPLH transmission line is shown in Fig. 8. The proposed NPLH transmission line consists of MIM (Metal-Insulate-Metal) capacitor and parallel inductor line. The physical size of componetns is calculated by distributed elements design.

The ground plane of proposed NPLH transmission line is simplified as line structure for reduction of parallel capacitor between ground and signal line. Also, to reduce series inductance, the transition line among cells is very short length. The substrate of proposed NPLH transmission line is Teflon, which is relative permittivity constant is 2.17. The S-parameter using 3D filed simulation is shown in Fig. 9. There is similarity between S-parameter results of 3D field simulation and equivalent circuit. The resonance frequencies are 1.17GHz and 2.15GHz. The pass bandwidth (over -3dB) of transmission coefficient is 0.94GHz. Also loci of transmission coefficients between equivalent circuit and 3D field simulation are very similar. The loci of transmission coefficient using 3D filed simulation are shown in Fig. 10. The proposed NPLH transmission line achieves near pure left handed characteristic.

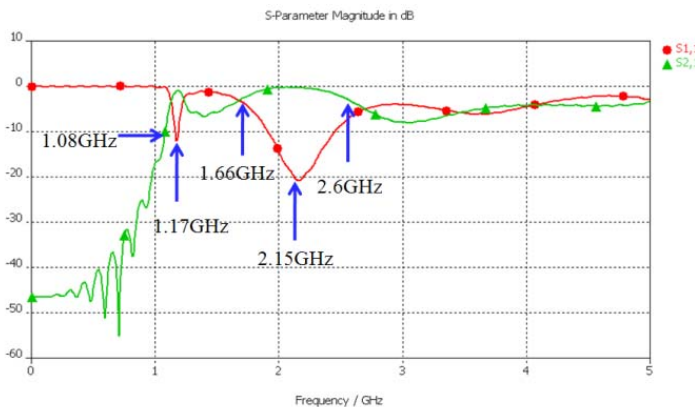


Fig. 9. The S-parameter using 3D filed simulation

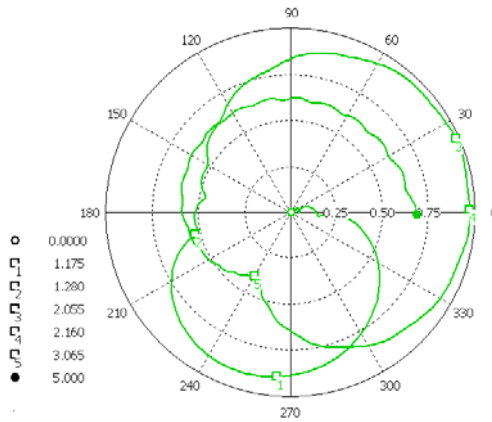


Fig. 10. The loci of transmission coefficient using 3D filed simulation

The backward wave characteristic is shown at frequency range below 3GHz. Due to limitation of a distributed elements design at frequency range over 3GHz The normal E-field distrigution at 2.15GHz is shon in Fig. 11.

The insertion loss is related with a radiation loss. In case of proposed NPLH transmission line, if the total power is 100%, the transmission power is calculated as following two equations.

$$S_{21r}[\%] = 100 - 100 * 10^{S_{11}[\text{dB}]/10}, \quad S_{21i}[\%] = 100 - 100 * 10^{S_{21}[\text{dB}]/10} \quad (4)$$

Where,  $S_{21r}$  and  $S_{21i}$  are calculated at reflection coefficient and insertion loss respectively. The radiation power( $P_{\text{rad}}$ )is expected as following equation

$$P_{\text{rad}}[\%] = S_{21r}[\%] - S_{21i}[\%] \quad (5)$$

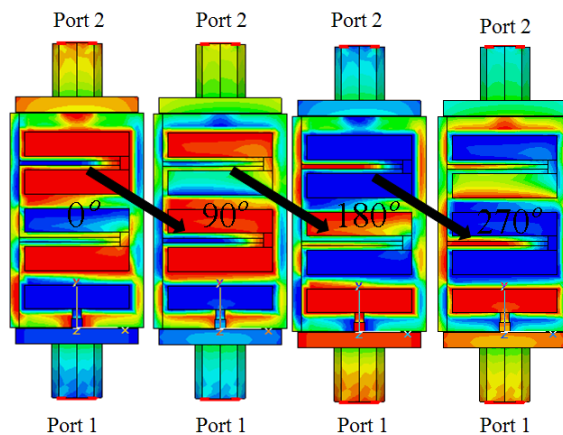


Fig. 11. The normal E-field distribution at 2.15GHz

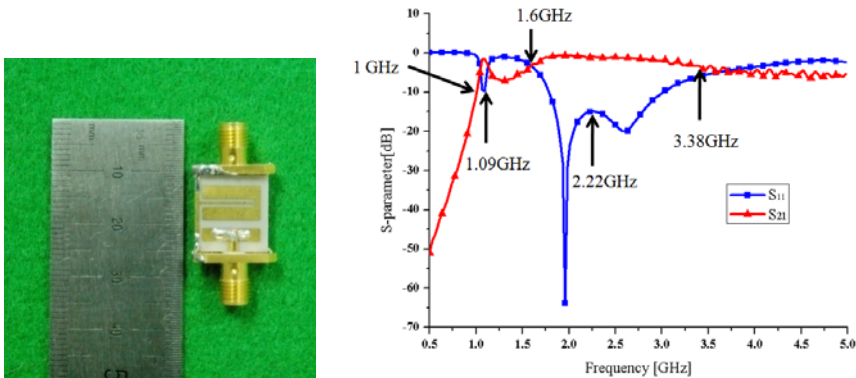
The  $P_{rad}$ , which is calculated at 2.6GHz, is about 33%. There are very similar results between  $P_{rad}[\%]$  and radiation efficiency of 3D simulation result. The radiation losses at each frequencies are shown in Table1.

The photo and measured S-parameter of fabricated NPLH transmission line is shown in Fig. 12. The pass bandwidth of transmission coefficient(over=3dB) is 1.78GHz.

The NPLH transmission line using prallel plate structure is proposed. The proposed structure shows backward wave characteristics which a PLH transmission line should have. The provided equivalent circuit model of a NPLH transmission line simulation results are similar with and ideal PLH transmission line characteristics. Also, The radiation loss which is delivered by  $S_{11}$  and  $S_{21}$ . We understand realization method of near pure left handed transmission line using distributed elements and means of meta-material concepts in paragraph. We will study compact antenna using metamaterial concepts in next paragraph.

Frequency(GHz)	Radiation loss(%)	Frequency(GHz)	Radiation loss(%)
1.7	0.21	2.2	6.18
1.8	0.43	2.3	10.73
1.9	0.96	2.4	17.16
2	1.82	2.5	24.53
2.1	3.39	2.6	31.16

Table 1. Radiation losses of NPLH transmission line



(a) The photo of NPLH transmission line (b) The measured S-parameter  
Fig. 12. The photo and measured S-parameter of NPLH transmission line

## 4. The compact antenna using meta-material concepts

### 4.1 Introduction

The electrically small antenna is defined as  $ka < 1$  where  $k$  is the wave number and  $a$  is the maximum length of antenna. For electrically small antennas efficiency, gain, impedance bandwidth and quality factor ( $Q$ ) vary as a function of maximum length of antenna. Miniaturization of an antenna typically results in narrower impedance bandwidth, higher  $Q$  and lower gain. The reduction of defects of small antennas is the main consideration in design of electrically small antennas.



Recently an EESA (Efficient Electrically Small Antenna) was proposed by Richard W.

Capacitance (unit: pF)		Inductance (unit: nH)		Resistance (unit: $\Omega$ )			
$C_f$	1.2	$L_m$	4	$R_1$	40.7k	$R_2$	0.637
$C_m$	0.15	$L_g$	36	$R_3$	81k	$R_4$	0.779

Table 2. The values of equivalent circuit elements

Ziolkowski in 2006 and simulated using HFSS. The EESA was achieved using a spherical shell of SNG (Single Negative) or DNG (Double Negative) materials. The SNG and DNG material characteristics are realized using electrical structures. These techniques will be applied for miniaturization of an antenna in this section.

#### 4.2 The equivalent circuit of small antenna using ENG material concepts

The concept of proposed antenna is shown in Fig. 13. The equivalent circuit of proposed small antenna is shown in Fig. 14. Generally the small monopole antenna has a high capacitance due to very short length. Therefore the inductance loading is necessary for the impedance matching of a small monopole antenna. The impedance matching can be achieved by negative permittivity meta-material structure, which is equivalent parallel inductance in this paragraph.

The two port equivalent circuit of proposed antenna is realized by open condition. The  $C_f$  is a capacitance of coaxial feed and feeding pad. The  $L_m$  is an inductance of monopole antenna and coaxial feed. The  $C_m$  is a capacitance among monopole antenna, ground and negative permittivity meta-material structure.

We find that parallel inductance is operated as negative permittivity in first paragraph. The  $L_g$  is an inductance of negative permittivity meta-material structure in effective material. The values of equivalent circuit elements are shown in table 2. The resonance frequency of equivalent circuit is 2.04GHz

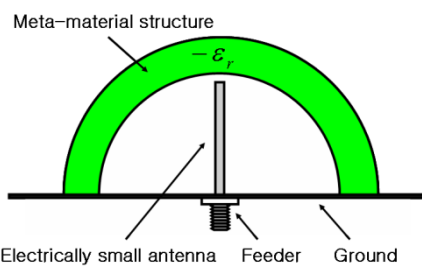


Fig. 13. The concept of proposed antenna

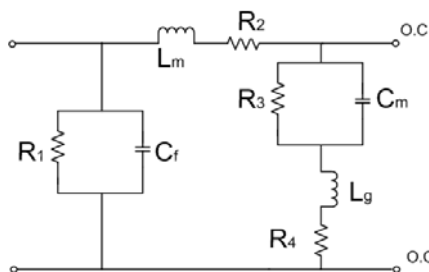


Fig. 14. The equivalent circuit

#### 4.3 The realization and experiment of small antenna using equivalent circuit

The idea and geometry of the proposed antenna are shown in Fig 15. The substrate is FR4 ( $\epsilon_r$ : 4.9) and the substrate thickness is 0.8mm. The proposed antenna is excited by a coaxial feed structure. The geometry is obtained by calculated passive components.

We consider thin wire in free space. The length of thin wire is about  $0.5\lambda$  for resonance condition. The resonated thin wire has high inductive characteristic at lower band of

resonance frequency. This factor can be applied for negative permittivity in proposed structure. But we have to reduce length of thin wire and apply shorted thin wire for small antenna. The shorted thin wire is alternated as defected ground structure, which is called meta-material structure in this geometry. The inductance of coaxial feed and monopole are insufficiency for resonance of antenna. Therefore, the additional inductance is needed and realized by meta-material structure.

The simulated characteristics of proposed antenna are shown in Fig. 16. The resonance frequency and the impedance bandwidth ( $VSRW \leq 2$ ) are 2.035GHz and 155MHz at 3D field simulated results. We find that loci of impedance are very similar between circuit simulation and 3D filed simulation. The geometry is corresponded with equivalent circuit. The field distribution of proposed antenna is shown in Fig. 17(a). The normal E-field is concentrated between monopole and negative permittivity meta-material structure.

We see that surface currents are flowed on negative permittivity meta-material structure in Fig. 17(b). Therefore the negative permittivity meta-material structure is operated as inductance  $L_m$  in equivalent circuit. The negative permittivity meta-material structure is used for impedance matching and high performance of small monopole antenna.

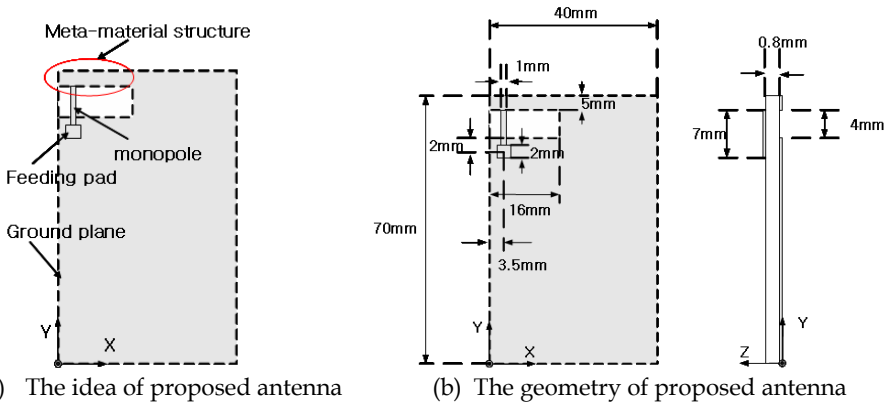


Fig. 15. The concept and geometry of proposed antenna

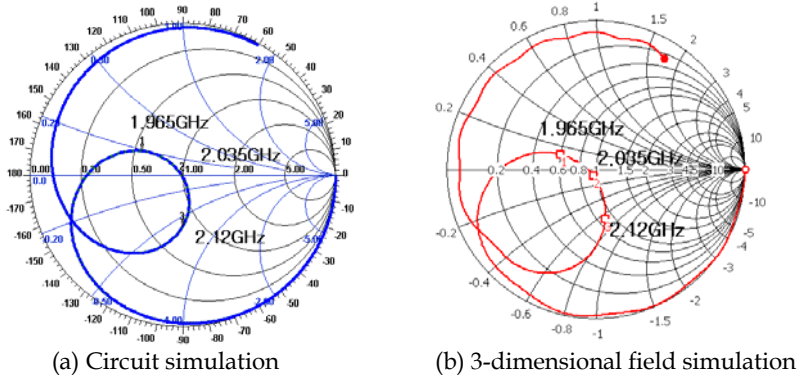


Fig. 16. The loci of input impedance on a smith chart for circuit simulation and 3D field simulation

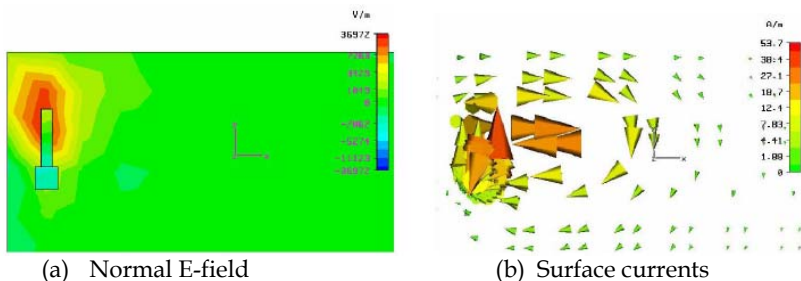


Fig. 17. The field distribution of proposed antenna

The photo of fabricated antenna is shown in Fig. 18(a). The measured return loss is shown in Fig. 18(b). The resonance frequency is 2.04GHz. The measured impedance bandwidth (VSRW  $\leq 2$ ) is 174MHz.

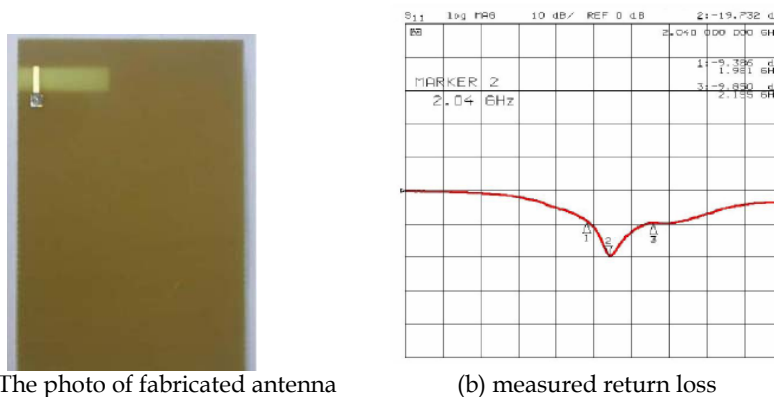


Fig. 18. The photo and measured return loss for proposed antenna

The inner cylinder of coaxial probe and monopole are dominant section of radiation pattern. Therefore, the omni directional pattern is achieved. The values of efficiencies and maximum gains are shown in Table 3. The maximum gain and efficiency are 3.6dBi and 77.8% respectively at the frequency of 2.1GHz. We calculate theoretical quality factor( $Q_L$ ), which is 108, using maximum length of monopole and measured quality factor ( $Q_m$ ), which is 7.21, using fractional bandwidth. We find that the quality factor is lowered by negative permittivity meta-material structure and the improvement of small antenna can be achieved by meta-material concepts.

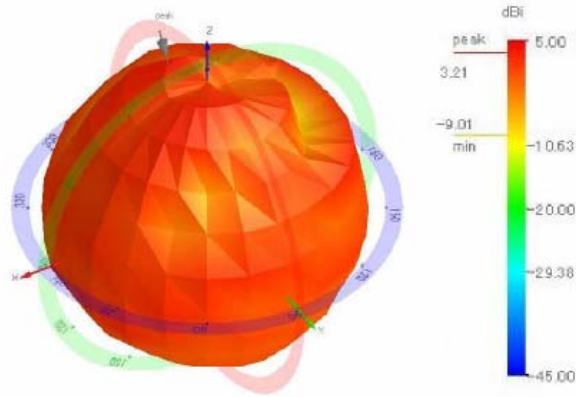


Fig. 19. The measured radiation pattern of fabricated antenna

Frequency [MHz]	Maximum gain [dBi]	Efficiency
1900	2.036	49.97%
2000	2.982	72.36%
2040	2.986	73.64%
2100	3.603	77.76%
2200	2.487	64.89%
2300	2.128	53.50%

Table 3. The values of efficiencies and maximum gains

## 5. Directive radiation of electromagnetic wave using dual-band artificial magnetic conductor structure

### 5.1 Introduction

In this paragraph, the FSS and AMC structures can be analyzed by a view point of effective medium. So we will find means of FSS and AMC using new analysis method, which will be proposed using periodic boundary condition. The verified FSS and AMC structure will be applied to enhance directivity of antenna. The enhancement of directivity of antenna will be achieved by febrly perot resonance condition between FSS and AMC structure.

### 5.2 The enhancement of directivity using FSS structure

The meta-materials concept can be realized by electrical structures, which adjust refractive index of material. So we can achieve enhancement of directivity using FSS structure, which is analyzed in negative permittivity of effective medium.

The febrly perot interferometer is shown in Fig. 20. The source generates wave power ( $P_1 \cos \theta$ ), which propagates to medium 2 and is reflected. The reflected wave power is

propagated to medium 1 and reflected by medium 1. The generated and reflected wave powers are combined. The reflected wave power ( $P_r$ ) and total power ( $P_t$ ) of generated and reflected wave are expressed by equation (6) and equation (7) briefly.

$$P_r = P_i \cos \left( 2 \frac{2\pi}{\lambda} \cdot d + \phi_1 + \phi_2 + \theta \right) \quad (6)$$

$$P_t = P_i \cos \theta + P_r \quad (7)$$

Where, the  $d$ ,  $\phi_1$ ,  $\phi_2$  and  $\theta$  are distance, phase variation at medium 1, shifted phase at medium 2 and initial phase respectively. These equations didn't consider radiation loss and additional reflected wave.

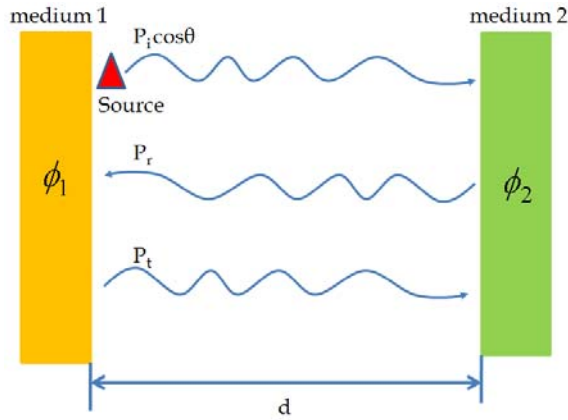


Fig. 20. The febry perot interferometer

If the medium 1 and medium 2 are perfect electric conductor, the shifted phase ( $\phi_1, \phi_2$ ) of medium is 180 degree. Therefore, if the distance is  $\lambda/2$  between medium 1 and medium 2, the total power is maxed.

The enhancement of directivity can be achieved by FSS structure. The source, medium 1 and medium 2 are replaced with antenna, ground and FSS structure. The optimized distance is about  $\lambda/2$  between ground and FSS structure. If the periodic spaces between lattices are very short below one wave length.

The FSS can be analyzed at a point view of effective medium. The equivalent effective permittivity ( $\epsilon_{\text{eff}}$ ) of FSS structure is expressed by equation (8).

$$\epsilon_{\text{eff}} = 1 - \omega_p^2 / \omega^2 \quad (8)$$

Where, the  $\omega_p$  is plasma angular frequency, the  $\omega$  is available angular frequency.

The effective permittivity is negative below plasma angular frequency, however the effective permittivity of FSS structure is near 0 over plasma angular frequency. This characteristic is applicable for enhancement of directivity. The concept of lens using FSS structure is shown in Fig. 21.

But this method has pebry ferot resonance distance, which is  $\lambda/2$ , between FSS structure and antenna. The physical height is very large in antenna using FSS structure. If we can adjust shifted phase of ground plane in antenna, we can reduce distance between FSS structure and antenna. So we will find AMC for miniaturization of distance in next paragraph.

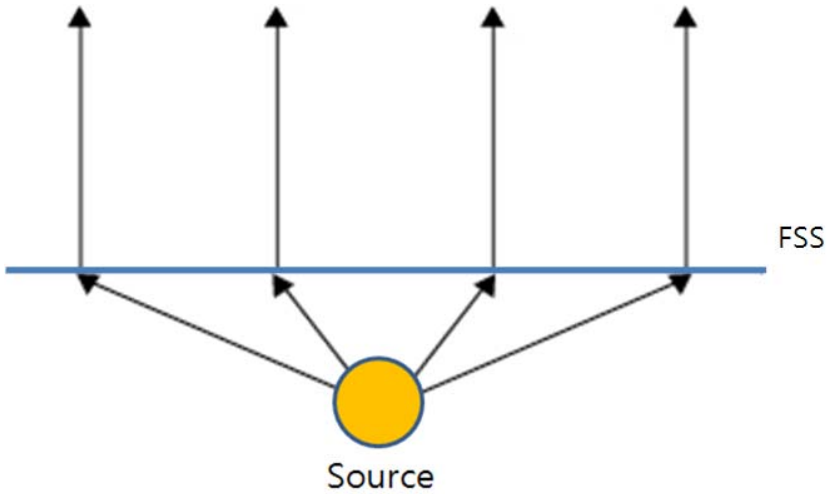


Fig. 21. The concept of lens using FSS structure

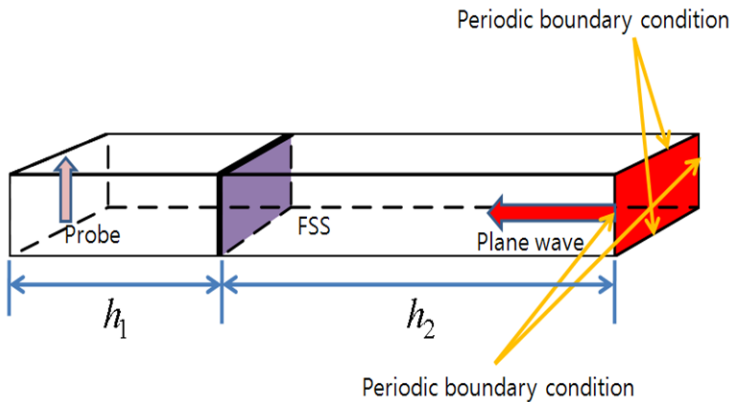


Fig. 22. The analysis method for FSS

**5.3 The enhancement of directivity using FSS structure**

In this paragraph, we propose analysis method for FSS, which is expressed by Fig. 22. The incident plane wave is propagated to unit cell of FSS. The space ( $h_2$ ) between unit cell of FSS and plane wave source is  $\lambda_0$ . The space ( $h_1$ ) between FSS and probe is  $\lambda_0/4$ . These are enclosed by periodic boundary condition.

We think that the plane wave, unit cell of FSS and probe are alternated with signal, FSS plate and receiving antenna. So if the electric field of received signal is maxed, the unit cell of FSS is operated as FSS lens. The unit cell of FSS structure is shown in Fig. 23. The unit cell is designed using square ring slit on substrate. The substrate is Rogers RO3210, the thickness and relative permittivity are 1.27mm and 10.2 respectively. The unit cell of FSS is alternated with infinite FSS plate using periodic boundary condition.

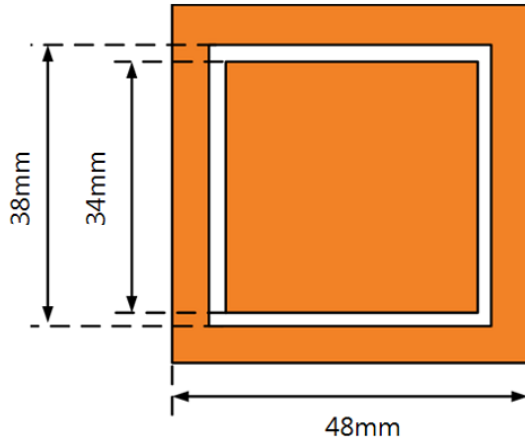
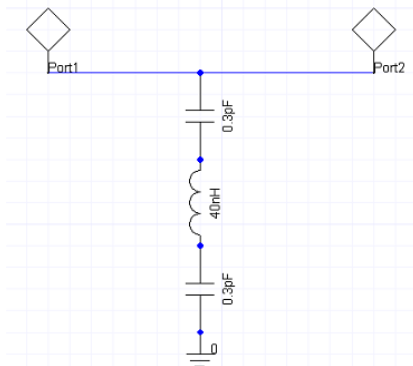
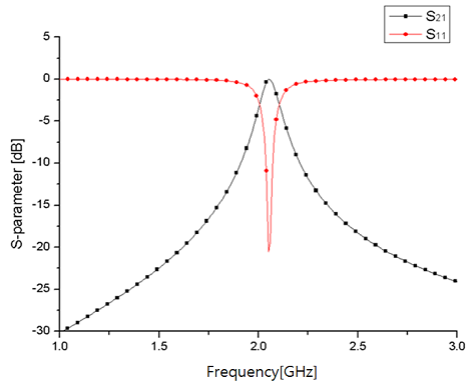


Fig. 23. The unit cell of FSS structure



(a) Equivalent circuit of unit cell



(b) The S-parameter of unit cell

Fig. 24. The unit cell of FSS structure

We think that the infinite conductor plate with periodic square ring slits. If the conductor plate with periodic square ring slits is excited by plan wave, the difference voltage between inner conductor and outer conductor is generated by square slits and the currents are induced along conductor. Therefore, the capacitance is generated between inner conductor and outer conductor.

The inductance is provided by induced currents. The equivalent circuit and S-parameter of unit cell is shown in Fig. 24. The generated capacitance and inductance are 0.3pF and 40nH.

The received E-field is shown in Fig. 25(a). It is maximum E-field at 2GHz. The fractional band width is 950MHz (1.6GHz~2.55GHz). The phase of received signal is expressed in Fig. 25(b). The phase of received signal is 90° at 2GHz.

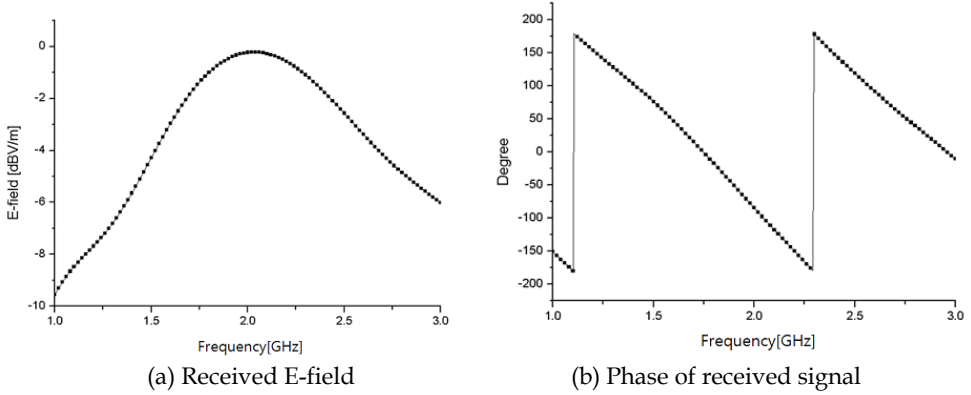


Fig. 25. The unit cell of FSS structure

### 5.3 The enhancement of directivity using AMC structure

In this paragraph, we find mean of AMC and propose the dual band AMC structure, because the defect of AMC technology is narrow operation bandwidth.

We suppose that the vertical plane wave is propagated to boundary between medium 1 and medium 2. The incident plan wave at boundary between medium 1 and medium 2 is shown in Fig. 26. The Electromagnetic field of incident plane wave can be expressed by equation (9)

$$\vec{E}_1(z) = \vec{a}_x E_{i0} e^{-j\beta_1 z}, \quad \vec{H}_1(z) = \vec{a}_y \frac{E_{i0}}{\eta_1} e^{-j\beta_1 z} \quad (9)$$

Where, the  $E_{i0}$ ,  $\beta_1$  and  $\eta_1$  are magnitude, phase constant and wave impedance at medium 1. The incident plane wave is divided by discontinuous mediums. A part of incident plane wave is transmitted continuously in medium 2. The rest part is reflected at boundary. The reflected plane wave is expressed by following equation.

$$\vec{E}_r(z) = \vec{a}_x E_{r0} e^{j\beta_1 z}, \quad \vec{H}_r(z) = -\vec{a}_z \times \frac{1}{\eta_1} \vec{E}_r(z) = -\vec{a}_y \frac{E_{r0}}{\eta_1} e^{j\beta_1 z} \quad (10)$$

The transmitted plane wave is expressed by following equation

$$\vec{E}_t(z) = \vec{a}_x E_{t0} e^{-j\beta_2 z}, \quad \vec{H}_t(z) = \vec{a}_z \times \frac{1}{\eta_2} \vec{E}_t(z) = \vec{a}_y \frac{E_{t0}}{\eta_2} e^{-j\beta_2 z} \quad (11)$$

Where,  $E_{t0}$ ,  $\beta_2$  and  $\eta_2$  are magnitude, phase constant and wave impedance respectively at  $z=0$ .

The relation of electric fields and magnetic fields can be expressed by equation (12)



$$\vec{E}_i(0) + \vec{E}_r(0) = \vec{E}_t(0), \quad \vec{H}_i(0) + \vec{H}_r(0) = \vec{H}_t(0) \quad (12)$$

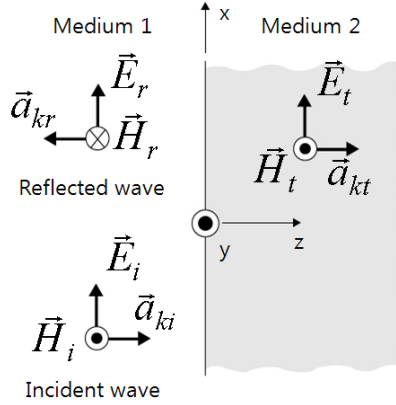


Fig. 26. The incident plan wave at boundary between medium 1 and medium 2

The magnetic field can be replaced with electric field using wave impedance and expressed by equation (13)

$$\frac{1}{\eta_1} (E_{i0} - E_{r0}) = \frac{E_{t0}}{\eta_2} \quad (13)$$

The reflection and transmission electric fields are expressed by equation (14) using equation (12) and (13).

$$E_{r0} = \frac{\eta_2 - \eta_1}{\eta_2 + \eta_1} E_{i0}, \quad E_{t0} = \frac{2\eta_2}{\eta_2 + \eta_1} E_{i0} \quad (14)$$

The reflection and transmission coefficient can be extracted using equation (14). The reflection and transmission coefficients are following equation (15).

$$\Gamma = \frac{E_{r0}}{E_{i0}} = \frac{\eta_2 - \eta_1}{\eta_2 + \eta_1}, \quad \tau = \frac{E_{t0}}{E_{i0}} = \frac{2\eta_2}{\eta_2 + \eta_1} \quad (15)$$

We see the reflection coefficient. If medium 2 is conductor, the wave impedance ( $\eta_2$ ) is 0. So reflection coefficient is -1. But if medium 2 has very high impedance like as infinity impedance, the reflection coefficient is 1. Therefore, the mean of AMC is electrical structure for infinity wave impedance. The wave impedance ( $\eta_2$ ) is following equation (16)

$$\eta_2 = \sqrt{\frac{\mu_2}{\epsilon_2}} \quad (16)$$

Finally, the AMC can be achieved by near zero permittivity or infinity high permeability. How can we achieve AMC structure? The realization of AMC can be found using resonance structure. The representative AMC structure, which is mushroom structure and equivalent circuit are shown in Fig 27.

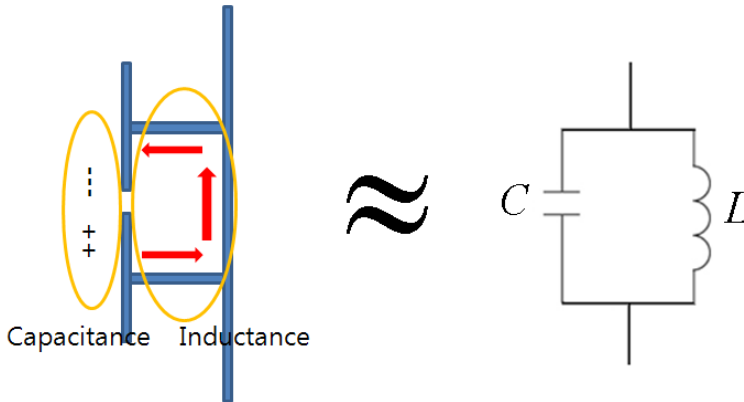


Fig. 27. The mushroom structure and equivalent circuit

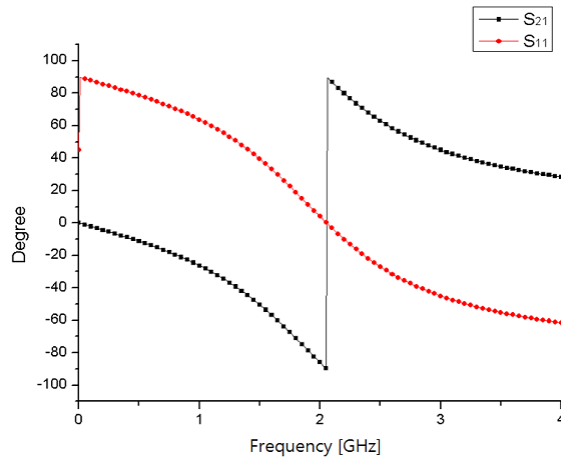


Fig. 28. The reflection coefficient phase and transmission coefficient phase

We find that the mushroom structure is like as split ring resonator. The mushroom structure is operated as parallel resonator. The capacitance is generated between plates of periodic mushroom structures. The inductance is induced by surface currents.

If the capacitance (C) and inductance (L) are 1pF and 6nH, the resonance frequency is 2.05GHz. The reflection coefficient phase and transmission coefficient phase are shown in Fig. 28. We analyze phase of transmission coefficient based on point view of effective medium. The negative phase is inductance section, which is alternated with negative epsilon medium or high permeability medium below 2.05GHz. otherwise the positive phase is expressed by high permittivity or negative permeability.

If the operating frequency is near 2.05GHz, the mushroom structure achieves high impedance structure. The proposed analysis method of AMC is shown in Fig. 29. The reflection coefficient is very important in AMC structure. The probe is set at location of plan

wave port. If the distance is — between unit cell of AMC and plan wave port, the received electric field is maximum strength, which is detected by probe. Because the reflected wave phase and excited phase has same phase. If the AMC is replaced with perfect electric conductor, the received electric filed is very small strength.

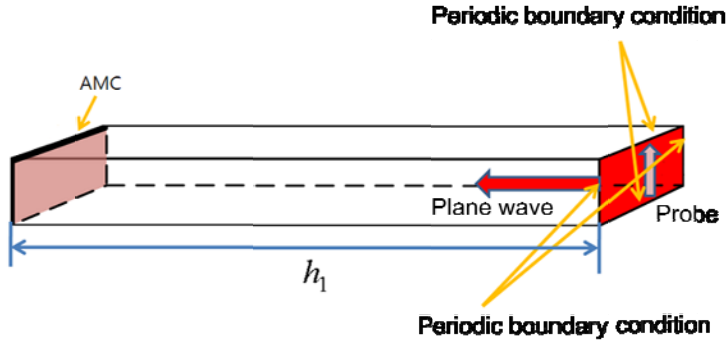


Fig. 29. The proposed analysis method of AMC

We try to design of dual band AMC using proposed method. The proposed unit cell of dual-band AMC structure is shown in Fig. 30. The substrates are RO3210 of Rogers , thickness is 1.27mm. We see tho middle layer. The vias are added for miniaturization of proposed AMC. The parallel short circuit structures, are used for wide AMC operation bandwidth, are realized by slits. The dual AMC operation frequency is realized using stacked thin lines above middle layer. The proposed unit cell of dual band AMC structure is analyzed by proposed analysis method of AMC. The received electric field strength of dual-band AMC is shown in Fig. 31. The operation bandwidth (E-field>0dB) are 120 MHz (1.85GHz~1.98GHz) and 70 MHz (2.11GH ~2.18GHz) respectively.

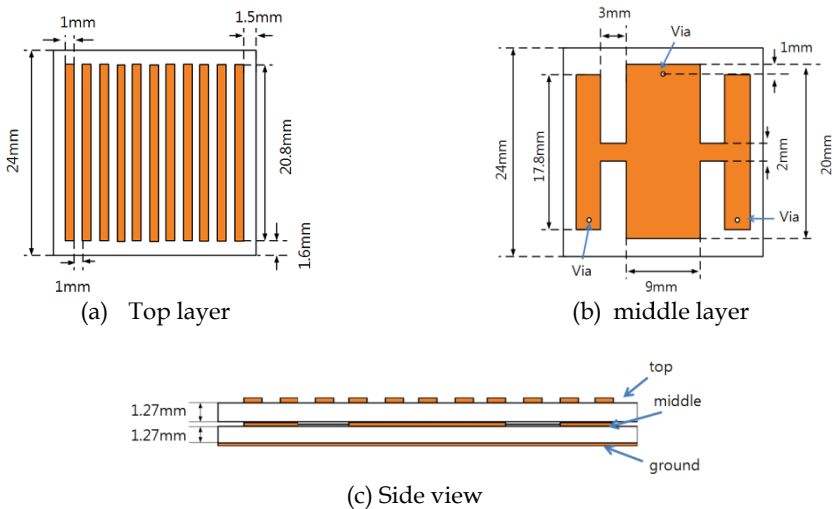


Fig. 30. The proposed dual-band AMC structure

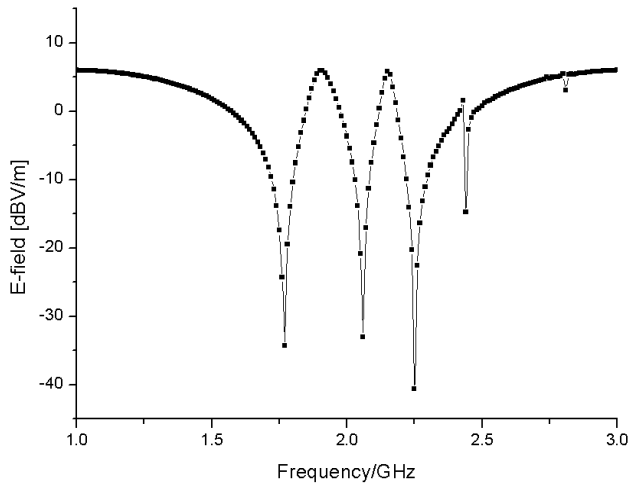


Fig. 31. The proposed dual-band AMC structure

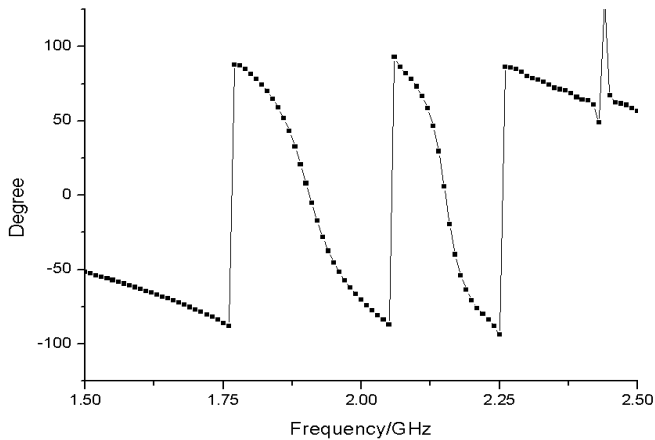


Fig. 32. The phase of proposed dual-band AMC structure

The phase response of dual band AMC is shown in Fig. 32. There are maximum received signal strengths and 0 phases at 1.91GHz and 2.15GHz respectively. Therefore, we find that proposed dual-band AMC is operated as AMC plane at 1.91GHz and 2.15GHz.

The antenna gain can be improved by FSS, but this method has defect of long height, which is febrly perot resonance condition ( $\frac{\lambda_0}{2}$ ) between FSS and antenna ground. However, if the antenna ground is replaced with dual-band AMC structure, the distance between antenna ground and FSS is reduced and compact size.

It is the composition structure of AMC and FSS analysis to spend very long time, because composition structure is analyzed fully in 3-D filed simulation, so we propose convenient analysis method for composition structure. We estimate composition of proposed unit cell

of FSS structure and dual-band AMC structure using proposed analysis method. The proposed analysis method for composition of AMC and FSS is shown Fig. 33.

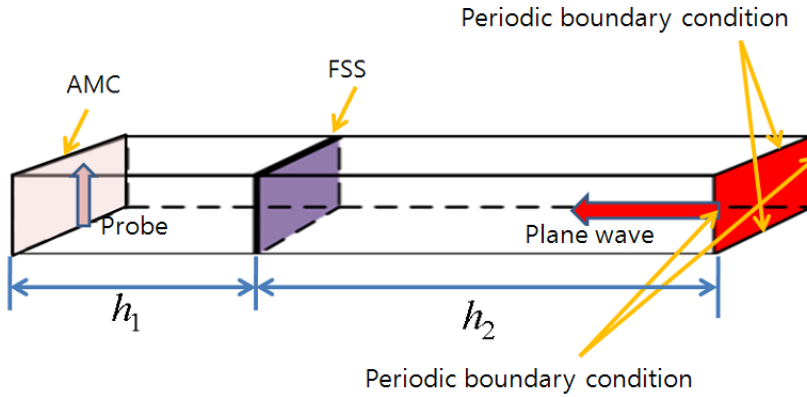


Fig. 33. The proposed analysis method for composition AMC and FSS

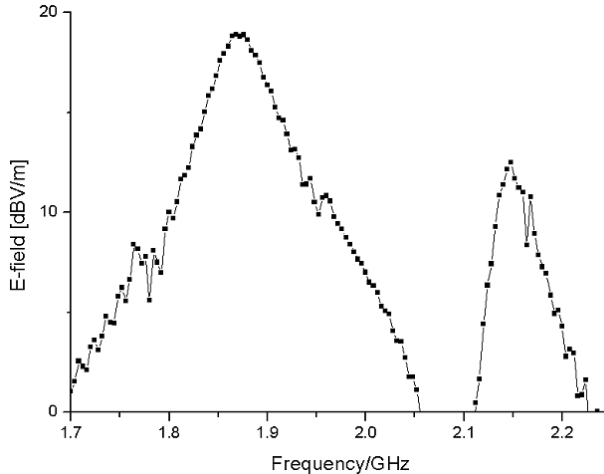


Fig. 34. The proposed analysis method for composition AMC and FSS

The proposed analysis method is very fast and convenient for optimization of distance between AMC and FSS. The distance( $h_1$ ) between AMC and FSS is about  $\lambda_0/4$ . The distance ( $h_2$ ) between plane wave source and FSS is  $\lambda_0$ . The probe is set on AMC plane. If the probe is regarded as antenna, the received electric field is max at operation frequency. The received electric field strength for proposed composition of FSS and AMC is shown in Fig. 34. The received electric field strengths are max at AMC operation frequencies, which are 1.87GHz and 2.15GHz.

The proposed composition structure will be applied to microstrip patch antennas. The proposed microstrip patch antenna using dual-band AMC is shown in Fig. 35. The proposed microstrip patch antennas are designed for 1.9GHz and 2.1GHz respectively. The 1.9GHz and 2.1GHz microstrip patch antenna size (p) are 23 mm and 20.4mm respectively. The

feeding positions (d) are 2.1mm and 2.4mm respectively against 1.9GHz and 2.1GHz microstrip patch antenna.

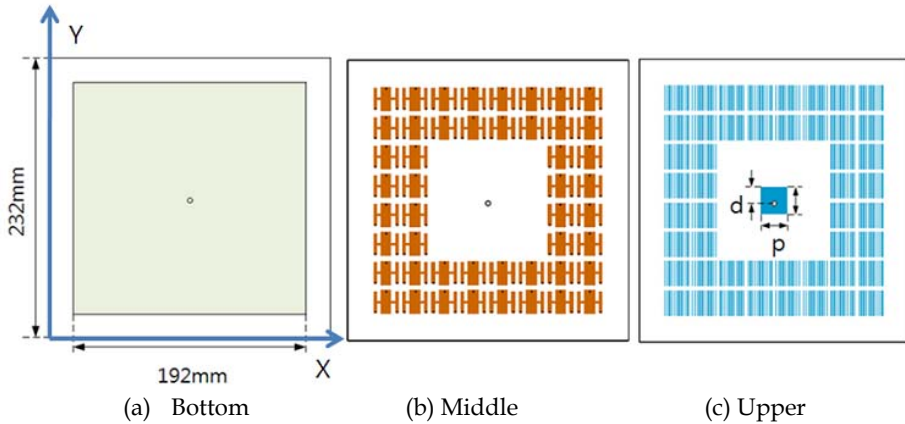


Fig. 35. The proposed microstrip patch antenna using dual-band AMC

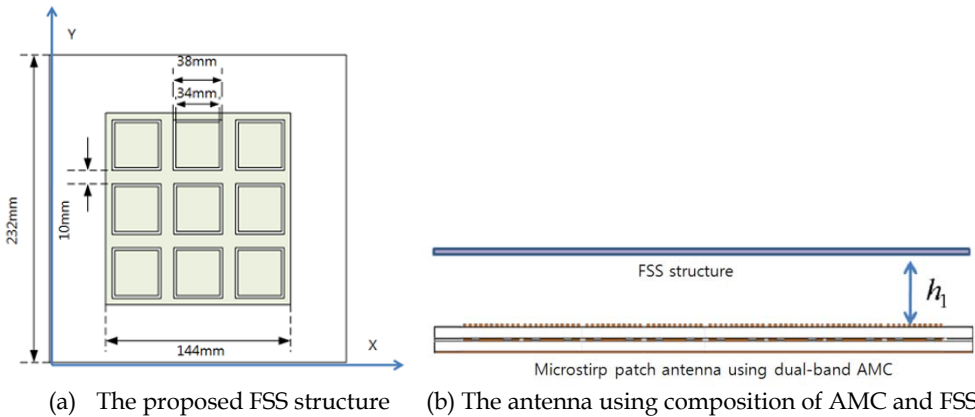


Fig. 36. The proposed FSS structure and the antenna using composition of AMC and FSS

The proposed FSS structure and the antenna using composition of AMC and FSS are shown in Fig. 36. The height ( $h_1$ ) between FSS structure and dual-band AMC is 10mm, which is very short length. The reduction of height can be adjusted using reflection phase of AMC structure. The photos of fabricated antennas are shown in Fig. 37. The total size of the antenna using composition is 232mm × 232mm × 13.81mm. The substrates of FSS and antenna are RO3210( $\epsilon_r$ : 10.2) of Rogers.

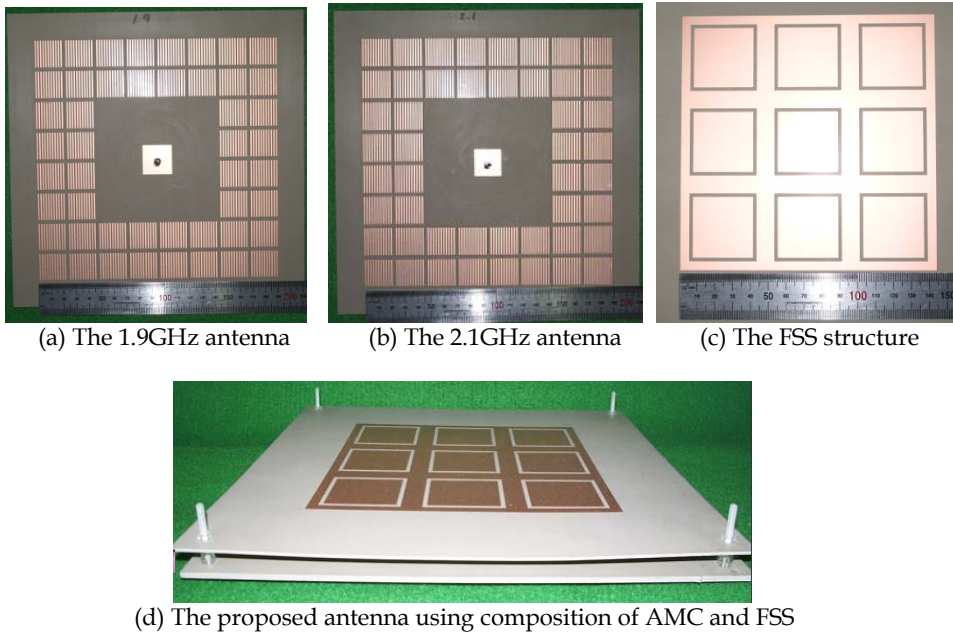


Fig. 37. The photos of fabricated antennas

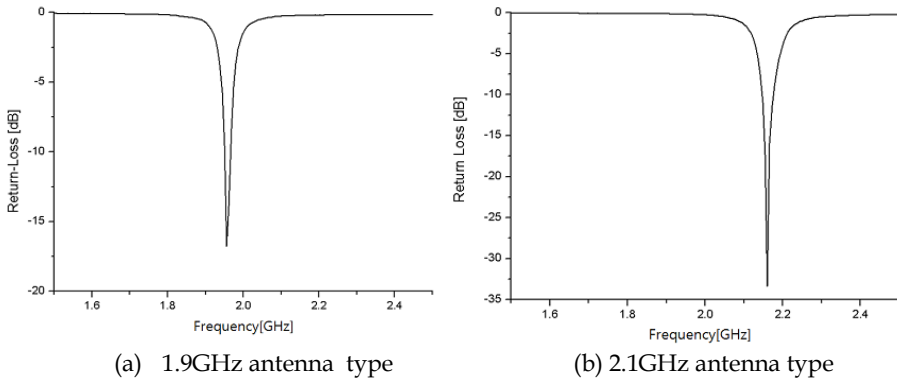


Fig. 38. The measured return-loss against antenna types

The measured return-losses against antenna types are shown in Fig. 38. The resonance frequency and impedance bandwidth ( $VSWR \leq 2$ ) are 1.97GHz and 20MHz respectively in the 1.9GHz antenna type. The resonance frequency and impedance bandwidth ( $VSWR \leq 2$ ) of 2.1GHz antenna type are 2.17GHz and 20MHz. The radiation patterns against antenna types are shown in Fig. 39. We measure antenna against three states. One state is conductor ground type, another state is AMC ground type. The other state is composition of AMC ground and FSS structure. The antenna gain and FBR (front back ratio) of 1.9GHz and 2.1GHz antennas are shown in table 4. We find that the back lobe of 1.9GHz antenna is reduced by AMC structure, because the surface wave is suppressed by AMC. The

maximum gain of composition type is 9.1 dBi although low profile, which is 10mm, between AMC and FSS. But the surface wave suppression is not good at 2.1GHz antenna type. The aspect of measured data is very similar to the estimation result for composition AMC and FSS. The maximum gain of 2.1GHz antenna is 9.1dBi.

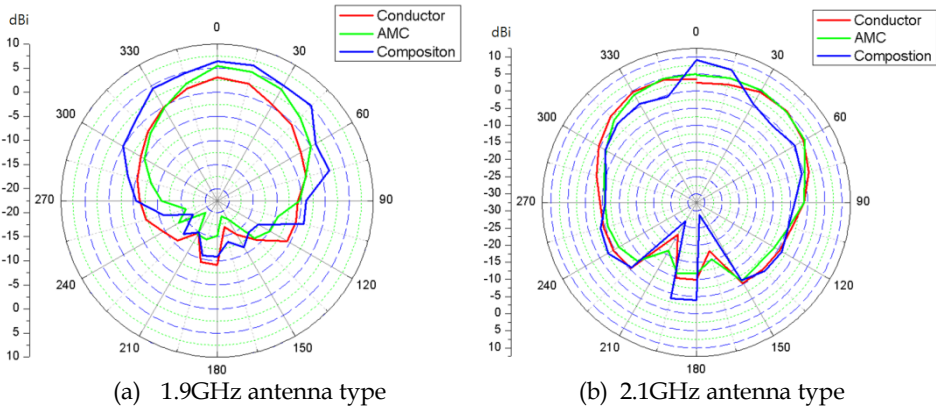


Fig. 39. The measured radiation patterns against antenna types

Types		Characteristic		
		Conductor	AMC	Composition
1.9GHz antenna	Gain [dBi]	4.6	7	8
	FBR [dB]	13.7	22.2	18.8
2.1GHz antenna	Gain [dBi]	4.6	6.5	9.1
	FBR [dB]	13.7	17.6	13

Table 4. The antenna gain and FBR against antenna types

The proposed antenna using composition FSS and dual-band AMC structure achieves low profile and high gain. We find that characteristic of the AMC and FSS structure is replaced with material point view.

The AMC is operated like as high permeability. The FSS has near 0 permittivity at operating frequency. Therefore, we can adjust material characteristic by additional electric structures like as meta-material structure.

## 6. EM waves shielding functional concrete

### 6.1 Introduction

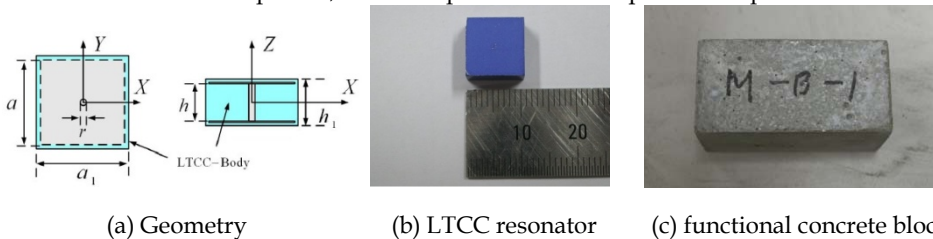
In this pragraph, we try to realize SNG meta-material using LTCC (low temperature cofired ceramic) resonator. The mushroom structure, which is resonator, is designed on ground and reduces surface wave. If the surface wave is replaced with plane wave, the image theory is not applicable in space. Therefore, the mushroom structure must be extended for stop-band characteristic. So we propose LTCC resonator, which is put into concrete for SNG concrete



block. we compare the results measured 1 year ago with the recent results. Because concrete block, loss is too high, includes water until it is dried perfectly.

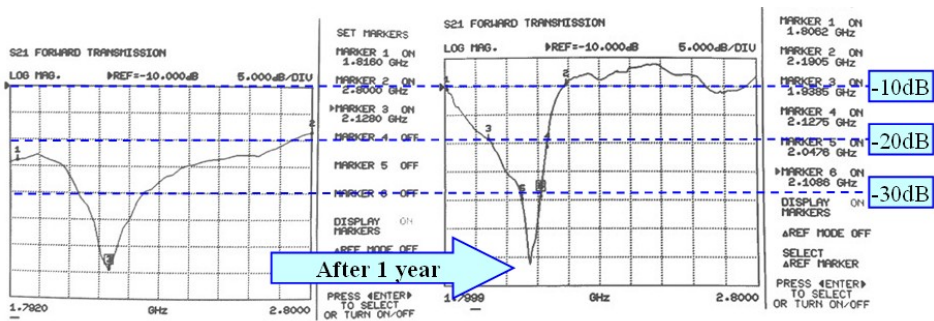
**6.2 The EM shielding concrete block using LTCC resonator**

The geometry of unit cell LTCC resonator and photos of resonator and concrete block are shown in Fig. 40. The proposed resonator consists of two square plates and one via in LTCC ( $\epsilon_r = 7.8$ ) body. The plate size is 10mm ( $a$ ) $\times$ 10mm( $a$ ). The via length ( $h$ ) is 5mm. LTCC body size is 10.2mm ( $a_1$ ) $\times$  10.2mm ( $a_1$ )  $\times$ 5.2mm ( $h_1$ ). The concrete block size is 80mm $\times$ 40mm $\times$ 40mm. The proposed structure is operated as parallel LC resonator which has a characteristic of stop band, and it is operated like an equivalent dipole.

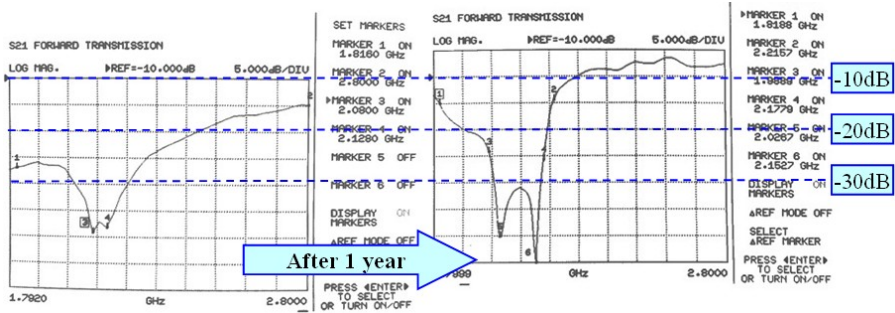


(a) Geometry (b) LTCC resonator (c) functional concrete block  
 Fig. 40. LTCC resonator and functional concrete block

The proposed structure is operated as parallel LC resonator which has a characteristic of stop band, and it is operated like an equivalent dipole. The coefficient comparison of a block with three resonators at 60 days and 1 year are shown in Fig. 41. The transmission coefficient variation of concrete block including only 1 type resonator is shown in Fig. 41 (a). As concrete loss level is lowered from -15dB (60 days) to -5dB (1 year), bandwidth of stop band is changed according to time. The transmission coefficient variation of concrete block including 2 kinds of resonator is shown in Fig. 41 (b). All these results show that the change in the dielectric properties strongly related to the amount of water in the concrete block and the permittivity changes may vary the stop band width and resonance frequency.



(a) Transmission coefficient of concrete block including 1 type resonator.

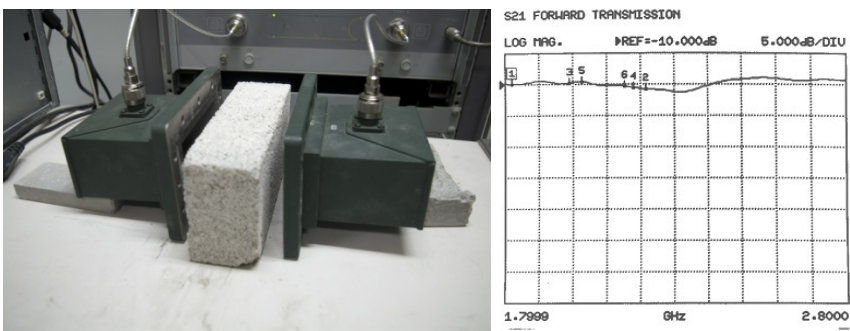


(b) Transmission coefficient of concrete block including 2 kinds of resonators  
Fig. 41. The coefficient comparison of a block with three resonators at 60 days and 1 year

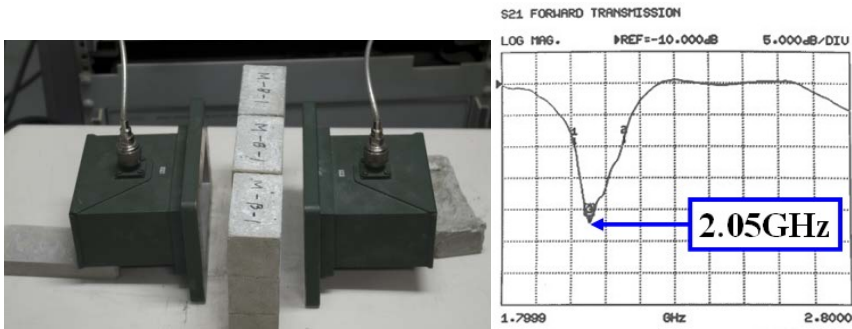
Block type	Mixer ratio	Resonance Frequency (GHz)		Bandwidth (MHz)					
				( $\leq -10\text{dB}$ )		( $\leq -20\text{dB}$ )		( $\leq -30\text{dB}$ )	
		60 days	1 year	60 days	1 year	60 days	1 year	60 days	1 year
M-B-1	73.42:1	2.12	2.07	-	395	-	191	215	90
M-AB-2	36.21:1	2.08	2.02	-	550	-	294	175	167
		2.12	2.15						

Table 5. The characteristic of functional concrete block against time

In order to apply the real building environment, concrete wall models are simulated. The pure concrete wall model is a single concrete block without resonator, and concrete wall model consists of 6 concrete blocks including resonator. The photos and transmission coefficients of concrete walls with/without LTCC resonators are shown in Fig. 42. We find that the functional concrete block achieve SNG material characteristic using LTCC resonator and is applicable for shielding structure.



(a) Concrete block without resonator



(b) Concrete block with LTCC resonators

Fig. 42. The photos and transmission coefficients of concrete walls with/without LTCC resonators

## 7. Conclusion

In this chapter, we study means of meta-material concept using transmission line, the NPLH transmission line, the compact antenna using meta-material concepts, the directive radiation of electromagnetic wave using dual-band artificial magnetic conductor structure and EM waves shielding functional concrete. It is proposed electrical structure to change characteristic of material at material point view. If we approach material point view of electrical structure, the component design method and analysis can be extended and will be improved by meta-material concepts

## 8. References

- J. B. Pendry, A. J. Holden, D. J. Robbins, and W. J. Stewart (1998). Low frequency plasmons in thin-wire structures, *Journal of Physics Condensed Matter*, vol. 10, pp. 4785-4810,
- J. B. Pendry, A. J. Holden, D. J. Robbins, and W. J. Stewart (1999). Magnetism from conductors and enhanced nonlinear phenomena, *Microwave Theory and Techniques*, IEEE Trans., vol. 47, pp. 2075-2084
- C. Caloz, H. Okabe, T. Iwai, and T. Itoh (2002). Anisotropic PBG surface and its transmission line model, *URSI Dig., IEEE-AP-S USNC/URSI National Radio Science Meet.*, pp. 224, San Antonio, TX, USA,
- A. Lai, T. Itoh, and C. Caloz (2004). Composite right/left-handed transmission line metamaterials, *Microwave Magazine, IEEE*, vol. 5, pp. 34-50
- A. Sanada, C. Caloz, and T. Itoh (2004). Characteristics of the composite right/left-handed transmission lines, *Microwave and Wireless Components Lett., IEEE*, vol. 14, pp. 68-70
- R. W. Ziolkowski and A. Erentok (2006). Metamaterial-based efficient electrically small antennas, *Antennas Propagat., IEEE Trans.*, vol. 54, pp. 2113-2130
- A. Erentok and R. W. Ziolkowski (2006). An efficient metamaterial-inspired electrically-small antenna, *Microwave Optical Technology Lett.*, vol. 49, pp. 1669-1672

- M. Thevenot, C. Cheype, A. Reineix, B. Jecko, F. des Sci, and L. Cnrs (1999). Directive photonic-bandgap antennas, *Microwave Theory and Techniques, IEEE Trans.*, vol. 47, pp. 2115-2122
- R. Biswas, E. Ozbay, B. Temelkuran, M. Bayindir, M. M. Sigalas, and K. M. Ho (2001). Exceptionally directional sources with photonic-bandgap crystals, *Journal of the Optical Society of America B*, vol. 18, pp. 1684-1689
- S. Enoch, G. Tayeb, P. Sabouroux, N. Gurin, and P. Vincent (2002), A Metamaterial for Directive Emission, *Physical Review Lett.*, vol. 89, pp. 2139-2142
- D. Sievenpiper, L. Zhang, R. F. J. Broas, N. G. Alexopolous, and E. Yablonovitch (1999). High-impedance electromagnetic surfaces with a forbidden frequencyband, *Microwave Theory and Techniques, IEEE Trans.*, vol. 47, pp. 2059-2074
- Feresidis, A.P., and Vardaxoglou, J.C. (2001). High gain planar antenna using optimised partially reflective surfaces, *Microwave Antennas Propag.*, IEE Proc., vol. 148, pp. 345-350
- N. C. Karmakar, M. N. Mollah, and S. K. Padhi (2002). Improved performance of a non-uniform ring patterned PBG assisted microstrip line, *Antennas and Propag. Society International Symposium, IEEE*, vol. 2, pp. 848-851
- E. Brown, C. Parker, E. Yablonovitch (1993). Radiation properties of a planar antenna on a photonic-crystal substrate, *Journal-Optical Society of America B*, vol. 10, pp. 404
- S. Cheng, R. Biswas, E. Ozbay, S. McCalmont, G. Tuttle, K.-M. Ho (1995). Optimized dipole antennas on photonic band gap crystals, *Applied Physics Lett.* vol. 67, pp. 3399
- E. Brown, O. McMahon (1996). High zenithal directivity from a dipole antenna on a photonic crystal, *Applied Physics Lett.*, vol. 68, pp. 1300
- M. Kesler, J. Maloney, B. Shirley, G. Smith (1996). Antenna design with the use of photonic band-gap materials as all-dielectric planar reflectors, *Microwave and Optical Technology Lett.*, vol. 11, pp. 169
- M. Sigalas, R. Biswas, Q. Li, D. Crouch, W. Leung, R. Jacobs-Woodbury, B. Lough, S. Nielsen, S. McCalmont, G. Tuttle, K.-M. Ho (1997). Dipole antennas on photonicband-gap crystals: Experiment and simulation, *Microwave and Optical Technology Lett.*, vol. 15, pp. 153
- C. Caloz and T. Itoh (2006). Electromagnetic Metamaterials: Transmission Line Theory and Microwave Applications: the Engineering Approach, *Wiley-IEEE Press*
- J. B. Pendry and D. R. Smith (2004). Reversing Light With Negative Refraction, *Physics Today*, pp. 37-44
- C. Caloz, H. Okabe, T. Iwai, and T. Itoh (2002). Transmission line approach of left-handed (LH) materials, *Proc. USNC/URSI National Radio Science Meeting*, vol. 1, pp. 39
- S. B. Cohn (2004). Electrolytic-Tank Measurements for Microwave Metallic Delay-Lens Media, *Journal of Applied Physics*, vol. 21, pp. 674
- S. Clavijo, R. E. Diaz, and W. E. McKinzie Iii (2003). Design methodology for Sievenpiper high-impedance surfaces: an artificial magnetic conductor for positive gain electrically small antennas, *Antennas and Propagation, IEEE Trans.*, vol. 51, pp. 2678-2690
- S. K. Hampel, O. Schmitz, O. Klemp, and H. Eul (2007). Design of Sievenpiper HIS for use in planar broadband antennas by means of effective medium theory, *Advances in Radio Science*, vol. 5, pp. 87-94

- C. R. Brewitt-Taylor (2006). Limitation on the bandwidth of artificial perfect magnetic conductor surfaces," *Microwaves, Antennas & Propagation*, IET, vol. 1, pp. 255-260
- N. Guerin, S. Enoch, G. Tayeb, P. Sabouroux, P. Vincent, and H. Legay (2006). A metallic Fabry-Perot directive antenna, *Antennas and Propagation*, IEEE Trans., vol. 54, pp. 220-224
- Z. Weng, N. Wang, Y. Jiao, and F. Zhang (2007). A directive patch antenna with metamaterial structure," *Microwave And Optical Technology Lett.*, vol. 49, pp. 456
- Yuehe Ge, Karu P. Esselle, and Trevor S. Bird (2007). A High-Gain Low-Profile EBG Resonator Antenna, *Antennas and Propag. Society International Symposium*, IEEE, pp. 1301-1304
- A. Alu, F. Bilotti, N. Engheta and L. Vegni (2006). Metamaterial covers over a small aperture, *Antenna and propagation*, IEEE Trans., vol. 54, pp. 1632-1642
- Q. Wu, P. Pan, F. Y. Meng, L. W. Li, and J. Wu (2007). A novel flat lens horn antenna designed based on zero refraction principle of metamaterials, *Applied Physics A: Materials Science & Processing*, vol. 87, pp. 151-156
- J. Huang (1991). Microstrip reflectarray, *Antennas and Propagation Society International Symposium*, IEEE, pp. 612-615
- Z.H. Wu & W.X. Zhang (2005). Circularly polarized reflectarray with linearly polarized feed, *Electron. Lett.*, vol. 41, pp. 387-388
- W. Menzel, & D. Pilz (1986). Millimeter-wave folded reflector antennas with high-gain, low loss and low profile, *IEEE Antenna and Propagation Magazine*, vol. 44, pp. 24-29
- D.T. Mc Grath (1986). Planar three-dimensional constrained lens, *Antennas and Propagation*, IEEE Trans., vol. 34, pp. 46-50
- H.L. Sun, & W.X. Zhang (2007). Design of Broadband Element of Transmitarray with Polarization Trans- form, *3rd iWAT*, IEEE, Cambridge, UK, pp. 287-290
- Z.C. Ge, W.X. Zhang (2006). Broadband and high-gain printed antennas constructed from Fabry-Perot resonator structure using EBG or FSS cover, *Microwave and Optical Technology Lett.*, vol. 48, pp. 1272-1274
- R. Gardelli, M. Albani & F. Capolino (2006). Array thinning by using antennas in a Fabry-Perot cavity for gain enhancement, *Antennas and Propagation*, IEEE Trans., vol. 54, pp. 1979-1990
- A.P. Feresidis, & G. Goussetis (2005). Artificial magnetic conductor surfaces and their application to low-profile high-gain planar antennas, *Antennas and Propagation*, IEEE Trans., vol. 53, pp.209-215
- W.X. Zhang, D.L. Fu & A.N. Wang (2007). A compound printed air-fed array antenna, *Proceeding International Conference on Electromagnetics in Advanced Applications*, Torino, Italy, pp. 1054-1057



# Microwave Filters

Jiafeng Zhou  
*University of Bristol*  
 UK

## 1. Introduction

Filters are two-port networks used to control the frequency response in a system by permitting good transmission of wanted signal frequencies while rejecting unwanted frequencies. Generally there are four types of filters: low-pass, high-pass, band-pass, and band-stop.

Microwave filter design has been a persistent and productive field for investigation from the very beginning of microwave engineering. Nowadays, high performance filters are needed in many microwave systems. Because of the importance of microwave filters, a great deal of material on the theory and design of filters is widely available in the literature. The purpose of this chapter is to introduce the basic theory of microwave filters, to describe how to design practical microwave filters, and to investigate ways of implementing high performance filters for modern communication systems.

## 2. The lowpass prototype

### 2.1 The lowpass prototype filters

The lumped-element circuit of an  $n$ -order lowpass prototype filter is shown in Fig. 1. The circuit shown in Fig. 1(b) is the dual form of that shown in Fig. 1(a). Both forms give identical responses. In Fig. 1,  $g_1$  to  $g_n$  are the values of the inductances or capacitances of the reactive elements.  $g_0$  and  $g_{n+1}$  are the values of terminal immittances (usually pure resistances or conductances) of the source and load respectively. The  $g$ -values for different types of lowpass filters are given in the following sections.

### 2.2 Butterworth lowpass prototype filter

A typical Butterworth, or “maximally flat”, lowpass response is shown in Fig. 2. The attenuation characteristic can be expressed by (Matthaei et al. 1980)

$$L_A(\omega') = 10 \log_{10} [1 + \varepsilon^2 (\frac{\omega'}{\omega'_c})^{2n}] \quad (1)$$

where  $\omega'$  is the radian frequency variable, and  $\omega'_c$  is the frequency of the passband edge, or cut-off frequency, as defined in Fig. 2. The value of  $\varepsilon$  is given by

$$\epsilon = \sqrt{10 \frac{L_{Ar}}{10} - 1} \tag{2}$$

where  $L_{Ar}$  is the attenuation at the cut-off frequency  $\omega'_c$ , In most cases for Butterworth filters,  $\omega'_c$  is defined as the frequency of the 3-dB passband edge point. That is,  $L_{Ar} = 3$  dB, and  $\epsilon = 1$ . The parameter  $n$  in equation (1) is the order of the filter, or the number of reactive elements in the circuit.

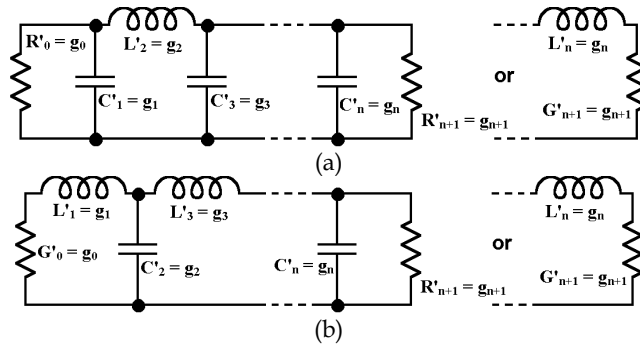


Fig. 1. (a) The prototype of lowpass filters and (b) its dual.

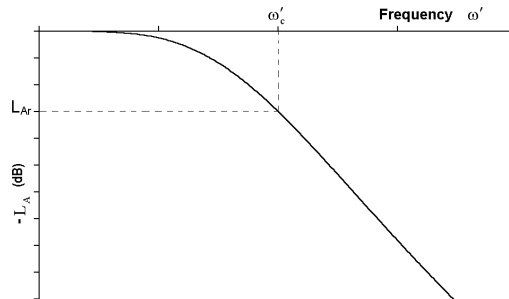


Fig. 2. A typical Butterworth lowpass filter response.

For the Butterworth filters with response of the form shown in Fig. 2, the element values, normalized to make  $g_0 = 1$  and  $\omega'_c = 1$ , can be calculated by

$$g_0 = g_{n+1} = 1$$

$$g_k = 2 \sin\left[\frac{(2k-1)\pi}{2n}\right] \quad (k = 1, 2, \dots, n) \tag{3}$$

The above values can be used to find out the required inductances and capacitances in a real filter having a different cut-off frequency and different terminal impedances (or admittance  $Y_0 = 1/Z_0$ ) by (Matthaei et al. 1980)

$$C_k = \frac{1}{Z_0} \frac{g_k}{\omega'_c} \quad (k \text{ even or odd}) \tag{4}$$



$$L_k = Z_0 \frac{g_k}{\omega'_c} \quad (k \text{ odd or even})$$

where  $\omega'_c$  is the new cut-off frequency and  $Z_0$  is the new source and load impedance.

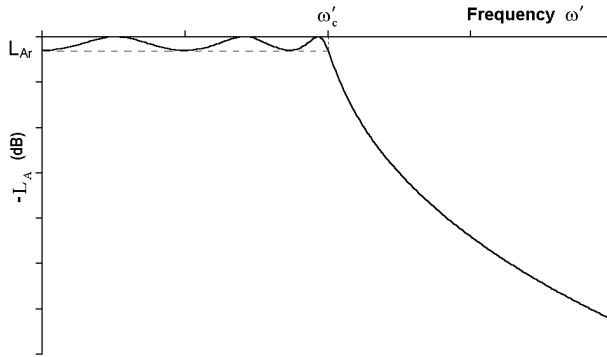


Fig. 3. A typical Chebyshev lowpass filter response (Matthaei et al. 1980) .

**2.3 Chebyshev lowpass prototype filter**

A typical Chebyshev, or “equal-ripple”, lowpass response is shown in Fig. 3. The attenuation characteristic can be expressed by (Matthaei et al. 1980)

$$L_A(\omega') = 10 \log_{10} \{1 + \epsilon^2 \cos^2 [n \cos^{-1}(\frac{\omega'}{\omega'_c})]\}, \quad (\text{for } \omega' \leq \omega'_c) \tag{5}$$

$$L_A(\omega') = 10 \log_{10} \{1 + \epsilon^2 \cosh^2 [n \cosh^{-1}(\frac{\omega'}{\omega'_c})]\}, \quad (\text{for } \omega' \geq \omega'_c)$$

where

$$\epsilon = \sqrt{10^{\frac{L_{Ar}}{10}} - 1} \tag{6}$$

In this case,  $L_{Ar}$  is the maximum attenuation in the pass band, while  $\omega'_c$  is the equal-ripple band edge. The parameter  $n$  is the order of the filter.

The normalized  $g$ -values for an  $n$ -order Chebyshev low-pass prototype filter can be calculated as follows:

$$\begin{aligned} g_0 &= 1 \\ g_1 &= \frac{2a_1}{\gamma} \\ g_k &= \frac{4a_{k-1}a_k}{b_{k-1}g_{k-1}} \quad (k = 2,3,4,\dots,n) \end{aligned} \tag{7}$$

$$g_{n+1} = \coth\left(\frac{\beta}{4}\right)^2 \quad (\text{n even})$$

$$= 1 \quad (\text{n odd})$$

where

$$\beta = \ln\left(\frac{\sqrt{1+\varepsilon}+1}{\sqrt{1+\varepsilon}-1}\right) \quad (8)$$

$$\gamma = \sinh\left(\frac{\beta}{2n}\right)$$

and

$$a_k = \sin\left[\frac{(2k-1)\pi}{2n}\right], \quad (k=1,2,\dots,n) \quad (9)$$

$$b_k = \gamma^2 + \sin^2\left(\frac{k\pi}{n}\right), \quad (k=1,2,\dots,n)$$

The above values can be used to find the required inductances and capacitances in a real filter to realize different cut-off frequency and source impedance by

$$C_k = \frac{1}{Z_s} \frac{g_k}{\omega'_c} \quad (\text{k even or odd})$$

$$L_k = Z_s \frac{g_k}{\omega'_c} \quad (\text{k odd or even}) \quad (10)$$

$$Z_L = \frac{g_{n+1}}{Z_s} \quad (\text{n even})$$

$$= g_{n+1} Z_s \quad (\text{n odd})$$

where  $\omega'_c$  is the new cut-off frequency,  $Z_s$  is the new source impedance and  $Z_L$  is the load impedance. It should be noticed that, in the prototype filter, the impedances of the source and load could be different for a Chebyshev filter, while they are the same for the Butterworth case.

Compared with a Butterworth filter of the same order, a Chebyshev response has a much sharper cut-off rate at the transition region, and usually a worse group delay distortion.

#### 2.4 Quasi-elliptic lowpass prototype filters

The synthesis procedures of lowpass prototype filters with Butterworth and Chebyshev characteristics are given above. For these two types of responses, all of transmission zeros (attenuation poles) are at infinite frequencies. The inverse Chebyshev filters and elliptic filters have all of the transmission zeros at finite frequencies. They have a much better cut-off rate in the transition region than Butterworth and Chebyshev filters (Rhodes, 1976). However, due to the difficulties in synthesis and realization of the inverse Chebyshev and elliptic filters, it is usually of more interest to develop alternative quasi-elliptic filters, which have transmission zeros at both finite and infinite frequencies (Rhodes & Alseyab, 1980). Especially quasi-elliptic filters with a single transmission zero (or a pair of transmission

zeros for the transformed bandpass filters) at finite frequency are very attractive. This is not only because these filters can be exactly synthesized and physically realized with little practical difficulty, but also because they give important improvements compared with conventional Butterworth and Chebyshev filters (Levy, 1976). The typical response of quasi-elliptic filters is shown in Fig. 4. The response of such filters has a generalized Chebyshev equal-ripple passband, and a different stopband with transmission zero(s). In filter realization, the transmission zero(s) are usually implemented by cross coupling a pair of nonadjacent elements of the filters.

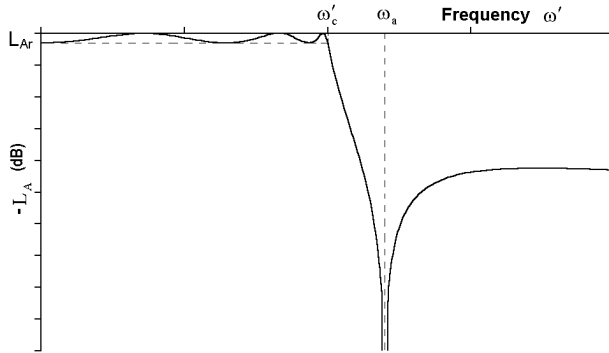


Fig. 4. A typical quasi-elliptic lowpass filter response (Rhodes & Aalseyab, 1980).

The attenuation characteristic of an  $n$ -order lowpass prototype filter with a single transmission zero at finite can be expressed by (Rhodes & Aalseyab, 1980)

$$L_A = 1 + \varepsilon^2 F_n^2(\omega') \tag{11}$$

where  $\varepsilon$  is given by equation (6) and the transfer function is given by

$$F_n(\omega') = \cosh[\cosh^{-1} \omega' + (n-1)\cosh^{-1}(\omega' \sqrt{\frac{\omega_a^2 - 1}{\omega_a^2 - \omega'^2}})] \tag{12}$$

where  $n$  is an odd number, and the transmission zeros are at  $\omega' = \pm\omega_a$  and infinity. The transmission zero at  $\omega' = \omega_a$  is shown in Fig. 4, while the other one  $\omega' = -\omega_a$  is the mirror image of the positive one.

Another similar form of the transfer function is given by (Hong & Lancaster, 2000),

$$F_n(\omega') = \cosh[(n-2)\cosh^{-1} \omega' + \cosh^{-1}(\frac{\omega' \omega_a - 1}{\omega_a - \omega'}) + \cosh^{-1}(\frac{\omega' \omega_a + 1}{\omega_a + \omega'})] \tag{13}$$

where the transmission zeros are at  $\omega' = \pm\omega_a$  and infinity. Some useful quasi-elliptic filters have been synthesized in the reference (Hong & Lancaster, 2000).

The general synthesis process to find the values of elements in the prototype quasi-elliptic lowpass filter has been given in the references (Rhodes & Aalseyab, 1980; Levy, 1976).

However, the exact synthesis procedure is quite complicated, and there does not exist closed-form formulas for the element values of quasi-elliptic filters as those for Butterworth and Chebyshev filters. Instead, a set of data is tabulated in the reference (Hong & Lancaster, 2000) for practical design of quasi-elliptic filters up to eighth-order.

### 3. The lowpass to bandpass transformation

In this section, only Chebyshev lowpass and bandpass filters are discussed. Butterworth and quasi-elliptic filters can be studied in a similar manner. The lowpass prototype shown in Fig. 1(a) is used for the discussion, while the result will be the same if Fig. 1(b) were used instead. The transformation from lowpass to highpass and bandstop filters can be accomplished similarly.

A typical Chebyshev bandpass filter response is shown in Fig. 5. The response can be related exactly to a corresponding lowpass prototype filter by the lowpass to bandpass mapping (Matthaei et al. 1980; Hong & Lancaster, 2001; Collin, 2001)

$$\frac{\omega'}{\omega'_c} = \frac{\omega_0}{\omega_2 - \omega_1} \left( \frac{\omega}{\omega_0} - \frac{\omega_0}{\omega} \right) \quad (14)$$

where  $\omega'$ ,  $\omega'_c$  are the frequency variable and the cut-off frequency of the lowpass prototype filter defined in the above sections respectively.  $\omega_1$  and  $\omega_2$  are the cut-off frequencies of the passband, and the centre frequency  $\omega_0$  is given by

$$\omega_0 = \sqrt{\omega_1 \omega_2} \quad (15)$$

Equation (14) may be solved for  $\omega$ , giving

$$\omega = \frac{\omega'}{\omega'_c} \frac{\omega_2 - \omega_1}{2} \pm \frac{1}{2} \sqrt{\left( \frac{\omega'}{\omega'_c} \right)^2 (\omega_2 - \omega_1)^2 + 4\omega_1 \omega_2} \quad (16)$$

The point  $\omega' = 0$  of the lowpass filter is seen to map into the points  $\omega = \pm\omega_0$  of the transformed filter, and  $\omega' = \pm\omega'_c$  map into four points  $\omega = \pm\omega_1$  and  $\omega = \pm\omega_2$ . Thus the lowpass band of the prototype filter maps into the passband extending from  $\omega_1$  to  $\omega_2$  and  $-\omega_1$  to  $-\omega_2$ , which represents bandpass filters with cut-off frequencies at  $\pm\omega_1$  and  $\pm\omega_2$ . The centre frequency  $\omega = \pm\omega_0$  is the geometric mean of the cut-off frequencies. The transformed response for  $\omega > 0$  is shown in Fig. 5, and the response for  $\omega < 0$  is the mirror image of the positive one.

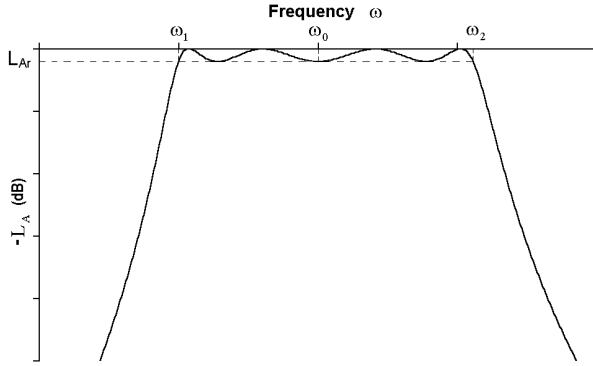


Fig. 5. A typical Chebyshev bandpass filter response.

According to equation (14), to obtain the transformed bandpass response, the shunt capacitance in the prototype lowpass filter needs to be changed to a new susceptance

$$\begin{aligned}
 jB_k &= j\left[\frac{\omega'_c \omega_0}{\omega_2 - \omega_1} \left(\frac{\omega}{\omega_0} - \frac{\omega_0}{\omega}\right)\right]g_k \\
 &= j\omega\left(\frac{\omega'_c g_k}{\omega_2 - \omega_1}\right) + \frac{1}{j\omega\left(\frac{\omega_2 - \omega_1}{\omega'_c \omega_1 \omega_2 g_k}\right)} \quad (k \text{ odd})
 \end{aligned} \tag{17}$$

which is equivalent to a shunt tuned resonator with a shunt capacitance  $C_k$  and a shunt inductance  $L_k$  given by

$$\begin{aligned}
 C_k &= \frac{\omega'_c g_k}{\omega_2 - \omega_1} \\
 L_k &= \frac{\omega_2 - \omega_1}{\omega'_c \omega_1 \omega_2 g_k} \quad (k \text{ odd})
 \end{aligned} \tag{18}$$

Similarly, the series inductance in the prototype filter should to be changed to a new reactance

$$\begin{aligned}
 jX_k &= j\left[\frac{\omega'_c \omega_0}{\omega_2 - \omega_1} \left(\frac{\omega}{\omega_0} - \frac{\omega_0}{\omega}\right)\right]g_k \\
 &= j\omega\left(\frac{\omega'_c g_k}{\omega_2 - \omega_1}\right) + \frac{1}{j\omega\left(\frac{\omega_2 - \omega_1}{\omega'_c \omega_1 \omega_2 g_k}\right)} \quad (k \text{ odd})
 \end{aligned} \tag{19}$$

which is equivalent to a series tuned resonator with a series capacitance  $C_k$  and a series inductance  $L_k$  given by

$$C_k = \frac{\omega_2 - \omega_1}{\omega_c' \omega_1 \omega_2 g_k} \tag{20}$$

$$L_k = \frac{\omega_c' g_k}{\omega_2 - \omega_1} \quad (\text{k even})$$

The equivalent circuit of the transformed bandpass filter is shown in Fig. 6.

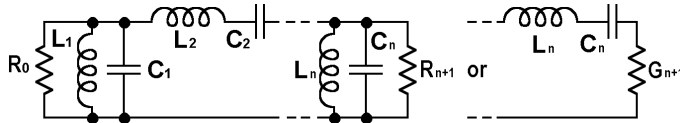


Fig. 6. The equivalent circuit of a bandpass filter transformed from a lowpass filter.

### 4. Transformation of bandpass filter using K- or J-inverters

The filter shown in Fig. 6 consists of series tuned resonators alternating with shunt-tuned resonators. According to equation (18) and equation (20), such a filter is difficult to implement, because the values of the components are very different in the shunt and series tuned resonators. A way to modify the circuit is to use J - (admittance) or K - (impedance) inverters, so that all resonators can be of the same type.

#### 4.1 Impedance and admittance inverters

An idealized *impedance inverter* operates like a quarter-wavelength line of characteristic impedance K at all frequencies. As shown in Fig. 7(a), if an impedance inverter is loaded with an impedance of Z at one end, the impedance  $Z_K$  seen from the other end is (Matthaei et al. 1980)

$$Z_K = \frac{K^2}{Z} \tag{21}$$

An idealized *admittance inverter*, which operates like a quarter-wavelength line with a characteristic admittance Y at all frequencies, is the admittance representation of the same thing. As shown in Fig. 7(b), if the admittance inverter is loaded with an admittance of Y at one end, the admittance  $Y_J$  seen from the other end is (Matthaei et al. 1980)

$$Y_J = \frac{J^2}{Y} \tag{22}$$

It is obvious that the loaded admittance Y can be converted to an arbitrary admittance by choosing an appropriate J value. Similarly, the loaded impedance Z can be converted to an arbitrary impedance by choosing an appropriate K value.

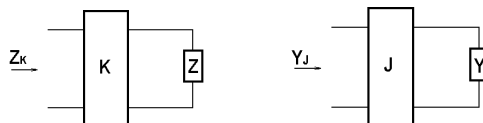


Fig. 7. Definition of K- (impedance) and J- (admittance) inverters.

As indicated above, both the impedance and admittance inverters are like ideal quarter-wave transformers. While  $K$  denotes the characteristic impedance of an inverter and  $J$  denotes the characteristic admittance of an inverter, there are no conceptual differences in their inverting properties. An impedance inverter with characteristic impedance  $K$  is identical to an admittance inverter with characteristic admittance  $J = 1/K$ . Especially for a unity inverter, with a characteristic impedance of  $K = 1$  and a characteristic admittance of  $J = 1$ .

Besides a quarter-wavelength line, there are some other circuits that operate as inverters. Some useful  $J$ - and  $K$ -inverters are shown in Fig. 8 and Fig. 9. It should be noticed that some of the inductors and capacitors have negative values. Although it is not practical to realize such components, they will be absorbed by adjacent resonant elements in the filter, as discussed in the following sections. It should also be noted that, since the inverters shown here are frequency sensitive, these inverters are best suitable for narrowband filters. It is shown in the reference (Matthaei et al. 1980) that, using such inverters, filters with bandwidths as great as 20 percent are achievable using half-wavelength resonators, or up to 40 percent by using quarter-wavelength resonators.



Fig. 8. Some circuits useful as J-Inverters.



Fig. 9. Some circuits useful as K-Inverters.

**4.2 Conversion of shunt tuned resonators to series tuned resonators**

Because of the inverting characteristic indicated by equation (22), a shunt capacitance with a  $J$ -inverter on each side acts like a series inductance (Matthaei et al. 1980). Likewise, a shunt tuned resonator with a  $J$ -inverter on each side acts like a series tuned resonator. To verify this, a shunt tuned resonator, consisting of a capacitor  $C$  and an inductor  $L$ , with a  $J$ -inverter on each side is shown in Fig. 10(a). Both  $J$ -inverters have a value of  $J$ . If the circuit is loaded with admittance  $Y_0$  of an arbitrary value at one end, from equation (22), the admittance  $Y$  looking in at the other end is given by

$$Y = \frac{J^2}{j\omega C + \frac{1}{j\omega L} + \frac{J^2}{Y_0}} \tag{23}$$

The impedance is, therefore,

$$Z = \frac{1}{Y} = \frac{j\omega C}{J^2} + \frac{1}{j\omega L J^2} + \frac{1}{Y_0} \tag{24}$$

This impedance is equivalent to a series tuned resonator loaded with an impedance of  $Z_0 = 1/Y_0$ , as shown in Fig. 10(b). The capacitor of  $C_1$  and inductor  $L_1$  of the equivalent circuit are given by

$$\begin{aligned} L_1 &= \frac{C}{J^2} \\ C_1 &= L J^2 \end{aligned} \tag{25}$$

Because the above equations are correct regardless the value of the load  $Y_0$ , the two circuits shown in Fig. 10 are equivalent to each other.

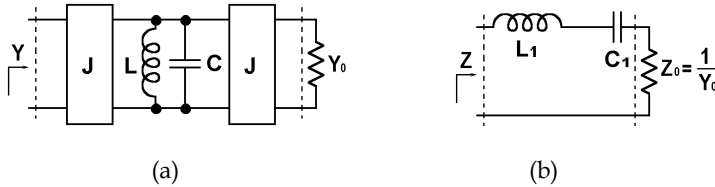


Fig. 10. A shunt tuned resonator with J-inverters on both sides and its equivalent circuit.

It is very useful for the discussion in the following sections to point out that, from equation (25), the transformed resonator can have an arbitrary impedance level  $\sqrt{L_1/C_1}$  tuned at the same frequency. That is, the shunt tuned circuit with J-inverters shown in Fig. 10(a) can be converted to a series tuned resonator with an arbitrary  $L_1$  or  $C_1$ , as long as  $L_1 C_1 = LC$ , by choosing the inverter

$$J = \sqrt{\frac{C}{L_1}} \tag{26}$$

Thus, the bandpass filter shown in Fig. 6 can be converted to a circuit with only shunt resonators by using J-inverters, as shown in Fig. 11.

The dual case of a series tuned resonator with a K-inverter on each side can be derived in a similar manner.

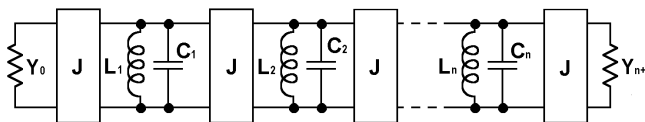


Fig. 11. The bandpass filter using only shunt resonators and J-inverters.



### 4.3 Conversion of shunt resonators with different J-inverters

In the above section, the shunt-tuned resonator is converted into a series tuned resonator by J -inverters of the same value at both ends. More generally, the inverters may have different values. Fig. 12(a) shows a shunt-tuned circuit with J -inverters at both ends. The resonator consists of a capacitor C and an inductor L. The J -inverters have a value of J<sub>1</sub> on one end and J<sub>2</sub> on the other. This circuit can be transformed to an equivalent circuit shown in Fig. 12(b), where the shunt tuned resonator has a capacitor C' and an inductor L', whereas LC=L'C', and the J -inverters have values of J'<sub>1</sub> and J'<sub>2</sub> respectively.

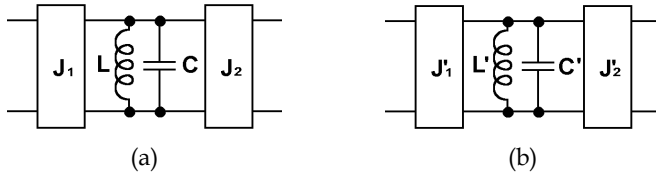


Fig. 12. (a) A shunt tuned resonator with J-inverters of different values, and (b) its equivalent circuit.

The circuit shown in Fig. 12(a) is not symmetrical. If the circuit is loaded with an admittance of Y<sub>OR</sub> at the right-hand-side end, the admittance Y<sub>L</sub> and impedance Z<sub>L</sub> looking in at the left-hand-side end are given by

$$Y_L = \frac{J_1^2}{j\omega C + \frac{1}{j\omega L} + \frac{J_2^2}{Y_{OR}}} \tag{27}$$

$$Z_L = \frac{1}{Y_L} = \frac{j\omega C}{J_1^2} + \frac{1}{j\omega L J_1^2} + \frac{J_2^2}{J_1^2 Y_{OR}}$$

Similarly, if the circuit is loaded with an admittance of Y<sub>OL</sub> at the left-hand-side end, the impedance Z<sub>R</sub> looking in at the other end are given by

$$Z_R = \frac{1}{Y_R} = \frac{j\omega C}{J_2^2} + \frac{1}{j\omega L J_2^2} + \frac{J_1^2}{J_2^2 Y_{OL}} \tag{28}$$

In a similar manner, with a load at the one end, the impedance from the other end of the circuit shown in Fig. 12(b) can be given by

$$Z'_L = \frac{1}{Y'_L} = \frac{j\omega C'}{J_1'^2} + \frac{1}{j\omega L' J_1'^2} + \frac{J_2'^2}{J_1'^2 Y_{OR}} \tag{29}$$

And

$$Z'_R = \frac{1}{Y'_R} = \frac{j\omega C'}{J_2'^2} + \frac{1}{j\omega L' J_2'^2} + \frac{J_1'^2}{J_2'^2 Y_{OL}} \tag{30}$$

If the two circuits shown in Fig. 12 are equivalent,  $ZL \equiv ZL'$  and  $ZR \equiv ZR'$ , from equation (27) to equation (30), it can be obtained

$$\begin{aligned} J'_1 &= J_1 \sqrt{\frac{C'}{C}} = J_1 \sqrt{\frac{L}{L'}} \\ J'_2 &= J_2 \sqrt{\frac{C'}{C}} = J_2 \sqrt{\frac{L}{L'}} \end{aligned} \quad (31)$$

This transformation is very useful in a sense that the bandpass the filter shown in Fig. 11 can be further converted to a circuit where all of the resonators have the same inductance and capacitance. Such conversion will be shown in the next section.

#### 4.4 Filter using the same resonators and terminal admittances

In filter design, it is usually desirable to use the same resonators in a filter, and have the same characteristic impedances or admittances at the source and load. In this section, an  $n$ -th order bandpass filter will be transformed to use the same shunt resonators tuned at the same frequency, with an inductance of  $L_0$  and a capacitance of  $C_0$ , and the same terminal admittances  $Y_0$  at both ends.

The equivalent circuit of a bandpass filter using only shunt resonators and J-inverters is shown in Fig. 11. As discussed in section 0, the admittance of the source and the load can be converted to the same value  $Y_0$  by adding a J-inverter, or changing the value of the J-inverter if there is a J-inverter directly connected to the source or load. By the transformation discussed in section 0, the circuit shown in Fig. 11 can be transformed to Fig. 13, where all resonators have the same inductances  $L_0$  and capacitance  $C_0$ . The values of the inverters are given by:

$$\begin{aligned} J_{0,1} &= \sqrt{\frac{Y_0 \omega_0 C_0 \Delta}{g_0 g_1 \omega'_c}} \\ J_{n,n+1} &= \sqrt{\frac{Y_0 \omega_0 C_0 \Delta}{g_n g_{n+1} \omega'_c}} \\ J_{k,k+1} &= \frac{\omega_0 C_0 \Delta}{\omega'_c} \sqrt{\frac{1}{g_k g_{k+1}}} \quad (k=1,2,\dots,n-1) \end{aligned} \quad (32)$$

where  $\Delta$  is the fractional bandwidth of the bandpass filter given by

$$\Delta = \frac{\omega_2 - \omega_1}{\omega_0} \quad (33)$$

where  $\omega_1$ , and  $\omega_2$  are the cut-off frequencies, and  $\omega_0$  is the centre frequency of the filter as defined in equation (15). The values of  $g_0, g_1, g_2 \dots g_{n+1}$  and  $\omega'_c$  are defined in the low-pass prototype filter discussed above.

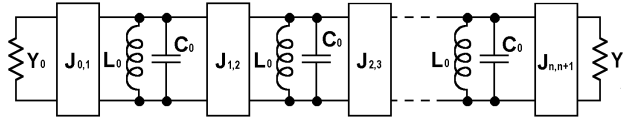


Fig. 13. A transformed bandpass filter using the same resonators.

The above equations are based on the lumped-element equivalent circuit of the filter. More generalized form of these equations will be given in section 0. This transformation is very useful because all the resonators in the filter have the same characteristics, which makes the design and fabrication of the filter much easier. The above transformation can also be implemented by using series tuned resonators and K -inverters in a similar manner.

### 5. Coupled-resonator filter

The J -inverters in the filter shown in Fig. 13 can be replaced by any of the equivalent circuits shown in Fig. 8 or other equivalent circuits. One form of such filters is shown in Fig. 14, using the equivalent circuit shown in Fig. 8(b) for those J -inverters. The results of this section would still hold if other equivalent circuit were chosen for the inverters.

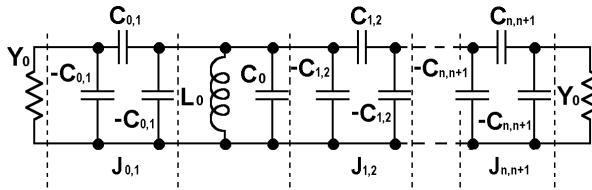


Fig. 14. The transformed filter using the same resonators with capacitive couplings between resonators.

In the filter shown in Fig. 14, the equivalent circuit of each J -inverter consists of one positive series capacitor and two negative shunt ones. In filter design, the positive capacitance represents the mutual capacitances between resonators, while the negative capacitors can be absorbed into the positive shunt capacitors in the resonators. It should be noted that the negative capacitances adjacent to the source and load cannot be absorbed this way. Further discussion about these negative capacitances will be given below in section 0. From equation (32), it is obvious that the knowledge of the equivalent circuit of the resonators will be needed to find out the values of the required J -inverters, whist the g -values can be obtained from the low-pass prototype filter. Once the values of the J -inverters are determined, the required mutual capacitances between resonators can then be calculated by the equation shown in Fig. 8(b). It should be noted that, as indicated in section 0, the inverters shown in Fig. 8 are actually frequency dependent. However, in the narrow-bandwidth near the centre frequency, the inverters can be regarded as frequency insensitive by approximating

$$J_{k,k+1}(\omega) \approx \omega C_{k,k+1} \approx \omega_0 C_{k,k+1} \tag{34}$$

where  $\omega_0 = 1/\sqrt{L_0 C_0}$ , and  $L_0, C_0,$  and  $C_{k,k+1}$  are defined in Fig. 14.

### 5.1 Internal and external coupling coefficients

Due to the distributed-element nature of microwave circuits, it is usually difficult to find out the equivalent circuit of the resonators directly. It is therefore difficult to determine the required the values of the J-inverters, or mutual capacitances between resonators. However, from equation (32), it is possible to obtain the required ratio of the mutual capacitance to the shunt capacitance of each resonator without the knowledge of the equivalent circuit. For example, the ratio of the required mutual capacitance between resonators to the capacitance of each resonator is, from equation (32) and equation (34),

$$M_{k,k+1} = \frac{C_{k,k+1}}{C_0} = \frac{\omega_0 C_{k,k+1}}{\omega_0 C_0} \approx \frac{J_{k,k+1}}{\omega_0 C_0} = \frac{\Delta}{\omega'_c} \sqrt{\frac{1}{g_k g_{k+1}}} \quad (k=1,2,\dots,n-1) \quad (35)$$

where  $\Delta$  is the fractional bandwidth of the bandpass filter, and  $\omega'_c \cdot g_k \cdot g_{k+1}$  are defined in the prototype lowpass filter.  $M_{k,k+1}$  is the strength of the internal coupling, or the *coupling coefficient*, between resonators.

The external couplings between the terminal resonators and the source and load are defined in a similar manner by, with the approximation of equation (34),

$$Q_{e0,1} = \frac{Y_0 C_0}{\omega_0 C_{0,1}^2} \approx \frac{\omega_0 C_0 Y_0}{J_{0,1}^2} = \frac{g_0 g_1 \omega'_c}{\Delta} \quad (a) \quad (36a)$$

$$Q_{en,n+1} = \frac{Y_0 C_0}{\omega_0 C_{n,n+1}^2} \approx \frac{\omega_0 C_0 Y_0}{J_{n,n+1}^2} = \frac{g_n g_{n+1} \omega'_c}{\Delta} \quad (b) \quad (36b)$$

The values of  $Q_{e0,1}$  and  $Q_{en,n+1}$  are the strength of the external couplings, or the *external quality factors*, between the terminal resonators and the source/load.

It can be seen from equation (35) and equation (36) that these required internal and external couplings can be obtained directly from the prototype low-pass filter and the passband details of the transformed bandpass filter, without specific knowledge of the equivalent circuit of the resonators. From equation (32), it can be proved that fixing the internal and external couplings as prescribed by equation (35) and equation (36) is adequate to fix the response of the filter shown in Fig. 14 (Matthaei et al. 1980). The following two sections will concentrate on experimentally determining these couplings.

### 5.2 Determination of internal couplings by simulation

After finding the required coupling coefficients and external quality factors for the desired filtering characteristics as discussed above, it is essential to experimentally determine these couplings in a practical circuit so as to find the dimensions of the filter for fabrication. This section describes the determination of the coupling coefficients between resonators by the use of full wave simulation. The details about the external couplings between the terminal resonators and the source and load are given in the next section.

As discussed above, the same resonators are usually used in a filter. The equivalent circuit of a pair of coupled identical resonators is shown in Fig. 15, which can be regarded as part

of the filter shown in Fig. 14. As the circuit is symmetrical, the admittance looking in at either side is,

$$Y_{in} = \frac{1}{j\omega L_0} + j\omega(C_0 - C_{k,k+1}) + \frac{1}{\frac{1}{j\omega C_{k,k+1}} + \frac{1}{j\omega(C_0 - C_{k,k+1}) + \frac{1}{j\omega L_0}}} \quad (37)$$

At resonance,  $Y_{in}=0$ . By equating the right-hand side of equation (37) to zero, four eigenvalues of the frequency  $\omega$  can be obtained. The two positive frequencies are given by

$$\begin{aligned} \omega_{01} &= \frac{1}{\sqrt{L_0(C_0 + C_{k,k+1})}} \\ \omega_{02} &= \frac{1}{\sqrt{L_0(C_0 - C_{k,k+1})}} \end{aligned} \quad (38)$$

The other two negative frequencies are the mirror image of these positive ones.

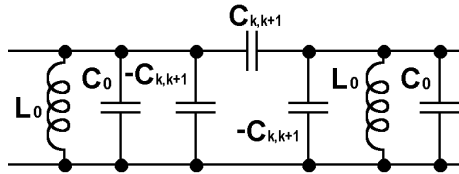


Fig. 15. The equivalent circuit of a pair of coupled identical resonators.

If this circuit is weakly coupled to the exterior ports for measurement or simulation, the typical measured or simulated response for the scattering parameter  $S_{21}$  is as shown in Fig. 16. More details of the measurement or simulation will be given in the next section. The two resonant frequencies as expressed in equation (38) are specified in Fig. 16. By inspecting equation (35) and equation (38), the coupling coefficient can be determined by,

$$M_{k,k+1} = \frac{C_{k,k+1}}{C_0} = \frac{\omega_{02}^2 - \omega_{01}^2}{\omega_{02}^2 + \omega_{01}^2} \approx \frac{\omega_{02} - \omega_{01}}{\omega_0} \quad (k = 1, 2, \dots, n - 1) \quad (39)$$

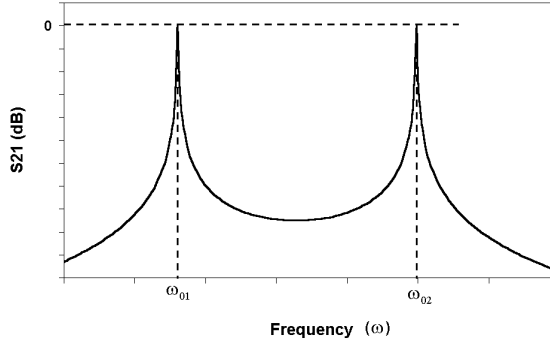


Fig. 16. A typical response of the coupled resonators shown in Fig. 15.

### 5.3 Determination of external couplings by simulation

The procedure to determine the strength of the external coupling, the external quality factor  $Q_e$ , is somewhat different from determining the internal coupling coefficient between resonators. It is possible to take the corresponding part of the circuit, for example, the load, the last resonator and the inverter between them, from Fig. 14, and determine the external quality factor by measuring the phase shift of group delay of the selected circuit (Hong & Lancaster, 2001).

More conveniently, a doubly loaded resonator shown in Fig. 17 is considered. One end of the circuit is the same as in Fig. 14, while another load and inverter of the same values are added symmetrically at the other end. The ABCD matrix of the whole circuit, except the two loads, is given by

$$\begin{pmatrix} A_Q & B_Q \\ C_Q & D_Q \end{pmatrix} = \begin{pmatrix} 0 & \frac{1}{j\omega C_e} \\ -j\omega C_e & 0 \end{pmatrix} \begin{pmatrix} 1 & 0 \\ j\omega C_0 + \frac{1}{j\omega L_0} & 1 \end{pmatrix} \begin{pmatrix} 0 & \frac{1}{j\omega C_e} \\ -j\omega C_e & 0 \end{pmatrix} \quad (40)$$

where  $C_e = C_{0,1}$ , or  $C_{n,n+1}$  as defined in Fig. 14. The scattering parameter  $S_{21}$  can be calculated by

$$S_{21} = \frac{2}{A_Q + Y_0 B_Q + \frac{C_Q}{Y_0} + D_Q} = \frac{2}{-2 - \frac{jY_0}{\omega^2 C_e^2} (\omega C_0 - \frac{1}{\omega L_0})} \quad (41)$$

By substituting equation (36) and  $\omega_0 = 1/\sqrt{L_0 C_0}$ , this equation can be rewritten as

$$S_{21} = \frac{-2}{2 + \frac{jY_0 \omega_0 C_0}{\omega^2 C_e^2} (\frac{\omega}{\omega_0} - \frac{\omega_0}{\omega})} = \frac{-2}{2 + jQ_e (\frac{\omega}{\omega_0} - \frac{\omega_0}{\omega})} \quad (42)$$

where  $Q_e = Q_{0,1}$  or  $Q_{n,n+1}$  is the external quality factor for the source or load as defined in equation (36). At a narrow bandwidth around the resonant frequency,  $\omega/\omega_0 - \omega_0/\omega \approx 2\Delta\omega/\omega_0$  with  $\omega = \omega_0 + \Delta\omega$ . The magnitude of  $S_{21}$  is given by

$$|S_{21}| = \frac{1}{\sqrt{1 + (Q_e \Delta\omega / \omega_0)^2}} \tag{43}$$

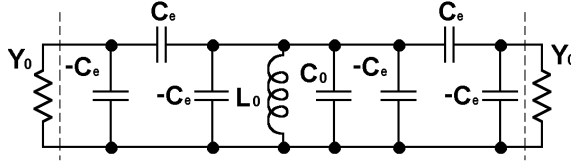


Fig. 17. The equivalent circuit of a doubly loaded resonator.

If this circuit is connected to the exterior ports for measurement or simulation, the typical measured or simulated response of the doubly coupled resonator is shown in Fig. 18. It can be found from equation (43) that  $|S_{21}|$  has a maximum value  $|S_{21}| = 1$  (or 0 dB) at  $\Delta\omega = 0$ , and the value falls to 0.707 (or -3 dB) at

$$\frac{Q_e \Delta\omega}{\omega_0} = \pm 1 \tag{44}$$

The two solutions of equation (44) are given by

$$\Delta\omega = \pm \frac{\omega_0}{Q_e} \tag{45}$$

The two corresponding frequencies  $\omega_1 = \omega_0 - \omega_0 / Q_e$  and  $\omega_2 = \omega_0 + \omega_0 / Q_e$  can be easily found by simulation or measurement as shown in Fig. 18. The external quality factor therefore can be given by

$$Q_e = \frac{\omega_0}{2(\omega_2 - \omega_1)} \tag{46}$$

As indicated above, the external quality factor  $Q_e$  is actually defined for a singly loaded resonator. One possible way to determine  $Q_e$  of a singly coupled resonator is to measure the phase shift of group delay of the reflection coefficient ( $S_{11}$ ) of a singly loaded resonator, and the external quality factor is given by (Hong & Lancaster, 2001)

$$Q_e = \left| \frac{\omega_0}{\omega_{+90^\circ} - \omega_{-90^\circ}} \right| \tag{47}$$

where  $\omega_{+90^\circ}$  and  $\omega_{-90^\circ}$  are the frequencies at which the phase shifts are  $\pm 90^\circ$  respectively. The external quality factor can also be given by (Hong & Lancaster, 2001)

$$Q_e = \frac{\omega_0 \tau(\omega_0)}{4} \tag{48}$$

where  $\tau(\omega_0)$  is the group delay of  $S_{11}$  at the centre frequency  $\omega_0$ .

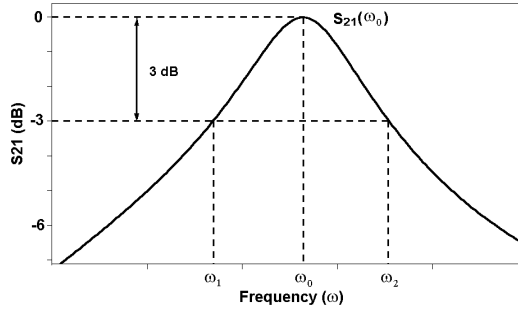


Fig. 18. The typical response of a doubly coupled resonator.

Another more practical way to determine the external quality factor of a singly loaded resonator is to use an equivalent circuit shown in Fig. 19. The circuit is similar to Fig. 14, except that one end of the circuit has the external coupling to be measured, while the other end has a relatively much weaker coupling, namely  $C_w \ll C_e$ . The ABCD matrix of the circuit can be expressed as, similar to equation (40),

$$\begin{pmatrix} A_{Q1} & B_{Q1} \\ C_{Q1} & D_{Q1} \end{pmatrix} = \begin{pmatrix} 0 & \frac{1}{j\omega C_e} \\ -j\omega C_e & 0 \end{pmatrix} \begin{pmatrix} 1 & 0 \\ j\omega C_0 + \frac{1}{j\omega L_0} & 1 \end{pmatrix} \begin{pmatrix} 0 & \frac{1}{j\omega C_w} \\ -j\omega C_w & 0 \end{pmatrix} \quad (49)$$

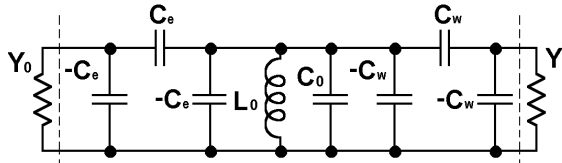


Fig. 19. The equivalent circuit of a singly loaded resonator. It is called “singly” loaded because the coupling at one end, represented by  $C_e$ ’s, is much stronger than the coupling at the other end, represented by  $C_w$ ’s.

The scattering parameter  $S_{21}$  can be obtained, similarly to equation (42), by

$$S_{21} = \frac{-2}{\left(\frac{C_e}{C_w} + \frac{C_w}{C_e}\right) - j\frac{C_e}{C_w} Q_e \frac{\Delta\omega}{\omega_0}} \quad (50)$$

It is obvious that if  $C_w = C_e$ , this equation is the same as equation (42). Here as  $C_w \ll C_e$ , equation (50) can be rewritten as,

$$S_{21} = -\frac{2C_w}{C_e} \frac{1}{\left(1 - j2Q_e \frac{\Delta\omega}{\omega_0}\right)} \quad (51)$$

The typical response of the circuit is very similar to Fig. 18, except that the value of  $|S_{21}|$  has a maximum value of  $2C_w/C_e$  [or  $20\log(2C_w/C_e)$  dB] at  $\Delta\omega = 0$ . The value is 3 dB lower at frequencies where  $\Delta\omega$  is given by,



$$\frac{2Q_e \Delta\omega}{\omega_0} = \pm 1 \quad (52)$$

The two corresponding frequencies are  $\omega_1 = \omega_0 - \omega_0/(2Q_e)$  and  $\omega_2 = \omega_0 + \omega_0/(2Q_e)$ . The external quality factor, therefore, can be determined by

$$Q_e = \frac{\omega_0}{\omega_2 - \omega_1} \quad (53)$$

#### 5.4 Equivalent circuit of the inverters at the source and load

In the above discussion, some negative shunt capacitances are used to realize the inverters. Most of these negative capacitances can be absorbed by the adjacent resonators. However, this absorption procedure does not work for the inverters between the end resonators and the terminations (source and load), as the terminations usually have pure resistances or conductances.

This difficulty can be avoided if another equivalent circuit, shown in Fig. 20, is used for the  $J$ -inverter. As indicated above, by using any equivalent circuits to realize the required inverters, the filter response will be the same. All the methods to determine the external quality factor as described by equations (46), (47), (48) and (53) are still valid.

In the circuit shown in Fig. 20, at the resonant frequency, the admittance looking in from the resonator towards the source is given by

$$Y_{in} = j\omega_0 C_a + \frac{1}{\frac{1}{Y_0} + \frac{1}{j\omega_0 C_b}} = \frac{1}{\frac{1}{Y_0} + \frac{Y_0}{\omega_0^2 C_b^2}} + j(\omega_0 C_a + \frac{1}{\frac{\omega_0 C_b}{Y_0^2} + \frac{1}{\omega_0 C_b}}) \quad (54)$$

Because the required value of the  $J$ -inverter is  $J_e = J_{0,1}$ , or  $J_{n,n+1}$  as defined in Fig. 13, the required admittance is therefore  $J_e^2/Y_0$ . By equating this value to the real part of  $Y_{in}$ , two solutions of  $C_b$  can be obtained, and the positive one is given by

$$C_b = \frac{J_e}{\omega_0 \sqrt{1 - (\frac{J_e}{Y_0})^2}} \quad (55)$$

By equating the imaginary part of  $Y_{in}$  to 0,  $C_a$  can be found by

$$C_a = -\frac{C_b}{1 + (\frac{\omega_0 C_b}{Y_0})^2} \quad (56)$$

This negative shunt capacitance can be absorbed by the resonator.

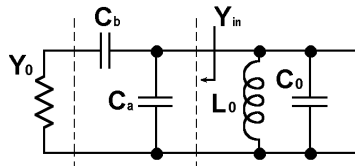


Fig. 20. Another equivalent circuit to realize the inverter between the end resonator and the termination.

### 5.5 More generalized equations

Since purely lumped elements are difficult to realize at microwave frequencies, it is usually more desirable to construct the resonators in a distributed-element form. Such a resonator can be characterized by its centre frequency  $\omega_0$  and its susceptance slope parameter (Matthaei et al. 1980)

$$\ell = \frac{\omega_0}{2} \left. \frac{dB(\omega)}{d\omega} \right|_{\omega_0} \quad (57)$$

where  $B$  is the susceptance of the resonator. For a shunt tuned lumped-element resonator, equation (57) can be simplified as  $\ell = \omega_0 C = 1/(\omega_0 L)$ . The values of  $J$ -inverters for filters using distributed-element resonators can be calculated by replacing  $\omega_0 C_0$  with  $\ell_0$  in equation (32), where  $\ell_0$  is the susceptance slope parameter of the distributed-element resonators. More generally, if the slope parameter of each resonator is different from the others, equation (32) can be rewritten as (Matthaei et al. 1980)

$$J_{0,1} = \sqrt{\frac{Y_0 \ell_1 \Delta}{g_0 g_1 \omega'_c}} \quad (58a)$$

$$J_{n,n+1} = \sqrt{\frac{Y_0 \ell_n \Delta}{g_n g_{n+1} \omega'_c}} \quad (58b)$$

$$J_{k,k+1} = \frac{\Delta}{\omega'_c} \sqrt{\frac{\ell_k \ell_{k+1}}{g_k g_{k+1}}} \quad (k=1,2,\dots,n-1) \quad (58c)$$

where  $\ell_k$  is the susceptance slope parameter of  $k$ -th resonator,  $\Delta$  is given in equation (33), and the values of  $g_0, g_1, g_2, \dots, g_{n+1}$  and  $\omega'_c$  are defined in the low-pass prototype filter. The definition of the coupling coefficient equation (35) can be modified to (Matthaei et al. 1980),

$$M_{k,k+1} = \frac{J_{k,k+1}}{\sqrt{\ell_k \ell_{k+1}}} = \frac{\Delta}{\omega'_c} \frac{1}{\sqrt{g_k g_{k+1}}} \quad (k=1,2,\dots,n-1) \quad (59)$$

If it is possible to find the equivalent capacitances  $C_k, C_{k+1}$  for the  $k$ -th and  $(k+1)$ -resonators, and the equivalent mutual capacitance  $C_{k,k+1}$  in the vicinity of the centre frequency, the coupling coefficient  $M_{k,k+1}$  can be expressed by

$$M_{k,k+1} = \frac{J_{k,k+1}}{\sqrt{\ell_k \ell_{k+1}}} \approx \frac{\omega_0 C_{k,k+1}}{\sqrt{\ell_k \ell_{k+1}}} = \frac{C_{k,k+1}}{\sqrt{C_k C_{k+1}}} \quad (k=1,2,\dots,n-1) \quad (60)$$

In a similar manner, equation (36) can be modified to

$$Q_{e0,1} = \frac{\ell_1 Y_0}{J_{0,1}^2} = \frac{g_0 g_1 \omega'_c}{\Delta} \quad (61a)$$

$$Q_{en,n+1} = \frac{\ell_n Y_0}{J_{n,n+1}^2} = \frac{g_n g_{n+1} \omega'_c}{\Delta} \quad (61b)$$

Or, if the equivalent capacitances in the vicinity of the centre frequency of the terminal resonators can be found,

$$Q_{e0,1} = \frac{\ell_1 Y_0}{J_{0,1}^2} \approx \frac{Y_0 C_1}{\omega_0 C_{0,1}^2} \quad (62a)$$

$$Q_{en,n+1} = \frac{\ell_n Y_0}{J_{n,n+1}^2} \approx \frac{Y_0 C_n}{\omega_0 C_{n,n+1}^2} \quad (62b)$$

For the case when a filter uses resonators tuned at different frequencies, the determination of the coupling coefficients are described in Chapter 8 of the reference (Hong & Lancaster, 2001).

## 6. Design example of a Chebyshev filter

At microwave and millimetre wave frequencies, filters are not usually built by using the lumped-element components as discussed above, but by utilizing transmission lines, usually called distributed-element components. The complex behaviour of the distributed-element components makes it very difficult to develop a complete synthesis procedure for microwave filters. It is, however, possible to approximate the behaviour of ideal capacitors and inductors by using appropriate microwave components in a limited frequency range. Thus the microwave filter is realized by replacing capacitors and inductors in the lumped-element filters by suitable microwave components with similar frequency characteristics in the frequency band of interest. The microwave filter design procedure is further simplified by the aid of CAD program.

### 6.1 Filter synthesis

In this section, a three-pole Chebyshev bandpass filter with a fractional bandwidth of 0.461% centred at 610 MHz, and a ripple of 0.01dB in the passband, will be designed by simulation (Sonnet Software, 2009) using the above theory.

Firstly, the  $g$ -values of the three-pole Chebyshev prototype lowpass filter, with a ripple of 0.01 dB, can be calculated by equation (7):  $g_0=1$ ,  $g_1=0.6291$ ,  $g_2=0.9702$ ,  $g_3=0.6291$  and  $g_4=1$ . Substituting these values with  $\omega'_c=1$  and the fractional bandwidth 0.461% into equation (35) and (36) results in,

$$M_{1,2} = M_{2,3} = 0.005901 \quad (63)$$

$$Q_{e0,1} = Q_{e3,4} = 136.5$$

where  $M_{1,2}$  and  $M_{2,3}$  are the coupling coefficients between resonators, and  $Q_{e0,1}$  and  $Q_{e3,4}$  are the external factors between the end resonators and the terminations (source and load).

## 6.2 Determination of the couplings by simulation

The shape and dimensions of a microstrip resonator centred at 610 MHz are shown in Fig. 21. The centre frequency can be tuned in a small range by changing the lengths of the stubs A and B. The resonator is designed on a 0.50 mm thick MgO substrate. More details on the design of this resonator can be found in the reference (Zhou et al., 2005).

To determine the coupling strength between resonators, the structure shown in Fig. 22(a) is used for simulation. The couplings between the resonators and the feed lines are much weaker than that between the two resonators. As discussed in section 0, two resonant frequencies will be obtained from the simulation as shown in Fig. 22(b), similar to Fig. 16. The coupling coefficient can be extracted by using equation (39). The coupling coefficient is a function of the distance  $d$  between the resonators, and the relationship between the coupling strength and the distance  $d$  is shown in Fig. 23. It can be found in Fig. 23 that two resonators with a distance of 0.60 mm have a coupling coefficient 0.0059, which is very close to the required value of 0.005901.

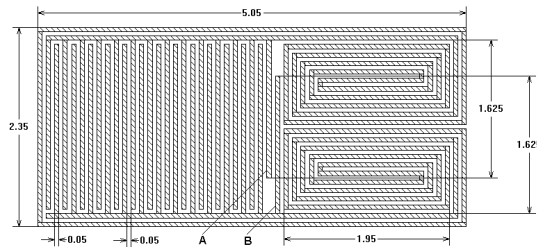


Fig. 21. Layout of the resonator centred at 610 MHz. The minimum line and gap widths are 0.050 mm. Other detailed dimensions are shown in the figure (unit: mm).

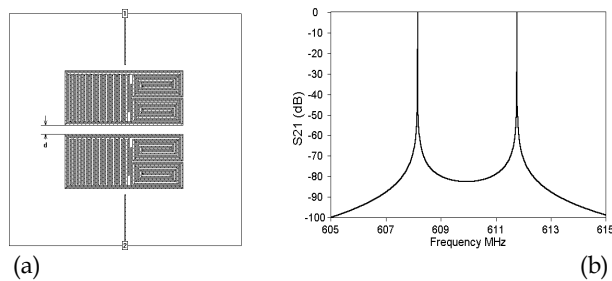


Fig. 22. (a) The structure to determine the coupling strength between resonators in the simulation, and (b) the simulated response for  $d = 0.6$  mm.

The external coupling between the end resonator and the termination is realized by a tapped line, as shown in Fig. 24(a). The length  $t$  along the signal line of the resonator, from the tapped line to the middle of the resonator, controls the strength of the external coupling. The

resonator is weakly coupled to the other feed line, so that the circuit can be regarded as a singly loaded resonator as discussed in section 0. The wide microstrip line connected to port 1 has a characteristic impedance of 50 ohm, the length of which does not affect the response of the circuit.

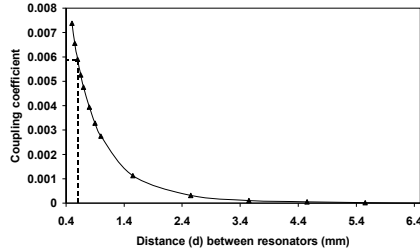


Fig. 23. The coupling coefficient against the distance between the resonators.

The simulated response is shown in Fig. 24(b), similar to Fig. 18, and the external quality factor can be extracted by using equation (53). The relationship between the external quality factor and the length  $t$  is shown in Fig. 25. It can be found that  $t = 4.2$  mm gives an external  $Q$  of 135, which is close to the required value of 136.5.

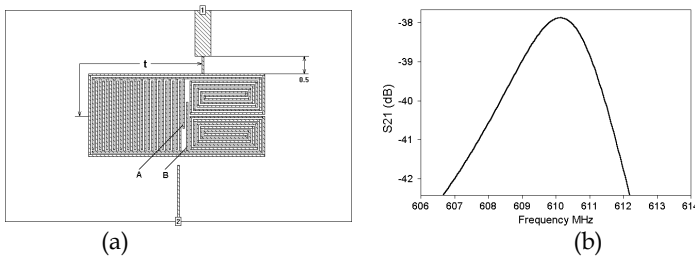


Fig. 24. (a) The structure to determine the external coupling between the end resonator and the termination in the simulation (unit: mm) and (b) the simulated response for  $t = 3.9$  mm.

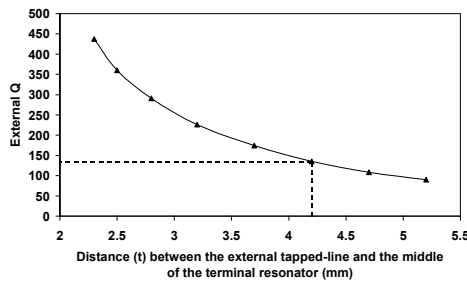


Fig. 25. The external coupling strength against the length from the tapped line to the middle of the resonator.

It should be noted that the position of the tapped line also affects the centre frequency of the end resonator. Therefore the dimensions of the end resonator need to be changed slightly to keep the desired centre frequency. This is done by changing the length of the stubs A and B as shown in Fig. 24.

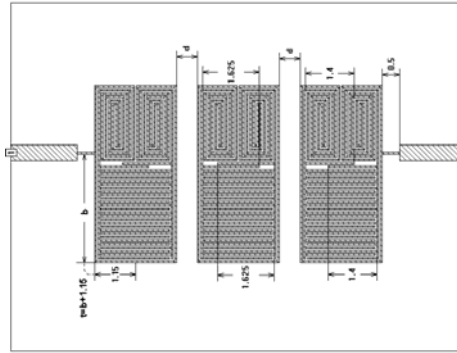


Fig. 26 Layout and dimensions of the three-pole Chebyshev filter (unit: mm), where  $t = 4.3$  and  $d = 0.60$  after optimisation. More detailed dimensions of the resonators can be found in Fig. 21 and Fig. 24(a).

For the required external  $Q$  for this filter, the length of  $A$  and  $B$  is found to be 1.4 mm, which compares to the length of 1.625 mm in the original resonator shown in Fig. 21. The filter is formed in a shape as shown in Fig. 26. It will be discussed below that further optimization of the filter is required to achieve optimal performance.

### 6.3 Circuit optimisation and simulated response

The theoretical response of the three-pole Chebyshev filter designed is shown in Fig. 27. The theoretical response is obtained by calculation using the coupling coefficients given in equation (63). More details on the calculation are given in Chapter 8 of the reference (Hong & Lancaster, 2001).

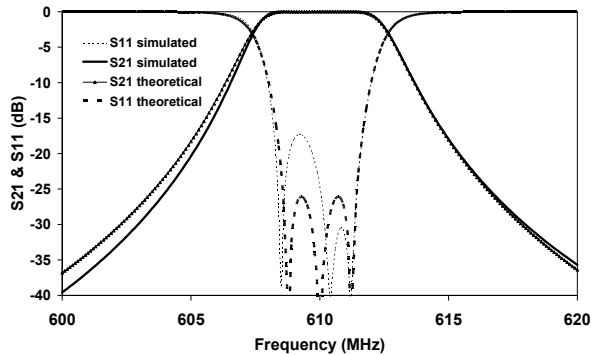


Fig. 27. The theoretical and simulated responses of the three-pole Chebyshev filter.

The dimensions obtained in section 0 are used by the full-wave simulator Sonnet (Sonnet Software, 2009). The simulated response of the filter is shown in Fig. 27. However, the simulated response using these dimensions is close to, but does not meet the theoretical response very well. Generally, there are two major reasons. One reason is that, in the simulator, the dimensions of the circuit are “discrete” rather than “continuous”, so that the

required coupling coefficients can usually be realized proximately, rather than precisely. This is because in the simulator a “cell” is the basic building block of the circuit. Thus any part of the circuit may be as small as one cell or may be multiple cells long or wide. For example, a typical circuit drawn in the simulator is shown in Fig. 28, which has a cell size of 0.05 mm × 0.025 mm. The black dots are the grid points. The dimensions of the circuit in the horizontal direction, such as  $w$  and  $d$ , can only be the multiple of 0.05 mm; while the dimensions in the vertical direction, such as  $h$ , can only be the multiple of 0.025 mm. If  $d = 0.75$  mm would give the required performance, in the simulator, only the proximate value  $d = 0.5$  or  $1.0$  mm could be used. The dimensions can be more precise if the cell size is smaller. But, on the other hand, the simulation time increases exponentially as the cell size decreases.

Another reason is that the unwanted cross couplings, among non-neighbouring resonators and between input and output ports, are not considered in the design. These cross couplings cannot be easily determined before the design as they are not independent to other couplings, and they become much more complicated in a filter having more resonators. Alternatively, the simulator (Sonnet Software, 2009) has an “optimisation function”, which can be used to optimise the dimensions of a circuit to get an optimised performance.

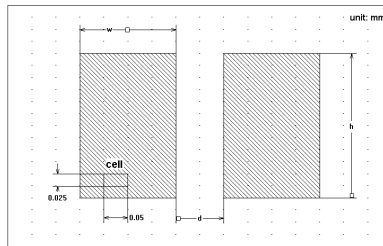
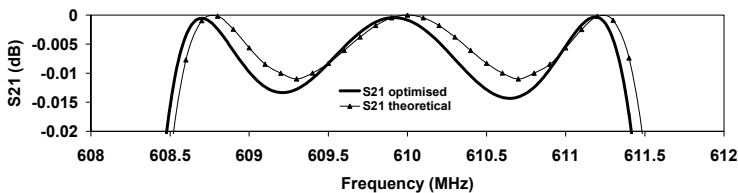


Fig. 28. An example circuit drawn in the EM simulator (Sonnet Software, 2009).

By using this function, the user may select dimensions of the circuit and define them as a parameter. In the analysis, the simulator controls the parameter value, within a user defined range, in an attempt to reach a user defined goal. More than one parameters can be used simultaneously in the simulation if necessary. More detailed information about the optimisation can be found in the reference (Sonnet Software, 2009).

The dimensions of the three-pole filter after optimisation by the simulator are shown in Fig. 26, where  $t = 4.3$  mm and  $d = 0.60$  mm. The optimised response is shown in Fig. 29, which agrees very well with the theoretical result. The optimised passband has a ripple of 0.014 dB, very close to the target of 0.01 dB; and the minimum return loss is better than 25 dB in the passband, also close to the theoretical value of 26.3 dB.



(a)

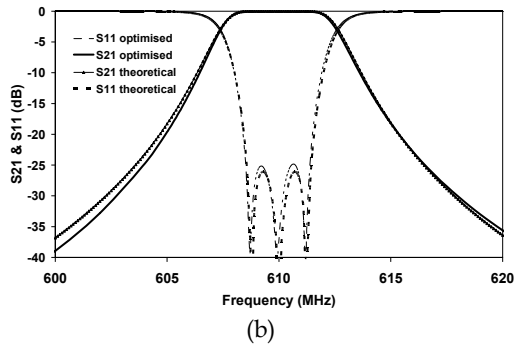


Fig. 29. The theoretical and optimised performances of the 3-pole Chebyshev filter.

## 7. Summary

The general theory of microwave filter design based on lumped-element circuit is described in this chapter. The lowpass prototype filters with Butterworth, Chebyshev and quasi-elliptic characteristics are synthesized, and the prototype filters are then transformed to bandpass filters by lowpass to bandpass frequency mapping. By using immittance inverters (J - or K -inverters), the bandpass filters can be realized by the same type of resonators. One design example is given to verify the theory on how to design microwave filters.

## 8. Reference

- Collin R. E. (2001). *Foundation for Microwave Engineering*, John Wiley & Sons, Inc. ISBN: ISBN 0-7803-6031-1. New Jersey.
- Hong, J. S. & Lancaster, M. J. (2000). Design of Highly Selective Microstrip Bandpass Filters with a Single Pair of Attenuation Poles at Finite Frequencies, *IEEE Transactions on Microwave Theory and Technology*, vol. 48, July 2000. pp. 1098-1107.
- Hong, J. S. & Lancaster, M. J. (2001). *Microstrip Filters for RF/Microwave Applications*, John Wiley & Sons, INC. ISBN: 0-471-38877-7, New York.
- Levy, R. (1976). Filters with single transmission zeros at real and imaginary frequencies, *IEEE Transactions on Microwave Theory and Technology*, vol. 24, Apr. 1976. pp. 172-181.
- Matthaei, G.; Young, L. & Jones, E.M.T. (1980). *Microwave Filters, Impedance-matching Networks and Coupling Structure*, Artech House, INC. 685 Canton Street, Norwood, MA 02062.
- Rhodes, J. D. (1976). *Theory of Electrical Filters*, Wiley. ISBN: 0-471-71806-8, New York.
- Rhodes, J. D. & Aloseyab, S. A. (1980). The generalized Chebyshev low-pass prototype filter. *Circuit Theory Application*, vol.8, 1980. pp.113-125.
- Sonnet Software (2009), *EM User's Manual*, Sonnet Software, Inc. Elwood Davis Road North Syracuse, NY 13212
- Zhou, J.; Lancaster, M. J.; Huang, F.; Roddis, N. & Glynn, D. (2005) HTS narrow band filters at UHF band for radio astronomy applications, *IEEE Transactions on Applied Superconductivity*, vol.15, June 2005. pp.1004 - 1007.



# Reconfigurable Microwave Filters

Ignacio Llamas-Garro and Zabdiel Brito-Brito  
*Technical University of Catalonia  
Spain*

## 1. Introduction

Reconfigurable microwave filters make microwave transceivers adaptable to multiple bands of operation using a single filter, which is highly desirable in today's communications with evermore growing wireless applications. Tunable filters can replace the necessity of switching between several filters to have more than one filter response by introducing tuning elements embedded into a filter topology.

Microwave tunable filters can be divided in two groups, filters with discrete tuning, and filters with continuous tuning. Filter topologies presenting a discrete tuning generally use PIN diodes or MEMS switches. On the other hand, filter topologies using varactor diodes, MEMS capacitors, ferroelectric materials or ferromagnetic materials are frequently used to obtain a continuous tuning device. Filter topologies can mix continuous and discrete tuning by combining tuning elements as well, e.g. the use of switches and varactors on a filter topology can form part of a discrete and continuous tuned device.

Center frequency is the most common filter parameter to reconfigure. Fewer designs reconfigure other parameters, such as the bandwidth or selectivity. When deciding which technology is adequate for a given application, the designer must consider the following issues: cost, power consumption, size, performance and operating frequency. This chapter intends to provide a broad view of the microwave reconfigurable filters field, where different technologies used to reconfigure filters are discussed through different chapter sections, and finally an overall view of the field is given in the conclusions section at the end of the chapter.

This chapter starts discussing filters that use active devices as tuning elements in section 2; these include the PIN diode, the varactor diode, the transistor and Monolithic Microwave Integrated Circuit (MMIC) implementation. Section 3 discusses the use of Micro Electro Mechanical Systems (MEMS) as tuning elements on filter topologies; the section discusses the use of MEMS switches and MEMS varactors. Section 4 contains tunable filters using ferroelectric materials, where devices using the most common ferroelectrics are discussed. Section 5 contains filters that use ferromagnetic materials as tuning elements, the section discusses circuits using Yttrium-Iron-Garnet (YIG) films and other ferromagnetic tuning mechanisms.

Section 6 describes devices that combine some of the technologies discussed in previous sections to achieve reconfigurable filter parameters. Section 7 contains a discussion of

traditional filter tuning techniques using dielectric or metallic mechanically adjustable tuning screws. Section 8 gives an overall conclusion of this chapter.

## 2. Tunable filters using active devices

This section covers tunable filters that use semiconductor based tuning elements. Devices using diodes are attractive below 10 GHz where diodes can still show quality factors above 50 with low bias voltages. Diodes usually involve simple packages and can be mounted on microwave boards, many of these designs are thought as potential monolithic designs. This section covers tunable filters that use PIN diodes, varactor diodes, transistors and ends with a discussion on monolithic designs.

### 2.1. Tunable filters using PIN diodes

PIN diodes are frequently used to produce reconfigurable discrete states on a filter response, and are very attractive for low cost implementations. In this section, tunable filters using PIN diodes are discussed in distributed and lumped topologies as well a design using periodic structures.

#### 2.1.1. Distributed designs

Recently in (Brito-Brito et al., 2008) the relation between fractional bandwidth and the reactance slope parameter of switchable decoupling resonators has been discussed. This technique has been used to implement two switchable bandstop filters (Brito-Brito et al., 2009 b); these filters can switch between two center frequency states, each having a defined fractional bandwidth. The filters have been implemented to provide the same fractional bandwidth at both center frequencies or different bandwidths defined by the shape of bended switchable resonator extensions, these two topologies are shown in Fig. 1.

The filter presented in (Lugo & Papapolymerou, 2004) can produce broad and narrow bandwidths by modifying inter-resonator couplings. The filter in (Koochakzadeh & Abbaspour-Tamijani, 2007) covers a frequency tuning range from 290 to 600 MHz in four steps using ten PIN diodes.

A tunable side coupled resonator filter with three center frequency states and two possible bandwidths for each state can be found in (Lugo & Papapolymerou, 2006 a). A reconfigurable bandpass filter for WiFi and UMTS transmit standards (Brito-Brito et al., 2009 a) is shown in Fig. 2, the filter has been designed to precisely provide the center frequency and bandwidth required for each application with low loss and low power consumption, since it only uses two PIN diodes.

The reconfigurable bandpass filter in (Lacombe, 1984) can obtain a pseudo all pass response or a bandpass response using PIN diodes. A Dual mode resonator filter can be found in (Lugo & Papapolymerou, 2005), the filter uses a triangular patch resonator to achieve a two state reconfigurable bandwidth. A reconfigurable bandwidth using a dual mode square resonator can be found in (Lugo et al., 2005).

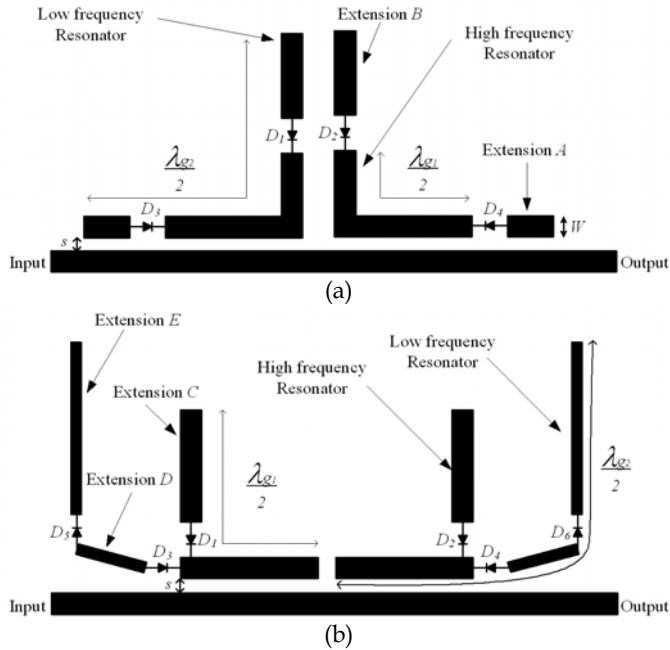


Fig. 1. Two state switchable bandstop filters using PIN diodes a) constant bandwidth b) different bandwidth, taken from (Brito-Brito et al., 2009 b).

Other dual mode resonator filter is presented in (Lugo & Papapolymou, 2006 b), this filter has an asymmetrical filter response, and can tune its center frequency, and transmission zero position using a modified square resonator. The filter in (Karim et al., 2008) can switch from a bandstop to a bandpass response for ultra wideband applications using four PIN diodes. A tunable non uniform microstrip combline filter with a reconfigurable center frequency of over an octave in the UHF band can be found in (Koochakzadeh & Abbaspour-Tamijani, 2008), the filter can maintain a constant bandwidth over the center frequency tuning range.

### 2.1.2. Lumped element designs

Lumped element filter designs using PIN diodes include a reconfigurable bandwidth design at 10 GHz able to switch between a 500 MHz and a 1500 MHz bandwidth (Rauscher, 2003). The filter presented in (Chen & Wang, 2007) uses low-temperature co-fired ceramic technology and can switch between two center frequency states.

### 2.1.3. Filters using periodic structures

The filter in (Karim et al., 2006) switches between a bandstop and a bandpass response using electromagnetic band gap periodic structures on a coplanar ground plane; the filter is centered at 7.3 GHz.

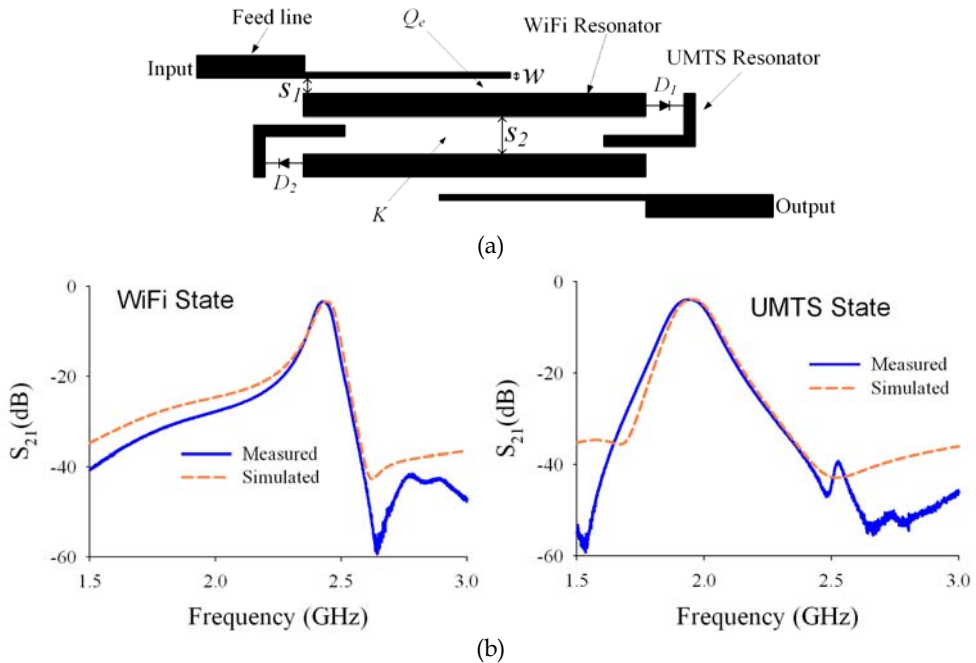


Fig. 2. Switchable bandpass filter using PIN diodes a) topology b) filter response, taken from (Brito-Brito et al., 2009 a).

## 2.2. Tunable filters using varactor diodes

Varactors are typically used for continuous tuned filters. Varactor diodes use the change in the depletion layer capacitance of a p-n junction as a function of applied bias voltage. Varactor tuned devices have been used for high tuning speeds; these devices do not exhibit hysteresis. Tuning speeds of varactor tuned filters are limited only by the time constant of the bias circuit. Varactor based tunable filters are mainly distributed designs as covered in this section.

The filter in (Musoll-Anguiano et al., 2009) can reconfigure center frequency, bandwidth and selectivity, resulting in a fully adaptable bandstop design. A photograph of this filter is shown in Fig. 3. The filter response when tuning these three parameters is shown in Fig. 4.

The filter in (Chung et al., 2005) can tune center frequency or bandwidth using a compact hairpin like resonator. The combline filters in (Hunter & Rhodes, 1982 a), (Hunter & Rhodes, 1982 b), (Sanchez-Renedo et al., 2005) and (Brown & Rebeiz, 2000) use suspended stripline transmission lines. The first design is a bandpass filter, and the second one is a bandstop filter. The bandpass design can tune its center frequency showing a good impedance matching for the different filter states. The third design provides both center frequency and bandwidth control on a bandpass filter topology. The fourth design is a bandpass filter with a reconfigurable center frequency, respectively.

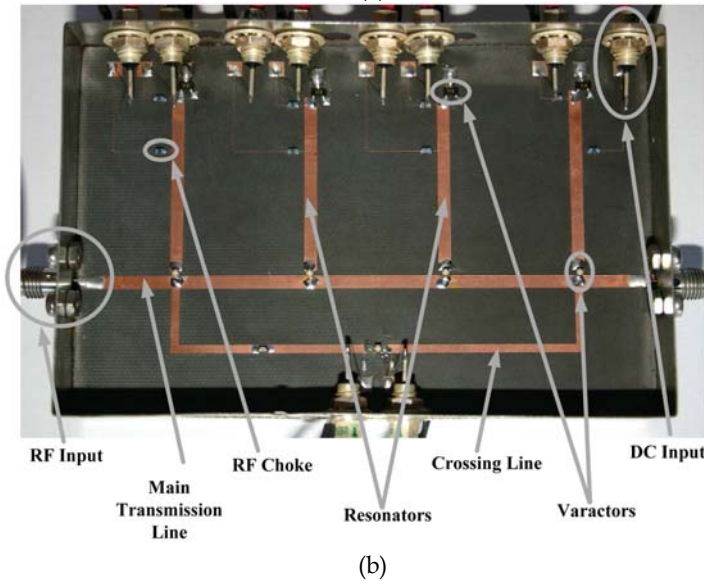
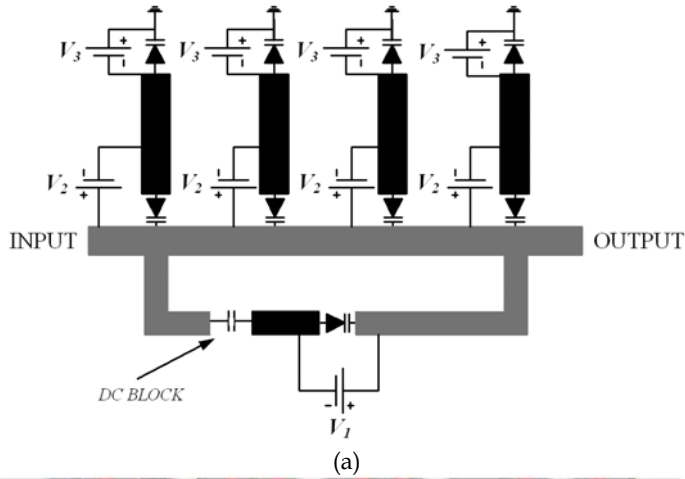


Fig. 3. Tunable bandstop filter using varactor diodes a) topology b) photography of the filter, taken from (Musoll-Anguiano et al., 2009).

In (Makimoto & Sagawa, 1986) a tunable bandpass filter using microstrip varactor loaded ring resonators is demonstrated, the device can reconfigure its center frequency. In (Liang & Zhu, 2001) a filter mixing combline and hairpin like resonators to achieve transmission zeros on the sides of the passband is presented, the device can tune its center frequency.

### 2.3. Tunable filters using PIN and varactor diodes

This section reviews filters which combine PIN and Varactor diodes, this results in filter topologies with discrete and continuous tuning.

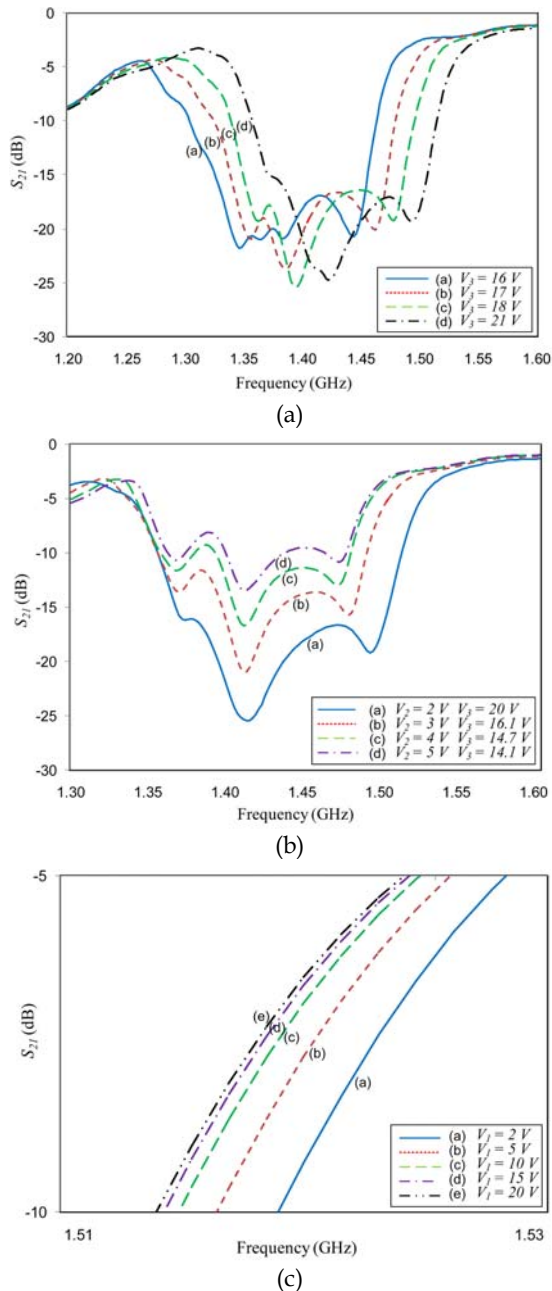


Fig. 4. Tunable bandstop filter measured responses according to applied bias voltages a) center frequency tuning b) bandwidth tuning c) selectivity tuning, taken from (Musoll-Anguiano et al., 2009).

PIN diodes have been used to vary resonator length for frequency tuning and varactor diodes to modify the bandwidth at each center frequency state in (Carey-Smith & Warr, 2007). This results in discrete center frequency tuning, and continuous bandwidth tuning.

#### 2.4. Tunable filters using transistors

A gallium arsenide field effect transistor has been used as a tuning element in (Torregrosa-Penalva et al., 2002), the filter topology and frequency response is shown in Fig. 5; the device is based on a combline topology and can tune its center frequency.

Center frequency tuning has been achieved on a two pole filter configuration using two metal semiconductor field effect transistors in (Lin & Itoh, 1992), one transistor is used for center frequency tuning and the other to provide a negative resistance to the circuit. The negative resistance technique can raise the resonator unloaded quality factor resulting in an improved filter response.

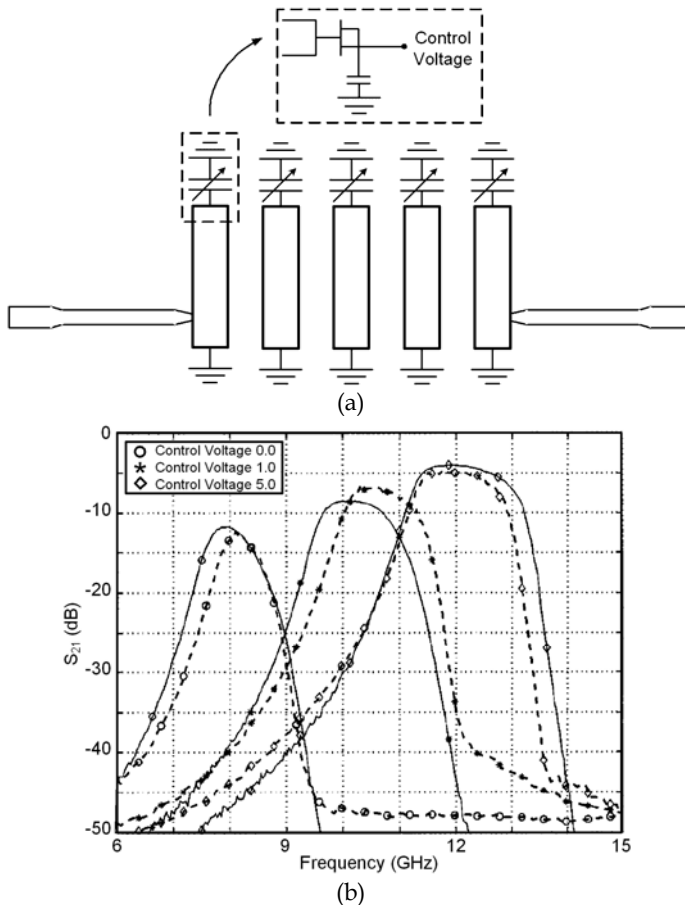


Fig. 5. Tunable bandpass filter using transistors a) topology b) filter response, taken from (Torregrosa-Penalva et al., 2002).

### 2.5. Tunable filters using transistors and varactor diodes

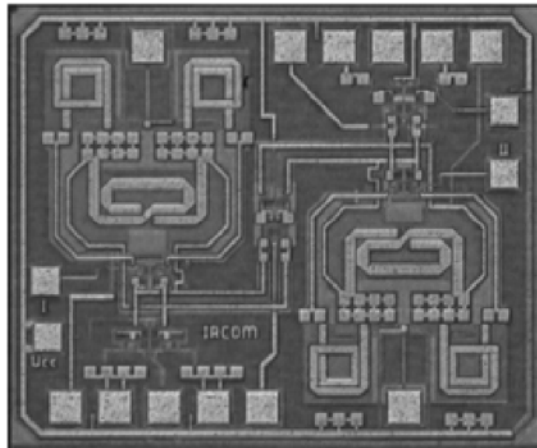
To compensate for filter losses, like those resulting from using a varactor diode, a negative resistance circuit using transistors can be added to the design. This technique has been used in (Chandler et al., 1993 b) where bandstop and bandpass filters are demonstrated, the transistor used was a silicon bi-polar transistor. In (Chandler et al., 1993 a) a bandpass filter is demonstrated using silicon bi-polar transistors as well. Finally in (Chang & Itoh, 1990) metal semiconductor field effect transistors were used on a bandpass filter topology.

### 2.6. MMIC Tunable filters

The silicon integrated reconfigurable filter in (Darfeuille et al., 2006) can tune center frequency, bandwidth and transmission gain, a photography and center frequency response of the chip is shown on Fig. 6. Two K-band filter designs using 0.15  $\mu\text{m}$  gallium arsenide technology have been reported in (Fan et al., 2005), both devices use negative resistance compensation for losses. The filter in (Takahashi et al., 2006) has an operating frequency range of around 120 GHz; the device can tune its center frequency or bandwidth, the device uses indium phosphide high-electron-mobility transistors. The tunable filter in (Wu & Chan, 1997) uses gallium arsenide metal semiconductor field effect transistors and provides frequency tuning with high resonator unloaded quality factors obtained using a negative resistance circuit which is also used as a tuning element.

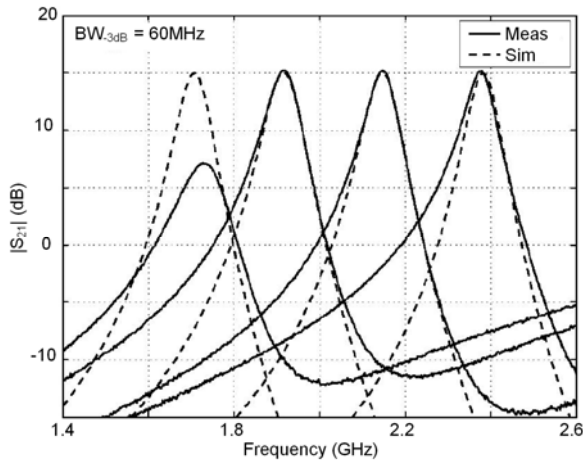
## 3. Tunable filters using MEMS

RF MEMS reconfigurable devices have good compatibility with technologies used in semiconductor industries. They offer small size and good integration capabilities with microwave electronics. RF MEMS in general require low currents to be operated, thus they consume low power compared to solid state devices, and they also can exhibit linear transmission with low signal distortion. This section contains tunable filters that use MEMS switches or MEMS varactors as tuning elements.



(a)





(b)

Fig. 6. MMIC tuneable bandpass filter a) fabricated chip b) filter response, taken from (Darfeuille et al., 2006)

### 3.1. Tunable filters using MEMS switches

This section reviews several filter topologies using MEMS switches to produce discrete tuning of reconfigurable parameters. The switches can be either a cantilever or a bridge type, and can be capacitive type switches or direct contact switches. Switches can have two states: on or off. Direct contact switches will generally make a metal to metal contact in the on state, direct contact switches are commonly used for low frequency applications. Capacitive switches will present two capacitances, one in the on state and another one in the off state, these switches can be used for high frequency operation.

#### 3.1.1. Filters using direct contact switches

This section discusses filters that use direct contact switches as tuning elements. The switches have an off state when the switch membrane is suspended and does not make contact with a bottom metallic pad. The switch in the on position results in a metal to metal contact of the switch membrane with a bottom metallic pad. Direct contact metal switches can be found as cantilever type, and bridge type. The switch on and off position is controlled by a bias voltage between the switch membrane and actuation electrodes. This section contains tunable filters in distributed designs, lumped element designs and finally a filter using periodic structures is described.

##### 3.1.1.1. Distributed designs

A microstrip bandpass filter using hairpin resonators with direct contact cantilever switches on the end of the resonators has been reported in (Ocera et al., 2006), the cantilever switches are used to enlarge the hairpin resonators when the switches are in the on state, thus tuning the device center frequency; a photography of the filter and cantilever switch is shown in Fig. 7, as well as its center frequency response. Tunable slotline resonators printed on a

microstrip ground plane have been used to make a lowpass filter using commercial MEMS switches to short-circuit the slot resonators in (Zhang & Mansour, 2007).

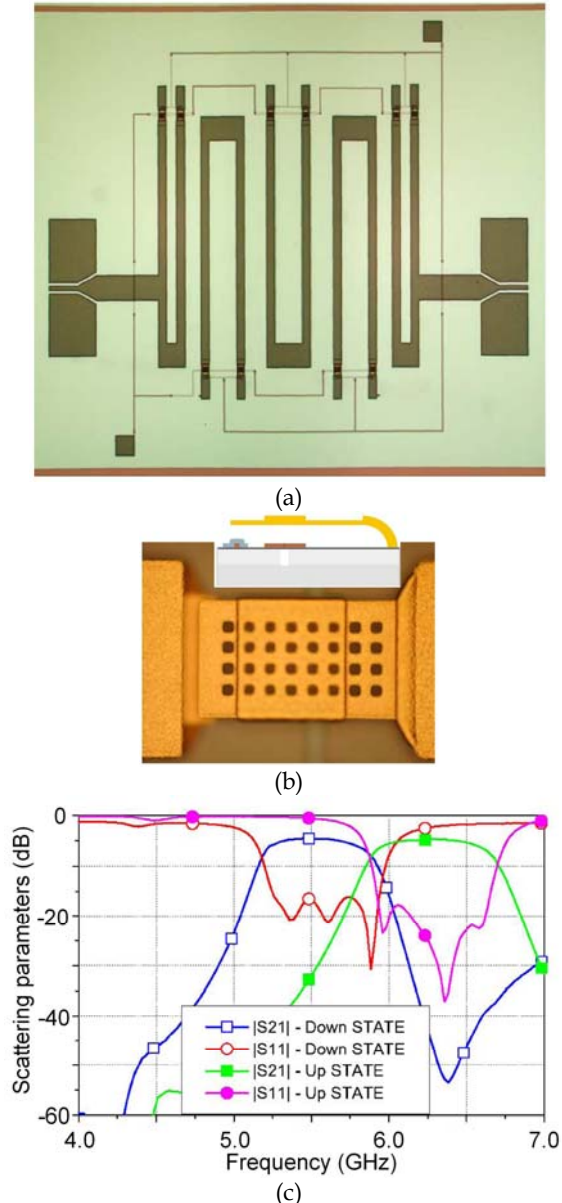


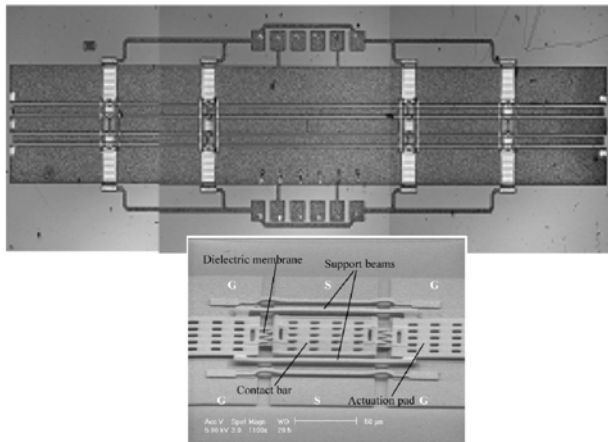
Fig. 7. Tunable bandpass filter using direct contact MEMS cantilever switches a) photography b) direct contact MEMS cantilever switch c) filter response, taken from (Ocera et al., 2006)

### 3.1.1.2. Lumped element designs

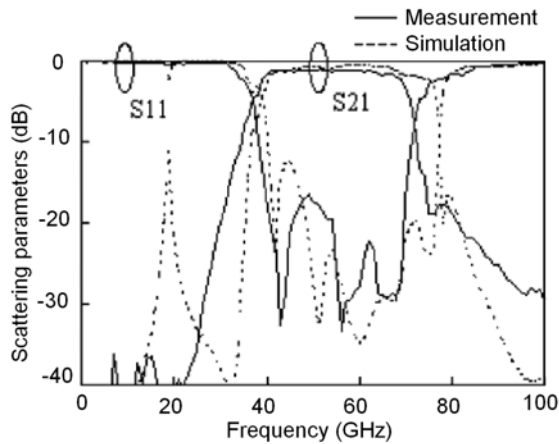
The bandpass lumped element tunable filter in (Entesari et al., 2007) uses commercial switches on an FR4 substrate; the device can reconfigure its center frequency from 25 to 75 MHz. A filter in (Kim et al., 2006) uses direct contact switches for wireless local area network applications to route the microwave signal on two different paths resulting in a two state reconfigurable center frequency filter.

### 3.1.1.3. Filters using periodic structures

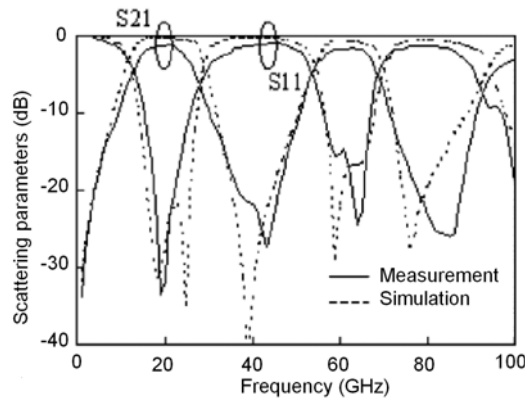
In (Park et al., 2005) a lowpass and a bandpass filter using direct contact switches have been designed and fabricated, the switches can make single and multiple contacts on coplanar transmission lines with periodic structures. Fig. 8 shows the fabricated bandpass filter and its frequency response.



(a)



(b)



(c)

Fig. 8. Tunable bandpass filter using direct contact MEMS switches a) photography of the fabricated filter b) filter response when the switches are in the off state c) filter response when the switches are in the on state, taken from (Park et al., 2005)

### 3.1.2. Filters using capacitive switches

This section contains filters that use capacitive type MEMS switches as tuning elements. The switches can produce two capacitances, one defined for the switch in the off state, and the other one is defined when the switch is in the on state. The two states are controlled by a bias voltage between the switch membrane and actuation electrodes. The capacitive switches can be of a cantilever type or a bridge type. This section contains designs using distributed and lumped elements.

#### 3.1.2.1. Distributed designs

A reconfigurable filter for wireless local area network applications can be found in (Park et al., 2006), the filter uses open loop ring resonators loaded with fixed metal air metal capacitors and capacitive switches. Capacitive bridge type MEMS switches have been used to load coplanar resonators in (Entesari & Rebeiz, 2005 b), were 16 different center frequency states have been achieved.

A switchable interdigital coplanar filter can be found in (Fourn et al., 2003 a), the design has two center frequency states, achieved by using a capacitive MEMS cantilever switch on the ends of coplanar resonators. MEMS cantilever capacitive switches have also been used in (Ong & Okoniewski, 2008), on a pair of microstrip parallel coupled line filters to achieve two center frequency states.

#### 3.1.2.2. Lumped element designs

A bandpass filter with a center frequency tuning range from 110 MHz to 2.8 GHz has been reported in (Brank et al., 2001), the design uses capacitive switches to form variable capacitor banks to reconfigure center frequency, the device also uses metal insulator metal capacitors on the lumped topology. One of the filters in (Kim et al., 2006) uses a capacitive switch bank to reconfigure filter center frequency for wireless local area network

applications. A differential filter that can tune its frequency from 6.5 to 10 GHz can be found in (Entesari & Rebeiz, 2005 a), the design uses metal air metal capacitors, and MEMS capacitive switches to reconfigure its center frequency.

### **3.2. Tunable filters using MEMS varactors**

The use of MEMS varactors can result in low filter insertion losses, and are used to provide a continuous filter parameter reconfiguration. MEMS varactors are suitable for miniature lumped element filters due to the high quality factor presented by the MEMS varactors, compared with conventional components like the metal insulator metal capacitor. MEMS varactors can also be used to load distributed resonators to achieve tunable filters. This section discusses filters made with bridge type and cantilever type MEMS varactors, where several filter topologies are described.

#### **3.2.1. Filters using bridge type varactors**

Filters that use MEMS varactors formed by bridge type actuators, can reconfigure filter parameters in a continuous fashion. The actuators are fixed on both ends, and are actuated using a bias voltage between the bridge and actuation electrodes, which will control the variable capacitance. This section discusses filters made using bridge type MEMS varactors on distributed and lumped topologies as well as a design based on periodic structures.

##### **3.2.1.1. Distributed designs**

In (Abbaspour-Tamijani et al., 2003) bridge type MEMS varactors are used to load coplanar transmission line resonators in order to achieve a reconfigurable center frequency. Fig. 9 shows the fabricated filter and the tunable center frequency response for different bias voltages supplied to bridge type varactors. The filters in (Mercier et al., 2004) use bridge varactors to adjust all filter design parameters at millimeter waves.

##### **3.2.1.2. Lumped element designs**

The filters in (Kim et al., 2002) use MEMS bridge varactors to tune V-band bandpass filters using compact lumped element filter designs. Other lumped element filter using spiral inductors and metal air metal capacitors can be found in (Kim et al., 2005), where bridge MEMS capacitors are used to tune center frequency at K-band.

##### **3.2.1.3. Filters using periodic structures**

A tunable bandstop filter designed using an electromagnetic bandgap periodic structure has been reported in (Karim et al., 2005), where MEMS bridge type varactors have been used in between the bandgap cells to tune the filter response.

### **3.2.2. Filters using cantilever type varactors**

This section contains filters using cantilever type MEMS varactors as tuning elements, these elements have been used to produce a continuous filter parameter reconfiguration by modifying the capacitance between a movable cantilever and a fixed metallic plate beneath it. The capacitance changes according to a bias voltage applied between the cantilever and

an actuation electrode, the bias voltage causes cantilever displacement thus forming the variable capacitance. This section discusses distributed and a lumped element design.

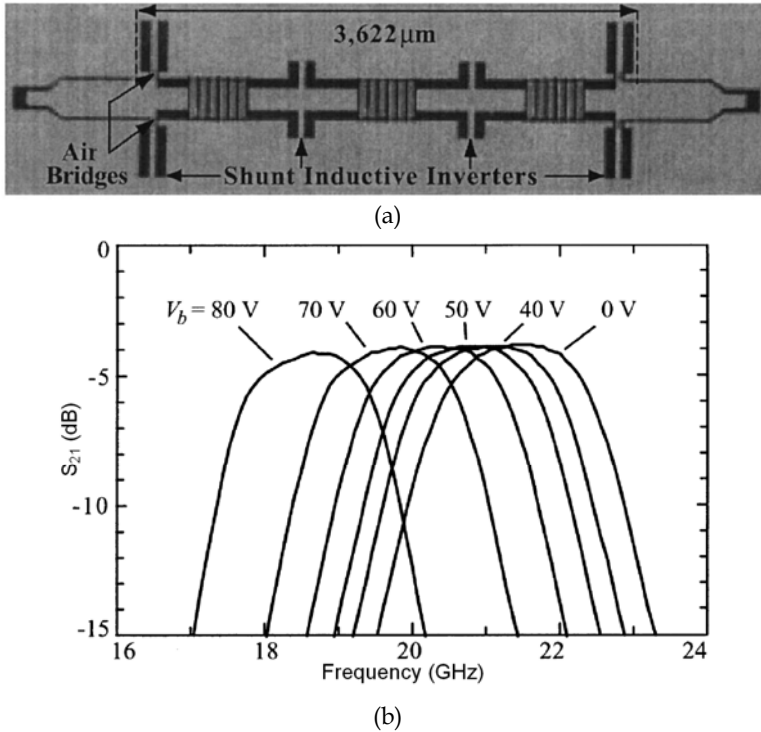


Fig. 9. Tunable bandpass filter using MEMS varactors a) photography of the fabricated filter b) filter response, taken from (Abbaspour-Tamijani et al., 2003)

### 3.2.2.1. Distributed designs

The device in (Fourn et al., 2003 b) uses MEMS cantilever type varactors to achieve center frequency and bandwidth tuning at Ka-band, the filter topology is based on dual behavior resonators, the device has two poles, and the MEMS varactors were placed at the ends of the proposed resonators. One of the filters in (Kim et al., 1999) uses MEMS cantilever varactors to modify the resonant frequency of distributed resonators on a bandpass filter topology at Ka-band. The slot resonator tunable bandstop filter in (Yan & Mansour, 2007 b) uses a thermal actuator as a tuning plate to produce a reconfigurable center frequency at around 6 GHz.

### 3.2.2.2. Lumped element designs

A lumped element tunable filter at Ka-band has been reported in (Kim et al., 1999), the device can reconfigure its center frequency according to bias voltages applied to a MEMS cantilever varactor.

## 4. Tunable filters using ferroelectric materials

Ferroelectric materials can change permittivity values proportionally to an applied DC electric field where some ferroelectrics are suitable for thin film deposition. This section focuses on tunable microwave filters using three of the most common ferroelectrics used to date, the Barium-Strontium-Titanate oxide (BST), the Strontium-Titanate Oxide (STO), and the lead Strontium-Titanate oxide (PST). Other ferroelectric materials considered for microwave tunable devices are the sodium potassium niobium oxide or the bismuth zinc niobate oxide ferroelectric which are not covered in this section. Ferroelectrics have been very attractive due to their compatibility with planar microwave electronics and technologies to produce high speed reconfigurable devices.

### 4.1 BST

A tunable quasi-elliptic bandpass filter using BST capacitors located on open loop ring resonators can be found in (Courreges et al., 2009), the filter topology and its tunable bandpass response is shown in Fig. 10.

The two pole bandpass filter using slow wave coplanar resonators in (Papapolymerou et al., 2006) can tune its center frequency by capacitive loading the resonators with ferroelectric varactor banks; the device can tune its center frequency from 11.5 to 14 GHz. The three pole combline filter in (Nath et al., 2005) uses ferroelectric varactors at one end of the resonators to produce a tunable center frequency from 2.44 to 2.88 GHz with good impedance matching for all states and a 400 MHz bandwidth.

A tunable bandstop filter using slotted ground resonators has been reported in (Chun et al., 2008 a), the device can tune its stopband bandwidth from 1.2 to 1.4 GHz. The lumped element tunable filter in (Sanderson et al., 2007) was designed to tune its center frequency from 31.5 MHz to 88 MHz with a 3 MHz bandwidth; the device uses 8 ferroelectric varactors.

### 4.2. STO

The tunable filter in (Subramanyam et al., 1998) uses a STO thin film to tune its center frequency, the permittivity of the ferroelectric film changes with temperature as well as with an applied bias voltage. The center frequency tuning range is from 18.3 to 19.15 GHz with a 4% fractional bandwidth.

### 4.3. PST

The filter in (Chun et al., 2008 b) uses high resistivity silicon as a substrate with integrated ferroelectric capacitors; this structure has been used to make a tunable resonator and a bandstop filter. The resonator and filter topology are based on a slotted coplanar resonator, and the device can tune its center frequency from 3.65 GHz to 4.23 GHz.

## 5. Tunable filters using ferromagnetic materials

Tunable filters using ferromagnetic materials like Yttrium-Iron-Garnet (YIG) results in high unloaded quality factor resonators with high power handling capabilities and high power consumption. Resonators using YIG spheres have been traditionally used (Carter, 1961),

despite the high unloaded quality factors obtained, the filters require very precise fabrication involving high costs, and also other drawbacks are a low tuning speed and a complex tuning mechanism involving coils near the spheres.

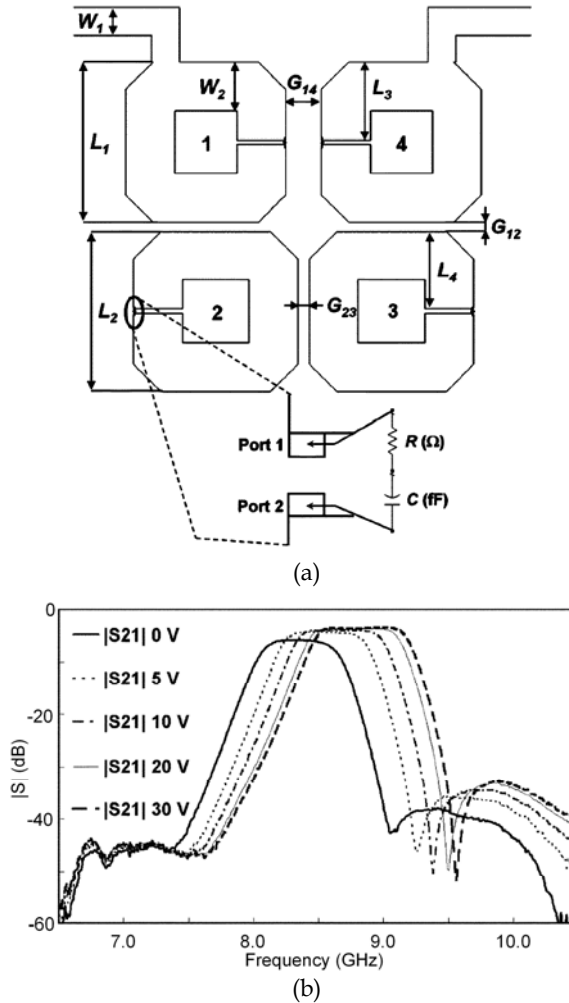


Fig. 10. Tunable bandpass filter using ferroelectric varactors a) topology b) filter response, taken from (Courreges et al., 2009)

This section discusses tunable filters using ferromagnetic materials in planar forms, which present ease of fabrication and integration with planar transmission lines or bias mechanisms. The section is divided in two, the first part deals with tunable filters using YIGs and the second part focuses on designs based on other ferromagnetic tuning structures.



### 5.1. Yttrium-Iron-Garnet films (YIG)

The device in (Murakami et al., 1987) uses a YIG film in a two pole filter topology, the design has a 16 MHz bandwidth and can tune its center frequency from 0.5 to 4 GHz. Fig. 11 contains the structure used for this filter, as well as its frequency response.

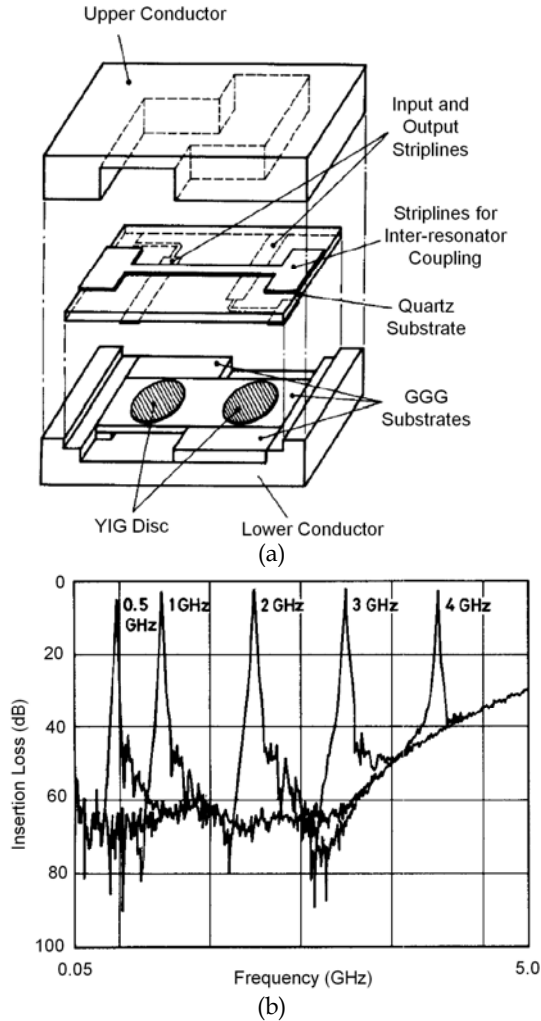


Fig. 11. Tunable bandpass filter using ferromagnetic disks a) filter structure b) filter response, taken from (Murakami et al., 1987)

The filters in (Tsai & Qiu, 2009) use a gallium arsenide substrate and ferromagnetic resonance tuning, bandstop and bandpass topologies are demonstrated, the bandpass filter can tune its center frequency from 5.9 to 17.8 GHz. These devices have wide tuning ranges, good power handling and tuning speed capabilities.

A single cavity resonator using ferromagnetic resonance has been reported in (Srinivasan et al., 2005), the proposed resonator uses ferrite-ferroelectric layers; the cavity design is tuned by magnetoelectric interactions between the layers used to form the resonator. A bandpass filter based on ferromagnetic resonance using piezoelectric-YIG layers has been reported in (Tatarenko et al., 2006), where a device is demonstrated with a tuning range from 6.65 to 6.77 GHz.

## **5.2. Other ferromagnetic tuning based devices**

The tunable bandstop filter in (Tsai et al., 1999) uses an iron film over a gallium arsenide substrate. The filter has a large tuning range from about 10 to 27 GHz, this device has been tuned at higher frequencies than the devices presented in previous section. In (Salahun et al., 2002), a laminated ferromagnetic and insulator composite material has been used to tune a pair of resonators, a stub resonator exhibited a frequency tuning range from 1.17 to 1.71 GHz.

## **6. Tunable filters using combined technologies**

This section discusses devices that combine different technologies to achieve reconfigurable filtering. The section describes filters that combine ferroelectric materials with either MEMS or active devices, and ends with a reconfigurable dielectric resonator filter using MEMS tuning elements.

### **6.1. Tunable filters using ferroelectric varactors and transistors**

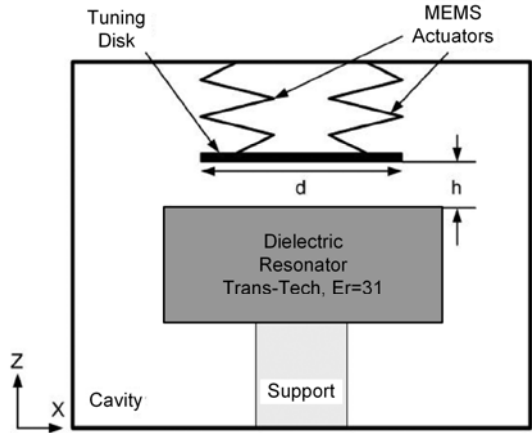
The negative resistance technique using a commercial transistor has been used to compensate ferroelectric and circuit losses in (Kim & Park, 2007). The filter topology is made out of commercial lumped elements and ferroelectric capacitors on a high resistivity silicon substrate. The bandpass device has two poles with a 110 MHz bandwidth and a center frequency tuning range from 1.81 to 2.04 GHz.

### **6.2. Tunable filters using ferroelectric varactors and MEMS switches**

A combination of BST varactors for center frequency tuning and cantilever direct contact MEMS switches for bandwidth tuning is presented in (Lugo et al., 2007); the filters can provide wide and narrow bandwidth configurations on two and three pole topologies. The continuous tunable center frequency goes from 30 to 35 GHz.

### **6.3. Tunable filters using dielectric resonators and MEMS actuators**

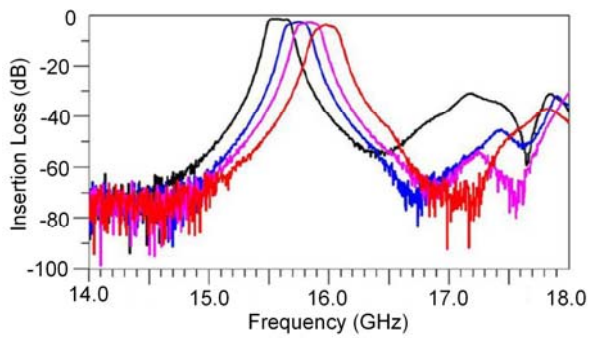
A tunable bandpass filter using high unloaded quality factor dielectric resonators has been reported (Yan & Mansour, 2007 a), the device is tuned using MEMS thermal actuators with large deflections to tune center frequency. Fig. 12 contains a schematic of the tunable structure, a view of a MEMS actuator and filter response.



(a)



(b)



(c)

Fig. 12. Tunable bandpass filter using dielectric resonators and MEMS thermal actuators a) tuning structure schematic b) MEMS thermal actuator isotropic view c) filter response, taken from (Yan & Mansour, 2007 a)

## 7. Mechanically tuned filters

Mechanically adjustable dielectric or metallic tuning screws are commonly used to tune microwave filters. These techniques are frequently used to compensate fabrication tolerances, where the screws can be moved manually while monitoring the measured response. Automated tuning programs can automatically find an optimum filter response by iterating tuning screw positions until a user defined response is found.

The tuning screws can be placed strategically on top or near microwave resonators to tune the resonant frequency of individual resonators. The screws can be placed between resonators to modify inter-resonator coupling coefficients, or screws can be placed between the input/output coupling structure to the filter and the first/last resonator to adjust the input and output coupling to the filter.

Also the type of screw is important depending on the electric and magnetic field distribution near the resonator to be tuned; in general, dielectric tuning screws are mostly used where the electric field maximums around the resonator can be found. Similarly metallic tuning screws are mostly used where magnetic field maximums around the resonator are found.

## 8. Conclusions

This chapter presented diverse methods for tuning microwave filters with the objective of providing an overall view of the field. The filters discussed in this chapter were classified by the technology used to tune filter parameters. Some devices are miniature type lumped element filters and others involve distributed designs with larger size but higher resonator unloaded quality factors in general. The chapter covered filters made using different technologies including active devices, MEMS, ferroelectric and ferromagnetic materials. Filters involving combined technologies were covered; and also the traditional tuning using mechanically adjustable screws was discussed. In this section a general technology summary is provided, pointing out some important features and drawbacks associated with each technology.

Microwave tunable filters can reconfigure filter parameters like center frequency, bandwidth or selectivity in a discrete or continuous fashion, according to the tuning element used to reconfigure the given filter parameter.

One important issue to look at is the operating frequency range of the filters according to the technology used for its fabrication. Diode tuned filters have been used at design frequencies ranging from VHF to X band (0.03 – 12.4 GHz). Filters made using MEMS technology have high potential of operating at much higher frequencies compared to diodes, for instance filter designs can be found with an operating frequency range from VHF to U band (0.03 – 60 GHz). Capacitive MEMS tuning elements have been used for high frequency operation, and direct contact type MEMS actuators are normally used for low frequency operation. Ferroelectric tuned filters have been mainly focused on operating frequency ranges from VHF to K band (0.03 – 26.5 GHz) where some few designs have center frequencies up to U band (60 GHz). Ferromagnetic tuned filters have been used in general for operating frequencies up to K-band.

Diodes have the advantage of being most of times a low cost tuning technology, where also fully monolithic designs can present the possibility of high integration with other

components on a single chip, or a System On Chip (SOP) approach. Also surface mount diodes can be used on microwave substrates, for a System On Package (SOC) approach. Diodes produce inter-modulation noise due to their intrinsic non linear response, and consume higher power compared to their MEMS counterpart.

RF MEMS devices have a small size and good integration capability and superior performance compared to diodes. RF MEMS have good compatibility with fabrication technologies used in semiconductor industries and have good performance in terms of losses and noise. MEMS devices consume very low currents resulting in low power consumption compared to using diodes as tuning elements. Currently the main drawback of MEMS tunable filters is related to reliability issues of the MEMS tuning elements, where the MEMS switches or varactors are frequently associated with life cycles before a MEMS tuning element break down. Also dielectric charging produces unwanted stiction effects degrading the MEMS tuning element reliability. Many efforts have been made to improve MEMS tuning reliability where hermetic packages have resulted in improved life cycles, however more effort to overcome this reliability limitation must be carried out before MEMS tuning elements can make it to successful commercialization.

Tunable filters that use ferroelectric materials as tuning elements have a good integration advantage due to thin film ferroelectric material deposition; suitable for highly integrated microwave devices compatible with planar circuits, with high tuning speeds. Ferroelectric materials have the main disadvantage of having a high loss tangent associated to them, and hence low resonator unloaded quality factors are generally related to resonators with embedded ferroelectric materials. In general a high permittivity tuning range on a ferroelectric material is associated with a high loss. A continuous effort is carried out to obtain a ferroelectric material with low loss tangent and high permittivity tuning range; this still is a challenge today.

Tunable filters that use ferromagnetic materials as tuning element like YIG tuned resonators, have a main advantage of having high unloaded quality factor resonators for the filter design. Other advantage is that the resonant frequency of the YIG crystals does not depend on the length of the resonators, and results in a circuit with compact tunable high unloaded quality factor fixed size resonators, which can be tuned over a large frequency range. The main drawbacks of ferromagnetic tuned filters is a complex bias circuit to tune the device with high power consumption, also a low tuning speed is generally associated with many of these devices.

## 9. References

- Abbaspour-Tamijani, A.; Dussopt, L. & Rebeiz, G., M. (2003). Miniature and tunable filters using MEMS capacitors, *IEEE Transactions on Microwave Theory and Techniques*, Vol. 51, No. 7, Jul. 2003, pp. 1878 - 1885.
- Brank, J.; Yao, J.; Eberly, M.; Malczewski, A.; Varian, K. & Goldsmith, Ch. (2001). RF MEMS-based tunable filters, *International Journal of RF and Microwave Computer-Aided Engineering*, Vol. 11, No. 5, Sep. 2001, pp. 276-284.
- Brito-Brito, Z.; Llamas-Garro, I.; Pradell, L. & Corona-Chavez, A. (2008). Microstrip Switchable Bandstop Filter using PIN Diodes with Precise Frequency and Bandwidth Control, *Proceedings of 38th European Microwave Conference*, pp. 126 - 129, Amsterdam, The Netherlands, 27-31 Oct. 2008.

- Brito-Brito, Z.; Llamas-Garro, I.; Navarro-Muñoz, G.; Perruisseau-Carrier, J. & Pradell, L. (2009)a. UMTS-WiFi Switchable Bandpass Filter, *Proceedings of 39th European Microwave Conference*, pp. 125-128, Rome, Italy, 28 Sep. - 2 Oct. 2009.
- Brito-Brito, Z.; Llamas-Garro, I. & Pradell, L. (2009)b. Precise Frequency and Bandwidth Control of Microstrip Switchable Bandstop Filters, *Microwave and Optical Technology Letters*, Vol. 51, No. 11, November 2009, pp 2573-2578.
- Brown, A., R. & Rebeiz, G., M. (2000). A varactor-tuned RF filter, *IEEE Transactions on Microwave Theory and Techniques*, Vol. 48, No. 7, Part 1, Jul. 2000, pp. 1157 - 1160.
- Carey-Smith, B., E., & Warr, P., A. (2007). Broadband-configurable bandstop-filter design employing a composite tuning mechanism, *IET Microwaves, Antennas & Propagation*, Vol. 1, No. 2, Apr. 2007, pp. 420 - 426.
- Carter, P., S. (1961). Magnetically Tunable Microwave Filters Using Single Crystal Yttrium Iron Garnet Resonators, *IRE Transactions on Microwave Theory and Techniques*, Vol. MTT-9, May. 1961, pp. 252-260.
- Chandler, S., R.; Hunter, I., C. & Gardiner, J., G. (1993)a. Active varactor tunable bandpass filter, *IEEE Microwave and Wireless Components Letters*, Vol. 3, No. 3, Mar. 1993, pp. 70 - 71.
- Chandler, S., R.; Hunter, I., C. & Gardiner, J., G. (1993)b. Active varactor tunable microwave filters, *Proceedings of 23rd European Microwave Conference*, pp. 244 - 245, Oct. 1993.
- Chang, C.-Y. & Itoh, T. (1990). A varactor-tuned, active microwave band-pass filter, *Proceedings of IEEE MTT-S International Microwave Symposium*, pp. 499 - 502, Vol. 1, 8-10 May 1990.
- Chen, Ch.-Ch. & Wang, Sh.-M. (2007). Design of an LTCC switchable filter for dual-band RF front-end applications, *Proceedings of IEEE TENCON Conference*, 3 pp., 30 Oct. - 2 Nov. 2007.
- Chung, M.-S.; Kim, I.-S. & Yun, S.-W. (2005). Varactor-tuned hairpin bandpass filter with an attenuation pole, *Proceedings of Asia-Pacific Microwave Conference*, 4pp., Vol. 4, 4-7 Dec. 2005.
- Chun, Y.-H.; Hong, J.-Sh.; Bao, P.; Jackson T. & Lancaster M., J. (2008)a. BST varactor tuned bandstop filter with slotted ground structure, *Proceedings of IEEE MTT-S International Microwave Symposium*, pp. 1115 - 1118, 15-20 Jun. 2008.
- Chun, Y.-H.; Fragkiadakis, C.; Bao, P.; Luker, A.; Wright, R., V.; Hong, J.-Sh.; Kirby, P., B.; Zhang, Q.; Jackson, T., J. & Lancaster, M., J. (2008)b. Tunable Bandstop Resonator and Filter on Si-Substrate with PST Thin Film by Sol-Gel Deposition, *Proceedings of 38th European Microwave Conference*, pp. 13 - 16, Amsterdam, The Netherlands, 27-31 Oct. 2008.
- Courreges, S.; Li, Y.; Zhao, Z.; Choi, K.; Hunt, A. & Papapolymerou, J. (2009). A Low Loss X-Band Quasi-Elliptic Ferroelectric Tunable Filter, *IEEE Microwave and Wireless Components Letters*, Vol. 19, No. 4, Apr. 2009, pp. 203 - 205.
- Darfeuille, S.; Gomez-Garcia, R.; Lintignat, J.; Sassi, Z.; Barelaud, B.; Billonnet, L.; Jarry, B.; Marie, H. & Gamand, P. (2006). Silicon-Integrated 2-GHz Fully-Differential Tunable Recursive Filter for MMIC Three-Branch Channelized Bandpass Filter Design, *Proceedings of IEEE MTT-S International Microwave Symposium*, pp. 776 - 779, 11-16 Jun. 2006.

- Entesari, K. & Rebeiz, G., M. (2005)a. A differential 4-bit 6.5-10 GHz RF MEMS tunable filter, *IEEE Transactions on Microwave Theory and Techniques*, Vol. 53, No. 3, Part 2, Mar. 2005; pp. 1103 - 1110.
- Entesari, K. & Rebeiz, G., M. (2005)b. A 12-18 GHz Three-Pole RF MEMS Tunable Filter, *IEEE Transactions on Microwave Theory and Techniques*, Vol. 53, No. 8, Aug. 2005, pp. 2566 - 2571.
- Entesari, K.; Obeidat, K.; Brown, A., R. & Rebeiz G., M. (2007). A 25-75 MHz RF MEMS Tunable Filter, *IEEE Transactions on Microwave Theory and Techniques*, Vol. 55, No. 11, Nov. 2007, pp.2399-2405.
- Fan, K.-W.; Weng, Ch.-Ch.; Tsai, Z.-M.; Wang, H. & Jeng, Sh.-K. (2005). K-band MMIC active band-pass filters, *IEEE Microwave and Wireless Components Letters*, Vol. 15, No. 1, Jan. 2005, pp. 19 - 21.
- Fourn, E.; Pothier, A.; Champeaux, C.; Tristant, P.; Catherinot, A.; Blondy, P.; Tanne, G.; Rius, E.; Person, C. & Huret, F. (2003)a. MEMS switchable interdigital coplanar filter, *IEEE Transactions on Microwave Theory and Techniques*, Vol. 51, No. 1, Part 2, Jan. 2003, pp. 320 - 324.
- Fourn, E.; Quendo, C.; Rius, E.; Pothier, A.; Blondy, P.; Champeaux, C.; Orlianges, J.C.; Catherinot, A.; Tanne, G.; Person, C. & Huret, F. (2003)b. Bandwidth and central frequency control on tunable bandpass filter by using MEMS cantilevers, *Proceedings of IEEE MTT-S International Microwave Symposium*, pp. 523 - 526, Vol. 1, 8-13 June 2003.
- Hunter, I., C. & Rhodes, J., D. (1982)a. Electronically Tunable Microwave Bandpass Filters, *IEEE Transactions on Microwave Theory and Techniques*, Vol. 30, No. 9, Sep. 1982, pp. 1354 - 1360.
- Hunter, I., C. & Rhodes, J., D. (1982)b. Electronically Tunable Microwave Bandstop Filters, *IEEE Transactions on Microwave Theory and Techniques*, Vol. 30, No. 9, Sep. 1982, pp. 1361 - 1367.
- Karim, M.,F.; Liu, A.,Q.; Yu, A.,B. & Alphones, A. (2005). MEMS-based tunable bandstop filter using electromagnetic bandgap (EBG) structures, *Proceedings of Asia-Pacific Microwave Conference*, 4 pp., Vol. 3, 4-7 Dec. 2005.
- Karim, M., F.; Liu, A., Q.; Alphones, A. & Yu, A., B. (2006). A Novel Reconfigurable Filter Using Periodic Structures, *Proceedings of IEEE MTT-S International Microwave Symposium*, pp. 943 - 946, Jun. 2006.
- Karim, M., F.; Guo, Y.-X.; Chen, Z., N. & Ong, L., C. (2008). Miniaturized reconfigurable filter using PIN diode for UWB applications, *Proceedings of IEEE MTT-S International Microwave Symposium*, pp. 1031 - 1034, 15-20 Jun. 2008.
- Kim, H.-T.; Park, J.-H.; Kim, Y.-K. & Kwon, Y. (1999). Millimeter-wave micromachined tunable filters, *Proceedings of IEEE MTT-S International Microwave Symposium*, pp. 1235 - 1238, Vol. 3, 13-19 June 1999.
- Kim, H.-T.; Park, J.-H.; Kim, Y.-K. & Kwon Y. (2002). Low-loss and compact V-band MEMS-based analog tunable bandpass filters, *IEEE Microwave and Wireless Components Letters*, Vol. 12, No. 11, Nov. 2002, pp. 432 - 434.
- Kim, J.-M.; Lee, S.; Park, J.-H.; Kim, J.-M.; Baek, Ch.-W.; Kwon, Y. & Kim, Y.-K. (2005). Low loss K-band tunable bandpass filter using micromachined variable capacitors; *Proceedings of 13th International Conference on Solid-State Sensors, Actuators and Microsystems*, pp. 1071 - 1074, Vol. 1, 5-9 Jun. 2005.

- Kim, J.-M.; Lee, S.; Park, J.-H.; Kim, J.-M.; Baek, Ch.-W.; Kwon, Y. & Kim, Y.-K. (2006). Digitally Frequency-Controllable Dual-Band WLAN Filters Using Micromachined Frequency-Tuning Elements, *Proceedings of 19th IEEE International Conference on Micro Electro Mechanical Systems*, pp. 158 - 161, 2006.
- Kim, K.-B. & Park, Ch.-S. (2007). Application of RF Varactor Using  $\text{Ba}_x\text{Sr}_{1-x}\text{TiO}_3/\text{TiO}_2/\text{HR-Si}$  Substrate for Reconfigurable Radio, *IEEE Transactions on Ultrasonics, Ferroelectrics and Frequency Control*, Vol. 54, No. 11, Nov. 2007, pp. 2227 - 2232.
- Koochakzadeh, M. & Abbaspour-Tamijani, A. (2007). Switchable Bandpass Filter for 0.3-0.6 GHz, *Proceedings of IEEE MTT-S International Microwave Symposium*, pp. 557 - 560, 3-8 Jun. 2007.
- Koochakzadeh, M. & Abbaspour-Tamijani, A. (2008). Tunable Filters With Nonuniform Microstrip Coupled Lines, *IEEE Microwave and Wireless Components Letters*, Vol. 18, No. 5, May. 2008, pp. 314 - 316.
- Lacombe, J., L. (1984). Switchable Band-Stop Filter for M.I.C., *Proceedings of 14th European Microwave Conference*, pp. 376 - 381, Oct. 1984.
- Liang, X.-P. & Zhu, Y. (2001). Hybrid resonator microstrip line electrically tunable filter, *Proceedings of IEEE MTT-S International Microwave Symposium*, pp. 1457 - 1460, Vol. 3, 20-25 May. 2001.
- Lin, J. & Itoh, T. (1992). Tunable active bandpass filters using three-terminal MESFET varactors, *Proceedings of IEEE MTT-S International Microwave Symposium*, pp. 921 - 924, Vol. 2, 1-5 Jun. 1992.
- Lugo, C., Jr. & Papapolymerou, J. (2004). Electronic Switchable Bandpass Filter Using PIN Diodes for Wireless Low Cost System-on-a-package Applications, *Proceedings of IEEE Microwave Antennas and Propagation*, Vol. 151, No. 6, Dec. 2004, pp. 497 - 502.
- Lugo, C., Jr.; Hadrick, J. & Papapolymerou, J. (2005). Dual Mode Reconfigurable Filter for 3D System on Package (SOP) Integration, *Proceedings of 55th Electronic Components and Technology Conference*, pp. 532 - 535, 31 May. - 3 Jun. 2005.
- Lugo, C., Jr. & Papapolymerou, J. (2005). Single switch reconfigurable bandpass filter with variable bandwidth using a dual-mode triangular patch resonator, *Proceedings of IEEE MTT-S International Microwave Symposium*, pp. 779 - 782, 12-17 Jun. 2005.
- Lugo, C., Jr. & Papapolymerou, J. (2006)a. Six-state reconfigurable filter structure for antenna based systems, *IEEE Transactions on Antennas and Propagation*, Vol. 54, No. 2, Part 1, Feb. 2006, pp. 479 - 483.
- Lugo, C., Jr. & Papapolymerou, J. (2006)b. Dual-Mode Reconfigurable Filter With Asymmetrical Transmission Zeros and Center Frequency Control, *IEEE Microwave and Wireless Components Letters*, Vol. 16, No. 9, Sep. 2006, pp. 499 - 501.
- Lugo, C., Jr.; Wang, G.; Papapolymerou, J.; Zhao, Z.; Wang, X. & Hunt, A., T. (2007). Frequency and Bandwidth Agile Millimeter-Wave Filter Using Ferroelectric Capacitors and MEMS Cantilevers, *IEEE Transactions on Microwave Theory and Techniques*, Vol. 55, No. 2, Part 2, Feb. 2007, pp. 376 - 382.
- Makimoto, M. & Sagawa, M. (1986). Varactor Tuned Bandpass Filters Using Microstrip-Line Ring Resonators, *Proceedings of IEEE MTT-S International Microwave Symposium*, pp. 411 - 414, Vol. 86, No. 1, Jun. 1986.
- Mercier, D.; Orlianges, J.-C.; Delage, T.; Champeaux, C.; Catherinot, A.; Cros, D. & Blondy, P. (2004). Millimeter-wave tune-all bandpass filters; *IEEE Transactions on Microwave Theory and Techniques*, Vol. 52, No. 4; Apr. 2004, pp. 1175 - 1181.



- Murakami, Y.; Ohgihara, T. & Okamoto, T. (1987). A 0.5-4.0 GHz Tunable Bandpass Filter Using YIG Film Grown by LPE, *IEEE Transactions on Microwave Theory and Techniques*, Vol. 35, No. 12, Dec 1987, pp. 1192 – 1198.
- Musoll-Anguiano, C.; Llamas-Garro, I.; Brito-Brito, Z.; Pradell, L. & Corona-Chavez, A. (2009). Characterizing a Tune All Bandstop Filter, *Proceedings of IEEE MTT-S International Microwave Workshop Series on Signal integrity and High-speed interconnects*, pp. 55 – 58, 19-20 Feb. 2009.
- Nath, J.; Ghosh, D.; Maria, J.-P.; Kingon, A., I.; Fathelbab, W.; Franzon, P., D.; Steer, M., B. (2005). An electronically tunable microstrip bandpass filter using thin-film Barium-Strontium-Titanate (BST) varactors, *IEEE Transactions on Microwave Theory and Techniques*, Vol. 53, No. 9, Sep. 2005, pp. 2707-2712.
- Ocera, A.; Farinelli, P.; Mezzanotte, P.; Sorrentino, R.; Margesin, B. & Giacomozzi, F. (2006). A Novel MEMS-Tunable Hairpin Line Filter on Silicon Substrate, *Proceedings of 36th European Microwave Conference*, pp. 803 – 806, 10-15 Sep. 2006.
- Ong, C., Y. & Okoniewski, M. (2008). Low-loss MEMS switchable microstrip filters, *Microwave and Optical Technology Letters*, Vol. 50, No. 10, Oct. 2008, pp. 2557-2561.
- Papapolymerou, J.; Lugo, C., Jr.; Zhao, Z.; Wang, X. & Hunt, A. (2006). A Miniature Low-Loss Slow-Wave Tunable Ferroelectric BandPass Filter From 11-14 GHz, *Proceedings of IEEE MTT-S International Microwave Symposium*, pp. 556 – 559, 11-16 Jun. 2006.
- Park, J.-H.; Lee, S.; Kim, J.-M.; Kim, H.-T.; Kwon, Y. & Kim, Y.-K. (2005). Reconfigurable millimeter-wave filters using CPW-based periodic structures with novel multiple-contact MEMS switches, *Journal of Microelectromechanical Systems*, Vol. 14, No. 3, Jun. 2005, pp. 456 - 463.
- Park, S.-J.; Lee, K.-Y. & Rebeiz, G., M. (2006). Low-Loss 5.15-5.70GHz RF MEMS Switchable Filter for Wireless LAN Applications, *IEEE Transactions on Microwave Theory and Techniques*, Vol. 54, No. 11; Nov. 2006; pp. 3931 – 3939.
- Rauscher, C. (2003). Reconfigurable bandpass filter with a three-to-one switchable passband width, *IEEE Transactions on Microwave Theory and Techniques*, Vol. 51, No. 2, Part 1, Feb. 2003, pp. 573 – 577.
- Salahun, E.; Tanne, G.; Queffelec, P.; Gelin, P.; Adenot, A.-L. & Acher, O. (2002) Ferromagnetic composite-based and magnetically-tunable microwave devices, *Proceedings of IEEE MTT-S International Microwave Symposium*, pp. 1185 – 1188, Vol. 2, 2-7 Jun. 2002.
- Sanchez-Renedo, M.; Gomez-Garcia, R.; Alonso, J., I. & Briso-Rodriguez, C. (2005). Tunable combline filter with continuous control of center frequency and bandwidth, *IEEE Transactions on Microwave Theory and Techniques*, Vol. 53, No. 1, Jan. 2005; pp. 191 – 199.
- Sanderson, G.; Cardona, A., H.; Watson, T., C.; Chase, D.; Roy, M.; Paricka, J., M. & York, R., A. (2007). Tunable IF Filter using Thin-Film BST Varactors, *Proceedings of IEEE MTT-S International Microwave Symposium*, pp. 679 – 682, 3-8 Jun. 2007.
- Srinivasan, G.; Tatarenko, A., S. & Bichurin, M., I. (2005). Electrically tunable microwave filters based on ferromagnetic resonance in ferrite-ferroelectric bilayers, *Electronics Letters*, Vol. 41, No. 10, 12 May. 2005, pp. 596 – 598.

- Subramanyam, G.; Van, K., F. & Miranda, F., A. (1998). A K-band tunable microstrip bandpass filter using a thin-film conductor/ferroelectric/dielectric multilayer configuration, *IEEE Microwave and Wireless Components Letters*, Vol. 8, No. 2, Feb. 1998, pp. 78 - 80.
- Takahashi, H.; Kosugi, T.; Hirata, A.; Murata, K. & Nagatsuma, T. (2006). Tunable coplanar filter for F-band wireless receivers, *Proceedings of Asia-Pacific Microwave Conference*, pp. 15 - 18, 12-15 Dec. 2006.
- Tatarenko, A., S.; Gheevarghese, V. & Srinivasan, G. (2006). Magnetolectric microwave bandpass filter, *Electronics Letters*, Vol. 42, No. 9, 27 April 2006, pp. 540 - 541.
- Torregrosa-Penalva, G.; Lopez-Risueno, G. & Alonso, J., I. (2002). A simple method to design wide-band electronically tunable combline filters, *IEEE Transactions on Microwave Theory and Techniques*, Vol. 50, No. 1, Part 1, Jan. 2002, pp. 172 - 177.
- Tsai, C., S.; Su, J. & Lee, C., C. (1999). Wideband electronically tunable microwave bandstop filters using iron film gallium arsenide waveguide structure, *IEEE Transactions on Magnetics*, Vol. 35, No. 5, Part 1, Sept. 1999, pp. 3178 - 3180.
- Tsai, C., S. & Qiu, G. (2009). Wideband Microwave Filters Using Ferromagnetic Resonance Tuning in Flip-Chip YIG-GaAs Layer Structures, *IEEE Transactions on Magnetics*, Vol. 45, No. 2, Part 1, Feb. 2009, pp. 656 - 660.
- Wu, H.-H. & Chan, Y.-J. (1997). Tunable high-Q MMIC active filter by negative resistance compensation, *Proceedings of Gallium Arsenide Integrated Circuit (GaAs IC) Symposium*, pp. 252 - 255, 12-15 Oct. 1997.
- Yan, W., D. & Mansour, R., R. (2007)a. Tunable Dielectric Resonator Bandpass Filter With Embedded MEMS Tuning Elements, *IEEE Transactions on Microwave Theory and Techniques*, Vol. 55, No. 1, Jan. 2007, pp. 154 - 160.
- Yan, W., D. & Mansour, R., R. (2007)b. Compact Tunable Bandstop Filter Integrated with Large Deflected Actuators, *Proceedings of IEEE MTT-S International Microwave Symposium*, pp. 1611 - 1614, 3-8 Jun. 2007.
- Zhang, R. & Mansour, R., R. (2007). Novel digital and analogue tunable lowpass filters, *IET Microwaves, Antennas & Propagation*, Vol. 1, No. 3, Jun. 2007, pp. 549 - 555.

# Electronically Tunable Ferroelectric Devices for Microwave Applications

Stanis Courrèges<sup>1</sup>, Zhiyong Zhao<sup>2</sup>, Kwang Choi<sup>2</sup>,  
Andrew Hunt<sup>2</sup> and John Papapolymerou<sup>1</sup>

<sup>1</sup> *School of Electrical and Computer Engineering, Georgia Institute of Technology*

<sup>2</sup> *nGimat Co.*

*USA*

## 1. Introduction

Tunable microwave devices provide added functionality, smaller form factor, lower cost, and lighter weight, and are in great demand for future communications and radar applications. Available tunable technologies include ferrites, semiconductors, microelectromechanical systems (MEMS), and ferroelectric thin films. While each technology has its own pros and cons, ferroelectric thin film based technology has attracted much attention due to its simple processes, low power consumption, high power handling, small size, and fast tuning. This chapter is not intended to provide an exhaustive overview of the ferroelectric technology, but to present several key points in materials optimization, capacitor structure, and device designs that Georgia Institute of Technology and nGimat have focused on in the last few years. Interested readers are suggested to read the large number of books, book chapters, review papers, workshop notes, and patents that are available (for example, Lancaster et al., 1998; Xi et al., 2000; York & Pond, 2000; Tagantsev et al., 2003; Jakoby et al., 2004).

## 2. Ferroelectric Technology

Ferroelectric material is a category of material with reorientable spontaneous polarization, a sub-category of pyroelectric materials. Because of their high dielectric constant and high breakdown voltage, ferroelectric materials have a wide range of applications: infrared (IR) detectors for security systems and navigation, high density capacitors, high-density DRAMs, non-volatile ferroelectric memory, and high frequency devices such as varactors, frequency multipliers, delay lines, filters, oscillators, resonators and tunable phase shifters (Chang et al., 1998; Cole et al., 2000; Fuflyigin et al., 2000; Joshi & Cole, 2000).

Among these applications, frequency agile devices based on ferroelectric thin films attract much research and development. Barium strontium titanate ( $\text{Ba}_{1-x}\text{Sr}_x\text{TiO}_3$  or BST) is the most studied ferroelectric material for tunable applications. A great characteristic of BST is that STO and BTO can form solid solution with virtually any value of  $x$ , as a result its dielectric properties varies in a relatively predictable fashion. While the Curie temperature of STO is

below 0 K, it is about 120° C for BTO. When  $x$  is varied, the Curie temperature of  $\text{Ba}_{1-x}\text{Sr}_x\text{TiO}_3$  changes accordingly. At temperatures above the Curie temperature, the material is said to be at the paraelectric state, and below the Curie temperature, the material is at the ferroelectric state, in which hysteresis exists. Nearly all-tunable BST devices are operated at the paraelectric state of the BST to reduce dielectric loss and eliminate hysteresis.

Bulk BST materials were studied decades ago, and their dielectric properties are well known. However, the high voltages (e.g., 1000's V) required to bias the bulk BST prevent it from many portable and commercial applications, and thin film BST becomes a good alternative. Even though thin film BST does not show the same dielectric properties as a bulk one, its tunability at low DC bias voltages (e.g., 2:1 tuning has been achieved at a bias of 10 V) opens door for many applications.

It is recognized that the technique used to deposit BST films plays a major role in determining the film's material properties, and consequently its dielectric and electrical properties. Several techniques are available to deposit BST films, such as RF sputtering (Chu & Lin, 1997), pulsed laser ablation deposition (PLD) (Bhattacharya et al., 1994), metal-organic deposition (MOD) (Fijii et al., 1992), chemical vapor deposition (CVD) (Yamamuka et al., 1998), metal-organic chemical vapor deposition (MOCVD) (Gao et al., 2000), and sol-gel processing (Zeng et al., 1999). In order to be successful, the process must be economical and the resultant films must exhibit controlled composition, good thickness uniformity, high density, a high degree of structural perfection, and required electrical properties. High quality BST thin films have been deposited by using MOCVD and PLD. However, these processes are expensive, require costly starting materials, and have low throughput and low yield due to composition variations and defects. The recently developed open atmosphere, low cost combustion chemical vapor deposition (CCVD) technology (Hunt et al., 1993) offers an attractive alternative to grow epitaxial BST thin films on sapphire substrates (Schmitt et al., 2006) with good yield and high throughput potential.

Despite the enormous application potential, the progress in ferroelectric technology has been elusive primarily due to the following reasons: (1) the loss was still high compared to its counterparts, attributed to the poor crystalline quality, (2) a process of making high-quality, large-area BST at reasonable cost did not exist, (3) the required DC bias voltage was too high (~100 V) or intermodulation distortion (IMD) performance was poor, and/or (4) the responses of the BST devices are temperature dependent.

In this chapter, we present some of our research and development results including materials development, capacitor structures, and device designs.

- Epitaxial BST thin films on inexpensive sapphire substrates (Zhao et al., 2006),
- Innovative capacitor structure that requires low DC bias voltage and shows improve IMD performance (Yoon et al., 2003),
- Tunable filters operated at microwave (6-20 GHz) and millimeter wave (30-45 GHz) frequencies (Courrèges et al. 2009; Papapolymerou et al., 2006; Lugo et al., 2007),
- Phase shifters operated at L- to C-band and up to Ka-band (nGimat, 2005; Kenney et al., 2006; Zhao et al., 2007).

### 3. Ferroelectric BST Materials and Varactors

#### 3.1 Epitaxial BST on Sapphire Substrate

In the CCVD process (Fig. 1), precursors, which are the metal-bearing chemicals used to coat an object, are dissolved in a solution, which typically is a combustible fuel. This solution is atomized to form microscopic droplets by means of the proprietary Nanomiser® Device. These droplets are then carried by an oxygen stream to the flame where they are combusted. A substrate (the material being coated) is coated by simply drawing it in front of the flame. The heat from the flame provides the energy required to vaporize the droplets and for the precursors to react and deposit (condense) on the substrates.

The key advantages of the CCVD technology include:

- Open-atmosphere processing,
- Use of inexpensive, environmentally friendly, soluble chemical reagents,
- Production of tailored and complex material.

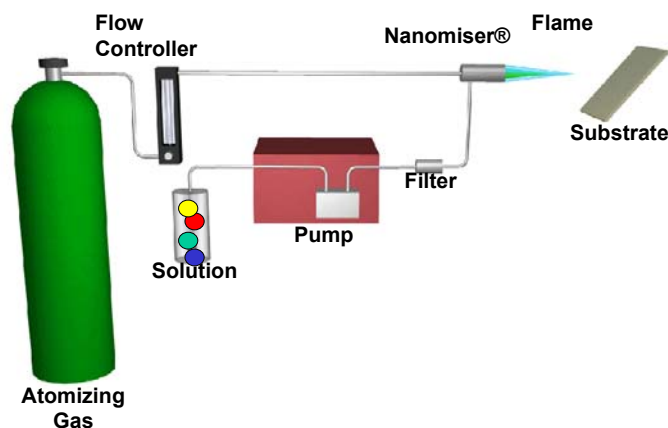


Fig. 1. Schematic representation of the CCVD system.

It is known that epitaxial BST films exhibit greater dielectric constant and tunability as well as lower loss tangent. Historically, complex oxides in the RF/microwave domain, such as BST, have not been applied to commercial products due to the difficulty in producing high-quality thin films. nGimat has developed its proprietary CCVD process for depositing epitaxial BST dielectric coatings on sapphire that provide the building blocks for a host of microwave and RF broadband devices. nGimat's significant advantage is the fact that the CCVD process can deposit BST thin films at lower costs and with better material properties, compared to other manufacturing processes.

Sapphire is chosen as the substrate because of its good insulating properties, low loss tangent, lower cost compared to MgO, LaAlO<sub>3</sub>, and SrTiO<sub>3</sub>, and availability of large size substrates (6" sapphire substrates available). Sapphire has a hexagonal crystal structure with  $a = 4.759 \text{ \AA}$  and  $c = 12.99 \text{ \AA}$ , but Ba<sub>1-x</sub>Sr<sub>x</sub>TiO<sub>3</sub> is cubic when  $x = 1$  (SrTiO<sub>3</sub>), with a lattice parameter of  $3.905 \text{ \AA}$ , and tetragonal when  $x = 0$  (BaTiO<sub>3</sub>), with  $a = 3.994 \text{ \AA}$  and  $c = 4.038 \text{ \AA}$ . We have developed an interface nanolayer between BST and sapphire that enabled an epitaxial BST growth. Fig. 2 shows an SEM micrograph of a cross section of a CCVD BST

thin film as well as a corresponding x-ray diffraction pole figure showing epitaxy between the coating and an r-sapphire substrate.

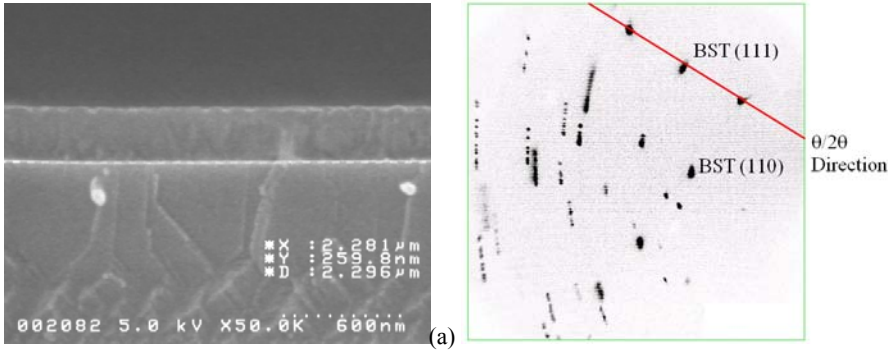


Fig. 2. (a) An SEM microphotograph of the cross section of a BST film. (b) Area detector XRD patterns.

### 3.2 BST Varactors

The core of a BST tunable device is a tunable capacitor, in which BST is the dielectric material. BST capacitors can be fabricated using parallel-plate or planar configurations. Parallel-plate thin film structures require lower tuning DC voltages (e.g., < 10 V), but the fabrications are sophisticated due to the patterning and etching of the bottom electrode and BST. Furthermore, the growth of a highly crystalline and defect-free BST film requires a chemically compatible and durable bottom electrode, which is electrically conductive at microwave frequencies. Pt has been the primary bottom electrode for the parallel-plate BST capacitors, but its poor conductivity leads to high device losses.

In contrast, planar configurations require fewer lithography steps, and single crystal substrates can be used to grow epitaxial BST films. But limited by the photolithographical techniques, the gap width of a planar capacitor is typically in the range of a few microns. This requires larger bias voltage to achieve the desired tunability. Georgia Institute of Technology and nGimat have developed an innovative planar capacitor structure (Yoon et al., 2003) that not only reduces bias voltage for the same tunability but also improves IMD performance.

The improved structure is shown schematically in Fig. 3. Both DC bias and RF signal are applied on the high conductive metal electrodes. The high resistivity electrode (e.g., indium tin oxide) fingers provide a constant DC bias voltage to the BST film, but they are “invisible” to RF signal due to their high impedance. Two-tone IMD tests at 1.9 GHz show that the IMD performance for the novel structure is improved by 6 dBm over the conventional reference structure ( $IIP_3 = 52$  dBm). Another beneficial outcome of this structure is that it allows for lower DC bias required to obtain the same tuning. Fig. 4 shows the tunability curve of the new capacitor structure. Q factor at 1 MHz is not reported due to the fact that it is not a good indicator of the loss tangent at microwave frequencies. Often times, it is misleading to report a higher Q at *megahertz*, while the devices are designed for *gigahertz* applications.

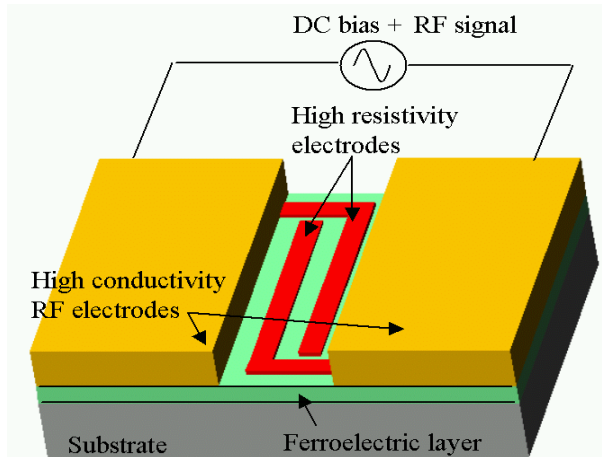


Fig. 3. An innovative planar capacitor structure that requires lower DC bias voltages and exhibits improved IMD performance.

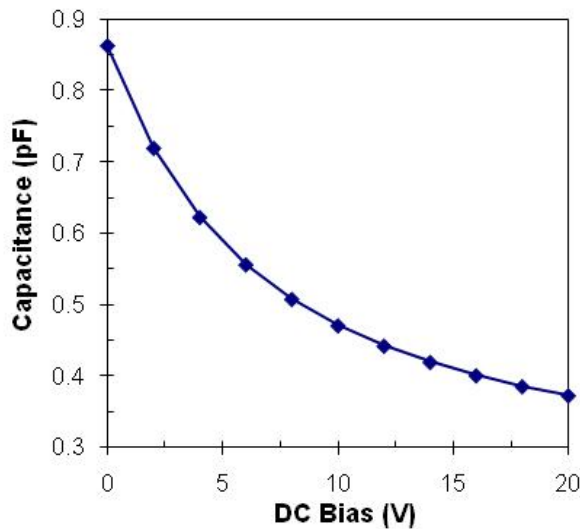


Fig. 4. Capacitance at 1 MHz versus tunability for the new planar capacitor.

## 4. Microwave and Millimetre-Wave Tunable Ferroelectric Filters

### 4.1 Interest of electronically tunable ferroelectric filters

With the pervasive growth of electronic systems in the defense and commercial marketplaces, there is a need for the development of microwave filters with compact size, inexpensive manufacturing process and precise filter response synthesis. Tunable filters are

a good alternative to switchable filter banks by offering smaller size and lower power consumption and requiring a simpler and lower-cost process. Tunable filters for wireless front-end applications have already been demonstrated using RF-MEMS switches (Palego et al, 2008; Park & Rebeiz, 2008), ferroelectric capacitors (Pleskachev & Vendik, 2004; Papapolymerou et al, 2006; Feng et al, 2009), and PIN diodes (Rauscher, 2003). The performance of these reconfigurable circuits mainly relies on these tunable components, and frequency reconfigurable filters are particularly sensitive to loss. Low-loss tunable filters based on PIN diodes are limited to frequencies below 5 GHz since the series resistance of the diodes increases considerably as frequency increases, resulting in high insertion loss. Even though better insertion loss can be achieved at high frequencies for RF-MEMS technology, the filters using these conventional components can only be switched in the microsecond range. The switches also need hermetic packaging. Furthermore, agile filters using PIN diodes or RF-MEMS are usually switchable filters and do not allow an analog frequency tuning. Unlike PIN diodes and RF-MEMS switches, ferroelectrics BST thin films represent an interesting way to design reconfigurable filters since their permittivity can be tuned in an analog way and the switching time is in the nanosecond range.

As explained above, nGimat's epitaxial BST on sapphire technology enables the fabrication of low-loss planar capacitors, simplifying the fabrication process and resulting in lower metal losses. The innovative tunable capacitor structure reduces the DC bias and improves the intermodulation distortion performance. This technology has been employed to design several electronically tunable ferroelectric filters with good performances for X-band and Ka-band applications.

#### 4.2 Method of simulation

Suitable electromagnetic software has to be used to design tunable devices, which includes ferroelectric thin-films. Indeed, for many reasons, these circuits are difficult to be rigorously simulated. First of all, there is an important difference between the thickness of ferroelectric layers (hundreds of nanometers) and the thickness of substrates (hundreds of micrometers), where the ferroelectric is deposited. For example, 2D simulation software, which includes the real topology, the layers of tunable elements and other metallization parts of the circuit, are not adequately efficient because the meshing elements of thin-films provide big approximations in the calculation. 3D electromagnetic softwares solve Maxwell's equations with the finite element method and must absolutely simulate with a high density of meshing, which increases the calculation time and the needed memory significantly. Secondly, the tuning of ferroelectric devices comes from the variation of ferroelectric material permittivity, which is not uniform in the 3D structure. For example, (Courrèges et al, 2007) presented these non-uniform effects in ferroelectric layers for tunable microstrip and coplanar resonators. Fast calculations were computed with 2D/3D analysis software developed at XLIM research institute (France), which takes into account the effects of inhomogeneous layers (ferroelectric thin-film and substrate) using a small computer memory. However, the time needed to draw complex topologies can be long.

The designs developed by Georgia Institute of Technology and nGimat use lumped-element model for BST tunable capacitors, while other metallization layers are simulated using their 3D structures. For our studies, we use commercial electromagnetic simulation software such as Agilent's ADS-Momentum (2½D), SONNET (2½D), or Ansoft's HFSS (3D). Hybrid



simulation approach consists in combining the electromagnetic calculation of the topology with the lumped element model of BST tunable capacitors, included in the filter design. Fig. 5 presents a simulation example of a Ka-band tunable ferroelectric filter with the software ADS. Identical simulations can be run using other softwares, such as those listed above.

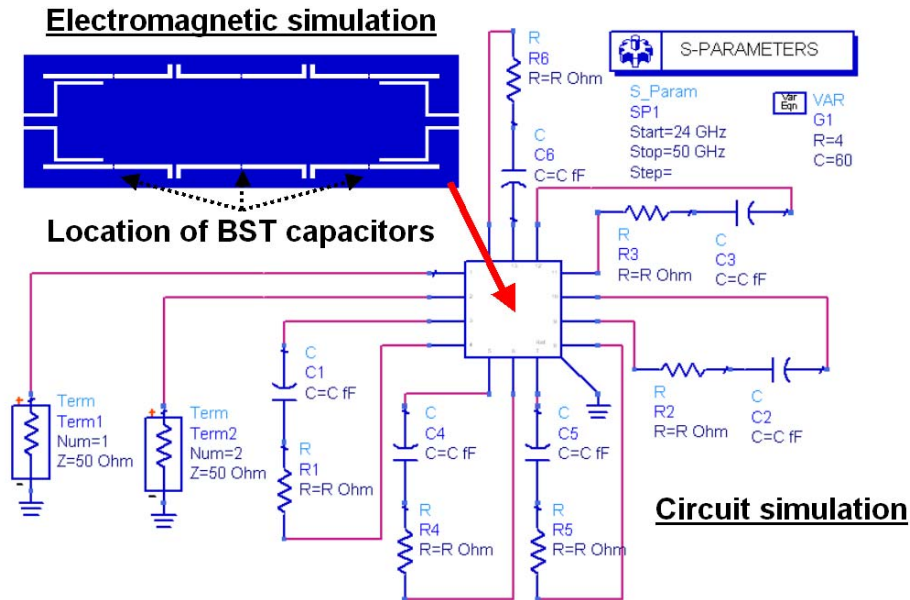


Fig. 5. Simulation of a Ka-band filter combining the electromagnetic calculation with the capacitive-resistive effects of BST capacitors.

Electromagnetic calculation of the filter (real pattern in blue color, in Fig. 5) is coupled with a schematic simulation. Two highly resistive internal ports are placed at the capacitor location. The method takes into account the capacitive-resistive effect of each BST varactor by connecting a lumped-element capacitor  $C$  with a series resistor  $R$  between both internal ports. The capacitor  $C$  ranges from the minimal and maximal capacitance value when the BST capacitors are biased by external DC voltages. The resistor  $R$  represents the overall loss of the ferroelectric capacitors. The values  $C$  and  $R$  are determined after an RF-characterization of the single BST capacitors. When BST tunable capacitor chips are connected to circuits with bonding-wires, the simulation has to take into account an additional series inductive effect. The value of the inductance mostly depends on the length and the diameter of wires at the working frequency.

### 4.3 X-band tunable ferroelectric filters

Compact 4-pole quasi-elliptic planar filters including epitaxial ferroelectric BST capacitors were designed on sapphire for X-band active electronically steered antenna (AESAs) arrays used in radar systems (Fig. 6) (Courrèges et al, 2009). This is the first time that a complex topology has been fabricated with the ferroelectric technology to meet the stringent

specifications: number of resonators, selectivity, flat bandwidth, high unloaded quality factor and compactness.

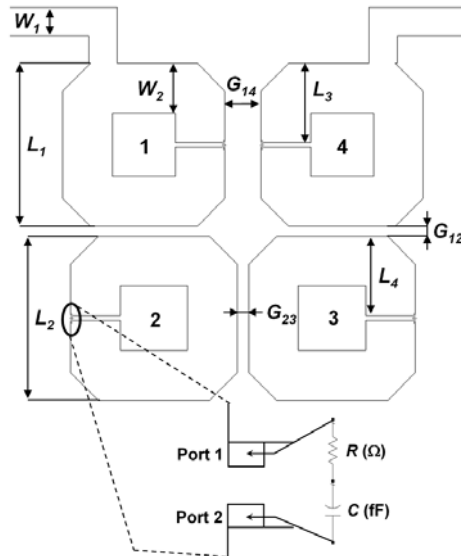


Fig. 6. Design of the 4-pole quasi-elliptic tunable filter including ferroelectric BST capacitors.

The frequency tuning required for the application is below 10%. The other specifications for the first filter are: a fractional 1-dB bandwidth between 5% and 8%, an insertion loss of over 30 dB at  $\pm 10\%$  of the central frequency ( $f_0$ ), a frequency tuning of about 650 MHz, an insertion loss in the bandwidth as low as possible and a maximum footprint of 10 mm x 10 mm.

The fabricated filter is composed of 4 cross-coupled open-loop resonators to meet the specifications. The four half-wavelength resonators are loaded by the BST tunable capacitors between both ends (1 BST capacitor for each resonator), which allow tuning of the center frequency by applying DC voltages. Since the electric field is maximum at the end of the resonator (capacitive part), a maximum frequency shift can be provided by loading with an external capacitor, which also reduces the initial length of the resonators  $\lambda_g/2$ , where  $\lambda_g$  is the guided wavelength with the fundamental resonant frequency ( $f_0$ ). The width of the resonators is increased to get smaller resonator impedances of 37  $\Omega$  and consequently a higher unloaded quality factor  $Q_0$ . The 50- $\Omega$  input and output feedlines are physically connected to resonators 1 and 4, respectively, to get the proper input-output impedances. The filter is made on a sapphire substrate with a thickness of 430  $\mu\text{m}$ . Its relative permittivity is  $\epsilon_r \text{ Sapphire} = 10$  and its loss tangent is below  $10^{-4}$ . The copper metallization of the resonators and the ground plane is 2- $\mu\text{m}$  thick with a conductivity of  $5.10^7 \text{ S/m}$ .

As described in section 4.2, a hybrid simulation approach coupled to the electromagnetic segmentation method (Bariant et al, 2002) is employed to optimize the S-parameter responses of the filter. We choose the normalized coupling matrix  $M_I$  for the required filter

specifications (Eq. 1).

$$[M_1] = \begin{bmatrix} 0 & 1.012 & 0 & -0.12 \\ 1.012 & 0 & 0.812 & 0 \\ 0 & 0.812 & 0 & 1.012 \\ -0.12 & 0 & 1.012 & 0 \end{bmatrix} \quad (1)$$

$$R_{in} = R_{out} = 1.143$$

The input/output impedances ( $R_{in}$  and  $R_{out}$ ) and the mutual inter-resonator coupling  $M_{ij}$  are used to find the external quality factor  $Q_{ext}$ , and the inter-resonator coupling  $k_{ij}$ . Then, the simulated S-parameters of the filter are optimized by adjusting  $Q_{ext}$ , and  $k_{ij}$  versus the filter dimensions: lengths of the resonators, positions of the feedlines and the gaps between the resonators. A final optimization of dimensions allows getting the right frequency responses (Table 1). The final size is very compact at this frequency: 5.7 mm x 5.5 mm. A photograph of the fabricated filter is shown in Fig. 7.

Parameter	( $\mu\text{m}$ )	Parameter	( $\mu\text{m}$ )	Parameter	( $\mu\text{m}$ )
$W_1$	407	$L_2$	1140	$G_{14}$	520
$W_2$	715	$L_3$	2360	$G_{12}$	145
$L_1$	2341	$L_4$	1144	$G_{23}$	168

Table 1. Optimized dimensions for the first filter design.

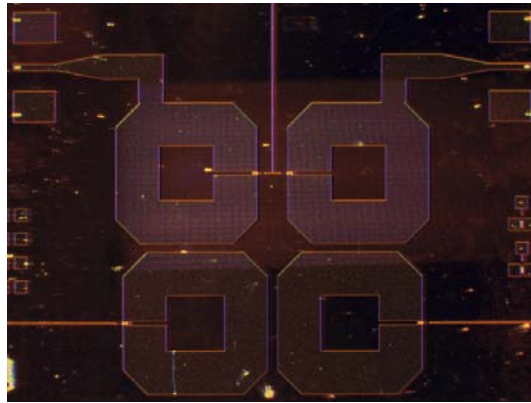


Fig. 7. Photograph of the first fabricated filter.

The DC bias is applied through bias tees. High-resistive thin strips are connected between the resonators in order to bias the resonators 2 and 3. The bias lines for the ground are connected to a copper square ring around the filter to use only one DC probe for the common ground. Coplanar pads are added to create vialess CPW transitions (Zheng et al, 2003) at the end of the feedlines to enable measurement using G-S-G probes. The measurements are performed with an Agilent Vector Network Analyzer 8510C calibrated

using the Short-Open-Load-Through (SOLT) standards and a pair of 800- $\mu\text{m}$  pitch probes (GGB Picoprobe). The S-parameters are measured with bias voltages ranging from 0 V to 30 V (Figs. 8 and 9).

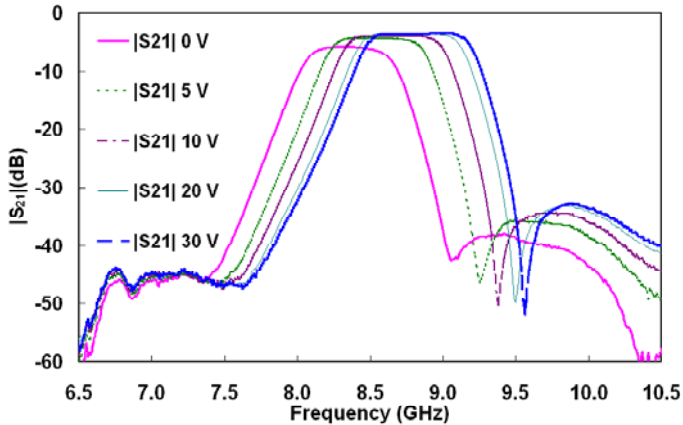


Fig. 8. Measured  $|S_{21}|$  of the 4-pole quasi-elliptic tunable filter.

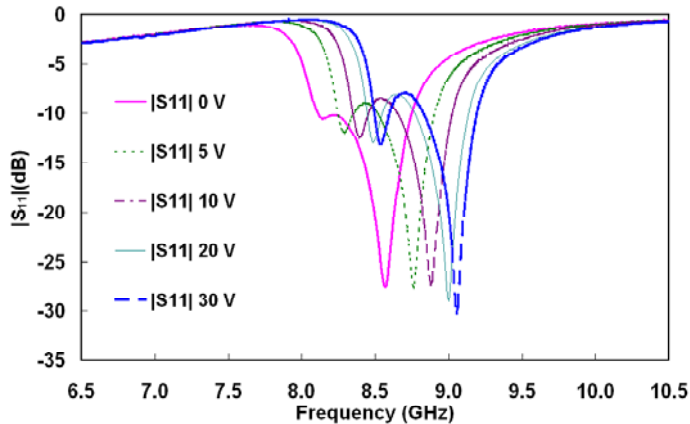


Fig. 9. Measured  $|S_{11}|$  of the 4-pole quasi-elliptic tunable filter.

The center frequency at 0 V is 8.35 GHz and the filter reaches a maximum frequency tuning of 500 MHz (6%) with a bias voltage of 30 V. The fractional 1-dB bandwidth ranges from 5.5% to 7.3%. The filter has an insertion loss and a return loss in the bandwidth of 5.7-3.5 dB, and 10.2-7.9 dB, respectively, between a DC bias of 0 V and 30 V. The insertion loss outside the passband is 30 dB as desired. By taking into account the values of the bandwidth, the frequency and the return loss, the unloaded quality factor is between 80 (0 V) and 115 (30 V). The measured results present very good loss performances for typical X-band tunable ferroelectric filters at room temperature.

This filter, with other values of bandwidth and center frequency, was improved with a second similar design (Fig. 10).



Fig. 10. Photograph of the second fabricated filter.

The biasing of the capacitors is realized with bias tees by applying DC bias on RF signal (positive DC bias) and RF ground (DC ground). To bias resonators 2 and 3, which do not have direct connection with the feedlines, the design uses high-resistive thin strips connected between the resonators 1 and 2, 2 and 3, and 3 and 4. The filter has a size of 4.9 mm x 4.9 mm. The experimental results are presented in Figs 11. and 12.

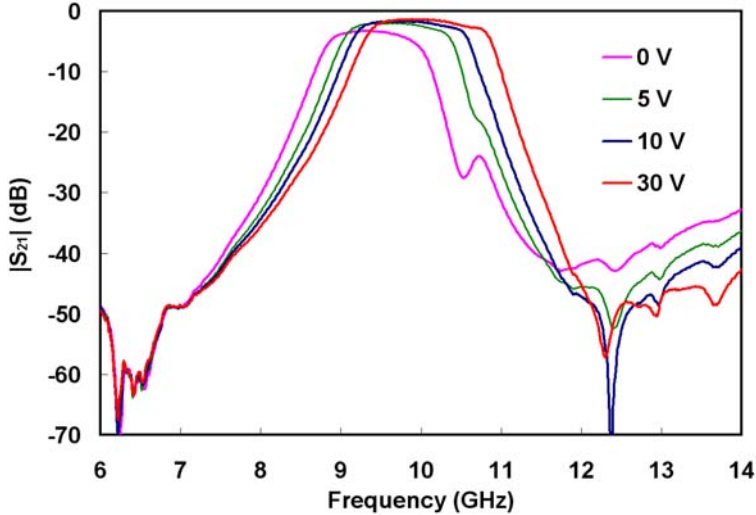


Fig. 11. Measured  $|S_{21}|$  of the second 4-pole tunable filter.

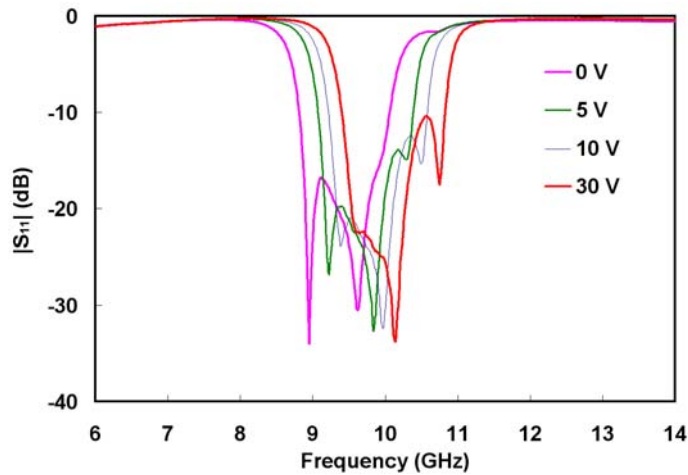


Fig. 12. Measured  $|S_{11}|$  of the second 4-pole tunable filter.

The center frequency of the second filter is 9.37 GHz without bias voltage. The frequency tuning at 30 V is 690 MHz (7.4%) that is better than the previous result. The fractional 1-dB bandwidth ranges from 11.4% up to 13.8%. The insertion loss and return loss in the passband are excellent, and better than those presented for the first design: 3.3-1.4 dB and 17-11 dB, respectively, between a DC bias of 0 and 30 V. This filter presents a low level of insertion loss and a good selectivity with the ferroelectric technology. The unloaded quality factor of the filter with a DC bias of 30 V is better than 130, an improvement with this second design.

For the same resonator topology, when we also added more BST tunable capacitors, which could be biased independently, allowing controlling the following three parameters independently and continuously: center frequency, bandwidth and return loss in the passband. Experimental results are presented in Figs. 13 and 14.

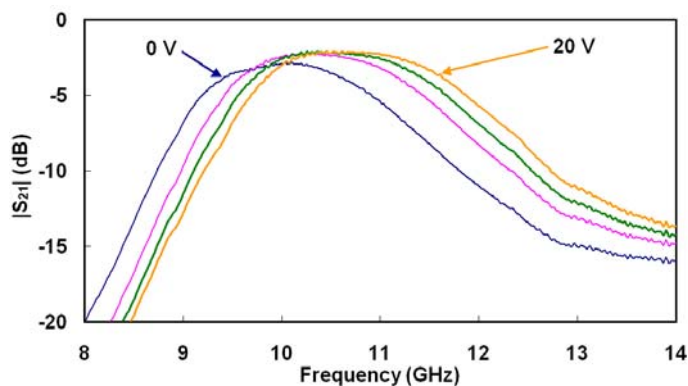


Fig. 13. Measured  $|S_{21}|$  of a 2-pole ferroelectric filter with constant fractional bandwidth.

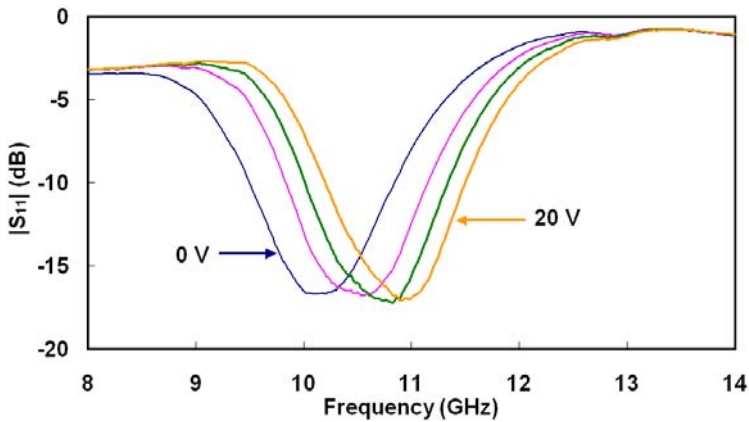


Fig. 14. Measured  $|S_{11}|$  of a 2-pole ferroelectric filter with constant fractional bandwidth.

The center frequency without bias voltage is 10 GHz and the frequency tuning is 740 MHz with a DC bias (controlling the resonant frequency) of 20 V (7.4%). The fractional equal-ripple bandwidth and the return loss are almost constant for all states of frequency: 8.1% ( $\pm 0.04\%$ ) and 16.7 dB ( $\pm 0.3\%$ ), respectively. Also, the insertion loss in the passband is great, between 2.75 dB and 2.2 dB.

These results open an interesting perspective for the design of complex tunable filtering functions. The third order intercept point (IP3) of these filters was measured by using a two-tone method. The output IP3 values are better than 20 dBm. The results are summarized in Table 2.

	Type	Band	Bandwidth	Insertion Loss: dB	$Q_0$	Tuning	Bias	Size (mm)
1 <sup>st</sup> design	4 poles microstrip Quasi-elliptic	X	5.5-7.3%	5.7-3.5	80-115	6%	30 V	5.7x5.5 Sapphire
2 <sup>nd</sup> design	4 poles microstrip Quasi-elliptic	X	11.4-13.8%	3.3-1.4	<130	7.4%	30 V	4.9x4.9 Sapphire
/	2 poles microstrip	X	8.5%	2.7-2.0	<100	Frequency Bandwidth Return loss 8.3% (max)	30 V	7x3 Sapphire

Table 2. Comparison between the designed X-band tunable ferroelectric filters.

#### 4.4 Ka-band tunable ferroelectric filters

Ferroelectric Ka-band tunable filters, working at room temperature, have been designed for commercial and defense applications. We present one coplanar design developed at 29 GHz (Courrèges et al, 2009). The filter is a 3-pole tunable bandpass filter working in the Ka-band (26-40 GHz), a fractional bandwidth of 10-12 %, a return loss of 20 dB, a frequency tuning greater than 15% and a minimum OIP3 value of 15 dBm. Fig. 15 presents the coplanar filter loaded with 6 BST capacitors (3 on each side).

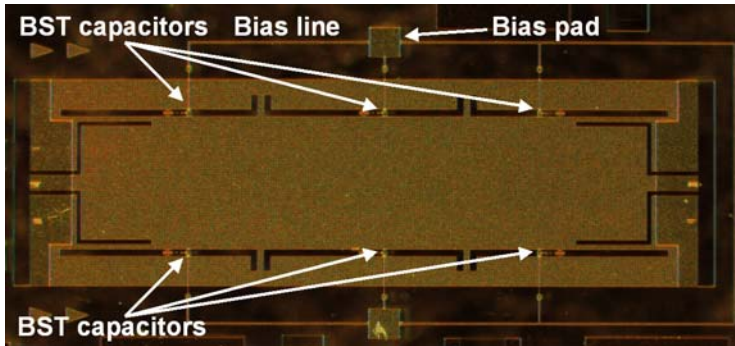


Fig. 15. Photograph of the fabricated Ka-band coplanar ferroelectric filter.

The filter is designed with 3 half-wavelength resonators and inductive impedance inverters. Since the electric field is maximal at the center of each resonator, the maximum frequency shift is achieved by loading the tunable capacitors at this position. The filter is fed by original feedlines (Paillot et al, 2002): the first part is a 50- $\Omega$  line connected to a wider short-circuited line. The filter does not need bridges with this feeding structure and the external quality factor can be easily optimized. It is also possible to get a wider resonator by keeping the same slot gap, which can increase the unloaded quality factor of the filter. The simulation procedure, the materials and the fabrication process are the same as those indicated in the section 4.3 with the X-band tunable filters. The final filter size is 4560 x 1400  $\mu\text{m}$ . The experimental S-parameters are presented in Figs. 16 and 17.

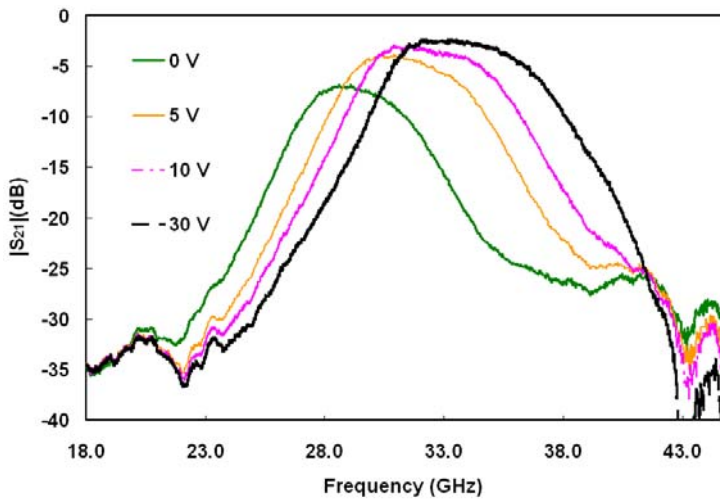


Fig. 6. Measured  $|S_{21}|$  of the Ka-band ferroelectric filter.



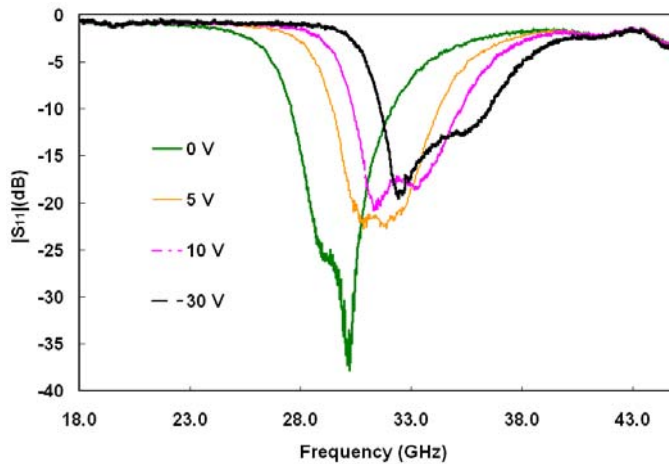


Fig. 17. Measured  $|S_{11}|$  of the Ka-band ferroelectric filter.

The S-parameters are measured with bias voltages ranging from 0 V up to 30 V. The frequency tunes from 29 GHz, at 0 V, up to 34 GHz with a bias voltage of 30 V. The frequency tuning is 17.2%. The fractional bandwidth ranges from 9.5% to 12.3%. For this technology in Ka-band, the planar filter has good insertion loss and return loss levels of 6.9-2.5 dB, and 24-13 dB, respectively, between a DC bias of 0 and 30 V at room temperature.

## 5. Ferroelectric phase shifters

Phase shifters are an essential component in electronically scanned phased-array antennas for communications and radar applications, and typically represent a significant amount of the cost, size and weight of producing military tactical antenna array. Jamming and interferers of mobile communication devices can be eliminated via phase shifters while still receiving the desired signal even with the interferer being at the same frequency. Phase shifting technology of choice includes ferrite, MMIC, MEMS, ferroelectrics, and others. Ferrite phase shifter has been very successfully employed in military systems despite its high cost, weight, large size and complex current switching circuitry. GaAs MMIC phase shifters have demonstrated good phase and amplitude error control. However, they involve a relatively large loss and have low power handling capability. MEMS use advanced IC processing techniques, which offer potential integration with GaAs MMIC or CMOS technologies. They provide low insertion loss, high isolation, negligible power consumption, and low IMD. Nevertheless, they require high driving voltage (e.g., 40 V or higher), have low switching speed ( $> 10 \mu\text{s}$ ), and suffer from reliability and packaging issues.

Several design options for BST phase shifters have been proposed (Kozyrev et al., 1998; Kim et al., 2002; Sherman et al., 2001; Kim et al., 2003; De Flaviis et al., 1997; Van Keuls et al., 1999). Reflection-type phase shifters consist of a 3-dB coupler and reflective loads (Kozyrev et al., 1998; Kim et al., 2002; Sherman et al., 2001). While wide bandwidths may be achieved with the reflection type topology, the coupler contributes directly to the insertion loss of the phase shifter, and requires a large portion of the die area. Loaded-line phase shifters are controlled by varying the capacitive loading on a coplanar waveguide transmission line (Lin

et al., 2000). The phase shifters using this topology show large size, and large numbers of capacitors are required for large phase shift, contributing substantial dielectric losses. nGimat and Georgia Tech have designed an S-band phase shifter using an all-pass network topology (Kim et al., 2003), which exhibited small size and low loss.

Fig. 18 shows the equivalent circuit of an all-pass phase shifter using tunable BST capacitors. While the circuit is all lumped elements, the  $L$ - $C$  sections may be considered equivalent to a transmission line of characteristic impedance  $Z_o = \sqrt{L_o / C_o}$ . Multiple phase shifters can be cascaded to achieve higher phase shift. We have achieved best-in-class performance for L-, S-, and C-band phase shifters with the Figure of Merit, defined as phase shift divided by insertion loss, being measured at 75°/dB (Kenney et al., 2006). Using the same topology, we have developed phase shifters up to 40 GHz.

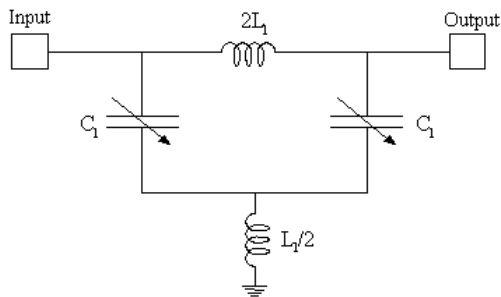


Fig. 18. Schematic of a low-voltage all pass network phase shifter.

Figs. 19 and 20 show, respectively, the measured S-parameters and phase shift of a Ka-band phase shifter. The insertion loss at 0 V is 7 dB, going down to 6 dB quickly at 5 V and even lower at most of the operational range. The return loss is better than 10 dB at all bias states. The phase shift is 370° at 30 V.

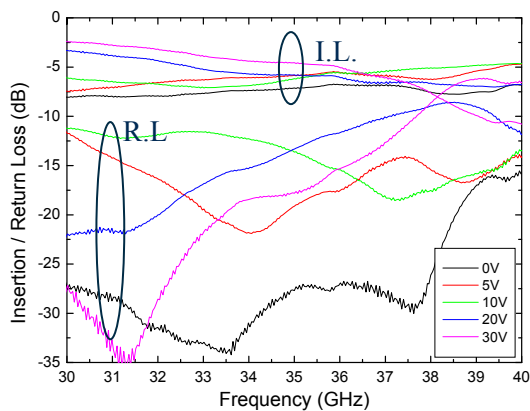


Fig. 19. Measured S-parameters of a 35-GHz phase shifter.

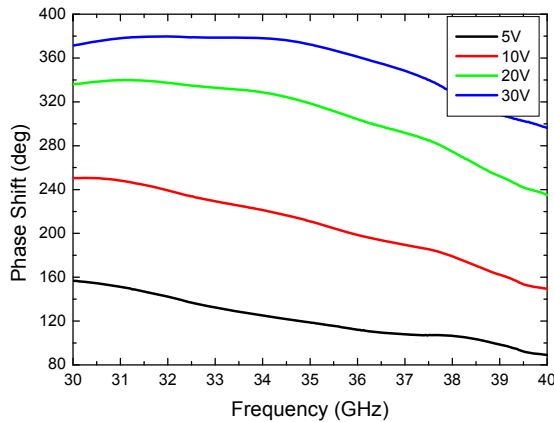


Fig. 20. Measured phase shift of a 35-GHz phase shifter.

Our phase shifters have the following features:

- Small size  $< 1 \times 1$  mm,
- Solder ball terminations for flip-chip mounting,
- Coplanar waveguide input and output to facilitate transitions to the antenna circuitry,
- Lumped-element designs for lower loss,
- Continuously tunable with a single DC bias voltage of 0-30 V,
- Fully passivated to prevent failures due to contaminations,
- No static state power consumption.

## 6. Conclusions

This chapter presents the latest research and development results by Georgia Institute of Technology and nGimat, including materials development, innovative capacitor structure, and device designs. Using proprietary process and interface layers, we are able to grow epitaxial BST films on inexpensive sapphire substrates. A new capacitor structure utilizing highly resistive film improves IMD performance and enables low DC bias voltages. We have used a hybrid design scheme to simulate the circuit, which saves simulation time and memory used. A few design examples are presented including tunable filters and phase shifters covering frequency range up to Ka-band. The devices are easy to fabricate, and exhibit low loss, small size, and low-power consumption.

## 7. References

Bariant, D.; Bila, S., Baillargeat, D., Verdeyme, S. & Guillon, P. (2002). Fast and accurate C.A.D. of narrow band waveguide filters applying an electromagnetic segmentation method, *IEEE Int. Micro. Symp. Dig.*, Vol. 2, (2002) pp. 979-982.

- Bhattacharya, P.; Park, K.H. & Mishioka, Y. (1994). Control of grain structure of laser-deposited  $(\text{Ba,Sr})\text{TiO}_3$  films to reduce leakage current. *Jpn. J. Appl. Phys. Part I*, Vol. 33, No. 9B, (September 1994) pp. 5231-5234.
- Chang, H.; Gao, C., Takeuchi, I., Yoo, Y., Wang, J., Schultz, P.G. & Xiang, X.D. (1998). Combinatorial synthesis and high throughput evaluation of ferroelectric/dielectric thin-film libraries for microwave applications. *Appl. Phys. Lett.*, Vol. 72, No. 17, (1998) pp. 2185-2187.
- Chu, C.M. & Lin, P. (1997). Electrical properties and crystal structure of  $(\text{Ba,Sr})\text{TiO}_3$  films prepared at low temperatures on a  $\text{LaNiO}_3$  electrode by radio-frequency magnetron sputtering. *Appl. Phys. Lett.*, Vol. 70, No. 2, (1997) pp. 249-251.
- Cole, M.W.; Joshi, P.C., Ervin, M.H., Wood, M.C., & Pfeffer, R.L. (2000). The influence of Mg doping on the materials properties of  $\text{Ba}_{1-x}\text{Sr}_x\text{TiO}_3$  thin films for tunable device applications. *Thin Solid Films*, Vol. 374, (2000) pp. 34-41.
- Courrèges, S.; Giraud, S., Cros, D., Madrangeas, V. & Aubourg, M. (2007). 2D and 3D analysis of ferroelectric thin-film planar microwave devices using method of line, *Ferroelectrics*, Vol. 353, (August 2007) pp 124-131.
- Courrèges, S.; Li, Y., Zhao, Z., Choi, K., Hunt, A. & Papapolymerou, J. (2009). A low-loss X-band ferroelectric tunable filter. *IEEE Microwave and Wireless Components Lett.*, Vol. 19, No. 4, (April 2009) pp 203-205.
- Courrèges, S., Li, Y., Zhao, Z., Choi, K., Hunt, A., Horst, S., Cressler, J. D. & Papapolymerou, J. (2009). A Ka-band electronically tunable ferroelectric filter. *IEEE Microwave and Wireless Components Lett.*, Vol. 19, No. 6, (June 2009) pp. 356-358.
- De Flaviis, F.; Alexopoulos, N.G. & Stafsudd, O.M. (1997). Planar microwave integrated phase-shifter design with high purity ferroelectric material. *IEEE Trans. Microwave Theory Tech.*, Vol. 45, No. 6, (June 1997) pp. 963-969.
- Feng, Z.; Fathelbab, W. M., Lam, P. G., Haridasan, V., Maria, J.-P., Kingon, A. I. & Steer, M. B. (2009). Narrowband Barium Strontium Titanate (BST) tunable bandpass filters at X-band. *IEEE Int. Micro. Symp. Dig.*, (June 2009) pp. 1061-1064.
- Fijii, E.; Uemoto, Y., Hayashi, S., Nasu, T., Shimada, Y., Matsuda, A., Kibe, M., Azuma, M., Otsuki, T., Kano, G., Scott, M., McMillan, L.C. & Paz de Araujo, C.A. (1992). ULSI DRAM technology with  $\text{Ba}_{0.7}\text{Sr}_{0.3}\text{TiO}_3$  film of 1.3nm equivalent  $\text{SiO}_2$  thickness and  $10^{-9}$  A/cm<sup>2</sup> leakage current. *IEDM Technical Digest*, (1992) pp. 267-270.
- Fuflyigin, V.; Wang, F., Jiang, H., Zhao J. & Norris, P. (2000). Electro-optic effect in  $\text{Ba}_{1-x}\text{Pb}_x\text{TiO}_3$  films. *Appl. Phys. Lett.*, Vol. 76, No. 13, (2000) pp. 1641-1643.
- Gao, Y.; He, S., Alluri, P., Engelhard, M., Lea, A.S., FINDER, J., Melnick, B. & Hance, R.L. (2000). Effects of precursors and substrate materials on microstructure, dielectric properties, and step coverage of  $(\text{Ba,Sr})\text{TiO}_3$  thin films grown by metalorganic chemical vapor deposition. *J. Appl. Phys.*, Vol. 87, No. 1, (2000) pp. 124-130.
- Hunt, A.T.; Carter, W.B. & Cochran, Jr., J.K. (1993). Combustion chemical vapor deposition: a novel thin-film deposition technique. *Appl. Phys. Lett.*, Vol. 63, No. 2, (July 1993) pp. 266-268.
- Jakoby, R.; Scheele, P., Muller, S. & Weil, C. (2004). Nonlinear dielectrics for tunable microwave components, *Proceedings of 15<sup>th</sup> International Conference on Microwaves, Radar and Wireless Communications (MIKON-2004)*, pp. 369- 378, Warsaw, Poland, May 17-19, 2004.

- Joshi P.C. & Cole, M.W. (2000). Mg-doped  $\text{Ba}_{0.6}\text{Sr}_{0.4}\text{TiO}_3$  thin films for tunable microwave applications. *Appl. Phys. Lett.*, Vol. 77, No. 2, (2000) pp. 289-291.
- Kenney, J. S.; Yoon, Y. K., Ahn, M., Allen, M. G., Zhao, Z., Wang, X., Hunt, A. & Kim, D. (2006). Low-voltage ferroelectric phase shifters from L- To C-band and their applications, *Proceedings of the 2006 IEEE Aerospace Conference*, 9 ps, Big Sky, MT, March 4-11, 2006, IEEE, Piscataway, NJ.
- Kim, D.S.; Choi, Y.S., Allen, M.G., Kenney, J. S. & Kiesling, D. (2002). A Wide bandwidth monolithic BST reflection-type phase shifter using a coplanar waveguide Lange coupler. *IEEE Trans. Microw. Theory Tech.*, Vol. 50, No. 12, (December 2002) pp. 2903-9.
- Kim, D.S.; Choi, Y. S., Ahn, M., Allen, M.G., Kenney, J.S. & Marry, P. (2003). 2.4 GHz continuously variable ferroelectric phase shifters using all-pass networks. *IEEE Microw. Wireless Comp. Lett.*, Vol. 13, No. 10, (October 2003) pp. 434-36.
- Kozyrev, A.; Ivanov, A., Keis, V., Khazov, M., Osadchy, V., Samoilova, T., Soldatenkov, O., Pavlov, A., Koepf, G., Mueller, C., Galt, D. & Rivkin, T., Ferroelectric films: Nonlinear properties and applications in microwave devices. *IEEE MTT-S 1998 Int. Mi-crowave Symp. Dig.*, (June 1998) pp. 985-988.
- Lancaster, M.J.; Powell, J., & Porch, A. (1998). Thin-film ferroelectric microwave devices. *Supercond. Sci. Technol.*, Vol. 11, (1998) pp. 1323-1334.
- Lugo, C.; Wang, G., Papapolymerou, J., Zhao, Z., Wang, X. & Hunt, A. T. (2007). Frequency and bandwidth agile-mm-wave filter using ferroelectric capacitors and MEMS cantilevers. *IEEE Trans. Microw. Theory Tech.*, Vol. 55, No. 2, (2007) pp. 376-382.
- Paillet, T.; Blondy, P., Cros, D. & Guillon, P.-Y. (2002). A novel compact coplanar filter. *IEEE MTT-S Int. Micro. Symp. Dig.*, Vol. 3, (June 2002) pp. 1793-1796.
- Palego, C.; Pothier, A., Crunteanu, A., Chatras, M., Blondy, P., Champeaux, C., Tristant, P. & Catherinot, A. (2008). A two-pole lumped-element programmable filter with MEMS pseudodigital capacitor banks. *IEEE Trans. on Micro. Theory Tech.*, Vol. 56, No. 3 (March 2008) pp. 729-735.
- Papapolymerou, J.; Lugo, C., Zhao, Z., Wang, X. & Hunt, A. (2006). A miniature low-loss slow-wave tunable ferroelectric bandpass filter from 11-14 GHz, *Proceedings of the IEEE MTT-S International Microwave Symposium*, pp. 556-559, San Francisco, CA, June 11-16, 2006, IEEE, Piscataway, NJ.
- Park, S.-J. & Rebeiz, G.M. (2008). Low-loss two-pole tunable filters with three different predefined bandwidth characteristics, *IEEE Trans. on Micro. Theory Tech.*, Vol. 56, No. 5, (May 2008) pp. 1137-1148.
- Pleskachev, V. & Vendik, I. (2004). Tunable microwave filters based on ferroelectric capacitors. *Microwaves, Radar and Wireless Communications, MIKON-2004*, Vol. 3, May 2004, pp. 1039-1043.
- Rauscher, C. (2003). Reconfigurable bandpass filter with a three-to-one switchable passband width, *IEEE Trans. on Microwave Theory Tech.*, Vol. 51, No. 2, (February 2003) pp. 573-577.
- Schmitt, J.; Cui, G.G., Luten, III, H.A., Yang, F., Gladden, F.A., Flanagan, S., Jian Y. & Hunt A.T. (2006). Electronic and optical materials, U.S. Patent 6,986,955, January 17, 2006.

- Sherman, V.; Astafiev, K., Setter, N., Tagantsev, A., Vendik, O., Vendik, I., Hoffmann, S., Böttger, U. & Waser, R. (2001). Digital reflection-type phase shifter based on a ferroelectric planar capacitor. *IEEE Microw. Wireless Comp. Lett.*, Vol. 11, No. 10, (October 2001) pp. 407-409.
- Tagantsev, A.K.; Sherman, V.O., Astafiev, K.F., Venkatesh, J. & Setter, N. (2003). Ferroelectric materials for microwave tunable applications. *J. Electroceramics*, Vol. 11, (2003) pp. 5-66.
- Van Keuls, F.W.; Mueller, C.H., Miranda, F.A., Romanofsky, R.R., Canedy, C.L., Aggarwal, S., Venkatesan, T., Ramesh, R., Horwitz, J.S., Chang, W. & Kim, W.J. (1999). Room temperature thin film  $\text{Ba}_x\text{Sr}_{1-x}\text{TiO}_3$  Ku-band coupled microstrip phase shifters: effects of film thickness, doping, annealing and substrate choice. *1999 IEEE MTT-S Int. Microwave Symp. Dig.*, pp. 737-740.
- Xi, X.X.; Li, H.-C., Si, W., Sirenko, A.A., Akimov, I.A., Fox, J.R., Clark, A.M., & Hao, J. (2000). Oxide thin films for tunable microwave devices. *J. Electroceramics*, Vol. 4, No. 2/3, (2000) pp. 393-405.
- Yamamuka, M.; Kawahara, T., Yuuki A. & Ono, K. (1998). Reaction mechanism and electrical properties of  $(\text{Ba,Sr})\text{TiO}_3$  films prepared by liquid source chemical vapor deposition, *IEICE Trans. Electronics*, E81-C47, (1998) pp. 497.
- Yoon, Y.-K.; Kim, D., Allen, M. G., Kenney, J. S. & Hunt, A.T. (2003). *IEEE Trans. Microwave Theory Tech.*, Vol. 51, (December 2003) pp. 2568-2576.
- York, B. & Pond, J. (2000). IMS Workshop Notes: Ferroelectric Materials and Microwave Applications. 2000 International Microwave Symposium (IMS), Boston, MA, June 11-16, 2000.
- Zeng, J.M.; Lin, C.L., Li, J.H. & Li, K. (1999). Low temperature preparation of barium titanate thin films by a novel sol-gel-hydrothermal method, *Materials Lett.*, Vol. 38, No. 2, (January 1999) pp. 112-115.
- nGimat (2006). A low cost analog phase shifter product family for military, commercial and public safety applications, *Microwave Journal*, Product release article, Vol. 49, No. 3, (March 2006) pp. 152-156.
- Zhao, Z.; Jiang, Y., Wang, X., Choi, K. & Hunt, A.T. (2006). Epitaxial growth of ferroelectric thin films by combustion chemical vapor deposition and their electrical properties, *Proceedings of the 15<sup>th</sup> IEEE Int'l Symp. Applications of Ferroelectrics (ISAF)*, pp. 356-359, Sunset Beach, NC, Jul. 30-Aug. 2, (2006) IEEE, Piscataway, NJ.
- Zhao, Z.; Wang, X., Choi, K. & Hunt, A.T. (2007). Ferroelectric Phase Shifters at 20 and 30 GHz, *IEEE Trans. Microwave Theory Tech*, Vol. 55, No. 2, (2007) pp. 430-437.
- Zheng, G.; Papapolymerou, J.; Tentzeris, M.M. (2003). Wideband coplanar waveguide RF probe pad to microstrip transitions without via holes, *IEEE Micro. Wireless Comp. Lett.*, Vol. 13, No. 12, (December 2003) pp. 544-546.

# Advanced RF MOSFET's for microwave and millimeter wave applications: RF characterization issues

<sup>1</sup> Julio C. Tinoco and <sup>2</sup> Jean-Pierre Raskin

<sup>1</sup> *Departamento de Ingeniería en Telecomunicaciones, División de Ingeniería Eléctrica, Facultad de Ingeniería, Universidad Nacional Autónoma de México (FI-UNAM)*

*Mexico*

<sup>2</sup> *Microwave Laboratory, Université catholique de Louvain*  
*Belgium*

## 1. Introduction

The communication industry has always been a very challenging and profitable market for semiconductor companies. The new communication systems are today very demanding; they require high frequency, high degree of integration, multi-standards, low power consumption, and they have to present good performance under harsh environment. The integration and power consumption reduction of the digital part will further improve with the continued downscaling of technologies. The bottleneck for further advancement is the analog front-end. Present-day transceivers often consist of a three or four chip-set solution combined with several external components. A reduction of the external components is essential to obtain a lower cost, power consumption and weight, but it will lead to a fundamental change in the design of analog front-end architectures. The analog front-end requires a high performance technology, like GaAs or silicon bipolar transistors, with devices that can easily achieve operating frequencies in the GHz range. For a digital signal processor, a small device feature size is essential for the implementation of complex algorithms. Therefore, it appears that only the best submicron CMOS technology is suitable for a feasible and cost-effective integration of the communication systems.

This last decade MOS transistors have reached amazingly high operation speed and the semiconductor community has noticed the Radio Frequency possibilities of such mainstream devices. Silicon-on-Insulator (SOI) MOSFET technology has demonstrated its potentialities for high frequency reaching cutoff frequencies close to 500 GHz for nMOSFETs and for harsh environment (high temperature, radiations) commercial applications.

From its early development phase till recent years, SOI has grown from a mere scientific curiosity into a mature technology. Partially Depleted (PD) SOI is now massively serving the 45-nm digital market where it is seen as a low cost - low power alternative to bulk silicon. Fully depleted (FD) devices are also widely spread as they outperform existing semiconductor technologies for extremely low power analog applications.

In this chapter, we are going to present the current state-of-the-art of advanced MOS transistors for microwave and millimeter wave applications. The importance of an accurate RF small-signal equivalent circuit of MOSFETs to properly design RF circuits is pointed out. Based on several experimental and simulation results the RF characterization issues of such advanced field effect transistors will be detailed. Several characterization techniques to extract an accurate small-signal equivalent circuit of MOSFET will be described.

## 2. Historical trend

The microelectronics area has gone through great developments during these last decades. The beginning of electronics technology can be situated in the beginning of the 20<sup>th</sup> century when the vacuum triode and pentode were developed. Since then, many applications have started to appear in several fields especially in communications: the radio and TV systems were developed.

The first step on the conception of solid state electronics devices was made by Lilingfiel (Iwai & Ohmi, 2002). He theoretically proposed a device called "Device for Controlled Electric Current". This theoretical device used the electric field generated across a dielectric film in order to control the flux of electrons between two electrodes called source and drain. The control terminal was called gate. Such device was not physically built because the technological possibilities did not allow its fabrication.

Some years later the first transistor was invented in the laboratories of the Bell Telephone Co. in 1947. This was a point-contact transistor made on germanium (Shockley, 1976). In 1958, Jack Kilby developed the first integrated circuit (IC). He integrated few devices on germanium to build a phase-shift oscillator, demonstrating the feasibility to integrate several devices in a semiconductor sample (Kilby, 1976). One year later, Robert Noyce developed a new technology and in fact a new conception of the IC's. This new technology was called "The planar technology" and was a revolutionary technology for microelectronics (Kilby, 1976).

Additionally in the 1950's and 1960's, many successful efforts were made looking for fabrication on reliable silicon Bipolar Junction Transistor's (BJT's). This promotes the growing of digital applications thanks to the called Transistor-Transistor Logic (TTL). At the same time, analog applications look for the use of BJT's in order to replace the vacuum triodes and pentodes. In fact, the first transistor with cut-off frequencies in the order of 1 GHz was developed in 1958-1959 based on germanium (Schwierz & Liou, 2001). At that time the community established that devices for high frequencies applications needed high carrier mobility and thus the silicon and germanium technologies were replaced by the III-V semiconductor technologies. Thus, in the 1960's different III-V based transistors with very high cut-off frequencies began to appear (Mead, 1966). In 1966, the first field-effect transistor based on GaAs was developed, this was a MESFET device which revolutionized the RF world (Schwierz & Liou, 2001).

Fig. 1 indicates the evolution of the record frequencies as a function of time (Schwierz & Liou, 2001) from the 1960's to the end of the century. As we can see in the late 90's the InP based transistors showed amazing cut-off frequencies near to 1 THz.

In the late 60's, the first silicon MOS transistor (MOSFET) was developed (Kahng, 1976). Due to its low carrier mobility, the silicon transistors were not considered for very high frequency applications but mainly for digital circuits. The n-MOS and p-MOS logic



technologies gained the attention of the digital community and a few years later the development of the CMOS technology revolutionized the digital applications. This technology allowed the development of the first microprocessors and high density memories (Iwai & Ohmi, 2002). In 1974, R. Denard established a new procedure with two objectives in mind: (i) increase the operation velocity of the MOSFETs and (ii) the integration density of the ICs (Denard *et al.*, 1974).

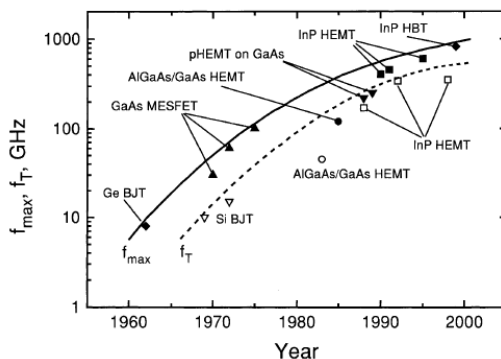


Fig. 1. Evolution of the record frequencies from 1960 to the end of the last century (Schwierz & Liou, 2001).

The downscaling of the MOSFET dimensions is the major way to reach both objectives. This has been the gold rule of microelectronics in the last three decades (Iwai, 2009). Thanks to downscaling, the digital electronics evolved enormously, in fact the integration density passed from hundreds of devices to millions of devices in the same silicon area and the microprocessors clock frequencies increased from a few MHz to the GHz range, through the fabrication of MOSFETs with channel lengths from 10  $\mu\text{m}$  to the current transistors with 65 nm (Iwai, 2009). Fig. 2 shows the evolution of the CMOS technology in the last decades (Iwai, 2009).

### 3. Development of high frequency MOSFET's

As established before, the MOS technology evolved enormously in the last decades allowing the development of very high performance circuits for digital applications. This evolution has been guided by the downscaling procedure (Iwai & Ohmi, 2002). Thanks to this, the channel length of the MOSFETs has been shrunk from 10  $\mu\text{m}$  down to 65 nm.

In recent years the RF community started to notice the potentialities of those devices and many efforts started to appear in order to optimize the RF performance of the MOSFETs. Due to the channel length reduction, the cut-off frequencies of the MOSFETs have grown enormously in such way that deep-submicron devices start to present values higher than 400 GHz (Schwierz & Liou, 2007).

Since then, many efforts began to look for the optimization of the MOSFETs for very high frequencies operation. Thanks to those researches, it was found that very important facts limiting the high performance at very high frequency are the series extrinsic resistances,

especially the gate resistance (Schwierz & Liou, 2007). Fig. 3 shows the evolution cut-off frequencies ( $f_t$  and  $f_{max}$ ) from the early 90's to the present (Schwierz & Liou, 2007).

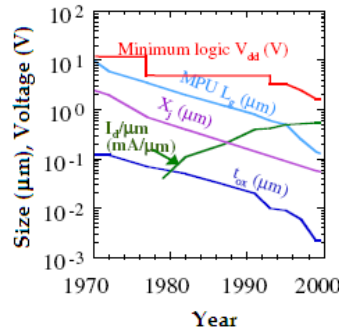


Fig. 2. Evolution of the main MOSFET parameters, gate length ( $L_g$ ), junction depth ( $X_j$ ), oxide thickness ( $t_{ox}$ ), normalized drain current ( $I_d/\mu m$ ) and minimum logic voltage ( $V_{dd}$ ) in the CMOS technology (Iwai, 2009).

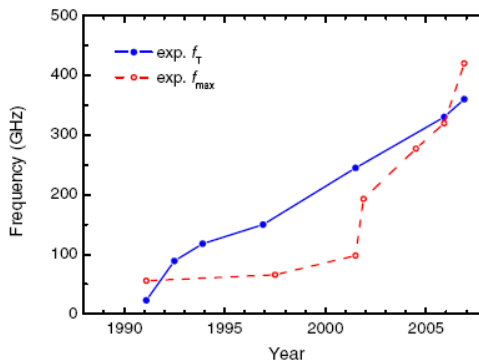


Fig. 3. Cut-off frequencies of MOSFETs, from early 90's to the present time (Schwierz & Liou, 2007).

As we can see in Fig. 3, the high frequency performance has recently grown amazingly and the current MOS transistors can present record frequencies higher than 460 GHz. Since the cut-off frequencies are inversely proportional to the channel length, cut-off frequencies as high as 1 THz can be expected for gate length in the order of 10 nm (Schwierz & Liou, 2007) as presented in Fig. 4.

### 3.1 Toward the Terahertz transistor

The standard MOS transistor is fabricated over a silicon substrate, however as the channel length is shrunk beyond 100 nm, some electrical degradations start to appear. Those effects include the loss of the gate electrostatic control on the carrier flow along the channel and they are called short channel effects, SCE (Colinge, 1991).

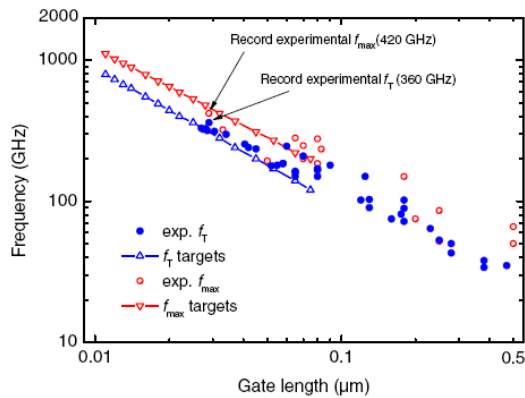


Fig. 4. Dependence of the cut-off frequencies of MOSFETs as a function of the channel length (Schwierz & Liou, 2007).

In order to keep a good electrostatic control of the channel by the gate and thus reduce the short-channel effects, Silicon-on-Insulator technology appears as a solution of great interest. Additionally, thanks to the buried oxide (BOX) underneath the transistor area, the source and drain capacitances to the silicon substrate are strongly reduced. The decrease of the capacitive coupling between the active silicon area of the transistor and the substrate contributes to the reduction of the parasitic capacitances and then the improvement of the high frequency capabilities of MOSFETs.

To reduce the SCE in nanometer scale MOSFETs, multiple-gate architectures (MuGFET) emerge as one of the most promising novel device structures, thanks to the simultaneous control of the channel by more than one gate. The idea of the double-gate (DG) MOSFET was first experimentally proven by J.-P. Colinge in 1990 (Colinge, 1990). Starting by the FinFET (Hisamoto *et al.*, 2000), other types of multiple-gate SOI MOSFETs have been introduced these last years (Cristoloveanu, 2001), (Tao Chuan Lim, 2009).

Additionally, new technologies like strained-silicon MOSFETs (s-Si MOSFETs) (Thompson, 2005) or Schottky barrier MOSFETs (SB MOSFETs) (Valentin *et al.*, 2008) appear as very interesting alternatives to replace the conventional bulk-technology and also promising devices for the TeraHertz era.

Theoretical analyses have proven that double-gate transistors (DG-MOSFETs) can reach cut-off frequencies as high as a few THz as shown in Fig. 5.

Some challenges must be solved in order to reach these projections. From a technological point of view, many efforts must be done to fabricate reproducible and feasible devices with channel length lower than 20 nm and engineers must figure out how to reduce as much as possible the access resistances and capacitances to the active useful area of the tiny transistor. Additionally, adequate modelling and characterization techniques are quite necessary to accurately simulate the device behaviour.

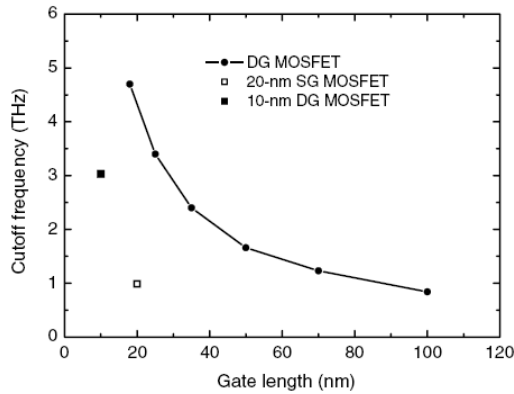


Fig. 5. Dependence of the cut-off frequencies of MOSFETs as a function of the channel length for DG-MOSFETs (Schwierz & Liou, 2007).

#### 4. RF Modelling and characterization

The modelling and characterization of MOS transistors at very high frequencies is of first importance and is made by the measurement of the scattering ( $S$ -) parameters. In general, there are two kinds of models: Polynomial and Physical-based small-signal models.

- Polynomial models: Those models describe the behaviour of the MOSFET as black boxes and usually require mathematical optimization routines. They are relatively easy to obtain but they do not give information about the physical nature of the transistors.
- Physical-based small-signal models: These models describe the behaviour of the MOSFET as equivalent electrical lumped circuits. The elements have a physically based origin but they are not easy to extract from the measurements.

The knowledge of the physically based small-signal equivalent circuit is very important because they are useful to determine circuit design methodologies or the influence of each parameter on the dynamic performance. In the following sections, a general equivalent circuit of MOS Transistor is presented.

##### 4.1 Useful effect

The useful effect of a MOSFET is the modulation of the current (labelled as  $I_{ds}$ ) flowing through the channel from the source terminal (S) to the drain terminal (D), by a control of the voltage applied on the gate terminal (G). Electrically this behaviour can be represented by a current controlled source connected between S and D terminals, while the control voltage is applied between the G and S terminals ( $V_{gs}$ ). The current source is defined by the intrinsic transconductance ( $g_{mi}$ ). Fig. 6 represents the equivalent circuit of the MOSFET considering only the useful effect.

The intrinsic transconductance can be mathematically expressed as:

$$g_{mi} = \left. \frac{\partial i_{ds}}{\partial v_{gs}} \right|_{v_{ds} = \text{const}} \quad (1)$$

**4.2 Quasi-static model**

The quasi-static regime is defined when an applied small signal varies sufficiently slowly that the carriers inside the transistor can follow it instantaneously. Additionally in the MOSFET, there are some influences from one terminal to the others. In such way that a small increment of the voltage applied on one terminal will produce a variation of the charge associated to the others. Fig. 7 shows the reduced scheme of the MOSFET when it is DC biased and an additional small signal is added to the gate terminal with a value  $\delta V_g$ . Such a voltage increment produces an increase of the channel charge represented by  $\delta Q$ . This charge increment is associated to both source and drain terminals noted as  $\delta Q_s$  and  $\delta Q_d$ , respectively.

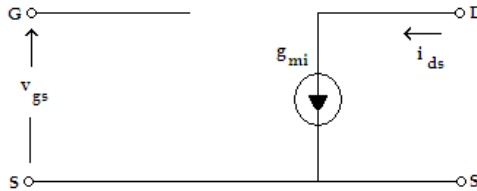


Fig. 6. Equivalent circuit for the useful effect of a MOSFET.

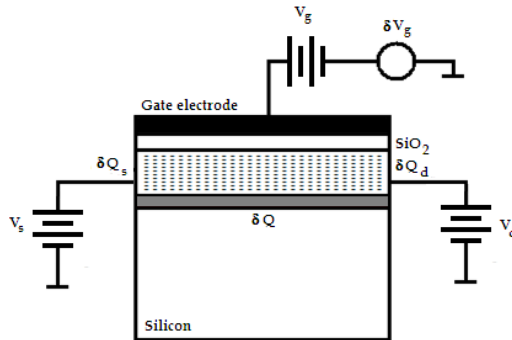


Fig. 7. Reduced scheme of a MOSFET showing the channel effect produced by a small increment of voltage applied on the gate terminal.

Those effects can be included in the equivalent small-signal model as capacitances due to the charge increment related to a voltage change. The capacitances between the source, drain and gate are defined by:

$$C_{gdi} = - \left. \frac{\partial q_g}{\partial v_d} \right|_{v_{gs} = \text{const}} \quad C_{dgi} = - \left. \frac{\partial q_d}{\partial v_g} \right|_{v_{gs} = \text{const}} \quad (2)$$

$$C_{gsi} = - \left. \frac{\partial q_g}{\partial v_s} \right|_{v_{gd} = \text{const}} \quad C_{sgi} = - \left. \frac{\partial q_s}{\partial v_g} \right|_{v_{gd} = \text{const}}$$

$$C_{dsi} = - \left. \frac{\partial q_d}{\partial v_s} \right|_{v_{gs} = \text{const}} \quad C_{sdi} = - \left. \frac{\partial q_s}{\partial v_d} \right|_{v_{gs} = \text{const}}$$

It is interesting to note that in general those capacitances are not reciprocal. For instance, if we consider a MOSFET biased in saturation, an increment on the drain voltage will not produce any change on the gate terminal, because of the pinch-off condition (Colinge, 1991) and thus  $C_{gdi} = 0$ . On the other hand, a small change on the gate voltage will produce a variation on the channel charge density and a drain current change which will lead to an associated drain charge change and therefore  $C_{dgi} \neq 0$ . Thus, under this condition we have  $C_{gdi} \neq C_{dgi}$ . This non-reciprocal effect can be modelled by adding an imaginary part to the transconductance called transcapacitance ( $C_{mi}$ ). Thus, the transadmittance ( $Y_{mi}$ ) is defined as:

$$Y_{mi} = g_{mi} - j\omega C_{mi} \quad (3)$$

Usually, the transcapacitance can be neglected for relatively low frequencies, however for very high frequencies it must be considered in order to accurately describe the MOSFET behaviour.

Additionally, the transistor acts as a real current source and thus it has a specific output conductance, defined by:

$$g_{di} = \left. \frac{\partial i_{ds}}{\partial v_{ds}} \right|_{v_{gs} = \text{const}} \quad (4)$$

Finally, the equivalent small-signal circuit will be modified as presented in Fig. 8, where all the parameters are bias dependent as equations (1-4) clearly indicate.

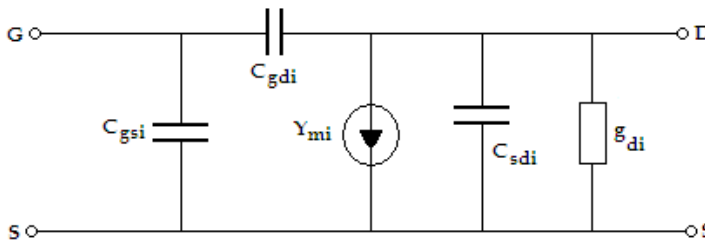


Fig. 8. Equivalent circuit of the quasi-static model of a MOSFET.

### 4.3 Non-Quasi-static model

As the operation frequency of the MOSFET increases, there will be a moment when the small-signal applied varies so fast that the charges inside the device cannot follow it anymore. In other words, at very high frequencies the charges will show inertial

phenomena, producing a delay between the applied signal (stimulus) and the charge redistribution in the channel (response). This delay cannot be modelled simply by the use of a capacitance effect.

The above phenomenon will be observed if the frequency exceeds the upper limit of validity of the quasi-static model presented in the previous section. Tsividis established this limit as proportional of  $1/L^2$ , where  $L$  is the transistor channel length (Tsividis, 1987).

One way to model the transistor under the non-quasi-static regime is to split the transistor into several small sections as Fig. 9 shows. The length of each section is chosen in such manner that the quasi-static model is valid in each section. The combination of the models for all sections will be valid for the whole device at the frequency of interest.

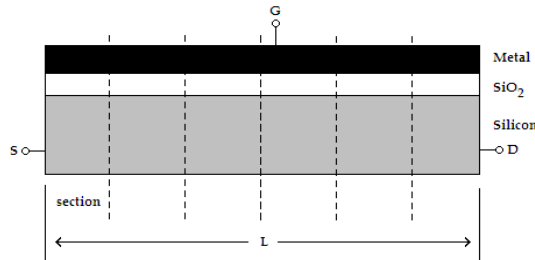


Fig. 9. MOS transistor split up in several sections along its channel.

However, this procedure is difficult to use due to the complexity of the analysis of several combined equivalent circuits and because if we change the frequency of analysis it is necessary to redefine the device subdivision. Another way to analyze the non-quasi-static regime is by the introduction of new elements in the equivalent circuit. The delay along the channel can be represented by the use of intrinsic series resistances connected between the gate and the drain ( $R_{gdi}$ ) and between the gate and the source ( $R_{gsi}$ ). Furthermore, the delay from the moment where the signal is applied to the gate and the moment at which the effect is transferred to the channel can be modelled by a complex transconductance, as represented in Fig. 10.

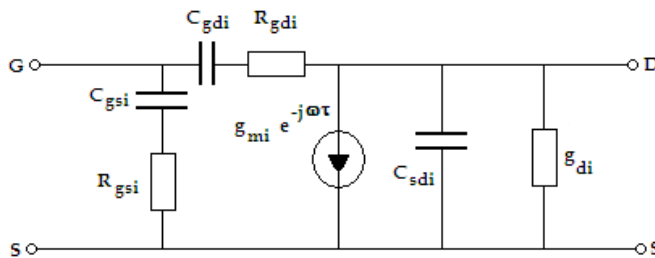


Fig. 10. Small-signal equivalent circuit of MOSFET under non-quasi-static condition.

This equivalent circuit can be represented by the admittance ( $Y$ -) matrix given by:

$$Y_{\pi} = \begin{bmatrix} j\omega \left( \frac{C_{gsi}}{1 + j\omega R_{gsi} C_{gsi}} + \frac{C_{gdi}}{1 + j\omega R_{gdi} C_{gdi}} \right) & -j\omega \left( \frac{C_{gdi}}{1 + j\omega R_{gdi} C_{gdi}} \right) \\ \frac{g_{mi} \cdot e^{-j\omega\tau}}{1 + j\omega R_{gsi} C_{gsi}} - j\omega \left( \frac{C_{gdi}}{1 + j\omega R_{gdi} C_{gdi}} \right) & g_{di} + j\omega \left( C_{sdi} + \frac{C_{gdi}}{1 + j\omega R_{gdi} C_{gdi}} \right) \end{bmatrix} \quad (5)$$

#### 4.4 Extrinsic model

In previous sections we established the equivalent circuit model under quasi-static and non-quasi-static regimes. Those models take into account only the intrinsic part of the transistor which is bias and geometry dependent. However, the structure of the MOSFET itself is surrounded by some parasitic effects originating mainly from the contacts and interconnections that must be considered in order to accurately describe its overall behaviour. Such parasitic extrinsic elements are in general bias independent.

##### 4.4.1 Extrinsic capacitances

Various extrinsic capacitances are associated to the physical structure of the transistor, as shown in Fig. 11. The extrinsic capacitances are associated to the gate, drain and source terminals. The gate-drain ( $C_{gde}$ ) and gate-source ( $C_{gse}$ ) capacitances originate from the parallel combination of: (i) the overlap regions due to the diffusion of source and drain doping atoms underneath the thin gate oxide and (ii) the fringing electric field from the gate electrode to the source and drain regions. The drain-to-source capacitance ( $C_{dse}$ ) corresponds to a proximity capacitance due to the coupling effects through the substrate.

The Y-matrix of the small-signal equivalent circuit presented in Fig. 12 is defined as:

$$Y_{\pi} = Y_{mi} + Y_e \quad (6)$$

$$\text{Where } Y_e = \begin{bmatrix} j\omega(C_{gse} + C_{gde}) & -j\omega C_{gde} \\ -j\omega C_{gde} & j\omega(C_{dse} + C_{gde}) \end{bmatrix}$$

##### 4.4.2 Extrinsic resistances and inductances

The doped source and drain semiconductor regions are characterized by a certain resistivity which, due to the geometry, will relate to access resistance values. Additionally, the transistor must be connected to the external world using metal lines. Those interconnection lines also introduce some series resistances with the intrinsic channel of the transistor. Finally, the contact between the metal lines and the doped semiconductor regions is characterized by a contact resistance which also contributes to the total parasitic resistances. Fig. 13 represents a top view of the transistor with the distributed extrinsic resistances.

Due to the interconnection lines the transistor structure might present some inductive effect at each electrode. Fig. 14 presents the small-signal equivalent circuit of the MOSFET including the all the intrinsic and extrinsic lumped elements. It is worth noting that due to the small size of the advanced MOSFETs the series extrinsic inductances are very small and can even be neglected for optimized layout.



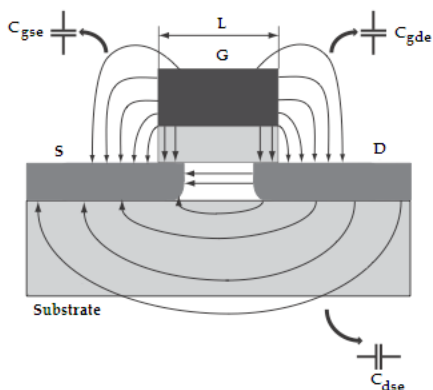


Fig. 11. Extrinsic capacitances associated to the physical structure of the MOS transistor.

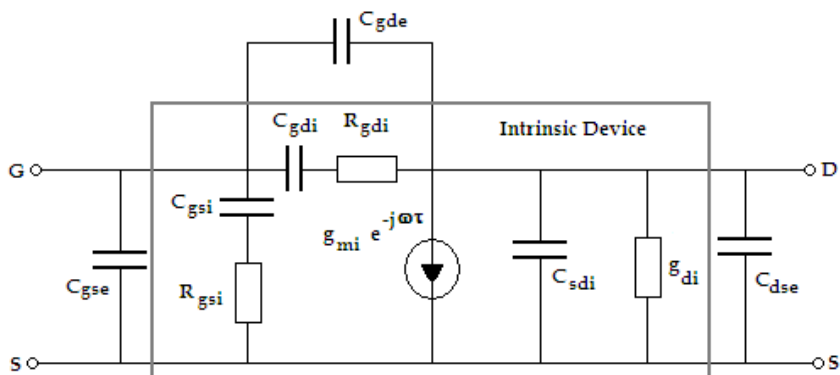


Fig. 12. Non-quasi-static intrinsic model including the extrinsic capacitances.

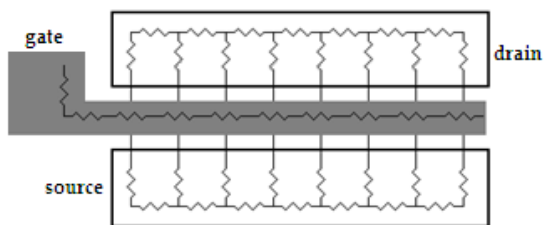


Fig. 13. Extrinsic series resistances distributed in the physical transistor structure.

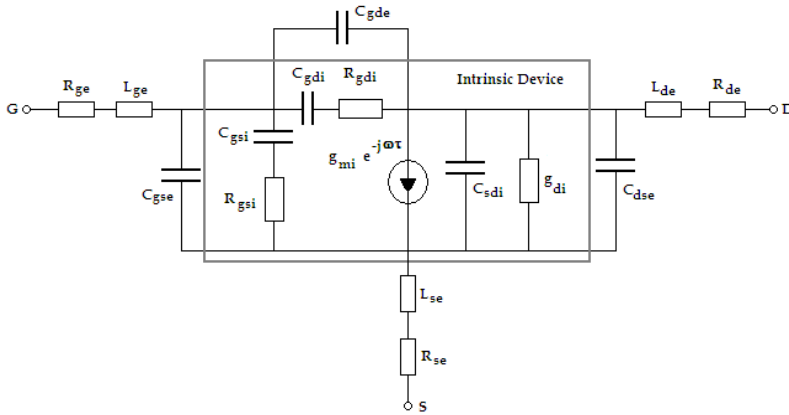


Fig. 14. Non-quasi-static small-signal equivalent circuit for a MOSFET including all intrinsic and extrinsic lumped elements.

The impedance ( $Z$ -) matrix of the whole circuit presented in Fig. 14 can be mathematically represented by:

$$Z_{\Sigma} = Y_{\pi}^{-1} + Z_e \tag{7}$$

$$\text{Where: } Z_e = \begin{bmatrix} (R_{ge} + R_{se}) + j\omega(L_{ge} + L_{se}) & R_{se} + j\omega L_{se} \\ R_{se} + j\omega L_{se} & (R_{de} + R_{se}) + j\omega(L_{de} + L_{se}) \end{bmatrix}$$

**4.5 Access parameters**

In order to characterize the MOSFET over a wide frequency band, it must be embedded into planar transmission lines and the most common ones are the coplanar-waveguide (CPW) presented in Figure 15. Those feed lines will of course introduce some additional series and parallel lumped elements at the input and output of the transistor under test.

Several procedures called de-embedding techniques are proposed in the literature (Cho & Burk, 1991) to withdraw those lumped elements related to the CPW structure. However, in the real scheme the de-embedding is not perfect and thus some access parasitic elements still remain at the input and output of the device.

For this reason the remaining parasitic access elements ( $Z_{ga}$ ,  $Z_{da}$ ,  $Y_{ga}$ ,  $Y_{da}$ ,  $Y_{gda}$ ) must be included in the equivalent circuit model as presented in Fig. 16.

The mathematical representation of the complete small-signal equivalent circuit presented in Fig. 16, needs two steps, first it is necessary to add the access impedances to the  $Z_{\Sigma}$  matrix and second the access admittances must be added. Thus we have:

$$Z_{\sigma} = Z_{\Sigma} + Z_{\alpha} \tag{8}$$

$$\text{Where } Z_{\alpha} = \begin{bmatrix} Z_{ga} & 0 \\ 0 & Z_{da} \end{bmatrix}$$

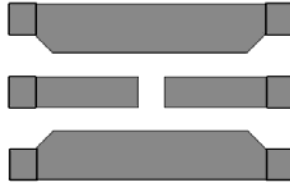


Fig. 15. Coplanar-waveguide structure.

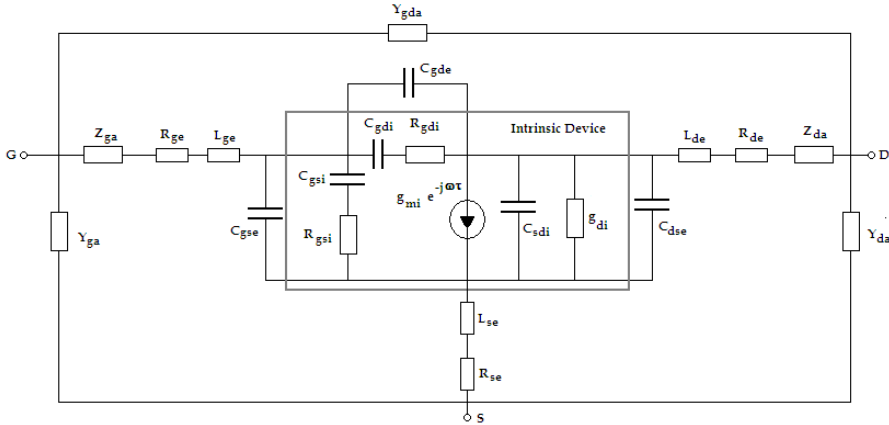


Fig. 16. Complete small-signal equivalent circuit of a MOSFET embedded in a CPW structure.

And finally:

$$Y_{\mu} = Z_{\sigma}^{-1} + Y_a \tag{9}$$

$$\text{Where } Y_{\alpha} = \begin{bmatrix} Y_{ga} + Y_{gda} & -Y_{gda} \\ -Y_{gda} & Y_{da} + Y_{gda} \end{bmatrix}$$

Thus,  $Y_{\mu}$  matrix represents the admittance parameters of the whole equivalent circuit of the MOS transistor. At the present time, the technology facilities are robust enough that the test structures used for the de-embedding procedures can adequately remove the access parasitic elements. Thus, for well optimized advanced transistors and de-embedding structures (open, short, lines, load), the access elements can be well withdrawn from the measured device under test.

### 5. Small-signal extraction procedure

As we mentioned above, the current technology is able to produce test structures to properly de-embed access lines. Thus, the extraction of the elements forming the equivalent circuit of the MOSFET as presented in Fig. 14 proceeds as follows:

- First, the extrinsic resistances and inductances are extracted and the matrix  $Z_e$  is constructed;
- Secondly, the  $Y_{\pi}^{-1}$  matrix is de-embedded from equation (9);
- Thirdly, the extrinsic capacitances are extracted and the matrix  $Y_e$  is defined;
- Finally, the matrix  $Y_{\pi i}$  is de-embedded from equation (8) and the intrinsic parameters are determined.

In general, the philosophy of the RF extraction methods is to bias the MOSFET under specific bias conditions in order to reduce the complexity of the equivalent circuit and thus obtain the direct extraction of the elements of the equivalent circuit.

### 5.1 Extraction of the series extrinsic resistances and inductances

There are several methods to extract the series extrinsic resistances. In general, they can be divided in two groups: (i) the methods which rely on DC measurements, and (ii) the methods that require RF measurements.

The RF methods allow determining independently the three series resistances  $R_{se}$ ,  $R_{de}$  and  $R_{ge}$ . The most widely used RF methods to extract the extrinsic series resistances have been proposed in the literature by (Lovell *et al.*, 1994), (Torres-Torres *et al.*, 2003), (Raskin *et al.*, 1998) and (Bracale *et al.*, 2000).

It is worth to mention that some of those RF methods require the extraction of intermediate parameters before the series resistances extraction (Pascht *et al.*, 2002) and other methods require complex mathematical optimization routines (Lee *et al.*, 1997). Such characteristics make them more sensitive to measurement noise and difficult to apply. For that reason, we are going to focus on the previously mentioned methods which are briefly described here below.

#### 5.1.1 Lovell's method

For this method the MOSFET is biased in depletion and under the quasi-static regime, i.e. with  $V_{gs} \ll V_T$  and  $V_{ds} = 0$  V. Under these bias conditions the intrinsic lumped elements vanish (Lovell *et al.*, 1994). Thus, the transistor can be represented by the simplified equivalent circuit shown in Fig. 17.

From the above equivalent circuit, the real parts of the impedance relationships can be written as:

$$\begin{aligned} \operatorname{Re}(Z_{11} - Z_{12}) &= R_{ge} \\ \operatorname{Re}(Z_{12}) &= \operatorname{Re}(Z_{21}) = R_{se} \\ \operatorname{Re}(Z_{22} - Z_{12}) &= R_{de} \end{aligned} \quad (10)$$

Thus, the series extrinsic resistances can be extracted at very high frequency from a plot of the corresponding real part of the impedance relationship as a function of the frequency. On the other hand, the imaginary part of the impedances follows the next relations:

$$\begin{aligned} \omega \operatorname{Im}(Z_{11} - Z_{12}) &= \omega^2 L_{ge} + C_A \\ \omega \operatorname{Im}(Z_{12}) &= \omega \operatorname{Im}(Z_{21}) = \omega^2 L_{se} + C_B \end{aligned} \quad (11)$$

$$\omega \text{Im}(Z_{22} - Z_{12}) = \omega^2 L_{de} + C_C$$

Where  $C_A$ ,  $C_B$  and  $C_C$  are values dependent on the extrinsic capacitances  $C_{gse}$ ,  $C_{gde}$  and  $C_{dse}$ . Thus, a plot of the corresponding imaginary part of the impedance relationship multiplied by  $\omega$  vs. the second power of  $\omega$  gives a linear function where the slope of such a plot corresponds to the respective series inductance.

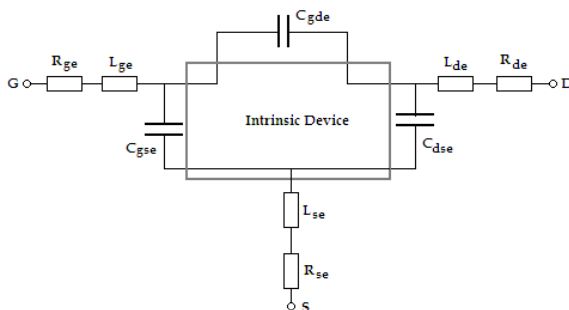


Fig. 17. Small-signal equivalent circuit under depletion regime:  $V_{gs} \ll V_T$  and  $V_{ds} = 0$  V.

### 5.1.2 Torres-Torres' method

For this method the MOSFET is biased in inversion and under quasi-static regime, i.e. with  $V_{gs} > V_T$  and  $V_{ds} = 0$  V. Under these bias conditions the intrinsic transconductance ( $g_{mi}$ ) vanishes. Additionally, the authors neglect the effect of the extrinsic series inductances, for that reason the equivalent circuit is simplified as presented in Fig. 18.

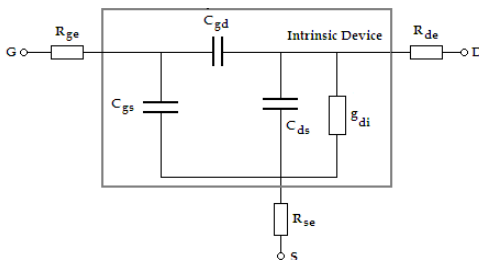


Fig. 18. Small-signal equivalent circuit under inversion regime:  $V_{ds} = 0$  V and  $V_{gs} > V_T$  with  $C_{gs} = C_{gsi} + C_{gse}$ ,  $C_{gd} = C_{gdi} + C_{gde}$  and  $C_{ds} = C_{sdi} + C_{dse}$ .

Under these bias conditions, the authors establish that the real parts of the impedances follow the following relationships (Torres-Torres *et al.*, 2003):

$$\begin{aligned} \text{Re}(Z_{11}) &= R_{ge} + R_{se} + A/2 \\ \text{Re}(Z_{12}) &= R_{se} + A/2 \\ \text{Re}(Z_{22}) &= R_{de} + R_{se} + A \end{aligned} \tag{12}$$

where  $A = \frac{R_{ch}}{1 + \omega^2 C_x R_{ch}^2}$ ,  $C_x = C_{ds} + \frac{C_{gs} C_{gd}}{C_{gs} + C_{gd}}$  and  $R_{ch} = \frac{1}{g_{di}}$

In order to determine the extrinsic series resistances it is necessary to know the values of  $R_{ch}$  and  $C_x$ . From the imaginary part of  $Z_{22}$  we have:

$$-\frac{\omega}{\text{Im}(Z_{22})} = C_x \omega^2 + \frac{1}{C_x R_{ch}^2} \quad (13)$$

Thus, a plot of  $-(\omega/\text{Im}(Z_{22}))$  gives a linear function respect to  $\omega^2$  where the slope corresponds to  $C_x$  and the intercept corresponds to  $1/C_x R_{ch}^2$ . Once those values are determined, the extrinsic series resistances can be obtained from equation (12).

### 5.1.3 Raskin's method

This technique biases the MOSFET in saturation or at the bias point of interest, with  $V_{gs} > V_T$  and  $V_{ds} > V_{gs} - V_T$  and under quasi-static regime. Under this condition, the device is asymmetric and its equivalent circuit is as shown in Fig. 19.

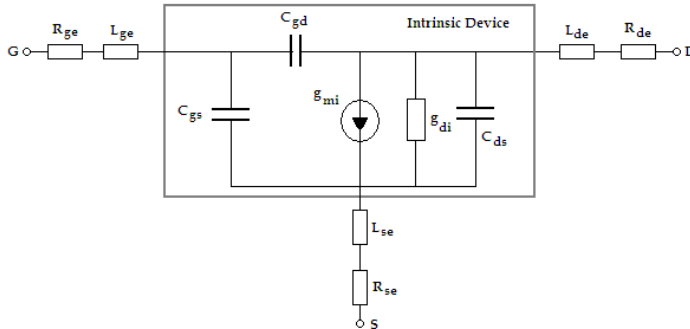


Fig. 19. Small-signal equivalent circuit under saturation regime:  $V_{gs} > V_T$  and  $V_{ds} > V_{gs} - V_T$ .

The real parts of  $Z$ -parameters can be expressed as (Raskin *et al.*, 1998):

$$\begin{aligned} \text{Re}(Z_{12}) &= R_{se} + \frac{A_s}{\omega^2 + B} \\ \text{Re}(Z_{22} - Z_{12}) &= R_{de} + \frac{A_d}{\omega^2 + B} \\ \text{Re}(Z_{11} - Z_{12}) &= R_{ge} + \frac{A_g}{\omega^2 + B} \end{aligned} \quad (14)$$

Thus, the extrinsic series resistances  $R_{ge}$ ,  $R_{se}$  and  $R_{de}$  are obtained, respectively, by using the parametric plots of the forms  $\{\text{Re}[Z_{\sigma\pi 11}(\omega)], \text{Re}[Z_{\sigma\pi 21}(\omega)]\}$ ,  $\{\text{Re}[Z_{\sigma\pi 12}(\omega)], \text{Re}[Z_{\sigma\pi 21}(\omega)]\}$  and  $\{\text{Re}[Z_{\sigma\pi 22}(\omega)], \text{Re}[Z_{\sigma\pi 12}(\omega)]\}$ .

### 5.1.4 Bracale's method

For this method the MOSFET is biased in inversion and under quasi-static regime, i.e. with  $V_{gs} > V_T$  and  $V_{ds} = 0$  V. Under these bias conditions the intrinsic transconductance ( $g_{mi}$ ) vanishes. Also, since  $V_{ds} = 0$  V the device becomes symmetric which implies  $C_{gs} = C_{gd} = C$ . Thus, the equivalent circuit is simplified as shown in Fig. 20.

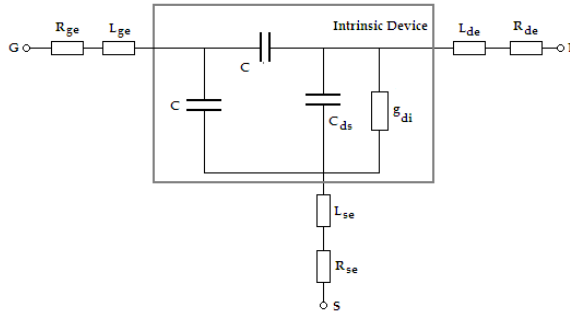


Fig. 20. Small-signal equivalent circuit under inversion regime:  $V_{gs} > V_T$  and  $V_{ds} = 0$  V.

Considering that  $C + 2CC_{ds} \ll 2g_{di} / \omega$  and a constant mobility (Bracale *et al.*, 2000) for each applied  $V_{gs}$ , the real parts of Z-parameters are related to the equivalent circuit elements as:

$$\begin{aligned} \text{Re}(Z_{22} - Z_{12}) &= R_{de} + \frac{1}{2K(V_{gs} - V_T)} \\ \text{Re}(Z_{12}) &= R_{se} + \frac{1}{2K(V_{gs} - V_T)} \\ \text{Re}(Z_{11} - Z_{12}) &= R_{ge} + \frac{1}{4K(V_{gs} - V_T)} \end{aligned} \quad (15)$$

Where  $K = \mu(W/L)C_{ox}$ ,  $\mu$  and  $C_{ox}$  are, respectively, the carrier mobility and the normalized gate oxide capacitance, and  $W$ ,  $L$ , the width and length of the MOS transistor channel, respectively.

Finally, the series resistances are determined by the intercept of a plot representing the real parts of the Z-parameters *vs.* the inverse of the gate overdrive ( $1/(V_{gs} - V_T)$ ). On the other hand, the imaginary parts of the Z-parameters are given by:

$$\text{Im}(Z_{22} - Z_{12}) = L_{de} + \frac{C + 2C_{ds}}{4K^2} \frac{1}{(V_{gs} - V_T)^2}$$

$$\begin{aligned} \text{Im}(Z_{12}) &= L_{se} + \frac{C + 2C_{ds}}{4K^2} \frac{1}{(V_{gs} - V_T)^2} \\ \text{Im}(Z_{11} - Z_{12}) &= L_{ge} + \frac{C_{ds}(C + 2C_{ds})}{4CK^2} \frac{1}{(V_{gs} - V_T)^2} - \frac{1}{2C\omega^2} \end{aligned} \quad (16)$$

Thus,  $L_{de}$  and  $L_{se}$  are obtained by the intercept of a plot of the corresponding Z-parameter imaginary part *vs.*  $(1/(V_{gs} - V_T))^2$ . For the case of  $L_{ge}$ , two steps are needed: (i) a linear regression of  $\text{Im}(Z_{11}-Z_{12})$  *vs.*  $\omega^2$  is required for different  $V_{gs}$  values and (ii) a new linear regression of each intercept of the step (i) *vs.*  $(1/(V_{gs} - V_T))^2$ . The intercept of the second step will give the corresponding  $L_{ge}$  value.

### 5.1.5 Tinoco's method

Recently, we showed that the Lovelace, Torres-Torres and Raskin's methods are quite sensitive to S-parameters measurement noise, for that reason a small noise signal mixed with the scattering parameters will disturb the extraction procedure enough to reduce the accuracy on the extracted lumped parameters (Tinoco & Raskin, 2008). On the other hand, the Bracale's method is more robust in terms of noise, however it cannot accurately extract the resistance values. Thus, we established a new extraction procedure of the extrinsic series resistances based on the Bracale's method (Tinoco & Raskin, 2009) but considering that the carrier mobility varies with  $V_{gs}$  and that the transistor is not perfectly symmetric. Under those new assumptions, the real parts of the Z-parameters are expressed as:

$$\begin{aligned} \text{Re}(Z_{22} - Z_{12}) &= R_{de} + \frac{1}{(\alpha^{-1} + 1)} \frac{L}{W\mu_0 C_{ox}} \left( \theta + \frac{1}{V_{gs} - V_T} \right) \\ \text{Re}(Z_{12}) &= R_{se} + \frac{1}{(\alpha + 1)} \frac{L}{W\mu_0 C_{ox}} \left( \theta + \frac{1}{V_{gs} - V_T} \right) \\ \text{Re}(Z_{11} - Z_{12}) &= R_{ge} - \frac{1}{(\alpha + \alpha^{-1} + 2)} \frac{L}{W\mu_0 C_{ox}} \left( \theta + \frac{1}{V_{gs} - V_T} \right) \end{aligned} \quad (17)$$

Where  $\alpha = C_{gs}/C_{gd}$  is defined as the symmetry coefficient and  $\theta$  is the mobility degradation coefficient (Tinoco & Raskin, 2009).

The mobility degradation factor  $\theta$  can be determined measuring an array of transistors characterized by different channel lengths ( $L$ -array) following by a two-step procedure as mentioned below:

- i. A linear regression of  $dV_{ds}/dI_{ds}$  *vs.*  $1/(V_{gs} - V_T)$  for each device in order to determine the intercept ( $\beta$ ) and the slope ( $m$ ) parameters;
- ii. A linear regression from the function  $\beta$  *vs.*  $m$  for the different channel lengths of the  $L$ -array is then traced to determine  $\theta$ , as detailed in (Tinoco & Raskin, 2009).

Additionally, the  $\alpha$  parameter can be obtained from:



$$\alpha = \frac{\text{Im}(Z_{22} - Z_{12})}{\text{Im}(Z_{12})} \tag{18}$$

Therefore, the correct series resistance can be obtained by the Bracale's method but applying the corrections related to the carrier mobility change with the applied gate voltage ( $\theta$ ) and the asymmetry of the device under test ( $\alpha$ ) (Tinoco & Raskin, 2009).

**5.2 Extraction of the extrinsic capacitances**

Once the series resistances and inductances are extracted, the matrix  $Z_e$  is constructed and removed from the  $Z_\Sigma$  matrix according to equation (7). Then, the extrinsic capacitances can be removed using the MOSFET biased in depletion with  $V_{ds} = V_{gs} = 0$  V. Under this condition, the equivalent circuit is shown in Fig. 21.

From that equivalent circuit, extrinsic capacitances can be obtained from the imaginary parts of the admittance parameters, and they are given by:

$$\begin{aligned} C_{gse} &= \frac{\text{Im}(Y_{11} + Y_{12})}{\omega} \\ C_{gde} &= -\frac{\text{Im}(Y_{12})}{\omega} \\ C_{dse} &= \frac{\text{Im}(Y_{22} + Y_{12})}{\omega} \end{aligned} \tag{19}$$

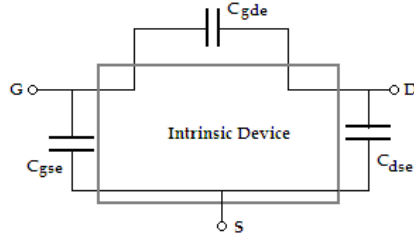


Fig. 21. Equivalent circuit under depletion bias condition after withdrawing the extrinsic series resistances and inductances.

**5.2 Extraction of the intrinsic parameters**

After extracting the extrinsic capacitances, the intrinsic matrix ( $Y_{in}$ ) can be determined by equation (6). From this matrix, the intrinsic parameters can be obtained from the following expressions.

$$\begin{aligned} C_{gsi} &= \frac{1}{\omega \text{Im}(1/(Y_{11} + Y_{12}))} \\ C_{gdi} &= -\frac{1}{\omega \text{Im}(1/Y_{12})} \end{aligned}$$

$$\begin{aligned}
C_{dsi} &= \frac{\text{Im}(Y_{22} + Y_{12})}{\omega} \\
R_{gdi} &= -\text{Re}(1/Y_{12}) \\
R_{gsi} &= \text{Re}\left(\frac{1}{Y_{11} + Y_{12}}\right) \\
g_{di} &= \text{Re}(Y_{22} + Y_{12}) \\
g_{mi} &= -\left|\frac{Y_{21} + Y_{12}}{Y_{11} + Y_{12}}\right| \cdot \frac{1}{\text{Im}(1/(Y_{11} + Y_{12}))} \\
\tau &= \frac{1}{\omega} \arctan\left\{\frac{\text{Im}\left[(Y_{21} - Y_{12})/(1 + j\omega R_{gsi} C_{gsi})\right]}{\text{Re}\left[(Y_{21} - Y_{12})/(1 + j\omega R_{gsi} C_{gsi})\right]}\right\}
\end{aligned} \tag{20}$$

## 6. Figures of merit (FOM's) for high frequency transistors

Three very important figures of merit (FOM's) are commonly considered to describe the high frequency performance of MOSFETs: the cut-off frequency of the current gain ( $f_T$ ), the maximum oscillation frequency ( $f_{max}$ ) and the minimum noise figure ( $NF_{min}$ ).

The cut-off frequency  $f_T$  can be defined as the frequency when the current gain decreases to 1 (0 dB). The current gain is related to the  $H_{21}$  parameter and is defined as the ratio of the output current to the input current. Based on the small-signal equivalent circuit presented in Fig. 14,  $f_T$  can be defined by the following expression:

$$f_T = \frac{g_{mi}}{2\pi} \frac{1}{(C_{gs} + C_{gd}) \cdot (1 + g_{di} R_{se}) + C_{gd} g_{mi} R_{se}} \tag{21}$$

As we can see from (21),  $f_T$  is strongly reduced by the extrinsic source resistance. In the literature, the intrinsic cutoff frequency,  $f_c$ , which measures the intrinsic ability of a field effect transistor (FET) to amplify high frequency signals is also defined.

$$f_c = \frac{g_{mi}}{2\pi} \frac{1}{C_{gs}} \tag{22}$$

The maximum oscillation frequency is defined as the frequency at which the device still provides power in a stable operation.  $f_{max}$  can be defined as:

$$f_{max} = \frac{f_T}{2\sqrt{2\pi \cdot f_T R_{ge} C_{gd} + g_{di} \cdot (R_{ge} + R_{se} + R_{gsi})}} \tag{23}$$

As we can see from (23),  $f_{max}$  is directly correlated to  $f_T$  and is strongly affected by the gate and source extrinsic resistances.

Another important FOM is the minimum noise figure ( $NF_{min}$ ). The main application of the transistors, in general, is to amplify the signal present at its input terminal. However, the signal is mixed with noise from several sources, one of them is the transistor itself. Thus, the noise introduced by the MOSFET must be as low as possible in order to assure good amplification performance.

$NF_{min}$  can be defined as the signal-to-noise ratio at the input divided by the signal-to-noise ratio at the output of the transistor and is expressed in dB.

$$NF_{min} = 10 \log \left( \frac{P_{Si} / P_{Ni}}{P_{So} / P_{No}} \right) \tag{24}$$

Where  $P_{Si}$  and  $P_{So}$  are the signal power at the input and output, respectively, and  $P_{Ni}$  and  $P_{No}$  are the noise power at the input and output, respectively.

### 7. Results of high frequency MOSFET's

Recently, we analyzed by simulation the ability and robustness of the above mentioned methods to extract the extrinsic series resistances (Tinoco & Raskin, 2009) of various advanced MOSFETs.

ELDO software has been used to simulate the S-parameters of Partially-Depleted (PD) SOI n-MOS transistors with a channel length of 0.13  $\mu\text{m}$ . The BSIM3SOI model, version 3.11, from ST Microelectronics, Crolles, France, is considered. The intrinsic core of the MOSFET is connected with lumped series resistances  $R_{se}$ ,  $R_{de}$  and  $R_{ge}$  and a noise signal is added to the simulated ideal S-parameters in order to emulate the noise floor of a Vectorial Network Analyzer (VNA), which corresponds to the most critical noise source.

Table I shows a summary of the resistances extracted using the different methods presented in Section 5.1 for simulated transistors with and without noise.

Method	Extracted series resistances without noise			Extracted series resistances with noise		
	$R_{se}$	$R_{de}$	$R_{ge}$	$R_{se}$	$R_{de}$	$R_{ge}$
Lovelace	2.82	2.94	5.05	---	---	---
Torres-Torres	2.84	2.93	5.1	6.0	6.2	3.5
Raskin	2.89	2.95	5.04	3.75	5.7	5.51
Bracale	4.3	3.95	4.4	4.28	3.97	4.39
Tinoco	2.79	2.89	5	2.79	2.9	5.01
Used in simulations	3	3	5	3	3	5

Table 1. Summary of the extracted series resistances in  $\Omega$  (Tinoco & Raskin, 2009).

As we can see from Table 1, the Torres-Torres and Raskin's methods give very different values for the simulations with noise signal added to the S-parameters. In the Lovelace's case, the noise disturbs enough the parameters that it makes impossible to determine the resistance values. On the other hand, the Bracale's method is more robust in terms of noise, however it cannot adequately determine the values used in simulations. This problem is adequately corrected by the Tinoco's method (Tinoco & Raskin, 2008).

Recently, we applied the Bracele's and mobility correction established by the Tinoco's series resistances extraction procedures on triple gate multifingered FinFETs with 50 gate fingers, 6 fins per finger and different channel lengths and widths. FinFETs are fabricated on a SOI wafer with 60-nm Si film on 145-nm of buried oxide, with <100> and <110> Si planes for top and lateral channels, respectively. From DC measurements a value of  $\theta = 0.3 \text{ V}^{-1}$  was extracted. Table II summarizes the aspect ratio of the measured FinFETs as well as the extracted series resistances using both extraction methods.

Measured FinFETs			Extracted Series Resistances							
Label	$L$ (nm)	$W_{fin}$ (nm)	Bracele's Method				Tinoco's Method			
			$R_{se}$ ( $\Omega$ )	$R_{de}$ ( $\Omega$ )	$R_{ge}$ ( $\Omega$ )	$R_{sd}$ ( $\Omega$ )	$R_{se}$ ( $\Omega$ )	$R_{de}$ ( $\Omega$ )	$R_{ge}$ ( $\Omega$ )	$R_{sd}$ ( $\Omega$ )
Fin1	60	27	4.75	7.77	5.66	12.52	4.08	7.1	5.99	11.18
Fin2	60	27	4.9	8.14	8.7	13.05	4.22	7.46	9.05	11.68
Fin3	60	92	0.86	2.92	11.13	3.78	0.58	2.63	11.27	3.21
Fin4	60	93	0.47	2.53	6.42	3	0.41	2.48	6.44	2.9
Fin5	79	27	5.22	7.94	7.05	13.16	4.42	7.14	7.45	11.56
Fin6	106	27	6.41	9.23	11.7	15.65	5.42	8.24	12.21	13.66
Fin7	106	53	1.14	4.14	31.46	5.29	0.42	3.42	31.8	3.85
Fin8	106	53	1	3.97	31.26	4.97	0.22	3.2	31.6	3.42
Fin9	280	27	8.04	10.3	4.39	18.34	6.11	8.39	5.35	14.47
Fin10	280	27	7.95	10.2	3.23	18.17	6.1	8.33	4.2	14.4
Fin11	920	34	0.71	4.96	58.2	5.68	0.11	4.36	58.5	4.48

Table 2. Summary of the experimental results for various FinFETs and the extracted series resistances (Tinoco & Raskin, B, 2009).

Using the extracted extrinsic resistances presented in Table II, we have demonstrated in (Tinoco & Raskin, B, 2009) the importance of using the Tinoco's method to accurately extract a wideband small-signal equivalent circuit. Those results highlight the importance of accurate and reliable RF characterization techniques to design wideband ICs.

As mentioned in the introduction, another important objective of developing accurate high frequency characterization techniques is the possibility to deeply analyze the dynamic behavior of the transistor and then identify the main high frequency limitations of a particular technology. As an example, using the developed RF characterization techniques presented in Section 5.1, the RF performance of FinFETs with various geometries (fin width,  $W_{fin}$ , channel length  $L_g$ ) has been deeply analyzed. The current gain ( $|H_{21}|$ ) as a function of frequency which yields the device cut-off frequency ( $f_T$ ) is presented in Fig. 22a for FinFETs characterized by different fin widths. Unfortunately, we can observe a reduction of the cutoff frequency with the shrinkage of  $W_{fin}$ . This degradation is mainly related to the increase of the source and drain resistances with the thinning down of the fin width (Raskin, 2009).

Fig. 22b presents the extracted RF cutoff frequencies of planar and FinFETs devices as a function of channel length. The so-called intrinsic ( $f_{Ti}$ ) and extrinsic ( $f_{Te}$ ) cutoff frequencies stand, respectively, for the current gain cutoff frequency related to only the intrinsic lumped parameter elements ( $g_{mir}$ ,  $g_{dir}$ ,  $C_{gsi}$  and  $C_{gdi}$ ) and the complete small-signal equivalent circuit (including the parasitic capacitances,  $C_{gse}$  and  $C_{gde}$ , as well as the series resistances  $R_{se}$ ,  $R_{de}$ , and  $R_{ge}$ ). It is quite interesting to see that both devices present similar intrinsic cutoff frequencies (around 400 GHz for a channel length of 60 nm) but the extrinsic cutoff

frequency,  $f_{Te}$ , of FinFET (90 GHz) is nearly twice lower than the one of the planar MOSFET (180 GHz) (Raskin, 2009), (Subramanian, 2008). This demonstrates that unfortunately the parasitic elements in the case of FinFETs are relatively more important than in the case of planar MOSFETs.

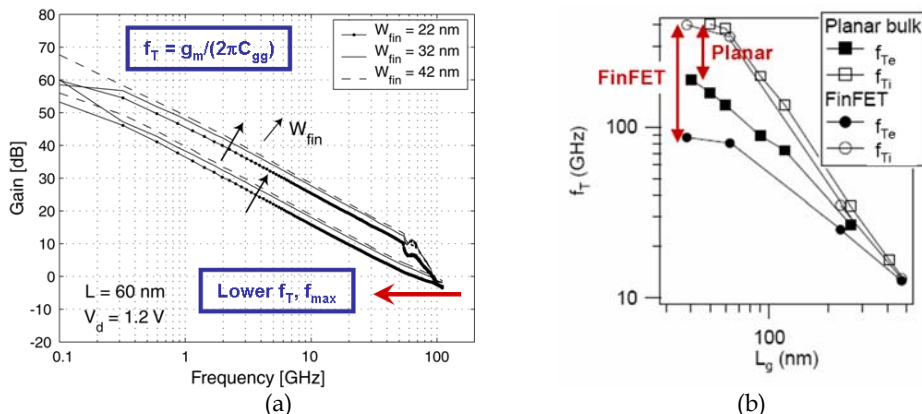


Fig. 22. (a) Current gain and maximum available power gain vs. frequency for a 60 nm-gate length FinFET for various fin widths ( $W_{fin}$ ). (b) Extracted intrinsic ( $f_{Ti}$ ) and extrinsic ( $f_{Te}$ ) current gain cutoff frequencies for a planar single gate MOSFET and a FinFET as a function of the channel length (Raskin, 2009), (Subramanian, 2008).

Again, thanks to the RF extraction techniques it was possible to analyze the relative importance of each lumped equivalent elements on the FinFET high frequency electrical behaviour. Indeed, based on a wideband analysis, the lumped small-signal equivalent circuit parameters are extracted from the measured S-parameters. Fig. 23 shows the relative impact of each parasitic parameter on the cutoff frequency ( $f_T$ , Fig. 23a) and maximum frequency of oscillation ( $f_{max}$ , Fig. 23b) in the case of a 60 nm-long FinFET. As expected from the expressions (21)-(23) the gate resistance has an important impact on  $f_{max}$  whereas  $f_T$  is unchanged. The sum of fringing capacitances  $C_{inner}$  directly linked to the FinFET three-dimensional (3-D) architecture has a huge impact on both cutoff frequencies. In fact,  $f_T$  and  $f_{max}$  drop down, respectively, by a factor of 3 and 2. Finally, the source and drain resistances as well as the parasitic capacitances related to the feed connexions outside the active area of the transistor slightly decrease both cutoff frequencies. Based on that analysis, it is quite clear that the fringing capacitances inside the active area of the FinFET are the most important limiting factor for this type of non-planar multiple gate transistor (Raskin, 2009), (Subramanian, 2008).

Finally, Fig. 24 shows the variations of the minimum noise figure  $NF_{min}$  and the available associated gain  $G_{ass}$  as a function of the DC drain current density at 10 GHz for three different channel lengths.  $G_{ass}$  is the available gain of the transistor when it is matched for minimum noise figure  $NF_{min}$ . The minimum noise figure decreases with the gate length, this variation is strongly linked to the increase of the intrinsic cutoff frequency when the gate length decreases, due to the  $g_{mi}$  increment.

In (Raskin, 2008), we demonstrated that the noise performance of FinFETs are mainly degraded by the important fringing capacitance ( $C_{gd}$ ) related to their 3-D and multifin

structure. However, a minimum noise figure of 1.35 dB could still be obtained with an associated available gain of 13.5 dB at 10 GHz for  $V_{dd} = 0.5$  V. This result is quite encouraging to bring solutions for future low-power RF systems.

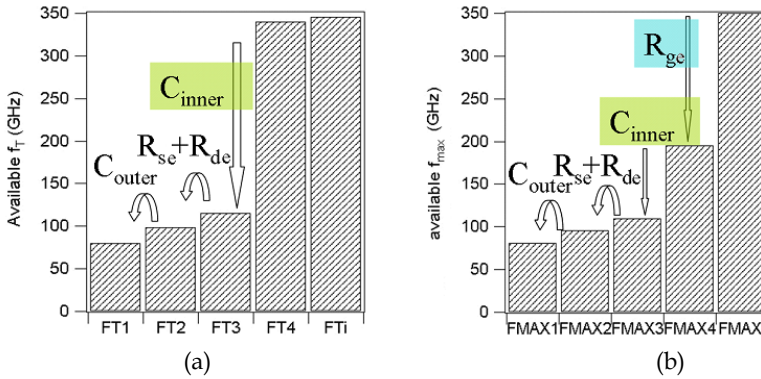


Fig. 23. Analysis of the relative impact of each lumped extrinsic parameters on (a) the cutoff frequency ( $f_T$ ) and on (b) the maximum frequency of oscillations ( $f_{max}$ ) for a 60 nm-long FinFET (Raskin, 2009), (Subramanian, 2008).

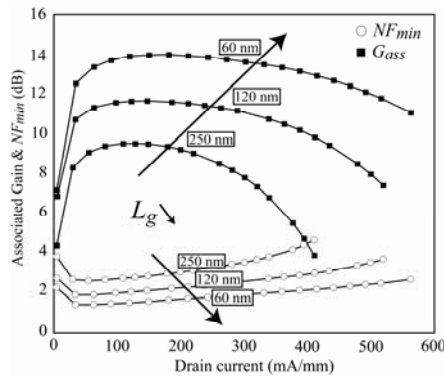


Fig. 24. Associated gain and minimum noise figure *vs.* normalized drain current at  $V_{dd} = 1$  V for FinFETs of various gate lengths, having a total width of  $68.4 \mu\text{m}$ ,  $N_{finger} = 50$  and  $W_{fin} = 32$  nm.

## 7. Conclusions

This chapter summarizes the current status of the MOSFETs for very high frequency applications. It also establishes the small-signal equivalent circuit for MOSFETs under quasi-static and non-quasi-static regimes. An efficient extraction method for the intrinsic and extrinsic lumped elements of the MOSFET electrical model has been presented and applied to various advanced MOS devices. Thanks to the development of accurate wideband characterization techniques, the static and dynamic (up to high frequencies) electrical behaviour of advanced MOSFETs can be modelled for supporting RF ICs designs but also

deeply analyzed to understand the limitations of present technologies and thus to pave ways to technological optimizations and innovations.

## 8. References

- Bracale, A.; Ferlet-Cavrois, V.; Fel, N.; Pasquet, D.; Gauthier, J. L.; Pelloie, J. L. & Du Port de Poncharra, J. (2000). A New Approach for SOI Devices Small-Signal Parameters Extraction. *Analog Integrated Circuits and Signal Processing*, vol. 25, no. 2, pp. 157, ISSN: 0925-1030.
- Cho, H. & Burk, D. E. (1991). A three-step method for de-embedding of high-frequency S-parameters measurements. *IEEE Trans. Electron Devices*, vol. 38, no. 6, pp. 1371-1375, ISSN: 0018-9383.
- Colinge, J.-P. (1991). *Silicon-on-Insulator technology: Material to VLSI*. Kluwer Academic Publishers, ISBN 0792391500, Dordrecht.
- Colinge, J.-P.; Gao, M.-H.; Romano, A.; Maes, H. & Claeys, C. (1990). Silicon-on-Insulator 'gate-all-around' MOS device, *Proc. IEEE SOS/SOI Tech. Conf.*, Oct. 2-4, pp. 137-138.
- Cristoloveanu, S. (2001). Silicon on insulator technologies and devices: From present to future. *Solid State Electron.*, vol. 45, no. 8, pp. 1403-1411, ISSN: 0038-1101.
- Dennard, R. H.; Gaensslen, F. H.; Yu, H.-N.; Rideout, V. L.; Bassouts, E. & LeBlank, A. R. (1974). Design of Ion-Implanted MOSFET's with Very Small Physical Dimensions. *IEEE J. Solid-State Cir.* vol. 9, no. 5, pp. 256-266, ISSN: 0018-9200.
- Hisamoto, D.; Lee, W.-C.; Kedzierski, J.; Takeuchi, H.; Asano, K.; Kuo, C.; Anderson, E.; King, T.-J.; Bokor, J. & Hu, C. (2000). FinFET – A self-aligned double-gate MOSFET scalable to 20 nm. *IEEE Trans. Electron Devices*, vol. 47, no. 12, pp. 2320-2325, ISSN: 0018-9383.
- Iwai, H. & Ohmi, S.-I. (2002). Silicon integrated circuit technology from past to future. *Microelectronics Reliability*, vol. 42, no.4, pp. 465-491, ISSN: 0026-2714.
- Iwai, H. (2009). Roadmap for 22 nm and beyond. *Microelectron. Eng.*, vol. 86, no. 6-7, pp. 1520-1528, ISSN: 0167-9317.
- Kahng, D. (1976). A historical perspective on the development of MOS transistors and related devices. *IEEE Trans. Electron Devices*, vol. 23, no. 7, pp. 655, ISSN: 0018-9383.
- Kilby, J. (1976). Invention of the Integrated Circuit. *IEEE Trans. Electron Devices*, vol. 23, no. 7, pp. 648-654, ISSN: 0018-9383.
- Lee, S.; Yu, H. K.; Kim, C. S.; Koo, J. G. & Nam, K. S. (1997). A novel approach to extracting small-signal model parameters of silicon MOSFET's. *IEEE Microwave and Guided Wave Letters*, vol. 7, no. 3, pp. 75, ISSN: 1051-8207.
- Lovelace, D.; Costa, J. & Camilleri, N. (1994). Extracting small-signal model parameters of silicon MOSFET transistors, *IEEE MTT-Symposium*, pp. 865-868, San Diego, CA, USA.
- Mead, C. A. (1966). Schottky barrier gate field effect transistor. *Proc. IEEE*, vol. 59, pp. 307-308, ISSN: 0018-9219.
- Pascht, A.; Grözing, M.; Wiegner, D. & Berroth, M. (2002). Small-signal and temperature noise model for MOSFET's. *IEEE Trans. on Microwave Theory and Techniques*, vol. 50, no. 8, pp. 1927, ISSN: 0018-9480.
- Raskin, J.-P. (2009). SOI technology: an opportunity for RF designers?, *8<sup>th</sup> Diagnostics & Yield Symposium*, Warsaw, Poland, June 22-24, 2009, paper #7.

- Raskin, J.-P.; Pailloucy, G.; Lederer, D.; Danneville, F.; Dambrine, G.; Decoutere, S.; Mercha, A. & Parvais, B. (2008). High Frequency Noise Performance of 60 nm gate length FinFETs, *IEEE Transaction on Electron Devices*, vol. 55, no. 10, pp. 2718-2727, ISSN: 0018-9383.
- Raskin, J.-P.; Gillon, R.; Chen, J.; Vanhoenacker-Janvier, D. & Colinge, J.-P. (1998). Accurate SOI MOSFET characterizations at microwave frequencies for device performance optimization and analog modeling, *IEEE Transaction on Electron Devices*, vol. 45, no. 5, pp. 1017-1025, ISSN: 0018-9383.
- Schwierz, F. & Liou, J. J. (2007). RF transistors: Recent developments and roadmap toward terahertz applications. *Solid-State Electronics*, vol. 51, no. 8, pp. 1079-1091, ISSN: 0038-1101.
- Schwierz, F. & Liou, J. J. (2001). Semiconductor devices for RF applications: evolution and current status. *Microelectronics Reliability*, vol. 41, no. 2, pp. 145-168, ISSN: 0026-2714.
- Shockley, W. (1976). The Path to the Conception of the Junction Transistor. *IEEE Trans. Electron Devices*, vol. 23, no. 7, pp. 597-620, ISSN: 0018-9383.
- Subramanian, V. T. (2008). Study of analog and RF performance of Multiple Gate Field Effect Transistors for future CMOS technologies, *PhD thesis*, Katholieke Universiteit Leuven, Leuven, Belgium.
- Torres-Torres, R.; Murphy-Arteaga, R. S. & Decoutere, S. (2003). MOSFET bias dependent series resistance extraction from RF measurements, *Electronics Letters*, vol. 39, no. 20, pp. 1476-1478, ISSN: 0013-5194.
- Thompson, S. E. (2005). Strained Si and the Future Direction of CMOS. *Proceedings of the 9<sup>th</sup> International Database Engineering & Application Symposium (IDEAS'05)*.
- Tinoco, J. C. & Raskin, J.-P. (2009). New RF extrinsic resistances extraction procedure for deep-submicron MOS transistors. *Accepted in International Journal of Numerical Modelling*.
- Tinoco, J. C. & Raskin, J.-P.; B (2009). Revised RF Extraction Method of Series Resistances for deep-submicron MOS Transistors: Mobility Correction. *Submitted to IEEE - Transaction on Electron Devices*, ISSN: 0018-9383.
- Tinoco, J. C. & Raskin, J.-P. (2008). RF-Extraction Methods for MOSFET Series Resistances: a fair comparison. *Proceedings of the 7<sup>th</sup> International Caribbean Conference on Devices, Circuits and Systems*, paper 64, April 28-30, 2008, Cancun, Mexico.
- Tao Chuan Lim; Bernard, E.; Rozeau, O.; Ernst, T.; Guillaumot, B.; Vulliet, N.; Buj-Dufournet, C.; Paccaud, M.; Lepilliet, S.; Dambrine, G. & Danneville, F. (2009). Analog/RF Performance of Multichannel SOI MOSFET. *IEEE Trans. on Electron Devices*, vol. 56, no. 7, 1473-1482, ISSN: 0018-9383.
- Tsividis Y. P. (1987). Operation and modelling of the MOS transistors. Mc-Graw Hill, ISBN: 978-0-07-065381-8, New York.
- Valentin R.; Dubois R.; Raskin J.-P.; Larrieu G.; Dambrine G.; Lim T.-C.; Breil N. & Danneville F. (2008). RF Small Signal Analysis of Schottky-Barrier p-MOSFET. *IEEE Trans. Electron Devices*, Vol. 55, No. 5, pp. 1192-1202, ISSN: 0018-9383.



# Development of Miniature Microwave Components by Using High Contrast Dielectrics

Elena Semouchkina  
*Michigan Technological University*  
USA

## 1. Introduction

Modern communication systems require microwave components of high performance and small size. In particular, microstrip components are always in demand because of low profile and lightweight. However, despite of many advances, microstrip component miniaturization still remains challenging. One of the ways to solve this problem is to introduce capacitive loading or stepped impedance in the device design. Capacitive loads of different types were often employed in monopole and patch antennas to reduce their dimensions (Lacey et al., 1996; Delaveaud et al., 1998). Stepped impedance (Sagava, 1997) has been also frequently used in resonators, including microstrip ones. For example, stepped impedance approach was used in the design of open-loop filter, in which the microstrip width gradually increased toward the slot that resulted in reduced size and wider upper stop-band (Hong & Lancaster, 1997). Size reduction and improvement of characteristics of an open-loop filter was also reported for filters when symmetrically located patches and open stubs were added in the design (Banciu et al., 2002). However, the efficiency of stepped impedance is limited by the maximum possible size of additional microstrip or patch sections. Another option for device miniaturization is using higher permittivity dielectric substrates. However, this approach meets serious problems, such as impedance mismatch and increased mutual coupling between components.

This Chapter describes an efficient way for microwave component miniaturization and parameter optimization by engineering device substrates with local inclusions or layers of higher permittivity dielectrics to provide local compression of the electromagnetic wave. Such approach utilizes the advantages of higher permittivity materials for miniaturization and parameter tuning, while simultaneously providing solutions for impedance matching and coupling problems. The Chapter outlines the materials and the strategy for their combination that were used to achieve miniaturization and enhanced device functions. A general concept that has been applied is to choose the optimal locations of high and low dielectric constant materials within the structure in accordance with the simulated electromagnetic field distributions at frequencies of device operation. Full-wave electromagnetic modeling has been used to develop device designs.

Low Temperature Co-fired Ceramic (LTCC) technology, which is efficient for fabrication compact multilayer microwave components and packages (Nishigaki et al., 1985), provides the means to co-process diverse ceramics in multilayer and planar architecture. Today several types of ceramic materials, such as columbites (having the relative dielectric permittivity  $K$  equal to 20), low-loss glass ceramics ( $K$  in the range 17 to 85) (Knijer et al., 1997), and Bi-pyrochlore ( $K$  between 40 to 150) (Kamba et al., 2001; Youn et al., 2002) are ready for integration in the modules based on commercial LTCC tapes with  $K$  in the range from 4.1 to 10, either by embedding into the cavities in the substrate or by thin-or thick-film technologies. These achievements in materials offer a possibility to use hybrid dielectric substrates in microwave devices. Technological solutions and examples of prototypes are presented in the Chapter, with emphasis on device modeling and design, prototype processing methods, fabrication tolerance issues, and electrical test results.

The Chapter starts from consideration of open-loop microstrip square ring band-pass filters. Such filters are known to provide elliptical function response notable due to narrow pass band and low insertion loss (Hong & Lancaster, 1995). The Chapter demonstrates that local wave compression due to strategic capacitive load placement enables altering the center and attenuation pole frequencies, the shape and width of the pass-band, and input impedance of the filter by modification of selected resonant modes. Capacitive loading with higher permittivity dielectrics is shown to be very efficient in decreasing the filter size. Different possibilities for designing narrow-band filters comprised of capacitively coupled resonators are demonstrated and prototypes of highly miniaturized filters are described. The examples of filters fabricated by using the LTCC-technology with dimensions decreased by a factor of four compared to unloaded devices are presented, in particular, a band-pass filter with the dimensions of  $(4.1 \times 5.6)$  mm<sup>2</sup> for the center frequency of 2.45 GHz.

Novel design opportunities for microstrip band-pass filters built on layered substrates of ceramic dielectrics having different permittivities are then demonstrated on the example of a filter for UHF band. A miniature LTCC-filter of  $(3.6 \times 2.8)$  mm<sup>2</sup> size for the center frequency of 750 MHz, *i.e.*, the frequency chosen for TV broadcasting to cell-phones in Europe, is described.

Finally, the Chapter presents a novel ultra-compact microstrip patch antenna with circular polarization of radiation built on the substrate composed of high contrast dielectrics. The engineered design targeted miniaturization and desired electric characteristics, mitigation of surface wave leakage, recovering of fringing fields and ease of fabrication. Prototype devices made from commercially available high permittivity powders and standard LTCC systems are described.

## 2. Miniaturization of Microstrip Filters Based on Open-Loop Ring Resonators

### 2.1 General Design Approach

Here we describe the strategy for the placement capacitive loads in a microstrip resonator to modify selected resonance modes and monitor transmission characteristics. First, open-loop microstrip resonators with capacitive loads placed at different locations are modeled and field distributions at resonance frequencies, as well as transmission spectra of the resonators, are simulated (Semouchkina et al., 2003).

Fig. 1 shows the geometries of several single-section microstrip open-loop square ring resonators: (a) without any loading so that the structure is composed of only the matrix

dielectric with the relative permittivity  $K_1$  and (b-d) with capacitive loads utilizing high permittivity dielectrics ( $K_2$  and  $K_3$ ) placed at three different locations: (b) near the slot, (c) in the middle of the front rib and (d) at the side ribs.

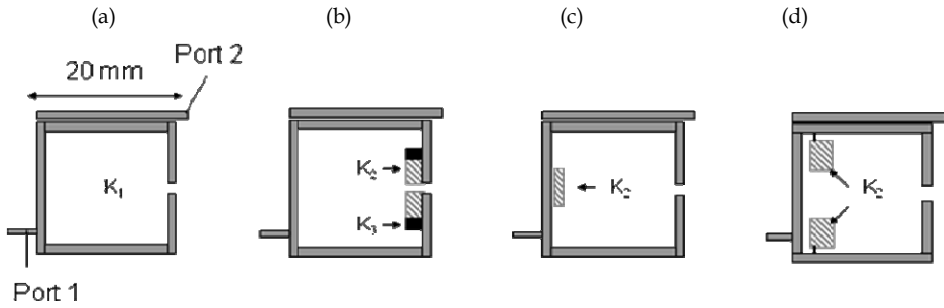


Fig. 1. Schematics of open-loop square ring resonators: (a) without capacitive loading, (b) with loading near the ring slot, (c) with loading in the middle of the front rib, and (d) with loading at the side ribs.

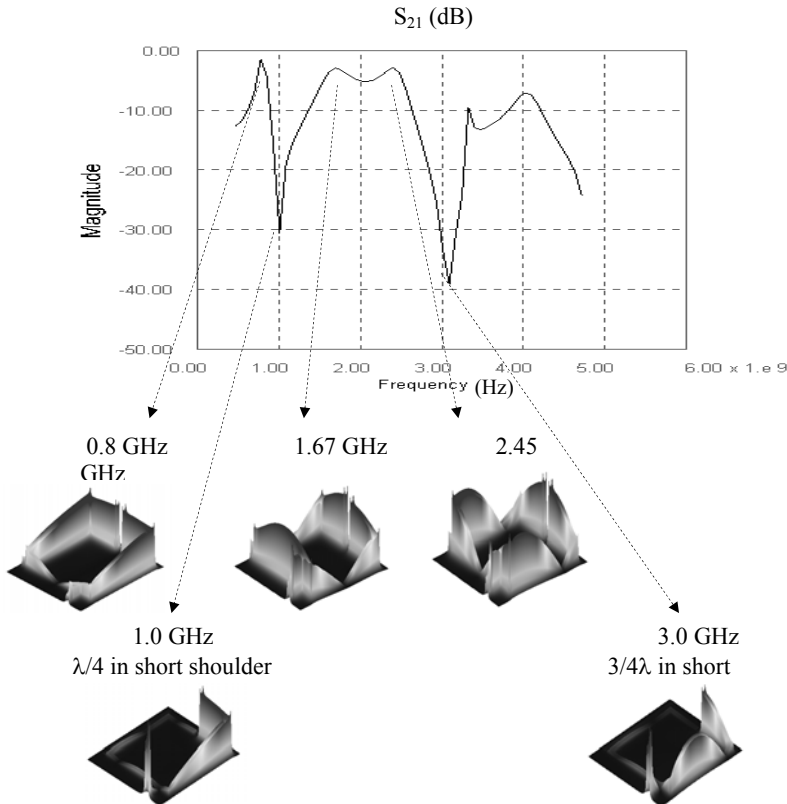


Fig. 2.  $S_{21}$  spectrum of open-loop square ring resonator depicted in Fig. 1a, and standing wave patterns corresponding to the peaks and attenuation poles of the spectrum.

The substrate has a thickness of 0.66 mm and a dielectric constant of 9; the width of the microstrips is 1 mm. The loads are either stepped impedance sections of a patch type placed on top of a uniform substrate or metal patches placed above the inclusions of higher-K inside the low-K substrate (as shown in Figs. 1b-d). In the case depicted in Fig. 1b, dielectric inclusions consist of two parts with different K values, with the higher-K ( $K_2$ ) sections placed closer to the slot than the lower-K ( $K_3$ ) sections. The resonator shown in Fig. 1d has patch sections separated from the side ribs by a 0.8 mm gap, and connected with them by 0.4 mm wide microstrips. An output microstrip line is added to the rings in order to model the coupling with the next section and to calculate the  $S_{21}$  spectrum.

The Finite-Difference Time Domain (FDTD) simulations have been used to simulate transmission and reflection characteristics of the resonators, as well as field distributions in the resonator substrates at different frequencies.

The simulated  $S_{21}$  spectrum of the unloaded resonator (see Fig. 1a) is presented in Fig. 2, which also shows the standing wave patterns of the normal electric field component at the frequencies corresponding to the  $\lambda/4$ ,  $\lambda/2$  mode and  $3/4\lambda$  resonant modes, respectively. It is also seen in Fig. 2 that the first attenuation pole in the  $S_{21}$  spectrum at 1 GHz corresponds to the  $\lambda/4$  resonance in the right shoulder of the square ring between the input feedline and the gap, while the second pole at 3 GHz is associated with the  $3/4\lambda$  resonance in the same shoulder.

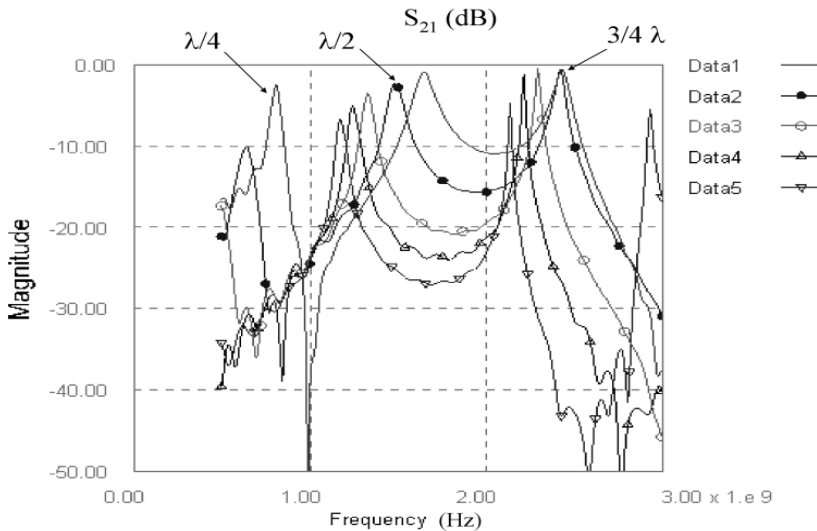


Fig. 3.  $S_{21}$  spectra for resonators: (Data1) without loading and (Data2-5) with capacitive load located near the slot (Fig. 1b), (Data2)-loading by metal patches with matrix dielectric ( $K_1$ ), (Data3)-loading by patches above inclusions with  $K_2=K_3=21$ , (Data4)-loading by patches above inclusions with  $K_2=45$  and  $K_3=21$ , and (Data5)-loading by patches above inclusions with  $K_2=90$  and  $K_3=21$ .

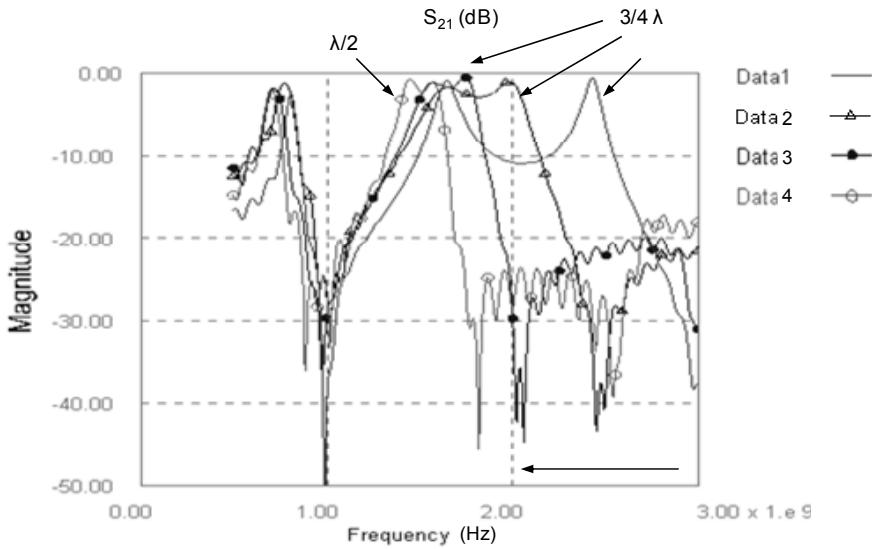


Fig. 4.  $S_{21}$  spectra for resonators: (Data1) without loading and (Data2-5) with capacitive load located at the side ribs (Fig. 1d); (Data2)-loading by metal patches; (Data3)-loading by patches above inclusions with  $K=21$ ; (Data4)-loading by patches above inclusions with  $K=30$

(a)

(b)

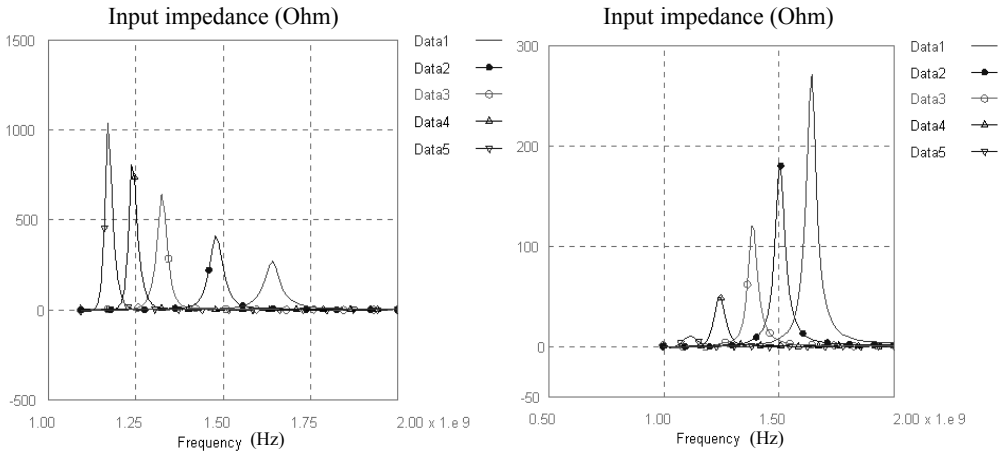


Fig. 5. Input impedance spectra for resonators with capacitive load located: (a) near the slot (Fig. 1b), area of each patch-15 mm<sup>2</sup>, (Data1-Data5) correspond to the same loading as in Fig. 3; and (b) in the middle of the front rib (Fig. 1c) with a patch area of 12 mm<sup>2</sup>; (Data1)-unloaded filters, (Data2)-filter loaded with capacitor patch with matrix dielectric ( $K_1=9$ ), (Data3)-capacitor patch with  $K_2=21$ , (Data4)-capacitor patch with  $K_2=45$ , and (Data5)-capacitor patch with  $K_2=90$ .

In order to decrease the resonant frequency of a particular mode of the microstrip resonator, capacitive loads are placed in a position of amplitude maximum of electric field for this mode. Conversely, capacitive load placed at the node of electric field standing wave of a resonant mode does not affect the resonant frequency of this mode. Thus resonant frequencies and transmission zeros can be independently manipulated by selectively loading high-K dielectrics within a low-K matrix structure. For the loading of the type shown in Fig. 1b, the resonant frequencies of all the modes depicted in Fig. 2 decrease, which results in shifting of the entire  $S_{21}$  spectrum to lower frequency (Fig. 3). Therefore, this type of loading can be used for the device miniaturization.

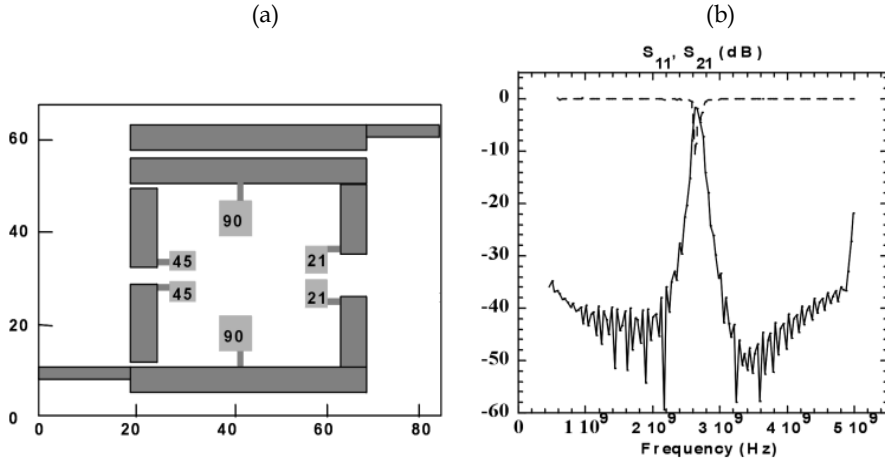


Fig. 6. (a) Geometry (dimensions are given in numbers of cells, the size of one cell is 0.2 mm) and (b)  $S_{11}$  (dotted curve) and  $S_{21}$  (solid curve) spectra of the filter with the substrate of  $K=9$  loaded by a combination of dielectric inclusions with  $K=21, 45$  and  $90$ .

When the load is located in the middle of the front rib (Fig. 1c), it affects the  $\lambda/2$  and  $\lambda$  modes in a similar way but does not alter the  $\lambda/4$  and  $3/4\lambda$  modes. Quite opposite, the loads placed at the locations of standing wave antinodes for the  $3/4\lambda$  mode at the side ribs of the filter (Fig. 1d) strongly affect this mode and the mode responsible for the second attenuation pole, while producing negligible effect on the  $\lambda/4$  and  $\lambda/2$  modes (compare field patterns in Fig. 2). As the result, strong shifts of the  $3/4\lambda$  peak and of the second attenuation pole can be observed in the  $S_{21}$  spectrum (Fig. 4). These data illustrate the possibility to modify the widths of the pass- and stop-bands, as well as their shapes, by affecting only selected modes of the spectrum through using proper load location.

Fig. 5 demonstrates changes in input impedance of the resonator due to the loading: input impedance increases for the loading shown in Fig. 1b (see Fig. 5a), while its behavior is opposite (Fig. 5b) for the loading shown in Fig. 1c. It points at the possibility to match impedance by varying the location and the permittivity of the loads.

It is worth noting that capacitive loads connected precisely to the points where the resonant mode has electric field maxima (see Fig. 1d), were found to be more efficient in modifying the resonant frequency of the mode and the input impedance, than adding stepped impedance sections in the areas of high electric fields (Figs. 1b, c).

By using the described strategy, a combination of different loads of higher permittivity than that of the substrate, with their placement governed by the simulated field distribution, can be used to design a filter with reduced size and optimized characteristics. An example of how the loading of initial open-loop square-ring resonator (Fig. 1a) can be optimized to provide a narrow pass band at 2.45 GHz is presented below. Instead of the passband of  $\lambda/4$  mode of the initial resonator, which is not accompanied by a low frequency attenuation pole (Fig. 2), the pass band between 1.5 GHz and 2.5 GHz, which results from the  $\lambda/2$  and  $3/4\lambda$  modes, can be used to form two attenuation poles in the transmission spectrum. Fig. 6a depicts the schematic of a one-section filter with the relative substrate permittivity of 9, in which the size and the permittivity of the loads placed at the front and back ribs were adjusted to provide the center frequency of 2.45 GHz and to match input impedance, the loads at the side ribs were used to shift the  $3/4\lambda$  mode closer to the  $\lambda/2$  mode, and additional slots in the microstrip ring were introduced to suppress undesirable modes. The size of this filter is  $(10 \times 10)$  mm<sup>2</sup> compared to  $(20 \times 20)$  mm<sup>2</sup> of an unloaded resonator (Fig. 1a), and the  $S_{21}$  spectrum (Fig. 6b) exhibits a narrow pass band.

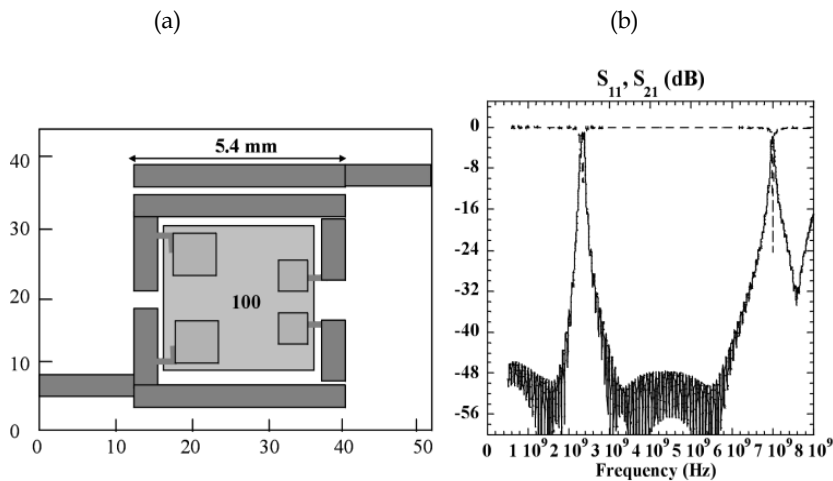


Fig. 7. (a) Geometry and (b)  $S_{11}$  (dotted curve) and  $S_{21}$  (solid curve) spectra of the filter with the substrate of  $K=7.8$  and thickness of 660 microns loaded by a dielectric plug with  $K=100$ .

Combining loads of different permittivity offers potentially many degrees of freedom in shaping the pass-band, however, it is technologically difficult to reproduce. The design example presented in Fig. 7a demonstrates that efficient pass-band shaping and size reduction of the filter could be achieved even when only one type of high- $K$  dielectric is used for loading. In this design, one plug of  $K=100$  is inserted in the substrate of  $K=7.8$  within the microstrip loop. Metal patches and parts of the connecting strips are located at the surface of the plug to provide local loading. The simulated S-parameter spectra of this filter show no spurious modes up to frequencies three times higher than the center one, and the pass-band of 3.6% (Fig. 7b), while its area is decreased from  $(20 \times 20)$  mm<sup>2</sup> for an unloaded resonator down to  $(5.4 \times 5.4)$  mm<sup>2</sup>.

## 2.2 Realization of Filters with Local Loading by High-Permittivity Materials

For practical realization of filters with hybrid dielectrics, either high-K superstrate layers over low-K substrates or high-K plugs embedded into low-K substrates could be implemented (Semouchkina et. al., 2004; Semouchkina et. al., 2005). The examples below describe the development of designs and approaches for the fabrication of a miniature microstrip filter for 2.45 GHz center frequency with a narrow band and low insertion loss in the pass-band.

In the design depicted in Fig. 8a, a square-shaped superstrate layer with the area slightly less than the area inside the ring is placed on top of the substrate. Metal patches located at the top and the bottom of the superstrate serve as the electrodes of the loads, and the bottom electrodes are connected to the ground through vias in the substrate. The substrate thickness is 660 microns, and its permittivity is 7.8. The superstrate is 55 microns thick and has the permittivity of 100. The size and the locations of the electrodes of the loads are adjusted to provide the central frequency of the filter equal to 2.45 GHz. To improve the pass-band characteristics, two open-loop resonators with 3.75 mm side are combined, and the coupling gap between them is optimized to provide low return loss level and symmetric slopes of the  $S_{21}$  spectrum Fig. 8b).

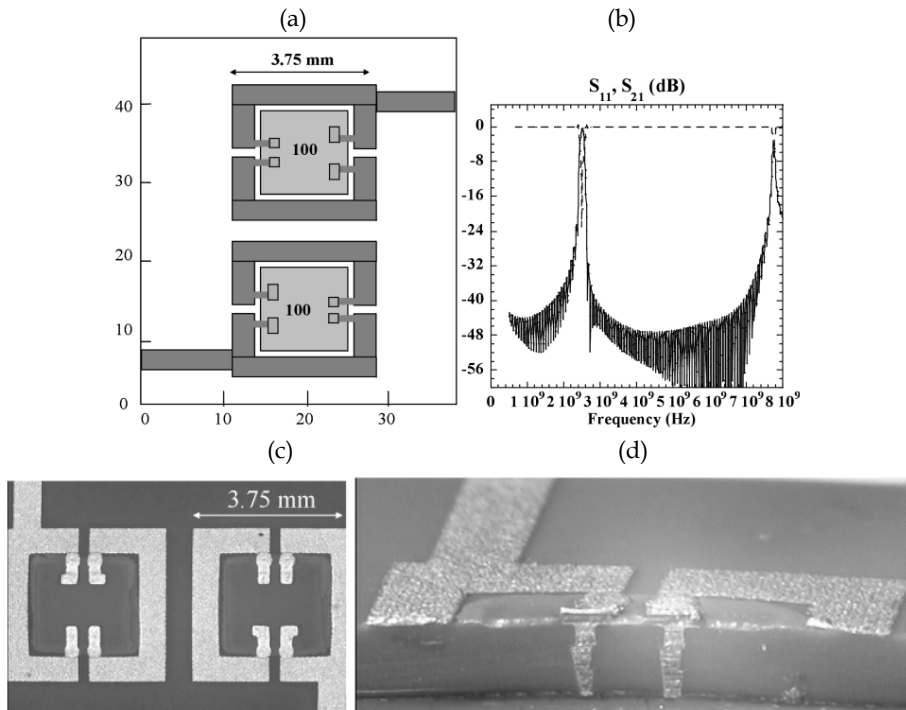


Fig. 8. (a) Geometry and (b)  $S_{11}$  (dotted curve) and  $S_{21}$  (solid curve) spectra of the filter with the substrate of  $K=7.8$  and thickness of 660 microns loaded by superstrate with  $K=100$  and thickness of 55 microns; (c) top and (d) cross sectional views on the prototype with the superstrate layer.



The latter design was reproduced with the substrate made of three layers of DuPont 951 commercial LTCC tape ( $K=7.8$ ). To make via-connection between the bottom electrodes of the loads and the ground, the tapes were punched with a 150-micron punch and then the holes were filled with silver via fill. The ground plane was printed on the backside of the lower layer with filled vias using commercial silver ink. Bottom electrodes of the loads and microstrip pattern were printed on the top layer using commercial silver ink. The superstrate was then printed on this electroded tape using Bismuth Pyroclor ink, and the top electrodes of the loads were printed on top of the superstrate using silver ink. Bottom layer with ground plane and filled vias, middle layer with filled vias and top layer with electroded superstrate were stacked, collated and laminated. Filters were then singulated and fired to 875°C peak temperature for 30-minute dwell time. Top and cross-section views of the prototype are shown in Figs. 8c, d. However, in the described prototype, the expected value of dielectric constant of 100 was not achieved for the printed superstrate apparently due to the interaction between the superstrate material and the conducting ink. As the result, the measured resonance frequency of the filter exceeded the targeted 2.45 GHz and corresponded to a superstrate having the dielectric constant of 49 that was confirmed by the independent measurements on fabricated capacitors.

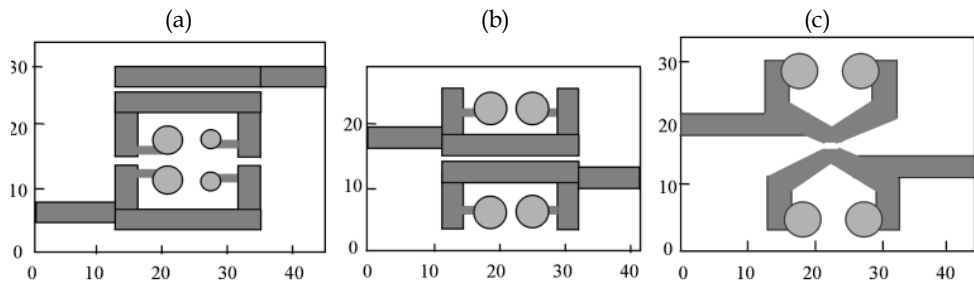


Fig. 9. Geometries of filters with substrates of  $K=7.8$  and high- $K$  plugs of  $K=74$  immersed in the holes punched in the substrate.

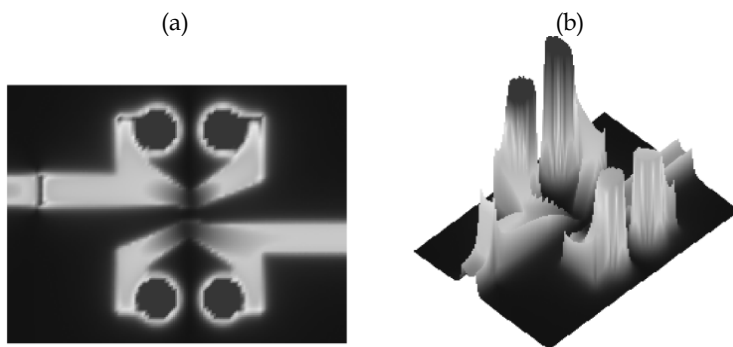


Fig. 10. (a) Contour plot and (b) 3D distribution of the electric field in the resonator depicted in Fig. 9c at the frequency 2.45 GHz.

Therefore, another fabrication approach, i.e. to embed plugs made of preliminary prepared high-K ceramic tape into a low-K substrate, has also been applied. For this purpose, three layers of DuPont 951 LTCC tape with dielectric permittivity of 7.8 and the thickness of 250 microns each have been used as the substrate material, while the 250 microns thick Bismuth Zinc Tantalate (BZT) LTCC tape with  $K=74$  and  $Q\approx 400$  (at 2.45 GHz) (Kamba et al., 2001; Youn et al., 2002) - as the material for plugs to be inserted in the top substrate layer. Fig. 9 illustrates the transformation of the filter design in the process of its adjustment to the fabrication opportunities.

Fig. 9a shows the initial design of a one-section open-loop resonator utilizing four round high-K pugs of 1.06 mm diameter with various diameters of the plug electrodes that provides the resonance frequency of 2.45 GHz. In order to simplify the processes of plug insertion and metallization, in the "back-to-back" design depicted in Fig. 9b, one half of the ring is flipped over and four equal plugs with completely metallized top and bottom surfaces are used. This design provides a stronger magnetic coupling between the half-rings, in difference from the design in Fig. 9a, in which the half-rings are coupled primarily via electric field in the coupling gaps.

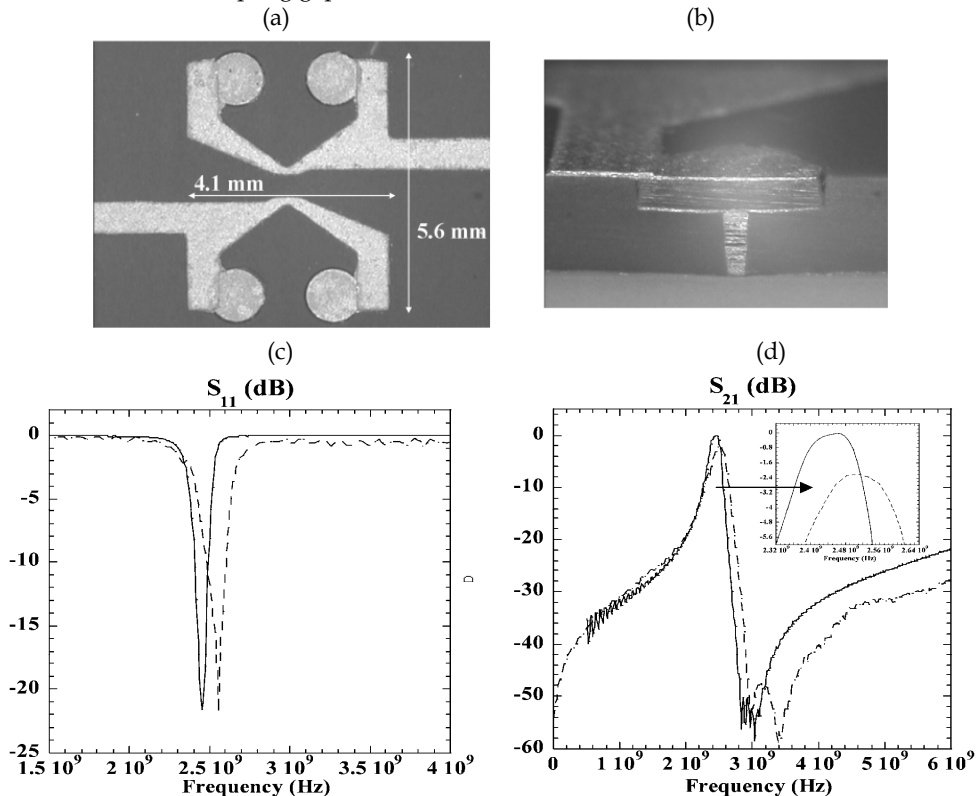


Fig. 11. (a) Top and (b) cross sectional views on the prototype with high-K plugs in the low-K substrate; and simulated (solid curves) and experimentally measured (dotted curves) (c)  $S_{11}$  and (d)  $S_{21}$  of the prototype.

Equal size of loading capacitors (Fig. 9b), however, does not provide sufficient degrees of freedom in optimizing the resonator characteristics. Therefore, in the final design shown in Fig. 9c, the shapes of the microstrips and the locations of the feedlines have been additionally adjusted. Fig. 10 shows the distribution of electric field normal component in the plane located below the substrate surface at the resonant frequency of 2.45 GHz, which points at half-wavelength resonance in the two half-rings at this frequency. The presented design consists of two resonators and is a two-pole (second order) filter with an asymmetric characteristic. Asymmetric insertion loss responses with one attenuation zero are often observed for multi-pole filters with one way for signal propagation, when none of the resonators is bypassed or cross-coupled (Amary et al., 2003). A second attenuation zero in such filter could be added by introduction cross-coupling in the filter design.

The prototype fabrication started with preparation vias by punching holes with the diameter of 150 microns in the two bottom substrate layers, and filling them with silver via fill ink. Then the top layer was punched using a 1.25 mm diameter punch. The three substrate layers were laminated in a platen press to form a “tray” for subsequent plug insertion, and PEOX „glue” was used to promote layer adhesion (Wilcox & Oliver, 2002). This lamination technique has been employed so that hole integrity could be maintained. BZT tape was printed on both bottom and top sides with silver ink and then punched using a 1.25mm punch. The resulting metallized BZT plugs were then pressed into slots formed in the LTCC tray. The filled tray was laminated and microstrip pattern was then printed using silver ink. Resonators were singulated and fired to peak temperature of 850°C for 30 minutes holding time. Air dried silver (Premetek 1228) was painted on the backs of the samples to form the ground plane.

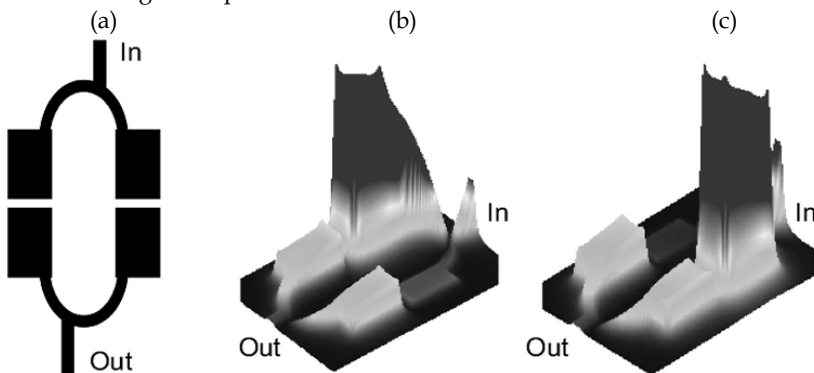


Fig. 12. (a) Schematic of the filter with double-coupled „horse-shoe” resonators and standing wave pattern of the normal electric field component in the vicinity of (b) the frequency of the lower transmission zero and (c) the frequency of the upper transmission zero.

Figs. 11a, b present top and cross-sectional views of the fabricated prototype. Inclusion of high permittivity dielectric, as well as a via connecting the bottom electrode of the plug with the ground, are clearly seen. Figs. 11c, d compare the simulated and measured S-parameters of the prototype. The achieved return loss level in the pass band agrees with the predicted value (-22 dB), which indicates that the input impedance of the prototype has been matched. The measured value of the center frequency is 2.50 GHz, which, in comparison with the simulated value of 2.45 GHz, corresponds to an error of 2 %. The measured insertion loss

level of  $(-2.23 \text{ dB})$  demonstrates that losses introduced by high-K plug insertion are small. It is worth noting that the main circuitry of the device is still located at the low-K substrate that decreases the influence of possible losses connected to high-K materials. The dimensions of the fabricated prototype are just  $(4.1 \times 5.6) \text{ mm}^2$ .

In real production environment, the tolerances on the material properties and the manufacturing process could require tuning of the narrow filter band, which depends on the capacitance of the inserted high-K loads. Taking into account that upper electrodes of the loads are located at the surface, this capacitance could be tuned by using fine laser trimming of the top electrodes. Metal removal with 50 microns accuracy will allow for resonant frequency shift by about 30 MHz at each trimming step.

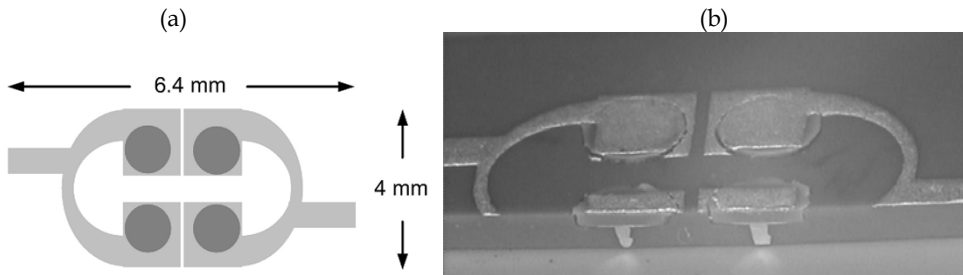


Fig. 13. (a) Layout of the filter loaded by high-permittivity plugs; and (b) cross-sectional view of the filter prototype showing high-permittivity dielectric plugs inserted into a commercial LTCC matrix. Vias connect metalized plugs to the ground plane at the bottom of the structure.

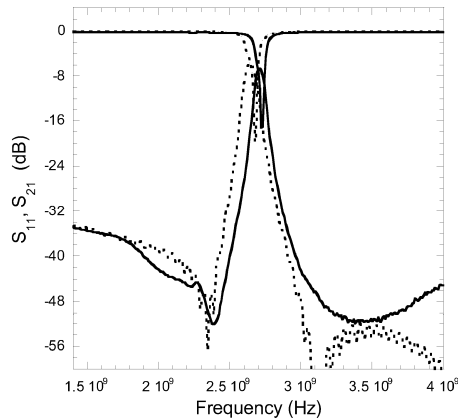


Fig. 14. Comparison of the measured  $S_{11}$  and  $S_{21}$  of the filter prototype depicted in Fig. 13b (solid curves) with the simulated ones (dashed curves).

In order to provide a second attenuation zero in the insertion loss response of the filter, a double-coupled design consisting of "horse-shoe" resonators has been developed (Hennings et al., 2003; Hennings et al., 2004; Hennings et al., 2006). Fig. 12 presents the schematic of such filter and standing wave patterns of electric field in the substrate at the frequencies of

the transmission zeros. As seen from Figs. 12 b, c; two quarter-wavelength resonances take place in either one of the shoulders of the input resonator, while the field amplitudes drop down to almost zero in the other shoulder.

To miniaturize the filter shown in Fig. 12a with the dimensions (7.68 x 12.61) mm<sup>2</sup>, a design having cylindrical plugs of high-permittivity dielectric located in the LTCC substrate underneath rectangular patches has been developed (Semouchkina et. al., 2005b). Fig. 13a presents the layout of this filter with the size of (4.0 x 6.4) mm<sup>2</sup>, while Fig. 13b shows the cross-sectional view of the prototype fabricated using the described above LTCC based approach and the same materials. The presented in Fig. 14 simulated and measured S-parameter spectra demonstrate that the filter's pass-band has two attenuation zeros. Thus dimensions of the filter have been decreased by a factor of 4 compared to unloaded one by using local insertion of higher permittivity dielectrics.

### 3. Development of Miniature Filters for TV Broadcasting Band by Using Layered Substrates of Mixed Ceramic Dielectrics

#### 3.1 Novel Filter Design with Double-Coupled Stepped Impedance Resonators

In many cases, there is a need for such filter transfer functions, which include a number of transmission zeroes. In particular, the zeroes are used to sharpen the transitions between the pass-band and the rejection-band regions. The transmission zeroes can be realized by providing multiple signal paths in cross-coupled structures (Hong & Lancaster, 1996) or adding a signal bypass between input- and output-ports (Amari, 2001). Alternative methods are described by (Hennings et. al., 2006; Belyaev et. el., 2001). Multilayer LTCC-filters described in literature are mainly designed for WLAN applications, e. g. (Lin et. al., 2006), and have rather broad bandwidth. In some cases, they suffer from low out-of-band rejection or exhibit unwanted spurious resonances. Moreover, several LTCC-filters succumb to high complexity and contain a big number of metallized LTCC-layers. In order to simplify the fabrication process, the quantity of metallized layers, vias, and dielectric layers should be kept low.

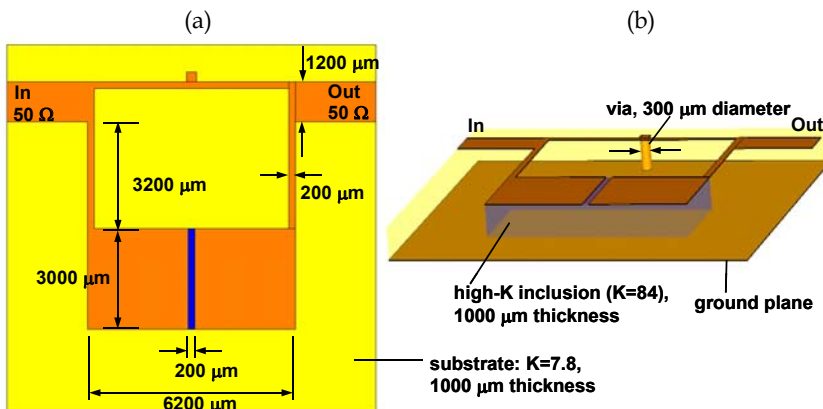


Fig. 15. Microstrip filter using mixed dielectrics: (a) top view, (b) perspective view.

Here, the development of a miniature narrow-band LTCC-filter with high performance but low degree of complexity is described (Hennings et. al., 2007). In order to retain small dimensions, only two-pole filters built of two quarter-wavelength resonators have been designed. The center frequency of the pass-band is 750 MHz, *i.e.*, the frequency chosen for TV broadcasting to cell-phones in Europe. It is worth noting that a DVB-H network is expected to be soon provided in the USA by using frequencies near 700 MHz. Therefore, small-size high-quality filters for UHF band are expected to get high priority.

The design of the filter employs stepped impedance microstrip resonators loaded by plugs of high permittivity underneath wide metal patches. Fig. 15a depicts the initial design consisting of two end-coupled quarter-wavelength stepped impedance resonators placed in parallel normally to the feed lines. A high-K plug is shown inserted in a low permittivity matrix in Fig. 15b. Simulations have been performed for dielectric constants of the matrix of 7.8, and of the plug of 84. The thickness of the plug was the same as one of the matrix, *i.e.*, 1 mm. The filter was designed to be mounted on an additional substrate, or, if necessary, another low-K layer could be placed on top of the structure to ensure material adhesion.

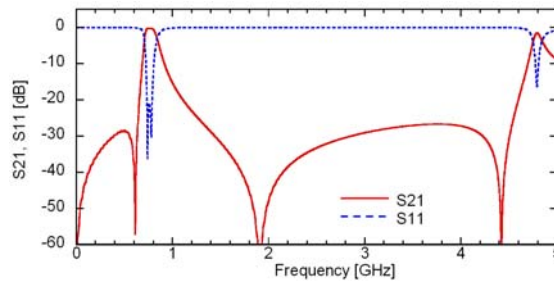


Fig. 16. Simulated S-parameters for the filter shown in Fig. 15.

The via seen in Fig.15b has the diameter of 300 microns and is used to connect the circuit to ground and to serve as shunt-inductance, providing for inductive coupling between the resonators, while capacitive coupling is achieved through the narrow gap (200 microns) between the patches of the two resonators. Without the via, the two quarter-wavelength resonators would merge to an open loop half wavelength resonator which could support only a single fundamental resonance (Semouchkina, 2003), while with the via, two fundamental modes could be supported in the filter. In comparison with filters based on open loop resonators (Semouchkina et. al., 2003; Semouchkina et. al, 2005a), the new design allows for obtaining the desired two-pole filter characteristics at more compact filter dimensions.

The use of mixed inter-resonator coupling is advantageous due to desirable possibility for capacitive and inductive coupling to compensate each other (Belyaev et. al, 2001; Hong & Lancaster, 2001), and to allow for obtaining transmission zeroes at frequencies located closely to the filter pass-band edge. Such compensation allows one to achieve a weak overall coupling coefficient that is required for a narrow band-width. Depending on the dimensions of the gap and the via, either capacitive or inductive coupling is dominant at center frequency. At the given in Fig. 15 dimensions, capacitive coupling was found to exceed inductive coupling, although the latter was meaningful. A design with pure capacitive coupling would have required a much wider gap between the patches to make coupling weak at employment the same high-K plug located underneath the coupled patches of the resonators.

The area consumption of the filter is  $(6.2 \times 7.4) \text{ mm}^2 = 45.88 \text{ mm}^2$  for the dimensions scaled for the center frequency of 0.75 GHz. The simulated S-parameter spectra of the novel filter design are displayed in Fig. 16. As seen from the figure, the filter characteristics look very promising and could be additionally improved at careful balance of capacitive and inductive coupling. In fact, lower transmission zero is observed very close to the pass-band edge. In modified filters with dominant inductive coupling other transmission zero was similarly close to the opposite pass-band edge.

However, since both the electric and the magnetic coupling coefficients in the described above design are relatively high, the weak overall coupling coefficient appears to be sensitive to the parameter choice. In addition, further miniaturization requires increased capacitive loading of the resonators, and, so, thinner plugs of the high-K material. As processing of the plugs is relatively complicated, a modified design is presented below, which has a thin planar layer of high permittivity material inserted in the LTCC matrix instead of local plugs and multilevel metallization to employ this layer for capacitive loading.

### 3.2 Realization of Multilayer LTCC Filters

Figs. 17a through 17d illustrate the filter design based on three-layer LTCC sandwich-like substrate (low-K, high-K, low-K) having  $3 \times 90$  microns height.

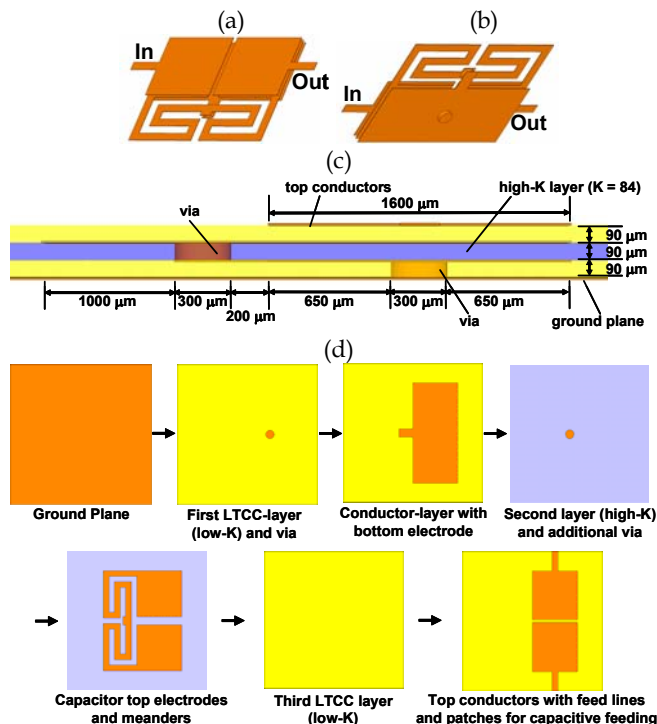


Fig. 17. Filter design: (a) and (b) perspective views with hidden substrate and ground plane, (c) cross sectional view, and (d) design schematics (top view).

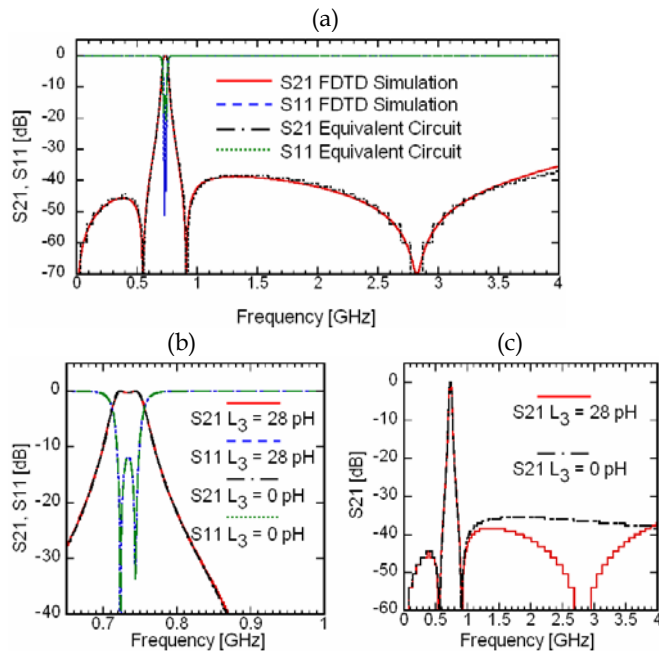


Fig. 18. (a) Comparison of simulated S-parameters for filter shown in Fig. 17 and calculated S-parameters for equivalent circuit. (b), (c) S-parameter spectra for the equivalent circuit in case of  $L_3 = 0$  and  $L_3 = 28$  pH.

In the new design, capacitively loaded low-impedance sections of two resonators are replaced by capacitors formed by using interlayer metallization. These capacitors have common bottom electrode, which is connected to ground plane by an additional via. Instead of straight microstrips used in the design depicted in Fig. 15, the space-saving meander lines are employed to connect top electrodes of the capacitors to via providing for inductive inter-resonator coupling. In the new design, the gap between the capacitors of two resonators is increased, and, therefore, the contribution of capacitive coupling is essentially decreased in comparison with the previous design. The resonators are fed capacitively (without a direct ohmic contact to feedlines) by using additional patches located just above the resonator capacitors on the upper substrate surface. The gap between these top patches is quite narrow to enable capacitive bypass path, which is known to cause a pair of transmission zeroes if applied to two inductively coupled resonators. This implementation with quasi-lumped elements allows for scaling the dimensions down to  $(3.6 \times 2.8) \text{ mm}^2 = 10.08 \text{ mm}^2$  at the center frequency of 0.735 GHz.

As seen in Fig. 18a, excellent characteristics with transmission zeroes near the pass-band edges have been obtained in FDTD simulations. The 3-dB bandwidth is as low as 6 %, and spurious bands occur at frequencies more than 7.9 times higher than the center frequency.

In order to get a deeper insight into the filter performance it was modeled by a lumped element equivalent circuit shown in Fig. 19. Here, the two resonator capacitors are represented by elements  $C_1$ , the capacitance between their common bottom electrode and



the ground plane - by element  $C_3$ , whereas  $L_3$  is related to the inductance of the via connecting this electrode to ground. The elements  $C_2$  describe capacitive feeding,  $C_4$  - capacitive bypass, and  $L_2$  and  $C_5$  - inductive and capacitive inter-resonator coupling. The meanders are represented by inductors  $L_1$ , and their associated parasitic capacitances - by elements  $C_6$ . The element values have been first roughly approximated and then gradually changed up/down to the levels providing for better coincidence of the calculated filter characteristics to the results of the FDTD simulations. The same filter characteristics could be realized by various combinations of element values, in particular, for an equivalent contour with neglected  $C_6$  and values of  $C_1$  and  $C_2$  corresponding to ideal parallel plate capacitors. We have used the following values of these and other elements:  $C_1 = 21.82$  pF,  $C_2 = 2.03$  pF,  $C_3 = 4.43$  pF,  $C_4 = 30$  fF,  $C_5 = 370$  fF,  $C_6 = 0$ ,  $L_1 = 1.86$  nH,  $L_2 = 115$  pH,  $L_3 = 28$  pH. As seen in Fig. 18a, the chosen values allowed for correct describing of the bandwidth, ripples, and the rejection performance of the filters. It means that physical design of the filter was close to an ideal lumped element circuit within the considered frequency range, while the impact of parasitic elements could be compensated by appropriate parameter choice. Introduction of  $C_6$  values in consideration has shown that the impact of these parasitics was relatively small. They could slightly reduce the resonant frequency and increase the external Q factor. The element  $C_5$  compensated only a small part of the inductive inter-resonator coupling. The capacitor  $C_3$  was found to be negligible. It had only a minor impact on the frequency of the third transmission zero at 2.82 GHz, which was found to be related to the presence of the inductor  $L_3$  (representing the via).

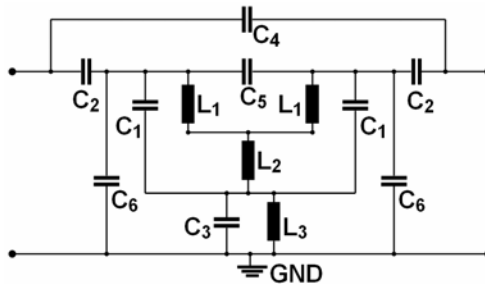


Fig. 19. Equivalent circuit of the Filter shown in Fig. 17.

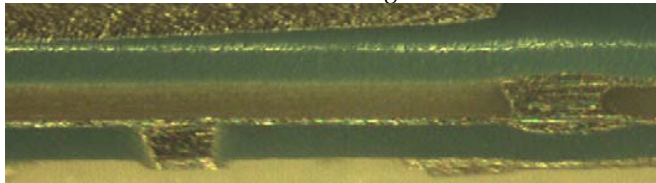


Fig. 20. Cross-section of fabricated sample with high K layer and vias.

Comparison of the filter characteristics obtained at different values of  $L_3$  is shown in Figs. 18b and 18c. As seen from the figures, the element  $L_3$  is useful for enhancement of the rejection band performance without affecting the pass-band characteristics. This holds as long as  $L_3$  does not exceed the order of magnitude of the value based on physical estimations (28 pH). It is also worth mentioning that the inductor  $L_3$  does not cause any

significant loss contribution, even if this element has a very low  $Q$ -factor. Hence, it is not critical. However, the presence of the elements  $C_3$  and  $L_3$  in the circuit causes an appearance of a spurious band at frequencies beyond 13 GHz. If this is undesirable, while the enhanced rejection at about 2.8 GHz is not necessary, then the filter design could be modified through complete removal of both the via and the lower LTCC layer.

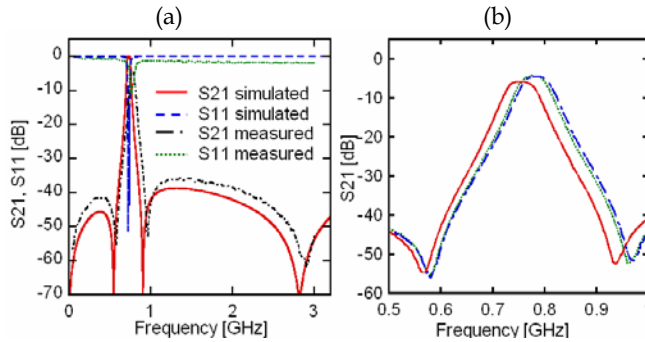


Fig. 21. (a) Measured and simulated S-parameter spectra in comparison. (b) Measured S21-spectra of three different samples.

The prototypes have been fabricated by using the layout given in Fig. 17. Metallization was provided by silver inks designed for LTCC technology. The upper and lower layers were made by using the LTCC DuPont 951 tape (the permittivity  $K=7.8$ ). The middle layer was made by using the BZT tape ( $K=60-84$ ). First, vias were punched and filled in layer 1 (low  $K$ ), and layer 2 (high  $K$ ). Then, the ground plane was printed on the backside of layer 1 and dried at  $80^\circ\text{C}$ . Next, the rectangle pattern was printed on topside of layer 1. After it, the meander including pattern was printed on backside of layer 3. Finally two patches with feed lines were printed on topside of layer 3. The layers were aligned and laminated using 3000 psi at  $70^\circ\text{C}$  for 15 minutes. Filters were singulated and fired at  $850^\circ\text{C}$  for 30 minutes dwell time. Fig. 20 presents the cross-section of one of the prototypes.

The results of measurements in comparison with the results of simulations are shown for one of the samples in Fig. 21a. The S-parameter spectra of the prototype agree well with the simulated results. Fig. 21b shows the measured results for three different samples, which demonstrate good repeatability of the fabrication process.

The described data confirm that employment of quarter wavelength resonators and layered substrates of mixed dielectrics allows one to develop highly miniaturized quasi-lumped LTCC-filters with excellent characteristics. In comparison to other LTCC-filters, they benefit from narrow bandwidth, reduced complexity and lower volume, since only three LTCC-layers are used.

## 4. Wearable Patch Antenna for Voice Communications with Substrate Composed of High Contrast Dielectrics

### 4.1 Designing Miniature Patch Antenna with CP

Future communication systems will require small and low cost antennae. It is especially true for wearable antennae for voice communications. However, small antenna size becomes a

severe problem in UHF band due to large resonance length of the antenna patch. The most direct way of reducing antenna dimensions is employment of substrates with high dielectric permittivity. However, such substrates cause narrow antenna bandwidth, impedance matching problems, transfer energy into substrate waves, and decreased fringing fields that leads to low efficiency (Zhang et. al., 1995; Hoofar & Perrotta, 2001; Hwang et al., 2003).

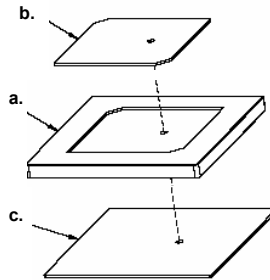


Fig. 22. Schematic diagram of a typical patch antenna for 915 MHz: (a) dielectric block, (b) patch, and (c) ground plane. Size of device is roughly 80 by 80 by 5.5 mm.

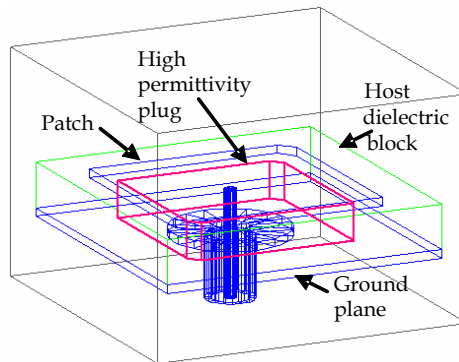


Fig. 23. Simulation model of the miniaturized antenna.

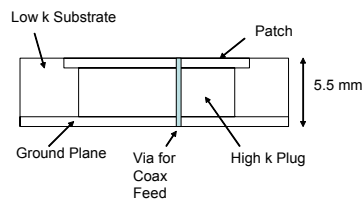


Fig. 24. Schematic cross-section of a miniaturized antenna with capacitive loading of the patch. Antenna area has been decreased by about 80%.

To mitigate these drawbacks, the antenna designers have explored various approaches. In particular, superstrates of higher permittivity with or without parasitic radiators are recommended for recovering the gain loss (Hwang et. al., 2003; Teo et. al., 2000). In order to recover the antenna bandwidth, it was proposed (Kiziltas et al., 2003) to employ textured substrates with optimized distribution of several high contrast materials. However, such

texturing is difficult for practical realization. Another well known method to increase antenna bandwidth is the employment of thicker substrates. However, it enhances surface modes generation. Although several solutions for suppressing surface wave leakage have been considered, most of them lead to increasing antenna dimensions. To mitigate surface wave generation, it was proposed (Kula et al., 2004) to truncate high permittivity substrates near the patch edges. In (Semouchkina et. al., 2002) it was earlier shown that truncation of high index dielectrics by low permittivity plugs significantly obstructs surface waves propagation.

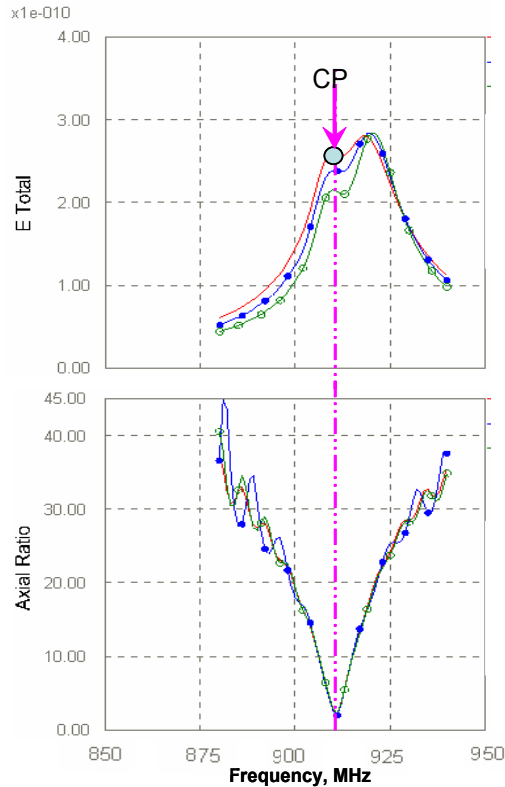


Fig. 25. Simulated spectra of radiation efficiency (upper plot) and axial ratio (lower plot) for antennas with optimized patch, plug, and cut corner dimensions; three curves correspond to a slightly different feed point locations.

In order to avoid drawbacks of higher permittivity substrates, it was proposed (Lee & Harackiewicz, 2002) to use partially filled substrates, with high permittivity dielectric bars placed in areas of high electric fields and with other areas filled with air. While this approach could be helpful to solve narrow bandwidth and low gain problems of antennas based on high permittivity substrates, it could not prevent fringing fields deterioration. An opposite proposed approach was to place high permittivity substrate underneath the antenna patch everywhere excluding the regions with peak radiation and fields (Chen &

Volakis, 2005). High permittivity substrate regions of the substrate were partly removed in proportion with electric field intensity and replaced by low permittivity dielectric. While antenna prototypes demonstrated high gain and bandwidth broadening, the graded design was not convenient for practical realization, and circular polarization (CP) could not be achieved.

A new approach to the development of a miniature microstrip patch antenna with CP based on employment of antenna substrates of high contrast dielectrics is described below (Semouchkina et al., 2007). The design targeted miniaturization and desired electric characteristics, mitigation of surface wave leakage, recovering of fringing fields and ease of fabrication.

As a starting point, conventional microstrip patch antennas designed for operation at 915 GHz have been analyzed. These antennas generally use alumina substrate having dimensions of  $(80 \times 80)$  mm<sup>2</sup> and a thickness of 5.5 mm. Patches are designed with cut corners to provide elliptical polarization. A schematic diagram of this type of antenna is shown in Fig. 22. Far-field radiation measurements confirmed that radiation patterns of these antennas were close to spherical with backward radiation intensity of about 3 dB less than the forward intensity and peak gain of about 1.5 dBi. They had split or wide radiation efficiency peak and axial ratio exceeding 5 dB. This antenna serves as a basis for the integration of higher permittivity material to achieve antenna miniaturization without performance deterioration.

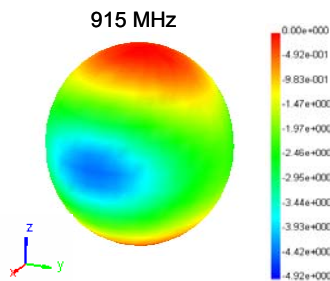


Fig. 26. 3D far-field radiation pattern of the novel antenna at the resonance frequency.

The conventional design is modified by inserting a square plug of higher permittivity material into the lower permittivity block substrate. The plug dimensions are smaller than the patch dimensions so that the fringing field distortion is mitigated. At the same time, capacitive loading of the patch by the high permittivity plug allows for compressing of the resonance wavelengths inside the plug. Plug dimensions and permittivity are optimized to get maximal possible miniaturization while maintaining antenna operation frequency of 915 MHz and preserving strong fringing fields to provide high antenna efficiency. CP of radiation is achieved by using plugs with properly cut corners and a precise feed location. The 3D model used in FDTD simulations is shown in Fig. 23. As seen from the figure, antenna feed is modeled by a coax cable. Its outer conductor is connected with the ground plane, and inner conductor - with the patch through a via in the plug. The perfectly matched (PML) boundary conditions are used at the second end of the coax to mitigate reflections. The antenna is excited by the current launched from the inner conductor of the coax.

Materials used in the model of the antenna included high permittivity ceramic powders of  $K = 84$  for plug fabrication, and LTCC material systems with the relative permittivity of 7.4 for

the fabrication of the host dielectric block. By employing the high permittivity material under the patch, the overall dimensions of the new antenna design were decreased to 35 by 35 mm, about one fifth the size of the conventional antenna. A schematic diagram of the miniaturized device is shown in Fig. 24. According to simulations the antenna efficiency was not degraded from miniaturization and the new design had a wider bandwidth. The results of simulations of the total electric far-field and the axial ratio are given in Figs. 25, while the 3D far-field pattern at the resonance frequency is presented in Fig. 26. As seen from the figures, the antenna radiates in zenith despite of the small ground plane and is capable of providing for axial ratio at the levels essentially less than 3dB at the resonance frequency.

#### 4.2 Miniature Antenna Fabrication

The prototypes of the novel antennas have been fabricated by using ceramic technologies. Dupont 951 LTCC material has been used for fabrication of the low permittivity dielectric block and Ferro COG820MW was chosen for fabrication of the high permittivity plug. Plugs fabrication starts with pressing a large rectangular slab at 16,000 psi using the Ferro COG powder coated with 3% acryloid binder. A template of the plug is generated using a drawing program. A factor of 1.226 should be applied to the template to account for shrinkage of the ceramic after firing. The template of the plug is placed on the slab, and the shape is cut from the soft green ceramic. The coax feed hole is drilled into the plug. The plug is then fired at a peak temperature of 1330°C. After firing, plugs are further machined on a grinding wheel to their final size. Dupont 6160 silver paste is applied to the front and back of the plug and dried.

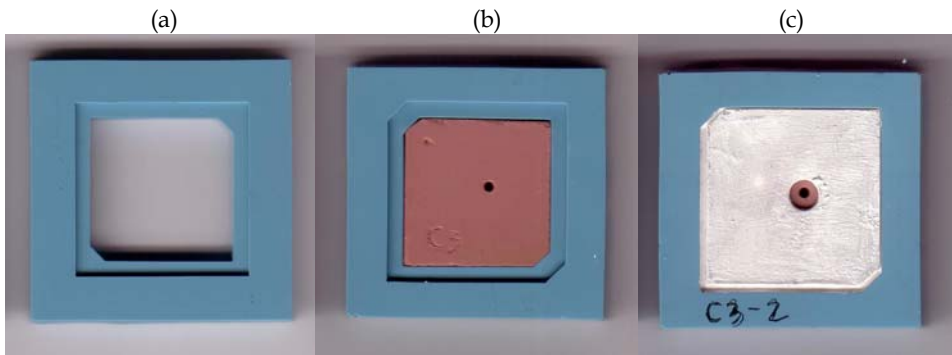


Fig. 27. Antennas are shown in process: (a) Low-K dielectric block, (b) dielectric block fired around the high-K plug, before final metallization is applied, and (c) finished miniaturized antennas with metallized LTCC patch with via for coax feed. Final size is 35 by 35 mm.

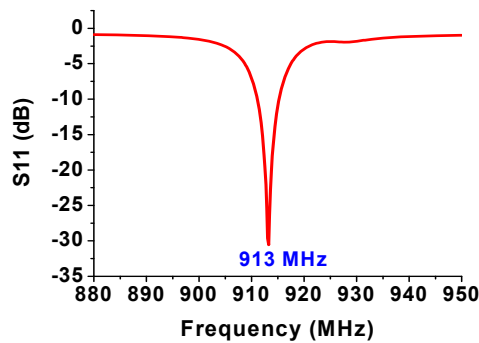


Fig. 28. Measured  $S_{11}$  spectrum of the miniaturized antenna

The host dielectric substrate block is fabricated from 50 layers of Dupont 951 LTCC. To build up the thickness, several layers of the LTCC should be first isostatically laminated at 70°C, 3000 psi for 10 minutes. The resulting 1 mm thick LTCC stacks are then punched to provide the open area for plug insertion. A shrinkage factor of 1.14 should be applied to this open area so that during firing the LTCC would shrink around the inserted plug. Metallization is printed onto the green layers using Dupont 6145 silver paste. Each punched LTCC stack is painted with a honey/water 75/25 mixture and placed on an alignment fixture. The honey mixture acts as glue between the LTCC layers and eliminates the need of further lamination steps that often result in the distortion and smashing of the soft ceramic devices (Rocha et. al., 2004).

The low permittivity LTCC block is then placed on an alumina setter and the metallized, fired plug is placed in the center of the cut out area in the block. The device is then fired to a peak temperature of 850°C for 30 minutes. The LTCC block substrate material shrinks about 14% to tightly surround and contact the edges of the plug.

Examples of the miniaturized antenna in process are presented in Fig. 27. Fig. 28 demonstrates the measured  $S_{11}$  spectrum with a -30dB minimum at the operating frequency of 913 MHz for the miniaturized antenna having the area of only 20% of the area of the original antenna.

## 5. Conclusion

The potential of high permittivity dielectric materials for local capacitive loading of microstrip components has been demonstrated in this Chapter. Capacitive loads are introduced in the device design based on the analysis of simulated field distribution at resonant frequencies. The use of hybrid dielectrics helps to substantially decrease device dimensions and to shape and optimize all characteristics of the device. The designs of miniature microstrip resonators, filters, and antennas with local high-permittivity dielectric loading have been developed, and the prototypes have been fabricated by using the LTCC technology that allowed for coprocessing different ceramic materials in multilayer and planar architecture. The results of the prototype measurements were found to agree with the simulation results.

## 6. References

- Amari, S. (2001). Direct synthesis of folded symmetric resonator filters with source-load coupling. *IEEE Microwave and Components Letter.*, Vol. 11, pp.264-266
- Amari, S.; Tadeson, G.; Cihlar, J. & Rosenberg, U. (2003). New parallel  $\lambda/2$ -microstrip line filters with transmission zeros at finite frequencies, *Proceedings of IEEE Microwave Theory Tech. Int. Symp.*, Vol. 1 , pp. 543-547, June 2003
- Banciu, M. G.; Ramer, R. & Ioachim, A. (2002). Microstrip filters using new compact resonators. *Electron. Lett.*, Vol. 38, pp. 228-229
- Belyaev, B.; Laletin, N. & Leksikov, A. (2001). Coupling coefficients of irregular microstrip resonators and selective properties of filters on their basis, *Proceedings of 2001 IEEE Conf. on Microwave Electronics: Measurements, Identification, Applicatio*, pp. 86-91
- Delaveaud, C.; Laveque, P. & Jecko, B. (1998). Small-sized low-profile antenna to replace monopole antenna. *Electron. Lett.*, Vol. 34, No. 8, (Apr. 1998) pp. 716-717
- Hennings, A.; Semouchkin, G.; Semouchkina, E. & Lanagan, M.. (2003). Design optimization of microstrip square-ring band-pass filter with quasi-elliptic function, *Proceedings of 33<sup>rd</sup> European Microwave Conf.*, pp. 175-178, Munich, germany, October 2003
- Hennings, A.; Semouchkina, E.; Semouchkin, G. & Lanagan, M. (2004). Novel compact band-pass filters with horse-shoe microstrip resonators, *Proceedings og 34th European Microwave Conf.*, Amsterdam, October 2004
- Hennings, A.; Semouchkina, E.; Baker, A. & Semouchkin, G. (2006). Design optimization and implementation of bandpass filters with normally fed microstrip resonators loaded by high-permittivity dielectric. *IEEE Trans. Trans. Microwave Theory Tech.*, Vol. 54, pp. 1253-1261
- Hennings, A.; Semouchkina, E.; Baker, A.; Semouchkin, G.; Waser, R. & Lanagan, M. (2007). Development of miniature LTCC filter for TV broadcasting band by using substrates of mixed dielectrics, *Proceedings of 37<sup>th</sup> European Microwave Conf.*, pp. 866-869, Munich, Germany, Sept. 2007
- Hong, J. S. & Lancaster, M. J. (1995). Canonical microstrip filter using square open-loop resonator. *Electron. Lett.*, Vol. 31, pp. 2021-2022
- Hong, J. S. & Lancaster, M. J. (1996). Couplings of microstrip square open-loop resonators for cross-coupled planar microwave filters. *IEEE Trans. Microwave Theory Tech.*, Vol. 44, pp. 2099-2109
- Hong, J. S. & Lancaster, M. J. (1997). Theory and experiment of novel microstrip slow-wave open-loop resonator filters, *IEEE Trans. Microwave Theory Tech.*, Vol. 45, pp. 2358-2365
- Hong, J. S. & Lancaster, M. J. (2001). *Microstrip Filters for RF/Microwave Applications*, Wiley, New York, pp. 249-251, pp. 73
- Hoofar, A. & Perrotta, A. (2001). An experimental study of microstrip antennas on very high permittivity ceramic substrates and very small ground planes. *IEEE Trans. Antennas Propagation*, Vol. 49, pp. 838-840
- Hwang, Y.; Zhang, Y. P. & TLo, T. K. (2003). Aperture-coupled microstrip antenna loaded with very high permittivity ceramics", [www.interscience.wiley.com](http://www.interscience.wiley.com), DOI 10.1002/mmce.10072



- Kamba, S.; Porokhonsky, V.; Pashkin, A.; Bovtin, V.; Petzelt, J.; Nino, J.; Trolier-McKinstry, S.; Randall, C. & Lanagan, M. (2001). Broad-band dielectric spectroscopy of Bi pyrochlores in the range 100 Hz - 100 THz, *Proceedings of the COST525 Meeting*, 2001, pp 49-53
- Kiziltas, G.; Psychoudakis, D.; Volakis, J. L. & Kikuchi, N. (2003). Topology design optimization of dielectric substrates for bandwidth improvement of patch antenna. *IEEE Trans. Antennas Propagation*, Vol. 52, pp. 2731-2743
- Knijer, G.; Dechant, K. & Apte, P. (1997). Low loss, low temperature cofired ceramics with higher dielectric constants for multichip modules (MCM), *Proceedings of IEEE Int. Conf. On Microchip Modules*, pp. 121-127
- Kula, J.; Psychoudakis, D.; Chen, C.-C.; Volakis, J. L. & and Halloran, J. H. (2004). Patch antenna miniaturization using thick truncated textured ceramic substrates, *Proceedings of IEEE AP-S Int. Symp.*, Vol. 4, pp. 3800-3803
- Lacey, D.; Drossos, G.; Wu, Z.; Davis, L. E.; Button, T. W. & Smith, P. (1996). Miniaturized HTS microstrip patch antenna with enhanced capacitive loading, *Proceedings of IEE Superconducting Microwave Circuits Colloq.*, Vol. 4, pp. 1-6, Apr. 1996
- Lin, K.-C.; Chang, C.-F.; Wu, M.-C. & Chung, S.-J. (2006). Dual bandpass filters with serial configuration using LTCC technology. *IEEE Trans. Microwave Theory Tech.*, Vol. 54, pp. 2321-2328
- Nishigaki, S.; Yano, S.; Fukuta, J. & Fuwa, T. (1985). A new multilayered low temperature fireable ceramic substrate, *Proceedings of Int. Hybrid Microelectron. Symp.*, pp.225-234
- Rocha, Z.; Garcia, N.; Oliveira, N.; Matos, J. & Gongora-Rubio, M. (2004). Low temperature and pressure lamination of LTCC tapes for meso-systems, *Proceedings of IMAPS Ceramic Interconnect Technology Conference*, pp 205 - 210, Denver Co., April 2004
- Sagava, M.; Makimoto, M. & Yamashita, S. (1997). Geometrical structures and fundamental characteristics of microwave stepped-impedance resonators. *IEEE Trans. Microwave Theory Tech.*, Vol. 45, pp.1078-1085
- Semouchkina, E.; Semouchkin, G.; Cao, W. & Mittra, R. (2002). FDTD study of surface waves in microstrip and patch structure, *Proceedings of IEEE Microwave Theory Tech. Int. Symp*, pp.1127-1130
- Semouchkina, E.; Semouchkin, G.; Lanagan, M. & Mittra, R. (2003). Field simulation based strategy for designing microstrip filters, *Proceedings of IEEE MTT-S Int. Symp.* pp. 1897-1900
- Semouchkina, E.; Baker, A.; Semouchkin, G. & Lanagan, M. (2004). Microwave component miniaturization by local embedding high-permittivity dielectric materials in low-permittivity substrates, *Proceedings of 34th European Microwave Conf.*, Amsterdam, October 2004
- Semouchkina, E.; Baker, A.; Semouchkin, G.; Lanagan, M. & Mittra, R. (2005a). New approaches for designing microstrip filters utilizing mixed dielectrics. *IEEE Trans. Microwave Theory Tech.*, Vol. 53, pp. 664-652
- Semouchkina, E.; Hennings, A.; Baker, A.; Semouchkin, G. & Lanagan, M. (2005b). Miniature filter with double-coupled horse-shoe microstrip resonators capacitively loaded by using high-permittivity material, *Proceedings of 35<sup>th</sup> European Microwave Conf.*, pp. 293-296, Paris, France, Oct. 2005

- Semouchkina, E.; Baker, A.; Semouchkin, G.; Kerr, T. & Lanagan, M. (2007). Wearable patch antenna for voice communications with substrate composed of high contrast dielectrics, *Proceedings of IEEE AP-S International Symposium*, Honolulu, Hawaii, June 2007
- Teo, P. T.; Vinoy, K. J.; Jose, K. A.; Varadan, V. K.; Varadan, V. V. & Gan, Y. B. (2000)., Design and development of tunable multi-layer smart antennas using ferroelectric materials. *J. Intell. Materials Systems Structures*, Vol. 11, pp.294-299
- Wilcox Sr. D. L. & Oliver, M. (2002). LTCC, an interconnect technology morphing into a strategic microsystem integration technology, *Proceedings of the IMAPS Advanced Technology Workshop*, pp. 1-4, Providence, RI, May 2002
- Youn, H.-J.; Randall, C.; Chen, A.; ShROUT, T. & Lanagan, M. (2002). Dielectric relaxation and microwave dielectric properties of  $\text{Bi}_2\text{O}_3\text{-ZnO-Ta}_2\text{O}_5$  ceramics. *J. Mater. Res.*, Vol. 17, pp. 1502-1506
- Zhang, Y. P.; Lo, T. K. & and Hwang, Y. (1995). A dielectric loaded miniature antenna for microcellular and personal communications, *Proceedings of IEEE AP-S Int.Symp.*, pp.1152-1155

# Broadband and Planar Microstrip-to-waveguide Transitions

Kunio Sakakibara

*Nagoya Institute of Technology  
Japan*

## 1. Introduction

Millimeter-wave systems consist of various components; MMICs, antennas and other microwave circuits in different transmission lines. Loss at the connections between components is significant problem in the millimeter-wave systems. Transitions between different transmission lines; microstrip line, coplanar line, suspended line, slot line, coaxial cable, waveguide et al. are required in the millimeter-wave band. Accurate impedance matching and complete mode transformation between the different transmission lines are important in the design.

Various kinds of microstrip-to-waveguide transitions have been proposed in the millimeter-wave band. Transitions with short-circuited waveguide of  $1/4$  guided wavelength on the substrate are very popular (Shin et al., 1988, Leong & Weinreb, 1999) because their principle of mode transformation is simple and almost the same with that of ordinary transitions of a waveguide and a coaxial cable (Collin, 1990). Slot-coupled transitions are also proposed by some authors (Grabherr et al., 1994, Hyvonen & Hujanen, 1996). An additional substrate with a radiating element is needed in the waveguide, although the short-circuited waveguide is not necessary. Single layer microstrip-to-waveguide transitions have been developed in the recent years. The short-circuited waveguide and the additional substrate are not necessary, which is advantageous from the industrial point of view for low cost and high reliability. However, narrow frequency bandwidth is essential disadvantage due to the high-Q resonant structure printed on the substrate (Simon et al., 1998, Iizuka et al., 2002, Sakakibara et al., 2003). Broad frequency bandwidth is obtained by using quasi-yagi antenna printed on the substrate in the waveguide (Kaneda et al., 1999). However, the microstrip line is parallel to the waveguide (Kaneda et al., 1999, Sakakibara et al., 2003), which is a different type from others. Here, we treat the transitions whose microstrip line and waveguide are perpendicular to each other.

We have proposed novel microstrip-to-waveguide transitions based on the ones with short-circuited waveguide, shown in Fig. 1(a), to realize broadband characteristic for uses to the broadband applications and for wide manufacturing-tolerance. No additional parts and no complicated structures are needed to extend the bandwidth. Broad frequency bandwidth is realized only by the change of the printed pattern on the substrate. The short-circuited waveguide is replaced by an additional substrate to compose a planar microstrip-to-

waveguide transition in a multi-layer substrate as shown in Fig. 1(b). Since the short-circuited waveguide of the substrate is filled with dielectric material, the bandwidth is narrower than the transition (a) with the hollow short-circuited waveguide. However, the two substrates are attached accurately and free from fabrication error. A planar transition in a single-layer substrate has been developed (Iizuka et al., 2002). Bandwidth is narrow but the transition consists of only one substrate set on the open-ended waveguide as shown in Fig. 1(c), which is attractive from the industrial point of view. The dependencies to the characteristics of these transitions on geometrical parameters of the structures are examined in detail. Various ways to control bandwidths and center frequencies are presented for required characteristics in the designs of the transitions.

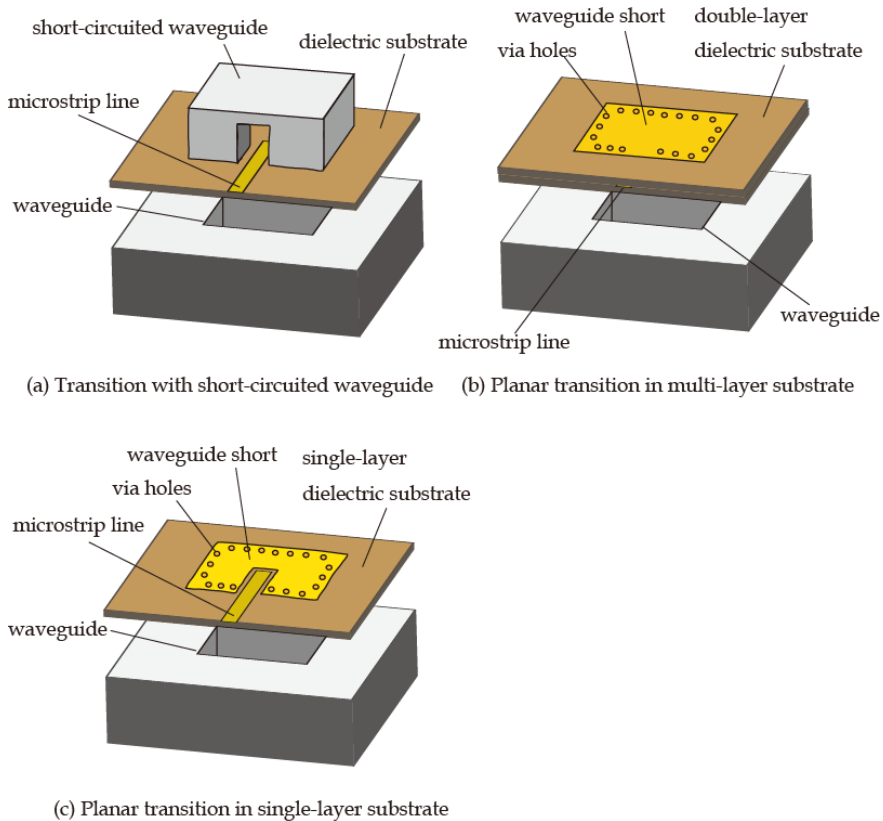


Fig. 1. Variety of microstrip-to-waveguide transitions

## 2. Configurations of Microstrip-to-waveguide Transitions

Three types of transitions with different features have been developed in the millimeter-wave band. Configurations of the transitions are shown in Fig. 1. The transition (a) with short-circuited waveguide has an advantage of broadband (Deguchi et al., 2005, Deguchi et

al., 2007). However, it requires an additional short-circuited waveguide on the substrate, which suggests the transition suffers from loss increasing due to fabrication error in setting the short-circuited waveguide on the substrate. On the other hand, the planar transition (c) in a single-layer substrate is free from loss increasing due to the fabrication error of the additional parts because the transition consists of only one substrate on the open-ended waveguide (Iizuka et al., 2002). However, bandwidth is narrow since the volume of the resonant circuit is limited in the thin substrate. Planar transition (b) in multi-layer substrate possesses intermediate property between (a) and (c) (Hirono et al., 2007, Sakakibara et al., 2008, Hirono et al., 2008).

## 2.1 Transition with short-circuited waveguide

Broad operation-bandwidth is in high demand for many applications. Wide tolerance in manufacturing is also advantageous from the industrial point of view. Then, we propose a broadband microstrip-to-waveguide transition with a novel printed pattern in the substrate. No additional parts and no complicated structures are needed. Only the printed pattern is modified in order to extend the frequency bandwidth.

The configuration of the proposed transition is almost the same as more conventional ones that have short-circuited waveguide on the substrate (Shin et al., 1988, Leong & Weinreb, 1999). The microstrip-to-waveguide transition connects a microstrip line and a perpendicular waveguide. A probe at one end of the microstrip line is inserted into the waveguide whose one end is short-circuited. A configuration of the proposed transition is shown in Fig. 1(a). A dielectric substrate with conductor patterns on its both sides is placed on an open-ended waveguide (WR-12,  $3.1 \times 1.55$  mm). An aperture of the dielectric substrate is covered with an upper waveguide. A short circuit of the upper waveguide is theoretically  $\lambda_g/4$  ( $\lambda_g$ : a guided wavelength of the waveguide) above the substrate. Consequently, electric current on the probe couples to magnetic field of TE<sub>10</sub> dominant mode of the waveguide. Via holes are surrounding the waveguide in the substrate to reduce leakage of parallel plate mode transmitting into the substrate.

Figure 2 shows cross-sectional views of the proposed transition. Two distinctive features are introduced in the upper conductor pattern (AA' plane) of the dielectric substrate as is shown in Fig. 2(a) and 3. First, the probe is shifted by  $d$  toward  $+y$ -direction from the center of the waveguide ( $y = 0$ ). Local impedance in the waveguide is defined as a ratio of electric field and magnetic field at each point and is lower at  $y = d$  rather than at the center of the waveguide where the magnitude of the electric field is the maximum. Therefore, a characteristic impedance of the waveguide becomes comparable with that of the microstrip line ( $60 \Omega$ , line width: 0.3 mm). Second feature is an extended ground at the opposite side of the waveguide from the probe. The extended ground works as a capacitive obstacle which can control the reactance of the probe (Marcuvitz, 1993). Consequently, impedance matching could be achieved by controlling the shift  $d$  of the probe and the length  $p$  of the extended ground. The length  $l$  of the probe and the length  $s$  of the short-circuited waveguide are also important parameters for the performance of the transition. Reducing leakage from the waveguide window at the insertion of the microstrip line, width of the window should be narrower than the width for the cut off condition and is 1.0 mm in this case. Taper structure of 0.5 mm long is adopted for gradually change of impedance. On the other hand in the substrate, cut off condition is much more significant because the wavelength is shorter than

the air. Distance between the via-hole centers is 1.5 mm at the both sides of the probe insertion.

A photograph of the fabricated transition is shown in Fig. 3. Top plate of the short-circuited waveguide is removed to see the inside. Shift  $d$  and length  $l$  of the probe, length  $p$  of the extended ground and length  $s$  of the upper waveguide are designed to obtain the required performance.  $d$ ,  $l$  and  $p$  are in the printed pattern and  $s$  is controlled by the thickness of the metal plate for the short-circuited waveguide shown in Fig. 3.

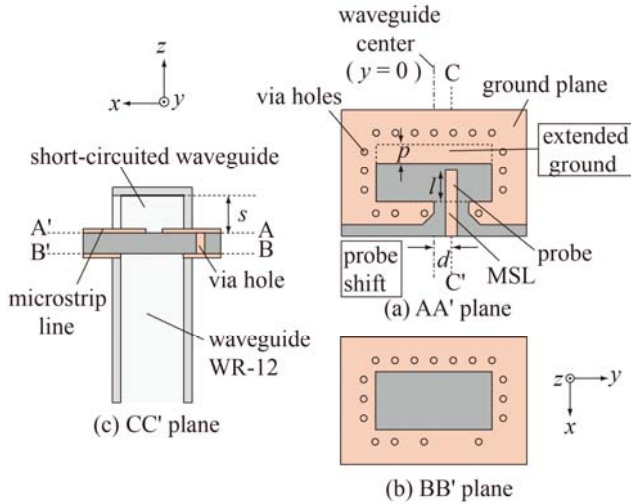


Fig. 2. Structure of the transition with a short-circuited waveguide

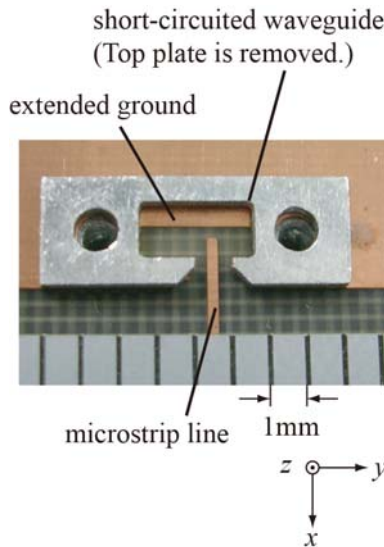


Fig. 3. Photograph of the transition inside

## 2.2 Planar transition in multi-layer substrate

To reduce the number of required parts and to avoid loss increasing due to alignment error in setting the short-circuited waveguide on the substrate, the short-circuited waveguide is replaced by an additional layer of the substrate, which results in a flat, planar and broadband transition in multi-layer substrate as is shown in Fig. 1(b) and 4. Two layers (Rogers RO4350B,  $\epsilon_r = 3.48$ ,  $\tan\delta = 0.0035$ ) are stuck by an adhesive layer (Rogers RO4450B,  $\epsilon_r = 3.54$ ,  $\tan\delta = 0.004$ ) as shown in Fig. 5. Quasi waveguide is formed in the multi-layer substrate by surrounding via-holes. The top plane is a short circuit of the quasi waveguide. The microstrip line is inserted at the upper plane of the lower substrate into the quasi waveguide with distance of approximately  $\lambda_g/4$  away from the short circuit, where  $\lambda_g$  is a guided wavelength in the quasi waveguide. The thickness  $t_1$  of the top layer is optimized as 0.25 mm, while both thicknesses of the lower and the adhesive layers are 0.1 mm.

Metal printed patterns and major parameters are indicated in Fig. 6. Two geometrical features are supplied in the conductor patterns. One is an extended ground as well as the previous transition shown in Fig. 2. Reactance can be controlled by the shunt capacitance caused by the extended ground in the quasi waveguide. Double resonance is expected as the transition with short-circuited waveguide. Probe shift was not applied because it was not necessary for double resonance in this transition. The other feature is the size of the quasi waveguide. The dimensions of the quasi waveguide (2.04 mm X 1.15 mm) composed of via-holes are designed to be smaller than that of the open-ended metal waveguide (WR-10: 2.54 mm X 1.27 mm) in order to suppress the higher order mode in the quasi waveguide because a wavelength in dielectric material is shorter than in the air. Electric field distributions in the transitions with narrow upper waveguide and with wide upper waveguide are shown in Fig. 7 (a) and (b), respectively. The field concentrates around the waveguide center and can couple to the probe in the narrow waveguide (a).

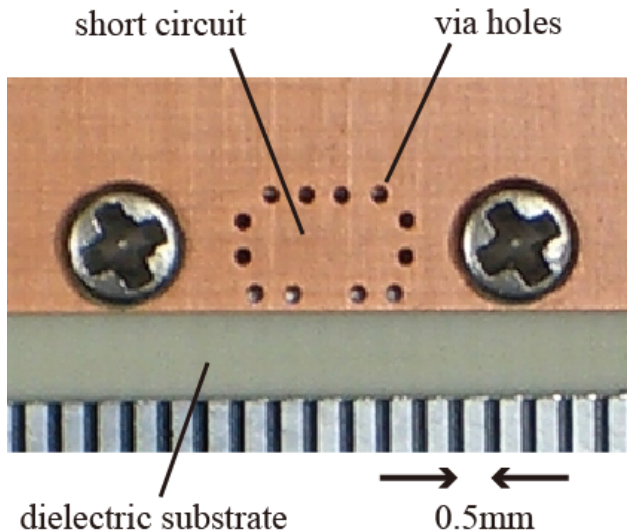


Fig. 4. Photograph of the fabricated planar transition in multi-layer substrate

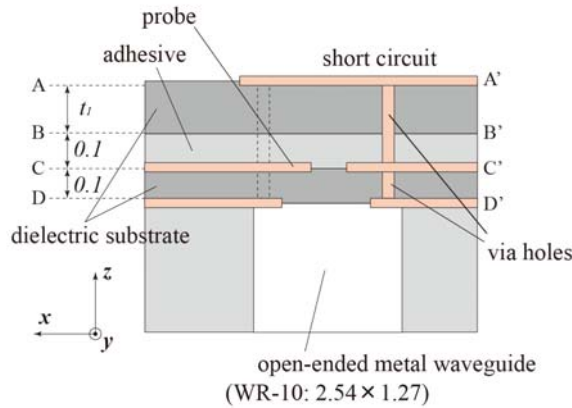


Fig. 5. Cross-sectional view of the planar transition in the multi-layer substrate

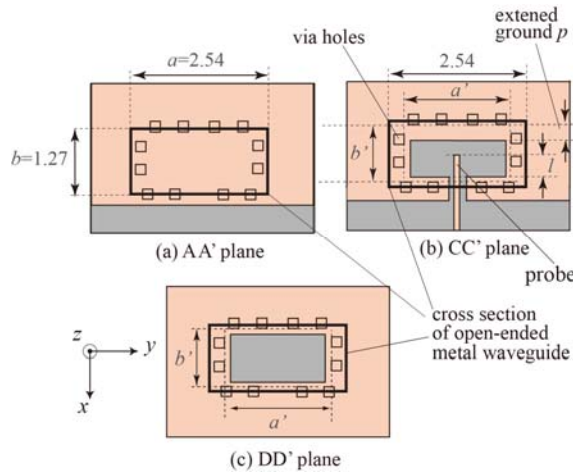


Fig. 6. Printed patterns of the planar transition in the multi-layer substrate

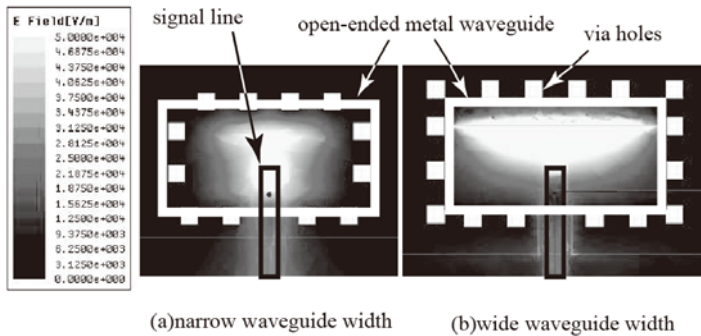


Fig. 7. Electric field distributions in the planar transitions of (a)narrow and (b)wide waveguides



**2.3 Planar transition in single-layer substrate**

Simple configuration of transition is constructed by setting a single-layer substrate ( $\epsilon_r = 2.2$ ) on the open ended waveguide (WR-12) as shown in Fig. 1(c). Microstrip line is inserted into the top ground plane to compose partly coplanar line. Via holes surrounds waveguide. The current on the line couples electromagnetically to the current on the patch of the lower plane in the aperture as shown in Fig. 8. Resonant frequency is controlled by the length of the patch and coupling magnitude is controlled by the insertion length of the microstrip line into the ground plane of the waveguide short circuit. Bandwidth would be narrow due to its high-Q characteristic of the patch.

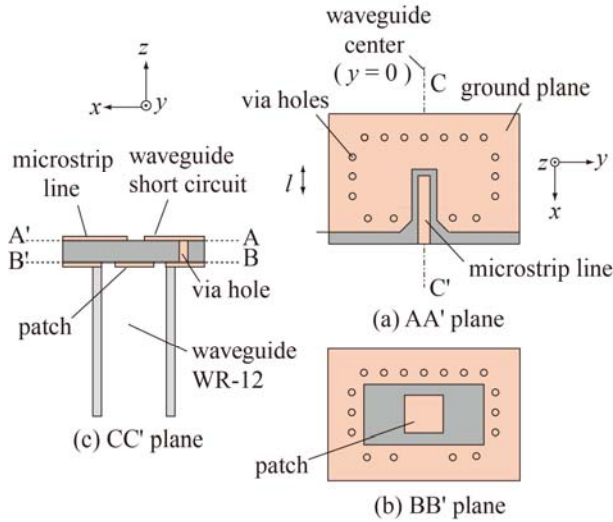


Fig. 8. Cross-sectional view and printed patterns of the transition in the single-layer substrate

**3. Performances**

**3.1 Measurement setup of scattering parameters**

Performance of the fabricated transitions is evaluated by experiment in the millimeter-wave band. Scattering parameters are measured in back-to-back configuration as shown in Fig. 9. Microstrip-line ports of two identical transitions are connected by a microstrip line. The other two waveguide-ports of them are connected to the vector network analyzer (Anritsu ME7808B). Frequency dependency of reflection  $S_{11}$  for one transition is evaluated by using the time gating function of the vector network analyzer. On the other hand, transmission  $S_{21_{exp}}$  [dB] for one transition is obtained by subtracting the loss of the microstrip line  $L_{msl}$  [dB] from the raw data  $S_{21_{raw}}$  [dB] of the two waveguide ports shown in Fig. 9, and dividing by two, that is,

$$S_{21_{exp}} = ( S_{21_{raw}}[dB] - L_{msl}[dB] ) / 2 [dB] \tag{1}$$

Loss of waveguide is quite small and is neglected in the measurement. Performances of transitions are evaluated by  $S_{21\_exp}$  in later sections.

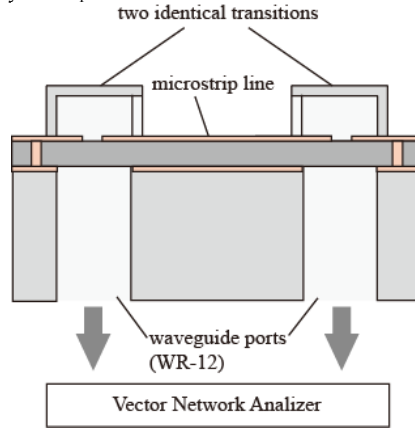


Fig. 9. Measurement setup of the developed transitions

### 3.2 Transition with short-circuited waveguide

The transitions with short-circuited waveguide are fabricated for experiment as shown in Fig. 3. A Teflon substrate (relative dielectric constant  $\epsilon_r = 2.2$ , thickness  $t = 0.127$  mm) with conductor pattern is located on the waveguide aperture. The short-circuited waveguide in the aluminium block is placed on the substrate. All these parts are screwed together. Scattering parameters of reflection  $S_{11}$  and transmission  $S_{21}$  are calculated by using a commercial electromagnetic simulator of the finite element method. Major parameters indicated in Fig. 2 (the length  $l$  and the shift  $d$  of the probe, the length  $p$  of the extended ground and the length  $s$  of the short-circuited waveguide) are optimized so that bandwidth where  $S_{11}$  is lower than  $-30$  dB (low-reflection design (1)) or  $-20$  dB (broadband design(2)) becomes the maximum.

Figures 10 and 11 show  $S_{11}$  and  $S_{21}$  for the transitions of low-reflection design (1) and broadband design (2), respectively. The dimensions are listed in Table 1. The geometrical difference between the designs (1) and (2) is only  $d$ . The simulated performance of the conventional transition ( $d = p = 0$ ) is also shown in Fig. 12 for reference. Only  $l$  and  $s$  are optimized in the condition of no probe shift  $d = 0$  and no extended ground  $p = 0$ . Low insertion loss of the proposed ones is achieved such that measured insertion loss is 0.35 dB (design (1)) and 0.33 dB (design (2)) at 76.5 GHz. The simulated loss is almost the same level with the conventional one. Moreover, two resonances are observed in the frequency dependency of  $S_{11}$ . Broad frequency bandwidth is obtained such that bandwidth for reflection below  $-30$  dB is 12.9 GHz (16.8 %) in the low-reflection design (1) and that below  $-20$  dB is 24.9 GHz (32.5%) in the broadband design (2). They are 1.95 and 1.37 times as broad as the bandwidth of the conventional ones. The frequency band of  $S_{11}$  lower than  $-20$  dB for low-reflection design (1) shifts by only 1 GHz, though both of the two resonant frequencies shift by approximately 3 GHz lower than that of the simulation. Loss increasing due to the frequency shift is quite small because this transition works well over broad frequency bandwidth.

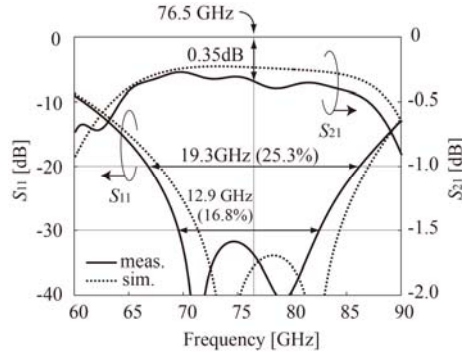


Fig. 10. Measured and simulated  $S_{11}$  and  $S_{21}$  of the transition of the low-reflection design (1).

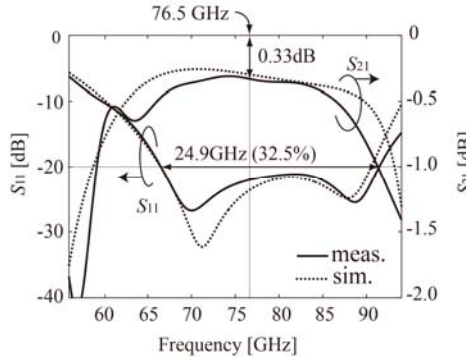


Fig. 11. Measured and simulated  $S_{11}$  and  $S_{21}$  of the transition of the broadband design (2).

Figures 13 and 14 show measured and simulated  $S_{11}$  depending on the shift  $d$  of the probe and the length  $p$  of the extended ground, respectively. Dependencies on  $d$  and  $p$  are clarified from the change of the curves. The two resonant frequencies approach as  $d$  grows or as  $p$  becomes small. Consequently, the number of resonant frequencies becomes one when  $d$  is larger than 0.45 mm or  $p$  is smaller than 0.50 mm. On the other hand, as  $d$  becomes small or as  $p$  grows, the interval between the two resonant frequencies extends and the frequency bandwidth becomes broader. Simultaneously, the reflection level at the middle of the two resonant frequencies grows higher. The shift  $d$  of the probe and the length  $p$  of the extended ground are designed in accordance with the required bandwidth and the admitted reflection level. Measured curves indicated as solid lines almost agree well with the simulated results indicated as dashed line.

Major parameters	Low-reflection design(1)	Broadband design(2)	Conventional design
$d$ [mm]	0.45	0.30	0.00
$p$ [mm]	0.50	0.50	0.00
$l$ [mm]	0.70	0.70	0.72
$s$ [mm]	0.50	0.50	0.71

Table 1. Optimized major parameters

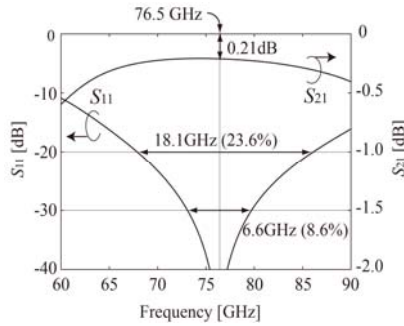


Fig. 12. Measured and simulated  $S_{11}$  and  $S_{21}$  of the conventional transition

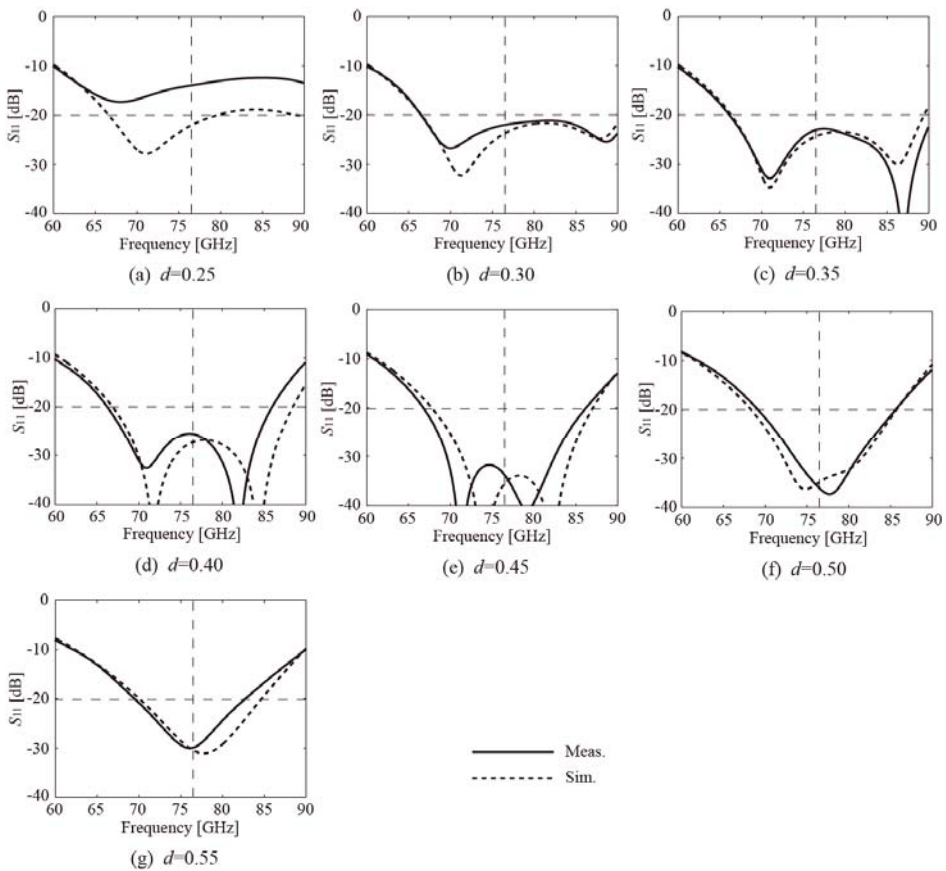


Fig. 13. Measured and Simulated  $S_{11}$  variation depending on the parameter  $d$

The change of the resonant frequencies is summarized in Fig. 15. Figure 15(a) shows simulated resonant frequencies versus  $d$  when the length  $p$  is 0.40, 0.50, and 0.60 mm.

Measured resonant frequency is also shown only for  $p = 0.50$  by dots. No second resonance is observed when  $p$  is 0.40 mm even though the shift  $d$  of the probe changes from 0.25 up to 0.65 mm. When  $p$  is 0.50 mm, only one resonant frequency is observed when  $d$  is larger than 0.47 mm. However, two resonant frequencies appear when  $d$  is smaller than 0.47 mm. The interval between the two resonant frequencies extends when  $d$  becomes small. Next, we investigate the effect of the extended ground as well. Figure 15(b) shows simulated resonant frequencies versus length  $p$  of the extended ground when the shift  $d$  is 0.30, 0.45, and 0.60 mm. Measured resonant frequency is also shown only for  $d = 0.45$  mm.

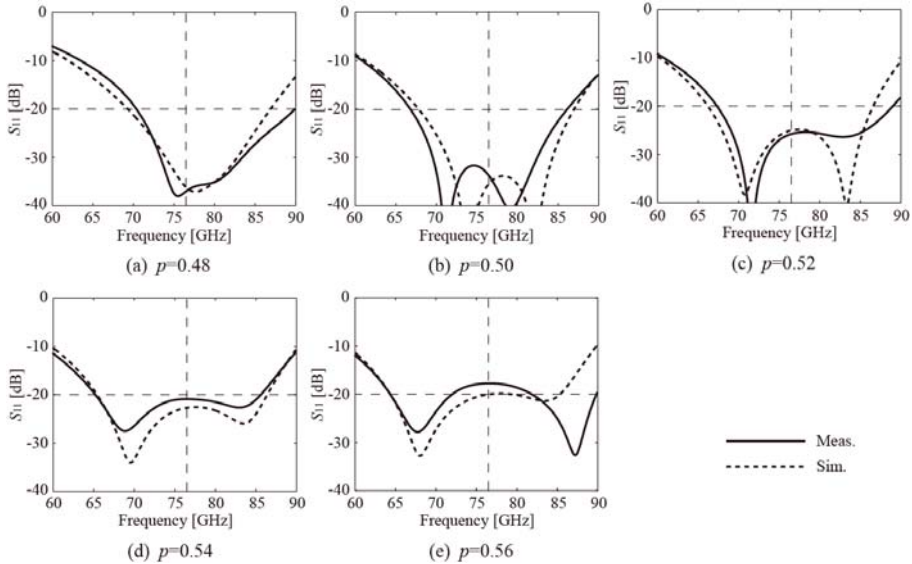


Fig. 14. Measured and Simulated  $S_{11}$  variation depending on the parameter  $p$

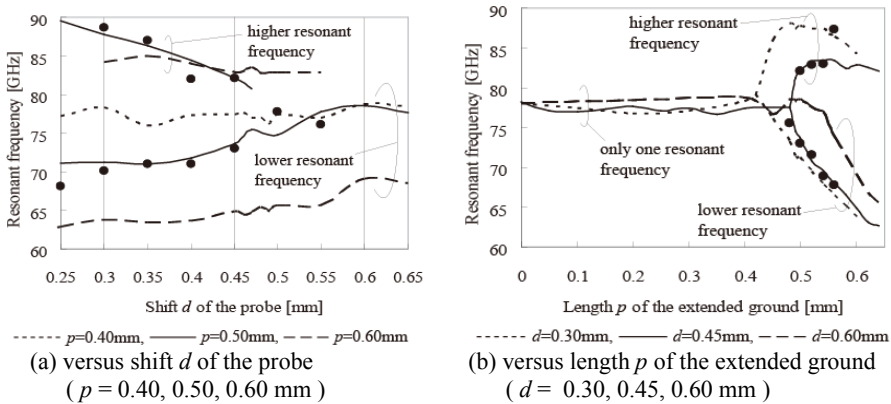


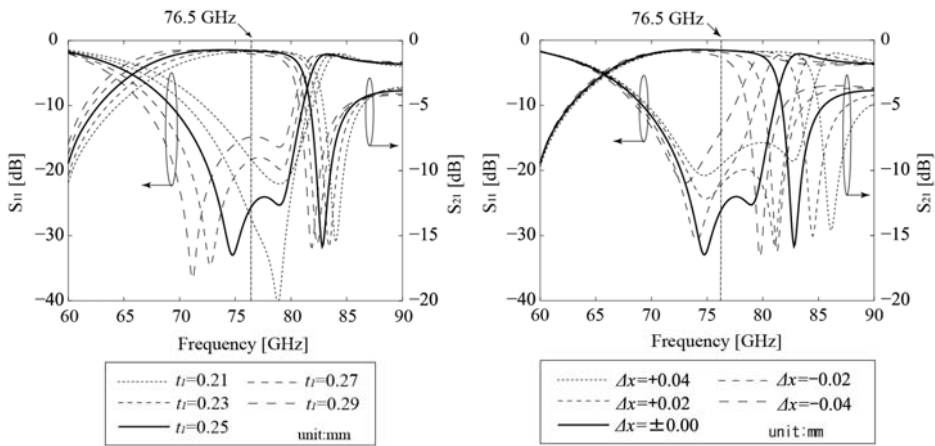
Fig. 15. Simulated resonant frequencies (lines) with measured resonant frequencies (dots)

No second resonance is observed when  $p$  is 0.60 mm even though the length  $p$  of the extended ground changes from 0.00 up to 0.65 mm. When  $d$  is 0.45 mm, only one resonant

frequency is observed when  $p$  is smaller than 0.48 mm. However, two resonant frequencies appear when  $p$  is larger than 0.48 mm. Furthermore, the higher resonant frequency is almost constant, while the lower resonant frequency shifts low when  $p$  becomes large. Consequently, bandwidth can be controlled by changing the two parameters  $d$  and  $p$ .

### 3.3 Planar transition in multi-layer substrate

Next, planar transition in multi-layer substrate is designed and its performance is evaluated by simulation and experiments. First, to verify the reason for the double resonance in  $S_{11}$ , scattering parameters are investigated by electromagnetic simulation based on the finite element method. Figure 16(a) shows variation of scattering parameters  $S_{11}$  and  $S_{21}$  depending on the length  $t_1$  of the short-circuited waveguide shown in Fig.5. Lower resonant frequency shifts according to the length  $t_1$  variation, while higher resonant frequency is stable. Consequently, lower resonant frequency is due to the resonance of the short-circuited waveguide. On the other hand, as shown in Fig. 16(b), the higher resonant frequency shifts according to the shift  $\Delta x$  of via-holes located at the opposite side of the microstrip-line probe. Consequently, higher resonant frequency is due to the resonance of the stub composed of the parallel plate waveguide short-circuited by the via-holes. So, the lower and higher resonant frequencies can be independently controlled by the length of the short-circuited waveguide and location of the via holes, respectively.



(a)  $S_{11}$  and  $S_{21}$  variation depending on the substrate thickness (b)  $S_{11}$  and  $S_{21}$  variation depending on the shift of via holes

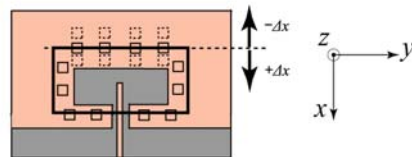


Fig. 16. Parameter dependency of double resonant-frequencies on scattering parameters

The planar transitions in multi-layer substrate are fabricated for experiment as shown in Fig. 4. The multi-layer substrate is fixed on the open-ended waveguide by screws. Surrounding

via holes form the quasi waveguide. The top metal in the via-hole arrangement is short circuit. Scattering parameters of fabricated transitions are measured in the millimeter-wave band. Figure 17 shows the measured  $S_{11}$  and  $S_{21}$  of the transition. The measured resonant frequencies shift by only 1 GHz lower than the simulated ones. Bandwidth of the transition for reflection lower than  $-20$  dB is 7.0 GHz (9.2 %). Measured insertion loss was approximately 0.7 dB which is the same level with the simulated one.

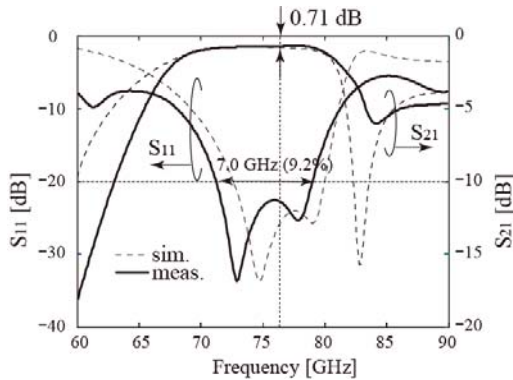


Fig. 17. Measured and simulated  $S_{11}$  and  $S_{21}$  of the transition in multi-layer substrate

Degradation of matching characteristics due to fabrication error in setting the substrate on the open ended waveguide is examined by electromagnetic simulation. Scattering parameters of the transition with shift of the substrate on the open-ended waveguide in  $x$ - and  $y$ -directions are shown in Fig. 18. The effect due to the shift of substrate in both  $x$ - and  $y$ -directions is quite small since the size of the aperture on the lower plane of substrate is much smaller than the waveguide open end and waveguide walls do not affect to the probe current until the waveguide wall appears in the aperture due to the shift. This phenomenon is one of the effective advantages of the transition from the industrial point of view.

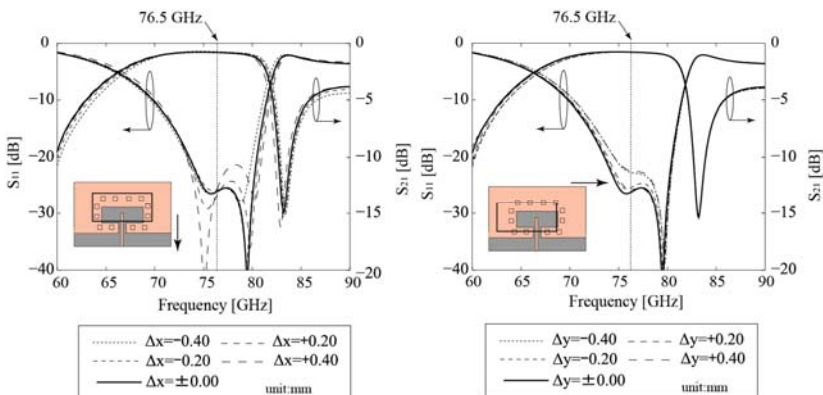


Fig. 18. Scattering parameters of the transition with shift of the substrate on the open ended waveguide in  $x$ - and  $y$ -directions

### 3.4 Planar transition in single-layer substrate

The planar transition in single-layer substrate is designed by electromagnetic simulation based on the finite element method. Patch length is designed to obtain resonant frequency at 76.5 GHz. Insertion length of the microstrip line is designed to couple between patch and microstrip line for low reflection-level at the resonant frequency. Figure 19 shows  $S_{11}$  and  $S_{21}$ . As resonant structure is a patch and is quite smaller size than short-circuited waveguide, Q-factor results high and bandwidth becomes narrow. Thus, bandwidth of reflection lower than  $-10$  dB is approximately 6 GHz.

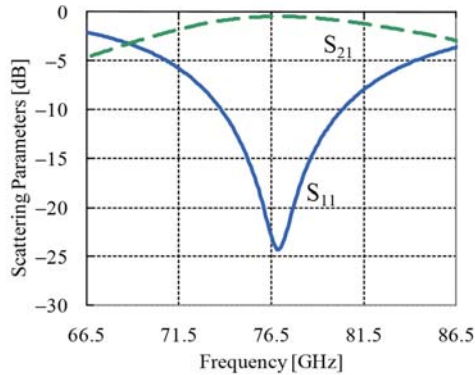


Fig. 19. Scattering parameters of planar transition in single-layer substrate

## 4. Conclusion

Three types of microstrip-to-waveguide transitions are presented in this chapter. One is a transition with a short-circuited waveguide which is quite broadband such that bandwidth of reflection below  $-20$  dB is 24.9 GHz (32.5 %). However, it requires an additional part of a short-circuited waveguide on the substrate. Second one is a planar transition in multi-layer substrate which is relatively broadband such that bandwidth of reflection below  $-20$  dB is 7.0 GHz (9.2 %) and is composed of the multi-layer substrate. Third one is also a planar transition in single-layer substrate. This is the most cost-effective transition due to its simple structure. However, bandwidth is quite narrow. We can choose the appropriate transition depending on the system requirement.

## 5. References

- Collin, R.E. (1990). *Field Theory of Guided Waves*, Chapter 7, IEEE Press., ISBN: 0-87942-237-8, Piscataway, NJ
- Deguchi, Y.; Sakakibara, K.; Kikuma, N. & Hirayama, H. (2005). Millimeter-wave microstrip-to-waveguide transition operating over broad frequency bandwidth, *IEEE MTT-S, Int. Microwave Symp. Dig.*, ISBN: 0-7803-8845-3, Long Beach, CA, June 2005.



- Deguchi, Y.; Sakakibara, K.; Kikuma, N. & Hirayama, H. (2007). Design and optimization of Millimeter-wave microstrip-to-waveguide transition operating over broad frequency bandwidth, *IEICE Trans. Electron.*, vol. E90-C, no. 1, Jan. 2007, pp. 157-164, ISSN: 0916-8516
- Grabherr, W.; Hudder, B. & Menzel, W. (1994). Microstrip to waveguide transition compatible with mm-wave integrated circuits, *IEEE Trans. Microwave Theory Tech.*, vol.42, no. 9, Sept. 1994, pp.1842-1843, ISSN: 0018-9480
- Hirono, M.; Sakakibara, K.; Kikuma, N. & Hirayama, H. (2007). Design of broadband microstrip-to-waveguide transition in multi-layer substrate, Proc. Int. Symp. Antennas and Propag. ISAP2007, 1C5-2, ISBN: 978-4-88552-223-9, pp. 125-128, Sendai, Japan, Aug. 2007
- Hirono, M.; Sakakibara, K.; Kikuma, N. & Hirayama, H. (2008). Measured performance of broadband microstrip-to-waveguide transition on multi-layer substrate in the millimeter-wave band, *IEICE Trans. Commun.*, vol. J91-B, no. 9, Sep. 2008, pp. 1057-1065, ISSN: 1344-4697
- Hyvonen, L. & Hujanen, A. (1996). A compact MMICcompatible microstrip to waveguide transition, *IEEE MTT-S Int. Microwave Symp. Dig.*, pp.875-878, ISBN: 0-7803-3246-6, San Francisco, CA, June 1996
- Iizuka, H.; Watababe, T.; Sato, K. & Nishikawa, K. (2002). Millimeter wave microstrip line to waveguide transition fabricated on a single layer dielectric substrate, *IEICE Trans. Commun.*, vol. E85-B, no. 6, June 2002, pp.1169-1177, ISSN 0916-8516.
- Kaneda, N.; Qian, Y. & Ito, T. (1999). A broad-band microstrip-to-waveguide transition using Quasi-Yagi antenna, *IEEE Trans. Microwave Theory Tech.*, vol. 47, no. 12, Dec. 1999, pp.2562-2567, ISSN: 0018-9480
- Leong, Y. & Weinreb, S. (1999). Full band waveguide to microstrip probe transition, *IEEE MTT-S Int. Microwave Symp. Dig.*, pp.1435-1438, ISBN: 0-7803-5135-5, Anaheim, CA, May 1999
- Marcuvitz, N. (1993). *Waveguide Handbook*, Chapter 5, IEE Press, ISBN: 0-86341-058-8, London, U.K.
- Sakakibara, K.; Saito, F.; Yamamoto, Y.; Inagaki, N. & Kikuma, N. (2003). Microstrip line to waveguide transition connecting antenna and backed RF circuits, *IEEE AP-S, Int. Symp. Dig.*, pp.958-961, ISBN: 0-7803-7846-6, , June 2003.
- Sakakibara, K.; Hirono, M.; Kikuma, N. & Hirayama, H. (2008). Broadband and Planar Microstrip-to-Waveguide Transitions in Millimeter-Wave Band, Proceedings ICMMT2008, I24A2, pp. 1278-1281, Nanjin, China, April 2008
- Shin, Y. C.; Ton, T. N. & Bui, L. Q. (1988). Waveguide-to-microstrip transitions for millimeter-wave applications, *IEEE MTT-S Int. Microwave Symp. Dig.*, pp.473-475, INSPEC Accession Number:3257643, New York, NY, May 1988
- Simon, W.; Werthen, M. & Wolff, I. (1998). A novel coplanar transmission line to rectangular waveguide transition, *IEEE MTT-S, Int. Microwave Symp. Dig.*, pp.257-260 ISBN: 0-7803-4471-5, Baltimore, MD, June 1998.



# Microwave and Millimeter Wave Technologies A New X-Band Mobile Direction Finder

Sergey Radionov<sup>1</sup>, Igor Ivanchenko<sup>1</sup>, Maksym Khruslov<sup>1</sup>,  
Aleksey Korolev<sup>2</sup> and Nina Popenko<sup>1</sup>

<sup>1</sup> *Usikov Institute for Radiophysics and Electronics  
of the National Academy of Sciences of Ukraine  
12 Ak. Proskura St., Kharkov, 61085, Ukraine  
ireburan@yahoo.com*

<sup>2</sup> *Institute of Radioastronomy  
of the National Academy of Sciences of Ukraine  
4 Krasnoznamennaya st., 61085, Kharkov, Ukraine*

## 1. Introduction

Nowadays, the radio direction finding (DF) has numerous applications in a variety of fields such as radio monitoring, navigation, disaster response, wildlife tracking, electronic warfare [Poisel, 2005], and personal locating service [Xiaobo & Zhenghe, 2002]. DF also forms an important branch of electronic intelligence. With the aim to get high resolution, a large baseline is usually used. In this case the most common DF approach uses phase interferometry method in which the phase delay across the array length (baseline) is measured. Many of DF techniques such as interferometer, correlative interferometer and multiple signal classification [Jnkins, 1991; Schmidt, 1986; Jun-Ho Choi et al., 2008] use the phase information to estimate the angle of arrival. It is well-known that increasing the element spacing increases the resolution, but also proportionally increases the phase ambiguities that must be resolved. These ambiguities occur when the spacing between antenna elements is greater than half of the signal wavelength. As a result of this, multiple baselines are commonly used to resolve ambiguities in DF systems [Pace, 2001; Kwai et al., 2008]. However, there is a need to take into account that the presence of unknown mutual coupling between array elements degrades significantly the performance of most high-resolution DF algorithms. Therefore, many array calibration methods have treated mutual coupling calibration as a parameter estimation problem [Friedlander & Weiss, 1991; See & Poh, 1999; Bu-hong et al., 2008]. It is appropriate mention here that fairly often the DF systems use very small individual radiators with degraded gain when the overall dimensions are important in contrast to the DF antennas in telecommunications systems, where gain or directivity is a prime requirement [Peyrot-Solis et al., 2005; Schantz, 2004; Chevalier et al., 2007]. As regards the wireless communications, during last decade the radio systems operating at frequencies higher 1GHz are widely used. Among them we can point

out the broadband radio-modems with data transmission rate higher 2Mbit/sec. The operational frequencies of those are usually found to be in limits ranging from 1GHz to 5.8GHz. At the same time the advancement to the state-of-the-art backbone links (for instance, WiMAX standards-based technology) compels moving to the higher frequencies. With these remarks in mind a problem of bearing, for example, the unauthorized local SHF sources becomes a topical question and there is a need of suitable broad-band mobile DF. In this respect we can note the compact dually polarized direction finding antenna system, working in the 500–3000MHz frequency band [Bellion et al., 2008] and hand held antenna array for localization of radio devices working on TETRA frequency ranges (380-390 MHz) [Sarkis et al., 2008].

The main objective of this paper is developing and designing X-band hand held DF system for localization the local SHF sources by using the “null-amplitude” technique.

## 2. Design and Experimental Technique

There is a set of canonical radiators, which are used as the individual antennas or the elementary radiators deployed in different array configurations. Here, the researchers offer and utilize various modifications of such the radiators to overcome the problems in the field of the state-of-the-art electromagnetics. Among a majority of individual radiators we have given preference to the usual cylindrical monopole antenna due to its simplicity of designing, omnidirectional radiation pattern in azimuth plane, broadbandness, as well as high values of the antenna gain and efficiency. In the process of our earlier comprehensive investigations of different radiators it has been found that the radiation characteristics of the cylindrical monopole antenna can be sufficiently changed by means of choice the suitable correlations between the monopole height and ground plane size [Ivanchenko et al., 2006; Khruslov & Pazynin, 2006]. In this respect, the revealed opportunity to produce the mono-beam conical radiation pattern with the high elevation angle of the peak directivity and relatively small ground plane of antenna attracted our attention especially. Just this result suggested us to apply such a monopole antenna as a sub-reflector of the reflector-type antenna for the DF [Ivanchenko et al., 2007; Radionov et. al. 2007; Ivanchenko et al., 2008]. Here, it should also be noted that in this case unlike the well-known reflector-type antenna with a dipole vibrator, the proposed antenna allows for connecting the sub-reflector directly to the standard 50 Ohm impedance coaxial feeder.

In this case the most preferable “null-amplitude” technique of the received signal should be applied. As a result of this, the following characteristics of the DF antenna should be provided, namely:

- we have to have the relatively narrow mono-beam conical radiation pattern;
- the elevation angle of the peak directivity should be as much as closer to zenith;
- the power ratio of signal in the antenna axis and in the direction of the radiation maximum as well as the power level of side lobes should at least be less than -10dB;
- the antenna should be essentially broadband one.

It is quite clear that in an effort to achieve the aforementioned characteristics of the reflector antenna, the radiation characteristics of the sub-reflector will have a defining value. Therefore, the main question we address is a choice of the optimal geometry of the monopole antenna from the point of view of designing a compact reflector antenna.

The experiments were carried out in the reactive, radiating and far-field regions of the monopole antennas differing by the monopole height and ground plane size. These experiments were performed with the help of the methods, facilities and special probes developed and designed in the Laboratory of High Frequency Technology and described in detail in our earlier papers [Ivanchenko et al., 2002; Cao et al., 2002; Andrenko et al., 2006; Chernobrovkin et al., 2006; Chernobrovkin et al., 2007]. As an example, the near-field distributions of the quarter-wave monopole antenna with different ground plane radii are shown in Fig. 1a. Thick solid lines at the bottom of pictures show the ground plane size of the monopole antenna. The EM field distributions in the far-field region were measured in the sweep mode of the SHF oscillator that allows for analysing the radiation pattern behaviour in the frequency band of interest. The respective far-field pictures of antenna in coordinates “frequency-radiation angle”, where the colour spectrum corresponds to the EM field power distribution, are presented in Fig. 1b.

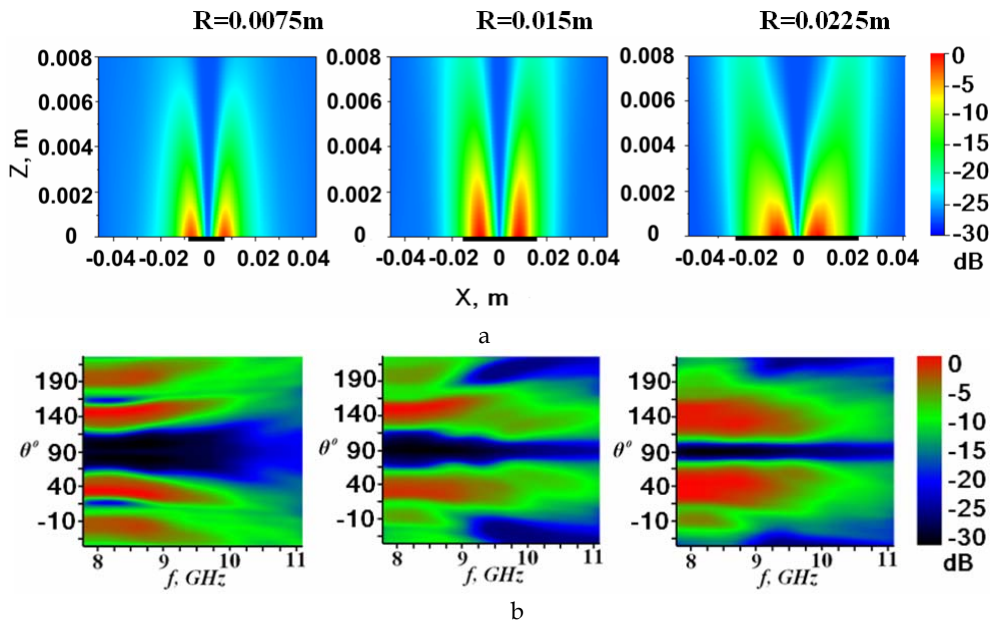


Fig. 1. Near-field distributions (a) and radiation patterns (b) of the quarter-wave cylindrical monopole antenna

### 3. Optimization of the Reflector Antenna

The vertical monopole as an extension of the central conductor of the coaxial cable with diameter  $2b=0.0014\text{m}$  is located above the circular metallic ground plane with thickness  $d=0.0005\text{m}$  (Fig. 2). We focus on the two monopole heights  $h$ , namely: quarter-wavelength ( $h=\lambda/4$ ) and three fourth-wavelength ( $h=3\lambda/4$ ) monopoles (the wavelength  $\lambda=0.030\text{m}$ ). The ground plane radius  $R$  varies from  $0.0075\text{m}$  to  $0.0375\text{m}$  with the step of  $0.0075\text{m}$ . The input reflection coefficient  $S_{11}$ , near-field distributions in the reactive region, radiation patterns, and antenna bandwidth are the characteristics for our analysis. The near-field distributions

in the reactive region are performed on the set-up described in [Ivanchenko et al., 2002]. The scan area in the XOY plane is adjusted to the ground plane size and located at the stand-off distance of 0.001m above the ground plane surface.

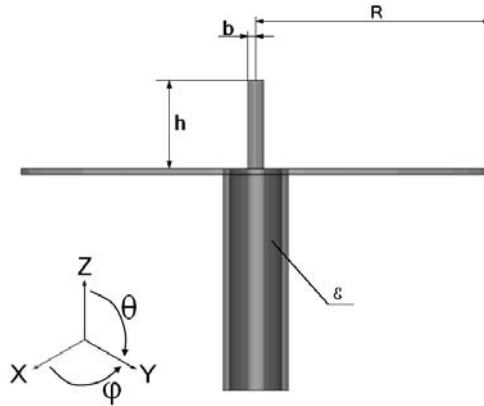


Fig. 2. Schematic view of the monopole antenna

The results obtained in the process of measuring the EM field distributions in the reactive region of the quarter-wavelength monopole antenna show that the field distributions of the  $H_\phi$ -component have two variations along the ground plane radius which equal to an integer number times  $\lambda/2$  (Fig. 3a and Fig. 3b). In this case the first maximum of the magnetic field component is observed near the antenna center, the first minimum of the magnetic field is located at the distance  $\approx \lambda/4$  from the ground plane edge, and the second maximum is located outside the ground plane edge. At the same time, the antennas with ground plane radii equal to the odd number times  $\lambda/4$  (Fig. 3c) have more than one oscillation along the ground plane radius thereby pointed out the interference nature of the fields in the close vicinity of the ground plane surface.

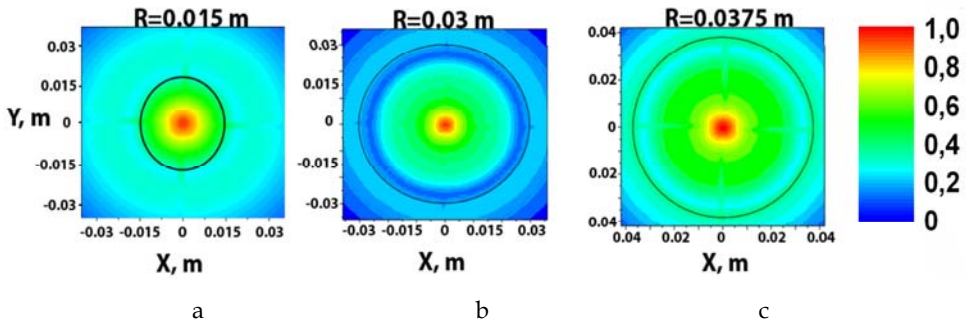


Fig. 3. Near-field distributions of the  $H_\phi$ -component measured in the reactive region of antennas with  $h=\lambda/4$  and different ground plane radii:  $R=0.015\text{m}$  (a);  $R=0.030\text{m}$  (b), and  $R=0.0375\text{m}$  (c). The black circles on the pictures show the ground plane size. The regularities revealed in the near-field distributions should also be reflected in the antenna beam pattern. In fact, the simulated radiation pattern shape of antennas undergoes

appropriate changes when increasing the ground plane radius (Fig. 4). In particular, the secondary beams appear in the backward direction of antennas with the ground plane radii  $R \geq 0.030\text{m}$  and in the broadside direction of antennas with the ground plane radii  $R \geq 0.0375\text{m}$ . The elevation angle of the peak directivity of antennas with different substrate radii  $R$  is oriented at  $\theta = 60^\circ$  ( $R = 0.015\text{m}$ ),  $\theta = 60^\circ$  ( $R = 0.03\text{m}$ ), and  $\theta = 54^\circ$  ( $R = 0.0375\text{m}$ ). It is the author's opinion that these changes in the elevation angle are just determined by the different EM distributions in the reactive region of antennas noted above (Fig. 3).

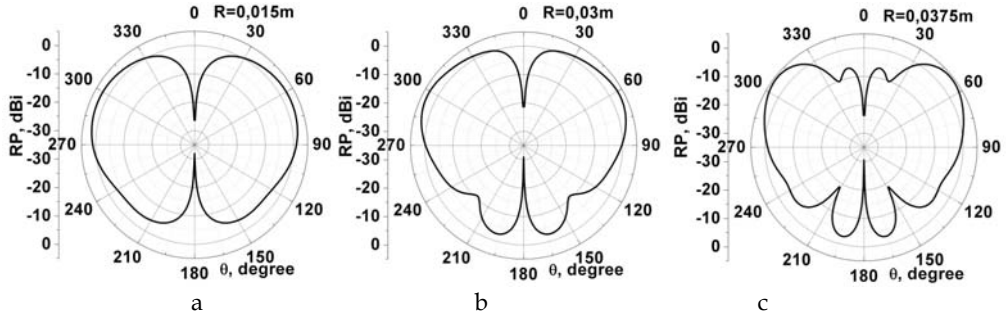


Fig. 4. Simulated radiation patterns of antennas with  $h = \lambda/4$  and different ground plane radii:  $R = 0.015\text{m}$  (a);  $R = 0.030\text{m}$  (b), and  $R = 0.0375\text{m}$  (c)

Unlike the antenna with  $h = \lambda/4$  (Fig. 4) the monopole antenna with  $h = 3\lambda/4$  produces mono-beam radiation pattern in the broadside direction without evident pattern shape transformations when increasing the ground plane radius (Fig. 5). However, the radiation patterns become the multi-beam ones in the backward direction though a power level of the lobes is substantially smaller than that of the antenna with  $h = \lambda/4$ . The elevation angle of the peak directivity of antennas with substrate radii  $R > 0.0225\text{m}$  is virtually the same, namely:  $\theta = 43^\circ$  ( $R = 0.015\text{m}$ ),  $\theta = 33^\circ$  ( $R = 0.0225\text{m}$ ), and  $\theta = 34^\circ$  ( $R = 0.03\text{m}$ ). The measured radiation patterns are in good agreement with simulated ones.

In the framework of these investigations some general regularities in the radiation pattern formation for both monopole heights have been determined, namely: (i) the differences in the near-field distributions lead to the changes in both the radiation pattern shape and the elevation angle of the peak directivity when varying the ground plane radius; (ii) the additional lobes in the broadside and backside directions appear when increasing the ground plane radius; (iii) the influence of the ground plane size on antenna performance is less for antennas with the monopole height  $h = 3\lambda/4$  than that for antennas with the monopole height  $h = \lambda/4$ . As it should be from measurements of near-fields and radiation patterns the monopole antenna with parameters  $h = 0.0075\text{m}$  and  $R = 0.015\text{m}$  seems to be the entirely acceptable one as the sub-reflector because the wave beam is to be wide enough for the effective illumination of the main reflector and the ground plane size is sufficiently small.

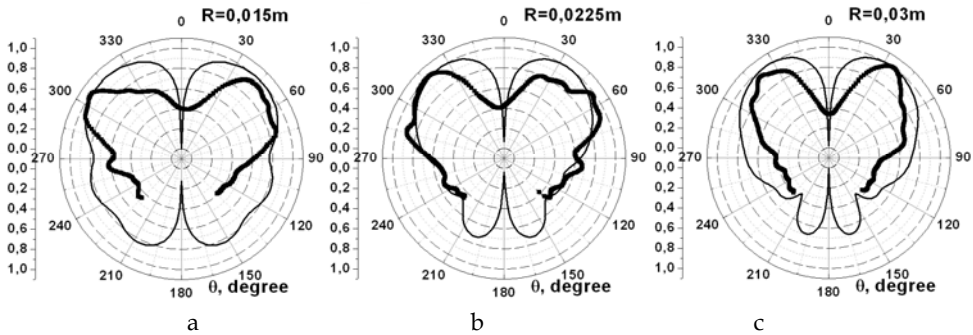


Fig. 5. Simulated (thin line) and measured (thick line) radiation patterns of antennas with  $h=3\lambda/4$  and different ground plane radii:  $R=0.015\text{m}$  (a);  $R=0.0225\text{m}$  (b),  $R=0.030\text{m}$  (c)

The geometrical parameters of the DF antenna consisting of the parabolic reflector and monopole antenna as a primary source are shown in Fig. 6. The primary source is fixed in the foam box and the distance  $D$  between the monopole and the reflector can be changed during the experiment.

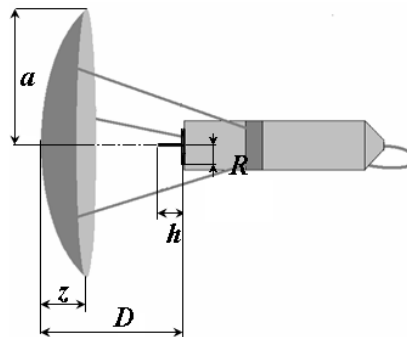


Fig. 6. Schematic view of the reflector antenna.

First, we have carried out a computational modeling of the reflector antenna with the following parameters of sub-reflector:  $h=0.075\text{mm}$  and  $R=0.015\text{m}$ . From our study it has been found that the radiation pattern demonstrates the high level of side lobes (Fig. 7a). Therefore, we have proceeded with computational modeling of the reflector antenna by varying its geometrical parameters in the following limits:  $0.015\text{m} < R < 0.0375\text{m}$ ,  $0.05\text{m} < a < 0.100\text{m}$ , and  $0.04\text{mm} < D < 0.06\text{m}$  for the two monopole heights  $h=0.0075\text{m}$  and  $h=0.0225\text{m}$  (Fig. 6) with the aim to optimize the reflector antenna prototype from the point of view of the main reflector blockage and the utilization factor of its surface. Furthermore, we have to take into account that the antenna should be a long-focus one ( $D > 2a/4$ ) in order to minimize the cross-polarization level and to provide a good matching of antenna with a feeding line in the wide frequency band. As a result of investigations the optimal parameters of the reflector antenna have been determined, namely: the aperture radius of the main reflector is  $a=0.080\text{m}$ , the monopole height  $h=0.0225\text{m}$ , the ground plane radius  $R=0.0225\text{m}$ , the focal



length of the parabolic reflector  $D=0.055\text{m}$ . As can be seen from the Fig. 7b, the simulated radiation pattern of the reflector antenna with aforementioned parameters shows substantially lower level of side lobes.

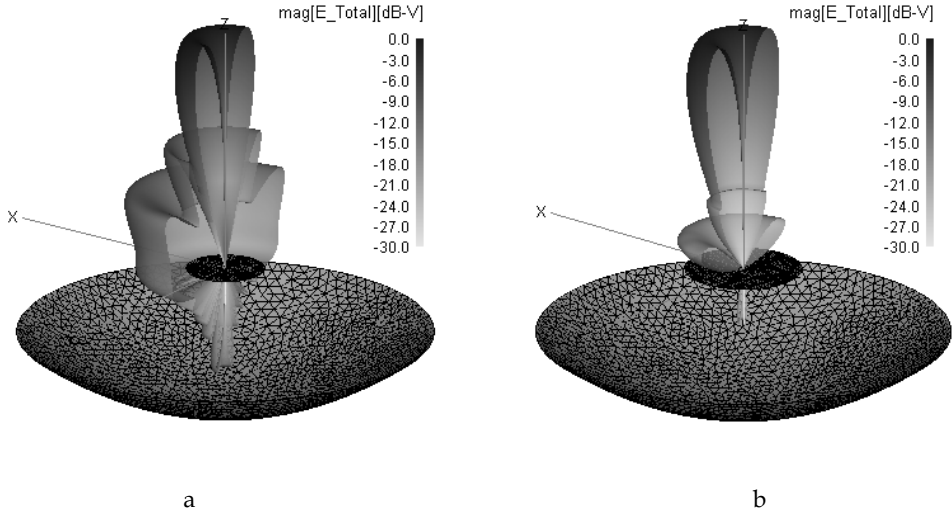


Fig. 7. Simulated radiation patterns of the reflector antenna with  $h=0.0075\text{m}$ ,  $R=0.015\text{m}$  (a) and  $h=0.0225\text{m}$ ,  $R=0.0225\text{m}$  (b) parameters.

The characteristics of the reflector antenna ( $\theta^0$  is the elevation angle;  $\Delta\theta^0$  is the beamwidth) are shown in Table 1. The angle  $\Delta\theta'$  is determined by the two positions of the DF antenna relative to the external SHF source when the signal amplitude increases on 3dB in comparison with the signal level in the “global” minimum of the radiation pattern.

$\theta$ (degree)	$\Delta\theta$ (degree)	$\Delta\theta'$ (degree)	Side lobe level (dB)	Gain (dB)
Theory				
10	10	1.5	-21	18
Experiment				
10	7	1.5	-19	17

Table 1. The characteristics of the reflector antenna

With these remarks in mind we have manufactured the novel reflector-type antenna. The measured VSWR of the antenna prototype is less than 2 in the wide frequency band (Fig. 8).

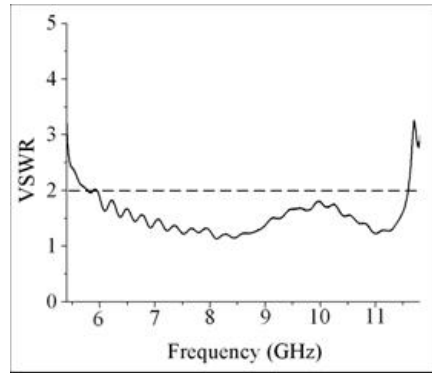


Fig. 8. VSWR of the antenna prototype

With the aim to study the process of radiation shaping of the reflector antenna and to optimize the mutual arrangement of supporting elements, we have carried out the simulations and measurements of EM field distributions in the radiating region of the reflector antenna prototype. The near-field distribution being measured at frequency  $f=10\text{GHz}$  is shown in Fig. 9a for the optimized DF antenna prototype. As one sees from this picture, one has the main lobe and the weak side lobe with a power level around  $-15\text{dB}$ . The simulations of near-field distribution at the same frequency  $f=10\text{GHz}$  (Fig. 9b) points out a qualitative agreement with the experiment. Thus, we can pronounce that the selected by us supporting elements do not virtually disturb the EM field distribution in the radiating region of the antenna prototype.

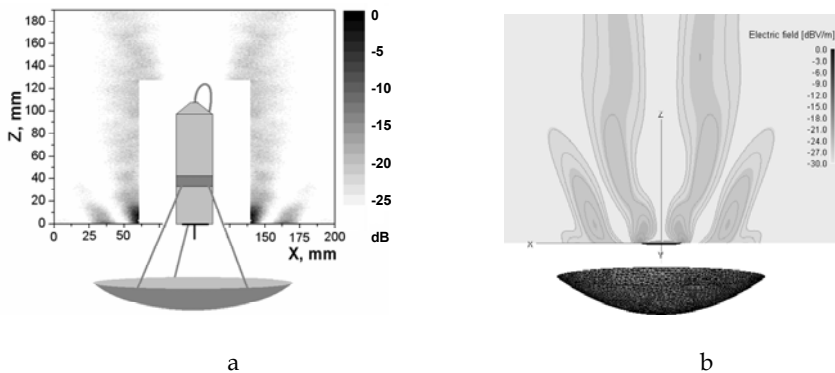
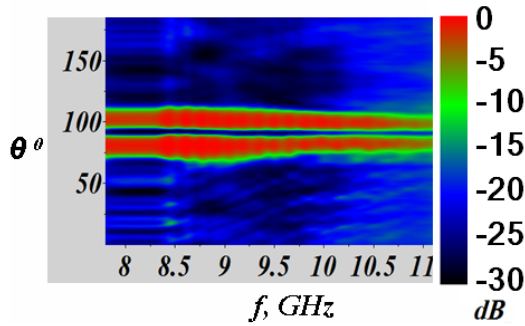


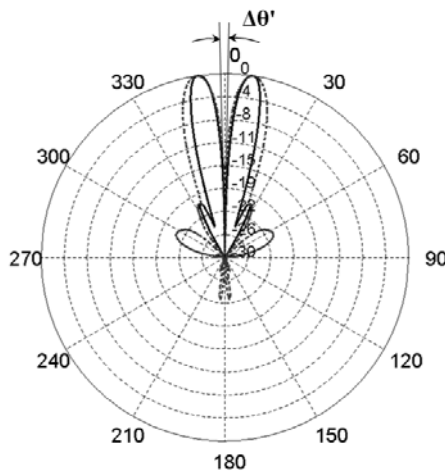
Fig. 9. Measured (a) and simulated (b) near-field distributions of the antenna prototype

The experiments being performed in the far-field region of the DF antenna have shown that the antenna produces mono-beam conical radiation pattern in the bandwidth of  $5.5\text{GHz}$  (Fig. 10a) with the elevation angle of the peak directivity equals to  $10^\circ$  and the beamwidth around  $10^\circ$ . We note that the radiation pattern shape remains virtually the same within the antenna bandwidth. The typical radiation pattern at frequency  $f=10\text{GHz}$  is shown in Fig. 10b. From the practical point of view it is important that the power signal ratio in the

antenna axis and in the main lobe maximum is less than -20dB. It should be also noted that the principal characteristic of the DF using the “null-amplitude” technique is the angular domain of the “global” minimum of the radiation pattern  $\Delta\theta'$  which equals to 1.50 in this case.



a



b

Fig. 10. Measured radiation pattern within the antenna bandwidth (a); simulated (dotted line) and measured (solid line) radiation patterns at  $f=10\text{GHz}$  (b) of the antenna prototype

Thus, the reflector antenna has the good principal characteristics such as elevation angle, beamwidth, bandwidth, and sharp power minimum along the antenna axis that allows us to expect high sensitivity and space resolution of the proposed DF.

#### 4. Direction Finder Prototype

The conceptual diagram of the DF is shown in Fig. 11a. The signal received from the SHF source enters into the low-noise amplifier for the signal pre-amplification over the entire operational frequency band. The subsequent logarithmic amplifier realizes the signal amplification to the level to be quite enough for the effective ultra wideband video detector operation ( $U=1\text{mV}$ ) and provides a suitable dynamic range of the received signal thereby guarantees a high accuracy of the center of “global” minimum location. The need in the UWB detector is determined by a large difference (up to 20dB) of the signal power in the main lobe and in the “global” minimum of the radiation pattern. The wideband low-noise video amplifier with a small integration time constant ( $\tau=0,1 - 1$  microseconds for the choice) increases the signal up to the level required to the stable flash encoder operation (around 2.5V). The photo of the DF prototype is shown in Fig. 11b.

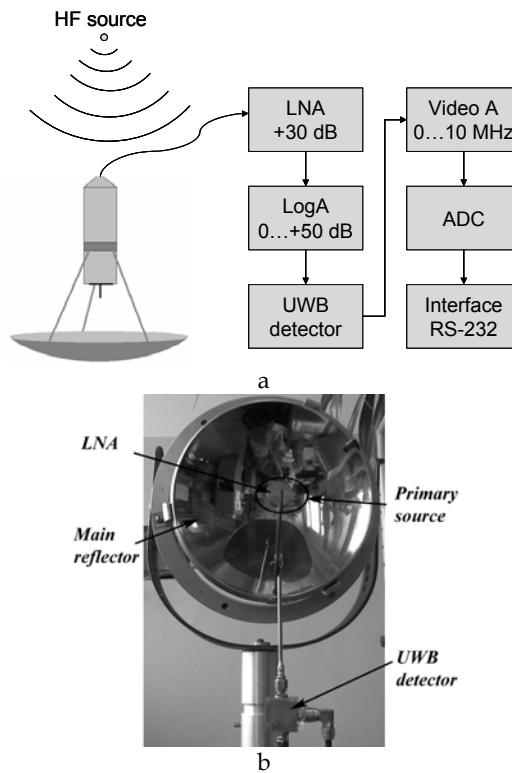


Fig. 11. Block-diagram of the direction finder (a) and direction finder prototype (b)

After video-amplifier the signal enters the interface, which serves for the registration, numeralization, and displaying the level of received signal, and then enters the working board of the control unit. The photo of the control unit is shown in Fig. 12a. As the radiation pattern looks like a “bell” shape we imitate a bearing process on the front panel of the

control unit by V-symbol of the light emitting diodes (LED) which are connected with the power level of the received signal (Fig. 12b).

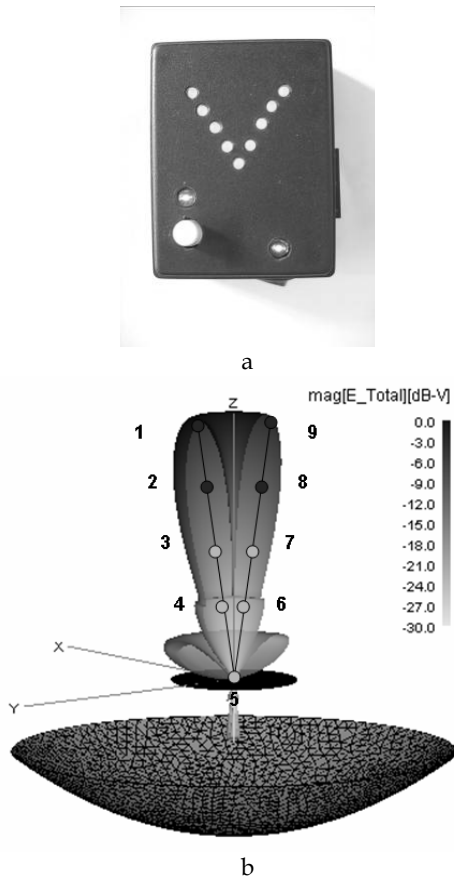


Fig. 12. Control unit (a) and conformity of the bearing process indication (b)

### 5. The Bearing Algorithm

The bearing algorithm is as follows. It is quite clear that first of all the preliminary scan of the space area of interest is carried out. Let us assume that only the one SHF source is located in the space. In this case we shall detect this source when it will hit the main lobe of the radiation pattern of the DF antenna. At that, the source bearing will be determined by the antenna position corresponding to the “global” minimum of the received signal. Below the bearing algorithm is described in detail by means of the diagram shown in Fig. 13.

Two operation modes so-called the “Search mode” and the “Bearing mode”, respectively, are realized here. Under the DF operation in the “Search mode” the angular domain of the source location and its power level are determined. In the “Search mode” operation and

under the external sources failing all the LED's on the front panel of the control unit frequently blink thereby indicating an availability of both the internal equipment noises and the environment background noise. The appearance of source signal is indicated by the ignition of all the LED's and the maximum power level of the received signal with the value 0dB remain in the microcontroller memory. Any deviation of the DF antenna from this position will lead to the signal power decrease and will be accompanied by LED's switching off in pairs top-down according to the introduced normalization. During the process of the consequent space scanning within the angular domain of the revealed source, every such a scan is completed by the memorization of the maximum signal level. In other words, the following conditions hold, namely: if  $\text{InpS} > \text{max}$ ;  $\text{max} = \text{InpS}$ . Thus, in the 'Search mode' operation the angular domain and the maximum signal level of the external SHF source are determined.

The parameters noted above are the initial ones for the "Bearing mode" operation. In this case a one of the upper two LED's on the working board of the control unit is shined. Let us propose that with the antenna rotation from the aforementioned initial position the received signal decreases by accompanied with the alternate LED's switching top-down so long as the lower LED goes out. These conditions correspond to the drift of antenna from the source. After that the antenna goes back to the initial position of the maximum signal reception and turns in the opposite direction (i.e., to the source). In this case the LED's will alternate switching along the appropriate branch of the symbol V on the working board of the control unit. After passing of antenna the point of the null signal reception, the LED's begin to shine in turn on the second branch of the symbol V on the working board of the control unit right up to the topmost LED. Thus, the source bearing corresponds to the antenna position when the lower LED shines on the working board of the control unit.

Let's now determine the conditions of the precise determination of the bearing angle. First of them consists in that the power level of the received signal for the antenna position corresponding the null reception must decrease to the signal level given in advance (in our case this upper level of the "global" minimum is determined by the radiation pattern of antenna and equals to -13dB). However, when holding only this condition, we can have the bearing uncertainty in view of the chaotic LED's switching between the left and right branches of the symbol V (the side lobes availability or the loss of signal at the drift of antenna from the source). In this respect the second condition is that the source must remain in the main lobe of the radiation pattern of antenna during the bearing process. Therefore, the complementary variable  $\text{max\_dB}$  with the initial value of -100dB is introduced in the program and we assign in advance the condition  $\text{max\_dB} > -5.5\text{dB}$  which is determined experimentally. Only in the case of the signal level exceeding -5,5dB again and subsequent its decreasing to the level  $< -13\text{dB}$ , we will observe the LED's switching from the one branch of the V-symbol to another one. It means that at first the antenna scan should be realized in the one selected direction right up to the total signal loss and only after that the antenna should turn in the opposite direction.

If the signal level (in the process of antenna scanning) becomes less than -12dB, the lower LED shines on the front panel of the control unit and with the subsequent signal level increase the LED's will be alternate shined on the another branch. It is worth noting that the lower LED goes out when the signal level becomes  $< -25\text{dB}$ . Just this condition corresponds to the signal loss. Thus, this is the lower limit of the received signal level at which all the LED's go out.

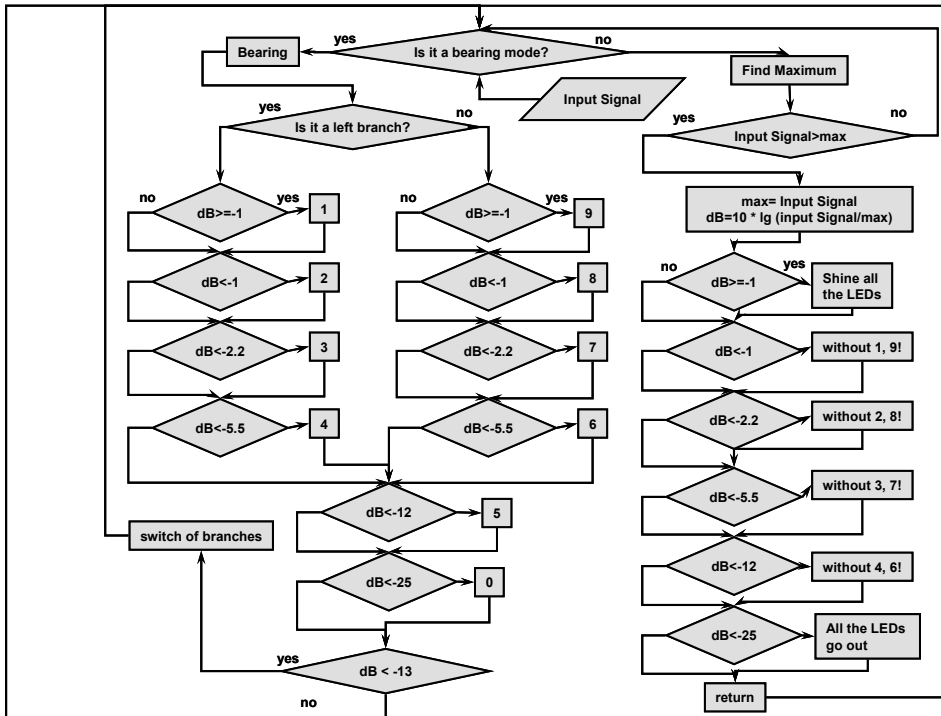


Fig. 13. Block-diagram illustrating the bearing algorithm

### 6. Model experiments

We have carried out a set of model experiments on the SHF source bearing by means of the aforementioned DF prototype. In these experiments we used the standard open-ended X-band waveguide as the isolated source, which was located at the distance 100m from the DF antenna (Fig. 14).

By using the algorithm noted above we have determined the direction on the SHF source with an evaluation accuracy of the source bearing equal to  $2^0$ . We note that the noise-factor of the DF integrally (excluding the DF operation in zenith directly) averages 2 - 4dB depending on the angle of arrival.

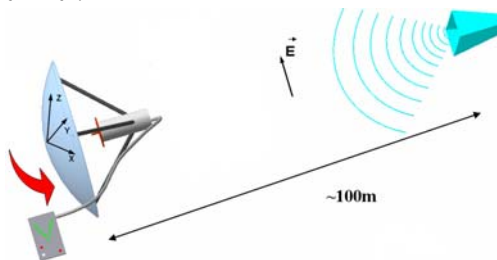


Fig. 14. Bearing the SHF source ( $f=10.3$  GHz)

Another situation is shown in Fig. 15. In the case when the angle between two incoherent sources equals to the two beamwidths  $2\theta_b$  or less, the sources bearing will not be determined correctly. In fact, one may assume that a single virtual source is located between two real sources. It is evident that we shall face the challenge like that in the case of several active SHF sources located in the analyzable space. Therefore, our further investigations will be aimed at the development of effective algorithms which allow one to solve this problem as well as to determine the source position and to improve the DF sensitivity.

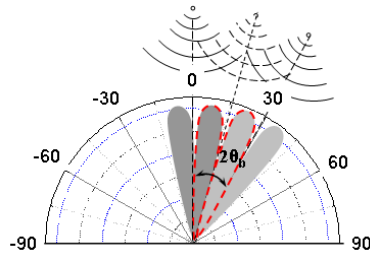


Fig. 15 Bearing of the two SHF sources operating at frequencies  $f_1=10.3\text{GHz}$  and  $f_2=9.2\text{GHz}$ , respectively

Finally, we have to take into account that the polarization of the source radiation will play a vital part in the bearing process. In spite of the fact that the DF antenna is able to receive the SHF signal with an arbitrary polarization, such an immovable antenna will be blind to the source having  $E_\varphi$ -polarization and moving in the same plane.

## 7. Conclusion

The original reflector antenna design with the cylindrical monopole antenna as a sub-reflector has been presented. The good matching of the reflector antenna to 50 Ohm feeding line has been achieved over the entire operational frequency band. The main features of the bearing algorithm have been described in detail. The capability and benefits of the proposed DF have been demonstrated by the model experiments on the external SHF source bearing. The results of model experiments with the DF prototype allow for estimating its basic characteristics:

Operational frequency band	6 - 11.5GHz
Dynamic range	50 dB
Noise factor	<3 dB
Bearing accuracy	$2^\circ$
Beamwidth	$10^\circ$
Elevation angle of peak directivity	$80^\circ$
Radiation power ratio in the antenna axis and in the radiation maximum	<-20dB
Power level of side lobes	-20dB
Cross-polarization level	<-15dB
Bearing method	"null-amplitude" technique



The proposed DF seems to be very attractive for BWLL, WLAN, and WiMAX applications.

## 8. References

- Andrenko, A. et. al. (2006). Active Broad X-Band Circular Patch Antenna, *IEEE ANTENNAS AND WIRELESS PROPAGATION LETTERS*, Vol. 5, 2006, pp. 529-533.
- Bellion, C. et. al. (2008). A New Compact Dually Polarized Direction Finding Antenna on the UHF Band, *Proceedings of the Antennas and Propagation International Symposium and USNC/URSI National Radio Science Meeting*, 526.7, July 2008.
- Bu-hong, W. et. al. (2008). Ambiguity Analysis and Solution for Direction Finding of Uniform Circular Array with Mutual Coupling, *Proceedings of the Antennas and Propagation International Symposium and USNC/URSI National Radio Science Meeting*, 225.10, July 2008.
- Cao, W. et. al. (2002). Modal Analysis of Rectangular Dielectric Resonator Antennas, *Proceedings of the International Symp. of Antennas*, pp.729-731, Nice (France), May 2002.
- Chernobrovkin, R. et. al. (2006). Millimeter wave nondestructive testing techniques for the embedded defects characterization, *Proceedings of the «Mediterranean Microwave Symposium MMS-2006»*, pp. 216-219, Genova (Italy), September 2006.
- Chernobrovkin, R. et. al. (2007). A Novel V-band Antenna for Nondestructive Testing Techniques, *Microwave and Optical Technology Letters*, Vol. 49, No. 7, Jul. 2007, pp. 1732-1735.
- Chevalier, P. et. al. (2007). Higher Order Direction Finding From Arrays With Diversely Polarized antennas, *Transactions on Signals Processing*, Vol. 55, No 11, Nov. 2007.
- Choi, Jun-Ho et. al. (2008). Indoor Sensor Array Test-Bed (SATB) for Direction Finding Applications at Communication-band, *Proceedings of the Antennas and Propagation International Symposium and USNC/URSI National Radio Science Meeting*, 439.7, July 2008.
- Friedlander, B. & Weiss, A. (1991). Direction finding in the presence of mutual coupling, *IEEE Trans. Antenna Propag.*, Vol. 39, No. 3, March 1991, pp.273-284.
- Ivanchenko, I. et. al. (2002). Experimental Studies of X-band Leaky-wave Antenna Performances, *Microwave and Optical Technology Letters*, Vol. 35, No. 4, April 2002, pp. 281-283.
- Ivanchenko, I. et. al. (2006). Effect of finite screen and monopole's height on radiation characteristics of monopole antenna, *Proceedings of the 16-th international conference on microwaves, radar and wireless communications MICON-2006*, pp.729-731, Krakov (Poland), May 2006.
- Ivanchenko, I. et. al. (2007). Compact broad-band SHF direction finder for WiMax applications, *Proceedings of the 10th European Conference on Wireless Technology. EuMW/07*, pp. 316-319, Munich (Germany), October 2007.
- Ivanchenko, I. et. al. (2008). Broadband SHF direction-finder, *Radioengineering*, Vol. 17, No. 2, June 2008, pp.61-65.
- Jinkins, H. (1991). Small aperture radio direction finding, In: *Artech House*.
- Khruslov, M. & Pazyinin V. (2006). Edge effect influence on a radiation formation of the cylindrical monopole antenna, *Proceedings of the «Mathematical methods in electromagnetic theory MMET-2006»*, pp. 178-180, Kharkov (Ukraine), June 2006.

- Kwai, K. et. al. (2008). Robust Symmetrical Number System Direction Finding Arrays with Virtual Spacing, *Proceedings of the Antennas and Propagation International Symposium, and USNC/URSI National Radio Science Meeting*, 237.3, July 2008.
- Pace, P. et. al. (2001). High Resolution Phase Sampled Interferometry Using Symmetrical Number Systems, *IEEE Transactions on Antennas and Propagation*, Vol. 49, No. 10, October 2001, pp. 1411-1423.
- Peyrot-Solis, M. et. al. (2005). State of the Art in Ultra Wideband Antennas, *Proceedings of the 2nd International Conference on Electrical and Electronics Engineering and XI Conference on Electrical Engineering* 2005.
- Poisel, R. (2005). Electronic Target Location Methods, In: *Artech House*.
- Radionov, S. et. al. (2007). Broadband SHF direction-finder, *Proceedings of the 19th International Conference on Applied Electromagnetics and Communications*, pp. 67-70, Dubrovnik (Croatia), October 2007.
- Sarkis, R. et. al. (2008). Amplitude and Phase Correction of the Radiation Pattern in Compact Planar Antenna Array for Direction Finding Applications, *Proceedings of the Antennas and Propagation International Symposium and USNC/URSI National Radio Science Meeting*, 435.3, July 2008.
- Schantz, H. (2004). A Brief History of UWB Antennas, *Proceedings of the IEEE A&E Systems Magazine*, April 2004.
- Schmidt, R. (1986). Multiple emitter location and signal parameter estimation, *IEEE Trans. on Antennas and Propagation*, Vol. AP-345, No. 3, Mar. 1986, pp. 276-280.
- See, C. & Poh, B. (1999). Parametric sensor array calibration using measured steering vectors of uncertain locations. *IEEE Trans. Signal Processing*, Vol.47, No.4, April 1999, pp.1133-1137.
- Xiaobo, V. & Zhenghe, R. (2002). A single channel correlative interferometer direction finder using VXI receiver, *Proceedings of the Int. Conf. on Microwave and Millimeter wave Technology*, Aug. 2002.

# Characterization techniques for materials' properties measurement

Hussein KASSEM, Valérie VIGNERAS and Guillaume LUNET  
*University of Bordeaux, IMS-Bordeaux Laboratory  
 France*

## 1. Introduction

The electromagnetic properties of materials are defined from the two following constitutive parameters: permittivity,  $\epsilon$ , and permeability,  $\mu$ ; ' $\epsilon'$ ' indicates how the medium reacts when an electric field is applied (field E of the electromagnetic wave), whereas  $\mu$  indicates how the material behaves further to a magnetic excitation (field H of the electromagnetic wave). To take into account the losses that occur in any material, permittivity and permeability need both to be expressed by complex values:  $\epsilon = \epsilon' - j\epsilon''$ ,  $\mu = \mu' - j\mu''$ .

But already, what represent these parameters?

As, during this chapter we will mostly be interested by the measurement of the permittivity of materials, we'll going to explain the dielectric properties and similar explanation can be mounted for the magnetic properties.

In general, a material is classified as "dielectric" if it has the ability to store energy when an external electric field is applied. Lets imagine a DC voltage source placed across a parallel plate capacitor, we'll have the ability to store an electric charge and called the capacitance ' $C$ ' defined to be the charge ' $q$ ' per applied voltage ' $V$ ' that is  $C_0 = q/V$ , where  $C$  is given in coulombs per volt or farad. The capacitance is higher, the larger the area  $A$  of the plates and the smaller the distance  $L$  between them. And so,  $C_0 = \epsilon_0 (A/L)$ , where  $\epsilon_0$  is a universal constant having the value of  $8.85 \times 10^{-12}$  F/m (farad per meter) and is known by the name permittivity of empty space (or of vacuum).

Now lets insert a material between the plates, the new value of the capacitance ' $C$ ' is increased by a factor  $\epsilon = C/C_0$ , which lead to  $C = \epsilon\epsilon_0 (A/L)$ , where ' $\epsilon'$ ' represents the magnitude of the added storage capability. It is called the (unit less) dielectric constant (or occasionally the relative permittivity  $\epsilon_r$ ). So, for the complex representation  $\epsilon_r = \epsilon_r' - j\epsilon_r''$ , the real part of permittivity ( $\epsilon_r'$ ) is a measure of how much energy from an external electric field is stored in a material. The imaginary part of permittivity ( $\epsilon_r''$ ) is called the loss factor and is a measure of how dissipative or lossy a material is to an external electric field. The imaginary part of permittivity ( $\epsilon_r''$ ) is always greater than zero and is usually much smaller than ( $\epsilon_r'$ ). the loss is usually denoted by: the loss tangent or 'tan  $\delta$ ' which is defined as the ratio of the imaginary part of the dielectric constant to the real part. The loss tangent 'tan  $\delta$ ' is called tan delta, tangent loss or dissipation factor.

Dielectric materials, that is, insulators, possess a number of important electrical properties which make them useful in the electronics industry. A type of dielectric materials is the ferroelectric materials, such as barium titanate. These materials exhibit spontaneous polarization without the presence of an external electric field. Their dielectric constants are orders of magnitude larger than those of normal dielectrics. Thus, they are quite suitable for the manufacturing of small-sized, highly efficient capacitors. Moreover, ferroelectric materials retain their state of polarization even after an external electric field has been removed. Therefore, they can be utilized for memory devices in computers, etc.

Taken together, these properties have been the key to the successful use of ceramics in microwave and optical domains. They are widely studied nowadays as potential replacements for semiconductors in modern tunable microwave devices such as tunable filters, phase-shifters, frequency mixers, power dividers, etc. This material integration, often in thin layers, for the miniaturization of components and circuits for telecommunications requires a preliminary knowledge of the dielectric and/or magnetic characteristics of these materials.

Accurate measurements of these properties can provide scientists and engineers with valuable information to properly incorporate the material into its intended application for more solid designs or to monitor a manufacturing process for improved quality control.

Variety of instruments, fixtures, and software to measure the dielectric and magnetic properties of materials are offered by the industries, such as network analyzers, LCR meters, and impedance analyzers range in frequency up to 325 GHz. Fixtures to hold the material under test (MUT) are available that are based on coaxial probe, coaxial/waveguide transmission line techniques, and parallel plate. Most of these serve to measure massive materials, but, with the advance in technology and miniaturizations of devices, thin film measurement became essential but still not yet industrialized.

In general, to measure the permittivity and permeability of a given material, a sample is placed on the path of a traveling electromagnetic wave, either in free space or inside one of the propagation structures mentioned. One can also put this sample at an antinode of the electric or magnetic field of a stationary wave, for example inside a resonator cavity. Reflection and transmission coefficients of the experimental device are directly related to electromagnetic properties of the material of concern; they are measured using a network analyzer. Then, the sample permittivity and permeability are determined from these coefficients and from the electromagnetic analysis of the discontinuities created within the material.

To select a characterization method, one should consider:

- the exploited frequency range,
- the physical properties of the material of concern: is it magnetic or not, low-loss or lossy, isotropic or anisotropic, homogeneous or heterogeneous, dispersive or not? And
- the shape and nature of the available samples, i.e. plate or thin films, liquid or solid, elastomeric or granular.

At microwave frequencies, generally higher than 1GHz, transmission-line, resonant cavity, and free-space techniques are commonly used. Here we present a brief coverage of both established and emerging techniques in materials characterization.

## 2. Methods of characterizations

A state of the art on the techniques for electromagnetic characterization of dielectric materials is carried out. The most common methods are classified into their main categories: resonant and broadband.

### 2.1 Massive materials measurements

#### (a) Coaxial probe

In a reflection method, the measurement fixture made from a transmission line is usually called measurement probe or sensor. There is a large family of coaxial test fixtures designed for dielectric measurements and those are divided into two types: open-circuited reflection and short-circuited reflection methods.

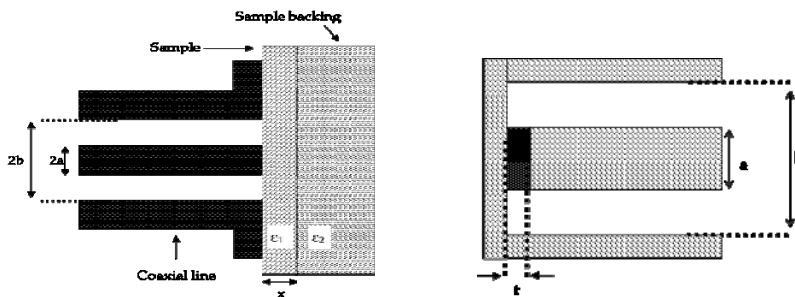


Fig 1. (left) open ended coaxial probe, (right) short ended coaxial probe test fixture

Open-ended coaxial test fixtures (OCP) (Fig 1-left) are the most popular techniques for measuring of complex dielectric permittivity of many materials. Non-destructive, broadband (RF and microwave ranges), and high-temperature ( $\leq 1200$  C) measurements can be performed with this method using commercially available instrumentation. The measurements are performed by contacting one flat surface of the specimen or by immersing the probe in the liquid sample. These techniques (Baker-Jarvis & Janezic, 1994; chen et al. 1994) has been widely used due to the convenience of using one port measurements to extract dielectric parameters and the relatively simple setup. Furthermore, minimal sample preparation is required compared to other techniques, such as the waveguide technique which will be seen later and which requires precisely machined bulk samples and is generally classified as a destructive testing method.

There are two basic approaches to the determination of complex permittivity from the measurements of the coaxial line open-circuit reflection coefficient; a rigorous solution (Baker-Jarvis & Janezic, 1994; chen et al. 1994) of the electromagnetic field equations, and the lumped equivalent approach utilising an admittance circuit to represent the probe fringing fields. Nevertheless, theoretical formulations for the open-ended coaxial probe assume that the MUT extends to infinity in the longitudinal and transverse directions, which is practical when considering finite thin samples.

(chen et al. 1994) presented a method using an open coaxial probe where the material to be measured (MUT) is backed by an arbitrary medium of semi-infinite thickness in a bi-layer configuration (Fig 1-a). The coaxial line is considered to have an infinite flange extending in

the radial direction, while the MUT is considered to be linear, isotropic, homogeneous and nonmagnetic in nature. It is further assumed that only TEM mode fields exist at the probe aperture. The total terminal capacitance  $C_T$  can be represented by:

$$C_T = C_f + C_{01} + C_{02} \quad (1)$$

Where  $C_f$  is the capacitance inside a Teflon-filled coaxial line while  $C_{01}$  represents the capacitance due to the fringing field outside the coaxial line into the finite sample and  $C_{02}$  represents the capacitance of the fringing field into the infinitely thick medium that is used to back the sample.

The final expression for the permittivity of the MUT after incorporating the error network is expressed as:

$$\epsilon_1 = \frac{a\rho + b}{c\rho + 1} = \frac{g_1(f, x, D, \epsilon_2)\rho + g_2(f, x, D, \epsilon_2)}{g_3(f, x, D, \epsilon_2)\rho + 1} \quad (2)$$

Where  $\epsilon_1$  and  $\epsilon_2$  are the dielectric constants of the MUT and the infinite medium (dielectric backing), respectively,  $x$  is the thickness of the MUT and  $D$  represents an empirical parameter with dimensions of length,  $\rho$  is the measured reflection coefficient,  $a$ ,  $b$  and  $c$  are complex coefficients that are functions of frequency  $f$ . corresponding to functions  $g_1$ ,  $g_2$  and  $g_3$  respectively which are, in turn, dependent on parameters  $f$ ,  $x$ ,  $D$  and  $\epsilon_2$ . To extract  $\epsilon_1$ , three simultaneous equations are required to determine  $a$ ,  $b$  and  $c$ , which are obtained by measuring the reflection coefficients of three materials with known dielectric properties. The model is valid at frequencies for which the line dimensions are small compared to the wavelength.

The OCP method is very well suited for liquids or soft solid samples. It is accurate, fast, and broadband (from 0.2 to up to 20 GHz). The measurement requires little sample preparation. A major disadvantage of this method is that it is not suitable for measuring materials with low dielectric property (plastics, oils, etc.) nor for thin films.

Short-circuited reflection: In these methods, a piece of sample is inserted in a segment of shorted transmission line. An interesting method is presented by (Obrzut & Nozaki, 2001) (Fig 1-right). A dielectric circular film (disk) specimen of thickness  $t$  is placed at the end of the center conductor of a coaxial airline. The diameter of the specimen 'a' matches that of the central conductor and forms a circular parallel-plate capacitor terminating the coaxial line. The incoming transverse-electromagnetic (TEM) wave approaches the sample section through the coaxial line. The lumped capacitance model applies to this structure at higher frequencies and still satisfies the quasi-static conditions as long as the length of the propagating wave is much larger than the film thickness. The structure is electrically equivalent to a network in which the dielectric film can be viewed as a transmission line inserted between 2 matched transmission lines. The permittivity of the sample material is written as follows:

$$\epsilon^* = \frac{G_s}{j\omega C_p} \frac{1 - S_{11}}{1 + S_{11}} - \frac{C_f}{C_p} \quad (3)$$

where  $G_s$  is the conductance,  $C_p$  is the capacitance of the sample,  $C_f$  is the fringing capacitor,  $S_{11}$  is the reflection coefficient resulting from wave multiple reflection + transmission components in the specimen section.

Short-terminated probes are better suited for thin film specimens. Dielectric materials of precisely known permittivity are often used as a reference for correcting systematic errors due to differences between the measurement and the calibration configurations. The properties of the sample are derived from the reflection due to the impedance discontinuity caused by the sample loading.

#### (b) Free space

Among the measurement techniques available, the techniques in free space (Varadan et al. 2000; Lamkaouchi et al., 2003) belong to the nondestructive and contactless methods of measurement. They consequently do not need special preparation of the sample; they can be used to measure samples under special conditions, such as high temperature and particularly appropriate to the measurement of non-homogeneous dielectric materials.

With such methods, a sample is placed between 2 antennas: a transmission antenna and a reception antenna placed facing each other and connected to a network analyzer.

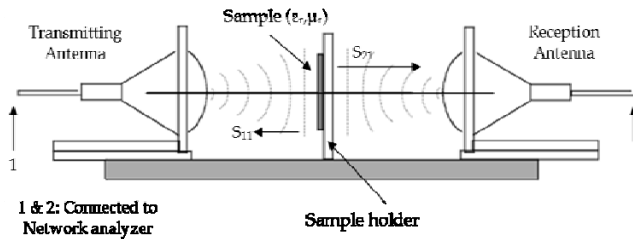


Fig. 2. Free space measurement bench with the sample placed between 2 antennas

Before starting the measurement, the VNA must first be calibrated. Then, using the de-embedding function of the VNA, the influence of the sample holder can be cancelled out and only the s-parameter of the MUT can be determined. Time domain gating should also be applied to ensure there are no multiple reflections in the sample itself, though appropriate thickness should be able to avoid this. It also eliminates the diffraction of energy from the edge of the antennas. Many conditions are requirement to obtain perfect results:

- Far field requirements: to ensure that the wave incident to the sample from the antenna can be taken as a plane wave, the distance  $d$  between the antenna and the sample should satisfy the following far-field requirement:  $d > 2D^2/\lambda$ , where  $\lambda$  is the wavelength of the operating electromagnetic wave and  $D$  is the largest dimension of the antenna aperture. For an antenna with circular aperture,  $D$  is the diameter of the aperture, and for an antenna with rectangular aperture,  $D$  is the diagonal length of the rectangular aperture.
- Sample size: if the sample size is much smaller than the wavelength, the responses of the sample to electromagnetic waves are similar to those of a particle object. To achieve convincing results, the size of the sample should be larger than the wavelength of the electromagnetic wave.
- Measurement environment: An anechoic room is preferable; we can also use time-domain gating to eliminate the unwanted signal caused by environment reflections and multi-reflections.

After that, from a precise phase measurement, a precise measurement of the permittivity on a broad frequency band can thus be carried out using generally the “Nicolson–Ross–Weir (NRW) algorithm” (Nicolson & Ross, 1970; Weir, 1974) where the reflection and transmission are expressed by the scattering parameters  $S_{11}$  and  $S_{21}$  and explicit formulas for the calculation of permittivity and permeability are derived.

## 2.2 Thin films measurements

### (a) Short frequency band methods

#### Capacitive methods:

The basic methods for measuring the electromagnetic properties of materials at low frequencies consists of placing the material in a measuring cell (capacitor, inductance) where we measure the impedance  $Z$  or the admittance  $Y=1/Z$  (Mathai et al, 2002). The permittivity of the material is deduced from the measured value of  $Z$  or  $Y$  using a localized elements equivalent circuit representing the measurement cell. Capacitance techniques (Fig. 3) include sandwiching the thin layer between two electrodes to form a capacitor. They are useful at frequencies extending from fractions of a hertz to megahertz frequencies. Yet, with very small conductors, specimens can be measured up to gigahertz frequencies (Park et al. 2005; Obrzut & Nozaki, 2001). Capacitance models work well if the wavelength is much longer than the conductor separation. The capacitance for a parallel plate with no fringing fields near the edges and the conductance (represent losses) at low frequency are written as:

$$C = \frac{\epsilon' A}{d} \text{ and } G = \omega \frac{\epsilon'' A}{d} \quad (4)$$

The permittivity can be obtained from measurements of  $C$  and  $G$  and is given by:

$$\epsilon_r = \frac{C - jG/\omega}{C_{\text{air}} - jG_{\text{air}}/\omega} \quad (5)$$

This model assumes no fringing fields. A more accurate model would include the effects of fringing fields. The use of guard electrodes as shown in Fig. 3 minimizes the effects of the fringe field.

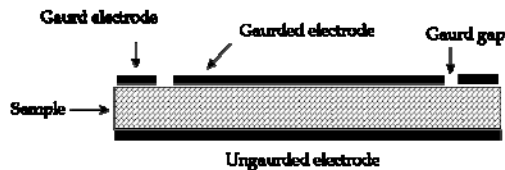


Fig. 3. A specimen in a capacitor with electrode guards.

Many procedures of measurement depending on the capacitive techniques have been widely reported during the last decade. These methods whether using transmission lines, interdigital capacitors or the classic capacitor, have their principle basics on measuring the equivalent total impedance of the cell using an impedance analyser where we can measure



directly the capacitance and conductance or using a network analyser thus measuring the reflection coefficient  $S_{11}$  and deducing the impedance of the whole structure using the formula:

$$Z_{in} = Z_0(1 + S_{11}) / (1 - S_{11}) \tag{6}$$

Then with an analytical work we go up with the dielectric permittivity of the material under test. Other methods use very complicated equivalent circuit to represent the measurement device and increase the accuracy of calculations.

**Resonant cavities:**

Resonant measurements are the most accurate methods of obtaining permittivity and permeability. They are widely utilized because of its simplicity, easy data processing, accuracy, and high temperature capabilities. There are many types of resonant techniques available such as reentrant cavities, split cylinder resonators, cavity resonators, fabry-perot resonators etc. This section will concentrate on the general overview of resonant measurements and the general procedure using a cavity resonator.

The most popular resonant cavity method is the perturbation method (PM) (Komarov & Yakovlev, 2003; Mathew & Raveendranath, 2001); it is designed in the standard TM (transverse magnetic) or TE (transverse electric) mode of propagation of the electromagnetic fields. It is particularly suited for medium-loss and low-loss materials and substances. Precisely shaped small-sized samples are usually used with this technique. But PM provides dielectric properties measurements only at a resonant frequency, indicated by a sharp increase in the magnitude of the  $|S_{21}|$  parameter. The measurement is based on the shift in resonant frequency and the change in absorption characteristics of a tuned resonant cavity, due to insertion of a sample of target material (Janezic, 2004; Coakley et al. 2003). The specimen is inserted through a clearance hole made at the center of the cavity and that's into region of maximum electric field.

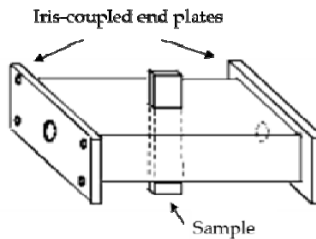


Fig. 4. Resonant cavity with a bar sample inserted at its center.

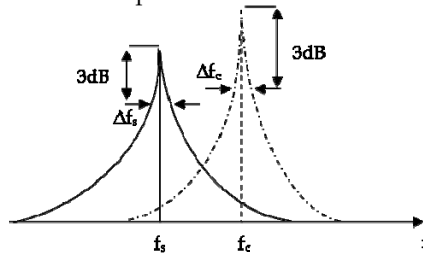


Fig. 5. The resonance response with and without the sample.

When the dielectric specimen is inserted to the empty (air filled) cavity the resonant frequency decreases from  $f_c$  to  $f_s$  while the bandwidth  $\Delta f$  at half power, i. e. 3 dB below the  $|S_{21}|$  peak, increases from  $\Delta f_c$  to  $\Delta f_s$  (see illustration in Fig. 5). A shift in resonant frequency is related to the specimen dielectric constant, while the larger bandwidth corresponds to a smaller quality factor  $Q$  (ratio of energy stored to energy dissipated), due to dielectric loss. The cavity perturbation method involves measurements of  $f_c$ ,  $\Delta f_c$ ,  $f_s$ ,  $\Delta f_s$ , and volume of the empty cavity  $V_c$  and the specimen volume  $V_s$ . The quality factor for the empty cavity and for the cavity filled with the specimen is given by the expressions:

$$Q_c = f_c / \Delta f_c, Q_s = f_s / \Delta f_s \quad (7)$$

The real and imaginary parts of the dielectric constant are given by:

$$\epsilon_r' = 1 + \frac{V_c}{2V_s} \frac{f_c - f_s}{f_s}, \epsilon_r'' = \frac{V_c}{4V_s} \left( \frac{1}{Q_s} - \frac{1}{Q_c} \right) \quad (8)$$

As indicated before, this method requires that:

- The specimen volume be small compared to the volume of the whole cavity ( $V_s < 0.1V_c$ ), which can lead to decreasing accuracy.
- The specimen must be positioned symmetrically in the region of maximum electric field.

However, compared to other resonant test methods, the resonant cavity perturbation method has several advantages such as overall good accuracy, simple calculations and test specimens that are easy to shape.

(b) Large frequency band methods:

#### Wave guides:

Two types of hollow metallic waveguides are often used in microwave electronics: rectangular waveguide and circular waveguide. Owing to the possible degenerations in circular waveguides, rectangular waveguides are more widely used, while circular waveguides have advantages in the characterization of chiral materials.

The waveguide usually works at TE<sub>10</sub> mode. The width "a" and height "b" of a rectangular waveguide satisfies  $b/a = 1/2$ . To ensure the single-mode requirement in materials property characterization, the wavelength should be larger than "a" and less than "2a", so that for a given waveguide, there are limits for minimum frequency and maximum frequency. To ensure good propagations, about 10% of the frequency range next to the minimum and maximum frequency limits is not used. Several bands of waveguides often used in microwave electronics and materials property characterization: X, Ka and Q bands.

The samples for rectangular waveguide method are relatively easy to fabricate, usually rectangular substrates, and films deposited on such substrates.

(Quéffélec et al., 1999; 2000) presented a technique allowing broadband measurement of the permeability tensor components together with the complex permittivity of ferrimagnetics and/or of partly magnetized or saturated composite materials. It is based on the measurement of the distribution parameters,  $S_{ij}$ , of a rectangular waveguide whose section is partly filled with the material under test (Fig. 6). The  $S_{ij}$ -parameters are measured with a

vector network analyzer. The sample is rectangular and having the same width of the waveguide, thus to eliminate any existence of air gap.

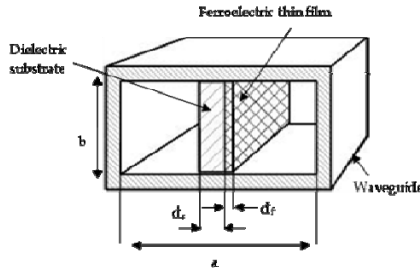


Fig. 6. Rectangular waveguide measurement cell, with a 2-layer sample fitting inside.

The determination of “ $\epsilon$ ” and “ $\mu$ ” of the material from the waveguide  $S_{ij}$  requires to associate an optimization program (inverse problem) to the dynamic electromagnetic analysis of the cell (direct problem). The electromagnetic analysis of the cell is based on the mode-matching method (Esteban & Rebollar, 1991) applied to the waveguide discontinuities. This method requires the modes determination in the waveguide and the use of the orthogonality conditions between the modes. The main problem in the modal analysis is the calculation of the propagation constant for each mode in the waveguide partly filled with the material; and then to match the modes in the plane of empty-cell/loaded-cell discontinuities. Such an analysis allows a rigorous description of the dynamic behavior of the cell. The electromagnetic analysis approach used is detailed in (Quéffelec et al., 1999).

The complex permittivity and complex components of the permeability tensor are computed from a data-processing program, taking into account higher order modes excited at the cell discontinuities and using a numerical optimization procedure (Quéffelec et al., 2000) to match calculated and measured values of the S-parameters.

Lately the same procedure was used for the measurement of the permittivity of ferroelectric thin film materials deposited on sapphire (Blasi & Queffelec, 2008) and good results were obtained in the X-band. The goal is to have the less possible error  $E(x)$  for the equation defined by:

$$E(x) = \sum \sum |S_{ij}^{th}(x) - S_{ij}^{mes}(x)|^2, \text{ where } x = (\epsilon', \epsilon''). \tag{9}$$

Where the indexes ‘th’ and ‘mes’ hold for the theoretical and measured parameters.

**Transmission lines:**

Transmission-line method (TLM) belongs to a large group of non-resonant methods of measuring complex dielectric permittivity of different materials in a microwave range. They involve placing the material inside a portion of an enclosed transmission line. The line is usually a section of rectangular waveguide or coaxial airline. “ $\epsilon_r$ ” and “ $\mu_r$ ” are computed from the measurement of the reflected signal ( $S_{11}$ ) and transmitted signal ( $S_{21}$ ). Free-space technique, open-circuit network and the short-circuited network methods are included as a part of this family. But, usually the main types of transmission lines used as the

measurement cell in TLM are: coaxial line (Vanzura et al. 1994; Shenhui et al., 2003), strip line (Salahun et al. 2001), and the planar circuits: micro-strip line (Queffelec & Gelin, 1994; Janezic et al. 2003), slot line (planar capacitor) (Petrov et al. 2005), coplanar waveguide (Lue & Tseng, 2001; Hinojosa et al., 2002) and inter-digital capacitors (Su et al., 2000; Al-Shareef et al. 1997).

**Coaxial line:** Due to their relative simplicity, coaxial line transmission or reflection methods are widely used broadband measurement techniques. In these methods, a precisely machined specimen (Fig. 7 **Error! Reference source not found.**) is placed in a section of coaxial line totally filling this section, and the scattering parameters are measured. The relevant scattering equations relate the measured scattering parameters to the permittivity and permeability of the material.

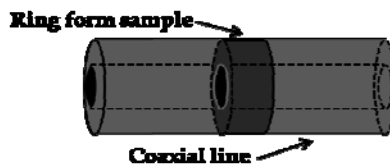


Fig. 7. Coaxial structure with the material to be tested filling completely a section part.

For TEM mode, the complex relative permeability and permittivity can be found as (Shenhui et al., 2003):

$$\epsilon_r = Z_0 \gamma \lambda / j Z_s 2\pi, \mu_r = Z_s \gamma \lambda / j Z_0 2\pi \quad (10)$$

Where  $Z_s$  is the characteristic impedance of the sample,  $Z_0$  is the characteristic impedance of the air for the same dimensions,  $\lambda$  is the free space wavelength and  $\gamma$  is the propagation constant written in terms of S-parameters as follows:

$$\gamma l = \cosh^{-1} \left( \frac{(1 - S_{11}^2 + S_{21}^2)}{2S_{21}} \right) \quad (11)$$

And "l" is the sample thickness.

Corrections for the effects of air gaps between the specimen holder and the sample can be made by analytical formulas (Vanzura et al., 1994). For coaxial lines, an annular sample needs to be fabricated. The thickness of the sample should be approximately one-quarter of the wavelength of the energy that has penetrated the sample. Although this method is more accurate and sensitive than the more recent coaxial probe method, it has a narrower range of frequencies. As the substance must fill the cross-section of the coaxial transmission line, sample preparation is also more difficult and time consuming.

**Strip line:** This method (Salahun et al., 2001) allows a broad-band measurement of the complex permittivity and permeability of solid and isotropic materials. The samples to be tested are either rectangular plates or thin films put (or mounted) on a dielectric holder. This method is based on the determination of the distribution parameters,  $S_{ij}$ , of a 3-plate transmission microstrip line that contains the material to be tested (Fig. 8).

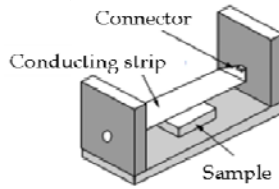


Fig. 8. Strip line measuring cell: Schematic drawing of an asymmetrical stripline structure. The sample is laid on the ground plane (Source: Salahun et al. 2001).

The method presents 3 steps: firstly, the theoretical effective permittivity and effective permeability are calculated from:

$$\varepsilon_{\text{eff}}^{\text{th}} = C/C_0 \text{ and } \mu_{\text{eff}}^{\text{th}} = L/L_0 \quad (12)$$

Where  $(L, C)$  and  $(L_0, C_0)$  are the inductance and capacitance per unit of length calculated in the cell with and without the sample. In the 2<sup>nd</sup> step, supposing a TEM mode in the cell, the effective permittivity and permeability are calculated using the Nicolson/Ross procedure mentioned in the free space method previously. In the last step, the complex electromagnetic parameters of the material are calculated by matching theoretical and measured effective values. Errors equations for the complex permeability and permittivity of the material are solved using a dichotomous procedure in the complex plane.

$$\begin{cases} F(\mu', \mu'') = |\mu_{\text{eff}}^{\text{m}} - \mu_{\text{eff}}^{\text{th}}|^2 \\ G(\varepsilon', \varepsilon'') = |\varepsilon_{\text{eff}}^{\text{m}} - \varepsilon_{\text{eff}}^{\text{th}}|^2 \end{cases} \quad (13)$$

The method enables one to get rid of sample machining problems (presented in the previous coaxial line methods) since the latter does not fully fill in the cross-section of the cell.

**Micro-strip line:** Microstrips have long been used as microwave components, and show many properties which overcome some of the limitations of non-planar components, thus making it suitable for use in dielectric permittivity measurement. These methods can be destructive and non-destructive. A destructive technique in presented by (Janezic et al., 2003), where the thin film is incorporated in the microstrip line. The advantage of this technique is the ability to separate the electrical properties of the metal conductors from the electrical properties of the thin film by separate measurements of the propagation constant and the characteristic impedance of the microstrip line. From the propagation constant and characteristic impedance, the measured distributed capacitance and conductance of the microstrip line are determined. Then knowing the physical dimensions of the microstrip lines, the thin-film permittivity is related to the measured capacitance by using a finite-difference solver. Yet precise, a more advantageous method is a non-destructive where the material to be measured is left intact for later integration in applications. A method of this type is published in the work of (Queffelec & Gelin, 1994) where the material to be measured is placed on the microstrip line. And as, it is well known that the effective permittivity (a combination of the substrate permittivity and the permittivity of the material above the line) of a microstrip transmission line (at least for thin width-to-height ratios) is

strongly dependent on the permittivity of the region above the line, this effect has been utilized in implementing microwave circuits and to a lesser extent investigation of dielectric permittivity.

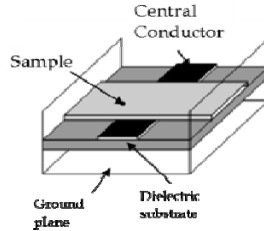


Fig. 9. Microstrip device loaded with the sample (Source: Queffelec et al. 1998).

This method (Fig. 9) allows a broad-band measurement of the complex permittivity and permeability of solid and isotropic materials. The samples to be tested are either rectangular plates or thin films. This method is based on the determination of the distribution parameters,  $S_{ij}$ , of a microstrip line that contains the material to be tested. The method is original because the sample is directly placed onto the line substrate without needing to fully fill in the cross-section of the cell as in the case of waveguides and coaxial cables. The analysis of measured data, that is, the determination of complex " $\epsilon$ " and " $\mu$ " from  $S_{ij}$  requires associating an optimization program (inverse problem) to the electromagnetic analysis of the cell (direct problem) as follows:

- The spectral domain approach was used in the direct problem, allows one to take into account several propagation modes in the calculation. and later in (Queffelec et al., 1998) the mode matching method.
- The inverse problem is solved using a numerical optimization process based on the Raphson-Newton method and the results for the permittivity and permeability were obtained on a large frequency band up to 18 GHz.

**Slot line (Planar capacitor):** One of the simplest devices for evaluating the electrical properties of ferroelectric materials is the capacitor. There are two types: parallel plate capacitors discussed above, where the ferroelectric layer is sandwiched between the electrodes; and planar capacitors, where the electrodes are patterned on the same side of a ferroelectric film and are separated by a small gap (Petrov et al., 2005).

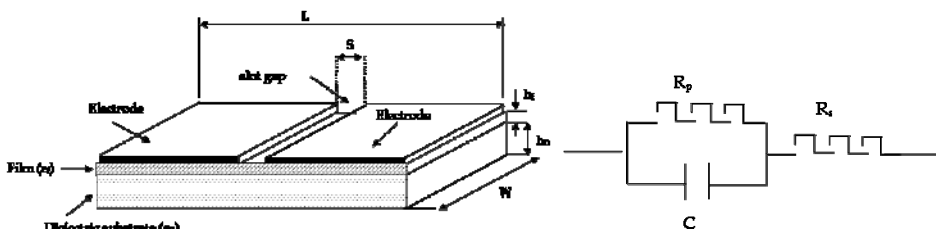


Fig. 10. Planar capacitor structure and its equivalent circuit ( $R_s$  and  $R_p$  are the series and parallel resistors representing loss).

Fig. 10 shows the planar capacitor device used for measurement of the dielectric permittivity of the ferroelectric thin film incorporated in the structure (destructive) and its equivalent circuit model used to go up with the total impedance of the structure through measuring the reflection coefficient  $S_{11}$  and then the impedance using equation (6). And the permittivity of the thin film is written as follows:

$$\epsilon_F = \left[ \frac{C}{w\epsilon_0} - \frac{2}{\pi} \ln\left(4 \frac{l}{s}\right) - \frac{(\epsilon_D - 1)}{\pi} \ln\left(16 \frac{(h_D + h_F)}{\pi s}\right) \right] \times \left[ \frac{s}{h_F} + \frac{4}{\pi} \ln(2) \right] + \epsilon_D \quad (14)$$

Where,  $C$  is the capacitance of the structure,  $h_F$  is the ferroelectric film thickness;  $h_D$  is the substrate thickness,  $s$

is the gap width,  $l$  is the electrode length,  $w$  is the electrode width and  $\epsilon_D$  is the dielectric constant of the substrate. It should be noted that equation (26) is valid under the following limitations:  $\epsilon_F / \epsilon_D \geq 10^2$ ,

$h_F < s < 10h_F$ ,  $s < 0.25l$  and  $s < 0.5h_D$ . Using this approach, the dielectric permittivity of the STO film was evaluated to be about  $\epsilon' \sim 3500$  at 77 K, 6 GHz.

**Coplanar lines:** The coplanar lines were the subject of increasing interest during the last decade in that they present a solution at the technical problems, encountered in the design of the strip and micro-strip standard transmission lines (their adaptation to the external circuits is easier and their use offers relatively low dispersion at high frequencies).

Many characterization methods using coplanar lines are published. (Hinojosa, et al. 2002) presented an easy, fast, destructive and very high broadband (0.05–110 GHz) electromagnetic characterization method using a coplanar line as a cell measurement to measure the permittivity of a dielectric material on which the line is directly printed (Fig. 11). The direct problem consists of computing the S-parameters at the access planes of the coplanar cell under test propagating only the quasi-TEM mode. The optimization procedure (the inverse problem) is based on an iterative method derived from the gradient method (Hinojosa et al., 2001), simultaneously carrying out the ' $\epsilon_r$ ' and ' $\mu_r$ ' computation and the convergence between ( $S_{11}$ ,  $S_{21}$ ) measured values and those computed by the direct problem through successive increment of the permittivity and permeability values.

Another method is presented by (Lue & Tseng, 2001). A technique using a coplanar waveguide incorporating the ferroelectric thin film deposited on a dielectric substrate.

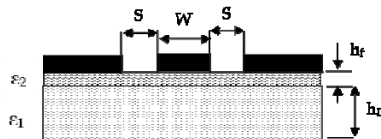


Fig. 11. Coplanar line incorporating the thin ferroelectric film.

It is based on an easy and fast processing method of the coplanar S-parameter measurements, which takes into account the quasi-TEM mode propagation. Analytical relationships compute the propagation constant and characteristic impedance of the coplanar cell instead of any numerical method, which considerably decreases computation time, and the effective permittivity of the multi-layered structure is deduced. The S-

parameter measurement bench of the coplanar cells employs vector network analyzers and commercially available high-quality on-coplanar test fixtures (probe station). The extraction of the permittivity of the thin film is done using the conformal mapping analysis.

Coplanar interdigital capacitor:

Another type of characterization methods which use the coplanar wave guide structure are those of the coplanar interdigital capacitor. These methods have the strip line or the central conductor in the form of interdigitated fingers (Fig. 12) in a way to increase the electromagnetic interaction between the propagating wave and the sample, thus increasing the sensitivity of the structure.

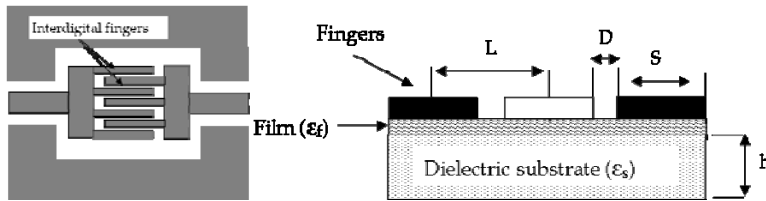


Fig. 12. coplanar IDC (left) with fingers parallel to the wave propagation with a schematic of a cross section of the capacitor structure (right).

As reported by (Al-Shareef et al., 1997); to calculate the dielectric constant of the thin film capacitors with the interdigital electrode configuration shown in Fig. 12, an analytical model previously derived by Farnell et al. was employed (Farnell et al., 1970). Based on Farnell's analysis, it can be shown that the dielectric constant of a thin film having the configuration shown in Fig. 1 can be calculated using the following expression:

$$\varepsilon_f = \varepsilon_s + \left\{ \frac{C - K(1 + \varepsilon_s)}{K \left[ 1 - \exp\left(-4.6h/L\right) \right]} \right\} \quad (15)$$

where  $\varepsilon_f$  and  $\varepsilon_s$  are the film and substrate dielectric constants, respectively;  $h$  is the film thickness,  $K$  is a constant which has units of pF, and  $C$  is the measured capacitance per unit finger length per electrode section of width  $L$  ( $L$  is half the IDE pattern period or  $l=2$ ).

Another procedure for low frequency measurement is to measure directly the impedance using an impedance analyzer (1 layer material case), or using the conformal mapping method to calculate analytically, the capacitance of the structure and compare this latter to the measured value thus deducing the permittivity of the material under test.

### 3. Non-destructive transmission line method: Characterization using a Coplanar line

Principles and techniques of permittivity measurements using transmission lines have been illustrated in the preceding part. Yet, most of these methods have the thin film incorporated inside the device (Lue & Tseng, 2001) (a destructive method), which prevent using the measured film material in an electronic circuit. And as ferroelectric film deposition and permittivity values still not well controlled, this poses a problem in their integration.



Therefore, a non-destructive method will be the most appropriate for such situation as well as for industrial use in general.

We present here a nouvelle and non-destructive Broadband characterization method which employs a coplanar line for the measurement of the complex permittivity of linear dielectric materials and precisely, that of ferroelectric thin films. The method uses the transmission coefficient supposing a quasi-TEM analysis to find the effective permittivity of the multilayer system. In the inverse problem, the coplanar conformal mapping technique is employed to extract the relative permittivity of the thin layer.

### 3.1 Theory and analysis

The theory of the method and its principle is very simple; the substrate to be measured is placed on the line for an assembly as described in Fig. 13 below, where the line is taken in sandwich between 2 dielectric substrates, that of the line and the material to measure.

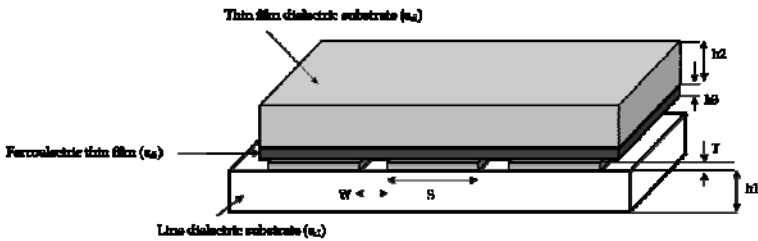


Fig. 13. Schematic of a CPW tight between two dielectrics: Alumina substrate from below and the ferroelectric thin film + MgO substrate from above.

The method includes measuring 'only' the transmission coefficient  $S_{21}$  of the device and that's in two steps: - the first for the coplanar line in air (without material), - and the other with the line loaded with material whether of one layer or multi-layers.

The effects of the different materials on the dispersion parameters of the line results of these measurements are presented in Fig. 14.

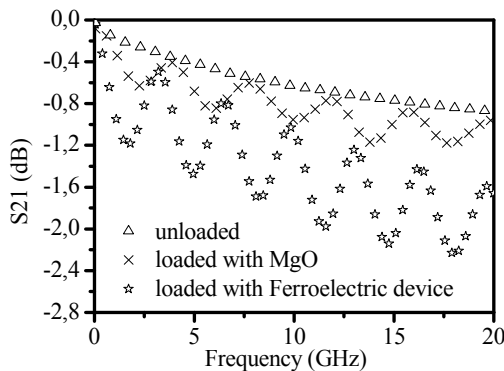


Fig. 14. S-parameters measured with 3 different samples placed on the coplanar line: unloaded (air), MgO substrate and 2-layered device: MgO + ferroelectric thin film

The measurement procedure is presented in 2 problems: a direct one and an inverse one.

### 3.2 Analysis of the direct problem

The analysis is based on the measurements of the S-parameters of the line and precisely the transmission coefficient  $S_{21}$ . We have for a standard transmission line the S-parameters written as follows:

$$S_{ij} = \begin{bmatrix} 0 & e^{-\phi} \\ e^{-\phi} & 0 \end{bmatrix} \quad (16)$$

Where  $L$  is the line length, and  $\phi = \gamma L$  is the  $S_{21}$  phase shift. The propagation constant of a coplanar wave guide is well known to be:

$$\gamma = j \frac{2\pi}{c} f \sqrt{\epsilon_{\text{eff}} \mu_{\text{eff}}} \quad (17)$$

The ratio of the two measurements mentioned gives the following formula:

$$\frac{S_{21}^{(\text{loaded})}}{S_{21}^{(\text{unloaded})}} = e^{-(\gamma_c - \gamma_v)} = e^{j \frac{2\pi}{c} f L (\sqrt{\epsilon_{\text{reff}_v}} - \sqrt{\epsilon_{\text{reff}_c}})} \quad (18)$$

Where  $(\gamma_c)$  and  $(\gamma_v)$  are propagation constant of the system with and without the load respectively,  $\epsilon_{\text{eff}}$  is the effective permittivity of the whole system,  $\mu_{\text{eff}}$  the effective permeability which is equal to '1' in the case of dielectric medium and ' $f$ ' is the frequency. This equation makes it possible to extract the effective permittivity of the complete system (line + DUT) that we will note " $\epsilon_{\text{eff}}$ ".

### 3.3 Quasi-TEM analysis and Inverse problem

From the previous analysis, we extracted the effective permittivity of the complete system (coplanar line+ coplanar substrate + the material to be measured (1-layer or 2-layers)). In this section, the conformal mapping analysis is carried out to solve the inverse problem. The conformal mapping technique assumes a quasi-static TEM mode of propagation along the line. Closed form expressions for the effective permittivity and the characteristic impedance for CPW are presented in (Simons, 2001). The simplified formulas for the sandwiched 3-layered CPW structure are given here; where we have the effective permittivity written as follows:

$$\epsilon_{\text{eff}} = 1 + q_1(\epsilon_{r1} - 1) + q_2(\epsilon_{r2} - 1) + q_3(\epsilon_{r3} - \epsilon_{r2}) \quad (19)$$

With  $\epsilon_{r1}$  is the dielectric constant of the line substrate,  $\epsilon_{r2}$  is that of the thin film substrate (the substrate on which the film is deposited),  $\epsilon_{r3}$  is the permittivity of the thin film and  $q_i$  is the partial filling factor equal to:

$$q_i = \frac{1}{2} \frac{K(k_i)}{K'(k_i)} \frac{K'(k_0)}{K(k_0)}, i = 1, 2, 3, \dots \tag{20}$$

$K(x)$  is the complete elliptical integral of first kind, and  $K'(x) = K(\sqrt{1-x^2})$  and their modulus  $k_0$  and  $k_i$  are written:

$$k_0 = s/(s + 2w), k_i = \sinh\left(\frac{\pi s}{4h_i}\right) / \sinh\left(\frac{\pi(s + 2w)}{4h_i}\right) \tag{21}$$

$s$  and  $w$  are the CPW conductor and slot width respectively,  $h_i$  is the thickness of the 3 different layers.

To simplify our calculations usually we employ the asymptotic formula for the ratio of elliptic function and that under the following conditions:

For

$$0 \leq k_i \leq 0.707 \Rightarrow \frac{K(k_i)}{K'(k_i)} = \pi / \ln\left(\frac{2(1 + \sqrt{J_i})}{1 - \sqrt{J_i}}\right) \text{ where } J_i = \sqrt{1 - k_i} \tag{22}$$

and for

$$k_i \geq 0.707 \Rightarrow \frac{K(k_i)}{K'(k_i)} = \ln\left(\frac{2(1 + \sqrt{k_i})}{1 - \sqrt{k_i}}\right) / \pi \tag{23}$$

For a thickness  $h_i$  too small compared to the line parameters, that is, if  $s, w \gg h_3$  (which is the case),  $k_3$  become too small ( $k_3 \ll 1$ ), which leads to a numerical error in calculating the elliptic function. To overcome this difficulty, for the special case (Zhao, 2005) when  $k_i \approx 0$ ;

$$\frac{K(k_i)}{K'(k_i)} = \pi / \ln\left(2 \frac{1 + \sqrt{\sqrt{1 - k_i}}}{1 - \sqrt{\sqrt{1 - k_i}}}\right) \approx \pi / \ln \frac{16}{k_i^2} \tag{24}$$

The resolution of the inverse problem is carried out by applying these formulas which makes it possible to determine the permittivity of material. In the quasi-TEM case, these simplified expressions for a tri-layer structure make it possible to extract the complex permittivity of the thin layer ' $\epsilon_{r3}$ ' from the following equation:

$$\epsilon_{r3} = \frac{\epsilon_{eff} - 1 - q_1(\epsilon_{r1} - 1) + q_2(\epsilon_{r2} - 1)}{q_3} + \epsilon_{r2} \tag{25}$$

### 3.4 Numerical Calculation (FEM, TLM)

An analysis based on the conformal mapping method was done using a Matlab program. With this program we studied the effect of the material placed on the line on the effective permittivity of the system (Figure 15):

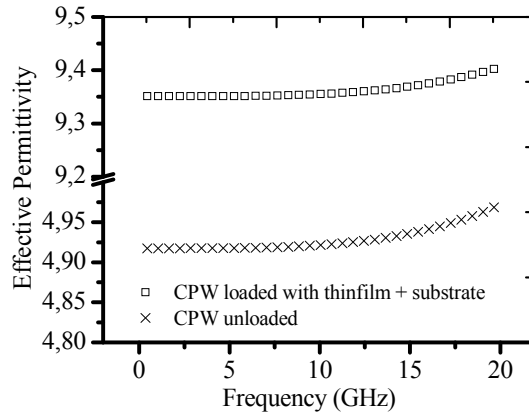


Fig. 15. Results for the effective permittivity calculated for the coplanar line when unloaded and loaded with the thin film device (thin film + substrate) where the substrate is MgO of permittivity 9.5 and the permittivity of the thin film considered 200 with a thickness of 500 $\mu\text{m}$  for the substrate and 0.5 $\mu\text{m}$  for the thin layer.

As shown in the figure, the effect is far being negligible. This result shows the high sensitivity of the coplanar device and the reliability of the method used in the calculations. The simulation with 3D electromagnetic commercial softwares gave comparable results.

### 3.5 Measurement bench

#### (a) Optimization of the coplanar device

A number of simulations are done using 3D electromagnetic simulation softwares in a way to optimize the coplanar device and the measurement method in general, and permittivity extractions took place with different line parameters employed as well.

The coplanar line employed here, was designed for a characteristic impedance of 50 $\Omega$  to match the coaxial cable of the network analyser used to measure the S-parameters. Alumina was taken as the device support substrate of permittivity 9.8 and different dimensions. The parameters for the coplanar printed on the substrate are as follows: Substrate thickness = 0.635mm, central conductor width  $w = 380\mu\text{m}$ , spacing between the central conductor and the ground plane  $s = 150\mu\text{m}$  with a metallic thickness  $t = 2\mu\text{m}$ .

#### (b) Measurements procedure

The measured samples are best to be rectangular yet, any form with known length with paralleled surfaces can be measured. The materials must have smaller length than the line but wider enough to cover the 2 ground planes in a way to confine the most possible field lines. The material to be measured is simply placed on the line; for a thin film deposited on a dielectric substrate and considering a higher permittivity for that film compared to its substrate ( $\epsilon_{r3} > 10 \cdot \epsilon_{r2}$ ), this device should be placed on the film side for the conformal mapping analysis to be valid. That is, going from the metallic line, the permittivity of the different layers should decrease on the 2 sides. The thin ferroelectric films measured here are barium strontium titanate (BST) deposited by RF-sputtering with thicknesses varied

between  $0.5\mu\text{m}$  and  $1\mu\text{m}$  on MgO and sapphire substrates. The S-parameters are measured using a vector network analyzer HP 8510C functioning to a frequency of 20 GHz. The line is mounted on a classical ANRITSU test-fixture. Both transmission coefficients measured in air and with material are integrated in a MATLAB program in order to extract the permittivity of the ferroelectric thin layer by applying the analysis described above.

TRL (Thru-Reflect-Line) and SOLT (Short-Open-Load-Thru) calibrations were carried out in order to eliminate systematic errors of the network analyzer and to place the reference planes of measurements at the needed positions, i.e.: at the levels the 2 coaxial cable for the SOLT and at the sample edges for the TRL case. The disadvantage of the TRL calibration is the necessity to have different line kits in order to measure different sample lengths. For the SOLT case, the reference planes are always at the CPW line edges and whatever sample can be measured, yet, because of the distance between the line edge and that of the sample, reflections take place causing a number of oscillations in the measured results all over the frequency band (Fig. 14). Solution for this problem is discussed in (Kassem et al., 2007).

### 3.6 Experimental results and discussion

To validate our method, we characterized several materials with well known dielectric properties (alumina, MgO, Sapphire...). The results obtained for MgO of rectangular shape ( $13\times 13$ ) mm<sup>2</sup> surface and 0.5mm thickness, as for other materials, show a good agreement with the awaited values. The result for the MgO substrate is presented in Fig. 16. which shows a number of oscillations over the whole frequency band with a mean of around 9.4 for the permittivity value and a fraction of  $< 10^{-3}$  for this low-loss substrate.

Concerning the ferroelectric thin film measurement, the thin layer deposited on the MgO substrate was measured by the same way like the MgO substrate and the results presented below in figure 17 also shows oscillations over the entire frequency band but with a mean value of around 62 for its relative permittivity.

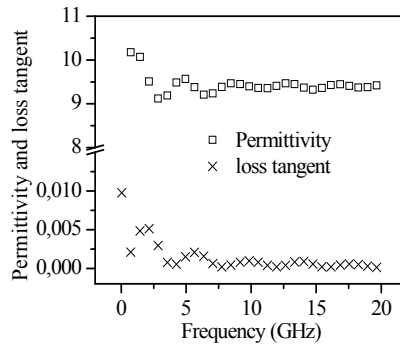


Fig. 16. permittivity and loss tangent measured for MgO.

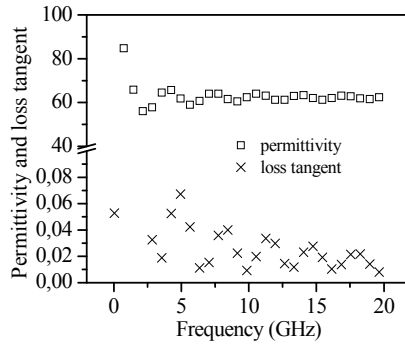


Fig. 17. permittivity and loss tangent measured for ferroelectric thin film layer.

The main reason behind the oscillations figured above is the calibration procedure followed before measurement. In fact, as we mentioned before, the SOLT calibration moves the reference planes to the side edges of the coplanar line, thus, for a sample less in dimension than that of the line, our device can be figured as a 3 regions structure (Fig. 18-left).

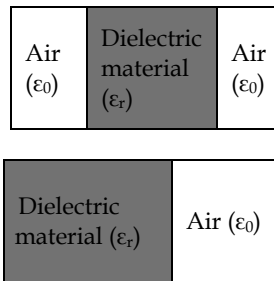


Fig. 18. coplanar line with the sample placed on it, in the 2 cases of: (left) 3 region systems (air, material, and then air), (right) 2 region system (air, material).

So, the EM wave will propagate in different regions each of different permittivity (Air/DUT/Air), thus reflections at the interfaces, which is not taken in our calculations. In a way to minimize this effect, we placed the sample at one edge of the line to have almost a 2 regions structure (Fig. 18-right). Oscillations are largely minimized over the entire frequency band after this procedure. TRL calibration can solve easily this problem.

### 3.7 Error analysis, losses and measurement limitation

The precision of the measurement method is limited by the percentage of errors and losses (Raj et al., 2001, kassem et al., 2007) and by the band of validity of the analysis used.

One of the major limitation of this method, and in general, for any non-destructive method is the presence of an air gap between the DUT and the metallic strips (Fig. 19) which in case of existence can lead to large uncertainties in the values of the permittivity measurement and result. This can be well noticed in

Fig. 20, which describes the effect of the presence of an air gap on the results of the permittivity of an alumina substrate.

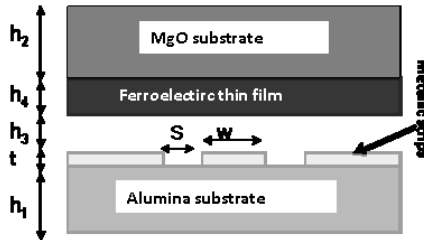


Fig. 19. Cut view of a multilayered coplanar waveguide monitoring the air-gap  $h_3$ .

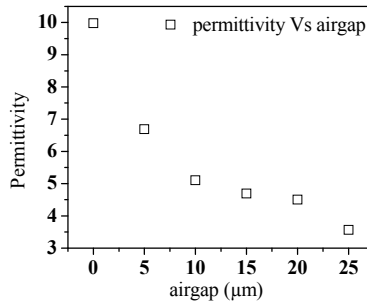


Fig. 20. variation of permittivity of alumina sample for different air gap thicknesses.

As it can be noticed from the graph, the error is more than 50% for a 20μm air-gap. Although, in our measurement, the metallic strips were well polished thus having a good contact, the effect of the air gap can be taken into consideration introducing a small factor  $q_3(\epsilon_{r3} - \epsilon_{r4})$  which takes in account the thickness of the existent air-gap  $h_3$  (M. Misra1 et al., 2003), thus we have the effective permittivity of the multilayered system with the air-gap written as follows:

$$\epsilon_{eff} = 1 + q_1(\epsilon_{r1} - 1) + q_2(\epsilon_{r2} - 1) + q_3(\epsilon_{r3} - \epsilon_{r4}) + q_4(\epsilon_{r4} - \epsilon_{r2}) \tag{26}$$

And then inverting the problem will give us the effective permittivity of the thin ferroelectric film material:

$$\epsilon_{r4} = [\epsilon_{eff} - 1 - q_1(\epsilon_{r1} - 1) - q_2(\epsilon_{r2} - 1) - q_3(\epsilon_{r3}) + q_4(\epsilon_{r2})] / (q_4 - q_3) \tag{27}$$

(a) Substrate Roughness (presentation of the problem):

Yet, for us, an air gap exists only if one forces the existence of such a layer. The fact is that, we'll always have a contact established between the substrate and the line; our problem here really relates the percentage of surface roughness of the substrate or thin layer. Fig. 21 gives an idea of the situation:

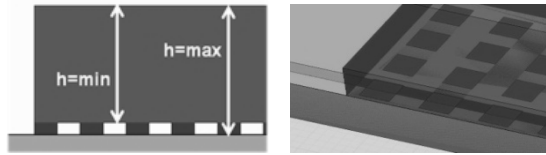


Fig. 21. Layer with a rough surface: (left) peaks, (right) holes, Substrate roughness (%) =  $(h_{\max} - h_{\min}) / h_{\max} \cdot 100$ .

One can imagine two types of problems, that is to say a layer with holes, or peaks. We simulated these two conditions with HFSS, for a 2-layers and 3-layers system, then using our program we calculated the permittivity of substrate and the film, and here are the obtained results for the thin film (Fig. 22).

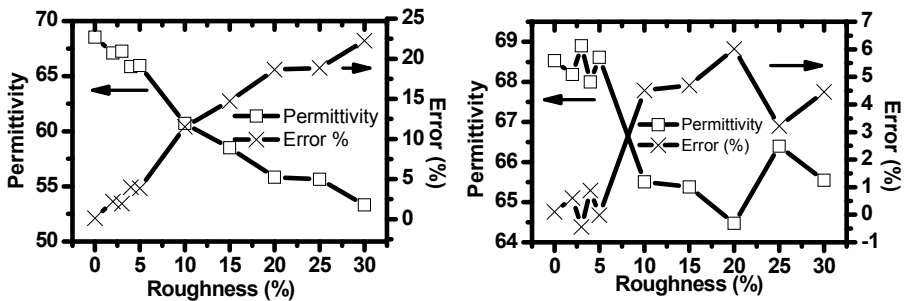


Fig. 22. Simulation made for Double-layered MgO + BST of permittivity 69 and a surface with peaks and 2 solutions proposed to solve the problem (left) calculating with a maximum thickness for the thin layer and (right) a minimum thickness.

Calculations of the permittivity of the film are done using the following 2 different procedures:

- Considering that the thickness of the film is maximal "h<sub>max</sub>".
- Calculating with the minimal thickness "h<sub>min</sub>"

The calculation with minimal thickness reduces the error to 5% maximum for 30% film roughness and even for 10% roughness; the error in the permittivity value will not bypass the 3%. In conclusion, all depends on the substrate of the layer. For that, a solution is proposed and validated.

#### 4. Conclusion and Future Research

The objective of the work is to point on an important part in nowadays electronic domain and that is, the characterization of materials; a necessary process before integrating them in electronic devices such as, tunable filters and tunable phase shifters. Our work concern studying the electrical properties of dielectrics and precisely those of thin ferroelectric materials and that, on a broad frequency band in a first step before their dynamic behavior study (response under application of external electric field). Thus, we can contribute in the realization of tunable circuits at high frequencies starting from such layers.



In the first part, we presented various methods of characterization allowing measuring the dielectric properties of dielectric materials. The methods were divided in a way that allows us to choose what tool of characterization is the most appropriate for each case, moreover, we put the light on the aspect of thin films characterizations which is not yet commercialized and always in the period of its development.

The broad band method proposed makes it possible to calculate the electric parameters of films of high permittivity mounted in a multi-layered device, on a coplanar line structure. The method presents an originality compared to normally used transmission lines methods and that in its nondestructive way of measurement, thus presenting an industrial advantage. Starting from the measurement of the propagation constant from the transmission coefficient of the S-parameters, an approach based on the method of Conformal Mapping is utilized to solve the inverse problem and thus, namely to determine the complex permittivity of a thin layer. The method was validated via the measurements made on various dielectric substrates such as alumina and MgO and of various thicknesses. The extraction of the dielectric properties of these substrates made it possible to include/understand well the process of measurement to follow. A rather good precision was reached for the permittivity like for the tangent of losses due to the advantage of using a differential measurement, thus eliminating various types of losses automatically. A satisfactory comparison of the results obtained on a layer of MgO and multi-layer BST/MgO was carried out between our broad band method and a cavity resonator method. After that, a study of the effect of air gap and material surface roughness is done giving larger understandings of the measurement results and solutions were proposed.

Various studies remain to be carried out, on the level of characterization with some proposals to widen the effectiveness of our method, in particular if the material ferroelectric is deposited on a metal substrate, as on the level of the temperature measurement which remains still a vital subject since it would make it possible to test stability electronic circuits in different environments.

The interest in tunable applications, open the way to advance towards the study of new characterization methods in the goal of integration of thin layers in the realization of controllable devices at ultra high frequencies, thus minimizing the price, volume and losses of today's' electronic circuits.

## 5. References

- Al-Shareef H.N., Dimos D., Raymond M.V. And Schwartz R.W. (1997), Tunability and Calculation of the Dielectric Constant of Capacitor Structures with Interdigital Electrodes, *Journal of Electroceramics* Vol. 1, Issue 2, pp. 145-153, ISSN: 1573-8663.
- Baker-Jarvis J., Janezic M.D. (1994), Analysis of an open-ended coaxial probe with lift-off for non-destructive testing, *IEEE Transactions on instrumentation and measurements*, Vol. 43, No. 5, ISSN: 0018-9456.
- Coakley Kevin J., Splett Jolene D., Janezic Michael D. And Kaiser Raian F. (2003), Estimation of Q-Factors and Resonant Frequencies, *IEEE Transactions On Microwave Theory And Techniques*, Vol. 51, No. 3, pp. 862-868, ISSN: 0018-9480.

- De Blasi, S. Queffelec, P. (2008), Non-Destructive Broad-Band Characterization Method of Thin Ferroelectric Layers at Microwave Frequencies, *38th European Microwave Conference EuMC*, pp. 793-796, ISBN: 978-2-87487-006-4, The Netherland, 27-31 Oct. 2008, IEEE, Amsterdam.
- Esteban J. and Rebollar J. M. (1991), Characterization of corrugated waveguides by modal analysis, *IEEE Trans. Microwave Theory Tech.*, vol.39, pp. 937-943, ISSN: 0018-9480.
- Farnell G.W., Cermak I.A., Silvester P. and Wong S.K. (1970), Capacitance and Field Distributions for Interdigital Surface-Wave Transducers, *IEEE Transaction on Sonics and Ultrasonics*, Vol. 17, Issue 3, pp. 188-195, ISSN: 0018-9537.
- Gagwu chen, Kang Li, and Zhong Ji (1994), Bilayer dielectric measurement with an opened coaxial probe, *IEEE Transactions On Microwave Theory And Techniques*, Vol. 42, No. 6, ISSN: 0018-9480.
- Hinojosa J, Lmimouni K., Lepilliet S. and Dambrine G. (2002), Very high broadband electromagnetic characterization method of film-shaped materials using coplanar, *Microwave and Optical Technology Letters*, vol. 33 n°5, pp. 352-355, ISSN: 1098-2760.
- Hinojosa J., Faucon L., Queffelec P., and Huret F. (2001), S-parameter broadband measurements of microstrip lines and extraction of the substrate intrinsic properties, *Microwave Opt Technol. Letters* Vol. 30, Issue 1, pp. 65-69, ISSN: 1098-2760.
- Janezic Michael D. (2004), Broadband complex permittivity measurements of dielectric substrates using a split-cylinder resonator, *Microwave Symposium Digest, IEEE MTT-S International Publication*, Vol. 3, pp. 1817- 1820, ISSN: 0149-645X.
- Janezic Michael D., Williams D. F., Blaschke V., Karamcheti A., and Chang C. S. (2003), Permittivity Characterization of Low-k Thin Films From Transmission-Line Measurements, *IEEE Transactions On Microwave Theory And Techniques*, Vol. 51, No. 1, pp. 132-136, ISSN: 0018-9480.
- Kassem H., Vigneras V., Lunet G. (2007), Non destructive dielectric characterization of thin ferroelectric films materials using coplanar line structure, *Integrated Ferroelectrics*, Vol. 94, Issue 1, pp. 82-93, ISSN: 1607-8489.
- Lamkaouchi K, Balana A, Delbos G and Ellison W J (2003), Permittivity measurements of lossy liquids in the range 26-110 GHz, *Institute Of Physics Publishing Measurement Science And Technology, Meas. Sci. Technol.* 14, pp. 444-450, ISSN: 0957-0233.
- Lue H-T Ting and Tseng T-Y, (2001), Application of on-wafer TRL calibration on the measurement of microwave properties of Ba<sub>0.5</sub>Sr<sub>0.5</sub>Ti O<sub>3</sub> thin films, *IEEE Transaction on ultrasonics, Ferroelectrics and Frequency Control*, vol. 48 n°6, pp. 1640-1647, ISSN: 0885-3010.
- Mathai C J, Saravanan S, Anantharaman M R, Venkitachalam S and Jayalekshmi S (2002) Characterization of low dielectric constant polyaniline thin film synthesized by ac plasma polymerization technique, *J. Phys. D: Appl. Phys.* 35 pp. 240-245, , ISSN: 0022-3727.
- Mathew K.T. & Raveendranath U. (2001), Cavity Perturbation Techniques for Measuring Dielectric Parameters of Water and Other Allied Liquids, *Sensors Update -Wiley interscience*, Volume 7 Issue 1, pp. 185-210, ISSN: 1616-8984.
- Misra M., Kataria N.D., Murakami H. and Tonouchi M. (2003), Analysis of a flip-chip bonded tunable high-temperature superconducting coplanar waveguide resonator using the conformal mapping technique, *Superconductor Science and Technology*, Vol. 16, pp. 492-497, ISSN: 0953-2048.

- Nicolson, A. M. and Ross, G. F. (1970), Measurement of the intrinsic properties of materials by time domain techniques, *IEEE Transactions on Instrumentation and Measurement*, Vol. 19, Issue 4, pp. 377-382, ISSN: 0018-9456.
- Obrzut J. and Nozaki R. (2001), Broadband Characterization of Dielectric Films for Power-Ground Decoupling, *Proceedings of the 18th IEEE Instrumentation and Measurement Technology Conference, IMTC*, Page(s):1000 - 1004, ISBN: 0-7803-6646-8, Hungary, 05/21/2001 - 05/23/2001, Budapest.
- Park Jaehoon, Lu Jiwei, Stemmer Susanne, York Robert A. (2005), Microwave dielectric properties of tunable capacitors employing bismuth zinc niobate thin films, *journal of applied physics*, Vol. 97, Issue 8, ISSN: 1089-7550.
- Petrov P. K., Alford N. and Gevorgyan S. (2005), Techniques for microwave measurements of ferroelectric thin films and their associated error and limitations, *Measurement Science And Technology* Vol. 16, Issue 1, pp.583-589, ISSN: 0957-0233.
- Quéffelec P., Le Floch M. and Gelin Ph., (2000), New method for determining the permeability tensor of magnetized materials in a wide frequency range, *IEEE Transactions on Microwave Theory and Techniques*, Vol. 48, No. 8, pp. 1344-1351, ISSN: 0018-9480.
- Quéffelec P., Le Floch M. and Gelin Ph. (1999), Nonreciprocal cell for the broad band measurement of tensorial permeability of magnetized ferrites, *IEEE Transactions on Microwave Theory and Techniques*, Vol. 47, No. 4, pp. 390-397, ISSN: 0018-9480.
- Queffelec P., Le Floch M., Gelin P. (1998), Broad-band characterization of magnetic and dielectric thin films using a microstrip line, *IEEE transactions on Instrumentation and measurements*, Vol. 47, Issue: 4, pp. 956-963, ISSN: 0018-9456.
- Queffelec Patrick, Gelin Philippe (1994), A microstrip device for the broadband simultaneous measurement of complex permeability and permittivity, *IEEE transactions on magnetics* Vol.30, No.2, pp. 224-231, ISSN: 0018-9464.
- Raj A., Holmes W.S. and Judah S.R. (2001), wide band width measurement of complex permittivity of liquids using coplanar lines, *IEEE Transactions on instrumentation and measurement* vol.50, No. 4, pp. 905-909, ISSN: 0018-9456.
- Salahun Erwan, Quéffelec Patrick, Le Floch Marcel, and Gelin Philippe (2001), A Broadband Permeameter for "in situ" Measurements of Rectangular Samples, *IEEE Transactions On Magnetics*, Vol. 37, No. 4, pp. 2743-2745, ISSN: 0018-9464.
- Shenhui Jing; Ding Ding; Quanxing Jiang (2003), Measurement of electromagnetic properties of materials using transmission/reflection method in coaxial line, *The 3rd Asia Pacific Conference on Environmental Electromagnetics CEEM 2003*, pp. 590-595, ISBN: 7-5635-0802-3, China, 4-7 Nov. 2003, IEEE, Hangzhou.
- Simons Rainee N. (2001), *Coplanar Waveguide Circuits, Components, and Systems*, John Wiley and Sons, Inc. ISBN: 978-0-471-16121-9, New York.
- Su H. T., Lancaster M. J., Huang F. and Wellhofer F. (2000), Electrically Tunable Superconducting Quasilumped Element Resonator Using Thin-Film Ferroelectrics, *Microwave And Optical Technology Letters*, Vol. 24, No. 3, pp. 155-158, ISSN: 1098-2760.
- Vanzura Eric J., Baker-Jarvis James, Janezic Michael D. (1994), Intercomparison of permittivity measurements using the transmission/reflection method in 7-mm coaxial transmission lines, *IEEE Transactions On Microwave Theory And Techniques*, Vol. 42, No. 11, pp. 2063-2070, ISSN: 0018-9480.

- Vasundara V. Varadan, K. A. Jose, and Vijay K. Varadan (2000), In situ Microwave Characterization of Nonplanar Dielectric Objects, *IEEE Transactions On Microwave Theory And Techniques*, Vol. 48, No. 3, pp. 388-394, ISSN: 0018-9480.
- Vyacheslav V. Komarov & Vadim V. Yakovlev (2003), Modeling Control Over Determination Of Dielectric Properties By The Perturbation Technique, *Microwave And Optical Technology Letters*, Vol. 39, No. 6, PP. 443-446, ISSN: 1098-2760.
- Weir, W. B. (1974), Automatic measurement of complex dielectric constant and permeability at microwave frequencies, *Proceedings of the IEEE*, Vol. 62, Issue 1, pp. 33-36, ISSN: 0018-9219.
- Zhao Ji-Xiang (2005), Characteristic Parameters For Cpws On A Very Thin Dielectric Layer, *Microwave & Optical Technology Letters*, Vol.45, No.3,pp. 240-241,ISSN: 1098-2760.

# Implementation of the Front-End-Module with a Power Amplifier for Wireless LAN

Jong-In Ryu, Dongsu Kim and Jun-Chul Kim  
*Korea Electronics Technology Institute*  
South Korea

## 1. Introduction

Recently, Wireless Local Area Network (W-LAN) market has been continuously growing in many filed and it become mature market. Therefore, a number of companies are researching and developing the W-LAN technology. Normally, W-LAN application is wildly used in the desktop computer, laptop computer, portable device, mobile phone, and so on. These application demands compact, small, low power consumption, slim, and many function in a module. These demands issue that a lot of components are integrated in a module. Low temperature co-fired ceramic (LTCC) continues to be attracted in wireless applications because it can implement a small, compact, and integrated module which embedding passive components by taking advantage of three-dimensional architecture. LTCC has high dielectric constant and low loss tangent that it has some benefits over other material substrates. The size of LTCC is shrunk after process of co-fired which makes some issues in design and implementation of LTCC. In spite of these disadvantages, many researches and companies have been researching and developing many passive components, RF modules, and front-end modules (FEM) by using the LTCC technology.

IEEE 802.11 a/b/g as W-LAN standard has been allocated two frequency bands for 2.4 GHz - 2.5 GHz (IEEE 802.11 b/g) and 5.15 GHz - 5.85 GHz (IEEE 802.11 a). The frequency band of IEEE 802.11 b/g and of IEEE 802.11 a are called as low-band and high-band, respectively.

The implemented W-LAN FEM coves low-band and high-band. It is composed of two matching circuits for low-band and high-band, two Tx low pass filters (LPFs) in order to reject 2<sup>nd</sup> harmonic frequency of a power amplifier module (PAM), two Rx band pass filters (BPFs) in order to reject interferers as blocker, a Rx diplexer to separate low-band from high-band, a Tx diplexer, a single-pole-double-throw (SPDT) switch for sharing the antenna between the RX and TX paths , and a PAM for low-band and high-band as shown in fig.1. Two Tx LPFs, two matching circuits, Tx diplexer, two Rx BPFs, and Rx diplexer are embedded in LTCC substrate. A DPDT IC and PAM IC are mounted on LTCC substrate. Embedded components are very sensitive to tolerance of LTCC and mutual coupling. A control of process LTCC and a layout of embedded components are important facts and are focused on being considered in design of a FEM. The design and layout are mainly discussed in this book.

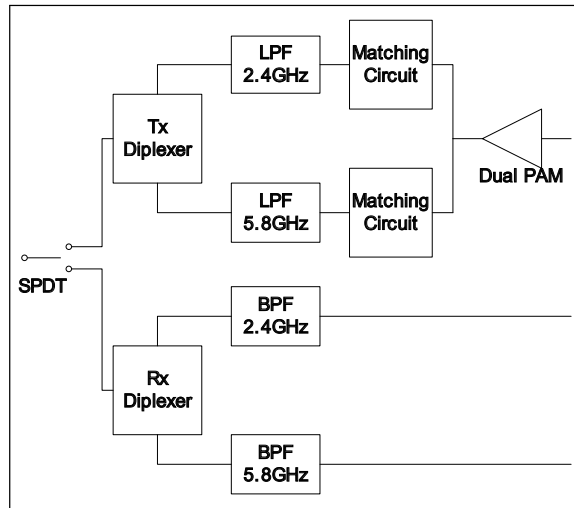


Fig. 1. Block diagram of W-LAN FEM.

## 2. Design for function blocks

### 2.1 Rx BPFs

The desired specifications of a LTCC BPF for low-band W-LAN FEM are as follows:

- A low insertion loss characteristic is required in the pass-band frequency range of 2.4 GHz - 2.5 GHz.
- A high attenuation is required in the stop-band frequencies of 1.91 GHz - 2.1 GHz, which can reduce the crosstalk from the image signal and local oscillator signal.
- A harmonic frequency in the range of 4.8 GHz - 5 GHz, needs to be reduced.
- The size of the BPF should be small, especially in its thickness, to be successfully embedded in the miniaturized FEM.

The step impedance quarter-wavelength comb line type filter with two resonators was chosen to satisfy the required specifications mentioned above and to minimize its size. Each step impedance resonator is composed of a shunt capacitor and stripline. The shunt capacitor and the stripline are connected with a via of 100  $\mu\text{m}$  diameter. With this structure, the impedance of resonators can be seen as step impedance. Fig. 2 depicts the schematic and geometry of this 2<sup>nd</sup> order filter.

The input and output ports are directly connected to the resonator at the middle of the point connecting the stripline and the shunt capacitor. For the large amount of the magnetic coupling between those two resonators, two resonators are connected by a short line in the middle point of the strip line. Without this connecting line between two resonators, it is not large enough of the magnetic coupling because of the small thickness of this embedded BPF. The design procedure of a high-band BPF is similar to a low-band BPF. The pass-band and the rejection band of a high-band BPF range from 5.15 GHz to 5.85 GHz and from 2.4 GHz to 2.5 GHz, respectively. The size of a high-band BPF is smaller than a low-band BPF because wavelength is decreased with increased frequency and quarter-wavelength in a BPF is depending on frequency.

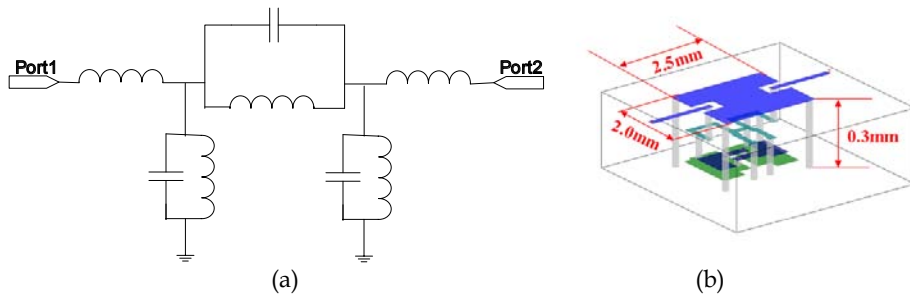


Fig. 2. A BPF for : (a) schematic, (b) Geometry of the 2nd order band pass filter.

## 2.2 Rx Diplexer

The Rx diplexer is designed by using two fabricated BPFs. Each s-parameter extracted through measuring BPFs is adapted as depicted in fig. 3. The Rx diplexer can be divided into a low frequency path and a high frequency path. The low frequency path is composed of a series inductor, a shunt capacitor, and a BPF for low-band. High frequency path is composed of a series capacitor, a shunt inductor, and a BPF for high band as shown in fig. 3. A low-band path in a diplexer is similar to a schematic of a LPF and a high band path in a diplexer is similar to a schematic of high pass filter (HPF). The Rx diplexer employs conjugate impedance matching method in order to match low-band path and high-band path. Conjugate impedance matching is complementary approach between impedance of low-band and of high-band. This method is therefore sensitive to BPF's s-parameter or port impedance.

The Rx diplexer is designed as follows steps:

- 2.4 GHz ~ 2.5 GHz BPF is designed and fabricated.
- 5.15 GHz ~ 5.85 GHz BPF is designed and fabricated.
- S-parameters of two BPFs are extracted by measuring with probe station.
- Extracted S-parameters of two BPFs are substituted as basic blocks in order to design the Rx diplexer.
- The Rx diplexer is designed and optimized in level of schematic by employing S-parameters.
- The Rx diplexer is designed and optimized in level of 2.5-Dimensin (2.5-D) by employing S-parameters.

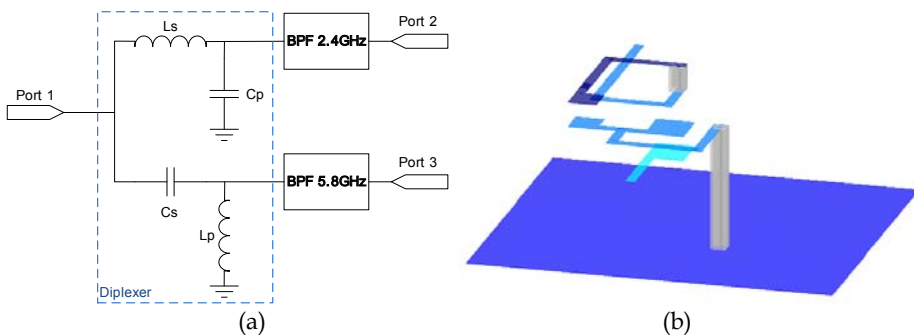


Fig. 3. A Rx diplexer for : (a) schematic, (b) Geometry.

**2.3 Tx matching stages**

Most products for PAM IC are necessary that the output matching circuit are fabricated in outside of PCB. The input matching circuit is usually included in the PAM IC. This type is used in this book, so only output matching circuit is required. Fig. 4 shows a block diagram for output matching stage. The DC power is supplied from the output port through the inductor which plays a role to a RF choke, and RF signal goes through a 50 ohm transmission line, a shunt capacitor and a series capacitor which blocks the DC. The value of each component is too large and the length of transmission line is too long, so it is hard to make the LTCC module as small size. The equivalent circuit is proposed in this book and the input impedance of a matching circuit has to be extracted in order to find out optimal impedance. The input impedance of a matching circuit is measured and extracted by following two method : (a) by using a probe station, and (b) by using load pull equipment. One method, by using a probe station, is explained as following : At first, the matching circuit stage was designed and implemented on PCB. After finding the optimal matching circuit on PCB, the input impedance (S11) of matching circuit was measured by using the Ground-Signal-Ground (GSG) probe as shown in fig. 5 (a). The input impedance of a matching circuit may be extracted by Ground-Signal (GS) probe as depicted in fig. 5 (b). Table 1 is the measured result of the input impedance which was performed at the frequency 2.45 GHz depending on the variation of samples by using the GSG probes because each sample has variation in input impedance.

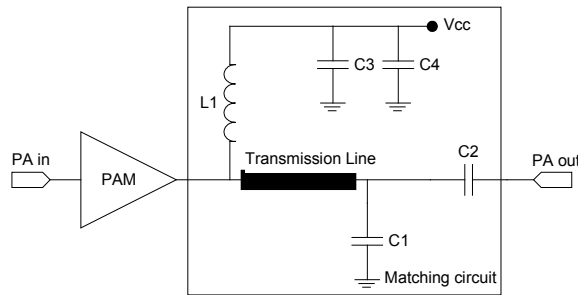


Fig. 4. Schematic of matching circuit.

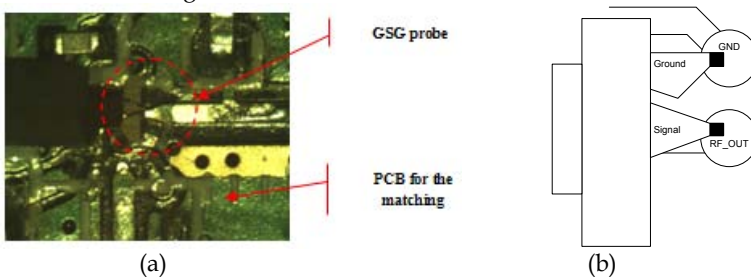


Fig. 5. The example of measurement by using : (a) GSG, (b) GS.

	#1	#2	#3	#4	#5
Z	6.4 + j5.2	5.7 + j6.2	5.5 + j6.5	5.7 + j6.5	5.6 + j7.0

Table 1. Summary of input impedance for matching circuit on PCB



The average value from table 1 is  $5.6 + j6.3$ . It is difficult to embed the inductor, capacitor, and transmission line in the LTCC. Therefore, the equivalent circuit as shown in fig. 6 is proposed. It consists of an inductor, a shunt capacitor, and a series capacitor. The equivalent value is induced to make the input impedance ( $S_{11}$ ) to be  $5.6 + j6.3$ . The LTCC module was designed and implemented on basis of these.

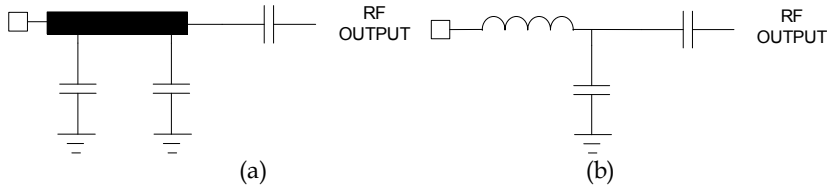


Fig. 6. The matching circuit for : (a) an original schematic. (b) a proposed schematic.

Second method, by using load pull equipment, is given as following : at first, load pull equipment is set-up as depicted in fig. 7. Test set-up is composed of the input load pull equipment, the s-parameter box of compensation for physical transmission line as connection between a device under test (DUT) and output load pull equipment. At second, the PAM is mounted on PCB without the matching circuit. The impedance of matching circuit can be changed by controlling setting the load pull equipment. The maximum output power, the maximum gain, the power circle and the gain circle can be obtained by using load pull equipment. The measured maximum output power and gain are depicted in fig. 8. This result is obtained in condition of 22pF at DC bias line which effects the performance of a PAM. The input impedance of matching circuit is extracted by measuring several samples which are different from previous mentioned sample in previous paragraph. The average value of samples which is applied and the optimal impedance is  $18.8 + j0.9$ . This value is the target of design and implementation

Power Block Diagram

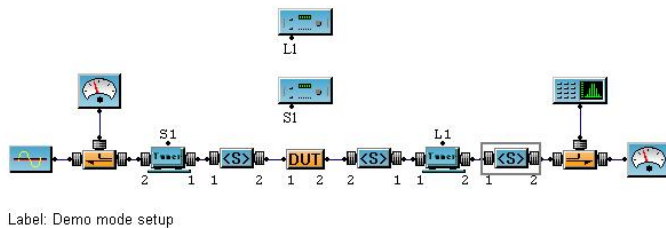


Fig. 7. Block diagram to extract the matching impedance by using load pull equipment

Fig. 9 shows the optimal gain circle and power circle depending on shunt capacitors in DC bias lines. The DC bias line of the PAM IC needs the shunt capacitor to reject DC bias noise. DC bias condition is major factor to meet the optimal performac of a PAM. The feedback in DC bias line causes the oscillation and cross modulation becaus of wanted signal and 2nd harmonic signal. Normally, shunt capacitors can remove the feedback signal. The value of the shunt capacitor is ranged from 100 pF to 1 nF. Fig. 9 depicts that the optimal impedance of matching circuit, maximum gain, and maximum power can be changed with variation of capacitor. In case of 100 pF, the maximum gain, the maximum power, and the optimal

impedance are 27.3 dB, 22.3 dBm, and  $14.1 - j 37.0$ , respectively. Table 2 describes the summary data. In case of 22 pF, the maximum gain, the maximum power, and the optimal impedance are 27.7 dB, 22.7 dBm, and  $17.7 - j 44.3$ , respectively. The optimal impedance, maximum gain, and maximum power are obtained when 22 pF as a shunt capacitor is connected with DC bias line.

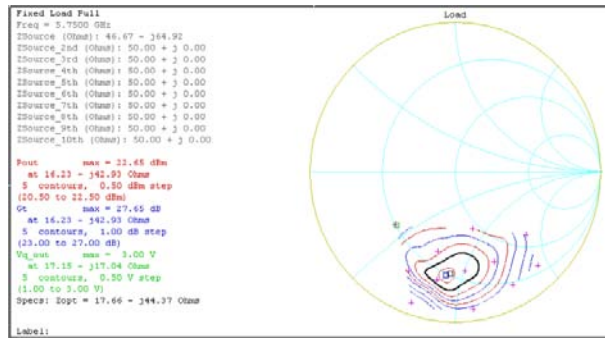
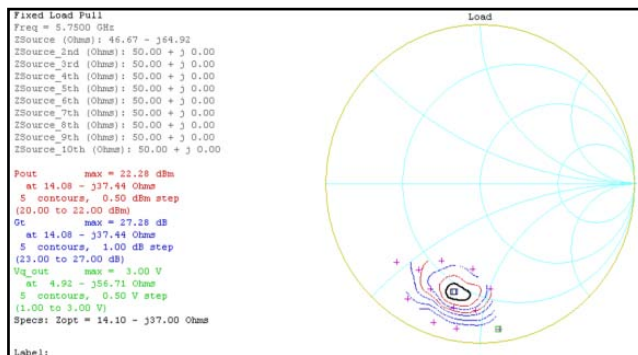


Fig. 8. Power and gain circle by using the load pull.

As a result, the optimal value can be obtained by trying to verify the various condition of DC bias line. These results mean that the power amplifier has different performance under DC bias condition. In order to merge the DC bias line, DC bias lines have to be maintain the isolation. The performance of a PAM is stable if isolation between ports are more than 20 dB. The optimal results can be extracted by attempting many trials at DC bias lines.

	100pF	22pF	5pF
Maximum Gain	27.28 dB	27.65 dB	24.99 dB
Maximum Pout	22.28 dBm	22.65 dBm	19.99 dBm
Optimal impedance	$14.10 - j37.0$	$17.66 - j44.3$	$23.97 - j65.1$

Table 2. Summary of Gain, Power, and Impedance depending on capacitors



(a)

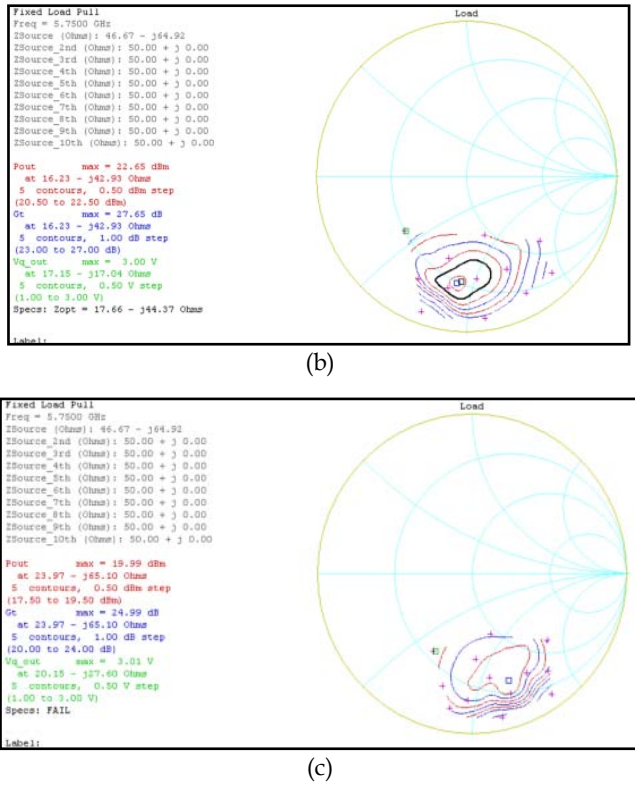


Fig. 9. Impedance of matching circuit depending shunt capacitors in DC bias line (a) 100 pF, (b) 22 pF, and (c) 5 pF.

Fig. 10 shows the presented a low-band matching equivalent circuit and a 3-D structure. This circuit is proposed and designed on basis of previous measured data. This circuit consists of a series inductor, series capacitor, and a shunt capacitor. L1 as a series inductor is given as 2 -turn coil shape in left side of fig. 9 (b). C1 as a shunt capacitor is induced by using parasitic capacitance. C2 as a series capacitor is given as parallel plate shape in center of fig. 9(b). 1-turn coil shape in right side of fig. 9 (b) is added to meet optimal impedance.

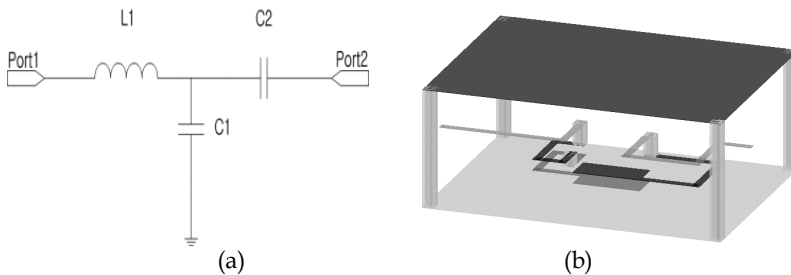


Fig. 10. Low band matching circuit : (a) Equivalent circuit (b) 3-D geometry.

Fig. 11 illustrates the high-band matching circuit which is composed of transmission line. This methodology of circuit is different from low-band matching circuit. The matching circuit for low-band is designed and fabricated by employing lumped elements in LTCC, but the matching circuit for high-band suffers from being designed by using lumped element because of parasitic capacitance at high frequency. As mentioned in previous, the matching impedance for high-band is designed by same procedure for low-band matching circuit. The optimal impedance of the output matching is given as  $18.1 + j 5.9$  at high-band. This target can be implemented by using an ideal shunt capacitor with  $0.5 \text{ pF}$ , but this can't be designed in the LTCC substrate. Because the parasitic shunt capacitor is more than  $0.8 \text{ pF}$  in W-LAN high frequency. This book proposed this matching circuit with the geometry of transmission line. The impedance and electrical length of the designed transmission line are  $27.05 \text{ ohm}$  and  $82.8 \text{ degree}$ , respectively. Fig. 11 (b) depicts 3-D geometry of strip line.

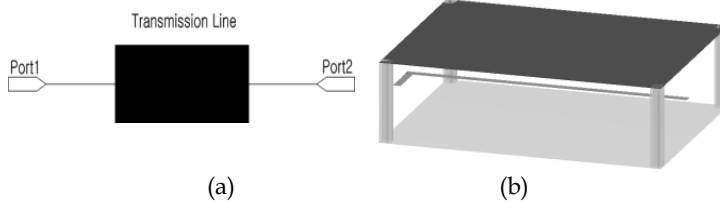


Fig. 11. High band matching circuit: (a) Equivalent circuit (b) 3-D geometry.

#### 2.4 Tx LPFs

The permittivity and dielectric loss tangent of LTCC substrate are  $9.0$  and  $0.0035$ , respectively. These LPFs play a role to reject  $2^{\text{nd}}$  harmonic of fundamental wireless LAN signal. In case of a low-band LPF, the pass band of a low-band LPF ranges from  $2.4 \text{ GHz}$  and  $2.5 \text{ GHz}$ . The stop band of low-band LPF ranges from  $4.8 \text{ GHz}$  and  $5 \text{ GHz}$ . In case of a high-band LPF, the pass band of a high-band LPF is given from  $5.15 \text{ GHz}$  to  $5.85 \text{ GHz}$  and the stop band of a LPF ranges from  $10.3 \text{ GHz}$  and  $11.7 \text{ GHz}$ .

A low-band LPF composed of inductors and capacitors as shape as T-junction or ladder. The size of each component according to this schematic is large, so it is difficult to make small module and to fabricate a LPF. The equivalent circuit for a low-band LPF as depicted in fig. 12 (a) is proposed. The equivalent circuit has two transmission zeros on basis of  $3^{\text{rd}}$  LPF as shown in fig. 12 (a). Transmission zero is generated by a series capacitor and a series inductor. Fig. 12 (b) illustrates a 3-D geometry for a low-band LPF. A shunt capacitor is designed by using one plate and a ground plane as depict in low side of fig. 12 (b).

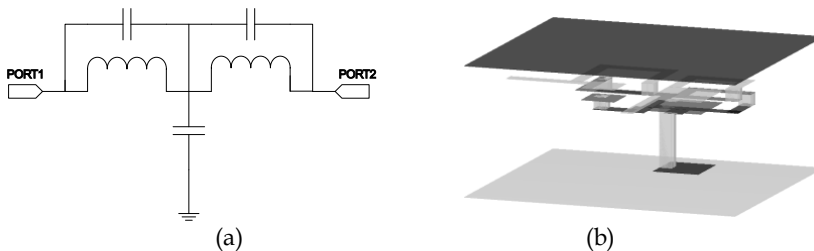


Fig. 12. Proposed low-band LPF : (a) schematic, (b) 3-D geometry.

A high-band LPF consists of inductors and capacitors. As mentioned in low-band LPF, an equivalent circuit of a high-band LPF is proposed as depicted in fig. 13. The proposed circuit adds two shunt capacitors in comparison to the low-band LPF in order to improve the characteristic of rejection. A high-band LPF is sensitive to dimension of designed components because the many parasitic facts occur in high frequency. For example, a series capacitor is composed of two parallel plates which occurs parasitic capacitance from ground plane to parallel plates in high frequency. The design and the control of parasitic component are key fact. RF components in high frequency are designed to avoid these facts, but these parasitic capacitors are employed in this book instead of avoiding it. A proposed high-band LPF is composed of series inductors, series capacitors, and shunt capacitors which are parasitic capacitors. Shunt capacitors as depicted in fig. 13 (a) don't appear in 3-D geometry as depicted in fig. 13 (b).

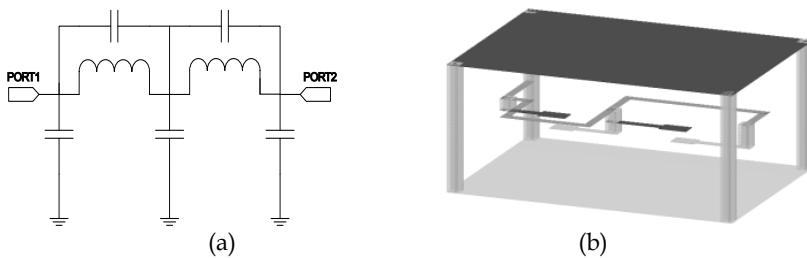


Fig. 13. Proposed high-band LPF : (a) schematic, (b) 3-D geometry.

## 2.5 Tx Diplexer

The concept of Tx diplexer and the flowchart for Tx part is similar to Rx part as mentioned in 2.2. The results of Tx LPFs are only employed instead of Rx BPFs. The Tx diplexer is designed as following step:

- (a) 2.4 GHz ~ 2.5 GHz LPF is designed and fabricated.
- (b) 5.15 GHz ~ 5.85 GHz LPF is designed and fabricated.
- (c) S-parameters of two LPFs are extracted by measuring with probe station.
- (d) Extracted S-parameters of two LPFs are substituted as basic blocks in order to design the Tx diplexer.
- (e) The Tx diplexer is designed and optimized in level of schematic by employing S-parameters,
- (f) The Tx diplexer is designed and optimized in level of 2.5-Dimensional (2.5-D) by employing S-parameters.

The Tx diplexer has the schematic and geometry as depicted in fig. 14. Each s-parameter box in fig. 14 (a) is obtained from measured Tx LPFs. The low frequency path is composed of a series inductor, and a Tx LPF for low-band. High frequency path is composed of two series capacitor, a shunt inductor, and a LPF for high-band. The part of low path consists of a series inductor and shunt capacitor but shunt capacitor is removed because a low-band LPF doesn't have 50 ohm but including shunt capacitance.  $Ls1$  and  $Lp1$  are designed by lines and series capacitors have shape of two parallel plates as illustrated in fig. 14 (b).

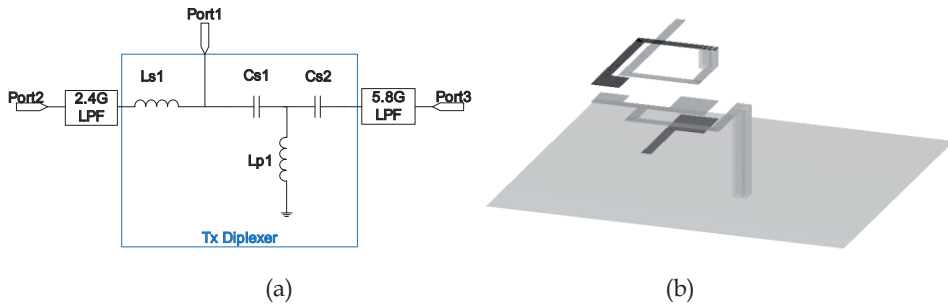
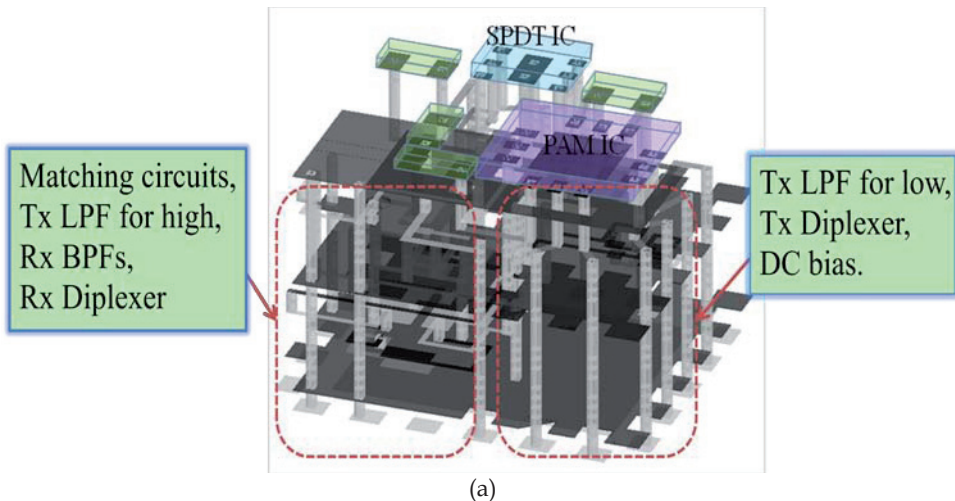


Fig. 14. Design for a Tx diplexer (a) equivalent circuit (b) 3-D layers.

### 3. Module design and fabrication

The whole module is composed of a SPDT IC, a PAM IC, and a LTCC substrate which integrates a Rx diplexer, a Tx diplexer, two Rx BPFs, two Tx LPFs, and two matching circuits. LTCC green sheets (X200) are obtained from Heraeus company. Its dielectric constant and loss tangent are given as 9 and 0.005, respectively. The size of LTCC substrate and whole module are given as 7.0 mm × 6.0 mm × 0.7 mm and 7.0 mm × 6.0 mm × 1.2 mm, respectively. The thickness of ICs is approximately 0.5 mm. Fig. 15 (a) illustrates the overall structure of the proposed module and the PAM, the SPDT, and external components are mounted on top layer. The PAM ( $\mu$ PG2317T5J) and SPDT ( $\mu$ PG2163T5N) are supplied from NEC company. GND planes are placed in the second layer, bottom, and middle. It distinguishes each component and isolates each part in order to maintain the performance of the components. Fig. 15 (b) shows the photograph of the implemented module.



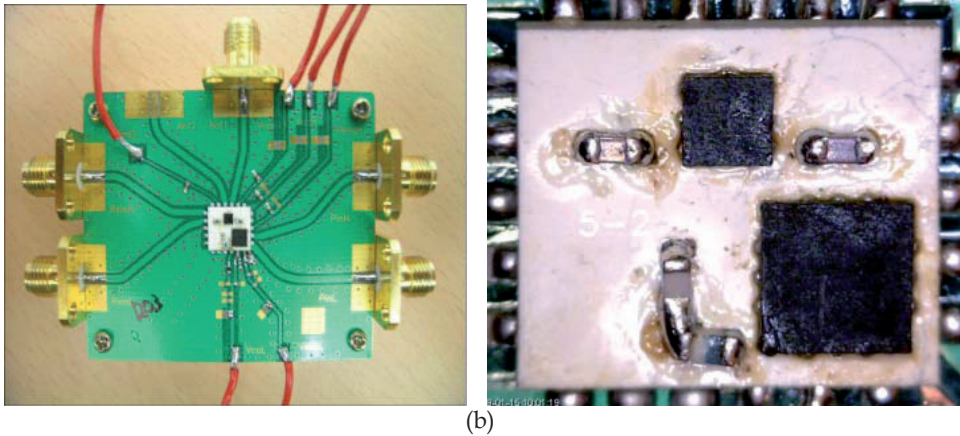
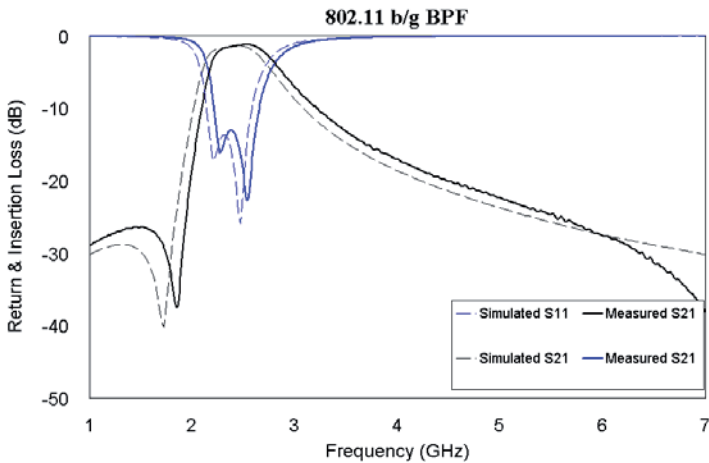


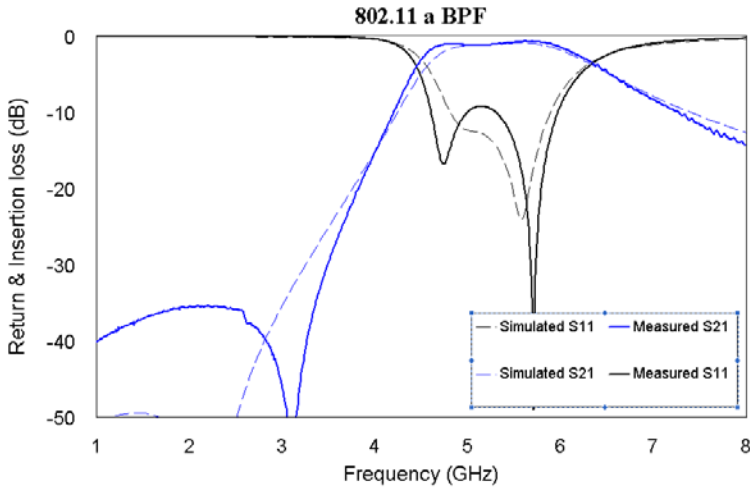
Fig. 15. W-LAN FEM: (a) 3-D geometry (b) Photograph

### 4. Measured performance

The implemented 802.11 a/b/g FEM with a PAM was measured by Agilent’s N5230 network analyzer, Agilent’s E4432B signal generator, and Agilent’s E4407B spectrum analyzer.

Two Rx BPFs, two Tx LPFs, and two matching stage are individually fabricated and measured because measured results of those can’t be obtained in the full module. Fig. 16 displays the simulated and measured data for a low-band BPF and a high-band BPF. Blue trace, black trace, solid trace, and dash trace are given as insertion loss, return loss, a simulated line, and a measured line as illustrated in fig. 16. A low-band BPF shows simulation and measurement has little difference. Insertion loss, rejection at 1.9 GHz, and rejection at IEEE 802.11 a are better than 1.3 dB, 25 dB and 20 dB, respectively.

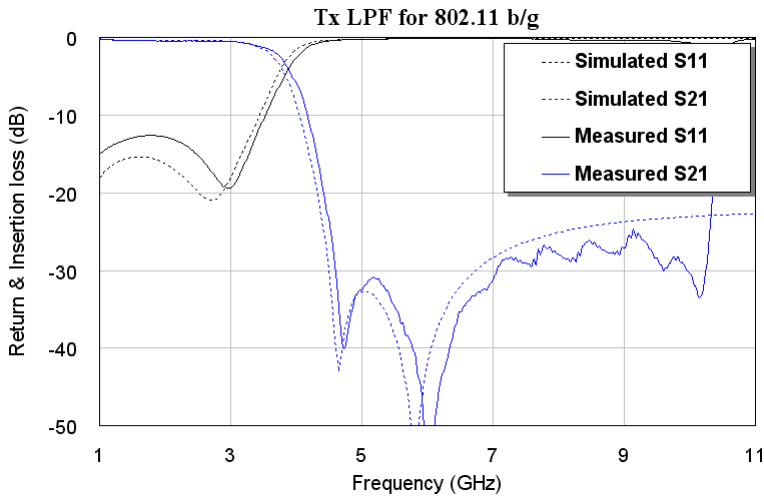




(b)

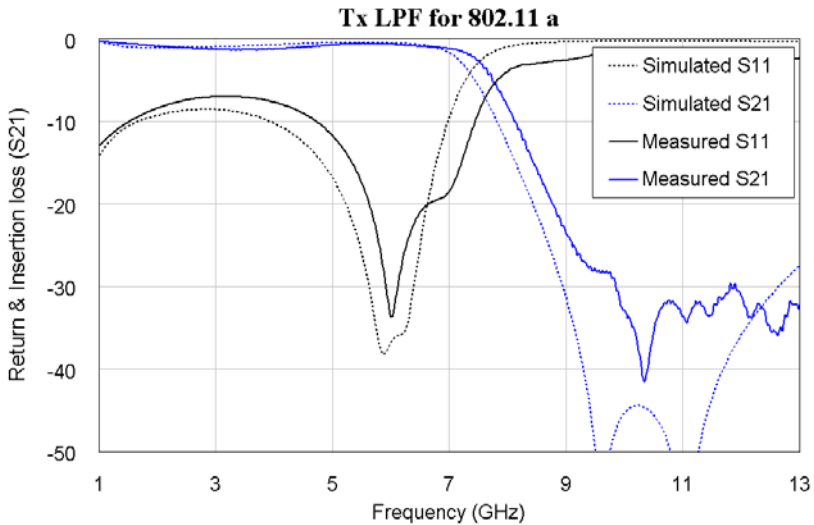
Fig. 16. Simulated and measured data for : (a) a low-band LPF, (b) a high-band LPF.

Fig. 17 illustrates the simulated and measured data for two Tx LFPs. Blue line, black line, solid line, and dash line are given as insertion loss, return loss, a simulated line, and a measured line as illustrated in fig. 17, respectively. Insertion loss and 2nd harmonic rejection for low- band LPF are 0.43 dB and 32 dB. In case of high band, the insertion loss and 2nd harmonic rejection are 0.64 dB and 32.6 dB, respectively.



(a)

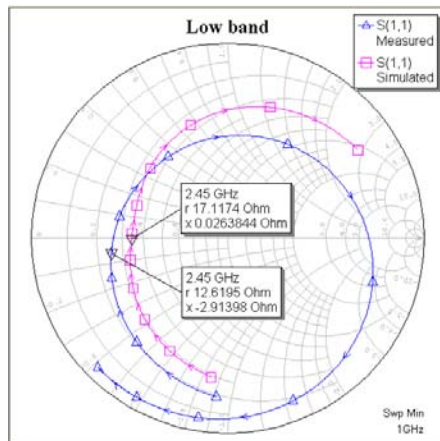




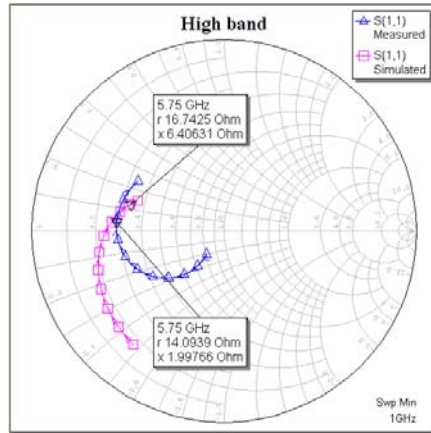
(b)

Fig. 17. Simulated and Measured data from LPF: (a) 802.11 b/g (b) 802.11 a

The simulated and measured data for two matching circuit are shown in fig. 18. Red trace and blue trace means simulation and measurement, respectively. Input impedance of matching circuit between required frequency ranges is measured and the results meet the target impedance.



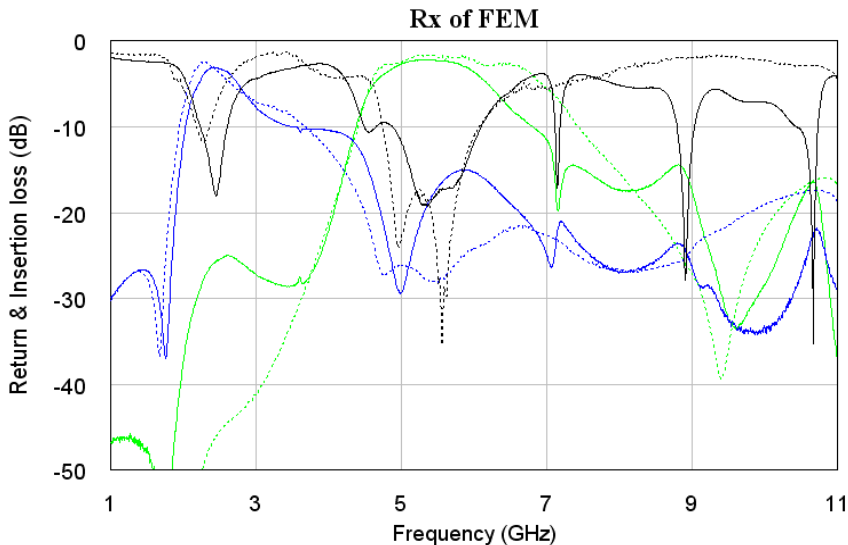
(a)



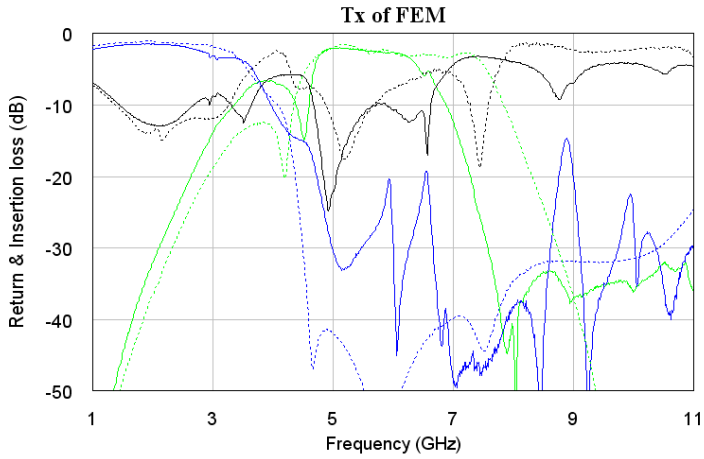
(b)

Fig. 18. Simulated and measured data from matching circuit.

Fig. 19 (a) illustrate measured data from Rx part which includes the SPDT switch, Rx diplexer, and two BPFs. Dash line and solid line display simulated and measured data, respectively. Black line, blue line, and green line express return loss, insertion loss of low-band, respectively. Insertion loss is less than 3.3 dB and return loss is better than 15.5 dB in each pass band as described in table 3. Fig. 19 (b) show measured data from Tx part which includes the SPDT switch, the Tx diplexer and two LPFs. Insertion loss is less than 2.6 dB and return loss is better than 11.3 dB as summarized in table 4.



(a)



(b)

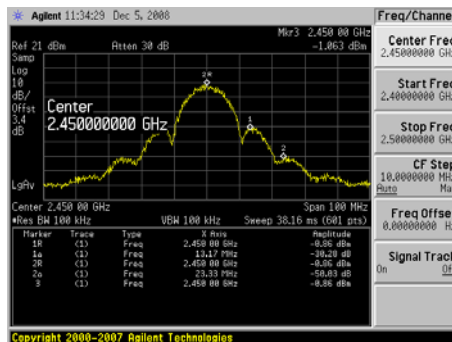
Fig. 19. Simulated and Measured data: (a) Rx part (b) Tx part.

Rx part	(Rx Diplexer + 2G BPF + 5G BPF+ SPDT)	
	2.4 GHz ~ 2.5 GHz	5.15 GHz ~ 5.85 GHz
Return loss	16.5 ~15.5 dB	16.5 ~15.5 dB
Insertion loss	3.11 ~3.26 dB	2.32 ~2.73 dB
Rejection	17.03 dB @ 5.50GHz 18.67 dB @ 1.90GHz	25.64 dB @ 2.45GHz 44.12 dB @ 1.90GHz

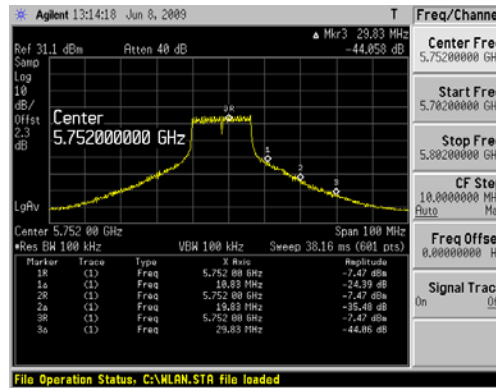
Table 3. Summary of measurement for Rx Part

Tx Part	Tx Diplexer + 2G LPF + 5G LPF + SPDT	
	2.4 GHz ~ 2.5 GHz	5.15 GHz ~ 5.85 GHz
Return loss	12.07 ~11.34 dB	16.98 ~9.93 dB
Insertion loss	1.72 ~1.84 dB	2.07 ~2.57 dB
Rejection	30.46 dB @ 5GHz	35.09 dB @ 11GHz

Table 4. Summary of measurement for Tx Part



(a)



(b)

Fig. 20. RF output spectrum (@18dBm) for: (a) 802.11 b/g (b) 802.11 a

The Tx performance of implemented module was measured at the 18 dBm output power. In case of low-band, measured adjacent-channel power ratios (ACPRs) of the presented module at first side-lobe and second side-lobe are -30.2 dBc and -50.0 dBc with 23.1 dB gain as shown in fig. 20 (a). In case of high band, first side-lobe, second side-lobe and third side-lobe are -24.3 dBc, -35.4 dBc, and -44.8 dBc with 24.5 dB gain as shown in fig. 20 (b), respectively.

## 5. Conclusion

The 802.11 a/b/g FEM with PAM was designed and implemented. It was composed of a SPDT switch, a Rx diplexer, two Rx BPFs, a Tx diplexer, two Tx LPFs, two matching circuits, and a dual-band PAM. The performance of the module was satisfied with IEEE 802.11 a/b/g regulation and the size of the module is very compact.

## 6. References

- Dongsu Kim, D.H Kim, J.I. Ryu, and J.C Kim, "Highly integrated triplexers for WiMAX applications," *2008 MTT-S*, pp. 614-617, 2008.
- J. I. Ryu, D. Kim, H. M. Cho, and J. C . Kim, "Implementation of WLAN front end module with a power amplifier," in *Proceeding of the Asia Pacific Microwave Conf.*, pp. 99-102, vol.1,2007..
- D. H. Kim, D. Kim, J. I. Ryu, J. C. Kim, C. D. Park, I. S. Song, "Implementation of an LTCC Quad-band module for WLAN and WiMAX applications," *Eur. Microwave. Conf.*, PP.614-617, 2008.
- J. I. Ryu, D. Kim, and J. C . Kim, "Isolation Effect Between DC supply Voltage Signal Lines in Wireless LAN Module," in *Proceeding of the 20<sup>th</sup> Inter. Zurich Sym.*, pp. 385-388, 2009.

# Millimeter-wave Imaging Sensor

Masaru Sato<sup>1</sup> and Koji Mizuno<sup>2</sup>

<sup>1</sup>*Fujitsu Ltd.*, <sup>2</sup>*Tohoku University*  
Japan

## 1. Introduction

Electromagnetic waves in the millimeter-wave band have attractive characteristics. One of their features is the wider usable frequency band compared with waves in the microwave band or lower bands. Another feature of using the millimeter-wave band is the fact that it becomes possible to design smaller and lighter equipment that utilizes that band. So it is useful to adapt millimeter waves for short-range broadband communication systems, high-resolution sensing systems and radio astronomy.

In this chapter, the authors describe imaging sensors using the millimeter-wave band. In simple terms, a millimeter-wave imaging sensor is a camera that uses millimeter waves. Receivers detect the millimeter-wave energy on the imaging plane, and record the relative intensity at each pixel. Then the millimeter-wave image is reconstructed using computers as shown in Fig. 1.

The most attractive feature of millimeter waves, when compared with optical, infrared, and terahertz waves, is their ability to penetrate obstacles. And a spatial resolution higher than that achievable with microwave imaging sensors is possible. Therefore, they can be used under low-visibility conditions such as in fog, rain, dust, or fire, where optical or infrared cameras cannot be used (Mizuno et al., 2005). Their most promising application is for security. As the radiometric temperatures of an object are different depending on its metallic or dielectric properties ( $\epsilon_r$ ) and its temperature, the sensors can detect concealed weapons or explosive materials. Consequently, these sensors have undergone test installation for use in security cameras at the entrances of airports (TSA, 2009) and buildings. In addition, these sensors are also useful for finding landmines, for offering all-weather vision, for detecting cracks in exterior walls, and for screening people for skin cancer.

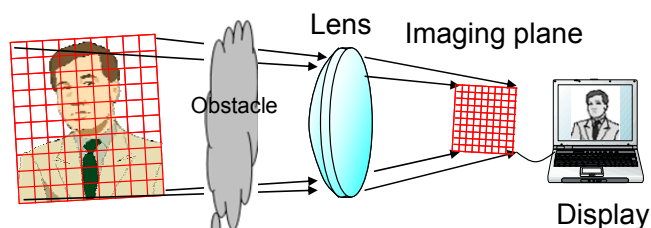


Fig. 1. Concept of millimeter-wave imaging sensor

In section 2, the authors describe the general principle and systems for millimeter-wave imaging sensors and show the published imaging sensors that have been developed so far. Section 3 shows in detail a 94-GHz-band passive millimeter-wave imaging sensor that was developed by Fujitsu.

## 2. Systems for millimeter-wave imaging sensor

### 2.1 Radiometric temperature

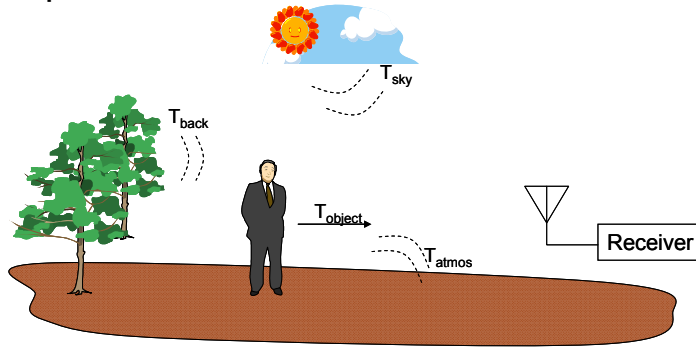


Fig. 2. Various emissions of radiometric temperatures

The total received radiometric temperature is the sum of an object's brightness,  $T_{obj}$ , downwelling temperature from the sky,  $T_{sky}$ , temperature from the background,  $T_{back}$ , and atmospheric effects,  $T_{atmos}$  as illustrated in Fig. 2.

$$T_{received} = T_{obj} + T_{sky} + T_{back} + T_{atmos} \quad (1)$$

$-T_{obj}$

The object's brightness temperature is comprised of the emission and reflection from the surroundings. The effective radiometric temperature is therefore:

$$T_{obj} = \varepsilon \cdot T_a + \rho \cdot T_{sur} \quad (2)$$

where  $T_a$  is the object's temperature (in K),  $T_{sur}$  is the temperature of the surroundings and  $\varepsilon$  is an emissivity of the object, which is a function of its dielectric properties, the roughness of its surface, and the observation angle.  $\rho$  is the reflectivity of the object, and is expressed as  $(1 - \varepsilon)$ .

A metallic object with  $\varepsilon = 0$  will have no emissions. But its high reflectivity will mean the second term in Equation 2 is high. For example, this will occur when  $T_{sur}$  is high or the object is illuminated from millimeter-wave sources (active imaging).

On the other hand, the human body has an emissivity in the order of 0.9.

The effective observed radiometric temperature,  $T_E$ , at a receiver is as follows:

$$T_E = \frac{\varepsilon T_a + \rho T_{sur}}{L_a} \cdot \eta \quad (3)$$

where  $L_a$  is the attenuation loss between the object and the antenna, and  $\eta$  is the area ratio between the object and the main lobe of the antenna.

$-T_{sky}$

$T_{sky}$  is the downwelling of radiation from the sky. The sky's brightness temperature at 94 GHz has a value in the order of  $\approx 60$  K (Bhartia & Bahl, 1984). In outdoor imaging, an important source of illumination is the downwelling of radiation from the sky. Typical values of the downwelling temperature as a function of the atmospheric conditions are shown in the following table.

Conditions	Downwelling Temperature (K)
Clear sky	10 - 60
Thick fog	120
Fog	180
Thick clouds	180
Moderate rain	240

Table 1. Downwelling temperatures in various conditions

$-T_{atmos}$

An atmosphere acts as a blackbody and will thermally generate millimeter waves itself. This is a consequence of the reciprocity between absorption and emission. The temperature of the atmospheric emission is expressed as:

$$T_{atmos} = T_a \left( 1 - \frac{1}{L_a} \right) \cdot \tag{4}$$

As is well known, atmospheric attenuation varies depending on its frequency, because electromagnetic waves are absorbed by  $O_2$  and  $H_2O$ , and the resonant frequencies of these are different. Figure 3 shows typical attenuations (with a water vapor density of  $7.5 \text{ g/m}^3$  at 20 deg) at sea level (Wills, 2009).

Absorption peaks due to the vapor line exist at 22, 184, and 324 GHz. There are  $O_2$  absorption bands at 60 and 118 GHz. This large attenuation causes a large emission temperature. Here the authors assume that an object with a brightness temperature of 300 K and that is at a distance of 1 km is being observed. The attenuation loss at 60 GHz is 13 dB. The radiometric temperature,  $T_{Er}$ , from the object was attenuated to 15 K. By contrast, the emission from the atmosphere,  $T_{atmos}$ , is almost 285 K. In this case, the brightness temperature from the object is buried in the atmospheric temperature,  $T_{atmos}$ .

On the other hand, there are low attenuation windows at 35, 94, 140, 220 and 360 GHz. Values for  $T_{atmos}$  of these bands are relatively low and the attenuation of brightness temperature from the object is low. So these low-attenuation windows are usually used for imaging sensors. Especially, the 94-GHz-band is often used because a high spatial resolution is possible due to its short wavelength ( $\approx 3 \text{ mm}$ ).

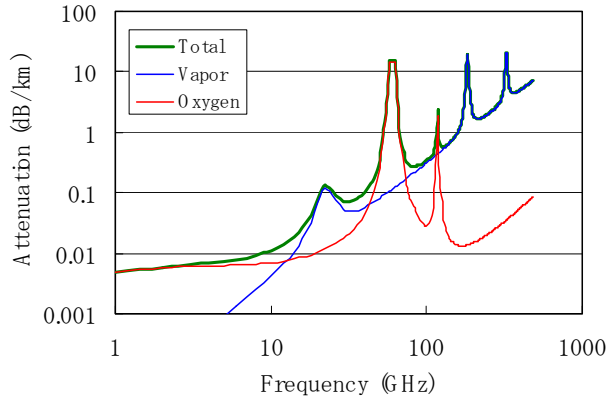


Fig. 3. Attenuations for atmospheric oxygen and water vapor

**2.2 Indoor and outdoor imaging considerations**

Fig. 4 compares the radiometric temperature of indoor and outdoor locations and shows the difference in such temperature between dielectric (a human) and metallic objects.

In outdoor imaging,  $T_{sky}$  is about 60 K. So the effective temperatures of a human ( $T_{obj\_human}$ ) and some metal ( $T_{obj\_metal}$ ) are calculated using Equation (2) are 285 K and 60 K, respectively, where the emissivity of the human and metal were set as 0.9 and 0, respectively. As the temperature difference is 225 K, the metallic object appears very cold in a millimeter-wave image.

By contrast, the radiometric temperature of a metallic object reflected in an indoor location,  $T_{obj\_metal}$ , is as high as 295 K. The temperature difference between the human and metallic object is only 13.5 K. Thus, the millimeter-wave camera has to detect this small temperature difference in order to distinguish between the dielectric and metallic object in an indoor location.

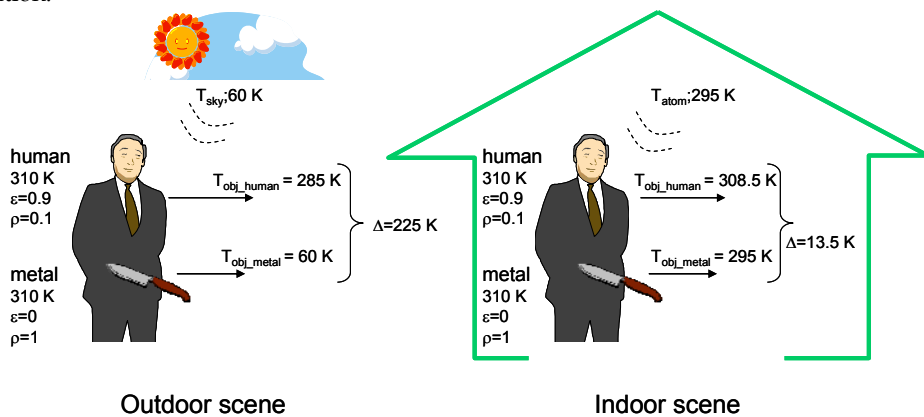


Fig. 4. Radiometric temperature observed outdoors and indoors



**2.3 Imaging method (passive or active imaging sensor)**

Broadly speaking, imaging sensors can be classified into two types: active imaging sensors and passive millimeter-wave sensors. Fig. 5 shows simplified diagrams of these active and passive imaging sensors.

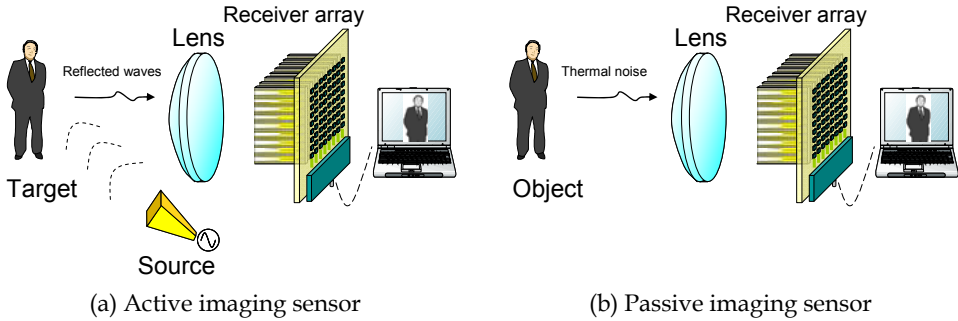


Fig.5. Active and passive imaging sensor

An active imaging sensor radiates millimeter waves from the millimeter-wave source and illuminates the object. The receiver array observes the amplitude or phase of the reflected waves. Using these signals, the millimeter-wave image is reconstructed using a computer. Since an active imaging sensor uses a millimeter-wave source, the signal to noise ratio (S/N) received at the RX antenna is relatively high. However, the millimeter-wave image has speckle or glint when using a coherent wave as the millimeter-wave source. So, adequate signal processes are usually needed. Recently, an incoherent wave source using an impulse generator (Nakashita et al., 2007) was reported, which might be useful for solving these problems.

On the other hand, a passive imaging sensor receives incoherent millimeter waves emitted from the object. The amplitude of the radiation depends on the object’s emissivity and temperature as described in section 2.1. Since passive millimeter-wave imaging sensors do not need a millimeter-wave source, the system block is simple when compared with active imaging and it lies outside the scope of the Radio Law regulations. Since the radiation from the object is the thermal noise, its power is quite small. So the receivers need to have both low noise and high sensitivity. This type of sensor is also often used in radiometers and in astronomy.

**2.4 Receiver system**

**-Receiver block**

Fig.6 shows various types of receiver block. Fig. 6 (a) has a traditional heterodyne structure using a mixer, which needs an LO oscillator. The recent development of a low-noise-amplifier (LNA) using InP, GaAs HEMTs or SiGe MMIC and a square-law detector have made it possible to use the direct detection as shown in Fig. 6 (b). An LNA boosts the signal above the detector’s noise floor. Furthermore, Sb-based heterostructure diodes (Siegwart et al., 2006) with high sensitivity have a possibility to remove the need for pre-amplification, which may lead to the development of imaging systems that are compact and inexpensive.

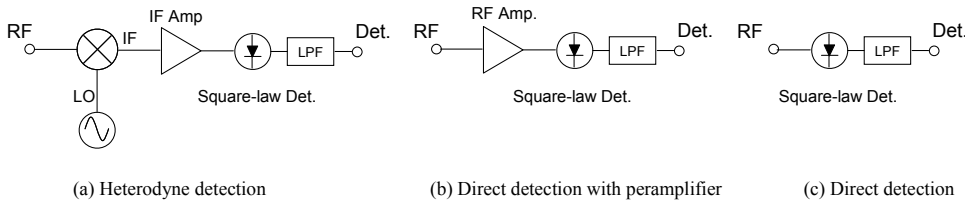


Fig. 6. Receiver block diagram

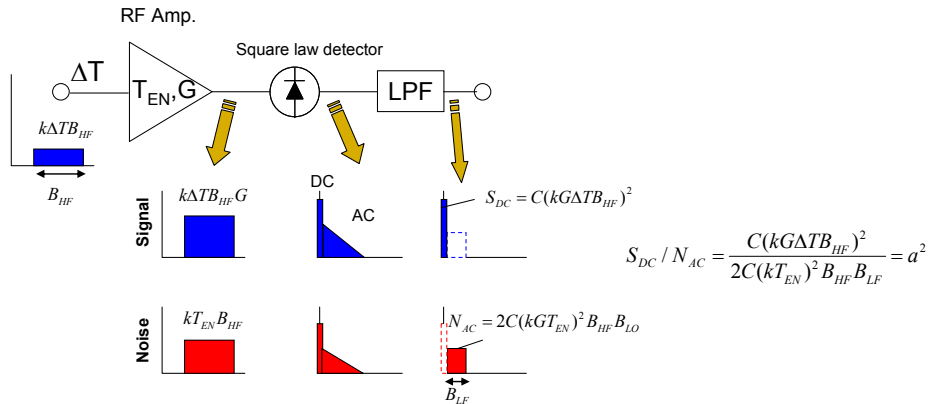


Fig. 7. Receiver block diagram and power spectrum at each stage

**-Total power receiver**

Here, the authors consider the relationship among minimum detectable temperature, noise figure, and integration time,  $\tau$ , of a receiver using the direct detection with a preamplifier, as shown in Fig. 6 (b).

Fig. 7 shows a receiver block diagram. The brightness temperature of an object,  $\Delta T$ , is observed and amplified in an LNA, then fed into a square-law detector. In the LNA, noise is also produced. The equivalent noise temperature,  $T_{EN}$ , is expressed using a noise factor,  $F$  and ambient temperature,  $T_a$ .

$$T_{EN} = (F - 1) \cdot T_a. \tag{5}$$

At the square-law detector, signals from the object and the noise produced in the LNA are converted to both DC and AC components. The DC component will be displayed as millimeter-wave intensity of the object. DC component of the detected signal is expressed by (Tiuri, 1964)

$$S_{DC} = C(kG\Delta TB_{HF})^2 \tag{6}$$

where  $k$  is the Boltzmann constant,  $B_{HF}$  is the bandwidth of the LNA and detector, and  $C$  is a constant that relates to the sensitivity of the detector. Although both DC and AC components are produced from the noise, the DC components of the noise can be removed by applying a proper offset voltage. An AC component of the signal also exists, its amount is small compared with the AC component of the noise.

The AC component converted from the noise at the output of LPF, which causes fluctuation in the detected voltage, is given by

$$N_{AC} = 2C(kGT_{EN})^2 B_{HF} \cdot B_{LF} \quad (7)$$

where  $B_{LF}$  is the bandwidth of the LPF.

So, the ratio of the DC component of the signal to the AC component of the noise determines the signal to noise ratio (S/N). Here, the authors define the S/N as  $a^2$ .

$$S_{DC} / N_{AC} = \frac{C(kG\Delta TB_{HF})^2}{2C(kGT_{EN})^2 B_{HF} B_{LF}} = a^2. \quad (8)$$

Using Equations (5) and (8), the relation between the bright temperature difference and the noise factor of the receiver is expressed in Equation (9):

$$F = 1 + \frac{\Delta T}{aT_a} \cdot \sqrt{\frac{B_{HF}}{2B_{LF}}}. \quad (9)$$

The relation between the integration time,  $\tau$ , and the bandwidth of the LPF based on an R-C circuit is given by:

$$B_{LF} = \frac{1}{2\pi\tau}. \quad (10)$$

Using Equation (9), the noise factor will therefore be:

$$F = 1 + \frac{\Delta T}{aT_a} \cdot \sqrt{\pi \cdot \tau \cdot B_{HF}} \quad (11)$$

$$\Delta T = \frac{aT_a(F-1)}{\sqrt{\pi \cdot \tau \cdot B_{HF}}}. \quad (12)$$

Equation (12) indicates that a larger  $B_{HF}$  with a smaller  $F$  of the receiver produces a smaller detectable temperature,  $\Delta T$ , which means an improved temperature resolution in the millimeter-wave image. Although a longer integration time will also make it possible to have a smaller  $\Delta T$ , it takes longer until the detected voltage is settled, which means that it would take a long time to acquire an image.

### -Dicke receiver

A Dicke receiver (Tiuri, 1964) is well-known architecture for decreasing fluctuations in a detected voltage. These fluctuations are caused from gain or temperature variations in the LNA or DC drift in the detector (1/f noise). A Dicke receiver consists of an RF switch, an LNA, a detector and a lock-in amplifier, as shown in Fig. 8. The RF switch alternately switches between the millimeter-wave signal from the scene and the reference noise at a repetition frequency of  $f_M$ . The output switch located in the lock-in-amplifier switches in synchronism with the antenna switch. By subtracting the received voltage in a lock-in

amplifier, fluctuations in the detected voltage can be decreased, if  $f_m$  is high enough in comparison with the gain instability frequencies.

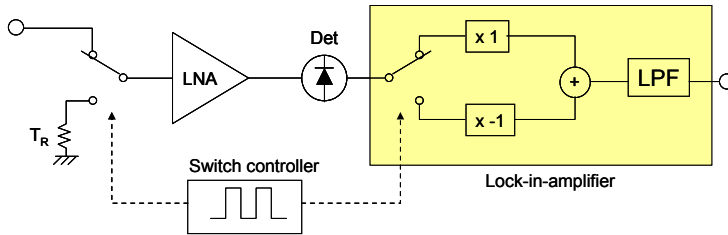


Fig. 8. Block diagram of a Dicke receiver

In the Dicke receiver, a receiver observes signals only half of the time, assuming there is a square wave modulation. The bandwidth of the receiver,  $B_{HF}$  is halved. Equation (6) is modified as:

$$S'_{DC} = C \left( \frac{kG\Delta T B_{HF}}{2} \right)^2. \tag{13}$$

On the other hand, the AC component converted from the noise is the same as in Equation (7) due to the halved integration time in LPF. So the noise factor of a Dicke receiver is modified as follows:

$$F' = 1 + \frac{\Delta T}{2aT_a} \cdot \sqrt{\pi \cdot \tau \cdot B_{HF}}. \tag{14}$$

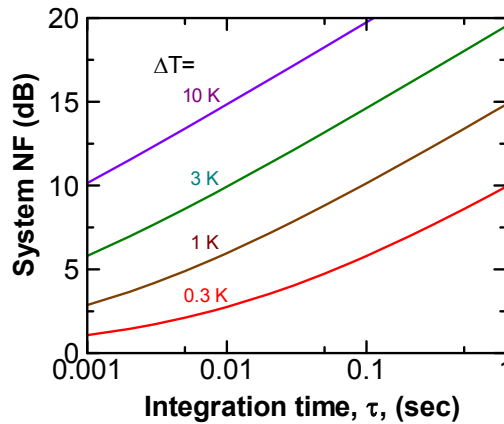
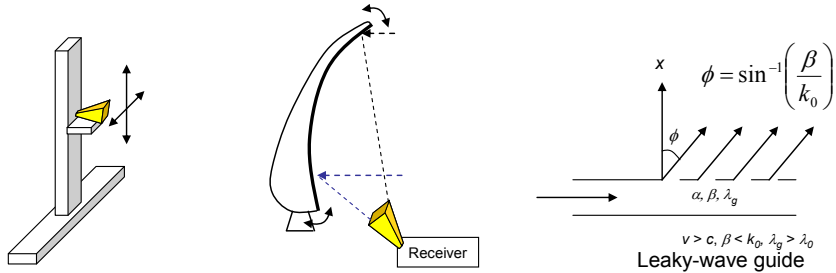


Fig. 9. System NF dependence on integration time

Fig. 9 shows the dependence of the system noise figure on integration time with various minimum detectable temperatures,  $\Delta T$ , where an ambient temperature of 300 K, a bandwidth of 10 GHz, and an  $a$  of 10 have been set. When observing millimeter waves in 0.01 second with  $\Delta T$  of 1 K, the required system noise should be within 6 dB.

**2.5 Scanning method**

The image acquisition time is composed of the integration time in the receiver and the time for moving the receivers. An X-Z mechanical scanning method is shown in Fig. 10 (a). It takes a long time to acquire an image with this method because the movement in the focal plane is large. The scanning method shown in Fig. 10 (b) uses a mirror. By moving the mirror slightly, the scanning direction can be changed. Fig. 10 (c) shows a frequency scanned antenna that uses a leaky-wave guide (Kuki, 2008). The angle of radiation depends on the frequency. Therefore, by scanning the amplitude on each frequency, a one-dimensional scan is possible using this antenna.



(a) X-Z mechanical scan      (b) Mechanical scan (Mirror)      (c) Frequency scanned antenna

Fig. 10. Scanning method for millimeter-wave imaging

**2.6 Published performances of millimeter-wave imaging sensors**

Table 2 shows the published performances of millimeter-wave images.

	Active/ Passive	Freq. (GHz)	Scan method	Sensitivity	Pixel format	Frame rate (frame/s)	Ref
Trex	Passive	75–93	Frequency + mechanical	2–3 K	128 × 60	0.5	(Kolinko et al., 2005)
Millivision	Passive	100	Mechanical	–	–	10	(Millivision, 2009)
QinetiQ	Passive	35	Mechanical	0.28 K	32 × 32	1	(Sinclair et al., 2001)
Northrop Grumman	Passive	84–94	Mirror	2 K	30 × 20	17	(Yujiri, 2006)
Farran Technolog y	Passive	94,140	Mirror	1 K	83 × 50	10	(Vizard & Doyle, 2006)
NHK	Active	60–62	Frequency+ Mechanical	–	30 × 20	0.1	(Kuki, 2008)
Tohoku University	Passive	30–40	Imaging Array	1 K	6 × 6	10	(Mizuno et al., 2009)
Fujitsu	Passive	84–99	Mechanical	1 K	40 × 40	0.1	(Sato et al., 2009)

Table 2. Published performances of millimeter-wave imaging sensors

### 3. 94-GHz-band PMMW imaging sensor

This section describes a 94-GHz-band passive millimeter-wave imaging sensor that was developed by Fujitsu. Fig. 11 shows a block diagram of the imaging system. In section 3.1 the authors describe the design and performance of the receiver MMIC based on InP HEMT technology. The development of the antipodal linearly tapered slot antenna (LTSA) and lens that are well suited for millimeter-wave sensors is shown in sections 3.2. and 3.3, respectively. Finally, the authors show an example of a millimeter-wave image captured by their imaging system.

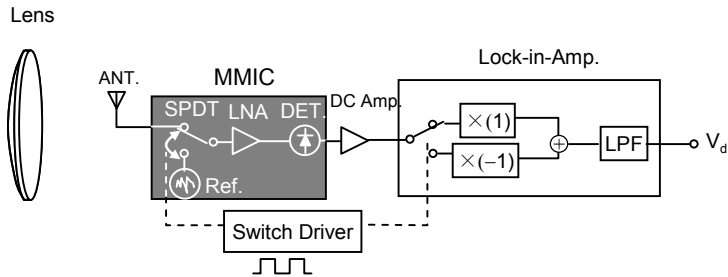
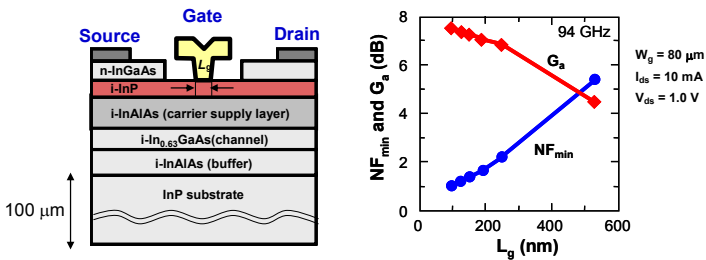


Fig. 11. Block diagram of passive millimeter-wave imaging sensor developed by Fujitsu.

#### 3.1 Receiver MMIC

The most challenging component to develop is the receiver MMIC. Especially an LNA is one of the key components. In order to detect a millimeter-wave signal in a short integration time without deteriorating the system noise figure, the NF of LNA should be extremely low. In addition, a gain of over 30 dB is required to provide a sufficient boost for the detector. The authors designed and fabricated an ultra-low-noise, high-gain LNA using InP HEMT. The authors also developed an SPDT switch and detector and integrated them into a single chip.

#### -InP HEMT technology



(a) Schematic of the InP HEMT technology (b) Noise performance on gate length

Fig. 12. Device structure and noise performance of InP HEMT technology

To meet these requirements, the authors used InP HEMT technology. The epitaxial wafer consists of an InGaAs channel layer and an InAlAs carrier supply layer. The gate had a T-shaped Ti/Pt/Au structure which was fabricated using electron beam (EB) lithography. The

thickness of the InP substrate was thinned to 100  $\mu\text{m}$ . A schematic of the InP HEMT is shown in Fig. 12 (a).

Fig. 12 (b) shows the dependence of the  $\text{NF}_{\text{min}}$  and the associated gain,  $G_a$ , on the gate length at a frequency of 94 GHz. The gate width was  $2 \times 40 \mu\text{m}$ , and the applied bias current,  $I_{\text{dsr}}$ , and voltage,  $V_{\text{dsr}}$ , are 10 mA and 1.0 V, respectively. Both the noise figure and associated gain have significant dependence on gate length. By decreasing the gate length to 100 nm, the authors could obtain an  $\text{NF}_{\text{min}}$  of 1 dB and an associated gain of 7.5 dB.

Schottky diodes constructed using HEMT technology were used for the detector. The gate length and width were 4  $\mu\text{m}$  and 5  $\mu\text{m}$ , respectively.

**-LNA**

The LNA requires a gain of over 30 dB, but it is difficult for a single amplifier to obtain such a high gain while maintaining stable operation. In the worst case, the amplifier oscillates. This instability is caused not only by feedback in the circuitry but also by the feedback path transmitted from the output to the input terminals via the MMIC (InP) substrate (Sato et al., 2007).

The authors estimated the feedback power that was transmitted in the MMIC substrate using a 3D electromagnetic simulation (HFSS). First, the authors extracted structure models from CAD data of the MMIC, from which the active devices were removed. Next, the authors simulated the feedback power from the output to the input terminals. Fig. 13 shows an E-field simulation of the feedback power at a frequency of 94 GHz. In this simulation, a conventional thin film microstrip structure for the transmission line was used, as shown in Fig. 14 (a). The blue shade in Fig. 13. represents the feedback power. Because a semiconductor’s substrate has high resistivity, electromagnetic waves can transmit in the substrate at high frequency. As the MMIC is mounted on a metal plate, most of the InP substrate was sandwiched between the second metal and the metal substrate. So the parallel-plate mode was excited, which caused the feedback. Dashed line in Fih. 14. (d) shows the feedback power. About -20dB feedback power was obserbed at W-band. And that feedback caused instability in the high-gain amplifier.

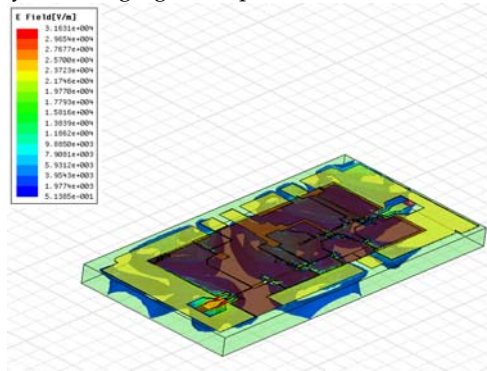


Fig. 13. E-field simulation of the feedback power at a frequency of 94 GHz

To isolate this feedback path, Tessmann et al. in 1997 reported the structure to stabilize it by thinning the MMIC’s substrate to 50  $\mu\text{m}$  and mounting them on an absorbing material. But with this method it is difficult to assemble the MMIC.

The authors proposed two structures. One is illustrated in Fig. 14 (b). An MMIC is flip-chipped on the interposer. In the MMIC, the authors employed an inverted microstrip line (IMSL). As the back side of the MMIC is exposed to the air, the parallel plate mode is hard to excite. The feedback power was decreased drastically as shown in Fig. 14 (d). In addition, the authors embedded a resistor layer in the areas except for the transistors and transmission line as shown in Fig. 14 (c). Using this resistor layer, an enhancement of about 5 dB is realized. Using this structure, it is possible to realize an amplifier with a gain of over 30 dB.

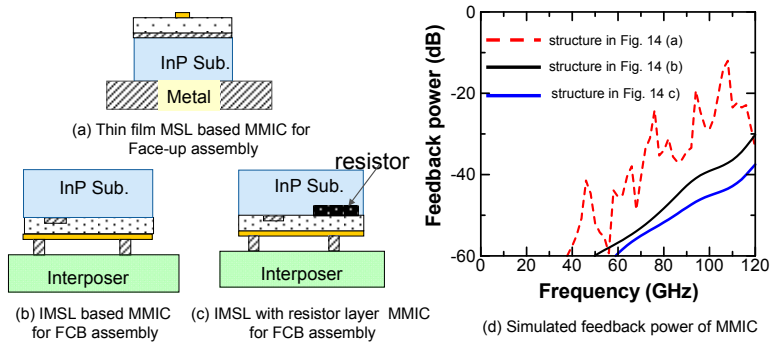


Fig. 14. Cross-sectional view of MMICs and simulated feedback power

Using these techniques, the authors designed and fabricated the LNA. The circuit consists of a 7-stage common-source amplifier. The gate widths of the transistors in each stage were  $2 \times 20 \mu\text{m}$ , the total power consumption was 60 mW, and the overall chip size was  $2.5 \times 1.2 \text{ mm}^2$ . Fig. 15(a) shows the measured S-parameters of the LNA. A linear gain of 35 dB was achieved between 90 and 110 GHz, and the measured input and output return loss in this frequency range was below 8 dB. In addition, the measured  $S_{12}$  was below  $-40 \text{ dB}$ . Thus, the MMIC structure using IMSL with a resistor layer can be used in high-gain amplifiers. The authors also measured the noise figure of the LNA as shown in Fig. 15 (b), which was about 4 dB. This high gain with low-noise performance achieved in the 130-nm InP HEMTs indicates the LNA can be used for a single-chip MMIC.

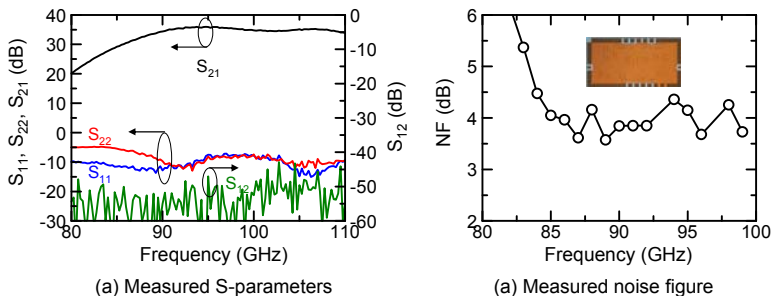


Fig. 15. Measured S-parameters and noise figure of the LNA



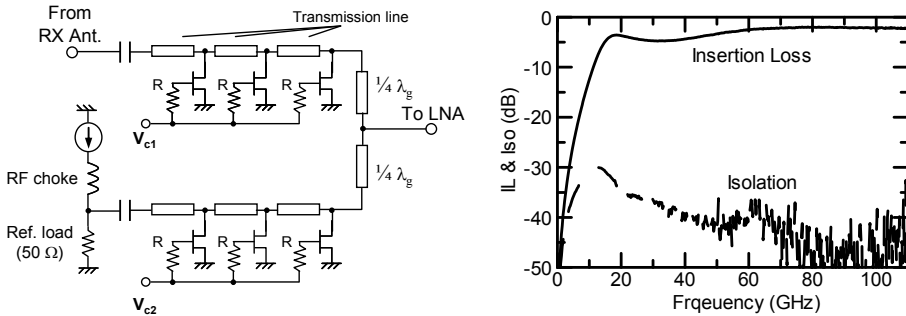
**-Detector**

A Schottky diode constructed on a HEMT device was employed for the detector. Although Schottky diodes are usually biased to increase the sensitivity, this causes an increase in noise. The authors chose a diode’s dimension of  $L_g=4 \mu\text{m}$  and  $W_g= 5 \mu\text{m}$  so that it could be used in a zero-bias condition. The sensitivity of the diode itself was  $150 \text{ V/W}$ . In order to increase the sensitivity, LNA was integrated with the detector, which will be discussed below.

**-SPDT switch**

An SPDT switch was used to control the direction between the antenna and reference noise. Fig. 16 (a) shows a schematic diagram of the distributed single-pole-double-throw (SPDT) switch, which is composed of two single-pole-single-throws (SPST) switches and two quarter-wavelength impedance transformers. The drain terminals of the transistors were connected to the transmission lines periodically. One port of the SPST switch was terminated in  $50 \Omega$  as a reference load. In addition, the authors added an RF choke and a current source to adjust the noise power from the reference load to be equal to the antenna noise.

The gates of the transistors in each SPST switch were biased below the pinch-off voltage; for example  $-1 \text{ V}$ , or alternately biased in the linear region such as at  $0.5 \text{ V}$ . When the bias applied is below the pinch-off voltage, the transistors act as capacitors. The authors chose the length and width of the transmission lines to give characteristic impedance  $Z_0$  for the artificial transmission line of  $50 \Omega$  (ON-state). On the other hand, when the bias applied is a positive voltage such as  $0.5 \text{ V}$ , the transistors act as small resistances. Since the transistors are shunted between the transmission lines, the SPST circuit works as a short circuit (OFF-state).



(a) Schematic diagram

(b) Measured insertion loss and isolation

Fig. 16. Schematic diagram and measured performance of SPDT switch

Using this technique, the authors fabricated an SPDT switch using InP HEMT technology. Fig. 16 (b) shows the insertion loss and isolation of the developed SPDT switch. The gate bias condition was  $-1 \text{ V}$  for the ON-branch, and  $0.5 \text{ V}$  for the OFF-branch. The measured insertion loss was within  $2 \text{ dB}$  between  $60$  and  $110 \text{ GHz}$  and the isolation was better than  $-40 \text{ dB}$ .

### -Single chip receiver MMIC

The authors integrated the switch, LNA, and detector onto a single MMIC. The die photo and measured performance of the receiver MMIC is shown in Fig. 17. The chip size is  $2.5 \times 1.2 \text{ mm}^2$ . The total power consumption was 64 mW.

Here are the measured results of the MMIC. The authors measured the sensitivity of the detector MMIC by calculating the ratio of the detected voltage,  $V_{\text{det}}$ , to the input millimeter-wave power,  $P_{\text{in}}$ . In this measurement, the authors used a 94-GHz CW source as the input. The bias voltages for the SPDT switch,  $V_{c1}$  and  $V_{c2}$  were  $-1$  and  $0.5 \text{ V}$ , respectively while the MMIC receiver was measuring the millimeter-wave signal (measuring mode). When the receiver was measuring the reference load (reference mode),  $V_{c1}$  and  $V_{c2}$  were set to  $0.5$  and  $-1 \text{ V}$ , respectively. As the isolation of the SPDT switch was better than  $-40 \text{ dB}$ , the difference in the detected voltage between the measuring and reference modes was detectable under  $-70 \text{ dBm}$ . Because the amplitude of the millimeter waves ( $kTB_{\text{HF}}$ ) was around  $-70 \text{ dBm}$  when the bandwidth was set to  $10 \text{ GHz}$ , it is possible to detect millimeter waves using the receiver MMIC.

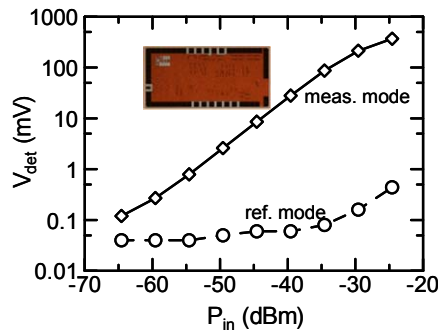


Fig. 17. Measured detected voltage as a function of input millimeter-wave power

### 3.2 Antipodal linearly tapered slot antenna

To collect 2D mapping of millimeter-wave energy, the authors placed receivers at the focus of the imager's lens and mechanically scanned the receivers on the focal plane. The resulting system can produce high-spatial-resolution images because the lens-coupled antenna has high directivity and a low sidelobe level. By using an array of receivers, the image collection time can be reduced by a factor equal to the number of receivers. To increase the number of receivers, the size of each receiver must be miniaturized. Although a waveguide horn antenna is usually used in front of the receivers, it is too large to be used in this case which makes it difficult to achieve a high-density receiver array.

The authors have developed a small tapered-slot antenna (Sato et al. 2008) called an antipodal linearly tapered-slot antenna (L TSA) with an aperture size as small as  $1.2 \lambda_0$  square, where  $\lambda_0$  is the wavelength in a vacuum at the centre frequency. The antenna has almost the same E-plane and H-plane patterns (circular radiation pattern), which make it well suited for use in a lens-coupled antenna. In addition, the antenna has a microstrip interface. Then the antenna and MMIC are connected by a low-cost flip-chip bonding assembly. The authors will discuss how to design this system to have an antenna that can obtain circular radiation patterns and have a low sidelobe level.

Fig. 18 shows the geometry of the antenna with a compact microstrip-slot transition. A metal pattern that forms the tapered-slot section is printed on the top and bottom sides of the dielectric layer. The slot profile is defined by the linear function

$$f(x) = \frac{W \cdot x}{2L} \tag{15}$$

where  $L$  and  $W$  are the antenna length and aperture width, respectively. Corrugated patterns are used on both sides of the metal edge. Corrugations work to suppress the surface-mode waves excited on the dielectric substrate and eventually widen the effective aperture size of the antenna. The dimensions of a corrugation with a width  $\omega_c$ , pitch  $p$  and length  $l_c$  were reported by Sato et al. in 2004 to be

$$\omega_c = 0.034\lambda_0, p = 0.069\lambda_0, l_c = 0.116\lambda_0. \tag{16}$$

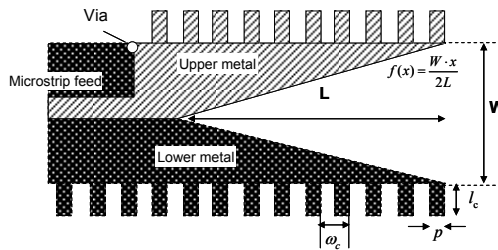


Fig. 18. Geometry of the linearly tapered slot antenna

The radiation pattern of the LTSA can be controlled by changing  $L$ ,  $W$ , the substrate thickness and the dielectric constant. To optimize these parameters in a shorter time, an antenna with fewer parameters must be developed.

The authors now turn to the design procedure to obtain a circular radiation pattern using 3D electromagnetic simulation (HFSS). In their simulation, the authors used a 125- $\mu\text{m}$  thick dielectric substrate ( $\epsilon_r = 2.9$ ). The antenna radiation patterns were controlled by two parameters: antenna length  $L$  and width of aperture. Fig. 19 (a) shows the simulated 10-dB-beam width of the radiation pattern as a function of  $L$ , when the width of the aperture,  $W$ , is  $0.78 \lambda_0$ . As the antenna length increased, the beam width in both the E- and H- planes decreased drastically. The authors chose an antenna length of  $4\lambda_0$  because it gives almost the same width in the E- and H-planes.

Fig. 19 (b) shows the simulated results for the 10-dB-beam width against the width of the aperture ( $0.3\text{--}1.3 \lambda_0$ ) when the antenna length,  $L$ , is  $4 \lambda_0$ . As the width of the aperture increased, the E-plane beam width decreased, but the H-plane beam width remained the same. Almost identical beam widths of 50.8 deg can be obtained by choosing a  $W / \lambda_0$  of 0.76. It can be seen in Figs. 19 (a) and (b) that the antenna length,  $L$ , rough-tunes the beam width, and the width of the aperture,  $W$ , fine-tunes it. Using this design procedure, the authors were able to design a circular radiation pattern that is well suited to their lens-coupled PMMW imaging system.

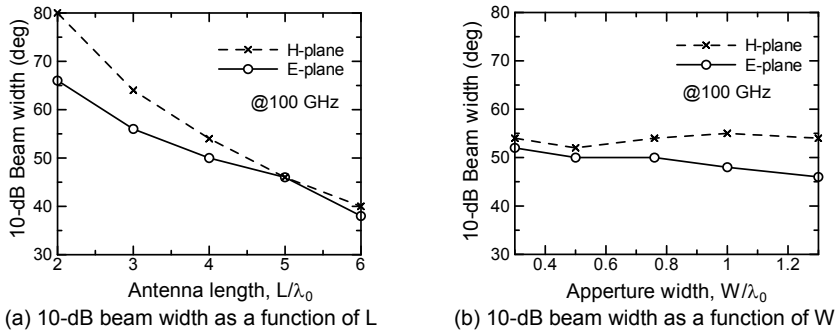


Fig. 19. Simulated 10-dB beam width of radiation patterns as a function of antenna length (a) and aperture width (b)

The authors fabricated an antipodal LTSA with a compact microstrip-slot transition using a PTFE substrate (Duroid 6002) with a thickness of 125  $\mu\text{m}$ . The authors chose  $L$  and  $W$  of  $4\lambda_0$  and  $0.78 \lambda_0$ , respectively, to obtain the circular radiation pattern. The size of the antenna was  $16 \times 3.7 \text{ mm}$ . Fig. 20 (a) shows a photograph of the antipodal LTSA. The authors mounted the antenna on a module with a W-1 connector. The measured and simulated radiation patterns are shown in Fig. 20 (b). The operating frequency was 94 GHz for both. The authors were able to obtain circular radiation patterns using the proposed design procedure. The measured 10-dB-beam widths of the E- and H-plane patterns were 50 and 54 deg respectively. In addition, the sidelobe level of the E-plane radiation pattern was less than  $-17 \text{ dB}$ , and the sidelobe level of the H-plane was less than  $-12 \text{ dB}$ .

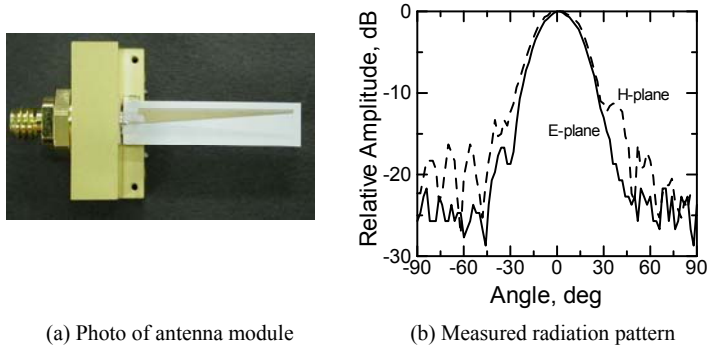


Fig. 20. Antipodal LTSA

### 3.3 Lens

When designing a lens, designers have to consider spatial resolution, aberration, viewing field, and matching between the lens and the antenna.

The authors chose polyethylene as the lens material because it has high permeability for millimeter waves and is very workable. As the imager will be used in a short range between 1 and 20 m, a lens with a diameter of 20 cm is sufficient for obtaining high spatial resolution. The authors used an even asphere function for the surface of the lens, and optimized

parameters in that function to realize a small aberration on the focal plane. This optimization was done using ZEMAX.

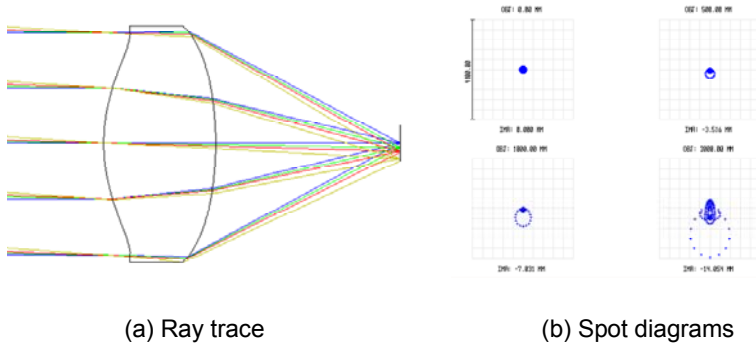


Fig. 21. Ray trace and spot diagram of lens

**3.4 94-GHz-band millimeter-wave image**

Using the components described above, the authors developed a PMMW imaging test system. The metal pattern of the antipodal LTSA was printed on polyamide. And the receiver MMIC was mounted on an antenna substrate by a flip-chip bonding assembly. A DC amplifier and bias circuits are also mounted on the antenna substrate. A photo of the receiver module is shown in Fig. 22. The size was as small as  $48 \times 12 \text{ mm}^2$ . The temperature resolution and integration time of the receiver module is about 1 K and 10 msec. Moreover, the authors arrayed the receiver module by  $10 \times 4$  to reduce the image collection time. The receiver array was set on the focal plane and scanned by a mechanical scanning system. The image acquisition time was 10 sec for  $40 \times 40$  pixels.

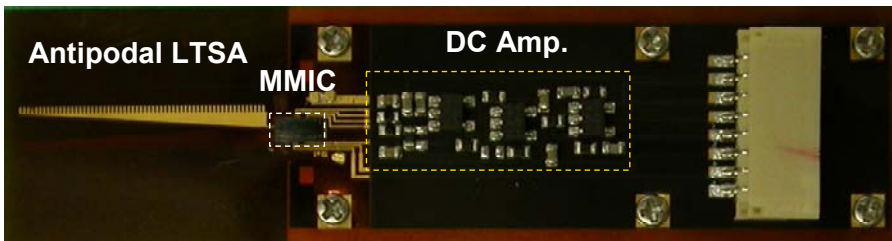


Fig. 22. Photo of the receiver module

The authors took images of a human indoors. The human was concealing a metallic object (simulating a gun). The distance between the human and the receiver was almost 2.5 meters. Fig. 23 shows the passive millimeter-wave image and corresponding photo and infrared image. The image size was  $40 \times 40$  pixels, and the spot size on the target was 2 cm. The blue area represents colder radiometric temperatures for the sample metal object and the ambient temperature, and the red areas represent warmer temperatures. As you can see, the

millimeter-wave image is able to distinguish between the human and the concealed metal object.

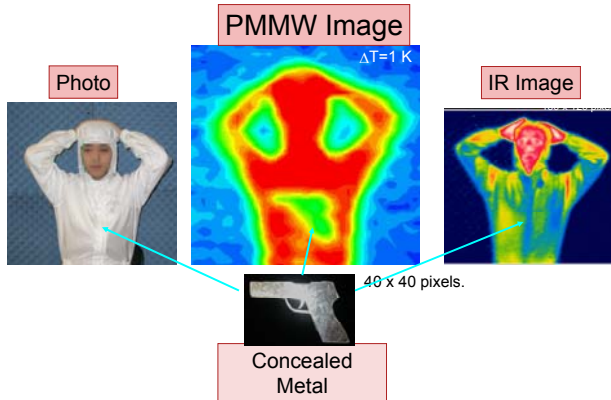


Fig. 23. Passive millimeter-wave image of a concealed metal object shown next to a photo and IR image

Part of this work was supported by the Ministry of Internal Affairs and Communications under the Strategic Information and Communications R&D Promotion Programme (SCOPE).

#### 4. Conclusion

In this chapter, the general principle and several systems for millimeter-wave sensors were discussed, and the state of development was also described. Furthermore, a 94-GHz-band passive millimeter-wave imaging sensor developed by Fujitsu Laboratories was shown in detail. The authors developed an ultra low-noise-receiver MMIC, and integrated it with a compact receiver module. The authors also realized a high-density imaging array to obtain millimeter-wave images in a short time. The considerations and the design method can also be used for other applications such as a broadband radio communication systems and radar.

#### 5. References

- Bhartia, P. & Bahl, I. J. (1984). *Millimeter Wave Engineering and Applications*, John Wiley & Sons, Ltd., pp. 660-671
- Kolinko, V. G.; Lin, S. H.; Shek, A.; Manning, W.; Martin, C.; Hall, M.; Kirsten, O.; Moore, J. & Wikner, D. A. (2005). A passive millimeter-wave imaging system for concealed weapons and explosives detection, *Proc. SPIE*, Vol. 5781, pp.85-92, USA
- Kuki, T. (2008). *RF world*, No. 4 pp. 88-92, ASIN:B001GWJWN2, 2008
- Millivision, (2009). <http://www.millivision.com/portal-350.html>
- Mizuno, K.; Matano, H.; Wagatsuma, Y.; Warashina, H.; Sato, H.; Miyanaga, S. & Yamanaka, Y. (2005). New applications of millimeter-wave incoherent imaging, *Proc. IEEE MTT-S Int. Microwave Symp.*, pp. 629-632, June 2007, USA
- Mizuno, K; Sato, H.; Hirose, T.; Sato, M.; Ohki, T. (2009). Development of Passive Millimeter-wave Imaging Sensors, 5<sup>th</sup> SCOPE meeting, pp. 50-51, June 9, Tokyo

- Nakasha, Y.; Kawano, Y.; Suzuki, T.; Ohki, T.; Takahashi, T. Makiyama, K; Hirose, T. & Hara, N. (2008). A W-band Wavelet Generator Using 0.13- $\mu\text{m}$  InP HEMTs for Multi-gigabit Communications Based on Ultra-Wideband Impulse Radio, *Proc. IEEE MTT-S Int. Microwave Symp. Digest*, pp. 109-112, June 15-20, Atlanta, USA
- Sato, H.; Sawaya, K.; Wagatsuma, Y.; & Mizuno, K., (2004). Design of narrow width Fermi antenna with circular radiation pattern, *Proc. IEEE Antennas and Propagation Society Symp.*, pp. 4312-4315, June 2004, USA
- Sato, M.; Hirose, T.; Ohki, T.; Sato H.; Sawaya K. & Mizuno K. (2007). 94 GHz band high-gain and low-noise amplifier using InP-HEMTs for passive millimeter wave imager, *Proc. IEEE MTT-S Int. Microwave Symp.*, pp. 1775-1778, June 2007, USA
- Sato, M.; Sato, H.; Hirose, T.; Ohki, T.; Takahashi, T.; Makiyama, K.; Kobayashi, H.; Sawaya, K. & Mizuno, K., (2009). Compact receiver module for a 94 GHz band passive millimetre-wave imager, *IET Microw. Antennas Propag.*, Vol. 2, No. 9, pp. 848-853
- Sato, M.; Hirose, T. & Mizuno, K. (2009). Advanced MMIC Receiver for 94-GHz Band Passive Millimeter-wave Imager, *IEICE TRANS. ELECTRON*, Vol. E92-C, No. 9, pp. 1124-1129
- Sinclair, G. N.; Anderton, R. N. & Appleby, (2001). Outdoor passive millimetre wave security screening, *2001 IEEE 35<sup>th</sup> International Carnahan Conference on Security Technology*, pp. 172-179, Oct 16-19, London, UK
- Tessmann, A.; Haydl, W. H.; Hulsmann, A. & Schlechtweg, M. (1998). High-Gain Cascode MMIC's in Coplanar Technology at W-band Frequencies, *IEEE Microwave and Guided wave Letters*, Vol. 8, No. 12, Dec 1998, pp. 430-431
- Tiuri, M. E. (1964). Radio astronomy receivers. *IEEE Transactions on Antenna and propagation*, Vol. 12, Issue 7, pp. 930-938
- TSA. (2009). TSA Continues Millimeter Wave Passenger Imaging Technology Pilot, [http://www.tsa.gov/press/happenings/mwave\\_continues.shtm](http://www.tsa.gov/press/happenings/mwave_continues.shtm)
- Yujiri, L. (2006). Passive Millimeter Wave Imaging, *2006 IEEE MTT-S Int. Microwave Symp. Digest*, pp. 98-101, June 13-16, USA
- Vizard, D. R.; Doyle, R. (2006). Advances in Millimeter Wave Imaging and Radar Systems for Civil Applications, *2006 IEEE MTT-S Int. Microwave Symp. Digest*, pp. 94-97, June 13-16, USA
- Wills, M. (2009). Gaseous attenuation, <http://www.mike-willis.com/Tutorial/gases.htm>





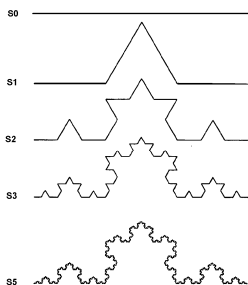
# Fractal Antenna Applications

Mircea V. Rusu and Roman Baican  
*University of, Bucharest, Physics Faculty, Bucharest*  
*„Transilvania” University, Brasov*  
*Romania*

## 1. Introduction

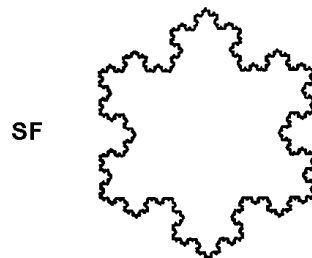
Fractals are geometric shapes that repeat itself over a variety of scale sizes so the shape looks the same viewed at different scales. For such mathematical shapes B.Mandelbrot [1] introduced the term of “fractal curve”. Such a name is used to describe a family of geometrical objects that are not defined in standard Euclidean geometry. One of the key properties of a fractal curve is his self-similarity. A self-similar object appears unchanged after increasing or shrinking its size. Similarity and scaling can be obtained using an algorithm. Repeating a given operation over and over again, on ever smaller or larger scales, culminates in a self-similar structure. Here the repetitive operation can be algebraic, symbolic, or geometric, proceeding on the path to perfect self-similarity.

The classical example of such repetitive construction is the Koch curve, proposed in 1904 by the Swedish mathematician Helge von Koch. Taking a segment of straight line (as *initiator*) and rise an equilateral triangle over its middle third, it results a so called *generator*. Note that the length of the generator is four-thirds the length of the initiator. Repeating once more the process of erecting equilateral triangles over the middle thirds of strait line results what is presented in figure (Figure 1). The length of the fractured line is now  $(4/3)^2$ . Iterating the process infinitely many times results in a "curve" of infinite length, which - although everywhere continuous - is *nowhere differentiable*. Following Mandelbrot, such nondifferentiable curves is a *fractal*.



Koch fractal

Fig. 1.



Koch snowflake

Fig. 2.

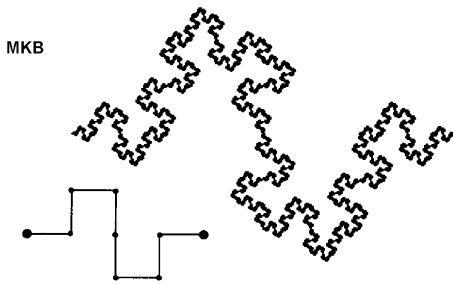


Fig. 3.

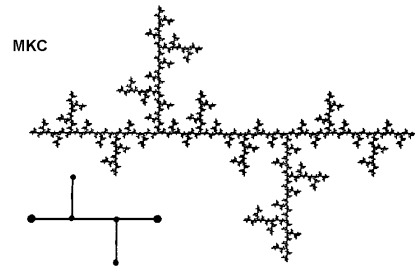


Fig. 4.

Applying the Koch generator to an equilateral triangle, after infinite iteration, converge to the Koch snowflake (Figure 2). The perimeter of the snowflake curve increase after  $n$  iteration  $(4/3)^n$ -fold over the perimeter of the initial triangle. Thus, as  $n$  approaches infinity, the perimeter becomes infinite long! In the next two images there are some variations on the same theme (Figure 3 and figure 4).

For a smooth curve, an approximate length  $L(r)$  is given by a product of the number  $N$  of straight-line segments of length  $r$  need to step along the curve from one end to the other end. The length will be:  $L(r) = N.r$ . As the step size  $r$  goes to zero,  $L(r)$  approaches a finite limit, the length of the curves. But for fractals the product  $N.r$  diverges to infinity because, as  $r$  goes to zero, the curve becomes more and more tortuous. Asymptotically this divergence behaves according to a well-define homogenous power law of  $r$ . There is some *critical exponent*  $D_H$ ,  $>1$  such that the product  $N.r^{D_H}$  stays finite. This critical exponent,  $D_H$ , is called *Hausdorff dimension*. Equivalently, we have

$$D_H = \lim_{r \rightarrow 0} \frac{\log N}{\log(1/r)}$$

For  $n$ th generation in the construction of the Koch curve or snowflake, choosing  $r = r_0/3^n$ , the number of pieces  $N$  is proportional to  $4^n$ . Thus,

$$D_H = (\log 4)/(\log 3) = 1.26\dots$$

For a smooth curve  $D_H = 1$ , for a smooth surface  $D_H = 2$ , and Koch or other fractals on the surface will have  $D_H$  between 1 and 2. Fractals are characterized by their dimension. It is the key structural parameter describing the fractal and is defined by partitioning the volume where the fractal lies into boxes of side  $\epsilon$ . For a real curve that mimic a fractal there is only a finite range over which the above scaling law will apply [2]. So, correct speaking, real curve are not true mathematical fractals, but intermediate stages obtained by iteration that could be called "fractal-like curves". The fractal dimension will be an important parametrization for the fractal antennas that could be explore, and will impact significantly the intensity and spatial structure of the radiated pattern.

The fractal design of antennas and arrays results from applying the new fractal geometry in the context of electromagnetic theory. Fractals help in two ways. First, they can improve the performance of antenna or antenna arrays. Traditionally, in an array, the individual antennas are either randomly scattered or regularly spaced. But fractal arrangement can combine the robustness of a random array and the efficiency of a regular array, with a quarter of the number of elements. "Fractals bridge the gap because they have short-range disorder and long-range order" [3].

A fractal antenna could be considered as a non uniform distribution of radiating elements. Each of the elements contributes to the total radiated power density at a given point with a vectorial amplitude and phase. By spatially superposing these line radiators we can study the properties of simple fractal antennae.

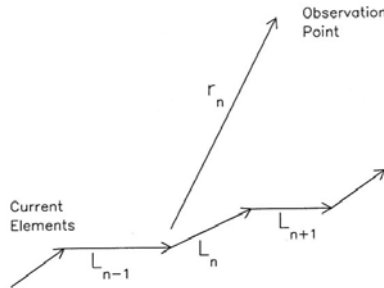


Fig. 5.

The energy radiated in the far field:

$$R(x, y, z, ) \propto \int E^2 dt .$$

The array factor can be normalized by maximum in the array factor corresponding to the single dipole, i.e.

$$R_0 \approx \frac{\beta^2 I_0^2 A}{4(1 - \beta a)^2 h^2} \text{ where } A = \frac{3\zeta^4 - \zeta^2 f[\eta, \zeta]}{2(4 + 5\zeta^2 + \zeta^4)} \approx 1$$

$$\text{and } f[\eta, \zeta] = \frac{\beta \Delta r - L}{\alpha v}, \quad \beta = v / c,$$

Where \$h\$ is the height of the detector \$\Delta r\$ is the difference in distance between the beginning and the end points of the dipole to the detector position, \$v\$ is the speed of the current thought the wire.

In the following parts we will exemplify from many fractals applications one possible use, fractal antenna for terrestrial vehicles.

## 2. Integrated Multi-Service Car Antenna

The system relates a multi-service antenna integrated in a plastic cover fixed in the inner surface of the transparent windshield of a motor car [4].

The miniaturized antennas are for the basic services currently required in a car, namely, the radio reception, preferably within the AM and FM or DAB bands, the cellular telephony for transmitting and receiving in the GSM 900, GSM 1800 and UMTS bands and for instance the GPS navigation system.

The antenna shape and design are based on combined miniaturization techniques which permit a substantial size reduction of the antenna making possible its integration into a vehicle component such as, for instance, a rear-view mirror (Figure 6 - the components are numbered).

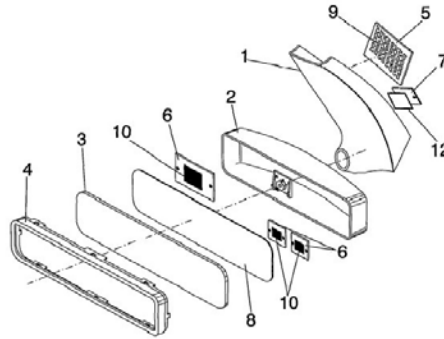


Fig. 6.

Until recently, the telecommunication services included in a automobile were limited to a few systems, mainly the analogical radio reception (AM/FM) bands). The most common solution for these systems is the typical whip antenna mounted on the car roof. The current tendency in the automotive sector is to reduce the aesthetic and aerodynamic impact of such whip antennas by embedding the antenna system in the vehicle structure. Also, a major integration of the several telecommunication services into a single antenna is especially attractive to reduce the manufacturing costs or the damages due to vandalism and car wash systems.

The antenna integration is becoming more and more necessary as we are assisting to a deep cultural change towards the information society. The internet has evoked an information age in which people around the globe expect, demand, and receive information. Car drivers expect to be able to drive safely while handling e-mails, telephone calls and obtaining directions, schedules, and other information accessible on the World Wide Web (www).

Telematic devices can be used to automatically notify authorities of an accident and guide rescuers to the car, track stolen vehicles, provide navigation assistance to drivers, call emergency roadside assistance and remote diagnostics of engine functions.

The inclusion of advanced telecom equipments and services in cars and other vehicles is very recent, and it was first thought for top-level, luxury cars. However, the fast reduction in both equipment and service costs are bringing telematic products into mid-priced automobiles. The massive introduction of a wide range of such new systems would generate a proliferation of antennas upon the bodywork of the car, in contradiction, unless an integrated solution for the antennas is used.

The patent PCT/EP00/00411 proposed a new family of small antennas based on the curves named as space-filling curves. An antenna is said to be a small antenna (a miniature antenna) when it can be fitted into a small space compared to the operating wavelength. It is known that a small antenna features are:

- A large input reactance (either capacitive or inductive) that usually has to be compensated with an external matching / loading circuit or structure.
- A small radiating resistance
- Small bandwidth
- Low efficiency

This is mean that is highly challenging to pack a resonant antenna onto a space which is small in terms of the wavelength at resonance. The space-filling curves introduces for the design and construction of small antennas improve the performance of other classical antennas described in the prior art (such as linear monopoles, dipoles and circular or rectangular loop)

The integration of antennas inside mirrors have been already proposed [5].

Patent US4123756 is one of the first to propose the utilisation of conducting sheets as antennas inside mirrors. Patent US5504478 proposed to use the metallic sides of a mirror as antenna for wireless car aperture [6]. Others configurations have been proposed to enclose wireless car aperture, garage opening or car alarm [7]. Obviously, these solutions proposed a specific solution for determinate systems, which generally require a very narrow bandwidth antenna, and did not offer a full integration of basic services antenna. Other solutions were proposed to integrate the AM/FM antenna in the thermal grid of the rear windshield [8].

However, this configuration requires an expensive electronic adaptation network, including RF amplifiers and filters to discriminate the radio signals from the DC source and is not adequate to the low antenna efficiency.

A main substantial innovation of the presented system consists in using a rear-view mirror to integrate all basic services required in a car: radio-broadcast, GPS and wireless access to cellular networks. The main advantages with respect to prior art are:

- Full antenna integration with no aesthetic or aerodynamic impact
- A full protection from accidental damage or vandalism
- Significant cost reduction.

The utilization of micro-strip antennas is already known in mobile telephony handsets [9], especially in the configuration denoted as PIFA (Planar Inverted F Antennas).

The reason of the utilization of micro-strip PIFA antennas reside in their low profile, their low fabrication costs and an easy integration within the hand-set structure.

One of the miniaturization techniques used in this antenna system are based on spacefilling curves. In some particular case of antenna configuration system, the antenna shape could be also described as a multi-level structure.

Multi-level technique has been already proposed to reduce the physical dimensions of micro-strip antennas.

The present integrated multi-service antenna system for vehicle comprising the following parts and features:

- The antenna includes a conducting strip or wire shaped by a space-filling curve, composed by at least two-hundred connected segments forming a substantially right angle with each

adjacent segment smaller than a hundredth of the free-space operating wavelength. This antenna is used for AM or DAB radio broadcast signal reception.

- The antenna system can optionally include miniaturized antenna, for wireless cellular services such as GSM900 (870-860 MHz), GSM1800 (1710-1880 MHz) and UMTS (1900-2170 MHz).

- The antenna system can include a miniaturized antenna for GPS reception (1575 MHz).

- The Antenna set is integrated within a plastic or dielectric cover fixed on the inner surface of the transparent windshield of a motor vehicle.

One of the preferred embodiments for the plastic cover enclosing the multi-service antenna system is the housing of the inside rear view mirror. This position ensures an optimised antenna behaviour, a good impedance matching, a substantially omnidirectional radiation pattern in the horizontal plane for covering terrestrial communication systems (like radio or cellular telephony), and a wide coverage in elevation for the case of satellite communication system (GPS).

The important reduction size of such antennas system is obtained by using space-filling geometries.

A space-filling curve can be described as a curve that is large in terms of physical length but small in terms of the area in which the curve can be included. More precisely, the following definition is taken for a general space-filling curve: a curve composed by at least ten segments forming an angle with each adjacent segment.

Whatever, the design of such space-filling curve is, it can never intersect with itself at any point except the initial and final point (that is, the whole curve can be arranged as a closed curve or loop, but none of the parts of the curve can become a closed loop).

A space-filling curve can be fitted over a flat or curved surface, and due to the angles between segments, the physical length of the curve is always larger than that of any straight line that can be fitted in the same area (surface).

Additionally, to properly shape the structure of a miniature antenna, the segments of the space-filling curves must be shorter than a tenth of the free-space operating wavelength.

The antenna is fed with a two conductor structure such as a coaxial cable, with one of the conductors connected to the lower tip of the multilevel structure and the other conductor connected to the metallic structure of the car which acts as a ground counterpoise.

This antenna type features a significant size reduction below a 20% than the typical size of a conventional external quarter-wave whip antenna; this feature together with the small profile of the antenna which can be printed in a low cost dielectric substrate, allows a simple and compact integration of the antenna structure.

Besides the key reduction of the antenna element covering the radio broadcast services, another important aspect for the integration of the antenna system into a small package or car component is reducing the size of the radiating elements covering the wireless cellular services. This can be achieved by using a Planar Inverted F Antenna (PIFA) configuration, consisting on connecting two parallel conducting sheets, separated either by air or a dielectric, magnetic or magnetodielectric material.

The sheets are connected through a conducting strip near a one of the sheets corners and orthogonally mounted to both sheets.

The antenna is fed through a coaxial cable, having its outer conductor connected to first sheet, being the second sheet coupled either by direct contact or capacitive to inner conductor of the coaxial cable.

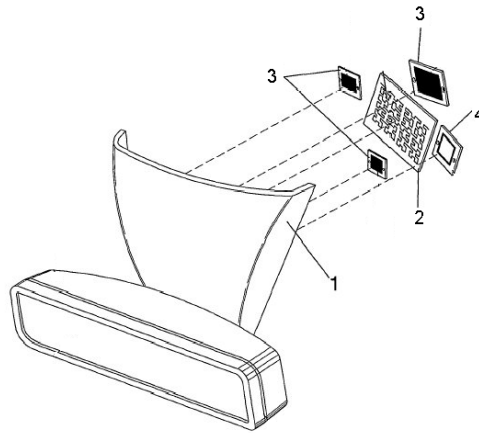


Fig. 7.

In the Figure 7 is shown another preferred embodiment of the present antenna system. The rear view mirror base support (1) to be fixed on the front windshield includes, a space-filling antenna for AM/FM reception (2), a set of miniature antennas (3) for wireless cellular system telephony transmitting or receiving GSM900 (870-960 MHz), GSM1800 (1710-1880 MHz) and UMTS (1900-2170 MHz) signals, and a GPS antenna (4).

In the Figure 8 is shown a detail of the space-filling structure antenna for reception of AM/FM bands. The antenna (1) is fed (2) as a monopole and is placed inside a rear view mirror support. The antenna can be easily adapted for DAB system by scaling it proportionally to the wavelength reduction.

In Figure 9 is presented a set of miniature antennas for cellular telephony system for transmitting GSM900, GSM1800 and UMTS. In this configuration, the antennas are composed by two planar conducting sheets, the first one being shorter than a quarter of the operation wavelength (1), and the second one being the ground counterpoise (2).

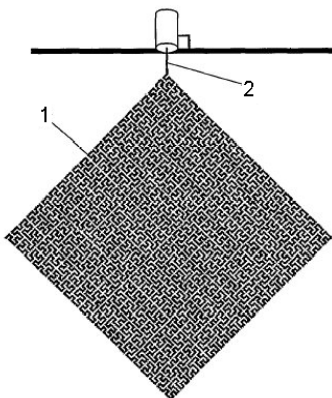


Fig. 8.

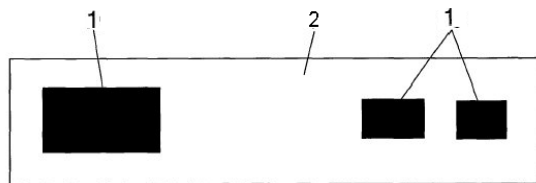


Fig. 9.

Both conducting sheet (1) and counterpoise are connected through a conducting strip. Each conducting sheet is fed by a separate pin.

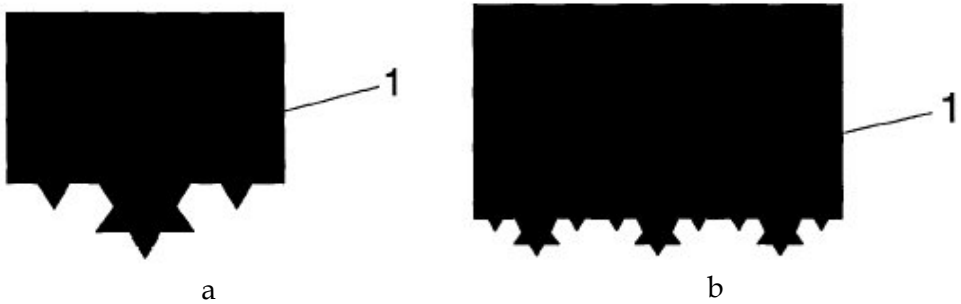


Fig. 10.a, b

In the Figures 10a,b is presented two examples of space-filling perimeter of the conducting sheet (1) to achieve an optimised miniaturization of the mobile telephony antenna. In the Figure 11 are presented four examples of miniaturization of the satellite GPS patch antenna using a space-filling or multilevel antenna technique.

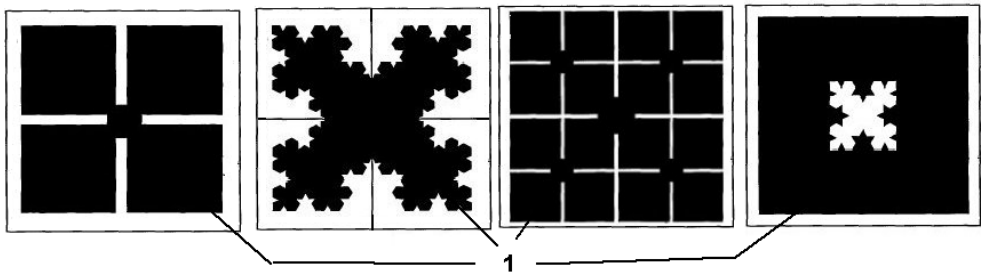


Fig. 11.

The GPS antenna is formed by two parallel conducting sheets spaced by a high permittivity dielectric material, forming a micro-strip antenna with circular polarisation. The circular polarization is obtained either by means of a two feeder schema or by perturbing the perimeter of the patch. The superior conducting sheet (1) perimeter is increased by confining it in space filling curve.

In the Figure 12 is presented another preferred embodiment wherein at least two space-filling antennas are supported by the same surface, one space-filling antenna for receiving radio broadcasted signals, preferably within the AM and FM or DAB bands, and the other second space-filling antennas for transmitting and receiving in the cellular telephony bands such as for GSM.

All the space-filling antennas (3) are connected at one end to one of the wires of a two conductor transmission line such as a coaxial cable (1, 2), being the other conductor of transmission line connected to the metallic car structure (1).



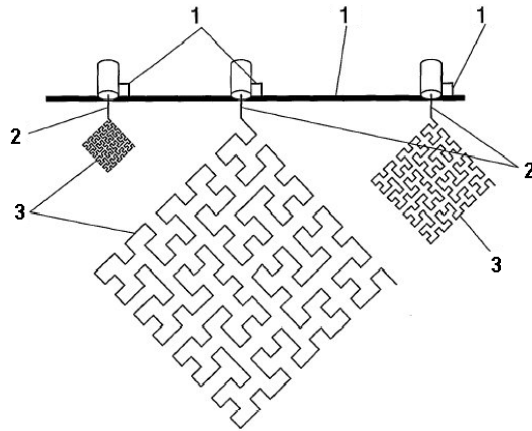


Fig. 12.

In the Figure 13 is presented an alternative position of GPS antenna (1). The antenna is placed in a horizontal position, inside the external housing (2) of an external rear view mirror.

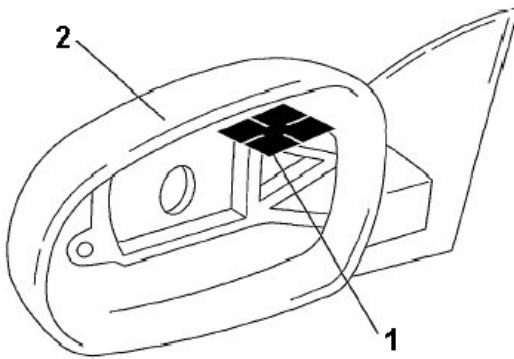


Fig. 13.

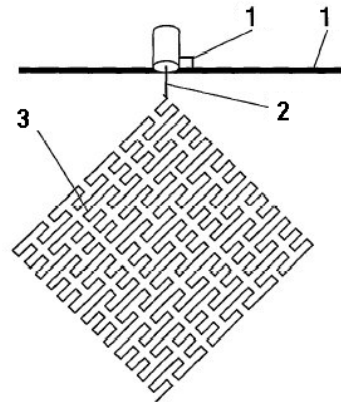


Fig. 14.

In the Figure 14 is shown another example of space-filling antenna, based of a fractal curve, for AM/FM reception. The antenna is fed as a monopole and is placed inside a rear view mirror support.

### 3. Anti-radar fractals and/or multilevel chaff dispersers

Chaff was one in the forms of countermeasure employed against radar. It usually consists of a large number of electromagnetic dispersers and reflectors, normally arranged in form of

strips of metal foil packed in a bundle. When they are released by an aircraft or distributed by rockets launched by a ship, most of the strips of foil which constitute the chaff bale are dispersed by the effect of the wind and become highly reflective clouds. Its vertical descent is determined by the force of gravity and for the properties to resist advance presented by the strips of individual leaves.

Chaff is usually employed to foil or to confuse surveillance and tracking radar.

Miscellaneous reference information on radar chaff can be found in [10], or in other patented publications [11].

Nevertheless, little attention has been paid to the design of the shape of the dispersers which form the cloud. Here are presented new geometry of the dispersers or reflectors which improve the properties of radar chaff [12]. Some of the geometries presented here of the dispersers or reflectors are related with some forms expounded for antennas. Multilevel and fractal structures antennas are distinguished in being of reduced size and having a multi-band behaviour, as has been expounded already in patent publications [13].

The main electrical characteristic of a radar chaff disperser is its radar cross-section (RCS) which is related with the reflective capability of the disperser. The new geometries facilitates a large RCS compared with dispersers presented in previous patents having the same size, surprisingly the RCS is equivalent to that of conventional dispersers of greater size.

Instead of using conventional rectilinear forms, multilevel and fractal geometries are introduced. Due to this geometric design, the properties of the clouds of radar chaff are improved mainly in two aspects: radar cross-section (RCD) and mean time of suspension.

A fractal curve for a chaff disperser is defined as a curve comprising at least ten segments which are connected so that each element forms an angle with its neighbours, no pair of these segments defines a longer straight segment, these segments being smaller than a tenth part of the resonant wavelength in free space of the entire structure of the disperser. In many of the configuration presented, the size of the entire disperser is smaller than a quarter of the lowest operating wavelength.

The space-filling curves (or fractal curves) can be characterized by:

1. They are long in terms of physical length but small in terms of area in which the curve can be included. The disperser with a fractal form are long electrically but can be included in a very small surface area. This means it is possible to obtain a smaller packaging and a denser chaff cloud using this technique.
2. Frequency response: Their complex geometry provides a spectrally richer signature when compared with rectilinear dispersers known in the state of the art.

Depending on the process of the form and of the geometry of the curve, some spacefilling curves (SFC) can be designed theoretically to characterise a larger Hausdorff dimension than their topological dimensions. These infinite theoretical curves cannot be constructed physically, but they can be approximated with SFC design.

The fractal structure properties of disperser not only introduce an advantage in terms of reflected radar signal response, but also in terms of aerodynamic profile of dispersers. It is known that a surface offers greater resistance to air than a line or a one-dimensional form. Therefore, giving a fractal form to the dispersers with a dimension greater than unity ( $D > 1$ ), increase resistance to the air and improve the time of suspension.

Multi-level structures are a geometry related with fractal structures. In that case of radar chaff a multi-level structure is defined as structure which includes a set of polygons, which are characterized in having the same number of sides, wherein these polygons are electro-

magnetically coupled either by means of capacitive coupling, or by means of an ohmic contact. The region of contact between the directly connected polygons is smaller than 50% of the perimeter of the polygons mentioned in at least 75% of the polygons that constitute the defined multilevel structure.

A multilevel structure provides both:

- A reduction in the size of dispensers and an enhancement of their frequency response, and
- Can resonate in a non-harmonic way, and can even cover simultaneously and with the same relative bandwidth at least a portion of numerous bands.

The fractal structure (SFC) are preferred when a reduction in size is required, while multilevel structures are preferred when it is required that the most important considerations be given to the spectral response of radar chaff.

The main advantages for configuring the form of the chaff dispensers are:

1. The dispensers are small; consequently more dispenser can be encapsulated in a same cartridge, rocket or launch vehicle.
2. The dispenser are also lighter, therefore they can remain more time floating in the air than the conventional chaff.
3. Due to the smaller size of the chaff dispensers, the launching devices (cartridges, rockets, etc.) can be smaller with regard to chaff systems in the state of the art providing the same RCS.
4. Due to lighter weight of the chaff dispensers, the launching devices can shot the packages of chaff father from the launching devices and locations.
5. Chaff constituted by multilevel and fractal structures provide larger RCS at longer wavelengths than conventional chaff dispensers of the same size.
6. The dispensers with long wavelengths can be configured and printed on light dielectric supports having a non-aerodynamic form and opposing a greater resistance to the air and thereby having a longer time of suspension.
7. The dispensers provide a better frequency response with regard to dispensers of the state of the art.

To complete the description being made and with the object of assisting in a better understanding of the characteristics of fractals and multilevel structures, a set of drawings are represented.

In the following images such size compression structures based on fractal curves are presented.

Figure 15 show examples of SZ fractal curves which can be used to configure a chaff dispenser.

Figure 17 shows several examples oh Hilbert fractal curves (with increasing iteration order) which can be used to configure the chaff dispenser. Figure 18 shows various examples of ZZ fractal curves (with increasing iteration order) which provide a size compression ratio. Figure 19 shows several examples of Peano fractal curves (with increasing iteration order) which can be used to configure chaff dispenser. These provide a size compression ratio. Figure 19 show two examples of fractal curves which define a loop which can be used to configure chaff dispensers.

Figure 21 shows several examples of multilevel structures built by joining various types of triangle.

Figure 22 shows several examples of multilevel structures built by joining various types of square.

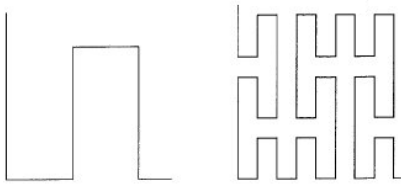


Fig. 15.

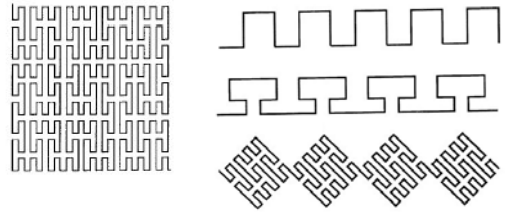


Fig. 16.

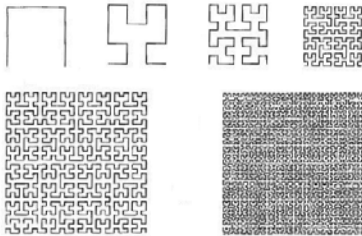


Fig. 17.

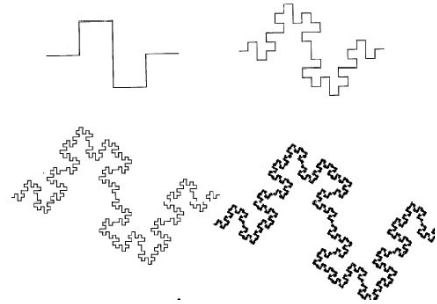


Fig. 18.

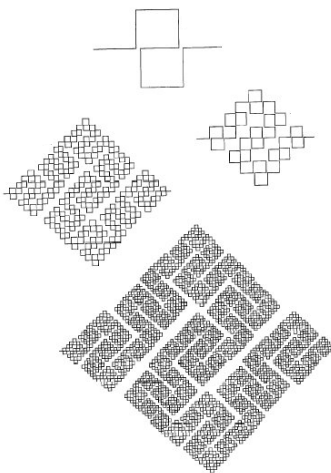


Fig. 19.

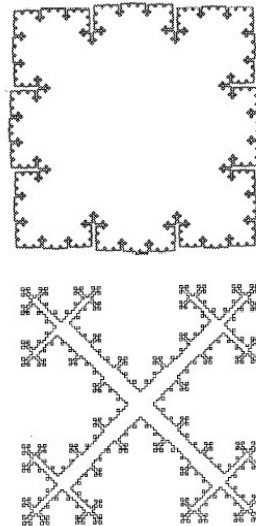


Fig. 20.

Figure 23 show some fractal dispersers forming a cloud of radar chaff. The disperser is formed by conducting, super-conducting or semi-conducting material configuring a fractal structure which is supported by a leaf of dielectric material.

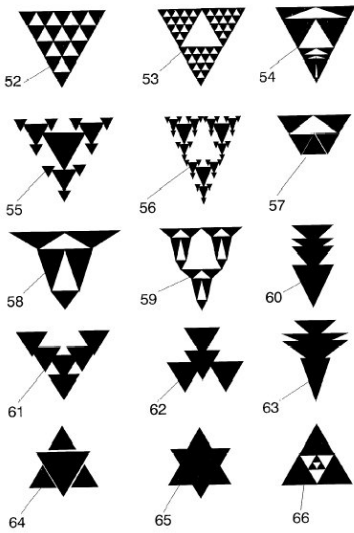


Fig. 21.

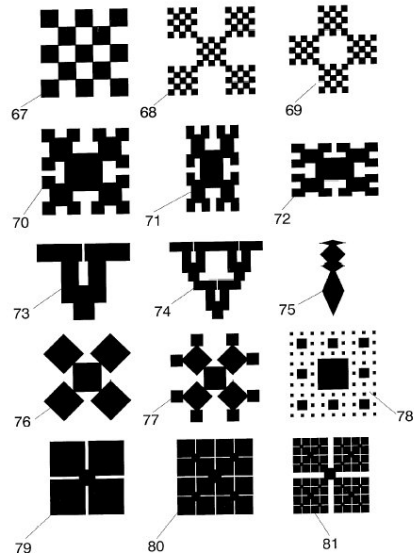


Fig. 22.

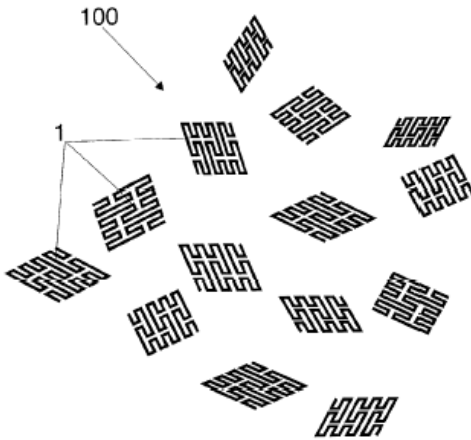


Fig. 23.

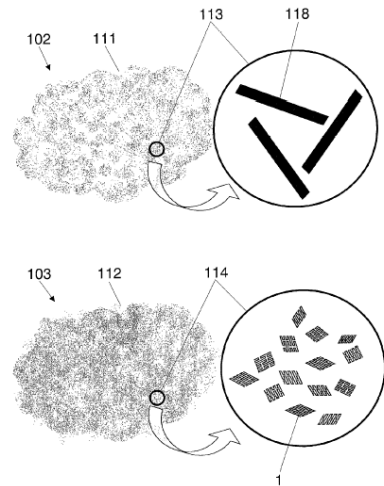


Fig. 24.

Figure 24 shows a comparison between a conventional chaff cloud with regard to a fractal or multilevel structure chaff cloud. Conventional chaff is formed substantially by linear or straight strip dispersers of a length determined by the wavelength of the radar. The fractal chaff are smaller for the same operating frequency, therefore a fractal chaff cloud can be made denser than a conventional one, providing a larger radar cross-section (RCS) and remaining floating in the air for a long time.

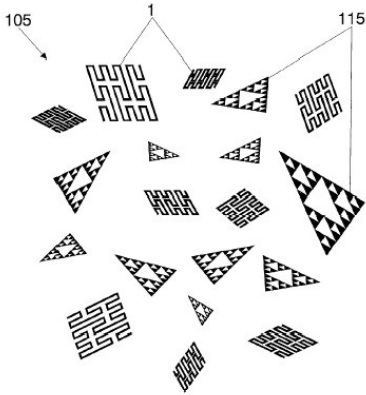


Fig. 25.

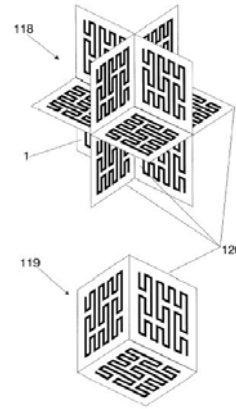


Fig. 26.

Figure 25 shows a mix of multilevel and fractal structures with diverse sizes forming a radar cloud. The sizes and geometries of the structures can be made to design the frequency signature for the whole chaff cloud.

Figure 26 shows a trihedron reflector with a fractal disperser on each side of the trihedron. The 3D disperser is constituted by up to 8 trihedrons. This type of reflector improves the backward dispersion in mono-static radar.

#### 4. Multilevel Advanced Antennas for Motor Vehicles

This application relates to an antenna for a motor vehicle, having the following parts and characteristics [14], Figure 27:

- A transparent windshield covered with a transparent, optically conductive plate on at least one side of any of the window material plates,
- A multilevel structure printed on the conductive plate. The multilevel structure consists of a set of polygonal elements pertaining to one same class, preferably triangles or squares.
- A transmission line powering two conductors
- A similar impedance in the power supply point and a horizontal radiation diagram in at least three frequencies within three bands.

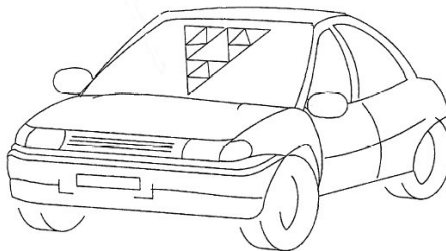


Fig. 27.

The main advantage of this advanced antenna system lies in the multi-band and multi-service performance of the antenna. This enables convenient and easy connection of a simple antenna for most communication systems of the vehicle.

The antenna is formed by a set of polygonal elements, supported by transparent conductive layer coated on the transparent window of motor vehicle.

The particular shape and design of the polygonal elements, preferably triangular or square, enhances the behaviour of the antenna to operate simultaneously at several bands.

The multi service antenna will be connected to most of the principal equipments available in a motor vehicle such as radio (AM/FM), Digital Audio and Video Broadcasting (DAB or DVB), Tire pressure control, Wireless car aperture, Terrestrial Trunked Radio (TETRA), mobile telephony (GSM 900 - GSM 1800 - UMTS), Global Positioning System (GPS), Bluetooth and wireless LAN (Local Area Network) access.

Until recently, telecommunication systems available in a automobile were limited to a few services, mainly the analogical radio reception (AM/FM bands).

The most common solution for these systems is the typical whip antenna mounted on the car roof. The current tendency in the automotive sector is to reduce the aesthetic and aerodynamic impact due to these antennas by embedding them in the vehicle structure. Also, a major integration of the several telecommunication services into a single antenna would help to reduce the manufacturing costs or the damages due to vandalism and car wash equipments.

The antenna integration is becoming more and more necessary as we are assisting to a profound change in telecommunication habits. The internet has evoked an information age in which people around the globe expect, demand, and receive information. Car drivers expect to be able to drive safely while handlings e-mail a telephone calls and obtaining directions, schedules, and other information accessible on the WWW.

Telematic devices can be used to automatically notify authorities of an accident and guide rescuers to the car, track stolen vehicles, provide navigation assistance to drivers, call emergency roadside assistance and remote diagnostics of engine functions.

High equipments and services have been available on some cars for very few years. The high costs of these equipments initially limited them to luxury cars.

However, rapid declines in both equipment and services prices are bringing telematic products into mid-priced automobiles.

The massive introduction of new systems will generate a proliferation of new car antennas, in contradiction with the aesthetic and aerodynamic requirements of integrated antenna.

Antennas are essentially narrowband devices. Their behaviour is highly dependent on the antenna size to the operating wavelength ratio.

The use of fractal-shaped multi-band antennas was first proposed in 1995 (Patent No. 9501019). The main advantages addressed by these antennas featured similar parameters (input impedance, radiation pattern) at several bands maintaining their performance, compared with conventional antennas. Also, fractal-shapes permit to obtain antenna of reduced dimensions compared to other conventional antenna, as well. In 1999, multilevel antennas [15] resolved some practical problems encountered with the practical applications of fractal antennas.

Fractal auto-similar objects are, in strict mathematical sense, composed by an infinite number of scaled iterations, impossible to achieve in practice. Also, for practical

applications, the scale factor between each iteration and the spacing between the bands do not have to correspond to the same number.

Multilevel antennas introduced a higher flexibility to design multi-service antennas for real applications, extending the theoretical capabilities of ideal fractal antennas to practical, commercial antennas.

Several solutions were proposed to integrate the AM/FM antenna in the vehicle structure. A possible configuration is to use the thermal grid on the rear windshield [16]. However, this configuration requires an expensive electronic adaptation network, including RF amplifiers and filters to discriminate the radio signals from the DC source. Moreover, to reduce costs, the AM band antenna often comes apart from the heating grid limiting the area of the heating grid.

Other configuration is based on the utilization of a transparent conducting layer.

This layer is coated on the vehicle windshield is introduced to avoid an excessive heating of the vehicle interior by reflecting IR radiations.

The utilization of this layer as reception antenna for AM or FM band has been already proposed with several antenna shapes [17].

Obviously all these antenna configurations can only operate at a determinate frequency band in reason of the frequency dependence of the antenna parameter and are not suitable for a multi-service operation.

One of the main substantial innovations of the antenna system presented here consists in using a single antenna element, maintaining the same behaviour for several applications, and to keep the IR protection.

The advantages reside in full antenna integration with no aesthetic or aerodynamic impact, a full protection from vandalism, and a manufacturing cost reduction.

The main advantage of this system is the multi-band and multi-service behaviour of the antenna. This permits a convenient and easy connection to a single antenna for the majority of communication systems of the vehicle.

The typical frequency bands of the different applications are the following:

- FM (80 - 110 MHz)
- DAB (205 - 230 MHz)
- TETRA (350 - 450 MHz)
- Wireless Car Aperture (433 MHz, 868 MHz)
- Tire Pressure Control (433 MHz)
- DVB (470 - 862 MHz)
- GSM 900 / AMP (820 - 970 MHz)
- GSM 1800 / DCS / PCS / DECT (1700 - 1950 MHz)
- UMTS ( 1920 - 2200 MHz)
- Bluetooth (2400 - 2500 MHz)
- WLAN (4,5 - 6,0 GHz)

This multi-band behaviour is obtained by a multilevel structure composed by a set of polygonal elements of the same class (the same number of sides), electro-magnetically coupled either by means of an ohmic contact or a capacitive or inductive coupling mechanism. The structure can be composed by whatever class of polygonal elements.

However, a preference is given to triangles or squares elements, being these structures more efficient to obtain an omni-directional pattern in the horizontal plane.



To assure an easy identification of each element composing the entire structure and the proper multiband behaviour, the contact region between each element has to be in at least the 75% of the elements, always shorter than 50% of the perimeters of polygonal structures.

The other main advantage of this antenna system resides in the utilization of a transparent conductive layer as support for the antenna.

Being transparent, this antenna can be coated in the windshield screen of a motor vehicle. Other possible positions are the side windows or the rear windows.

The most common material used is ITO (Indium Tin Oxide), although other materials may be used (like for instance TiO<sub>2</sub>, SnO or ZnO), by sputtering vacuum deposition process. An additional passive layer can be added to protect the conducting layer from external aggression (for instance SiO<sub>2</sub>).

Other advantage of the multi-band antenna is to reduce the total weight of the antenna comparing with classical whip. Together with the costs, the component weight reduction is one of the major priorities in the automotive sector. The cost and weight reductions are also improved by the utilization of only single cable to feed the multi-service antenna.

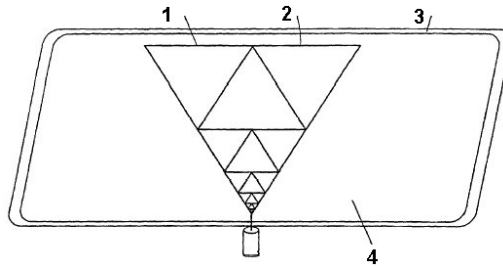


Fig. 28.

In Figure 28 is show a possible configuration for the multi-band antenna which support is an optically transparent conducting layer: A triangular multilevel structure (2) fed as a monopole and with the transparent conducting layer (1) filling the inside area of the polygonal elements and wherein the rest of the windows surface (4) is not coated with conducting layer.

In figure 29 is show an example of how several multilevel structures (1) can be printed at the same time using the same procedure and scheme described above.

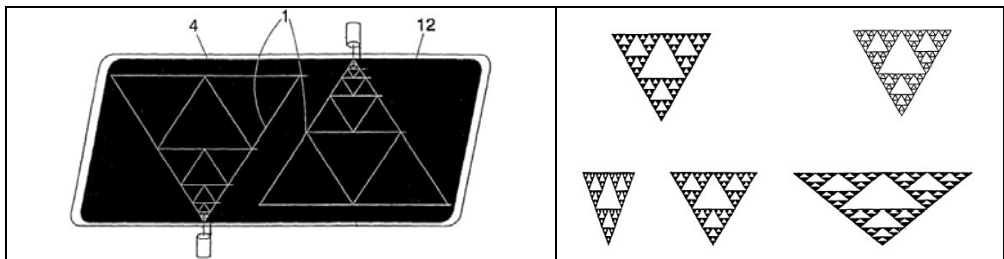


Fig 29.

Fig. 30.

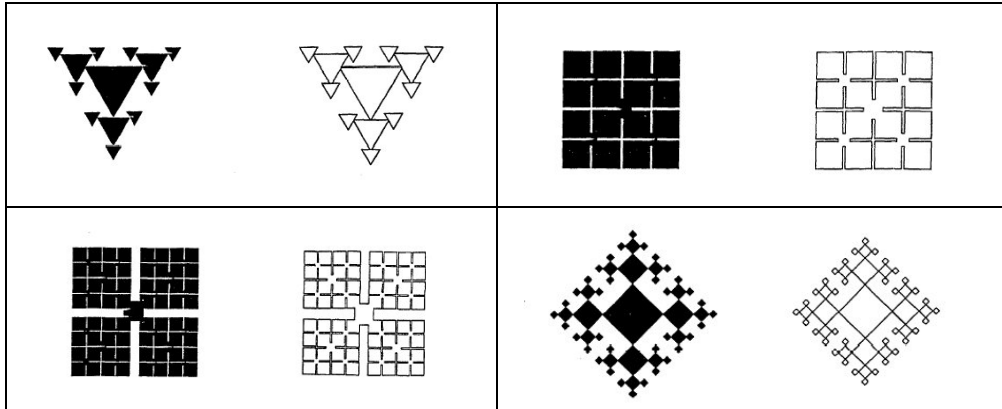


Fig. 31.

## 5. Vehicle Windshields with Fractal Antenna

A fractal antenna is patterned out of a conductive layer (e.g., Cu, Au, ITO, etc.) and is provided between first and second opposing substrates of a vehicle windshield.

A polymer inclusive interlayer function to both protect the fractal antenna(s) and laminate the opposing substrates to one another. In other embodiments, a multiband fractal antenna is provided which includes a first group of triangular shaped antenna portions, and a second triangular shaped antenna portion(s), wherein each of the triangular shaped antenna portions of the first group is located within a periphery of the second triangular shaped antenna portion. The first group of antenna portions transmits and/or receives at a first frequency band, while the second antenna portion(s) transmits and/or receive at a second frequency band different than the first band [18].

More particularly, one embodiment relates to a vehicle windshield including a fractal antenna(s). Another embodiment relates to a multiband fractal antenna. Yet another embodiment of this invention relates to an array of fractal antennas.

Generally speaking, antennas radiate and/or receive electromagnetic signals. Design of antennas involves balancing of parameters such as antenna size, antenna gain, bandwidth, and efficiency.

Most conventional antennas are Euclidean design/geometry, where the closed antenna area is directly proportional to the antenna perimeter. Thus, for example, when the length of a Euclidean square is increased by a factor of three, the enclosed area of the antenna is increased by a factor of nine.

Unfortunately, Euclidean antennas are less than desirable as they are susceptible to high Q factors, and become inefficient as their size gets smaller.

Characteristics (e.g., gain, directivity, impedance, efficiency) of Euclidean antennas are a function of the antenna's size to wavelength ratio.

Euclidean antennas are typically desired to operate within a narrow range (e.g., 10- 40%) around a central frequency  $f_c$  which in turn dictates the size of the antenna (e.g., half or quarter wavelength). When the size of a Euclidean antenna is made much smaller than the operating wavelength ( $\lambda$ ), it becomes very inefficient because the antenna's radiation

resistance decreases and becomes less than its ohmic resistance (i.e., it does not couple electromagnetic excitations efficiently to free space). Instead, it stores energy reactively within its vicinity (reactive impedance  $X_c$ ).

These aspects of Euclidean antennas work together to make it difficult for small Euclidean antennas to couple or match to feeding or excitation circuitry, and cause them to have a high Q factor (lower bandwidth). Q (Quality) factor may be defined as approximately the ratio of input reactance to radiation resistance,

$$Q = X_{in}/R_r$$

The Q factor may also be defined as the ratio of average stored electric energies (or magnetic energies stored) to the average radiated power. Q can be shown to be inversely proportional to bandwidth. Thus, small Euclidean antennas have very small bandwidth, which is of course undesirable (e.g., tuning circuitry may be needed).

Many known Euclidean antennas are based upon closed-loop shapes. Unfortunately, when small in size, such loop-shaped antennas are undesirable because, as discussed above, e.g., radiation resistance decreases significantly when the antenna size/area is shortened/dropped. This is because the physical area  $A$  contained within the loop-shaped antenna's contour is related to the latter's perimeter. Radiation resistance ( $R_r$ ) of a circular (i.e., loop-shaped) Euclidean antenna is defined by,

$$R_r = \eta \left( \frac{2}{3} \right) \pi \left( \frac{kA}{\lambda} \right)^2 = 20\pi^2 \left( \frac{C}{\lambda} \right)^2$$

where  $k$  is a constant.

Since ohmic resistance  $R_c$  is only proportional to perimeter ( $C$ ), then for  $C < 1$ , the ohmic resistance  $R_c$  is greater than the radiation resistance  $R_r$  and the antenna is highly inefficient. This is generally true for any small circular Euclidean antenna.

A small-sized antenna will exhibit a relatively large ohmic resistance and a relatively small radiation resistance  $R_r$ , such that low efficiency defeats the use of the small antenna.

Fractal geometry is a non-Euclidean geometry which can be used to overcome the aforesaid problems with small Euclidean antennas. Radiation resistance  $R_r$  of a fractal antenna decreases as a small power of the perimeter ( $C$ ) compression, which a fractal loop or island always having a substantially higher radiation resistance than a small Euclidean loop antenna of equal size. Accordingly, fractals are much more effective than Euclidean when small sizes are desired. Fractal geometry may be grouped into:

- Random fractals, which may be called chaotic or Brownian fractals and include a random noise component
- Deterministic or exact fractals. In deterministic fractal geometry, a self-similar structure results from the repetition of a design or motif (or generator) (i.e., self-similarity and structure at all scales). In deterministic or exact self similarity, fractal antennas may be constructed through recursive or iterative means. In other words, fractals are often composed of many copies of themselves at different scales, thereby allowing them to defy the classical antenna performance constraint which is size to wavelength ratio.

Recent growth in technology such as the Internet, cellular telecommunications, and the like has led to personal users desiring wireless access for: Internet access, cell phones, pagers, personal digital assistants, etc., while competing types of wireless broadband such as TDMA (Time Division Multiple Access), CDMA (Code Division Multiple Access) and GSM are being pushed by wireless manufacturers.

Unfortunately, current vehicle antenna systems do not have the capability of efficiently enabling such desired wireless access.

In view of the above, it will be apparent that there exists a need in the art for a vehicle antenna system that enables efficient access to the Internet, cell phones, pagers, personal digital assistants, radio, and/or the like. There also exists a need in the art for a multiband fractal antenna. These and other needs which will become apparent to the skilled artisan from a review of the instant application are achieved by the present antenna system.

Certain embodiments of this system relate to a fractal antenna printed on dielectric substrates (e.g., glass substrate or other suitable substrate).

Other embodiments of this system relate to a vehicle windshield with fractal antenna(s) provided therein.

Other embodiments of this system relate to a multiband fractal antenna.

Other embodiments of this system relate to an array of fractal antennas provided on a substrate.

Certain other embodiments of this system relate to a method of making fractal antennas, or arrays thereof. While fractal antennas are illustrated and described herein as being used in the context of a vehicle windshield, the system is not limited as certain fractals (e.g., multiband fractal antennas) may be used in other contexts where appropriate and/or desired.

Figure 32 is a cross sectional view of a vehicle windshield, including a fractal antenna (3). The windshield (curved or flat) includes first glass substrate (5) on the exterior side of the windshield, second glass substrate (7) on the interior side of the windshield adjacent the vehicle interior, polymer interlayer (9) for laminating the substrates (5, 7) to one another, and fractal antenna(s) (3).

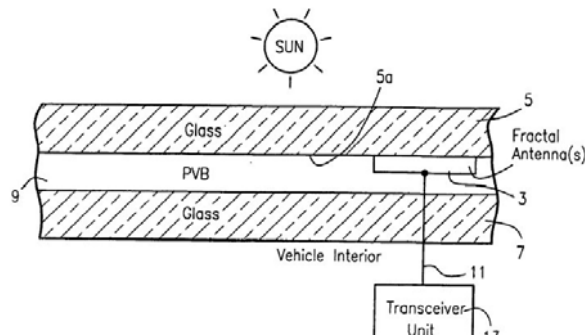


Fig. 32.

Polymer inclusive interlayer (9) may be of or include polyvinyl butyral (PVB), polyurethane(PU), PET, polyvinylchloride (PVC), or any other suitable material for laminating substrates (5) and (7) to one another.

Substrates (5) and (7) may be flat in certain embodiments, or bent/curved in other embodiments in the shape of a curved vehicle windshield. Substrates (5) and (7) are preferably of glass such as soda-lime-silica type glass, but may be of other materials (e.g., plastic, borosilicate glass, etc.) in other embodiments of this system.

As shown in Figure 32, the fractal antenna includes a conductive layer (3) provided on the interior surface of substrate (5). Fractal antenna layer (3) may be of or include opaque copper (Cu), gold (Au), substantially transparent indium-tin-oxide (ITO), or any other suitable conductive material in different embodiments of this system. Transparent conductive oxides (TCOs) are preferred for fractal antenna layer (3) in certain embodiments; example TCOs includes ITO, SnO, AlZnO, RuO, etc. Layer (3) is patterned into the shape of a fractal antenna.

The first major surface of fractal antenna layer (3) contacts insulative polymer inclusive interlayer (9). Interlayer (9) functions to both protect fractal antenna layer (3), and laminate the opposing substrates (5) and (7) to one another. Interlayer (9) is substantially transparent (i.e., at least about 80% transparent to visible light).

In the embodiment presented in Figure 32, fractal antenna (3) is shown as being located directly on the interior surface 5a of substrate 5. However, in other embodiments, the fractal antenna (3) may be located on substrate (5) with one or more additional layer(s) being provided there between.

In other embodiments, fractal antenna(s) may be printed on a PVB layer located between the substrates, or located on a polymer inclusive film located between the substrates. In all of these scenarios, antenna (3) is considered to be “on” and “supported by” substrate (5).

Because fractal antenna (3) herein may be printed on a substrate (e.g., glass substrate), the dielectric nature of the substrate may slightly change the effective dimension of the antenna by slowing electromagnetic waves passing there through. This may cause the antenna to look bigger than it actually is. However, it has been found that this effect can be compensated, for example, using the following equation,

$$\lambda_e = \frac{\lambda_0}{\sqrt{0.5(\epsilon_r + 1)}}$$

Figure 33 is a plan view of a windshield. As shown, a single fractal antenna FA (3) may be located at an upper portion of the windshield (i.e., near where a rear view mirror is to be attached thereto) so that it is not located in a primary viewing area of the windshield.

Instead of a single fractal antenna, an array(s) of fractal antennas (3) may be provided on the windshield in any of the manners described herein.

One array may be provided at an upper portion of the windshield, and another array at a bottom portion of the windshield (one array for a first frequency band, and another array for the second frequency band). In other embodiments, only a single array may be provided either at the upper portion or the lower portion of the windshield.

In the Figure 34 is illustrated a base element (20) in the form of a straight line or trace (a curve could instead be used). A fractal motif or generator (21), V-shape, is inserted into the base element to form a first order iteration N=1, the second iteration N=2, and the third iteration N=3. The iteration may go on and on (N may increase up to 10, up to 100, up to 1000, etc.) in different embodiments. Preferable, fractal antenna (3) herein take the shape of any fractal iteration herein, of N=2 and higher.

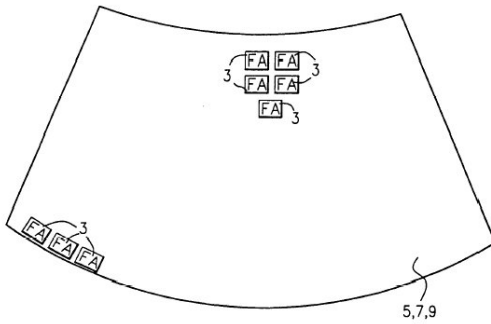


Fig. 33.

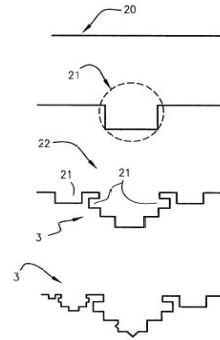


Fig. 34.

Figure 35 illustrate a loop shaped Koch fractal antenna (3) and a loop shaped Euclidean antenna (28) overlaid with one another, where both take up about the same volume or extend.

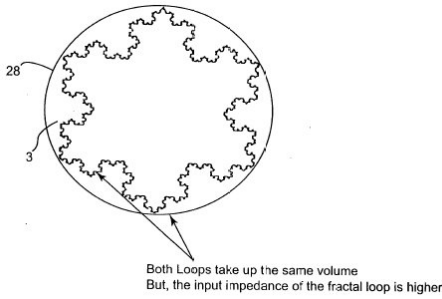
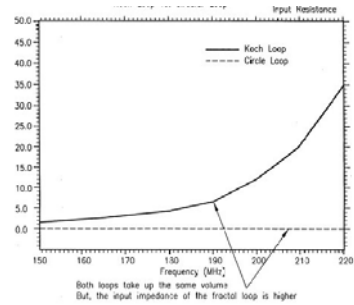


Fig. 35.



Figures 36a,b,c illustrate another way in which vehicle windows may be made according to certain embodiments.

In the upper Figure, one or more fractal antenna(s) (3) are printed on polymer (PET) film (40). Polymer inclusive film (40) also supports adhesive layer (41) and backing/release layer (42). If many antennae (3) are printed on film (40) via silkscreen printing, or any other suitable technique, then the coated article may be cut into a plurality of different pieces as shown by cutting line (45). After cutting (which is optional), release layer (42) is removed (peeled off), and film (40) with fractal antenna (3) printed thereon is adhered to substrate (5) via exposed adhesive layer (41) (see Figure 36b).

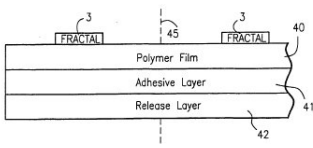


Fig. 36.a

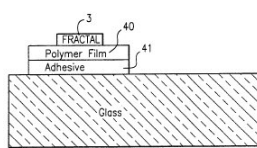


Fig. 36.b

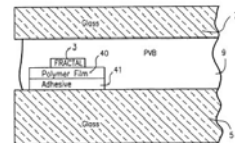


Fig. 36.c

The structure (Figure 36b) is laminated to the other substrate (7) via PVB interlayer (9). In such a manner, fractal (3) can be more easily formed in the resulting vehicle window that is shown in Figure 36c.

## 6. Multilevel and Space-Filling Ground-Planes for Miniature and Multi-Band Antennas

A new family of antenna ground-planes of reduced size and enhanced performance based on an innovative set of geometries.

These new geometries are known as multilevel and space-filling structures, which had been previously used in the design of multiband and miniature antennas. A throughout description of such multilevel or space-filling structures can be found in [19].

One of the key issues of the present antenna system is considering the ground-plane of an antenna as an integral part of the antenna that mainly contributes to its radiation and impedance performance (impedance level, resonant frequency, and bandwidth).

A new set of geometries are disclosed here, such a set allowing to adapt the geometry and size of the ground-plane to the ones required by any application (base station antennas, handheld terminals, cars, and other motor-vehicles), yet improving the performance in terms of, for instance, bandwidth, VSWR (Voltage Standing Wave Ratio), or multiband behaviour.

The use of multilevel and space-filling structures to enhance the frequency range an antenna can work within was well described in patent publications [19].

Such an increased range is obtained either through an enhancement of the antenna bandwidth, with an increase in the number of frequency bands, or with a combination of both effects.

The multilevel and space-filling structures are advantageously used in the ground plane of the antenna obtaining this way a better return loss or VSWR, a better bandwidth, a multiband behaviour, or a combination of all these effects. The technique can be seen as well as a means of reducing the size of the ground-plane and therefore the size of the overall antenna.

A first attempt to improve the bandwidth of micro-strip antennas using the ground plane was described in [20, 21]. There, a particular case of a ground-plane composed by three rectangles with a capacitive electromagnetic coupling between them was used.

Some of the geometries described here are inspired in the geometries already studied in 19th century by several mathematicians such as Giuseppe Peano and David Hilbert.

In all these cases the curves were studied from the mathematical point of view but were never used for any practical engineering application. Such mathematical abstraction can be approached in a practical design by means of the general space-filling curves described for this antenna system. It is interesting to notice that in some cases, such space-filling curves can be used to approach ideal fractal shapes as well.

The key point of the present antenna system is shaping the ground-plane of an antenna in such a way that the combined effect of the ground-plane and the radiating element enhances the performance and characteristics of the whole antenna device, either in terms of bandwidth, VSWR, multiband behaviour, efficiency, size, or gain.

Instead of using the conventional solid geometry for ground-planes as commonly described in the prior art, here are introduced a new set of geometries that forces the currents on the ground-plane to flow and radiate in a way that enhances the whole antenna behaviour.

The basis of this new system consists of breaking the solid surface of a conventional ground-plane into a number of conducting surfaces (at least two of them), which are electromagnetically coupled either by the capacitive effect between the edges of the several conducting surfaces, or by a direct contact provided by a conducting strip, or a combination of both effects.

The resulting geometry is no longer a solid, conventional ground-plane, but a groundplane with a multilevel or space-filling geometry, at least in a portion of ground-plane.

A multilevel geometry for a ground-plane consists of a conducting structure including a set of polygons, featuring the same number of sides, electromagnetically coupled either by means of a capacitive coupling or ohmic contact. The contact region between directly connected polygons is narrower than 50% of the perimeter of polygons in at least 75% of polygons defining conducting ground-plane.

In this definition of multilevel geometry, circles and ellipses are included as well, since they can be understood as polygons with infinite number of sides.

A Space-Filling Curve (hereafter SFC) is a curve that is large in terms of physical length but small in terms of the area in which the curve can be included. More precisely, the following definition is taken in this document for a space-filling curve:

A curve composed by at least ten segments which are connected in such a way that each segment forms an angle with their neighbours, that is, no pair of adjacent segments define a larger straight segment, and wherein the curve can be optionally periodic along a fixed straight direction of space if, and only if, the period is defined by a non-periodic curve composed by at least ten connected segments and no pair of adjacent and connected segments defines a straight longer segment.

Also, whatever the design of such SFC is, it can never intersect with itself at any point except the initial and final point (that is, the whole curve can be arranged as a closed curve or loop, but none of the parts of the curve can become a closed loop).

A space-filling curve can be fitted over a flat or curved surface, and due to the angles between segments, the physical length of the curve is always larger than that of any straight line that can be fitted in the same area (surface).

Additionally, to properly shape the ground-plane, the segments of the SFC curves included in the ground-plane must be shorter than a tenth of the free-space operating wavelength.

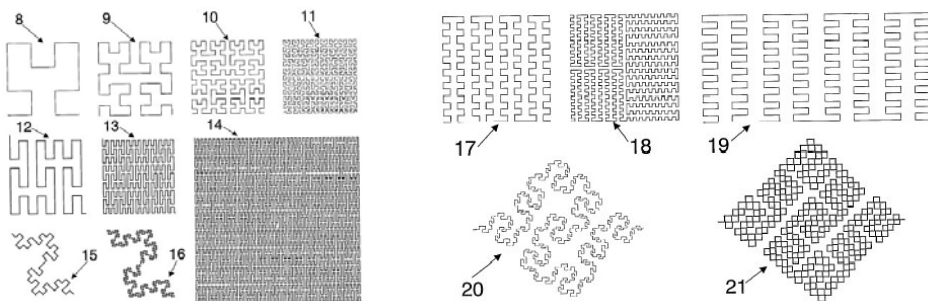


Fig. 37.



Depending on the shaping procedure and curve geometry, some infinite length SFC can be theoretically designed to feature a Hausdorff dimension larger than their topological-dimension (see Figure 37).

That is, in terms of the classical Euclidean geometry, it is usually understood that a curve is always a one-dimension object; however when the curve is highly convoluted and its physical length is very large, the curve tends to fill parts of the surface which supports it. In that case, the Hausdorff dimension can be computed over the curve (or at least an approximation of it by means of the box-counting algorithm) resulting in a number larger than unity. The curves shown in the Figure 37 are some examples of such SFC, in particular drawings 11,13,14 and 18 show some examples of SFC curves that approach an ideal infinite curve featuring a dimension  $D = 2$ .

From an initial curve (8), other curves (9), (10), and (11) are formed (called Hilbert Curves). Likewise, other set of SFC curves can be formed, such as set (12), (13), (14), called SZ curves; set (15) and (16), known as ZZ curves; set (17), (18) and (19), called Hilbert ZZ curves; set (20) Peanodec curve, and set (21) based on the Giuseppe Peano curve.

Depending on the application, there are several ways for establishing the required multilevel and space-filling metallic pattern according to the present antenna system.

Due to the special geometry of multilevel and space-filling structure, the current distributes over the ground-plane in such a way that it enhances the antenna performance and features in terms of:

- Reduced size compared to antennas with a solid ground-plane
- Enhanced bandwidth compared to antennas with a solid ground-plane
- Multi-frequency performance
- Better VSWR feature at the operating band or bands
- Better radiation efficiency
- Enhanced gain

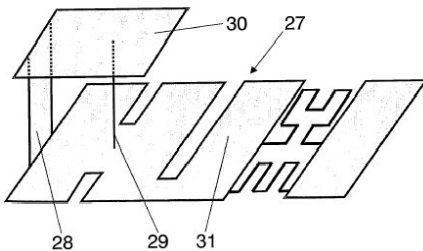


Fig. 38.

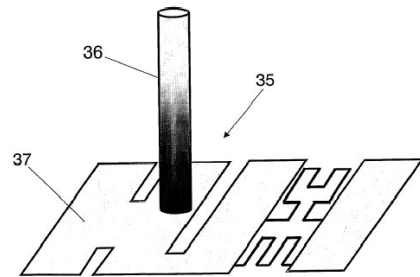


Fig. 39.

Figure 38 shows a new configuration (27) for a PIFA (Planar Inverted F Antenna), formed by an antenna element (30), a feed point (29), a short-circuit (28), and a particular example of a new ground-plane structure (31) formed by both multilevel and space-filling geometries.

Figure 39 shows an improved monopole antenna (36) configuration (35) where the ground-plane (37) is composed by multilevel and space-filling structures.

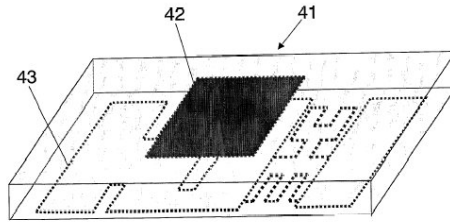


Fig. 40.

Figure 40 shows an improved antenna patch system composed by a radiating element (42) and a multilevel and space-filling ground-plane (43).

Figure 41 shows several examples of different contour shaped for multilevel groundplanes, such as rectangular (44), (45), and (46); and circular (47), (48), and (49). In this case, circles and ellipses are taken as polygons with infinite number of sides.

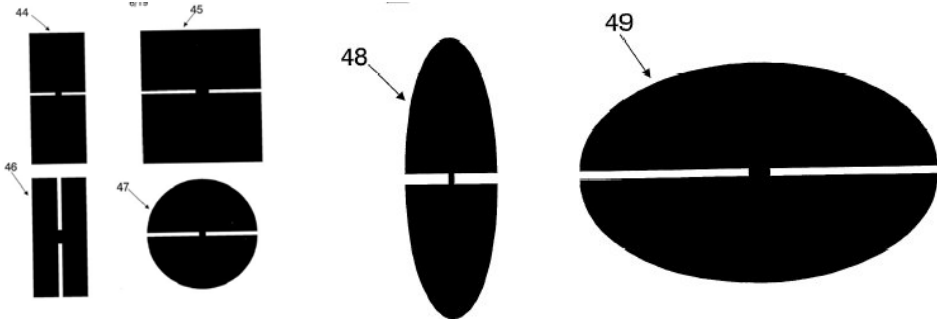


Fig. 41

Figure 42 shows alternative schemes of multilevel ground-planes. The ones being showed in the drawings (68) to (76) are being formed from rectangular structure, but any other shape could have been used.

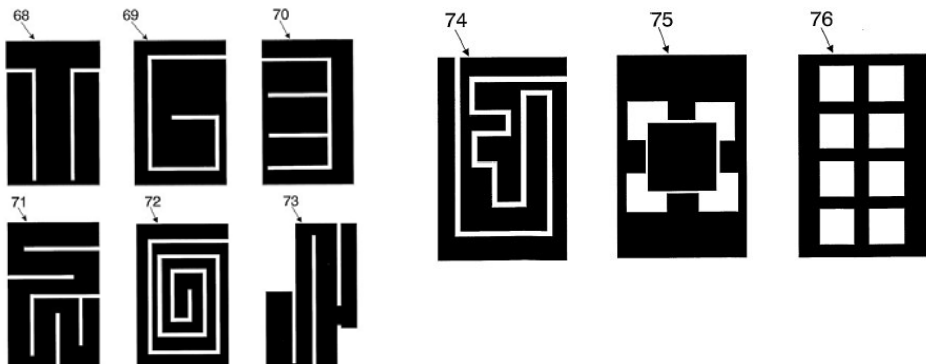


Fig. 42.

Figure 43 shows examples (77) and (78) of two conducting surfaces (5) and (6) being connected by one (10) or two (9) and (10) SFC connecting strips.

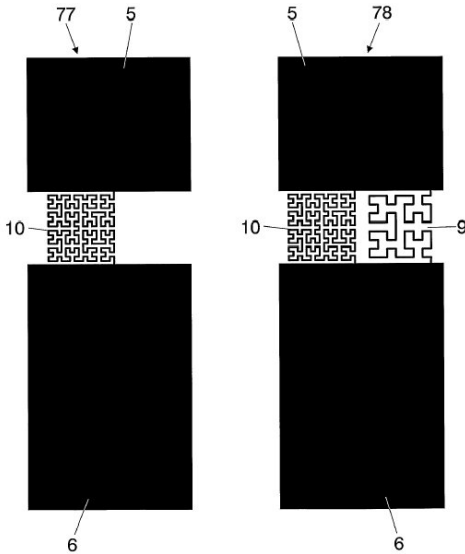


Fig. 43.

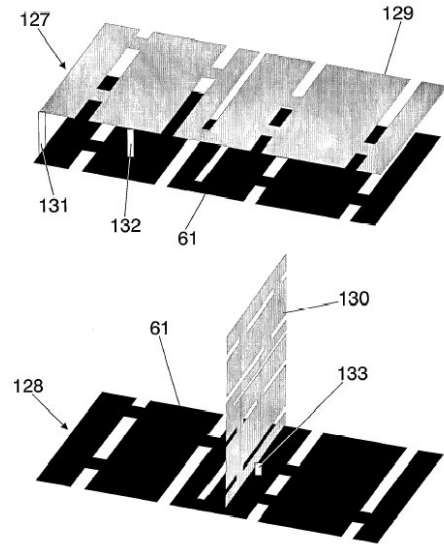


Fig. 44.

Figure 44 shows examples of antennas wherein the radiating element has substantially the same shape as the ground-plane, thereby obtaining a symmetrical or quasi-symmetrical configuration, and where the radiating element is placed parallel (drawing (127) or orthogonal, drawing (128) to ground-plane.

### 7. Miniature Broadband Ring-Like Micro-strip Patch Antenna

A miniature broadband stacked micro-strip patch antenna formed by two patches, an active and a parasitic patches, where at least one of them is defined by a Ring-Like Space-Filling Surface (RSFS) is presented [22], Figure 45

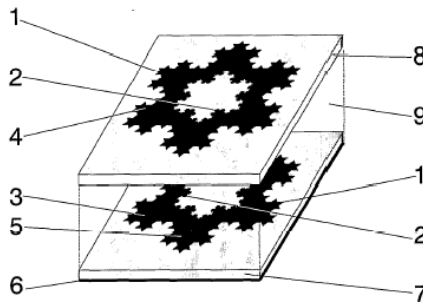


Fig. 45.

By means of this new technique, the size of the antenna can be reduced with respect to prior art, or alternatively, given a fixed size the antenna can operate at a lower frequency with respect to a conventional micro-strip patch antenna of the same size and with an enhanced bandwidth. Also, the antennas feature a high gain when operated at a high order mode.

An antenna is said to be small antenna (a miniature antenna) when it can be fitted in a space which is small compared to the operating wavelength. More precisely, the radian-sphere is taken as the reference for classifying an antenna as being small.

The radian-sphere is an imaginary sphere of radius equal to the operating wavelength divided by two times  $\pi$ .

An antenna is said to be small in terms of wavelength when it can be fitted inside a radian-sphere.

The fundamental limits of small antennas were theoretically established by H.Wheeler and L.J.Chu in the middle 1940's. They basically stated that a small antenna has a high quality factor (Q) because of the large reactive energy stored in the antenna vicinity compared to the radiated power. Such a high quality factor yields a narrow bandwidth.

In fact, the fundamental limit derived in such theory imposes a maximum bandwidth given a specific size of a small antenna. Other characteristics of a small antenna are its small radiating resistance and its low efficiency.

According to [23], the performance of a small antenna depends on its ability to efficiently use the small available space inside the imaginary radian-sphere surrounding the antenna.

In the antenna system presented here, a novel set of geometries named ring-like spacefilling surfaces (RSFS) are introduced for the design and construction of small antennas that improve the performance of other classical micro-strip patch antennas described in the prior art.

A general configuration for micro-strip antennas (also known as micro-strip patch antennas) is well known for those skilled in the art and can be found in [24].

The advantages such antennas compared to other antenna configurations are:

- Its low, flat profile (such as the antenna can be conformally adapted to the surface of a vehicle, for instance),
- Its convenient fabrication technique (an arbitrary shaped patch can be printed over virtually any printed circuit board substrate),
- And low cost.

A major draw-back of this kind of antennas is its narrow bandwidth, which is further reduced when the antenna size is smaller than a half-wavelength.

A common technique for enlarging the bandwidth of micro-strip antennas is by means of a parasitic patch (a second patch placed on top of the micro-strip antenna with no feeding mechanism except for the proximity coupling with the active patch) which enhances the radiation mechanism [25].

A common disadvantage for such a stacked patch configuration is the size of whole structure.

The advantage of this new antenna system is obtaining a micro-strip patch antenna of a reduced size when compared to the classical patch antennas, yet performing with a large bandwidth. The proposed antenna system is based on a stacked patch configuration composed by a first conducting surface (the active patch) substantially parallel to a conducting ground counterpoise or ground-plane, and a second conducting surface (the parasitic patch) placed parallel over such active patch.

Such parasitic patch is placed above the active patch so the active patch is placed between parasitic patch and the ground-plane.

One or more feeding source can be used to excite the active patch. The feeding element of the active patch can be any of the well known feeding element described in the prior art (such as for instance a coaxial probe, a co-planar micro-strip line, a capacitive coupling or an aperture at the ground-plane) for other micro-strip patch antennas.

The essential part of the antenna system is the particular geometry of either the active or the parasitic patches (or both).

The RSFS geometry consists on a ring, with an outer perimeter enclosing the patch and an inner perimeter defining a region within the patch with no conducting material.

The characteristic feature of the antenna system is the shape of either the inner or outer perimeter of the ring, either on the active or parasitic patches (or in both of them).

The ring perimeter is shaped as a space-filling curve (SFC), i.e., a curve that is large in terms of physical length but small in terms of the area can be included.

More precisely, the following definition is taken in this presentation for a space-filling curve: A curve composed by at least ten segments which are connected in such a way that each segment forms an angle with their neighbours, i.e., no pair of adjacent segments define a larger straight segment, and wherein the curve can be optionally periodic along a fixed straight direction of space if and only if the period is defined by a non-periodic curve composed by at least ten connected segments and no pair or adjacent and connected segments define a straight longer segment.

Also, whatever the design of such SFC is, it never intersects with itself at any point except the initial and final points (that is, the whole curve is arranged as a closed loop defining either the inner or outer perimeter of one patch within the antenna configuration).

Due to the angle between segments, the physical length of space-filling curve is always larger than that of any straight line than can be fitted in the same area (surface) as space-filling curve. Additionally, to properly shape the structure of the miniature patch antenna, the segments of the SFC curves must be shorter than a tenth of the free space operating wavelength.

The function of the parasitic patch is to enhance the bandwidth of the whole antenna system. Depending on the thickness and size constrain and the particular application, a further size reduction is achieved by using the same essential configuration for the parasitic patch placed on top of the active patch.

It is precisely due to the particular SFC shape of the inner or outer (or both) perimeters of the ring on either the active or parasitic patches that the antenna features a low resonant frequency, and therefore the antenna size can be reduced compared to a conventional antenna. Due to such a particular geometry of the ring shape, the antenna system is named Micro-strip Space-Filling Ring antenna (also MSFR antenna).

The advantage of using the MSFR configuration disclosed in this presentation is threefold:

1. Given a particular operating frequency or wavelength, the MSFR antenna has a reduced electrical size with respect to prior art.
2. Given the physical size of the MSFR antenna, the antenna operates at a lower frequency (a longer wavelength) than prior art.
3. Given a particular operating frequency or wavelength, the MSFR antenna has a larger impedance bandwidth with respect to prior art.

Also, it is observed that when these antennas are operated at higher order frequency modes, they feature a narrow beam pattern, which makes the antenna suitable for high gain applications.

As it will be readily notice by those skilled in the art, other features such as crosspolarisation or circular or elliptical polarization can be obtained applying to the newly disclosed configurations the same conventional techniques described in the prior art.

Figure 46 shows three preferred embodiments for a MSFR antenna. The top one describes an antenna formed by an active patch (3) over a ground plane (6) and a parasitic patch (4) placed over active patch.

At least one of the patches is a RSFS (e.g. top) both patches are a RSFS , only the parasitic patch is a RSFR (middle) and only the active patch is a RSFS (bottom).

Active and parasitic patches can be implemented by means of any of the well-known techniques for micro-strip antennas already available in the state of the art. For instance, the patches can be printed over a dielectric substrate (7) and (8) or can be conformed through a laser cut process upon a metallic layer.

The medium (9) between the active (3) and parasitic patch (4) can be air, foam or any standard radio frequency and microwave substrate.

The dimension of the parasitic patch is not necessarily the same than the active patch.

Those dimensions can be adjusted to obtain resonant frequencies substantially similar with a difference less than a 20% when comparing the resonance of the active and parasitic elements.

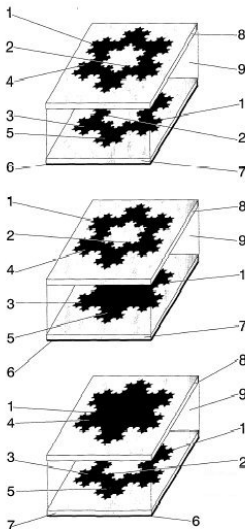


Fig. 46.

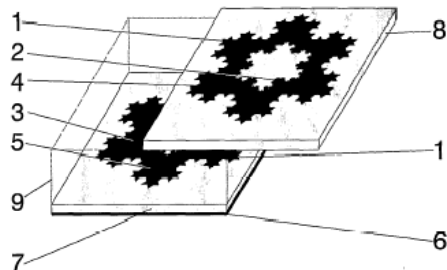


Fig. 47.

Figure 47 shows another preferred embodiment where the centre of active (3) and parasitic patches (4) are not aligned on the same perpendicular axis to the groundplane (7). This misalignment is useful to control the beam width of radiation pattern.

To illustrate several modification either on the active patch or the parasitic patch, several examples are presented.

Figure 48 and 49 described some RSFS either for the active or the parasitic patches where the inner (1) and outer perimeters (2) are based on the same SFC.

To illustrate some examples where the centre of the removed part is not the same than the centre of patch, in Figure 50 are presented other preferred embodiments with several combinations: centre misalignments where the outer (1) and inner perimeter of the RSFC are based on different SFC.

The centre displacement is especially useful to place the feeding point on the active patch to match the MSFR antenna to specific reference impedance. In this way they can features input impedance above 5 Ohms.

Other, non-regular (or mathematical generated fractal) curves was investigated for fractal antenna use in automotive industry and other applications like in RFID tags, with good results [26, 27]. The field is in rapid change, the potential of fractal antenna applications being far to be fully explored.

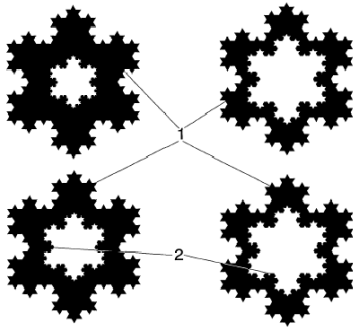


Fig. 48.

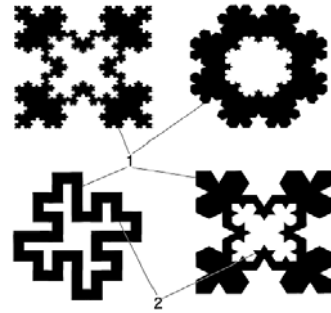


Fig. 49.

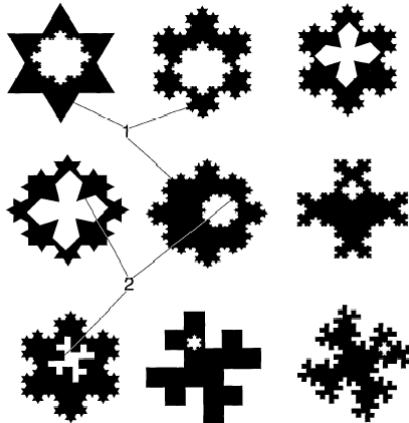


Fig. 50.

## 8. References

1. B.B. Mandelbrot, *The Fractal Geometry of Nature*, W.H. Freeman and Company, 1983; Mandelbrot, B.B., How long is the coast of Britain? Statistical self-similarity and fractional dimension, *Science* **156**, (1967) 636-638.
- 2 F.J.Falkoner, *The geometry of fractal sets*, Cambridge Univ. Press, 1990
- 3 D.Jaggard, <http://pender.ee.upenn.edu/facu5.htm>, D. Werner <http://www.psu.edu>
- 4 Balanis, Constantine A., *Antenna Theory Analysis and Design*, Second Edition, John Wiley & Sons, Inc., 1997
- 4 Puente Balliarda Carles, Rozan Edouard, Fractus-Ficosa International U.T.E, Patent, International Publication Number WO 02/35646 A1, 02.05.2002
- 5 Patent US4123756
- 6 Patent US5504478
- 7 Patent US5798688
- 8 Patent WO 95/11530
- 9 Virga K., Rahmat-Samii Y., "Low-Profile Enhanced-Bandwidth PIFA Antennas for Wireless Communications Packaging", *IEEE Trans. On Microwave Theory and Techniques*, October 1997.
- 10 Skolnik M.I, "Introduction to Radar Systems", Mc. Graw Hill, London, 1981
- 11 Patent US 5087515, Patent US 4976828, Patent US 4763127, Patent US 4600642, Patent US 3952307, Patent US 3725927
- 12 European Patent Application EP 1317018 A2 / 27.11.2002
- 13 Patent WO 0154225, Patent WO 0122528
- 14 Patent EP 1313166 A1
- 15 Patent PCT/ES/00296
- 16 Patent WO 95/11530
- 17 Patent JP-UM-49-1562; Patent US 445884; US Patent 5355144; US Patent 5255002
- 18 Patent WO 03017421 A2
- 19 Patent WO 03/023900 A1; Patent WO 01/22528; Patent WO 01/54225
- 20 Chiou T., Wong K., „Design of Compact Microstrip Antennas with a Slotted Ground Plane“ *IEEE-APS Symposium*, Boston, 8-12 July,2001
- 21 Patent US No. 5,703,600
- 22 Patent WO 02/063714 A1
- 23 Hansen R.C., "Fundamental limitations on Antennas", *Proc.IEEE*, vol.69, no.2, February 1981
- 24 Pozar D., "The Analysis and Design of Microstrip Antennas and Arrays", *IEEE Press*, Piscataway, NJ 08855-1331
- 25 Zurcher J.F., Gardiol F.E., "Broadband Patch Antennas", *Artech House* 1995
- 26 M. Rusu, R. Baican, Adam Opel AG, *Patent 01P09679, "Antenne mit einer fraktalen Struktur", die auf der Erfindungsmeldung 01M-4890 "Fractal Antenna for Automotive Applications" basiert*, 18 Okt. 2001.
- 27 M.V. Rusu, M. Hirvonen, H. Rahimi, P. Enoksson, C. Rusu, N. Pesonen, O. Vermesan, H. Rustad, "Minkowski Fractal Microstrip Antenna for RFID Tags", *Proc. EuMW2008 Symposium*, Amsterdam, October, 2008; Rahimi H., Rusu M., Enoksson P, Sandström D., Rusu C., Small Patch Antenna Based on Fractal Design for Wireless Sensors, *MME07, 18th Workshop on Micromachining, Micromechanics, and Microsystems*, 16-18 Sept. 2007, Portugal.



# Analysis and Design of Radome in Millimeter Wave Band

Hongfu Meng and Wenbin Dou

*State Key Laboratory of Millimeter Waves, Southeast University,  
China*

## 1. Introduction

Antenna is a very important component in a radar system. In order to protect the antenna from various environments, dielectric radome is always covered in front of the antenna. However, the presence of the radome inevitably affects the radiation properties of the enclosed antenna, such as loss and distortion of the radiation pattern. For the monopulse tracing radar, the appearance of the radome will deviate the null direction of the difference radiation pattern from the look angle of the antenna, which is called the boresight error (BSE) of the radome. Thus, an accurate analysis of the antenna-radome system is very important.

As the wavelength of the millimeter wave is shorter than microwave, the millimeter wave radar is more and more popular in monopulse radar system to improve the tracing precision. However, as the size of the radome in millimeter wave band is always tens of wavelengths or larger, the full-wave methods, such as the method of moments (MoM) [Arvas et al, 1990] and the finite element method (FEM) [Gordon & Mittra, 1993], are very difficult to be implemented. Whereas, the high-frequency methods [Gao & Felsen, 1985; Paris, 1970], e.g., the aperture integration-surface integration (AI-SI) method [Paris, 1970; Volakis & Shifflett, 1997], are very efficient and can provide an acceptable solution for the radome with smooth surface. But for the tangent ogive radome, as there is a nose tip in the front of the radome, the AI-SI method is also not suitable and can not get the accurate results.

In 2001, the hybrid physical optics-method of moments (PO-MoM) was proposed to analyze the radome with nose tip [Abdel et al., 2001]. In the hybrid method, the radome was divided into two parts: the high frequency part with the smooth surface and the low frequency part with the tip nose region. The high frequency part was analyzed by the high frequency method, such as the AI-SI method. Then, the surface integration equation was established on the radome surface, and the equivalent currents on the high frequency part of the radome were substituted into the equation to reduce the unknowns. Finally, the equation with the unknowns in the low frequency region was solved to obtain the surface currents on the radome. However, for the radome with some complex small structures, such as the multilayer radome or the radome with the metallic cap, this hybrid method is very difficult. So some new hybrid methods must be proposed to solve these problems.

The aim of antenna-radome analysis is to improve the performance of the radar system. So, the optimal design of the antenna-radome system is very necessary. During the last two decades,

many researches have been done to optimize the antenna-radome system. Hsu, et al. optimized the BSE of a single-layered radome using simulated annealing technique in 2D [Hsu et al., 1993] and 3D [Hsu et al., 1994] with variable thickness radome. The polarization and frequency bandwidth performances of a C-sandwich uniform thickness radome have been optimized in [Fu et al., 2005] using the genetic algorithm (GA). The power transmission property and BSE of a variable thickness A-sandwich radome have also been compromised between two uniform thickness radomes [Nair & Jha, 2007].

As there are few literatures to discuss about the radome in millimeter wave band, in this chapter, we mainly focus on the analysis and optimal design of the radome in millimeter wave band. This chapter is divided into the following three parts.

In section 2, we discuss about the high frequency method for the radome analysis. Firstly, the general steps of the AI-SI method to analyze the electrically large radome are given. Then, the transmission coefficient in the case when the wave is passing through the radome is derived from the transmission line analogy. As the incident angles of the millimeter wave antenna-radome system are always very large and the electrical thickness of the radome is large, the traditional AI-SI method, which is very popular in microwave band, must be modified to analyze the radome in millimeter wave band. So, a phase factor of the lateral transmission is deduced to modify the conventional transmission coefficient. With this modified transmission coefficient, a conical radome at W-band is analyzed by the AI-SI method, and the computational and experimental results are compared.

To analyze the radome with some small complex structures, we present a hybrid method that combines high frequency (HF) and boundary integral-finite element method (BI-FEM) together in section 3. The complex structures and their near regions (LF part) are simulated using BI-FEM, and the other flat smooth sections of the radome (HF part) are modeled by the AI-SI method. The fields radiated from the equivalent currents of the HF part determined by the AI-SI method are coupled into the BI-FEM equation of the LF part to realize the hybridization. In order to account for the higher-order interactions of the radome, the present hybrid method is used iteratively to further improve the accuracy of the radome analysis. Also, some numerical results are given to show the validation of the hybrid method.

In the last section of this chapter, in order to optimize the radome in millimeter wave band, we employ GA combined with the ray tracing (RT) method to optimize the BSE and power transmittance of an A-sandwich radome in millimeter wave band simultaneously. In the optimization process, the RT method is adopted to evaluate the performances of the desired radome, and GA is employed to find the optimal thickness profile of the radome that has the minimal BSE and maximal power transmittance. In order to alleviate the difficulties of the manufacture, a new structure of local uniform thickness is proposed for the radome optimization. The thickness of the presented radome keeps being uniform in three local regions and only varies in two very small transitional regions, which are more convenient to be fabricated than the variable thickness radome [Hsu et al., 1994; Fu et al., 2005; Nair & Jha, 2007].

## **2. High Frequency Method for Radome Analysis (Meng et al., 2009a)**

### **2.1 General Steps**

The AI-SI method is a high-frequency approximate method and can analyze the electrically large radome in millimeter wave band efficiently. It was introduced to analyze the antenna-

radome system by Paris [Paris, 1970] and many other researchers have done a lot of work on it [Kozakoff, 1997, Meng et al., 2008a]. The general steps of this method are as follows:

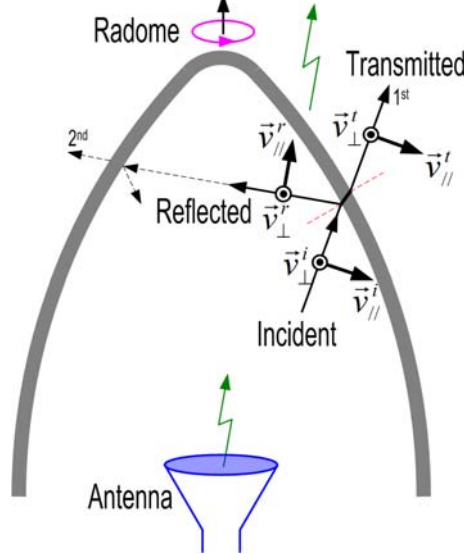


Fig. 1. Model of the AI-SI method for the antenna-radome analysis.

When the electromagnetic fields on the aperture of the antenna are known, the incident wave on the inner surface of the radome can be obtained by integrating over the aperture using the Stratton-Chu formulas. The incident vector at the intersection point on the inner surface of the radome is established by the direction of the Poynting vector [Wu & Rudduck, 1974]

$$\hat{S}_i = \text{Re}(\vec{E}_i \times \vec{H}_i^*) / |\text{Re}(\vec{E}_i \times \vec{H}_i^*)| \tag{1}$$

where  $\vec{E}_i$  and  $\vec{H}_i$  are the incident fields at the intersection point.

The incident vector and the normal vector at the intersection point on the inner surface define the plane of incidence. The incident fields at the intersection point are decomposed into the perpendicular and parallel polarization components to the plane of incidence. After reflection and refraction in the radome wall, the reflected fields  $\vec{E}_r, \vec{H}_r$  and the transmitted fields  $\vec{E}_t, \vec{H}_t$  are recombined as

$$\begin{aligned} \vec{E}_r &= (\vec{E}_i \cdot \vec{v}_\perp^i) R_\perp \vec{v}_\perp^r + (\vec{E}_i \cdot \vec{v}_\parallel^i) R_\parallel \vec{v}_\parallel^r \\ \vec{H}_r &= (\vec{H}_i \cdot \vec{v}_\perp^i) R_\parallel \vec{v}_\perp^r + (\vec{H}_i \cdot \vec{v}_\parallel^i) R_\perp \vec{v}_\parallel^r \end{aligned} \tag{2}$$

$$\begin{aligned} \vec{E}_t &= (\vec{E}_i \cdot \vec{v}_\perp^i) T_\perp \vec{v}_\perp^t + (\vec{E}_i \cdot \vec{v}_\parallel^i) T_\parallel \vec{v}_\parallel^t \\ \vec{H}_t &= (\vec{H}_i \cdot \vec{v}_\perp^i) T_\parallel \vec{v}_\perp^t + (\vec{H}_i \cdot \vec{v}_\parallel^i) T_\perp \vec{v}_\parallel^t \end{aligned} \tag{3}$$

where  $\vec{v}_\perp$  and  $\vec{v}_\parallel$  are the unit vectors illustrated in Fig.1, the superscripts  $i, r$  and  $t$  represent the incident, reflected, and transmitted fields, respectively.  $R_\perp, R_\parallel, T_\perp, T_\parallel$  are the reflection and transmission coefficients for the perpendicular and parallel polarizations, and they will be discussed later.

The reflected wave on the inner surface may bounce between the opposite sides of the radome. At this time, it is regarded as the incident wave for the second time step as an ordinary incident wave. The same process is repeated for the 3rd, 4th...inner reflections. Finally the total fields on the outer surface of the radome are the vector sum of the 1st, 2nd... transmitted fields.

When the fields on the outer surface are known, the far field radiation pattern of the antenna-radome system can be determined by integrating the fields over the outer surface of the radome using the Stratton-Chu formulas again.

## 2.2 Modified Transmission Coefficient

Now, we will concentrate on the reflection coefficients  $R_{\perp}$ ,  $R_{\parallel}$  and the transmission coefficients  $T_{\perp}$ ,  $T_{\parallel}$  in (2) and (3).

When a planar wave is incident from medium  $i$  to medium  $j$ , the Snell's law must be satisfied on the interface. The Fresnel reflection and refraction coefficients for the perpendicular and parallel polarizations are given by [Ishimaru, 1991]

$$\begin{aligned} r_{ij}^{\perp} &= \frac{Z_j \cos \theta_i - Z_i \cos \theta_j}{Z_j \cos \theta_i + Z_i \cos \theta_j} & r_{ij}^{\parallel} &= \frac{Z_i \cos \theta_i - Z_j \cos \theta_j}{Z_i \cos \theta_i + Z_j \cos \theta_j} \\ t_{ij}^{\perp} &= \frac{2Z_j \cos \theta_i}{Z_j \cos \theta_i + Z_i \cos \theta_j} & t_{ij}^{\parallel} &= \frac{2Z_i \cos \theta_i}{Z_i \cos \theta_i + Z_j \cos \theta_j} \end{aligned} \quad (4)$$

where  $Z_i = Z_0 \sqrt{\mu_i / \varepsilon_i}$  and  $Z_j = Z_0 \sqrt{\mu_j / \varepsilon_j}$  are the characteristic impedances of the two media,  $Z_0$  is the characteristic impedance of free space,  $\varepsilon_i, \varepsilon_j, \mu_i, \mu_j$  are the relative permittivities and permeabilities of the two media, and  $\theta_i, \theta_j$  are the angles of incidence and refraction, respectively.

For the antenna-radome system in millimeter wave band, the radome is always far away from the antenna, and the curvature radius of the radome is larger than the wavelength, so the incidence of the radiation field upon the radome wall can be simulated as locally planar wave impinging upon locally planar dielectric. In this case, the transmission coefficient of the dielectric plane is always determined by the transmission line analogy [Kozakoff, 1997]. As shown in Fig.2, the N-layered dielectric plane is equivalent to the cascade of the transmission lines with different impedances. For the  $n^{\text{th}}$  equivalent transmission line, the length is  $d_n$ , the equivalent propagation constant is  $k_n \cos \theta_n$ , and the effective impedances of the perpendicular and parallel polarizations are  $Z_n^{\perp} = Z_n \sec \theta_n$  and  $Z_n^{\parallel} = Z_n \cos \theta_n$ , in which  $\theta_n$  is the angle of refraction and  $Z_n = Z_0 \sqrt{\mu_n / \varepsilon_n}$  is the characteristic impedance in this layer.

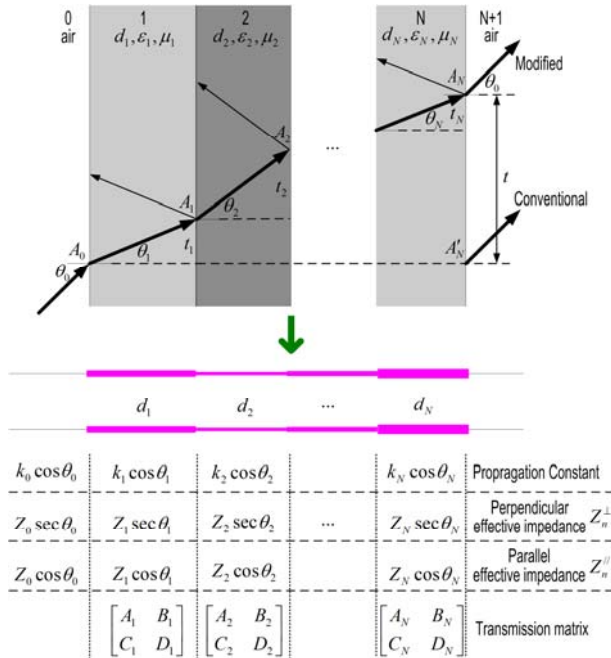


Fig.2. Transmission line analogy of the multi-layered dielectric plane.

For the perpendicular polarization, the transmission matrix of the  $n^{\text{th}}$  layer is

$$\begin{bmatrix} A_n & B_n \\ C_n & D_n \end{bmatrix} = \begin{bmatrix} \cosh(jk_n \cos \theta_n d_n) & Z_n^\perp \sinh(jk_n \cos \theta_n d_n) \\ \sinh(jk_n \cos \theta_n d_n)/Z_n^\perp & \cosh(jk_n \cos \theta_n d_n) \end{bmatrix} \tag{5}$$

Therefore, the transmission matrix of the N-layered dielectric plane is the cascade of the transmission matrix of each layer

$$\begin{bmatrix} A & B \\ C & D \end{bmatrix} = \begin{bmatrix} A_1 & B_1 \\ C_1 & D_1 \end{bmatrix} \begin{bmatrix} A_2 & B_2 \\ C_2 & D_2 \end{bmatrix} \dots \begin{bmatrix} A_N & B_N \\ C_N & D_N \end{bmatrix} \tag{6}$$

Then, the conventional reflection and transmission coefficients of the multi-layered dielectric plane are determined by the network theory as [Ishimaru, 1991]

$$R_\perp = \frac{(A + B/Z_{N+1}^\perp) - Z_0^\perp(C + D/Z_{N+1}^\perp)}{(A + B/Z_{N+1}^\perp) + Z_0^\perp(C + D/Z_{N+1}^\perp)}$$

$$T_\perp = \frac{2}{(A + B/Z_{N+1}^\perp) + Z_0^\perp(C + D/Z_{N+1}^\perp)} \tag{7}$$

For the parallel polarization, the reflection and transmission coefficients can be determined by replacing the perpendicular effective impedance  $Z_n^\perp$  in (5-7) with the parallel effective impedance  $Z_n^\parallel$ , and the results are given by

$$\begin{aligned} R_{\parallel} &= \frac{(A + B/Z_{N+1}^\parallel) - Z_0^\parallel (C + D/Z_{N+1}^\parallel)}{(A + B/Z_{N+1}^\parallel) + Z_0^\parallel (C + D/Z_{N+1}^\parallel)} \\ T_{\parallel} &= \frac{2}{(A + B/Z_{N+1}^\parallel) + Z_0^\parallel (C + D/Z_{N+1}^\parallel)} \end{aligned} \quad (8)$$

As indicated in Fig.2, when a planar wave is propagating in the dielectric plane, the equivalent propagation constants of the equivalent transmission lines are only the longitudinal components of the propagation constants in the dielectrics, and the departure point is at  $A'_N$ . By tracing the ray in the dielectrics, it is clearly that the main route of the wave passing through the dielectric plane is  $A_0 A_1 \dots A_N$ , and the departure point of the wave on the back surface is at  $A_N$ . Therefore, there is a lateral displacement  $t$  between the incident point  $A_0$  and the departure point  $A_N$ .

In the  $n^{\text{th}}$  layer, the transmission distance of the wave in the lateral direction is

$$t_n = d_n \tan \theta_n \quad (9)$$

and the lateral component of the propagation constant is

$$k_n^\tau = k_n \sin \theta_n \quad (10)$$

From the Snell's law

$$k_0 \sin \theta_0 = k_1 \sin \theta_1 = \dots = k_n \sin \theta_n = \dots = k_N \sin \theta_N \quad (11)$$

we can get the lateral transmission phase shift in the  $n^{\text{th}}$  layer

$$\varphi_n^\tau = k_n^\tau t_n = k_n \sin \theta_n \cdot d_n \tan \theta_n = k_0 \sin \theta_0 d_n \tan \theta_n \quad (12)$$

For the N-layered dielectric plane, the total lateral phase shift from  $A_0$  to  $A_N$  is the sum of the phase shift in each layer

$$\begin{aligned} \varphi^\tau &= \varphi_1^\tau + \varphi_2^\tau + \dots + \varphi_N^\tau \\ &= k_0 \sin \theta_0 d_1 \tan \theta_1 + k_0 \sin \theta_0 d_2 \tan \theta_2 + \dots + k_0 \sin \theta_0 d_N \tan \theta_N \\ &= k_0 \sin \theta_0 (d_1 \tan \theta_1 + d_2 \tan \theta_2 + \dots + d_N \tan \theta_N) \\ &= k_0 \sin \theta_0 (t_1 + t_2 + \dots + t_N) \\ &= k_0 \sin \theta_0 t \end{aligned} \quad (13)$$

in which

$$t = d_1 \tan \theta_1 + d_2 \tan \theta_2 + \dots + t_N \tan \theta_N \quad (14)$$

In order to simulate the wave propagating through the dielectric plane more exactly, the lateral phase shift must be taken into consideration. Thus, we modify the transmission coefficient determined by the transmission line analogy with the following lateral phase factor

$$P^\tau = e^{-j\phi^\tau} = e^{-jk_0 \sin \theta_0 t} \quad (15)$$

Then, we get the modified transmission coefficient for the perpendicular polarization

$$T_{\perp}^m = T_{\perp} P^\tau = \frac{2}{\left(A + B/Z_{N+1}^{\perp}\right) + Z_0^{\perp} \left(C + D/Z_{N+1}^{\perp}\right)} e^{-jk_0 \sin \theta_0 t} \quad (16)$$

Whereas, for the parallel polarization, there is

$$T_{\parallel}^m = T_{\parallel} P^\tau = \frac{2}{\left(A + B/Z_{N+1}^{\parallel}\right) + Z_0^{\parallel} \left(C + D/Z_{N+1}^{\parallel}\right)} e^{-jk_0 \sin \theta_0 t} \quad (17)$$

### 2.3 Numerical and Experimental Results

In order to verify the modification of the transmission coefficient, an antenna-radome system at W-band is investigated experimentally. The measured radiation patterns are compared with the calculated results.

The conical radome is shown in Fig.3. The radome has a height of 200mm and a base diameter of 156mm. In the front part of the radome, there is a dome with the curvature radius of 8mm. This radome with the thickness of 5mm is made of Teflon. The permittivity of the dielectric is 2.1. A conical horn with the aperture diameter of 20mm is enclosed by the radome. The horn can rotate around the gimbal center, which is located at the base center of the radome. The antenna-radome system is operating at 94GHz.

When the antenna points to the axial direction of the radome, Fig.3 shows the radiation patterns of the antenna-radome system calculated with the modified transmission coefficient and the conventional one. The measured radiation patterns are also given in these figures. In Fig.3 (a), the calculated E plane radiation pattern with the conventional transmission coefficient is wider than the measured pattern, and the result of the modified one agrees with the measured pattern much better. In the H plane as given in Fig.3 (b), the modified transmission coefficient predicts the sidelobe level of the pattern precisely; however, the calculated radiation pattern with the conventional transmission coefficient has an error of 5dB comparing with the measured data.

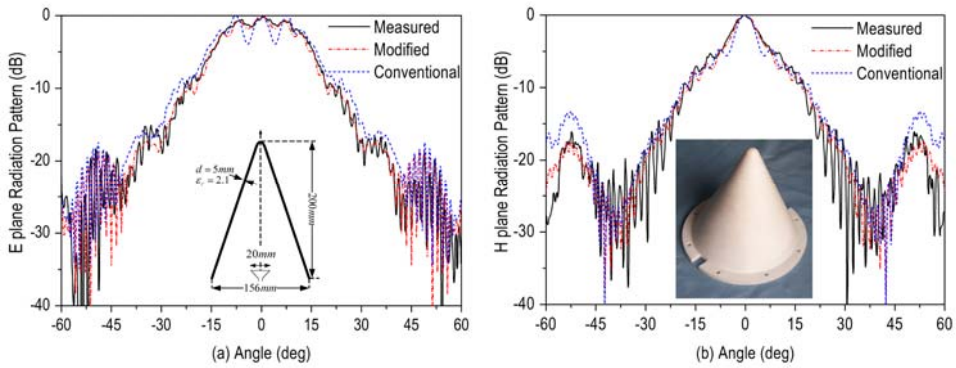


Fig.3. Measured and calculated radiation patterns of the conical horn enclosed by the conical radome: (a) E plane, (b) H plane.

Then, the antenna tilts  $10^\circ$  in the E plane and H plane respectively. The calculated radiation patterns with the two transmission coefficients and the measured results are illustrated in Fig.4. Comparing these radiation patterns, the patterns calculated with the modified transmission coefficient have good agreements with the measured results; however, there is an error of 7dB in the left sidelobe between the measured H plane pattern and the one calculated with the conventional transmission coefficient.

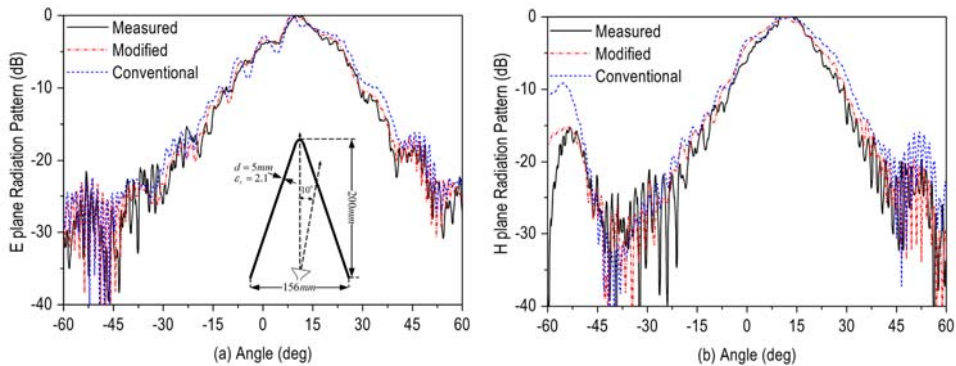


Fig.4. Measured and calculated radiation patterns of the conical horn enclosed by the conical radome when the horn tilts  $10^\circ$  in the E plane and H plane respectively: (a) E plane, (b) H plane.

### 3. Hybrid Method for Radome Analysis (Meng & Dou, 2009b)

#### 3.1 General Steps

As illustrated in Fig.5, the radome is divided into two parts: a) LF region with the length of  $L_{LF}$  from the vertex of the radome, in which there are complex structures. b) HF region, the



remainder portion of the radome with the length of  $L_{HF}$ , where the surface is smooth and the curvature radius is larger than the wavelength.

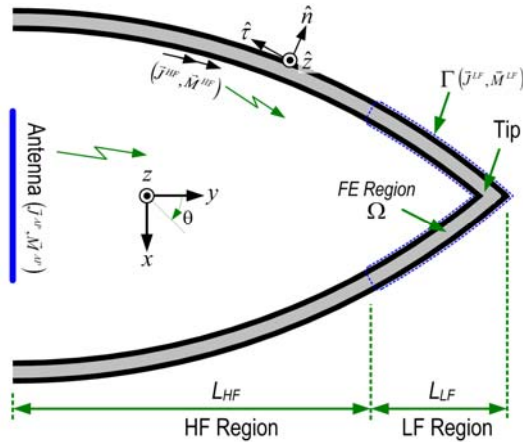


Fig. 5. Configurations of the electrically large A-sandwich tangent ogive radome

In the HF region, the radome surface is smooth and the curvature radius is much larger than the wavelength, so the assumption of locally planar dielectric can be adopted. The AI-SI method has been found very efficient and can get acceptable result for this structure. Firstly, the incident fields  $(\vec{E}_i, \vec{H}_i)$  on the inner surface of the radome are assumed only the radiation fields from the antenna as the traditional antenna-radome analysis [Abdel et al., 2001].

$$\begin{aligned} \vec{E}_i &= E_J(\vec{J}^{Ap}) + E_M(\vec{M}^{Ap}) \\ \vec{H}_i &= H_J(\vec{J}^{Ap}) + H_M(\vec{M}^{Ap}) \end{aligned} \tag{18}$$

where  $(\vec{J}^{Ap}, \vec{M}^{Ap})$  are the electric and magnetic currents on the aperture of antenna, and the operators  $E_J(\vec{J})$  and  $E_M(\vec{M})$  are defined as:

$$\begin{aligned} E_J(\vec{J}) &= -jk_0 Z_0 \int_S \vec{J} G(r, r') dr' \\ E_M(\vec{M}) &= \int_S \vec{M} \frac{\partial G(r, r')}{\partial n'} dr' \end{aligned} \tag{19}$$

in which  $S$  is the aperture of the antenna and  $G(r, r')$  is the 2D free space green's function. The operators  $H_M(\vec{M})$  and  $H_J(\vec{J})$  in (18) are duality of (19).

Then, the reflected fields  $(\vec{E}_r, \vec{H}_r)$  on the inner surface and the transmitted fields  $(\vec{E}_t, \vec{H}_t)$  on the outer surface of the radome can be determined by transmission line analogy as in [IP & Yahaya, 1998]. The equivalent currents on the inner surface of the HF region of the radome are determined by equivalence theorem as follows

$$\begin{aligned}\vec{J}^{HF} &= \hat{n} \times (\vec{H}_i + \vec{H}_r) \\ \vec{M}^{HF} &= -\hat{n} \times (\vec{E}_i + \vec{E}_r)\end{aligned}\quad (20)$$

and the currents on the outer surface are

$$\begin{aligned}\vec{J}^{HF} &= \hat{n} \times \vec{H}_i \\ \vec{M}^{HF} &= -\hat{n} \times \vec{E}_i\end{aligned}\quad (21)$$

where  $\hat{n}$  is the unit normal vector on the surface of the radome.

For 2D TM case, the electrical field  $E_z$  in the LF region satisfies the following Helmholtz equation

$$\begin{cases} \frac{\partial}{\partial x} \left( \frac{1}{\mu_r} \frac{\partial E_z}{\partial x} \right) + \frac{\partial}{\partial y} \left( \frac{1}{\mu_r} \frac{\partial E_z}{\partial y} \right) + k_0^2 \varepsilon_r E_z = 0 & \text{in } \Omega \\ \frac{1}{\mu_r} \frac{\partial E_z}{\partial n} = jk_0 Z_0 J_z & \text{on } \Gamma \end{cases}\quad (22)$$

where  $\Omega$  is the interior area of the FE region and  $\Gamma$  is its boundary.  $J_z$  is the unknown electric current on  $\Gamma$ .  $\varepsilon_r, \mu_r$  are the relative permittivity and permeability in  $\Omega$ . For the non-uniform region,  $\varepsilon_r, \mu_r$  are the functions of the position.

The field  $E_z$  can be solved by minimizing the following functional [Jin, 1993]

$$\begin{aligned}F(E_z) &= \frac{1}{2} \iint_{\Omega} \left[ \frac{1}{\mu_r} \left( \frac{\partial E_z}{\partial x} \right)^2 + \frac{1}{\mu_r} \left( \frac{\partial E_z}{\partial y} \right)^2 - k_0^2 \varepsilon_r E_z^2 \right] d\Omega \\ &+ jk_0 Z_0 \int_{\Gamma} E_z J_z d\Gamma\end{aligned}\quad (23)$$

As described in [Jin, 1993], the field  $E_z$  in  $\Omega$  is expanded in terms of finite element function defined in triangle and the electric current  $J_z$  is expanded using the triangular basis function. Applying the finite element analysis to (23), the linear equation of FEM is obtained as follows:

$$\begin{bmatrix} K_{II} & K_{IS} & 0 \\ K_{SI} & K_{SS} & B \end{bmatrix} \begin{bmatrix} E_I^{LF} \\ E^{LF} \\ J^{LF} \end{bmatrix} = \begin{bmatrix} 0 \\ 0 \\ 0 \end{bmatrix}\quad (24)$$

where  $K, B$  are the coefficient matrices,  $E_I^{LF}$  is the field in  $\Omega$  and  $E^{LF}, J^{LF}$  are the field and current on  $\Gamma$ , respectively.

The LF region can also be analyzed as a scattering problem. The scatter is the LF region of radome and the excitation is the radiation fields from the antenna and the PO currents on

HF region together. The electric field integral equation in the exterior of LF region is established as

$$\vec{E}^{LF} - E_J(\vec{J}^{LF}) - E_M(\vec{M}^{LF}) = \vec{E}_i \quad (25)$$

where  $\vec{J}^{LF}, \vec{M}^{LF}$  are the unknown currents on the boundary  $\Gamma$  and the incident field  $\vec{E}_i$  is sum of the following parts:

$$\vec{E}_i = E_J(\vec{J}^{Ap}) + E_M(\vec{M}^{Ap}) + E_J(\vec{J}^{HF}) + E_M(\vec{M}^{HF}) \quad (26)$$

in which  $E_J(\vec{J}^{Ap}), E_M(\vec{M}^{Ap})$  are the radiation fields from the aperture antenna and  $E_J(\vec{J}^{HF}), E_M(\vec{M}^{HF})$  are the fields radiated by the PO currents of the HF region.

Then, MoM is applied to equation (25). On the boundary  $\Gamma$  we have the relationship of

$$E^{LF} \hat{t} = E^{LF} \hat{z} \times \hat{n} = \vec{E}^{LF} \times \hat{n} = \vec{M}^{LF} = M^{LF} \hat{t} \quad (27)$$

So the currents  $J^{LF}, M^{LF}$  are expanded in terms of triangular basis functions and the Galekin's testing is employed. We obtain the following matrix equation:

$$\begin{bmatrix} P & Q \end{bmatrix} \begin{bmatrix} M^{LF} \\ J^{LF} \end{bmatrix} = [b] \quad (28)$$

where P, Q are the coefficient matrices of MoM and b is the excitation column.

As we have the relationship of (27) on the boundary  $\Gamma$ , we find that (24) and (28) have the same unknowns  $M^{LF}, J^{LF}$ . Combining the two equations together, we obtain the hybrid equation of PO-BI-FEM [Jin, 1993]

$$\begin{bmatrix} K_{II} & K_{IS} & 0 \\ K_{SI} & K_{SS} & B \\ 0 & P & Q \end{bmatrix} \begin{bmatrix} E_i^{LF} \\ M^{LF} \\ J^{LF} \end{bmatrix} = \begin{bmatrix} 0 \\ 0 \\ b \end{bmatrix} \quad (29)$$

Solving this hybrid equation, the currents  $J^{LF}, M^{LF}$  on the boundary  $\Gamma$  of the LF region are obtained. The currents  $J^{HF}, M^{HF}$  in HF region are already determined by PO modeling in (20) (21), then the far field radiation pattern of the antenna-radome system can be determined by integrating the currents over the outer surface of the radome.

In our former PO modeling, the incident fields (18) on the inner surface of the radome are assumed only the radiated fields from the antenna and the mutual interactions among the different parts of the radome are ignored. Actually, the equivalent currents  $\vec{J}^{LF}, \vec{M}^{LF}, \vec{J}^{HF}$ , and  $\vec{M}^{HF}$  on the surface of the radome will radiate for the second time (secondary radiation).

In order to take this high-order interaction into radome analysis, we modify the incident fields (18) on the inner surface of the radome by

$$\begin{aligned}\vec{E}_i &= E_J(\vec{J}^{Ap}) + E_M(\vec{M}^{Ap}) \\ &\quad + E_J(\vec{J}^{HF}) + E_M(\vec{M}^{HF}) + E_J(\vec{J}^{LF}) + E_M(\vec{M}^{LF}) \\ \vec{H}_i &= H_J(\vec{J}^{Ap}) + H_M(\vec{M}^{Ap}) \\ &\quad + H_J(\vec{J}^{HF}) + H_M(\vec{M}^{HF}) + H_J(\vec{J}^{LF}) + H_M(\vec{M}^{LF})\end{aligned}\quad (30)$$

These new incident fields are the sum of the fields from the antenna aperture and the surface currents on the radome. The other steps are the same as before and we repeat the antenna-radome analysis again. After the second iteration, the currents on the surface of the radome are updated and the radiation pattern is calculated again.

It can be predicted that the results of the second iteration are more accurate because of approximately considering the mutual interactions of the radome. In a similar way, we can determine the secondary radiation fields using the updated currents, and then we start the third iteration. The same process can be done for the fourth, fifth... iteration. As more iteration is done, the results will be more accurate; however, it will cost more time. Compromising between the accuracy and efficiency, when the results of two adjacent iterations have no significant difference, the iterative step can be stopped.

### 3.2 Numerical Results

Firstly, a moderate size A-sandwich tangent ogive radome is analyzed using the present IPO-BI-FEM and the results are compared with that of the full wave method to verify the validity of the method. The three-layered radome is  $17.3\lambda_0$  in length,  $20\lambda_0$  in based diameter with the thicknesses of  $0.08\lambda_0, 0.12\lambda_0, 0.08\lambda_0$  and dielectric relative permittivity of 4.0, 1.8, and 4.0, respectively. An antenna with the aperture diameter of  $5.5\lambda_0$  locates at the base center of the radome. The aperture currents are cosine distribution. The section with the length of  $L_{LF} = 2.5\lambda_0$  from the tip is chosen as the LF region and the other smooth portion of the radome is HF region.

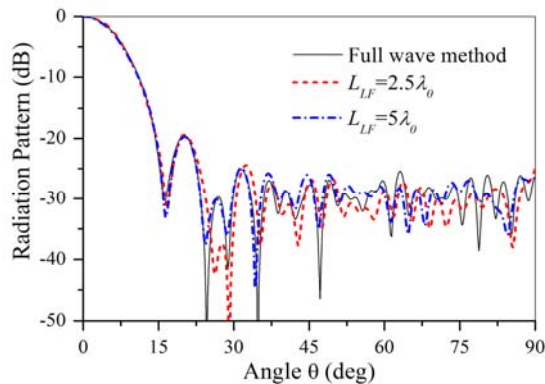


Fig.6. Radiation patterns of the A-sandwich tangent ogive radome determined by full wave method and IPO-BI-FEM with  $L_{LF} = 2.5\lambda_0$  and  $L_{LF} = 5.0\lambda_0$

The normalized radiation pattern of the antenna-radome system determined by IPO-BI-FEM after three iterations is given in Fig.6. The result determined by the full wave method is also shown as a comparison. It is clear that, the main lobe and first side lobe of the pattern determined by IPO-BI-FEM agree well with the full wave result, but some differences appear in the far side lobes. As in Fig.6, when the LF region extends to  $L_{LF} = 5.0\lambda_0$ , the second and third side lobes are also well predicted and the other side lobes are more close to the reference. It can be predicted that as the LF region becomes longer, the radiation pattern will agree better with the full wave result, but it will cost more time. When  $L_{LF}$  is set as the total length of the radome, the hybrid method becomes pure BI-FEM, which is a full wave method, and our reference result is obtained, but the efficiency is lowest. Considering the accuracy and efficiency of the hybrid method, setting  $L_{LF}$  about  $5\lambda_0$  from the tip is a compromise.

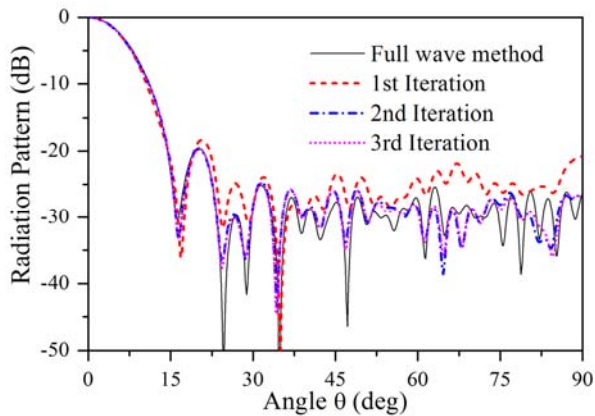


Fig. 7. Radiation patterns of the A-sandwich radome determined by the full wave method and IPO-BI-FEM in different iteration

Fig.7 shows the normalized radiation patterns of the tangent ogive radome in the three iterations when simulated using IPO-BI-FEM with  $L_{LF} = 5.0\lambda_0$ . It is seen that, the pattern of the first iteration has considerable differences with that determined by full wave method; however, the patterns of the second and third iteration are about the same and both agree very well with the reference result. As the mutual interactions of the radome are accounted in the last two iterations, this iterative use of the hybrid method indeed improve the accuracy of the result, but it need additional time for the iteration. In practical simulation, three iterations are enough to obtain the convergent results.

At the same time, IPO-BI-FEM only spends 31 minutes to simulate this moderate size radome; however, the full wave method takes about 4 hours and 10 minutes. A reduction in CPU time by a factor of 8 is reached. The improvement of efficiency of the present method is obvious. For electrically large radome, the efficiency of the present method will be much higher.

Then, an electrically large A-sandwich radome as in Fig.5 is analyzed as the first application. This radome is also tangent ogive shape with the electrically large size of  $100\lambda_0$  in length and  $80\lambda_0$  in base diameter. The thicknesses of the three layers are  $0.035\lambda_0$ ,  $0.33\lambda_0$  and  $0.035\lambda_0$ . The

three layers are low lossy dielectrics with the permittivity of 4.0, 1.8, 4.0 and loss tangent of 0.002, 0.001, and 0.002, respectively. An antenna with the diameter of  $20\lambda_0$  is located at the base center of the radome. The aperture distribution is cosine function. Two different LF region lengths ( $L_{LF} = 5.0\lambda_0, 10.0\lambda_0$ ) are chosen. This radome is simulated by IPO-BI-FEM with three iterations. The radiation patterns of this antenna-radome system are compared with the pattern of the antenna without radome in Fig.8. As we can see, when the radome is covered, there is an attenuation of 1.1dB in the maximal gain, a shoulder appears in the main lobe, and all the far side lobes are raised significantly. Comparing the radiation patterns determined with  $L_{LF} = 5.0\lambda_0$  and  $L_{LF} = 10.0\lambda_0$ , the main lobe and the first two side lobes are very close to each other, which verifies the convergence of IPO-BI-FEM.

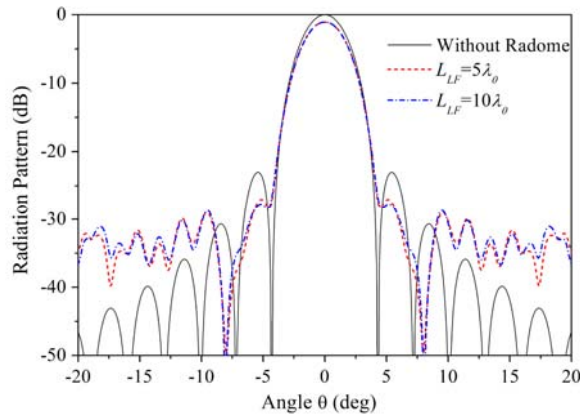


Fig. 8. Radiation patterns of the antenna without radome and with the electrically large A-sandwich tangent ogive radome when  $L_{LF} = 5.0\lambda_0$  and  $L_{LF} = 10.0\lambda_0$

For the antenna-radome system on high-speed aircraft, the radome always suffers from the rain erosion, especially in the tip region. In the purpose of overcoming this problem, a metallic cap is covered in the front of the radome to protect the radome (Fig.9). Unfortunately, very little open literature is available for accurately analyzing this complex radome [Kozakoff, 1997]. However, it can be analyzed easily by the presented hybrid method.

As in Fig.9, the radome with the length of  $86\lambda_0$ , base diameter of  $30\lambda_0$ , and thickness of  $0.32\lambda_0$  has a Von-Karman outer profile to satisfy the aerodynamic requirement. The metallic cap with the thickness of  $1.0\text{mm}$  is embedded in the front of radome to resist the rain erosion. A phase array antenna with 26 elements and element distance of  $6.5\text{mm}$  can rotate around the gimbal, which is  $200\text{mm}$  from the base center of the radome. The operating frequency is at Ka band.

In our model, the radomes with three different sizes of metallic cap are investigated. They are  $D_c = 0\text{mm}$  (means without metallic cap),  $12\text{mm}$ , and  $18\text{mm}$  respectively. The LF region is extended  $5\lambda_0$  from the cap. The radiation patterns of the antenna-radome system with different metallic caps are compared in Fig. 10. The radiation pattern of the array antenna without radome is also given as a reference. It is clear that, the radome without metallic cap

only induces an attenuation of  $0.4\text{dB}$  in the main beam and the sidelobe level rises from  $-27.3\text{dB}$  to  $-19.4\text{dB}$ . However, when the metallic cap with  $D_c = 12\text{mm}$  covered, the attenuation increases to  $1.1\text{dB}$  and all the sidelobe are raised significantly. As the metallic cap increasing to  $D_c = 18\text{mm}$ , an additional attenuation of  $0.6\text{dB}$  appears and the side lobes are much higher. This IPO-BI-FEM can analyze the effects of the metallic cap on the antenna-radome system accurately and conveniently.

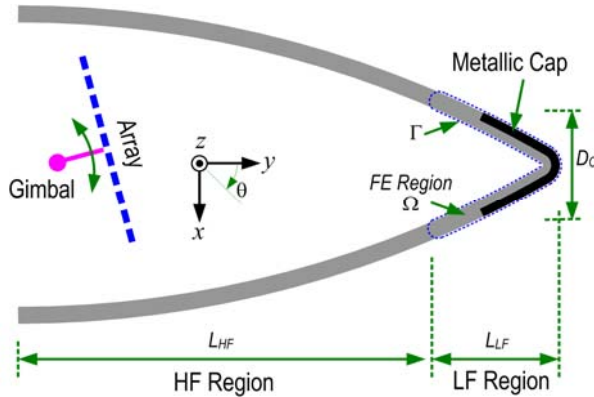


Fig. 9. Configurations of the electrically large Von-Karman radome with metallic cap

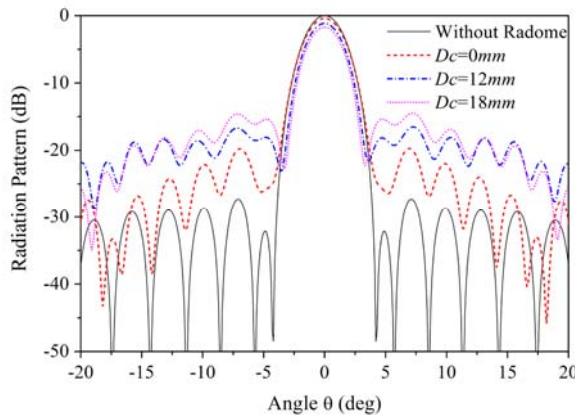


Fig. 10. Radiation patterns of the antenna-radome system with different metallic caps

Then the array antenna tilts with  $10^\circ$  to the left of the  $y$  axis. The radiation patterns of the antenna-radome system are given in Fig. 11. As we can see, when the antenna tilted, the metallic cap is removed from the main beam, the blockages of the cap and the high-order interactions between the metallic cap and radome are much smaller. Compared with the patterns in Fig.10, the influences of these radomes on the radiation patterns of the antenna are much smaller.

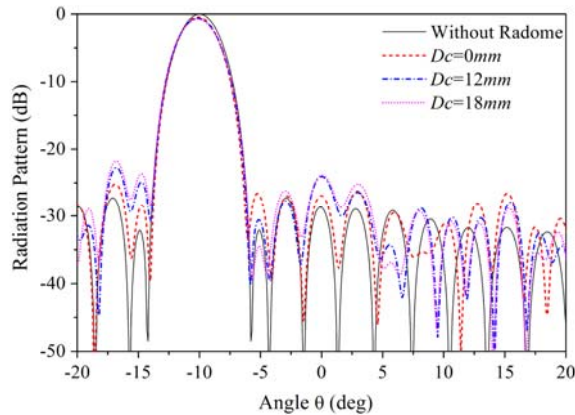


Fig. 11. Radiation patterns of the antenna-radome system when the antenna tilted with  $10^\circ$

## 4. Antenna-radome Optimization (Meng & Dou, 2008b)

### 4.1 General Steps

For the antenna-radome system in millimeter wave band, the electrical sizes of the radome are always very large. The high frequency method, such as RT method [Kozakoff, 1997] is very efficient and can get acceptable results, especially for radome with smooth surface. The RT method assumes that the fields radiate from the aperture of the antenna like a bunch of rays and transmit through the radome as the wall is locally plane at each intercept point. The fields outside the radome are obtained by accounting for the effects of the radome wall on the amplitude and phase of the propagation rays. The radiation performances of the antenna-radome system are determined by integrating the fields over the outer surface of the radome using Stratton-Chu formula.

As the radome wall has different transmission effects on different rays, the radiation patterns of the antenna-radome system are distorted. For the radome covered monopulse antenna, the gain loss of the sum radiation pattern is the power transmittance, and the angular difference between the null direction of the difference radiation pattern and the look angle of the antenna is the BSE induced by the radome. In order to improve the performances of the antenna-radome system, we can change the thicknesses of the radome wall at different parts to compensate the amplitude and phase distortion of the rays.

In general optimization of the radome, the thickness of the radome varies in the entire region [Hsu et al., 1993; Hsu et al., 1994; Nair & Jha, 2007]. However, the grind of this variable thickness radome is very laborious and the accuracy is difficult to control, especially for the electrically large radome in millimeter wave band. For the purpose of overcoming this problem, the region with variable thickness must be as small as possible. Thus, we propose the structure of local uniform thickness radome in the present work. The radome wall is described as below.

The A-sandwich wall consists of two high-density dielectric skins separated by a low-density core having a lower relative permittivity than the skins. The thickness profile  $d(z)$  of the local uniform thickness A-sandwich radome is expressed as the following piecewise function:



$$d(z) = 2d_s + \begin{cases} d_1 & 0 \leq z < z_1 - \lambda \\ f_1(z) & z_1 - \lambda \leq z < z_1 + \lambda \\ d_2 & z_1 + \lambda \leq z < z_2 - \lambda \\ f_2(z) & z_2 - \lambda \leq z < z_2 + \lambda \\ d_3 & z_2 + \lambda \leq z \leq L \end{cases} \quad (31)$$

where  $d_s$  is the thickness of the skin layers,  $d_1$ ,  $d_2$ , and  $d_3$  are the thicknesses of the core layer in the three local uniform regions,  $z_1$ ,  $z_2$  are the locations of the transitional regions as in Fig.12 (a).  $\lambda$  is the wavelength in free space and  $L$  is the total length of the radome. The thickness profile of the radome wall is guaranteed to be smooth by the function  $f_1(z)$ ,  $f_2(z)$  in the transitional regions:

$$\begin{aligned} f_1(z) &= d_1 + \frac{d_2 - d_1}{4\lambda^2} (z - z_1 + \lambda)^2 - \frac{d_2 - d_1}{4\lambda^3} (z - z_1 + \lambda)^2 (z - z_1 - \lambda) \\ f_2(z) &= d_2 + \frac{d_3 - d_2}{4\lambda^2} (z - z_2 + \lambda)^2 - \frac{d_3 - d_2}{4\lambda^3} (z - z_2 + \lambda)^2 (z - z_2 - \lambda) \end{aligned} \quad (32)$$

Compared with the transitional length ( $2\lambda$ ), the thickness changes (from  $d_1$  to  $d_2$  or from  $d_2$  to  $d_3$ ) in the transitional region are very small and the curvature radius of the radome wall is very large, so the RT method is still applicable. The 3D radome is a body of revolution (BOR) by revolving the thickness profile of the radome around the  $z$  axis.

In the optimization process, we employ GA to find the best thicknesses at different parts of the radome. GA is a global optimization method and is more and more popular in electromagnetic engineering [Weile & Michielssen, 1997]. The variables  $d_s$ ,  $d_1$ ,  $d_2$ ,  $d_3$ ,  $z_1$ ,  $z_2$  of the local uniform thickness radome are chosen as the optimal parameters and the objects are to minimize the maximum BSE and maximize the minimum power transmittance when the antenna scans in the desired angle of azimuth (AZ) and elevation (EL) planes. The objective function  $ObjF$  of the GA model is defined as:

$$ObjF = \min_{d(z)} \left\{ \max_{\theta} [BSE(\theta, d(z))] \right\} + \max_{d(z)} \left\{ \min_{\theta} [PTrans(\theta, d(z))] \right\} \quad (33)$$

Where  $\theta$  is the scanning angle in the two planes.  $\min\{f\}$ ,  $\max\{f\}$  are the minimum and maximum of the function  $f$ .  $BSE(f)$ ,  $PTrans(f)$  are the BSE and power transmittance of the desired radome, respectively.

## 4.2 Numerical Results

The configuration of our antenna-radome system is illustrated in Fig.12 (a). The outer profile of the radome is a Von-Karman curve to satisfy the aerodynamic requirement and the inner surface varies with the thickness profile. The radome with the length of  $86\lambda_0$  and the base diameter of  $30\lambda_0$  covers a waveguide slot antenna with a circular aperture. The aperture is divided into four parts to form the sum and difference patterns in the AZ and EL plane, respectively. The antenna can rotate from  $-30^\circ$  to  $+30^\circ$  in the two main planes around the gimbal, which is 200 mm away from the base center of the radome, and the radius of rotation is 50 mm. The two skin layers of the A-sandwich radome have the dielectric with relative permittivity of  $\epsilon_r = 6.0$  and loss tangent of  $\tan \delta = 0.002$ . The core layer is made of foam with  $\epsilon_r = 1.2$  and  $\tan \delta = 0.001$ . The antenna-radome system works at Ka band.

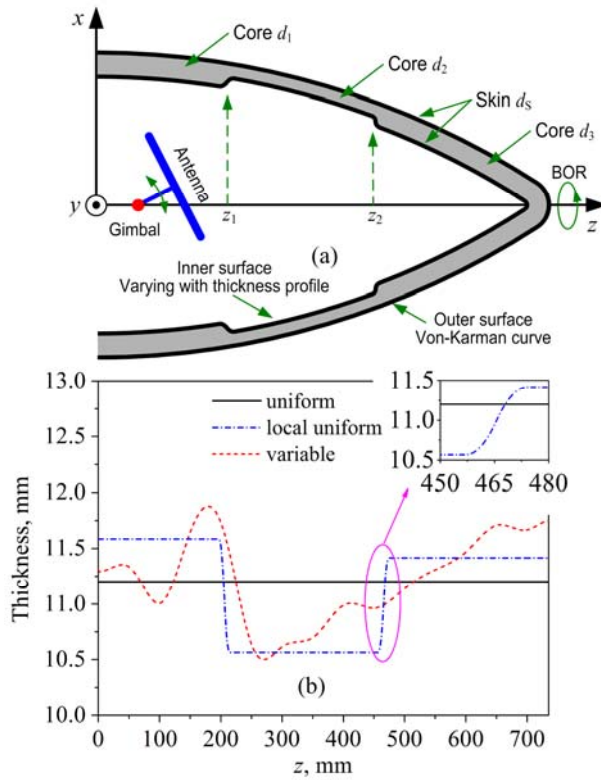


Fig. 12. (a) Configuration of the antenna-radome system, (b) thickness profiles of the uniform, local uniform thickness, and variable thickness radome

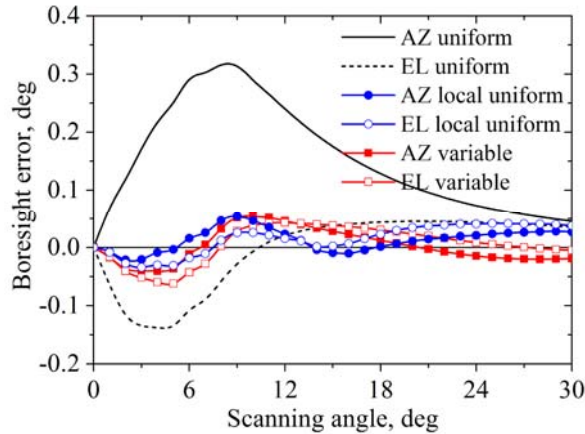


Fig. 13. Bore sight errors of the uniform, local uniform thickness, and variable thickness radome in AZ and EL plane

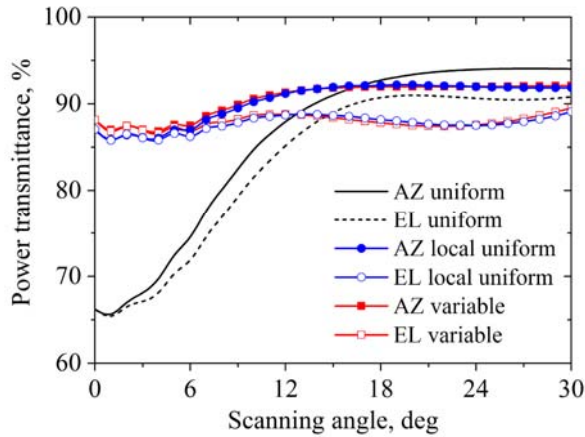


Fig. 14. Power transmittances of the uniform, local uniform thickness, and variable thickness radome in AZ and EL plane

As an example, the proposed structure of local uniform thickness is adopted for the radome optimization. The thicknesses  $d_s$  of two skin layers are limited between 1.7 mm and 2.0 mm, the thicknesses of the core layer in the three local regions can vary from 6.5 mm to 8.5 mm, and the positions of the two transitional regions are constrained as  $0 < z_1 < z_2 < 86\lambda_0$ . After optimization by the multi-objective GA, the optimal thickness profile of the local uniform thickness radome is shown in Fig.12 (b), and the BSE and power transmittance against the scanning angle are given in Fig.13-14. As a reference, the BSE and power transmittance of a uniform thickness radome with the skin thickness of  $d_s=1.85$  mm and uniform core thickness of  $d_c=7.5$  mm are also shown in Fig.13-14. Compared with the results of uniform thickness radome, the maximal BSE of the optimal antenna-radome system is reduced from  $0.30^\circ$  to  $0.05^\circ$  and the minimal power transmittance is increased from 66% to 86%. In the entire scanning range, the changes of the BSE and power transmittance are more slowly, which is more favorable for the radar tracing system. The above results verify the validities of the local uniform thickness radome and the multi-objective optimization model.

The variable thickness optimization described in [Hsu et al., 1994] is also implemented as a comparison. The thicknesses of the skin and core layers are restricted the same as the local uniform optimization. The thickness profile of the optimal radome is shown in Fig.12 (b) and the BSE and power transmittance are also given in Fig.13-14. It is clear that the present local uniform thickness radome obtains the similar BSE and power transmittance as the variable thickness optimization; however, the proposed radome keeps being uniform in most parts of the radome and the thickness only varies in two very small regions, which is easier to be fabricated than the variable thickness radome.

## 5. Conclusion

As the development of millimeter wave technology, the millimeter wave antenna-radome systems have been used more and more popular. In this chapter, we mainly concentrate on the methods for radome analysis and design. The general AI-SI method is modified to

improve the accuracy of millimeter wave radome analysis. The hybrid IPO-BI-FEM method is proposed to deal with the radome with small complex structures. Also, the GA combined with the RT method is adopted to optimize the BSE and power transmittance of the millimeter wave radome. All these methods have been verified validity by the numerical and experimental results. Some analysis and design examples are given.

## 6. Acknowledgment

This work is supported by the National Natural Science Foundation of China under grant 60571028.

## 7. References

- Abdel Moneum M. A., Shen Z. X., Volakis J. L. and Graham O. (2001), Hybrid PO-MoM Analysis of Large Axi-Symmetric Radomes, *IEEE Trans Antennas Propagat* 49, 1657-1666.
- Arvas E., Rahhalarabi A., Pekel U. and Gundogan E. (1990), Electromagnetic transmission through a small radome of arbitrary shape, *Microwaves, Antennas and Propagation, IEE Proceedings H*, 137(6), 401-405.
- Einzig P. and Felsen L. (1983), Ray annalysis of two-dimensional radomes, *IEEE Transactions on Antenna and Propagation*, 31(6), 870-884.
- Fu wen-bin, Chen Zhong-kuan, and Chang Yi-tao, (2005)“Multi-objective optimization of electric performance of sandwich antenna radome wall using genetic algorithm”, *Chinese Journal of Radio Science*, Vol.20, No.3, pp.289-294.
- Gao X. J. and Felsen L. B. (1985), Complex ray analysis of beam transmission through two dimensional radomes, *IEEE Transactions on Antenna and Propagation*, 33(9), 963-975.
- Gomez-Revuelto I., Garcia-Castillo L. E., Salazar-Palma M., and Sarkar T. K. (2005), Fully coupled hybrid-method FEM/high-frequency technique for the analysis of 3D scattering and radiation problems, *Microwave Opt Tech Lett* 47, 104-107.
- Gordon R. K. and Mittra R. (1993), Finite element analysis of axisymmetric radomes, *IEEE Trans Antennas Propagat* 41, 975-981.
- Hsu Fang, Chang Po-Rong, and Chan Kuan-Kin (1993), “Optimization of two-dimensional radome boresight error performance using simulated annealing technique,” *IEEE Trans. Antennas Propag.*, Vol.41, No.9, pp.1195-1203.
- Hsu Fang, Chan Kuan-Kin, Chang Po-Rong, and Chao S. H. (1994), “Optimal boresight error design of radomes of revolving symmetry”, *Electron. Lett.*, Vol.30, No.19, pp.1561-1562.
- Han D. H., Polycarpou A. C., and Balanis C. A. (2002), Hybrid analysis of reflector antennas including higher order interactions and blockage effects, *IEEE Trans Antennas Propagat* 50, 1514-1524.
- Ishimaru A. (1991), *Electromagnetic wave propagation, radiation, and scattering*, (NJ: Prentice Hall, Englewood Cliffs, , pp.31-76.
- Ip H. P. and Yahya Rahmat-Samii (1998), Analysis and characterization of multilayered reflector antennas: Rain/Snow accumulation and deployable membrane, *IEEE Transactions on Antenna and Propagation*, 46(11), 1593-1605.

- Jin J. M. (1993), *The finite element method in electromagnetics*, New York, Wiley.
- Kozakoff D. J. (1997), *Analysis of radome-enclosed antennas*, (Artech House, Boston London).
- Kong J. A. (1986), *Electromagnetic wave theory*, (Wiley-Interscience, New York).
- Lu C. C. (2003), A fast algorithm based on volume integral equation for analysis of arbitrarily shaped dielectric radomes, *IEEE Transactions on Antennas and Propagation*, 51(3), 606-612.
- Mark J. Povinelli and John D'Angelo (1991), Finite element analysis of large wavelength antenna radome problems for leading edge and radar phased arrays, *IEEE Transactions on Magnetics*, 27(5), 4299-4302.
- Meng H. F. Dou W. B. and Yin K. (2008a), Analysis of Antenna-Radome System at Millimeter Wave Band, 2008 Global Symposium on Millimeter Waves Proceeding, *GSMM 2008*, pp.380-383.
- Meng H. F. and Dou W. B. (2008b), Multi-objective optimization of radome performance with the structure of local uniform thickness, *IEICE Electronics Express*, Vol.5, No.20, pp.882-887.
- Meng H. F., Dou W. B., Chen T. T. and Yin K. (2009a), Analysis of radome using aperture integration-surface integration method with modified transmission coefficient. *Journal of Infrared Millimeter and Terahertz Waves*, Vol.30, No.2, pp.199-210.
- Meng H. F. and Dou W. B. (2009b), Hybrid IPO-BI-FEM for the analysis of 2D large radome with complex structure, *Microwave and Optical Technology Letters*, Vol.51, No.5, pp.1348-1353.
- Nair R. U. and Jha R. M. (2007), "Novel A-sandwich radome design for airborne applications", *Electron. Lett.*, Vol.43, No.15, pp. 787-788.
- Paris D. (1970), Computer-aided radome analysis, *IEEE Transactions on Antennas and Propagation*, 18(1), 7-15.
- Rudge A. W. et al. (1983), *The handbook of antenna design*, (Peter Pergrinus Ltd., London,), Vol.2 pp. 457-553.
- Tricoles G. (1963), Radiation patterns of a microwave antenna enclosed by a hollow dielectric wedge, *Journal of Optical Society of America*, 53(5), 545-557.
- Tzoulis A. and Eibert T. F. (2005), A hybrid FE-BI-MLFMM-UTD method for numerical solutions of electromagnetic problems including arbitrarily shaped and electrically large objects, *IEEE Trans Antennas Propagat* 53), 3358-3366.
- Volakis John L. and Shifflett James A. (1997), CADDRAD: A physical optics radar/radome analysis code for arbitrary 3D geometries, *IEEE Antennas and Propagation Magazine*, 39(6), 73-79.
- Wu D. C. F. and Rudduck R. C. (1974), Plane wave spectrum-surface integration technique for radome analysis, *IEEE Transactions on Antenna and Propagation*, 22(3), 497-500.
- Weile D. S. and Michielssen E. (1997), "Genetic algorithm optimization applied to electromagnetics: a review", *IEEE Trans. Antennas Propag.*, Vol.45, No.3, pp.343-353.
- Walter D. Burnside and Ken W. Burgener (1983), High Frequency Scattering by a thin lossless dielectric slab, *IEEE Transactions on Antenna and Propagation*, 31(1), 104-110.



# Design of dielectric lens antennas by multi-objective optimization

Yoshihiko Kuwahara † and Takashi Maruyama ‡

† *Shizuoka University*, ‡ *NTT Japan*

## 1. Introduction

Lens antennas are a promising device for realizing the anti-collision radars needed in intelligent transport systems (ITS) and multibeam antennas for satellite communication. They have simple structure, high gain and no feed blockage. Especially if the operating frequencies are above the microwave band, the resulting apertures with several tens of wavelengths, become practical.

In advance ITS application, the antenna is expected to resolve several objects in azimuth plane. In satellite application, the terrestrial station should catch multiple satellites at various directions. These applications demand multibeam antennas.

Typical antennas with multibeam attributes include the dual-reflector bifocal antenna (Rao, 1974). Another proposal is the bifocal lens (Brown, 1956), its multibeam characteristics has been evaluated (Peebles, 1988). Multibeam antennas have to form high gain and low sidelobe radiation patterns at different directions. The bifocal lens is guaranteed to equalize the aperture phase distribution on the specified design directions in the scanning plane. However, it is not guaranteed on the transverse plane due to its astigmatism, and no previous report has adequately addressed the design issues, especially the resulting degradation of the radiation pattern. Another multibeam lens antenna is the Luneburg lens (Luneburg, 1964). Though it offers many focal points at arbitrary directions, it has manufacturing problems, tapered dielectric constant, and heavy weight.

Our solution is to propose an effective method that optimizes multibeam lens antennas by gain, beamwidth, and sidelobe level. Antenna designs based on GA are very attractive and various methods have been proposed (Altshuler & Linden, 1997; Jones & Joines, 1997); we have already proposed a Yagi-Uda antenna design based on the pareto-GA (Kuwahara, 2005).

This chapter presents the design of a multibeam lens antenna based on the pareto-GA. The coordinates of the lens shape and the feed position are given as variables and are associated with GA chromosomes. From the variables, the radiation patterns are calculated. The values of the objective functions are evaluated from the radiation pattern. The objective functions are given as the gain and the sidelobe level on the scanning plane and the transverse plane. To balance these objective functions, we adopt the pareto-GA (Fonseca & Fleming, 1993). In the pareto-GA, individuals are ranked through multiple objective functions and selection

and crossover are carried out. To obtain rapid convergence, elitist preserving selection (Jong, 1975) is applied. As a result, various lenses that offer well balanced performance including the gain-tuned lens and the sidelobe level-tuned lens are obtained.

For the collision avoidance radar in the short range, it is necessary to search targets over wide angle in the azimuth plane. In addition, considering the road inclination, the beamwidth in the elevation plane should be wide enough so as not to miss any of the targets. That is, the antenna should form multibeam with the fan beam in the elevation plane. To achieve such characteristics, we introduce the elliptical aperture. We demonstrate the proposed method can balance three objects; the desired beam width in the elevation plane in addition to multibeam with high gain and low sidelobe levels.

## 2. Multi-objective Optimization by the Genetic Algorithm

### 2.1 Overview

The Genetic algorithm (GA) is one of the techniques used for solving the optimization problem under specified constraint conditions. The antenna is designed to obtain structural parameters that satisfy the requirements of various performances such as gain, beam width, largest side lobe level, and input impedance. In the case of an optimization method such as the steepest gradient method, it is difficult to apply a suitable initial parameter because structural parameters have complex influences on antenna performances. The GA is very attractive because it can globally obtain optimal solutions (Haupt & Haupt, 1998; Rahmat-Samii & Michielessen, 1999; Werner & Mittra, 2000; Alshuler & Linden, 1997; Jones & Joines, 1997).

Using the GA, the structural parameters of the Yagi-Uda antenna were optimized. And the gain, backlobe, and input impedance obtained by the GA and the values obtained by the steepest gradient method were compared (Jones & Joines, 1997). They have reported that the design parameters obtained by the GA yield better performances than those obtained by the gradient method. In their paper, the objective function of the GA is expressed by weighting the sum of a large number of objective functions to optimize multiple performances. In other words, the multi-objective optimization problem was transformed into a simple optimization problem with a single objective function. Although the weight determination method was not mentioned in their paper, it can be considered that they have repeatedly conducted computer experiments using empirical values.

The Pareto GA addresses a multi-objective optimization problem with a Pareto-optimal set (non-dominated solutions) in a very efficient manner (Fonseca & Fleming, 1993) since it can obtain a Pareto-optimal set in a single trial of a numerical simulation. Recently, the Pareto GA has been applied to the electromagnetic field and antenna design. The multi-layer microwave absorbers were optimized and the trade-off between reflectivity and thickness were studied (Weile et al., 1996; Weile & Michielssen, 1997). Further, they applied the Pareto GA to the array antenna with digital phase shifters for a low beamwidth and side lobe level (Weile & Michielssen, 1996). Furthermore, the feed circuits of a wing mounted Log-Periodic monopole array were optimized (Fisher et al., 1999). In their paper, the trade-off among the field degradation, feed reflection, and feed inefficiency over the operating band has been investigated. Electrically small planar antennas with an inductively coupled feed structure were designed (Choo & Ling, 2003). In this case, the trade-off between the efficiency-bandwidth product and the antenna size has been discussed.



We have also introduced the Pareto GA into the Yagi-Uda antenna design. In order to ensure diversity in Pareto-optimal solutions, individual fitness values selected by the Pareto ranking (Fonseca & Fleming, 1993) were corrected using fitness sharing (Horn et al., 1994). In addition, the elitist preserving selection process (Jong, 1975) was applied to accelerate convergence. We have demonstrated that the Pareto GA was able to search various Pareto-optimal solutions in a single trial of the GA process including the relatively small number of generations, and that it was a design method that was able to solve a multi-objective optimization problem such as the Yagi-Uda antenna design in a highly efficient manner.

## 2.2 Various multi-objective optimization

### (1) Transforming a Multiobjective Optimization Problem into a Single Objective Optimization Program.

In order to apply the conventional GA to a multi-objective optimization problem, this method weighs multi-objective functions and combines them linearly to form a single-objective function that is to be solved. Assuming that the parameter vector  $x$  represents the structure of an antenna, the antenna is designed to determine the  $x$  that minimizes the side lobe level  $SLL(x)$ , maximizes the gain  $G(x)$ , and achieves an input impedance  $Z(x)$  of approximately  $50 \Omega$ . Thus, the objective function  $y$  expressed by Equ. (1) is maximized to solve a single-objective optimization problem.

$$y = aG - b|50 - \text{Re}(Z(x))| - c|\text{Im}(Z(x))| - dSLL(x) \quad (1)$$

where  $a$ ,  $b$ ,  $c$ , and  $d$  are positive weight constants. The only guiding principles for determining their values are to increase  $a$  when priority is given to the gain, to increase  $b$  and  $c$  when priority is given to the impedance matching, and to increase  $d$  when priority is given to the side lobe level. In order to obtain Pareto-optimal solutions, the GA process should be attempted for several combinations of weight constants ( $a$ ,  $b$ ,  $c$ , and  $d$ ). The process of determining the weight constants has not been mentioned in literature (Alshuler & Linden, 1997; Jones & Joines, 1997). Accordingly, previous studies might have determined the weight constants by numerical experiments, resulting in a less efficient calculation.

### (2) VEGA (Scaffer, 1985)

The algorithm of VEGA (Vector Evaluated GA) begins with the selection of individuals that are to be left behind for the next generation, with every objective function to form a new population. It then carries out crossover and mutation processes following the random selection of individuals on the basis of the size of the original population from which the new population is generated. Although VEGA does not require uniquely undeterminable weight constants, such as  $a$ ,  $b$ ,  $c$ , and  $d$ , which are used in Equ. (1), it has difficulties in obtaining various Pareto-optimal solutions. These difficulties are due to the fact that the Pareto-optimal solutions obtained by VEGA have a tendency of lying very close to each other in solution space.

### (3) Pareto GA

In order to efficiently obtain various Pareto-optimal solutions in a single trial of the GA process, we apply the Pareto GA. Further, the elitist preserving selection process is applied for rapid convergence.

#### 1) Pareto GA

The VEGA is a non-Pareto approach that selects every objective function of the individuals. On the other hand, Pareto ranking is a Pareto approach that selects on the basis of the merits and demerits of the solutions from among the Pareto-optimal solutions.

The Pareto ranking procedure for optimizing two objective functions is shown in Fig. 1. The horizontal and vertical axes of Fig. 1 indicate the values of the objective functions 1 and 2, respectively. The further the point of the objective function is from the origin, the larger is its value. The white circle represents the set of values of the objective functions 1 and 2, which is a function of each individual  $x_i$ . The ranking of the Pareto-optimal solution in the group is assigned as 1. As regards the individuals that are not Pareto-optimal solutions, the ranking is lowered by the number of individuals that are dominated by others. The individual denoted by 1 in Fig. 1 is a Pareto-optimal solution. The ranking of individual E is 2 because it is dominated by individual B. The ranking of G is also 2 because it is dominated by individual C in a similar manner. The ranking of F is 3 because it is dominated by individuals B and C. The ranking of individual H is 5 because it is dominated by individuals B, C, E, and F. When the Pareto ranking is applied, the fitness  $f(x_i)$  of an individual  $x_i$  is expressed by Equ. 2.

$$f(x_i) = \frac{1}{N_i} \quad (2)$$

where  $N_i$  is the ranking of an individual  $x_i$ , which is obtained by the Pareto ranking.

## 2) Elitist preserving selection

The following methods are examples of individual selection schemes after crossover.

- (1) SGA (Simple GA), by which children are unconditionally chosen after crossover.
- (2) ER (Elitist Recombination), by which two individuals whose fitness is higher than the others are chosen from among four individuals, two parents and two children.
- (3) Elitist preserving selection, by which individuals are chosen on the basis of the original population size in a descending order of fitness from among all the individuals of two generations, before and after the crossover.

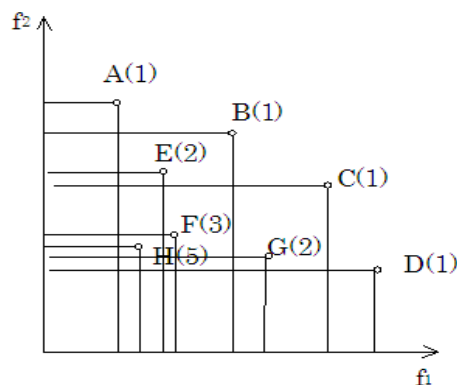


Fig. 1. Pareto Ranking

The elitist preserving selection scheme accelerates convergence because the population after the crossover consists of individuals with higher fitness. According to our numerical experiments, elitist preserving selection causes acceleration in the convergence speed that is several times higher than the SGA.

### 3. Design of dielectric lens antennas by Pareto Genetic Algorithm

#### 3.1 Radiation Pattern of the Lens Antenna

##### (1) Basic Theory

To calculate the radiation pattern of a lens antenna, it is necessary to obtain the amplitude distribution and the phase distribution on the aperture. These are calculated by means of ray tracing (Tajima, 2004). The ray tracing model is shown in Fig. 2. Here the inner side of the lens is defined as the first plane and outer side is defined as the second plane. The feed is placed away from the center axis of the lens. In this situation, the whole lens plane is swept by ray tracing to obtain the amplitude and the phase distribution as  $E(x,y)$  and  $\Theta(x,y)$ , respectively.  $\Theta(x,y)$  is given by,

$$\Theta(x,y) = -k l_e(x,y) \tag{3}$$

$$l_e(x,y) = l_1(x,y) + ref l_2(x,y) + l_3(x,y), \tag{4}$$

where,  $k$  is the wavenumber,  $l_e(x,y)$  is the path length from the feed to the aperture plane, and  $ref$  is the refractive index of the lens. From the power conservation law, the power incident to the first plane is preserved at the aperture plane. The calculation involves multiplying the power density by its associated area. Thus  $E(x,y)$  can be calculated from the next relation (Lee, 1988).

$$D_0(\theta_0) dS = E(x,y)^2 dS' \tag{5}$$

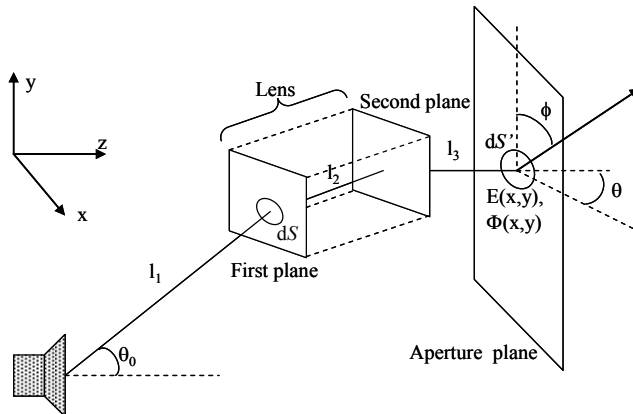


Fig. 2. Ray tracing model

The left term represents the incident power to the lens.  $D_0(\theta_0)$  is the feed power pattern, and  $\theta_0$  is the angle from the direction of the normal to the feed aperture.  $dS$  is a small area that is perpendicular to the ray.  $dS'$  is the projection of  $dS$  on the aperture plane. The radiation pattern,  $E_r(\theta, \phi)$ , is calculated by the next formula.

$$E_r(\theta, \phi) = \iint E(x, y) \exp(j\Theta(x, y) + jk(x \sin(\theta) + y \cos(\phi))) \, dydx \tag{6}$$

$\phi$  is the angle from the  $x$ -axis on the  $xy$ -plane and  $\theta$  is the angle from the  $z$ -axis on the plane including  $\phi$ .

**(2) Single Focal Lens**

We describe an analysis for a single focal lens. The coordinate system is shown in Fig.3.  $P_1(n)$  and  $P_2(n)$  denote coordinates of first and second plane in the cross section including the lens' center axis. Rotating symmetry around the center axis is assumed for the lens. When ray tracing from Feed(1) to the reference plane for each path is carried out, all phase should be arranged on the reference plane. The reference plane is set above second plane. All coordinates are decided so as to satisfy with Equ. (7).

$$l_e(n) = \text{const} \quad (n=1 \cdots N) \tag{7}$$

Fig.4 shows a ray tracing example for the plano-convex lens. The second plane coordinates are decided so as to satisfy Equ. (7) and Snell's law. At  $z=25$  (the reference plane), all path lengths are the same and all paths are parallel. The radiation pattern is also shown Fig.5.

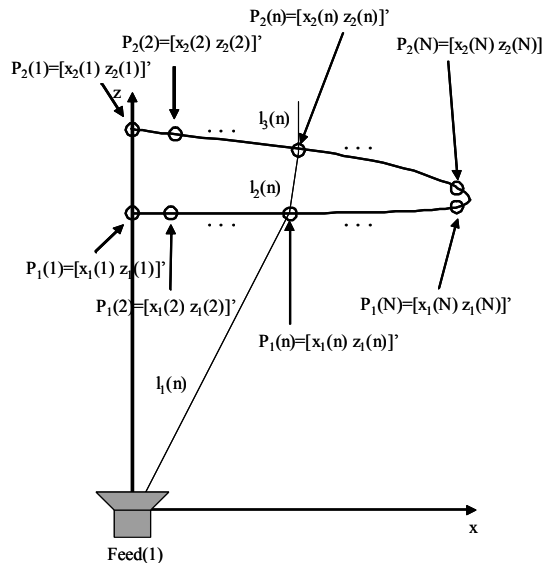


Fig. 3. The coordinate system for analysis

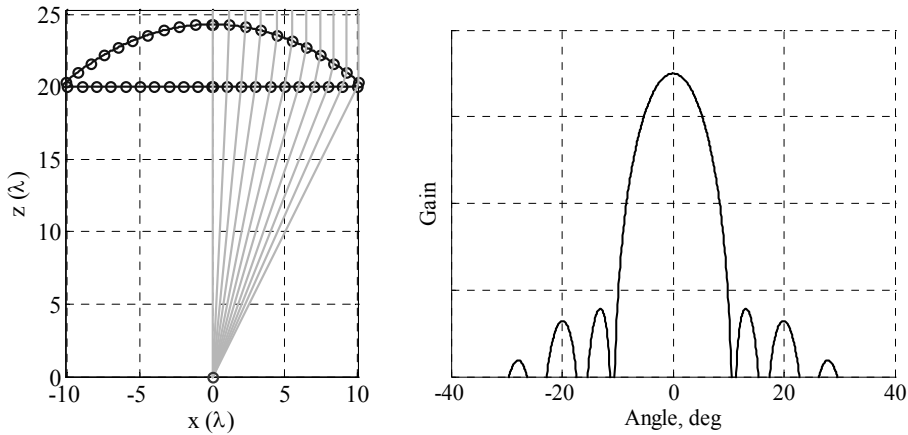


Fig. 4. Ray tracing example for the single focal lens and its radiation pattern

Then, we describe how to decide the focal points.  $z_1(1)$  in  $P_1(1)$  is determined so as to maximize the radiation efficiency. The radiation efficiency  $\eta$  of the space feed antenna is expressed by Eq.(8).

$$\eta = \frac{8}{\tan^2 \Phi} \frac{n_0 + 1}{(n_0 - 1)^2} \left\{ 1 - (\cos \Phi)^{\frac{n_0 - 1}{2}} \right\}^2 \tag{8}$$

The feed power pattern is assumed by,

$$D_0(\theta_0) = 2(n_0 + 1) \cos^{n_0}(\theta_0) \tag{9}$$

where  $n_0$  is a power index, and  $\theta_0$  is an angle from the centre axis.  $\Phi$  is the angle between the z-axis and the line from the origin to the lens edge. When the aperture size is fixed,  $\Phi$  is becomes a function of  $z$ , We assume  $D_0(\theta_0)$  in both the E-plane and H-plane is the same. Fig.5 shows the radiation efficiency in case of  $n_0=20$ . When  $\Phi=28^\circ$ ,  $\eta$  is maximized.  $z_1(1)$  can be determined by the aperture radius and  $\Phi$ .

**(3)Bifocal lens**

We briefly explain the design of a bifocal lens; the results of (Peebles, 1988) are used.  $P_1(1)$  was determined so that the efficiency on the z-axis was maximized. The initial parameters,  $P_1(1)= 19.9\lambda$ , the thickness  $T_b=5.25\lambda$  and the scanning angle  $\alpha=20^\circ$  are given, all lens coordinates can be calculated iteratively. Fig. 6 shows a ray tracing example for the bifocal lens. First,  $P_2(1)$  is determined by the Snell’s law so that the ray direction from left focal point takes a after passing through the lens. Second, after a ray incident to  $P_2(1)$  from  $-\alpha$  is assumed,  $P_1(2)$  is determined so as to arrive to right focal point through the lens. These procedures are carried out iteratively.

The focal point of  $xz$ -plane and  $yz$ -plane differs due to astigmatism. The focal point on the scanning plane is

$$R = F \cos^2(\theta) , \tag{10}$$

where  $F$  is focal length. The focal point on the transverse plane is

$$R = F. \tag{11}$$

The focal point of  $xz$ -plane and  $yz$ -plane differs due to astigmatism. Because the phase on the transverse plane is not considered, the radiation pattern may be degraded.

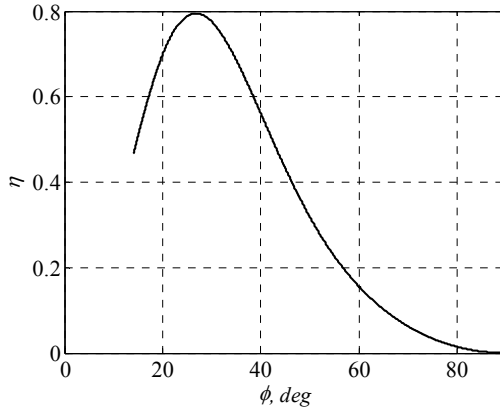


Fig. 5. Radiation efficiency ( $n_0=20$ )

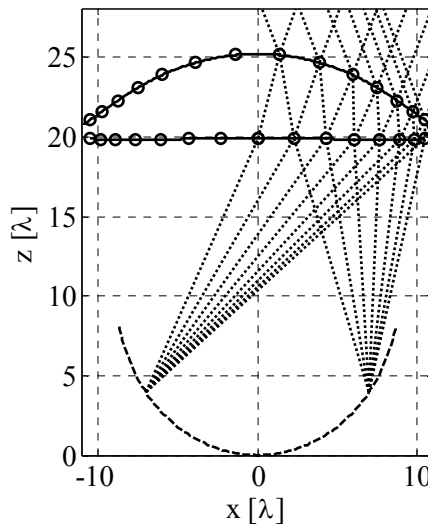


Fig. 6. Bifocal lens

### 3.2 Design of the lens for the multi-beam antenna

In this section, we discuss a multibeam antenna which forms 7 beams in the azimuth plane. The beam interval is  $10^\circ$ . That is, the beam directions are  $-30^\circ, -20^\circ, \dots, 30^\circ$ . Our objective is to achieve several candidates for performance (gain and sidelobe level) trade off. Where, the lens structure is assumed to be rotating symmetry, and we examine 4 beams taking into account of symmetric multibeam in the azimuth plane.

#### (1) Design procedures

In our approach, the initial shape of lens is determined so as to yield a single focal lens. Next, the shape of the lens is modified so as to obtain the multibeam characteristics. The modifying values are given by the chromosomes. The positions of the feeds are also determined from the chromosomes. The radiation pattern of each structure is calculated and evaluated by the pareto ranking method. The individuals and the calculation procedure are shown in Fig. 7. The lens configuration considering the multibeam goal is also shown in Fig. 7.

First of all,  $P_1(1)$  is defined.

$$P_1(1)=[0 \ z_1(1)+\Delta z_1(1)]' \tag{12}$$

When Feed(1) is placed at the origin,  $z_1(1)$  in  $P_1(1)$  is determined so as to maximize the radiation efficiency.  $z_1(1)$  is the value yielded by the maximization of the radiation efficiency.  $\Delta z_1(1)$  is the correction value derived from the individuals. Though the optimized lens including  $\Delta z_1(1)$  may not offer maximum efficiency, it offers better performance from the viewpoint of the multibeam characteristics.

The coordinates of the first plane that starts from  $P_1(1)$  are determined. The interval, in the  $x$ -direction, of each  $P_1(n)$  is constant,  $\Delta x_1$ . The difference, in the  $z$ -direction, from the previous point is defined as  $\Delta z_1(n)$ . Accordingly,  $P_1(n)$  is expressed by the following recursion.

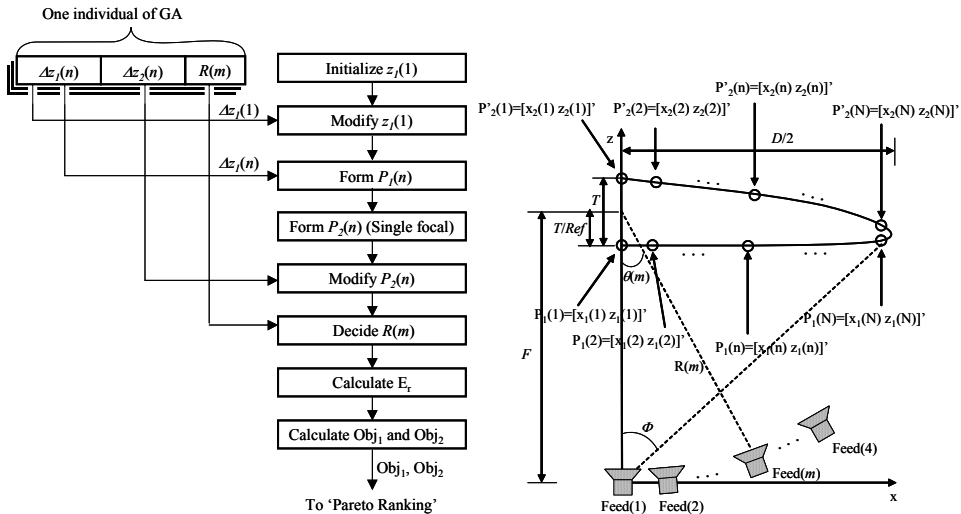


Fig. 7. Calculation procedure and lens configuration

$$P_1(n) = \begin{bmatrix} x_1(n-1) + \Delta x_1 \\ z_1(n-1) + \Delta z_1(n) \end{bmatrix} \quad (2 \leq n \leq N) \quad (13)$$

$\Delta z_1(n)$  are derived from the individuals. Referring to  $P_1(n)$ , the coordinates of the second plane are determined so that a single focal lens can be formed. The criterion of the path length is satisfied when the ray from the feed (1) to  $P_1(N)$  becomes parallel to the  $z$ -axis after refraction at the lens. Considering this path length and the refraction at the first plane, all  $P_2(n)$  can be determined so that  $l_e(x,y)$  is constant. The result is a single focal lens with modified first plane.

Next,  $P_2(n)$  are modified to  $P'_2(n)$  to obtain the desired multibeam characteristics. Similar to  $P_1(n)$ ,  $x_2(n)$  in  $P_2(n)$  are unchanged and  $z_2(n)$  are modified to  $z'_2(n)$ .

$$P'_2(N) = [x_2(N) \ z_2(N) + \Delta z_2(N)]^T \quad (14)$$

$$P'_2(n) = \begin{bmatrix} x_2(n) \\ z_2(n) + \Delta z_2(n) + z'_2(n+1) - z_2(n+1) \end{bmatrix} \quad (N-1 \geq n \geq 1) \quad (15)$$

$\Delta z_2(n)$  are also derived from the individuals.  $\Delta z_2(n) + z'_2(n+1) - z_2(n+1)$  represents the accumulation of correction value from the lens edge. Equ.(15) can gradually change toward the lens centre. The result is a lens with both planes modified.

Feed (2) is placed on the line formed by  $\theta(2) = 10^\circ$ . When the lens thickness on  $z$ -axis is  $T$ , the intersection point between the  $z$ -axis and  $R(m)$  is defined as  $T/ref$  from  $P_1(1)$  (Rao, 1974). Feed (3) and Feed (4) are placed at 20 and 30 degrees, respectively. Each feed is directed to  $P_1(1)$  to reduce the spillover. The focal lengths have yet to be determined. Because the focal point of  $xz$ -plane and  $yz$ -plane differs due to astigmatism, GA decides the focal lengths. The guesses of  $R(m)$  are calculated from (Brown, 1956). The focal point on the scanning plane is

$$R(m) = F \cos^2(\theta(m)) \quad (m = 1 \dots 4), \quad (16)$$

where  $F$  is the focal length shown in Fig. 7. The focal point on the transverse plane is

$$R(m) = F \quad (m = 1 \dots 4), \quad (17)$$

From (16) and (17), the search range of feed locations is determined. The positions are also derived from the individuals to obtain better performance.

To evaluate the modified lens performance, the radiation patterns of the designed shapes are calculated by Equ.(6). Here, three cross sections for the pattern calculation are defined. They are shown in Fig.8, Fig.8(a) is the scanning plane pattern:  $\varphi=0^\circ$  and  $\theta$  is swept on the  $xz$ -plane. It is named  $E_{m}(\theta)$ . Fig.8(b) is the transverse plane pattern:  $\Theta_{90}$ , newly defined, is swept on the vertical plane from the  $xz$ -plane, including the maximum radiating direction as  $\theta_m$ ,  $\theta_1=0^\circ$ ,  $\theta_2=10^\circ$ , and so on. It is named  $E_{r_m}(\Theta_{90})$ . Fig.5(c) is the  $45^\circ$  cut plane from the  $xz$ -plane, and includes the maximum radiating direction of each feed. It is named  $E_{r_m}(\Theta_{45})$ .



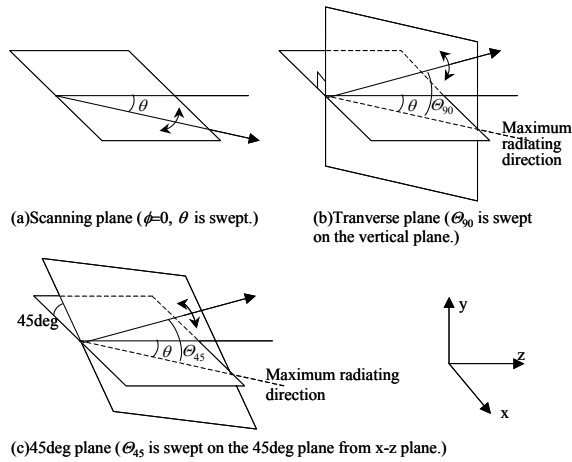


Fig. 8. Coordinate system for calculating the radiation pattern

Two objective functions for evaluating the obtained patterns  $Er_m(\theta)$ ,  $Er_m(\Theta_{90})$  and  $Er_m(\Theta_{45})$  are defined. The first object is the minimum gain on the desired angle  $\theta_m$  ( $m=1, \dots, 4$ ) of each feed.

$$Obj_1 = \min[Er_m(\theta_m)] \quad (m = 1 \dots 4) \quad (18)$$

The second object is the minimum value of the ratio between the gain and the sidelobe level (SLL).

$$Obj_2 = \min[Er_m(\theta_m)/SLL(Er_m(\theta)) \quad Er_m(\theta_m)/SLL(Er_m(\Theta_{90})) \quad Er_m(\theta_m)/SLL(Er_m(\Theta_{45}))] \quad (m = 1 \dots 4) \quad (19)$$

$SLL(\cdot)$  represents the calculated value of the maximum sidelobe level. The shoulder of the mainlobe at which the polarity of 2nd order difference for directivity change is included in this sidelobe level. The first element in Equ.(19) represents the ratio on the scanning plane. The second element represents the ratio on the transverse plane. The third element represents the ratio on 45°cut plane. Equ. (18) and (19) are evaluated for all individuals.

Though we calculated the results using Equ. (18) and (19), lens configuration satisfying other performance requirements can be achieved by changing or adding objective functions; for example, the objective function for every feed can be defined individually, the sidelobe condition is defined on the scanning plane and the transverse plane separately instead of Equ.(19), or the beamwidth is defined as the objective function.

## (2) Numerical simulation

### A. Simulation Model

The validity of the proposed method is demonstrated in this section. The simulation conditions are shown in Table 1. The lens coordinates on the x-axis are defined up to  $10.5\lambda$  to obtain accurate refraction at the lens edge, i.e.,  $N$  is set to 22.

Calculation of all possible combinations of the chromosomes is impractical since  $2^{376}$  combinations (about  $10^{113}$ ) would have to be assessed. On the other hand, our procedure with GA yields improved performance quickly. Mutation probability was gradually reduced by the convergence of the results. The radiation pattern of the feed with the normalized gain of 0dB is shown in Fig. 9. The two broken lines represent the lens edges for Feed (1) in Fig. 7.

Elements	Values
Lens aperture diameter $D$	$20\lambda$
Refractive index $Ref$	1.6
Interval of $x_1(n)$ ( $=\Delta x_1$ )	$0.5\lambda$
Number of $x_1(n)$ $N$	22
Range of $\Delta z_1(1)$	$\pm 1\lambda$
Range of $\Delta z_1(n)$ ( $n \neq 1$ ), $\Delta z_2(n)$	$\pm 0.05\lambda$
Distance between lens and feed $R(m)$	Min: $F\cos(\theta(m))$ Max: $F$
Exponential index of feed $n_0$	20
Initial coordinate of first plane $z_1(1)$	$19.9\lambda$
Number of individual	40
Number of elements composing one individual	47 (22 for $P_1(n)$ , 22 for $P_2(n)$ , 3 for $R(m=2,3,4)$ )
Number of bits for each element	8 (256 levels)
Number of bits in one individual	376 ( $=47 \times 8$ )
Number of generations	100
Mutation probability	Start: 0.2 End: 0.1
Crossover probability	0.01

Table 1. Simulation conditions

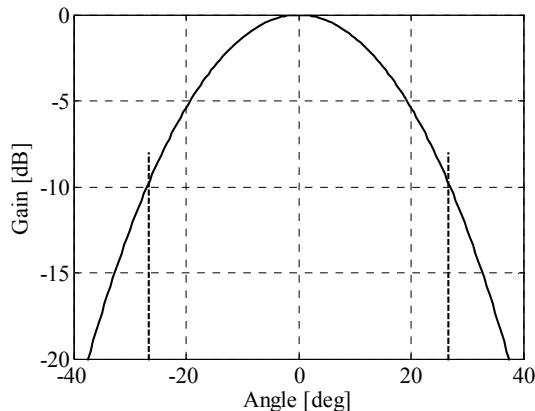


Fig. 9. Characteristics of the feed

### B. Results

The calculation result is shown below. The values of objective functions Equ. (18) and (19) at the final generation are shown in Fig. 10. The circles in this figure represent each individual's performance. The asterisk shows the performance of the bifocal lens with the same diameter lens and feed characteristics. From Fig. 10, we can see that the pareto-optimal solutions offer high gain and/or low sidelobe level and each individual was diffused.

Individual A in Fig. 10 is pareto-optimal. It has almost the same sidelobe level as the bifocal lens and its gain is improved by 1.7dB. It has well balanced characteristics. Individual B is also pareto-optimal. Its design targeted the sidelobe level. Though it seems that the sidelobe level was lowered from the bifocal lens in our criterion, the sidelobe performance is almost the same with the bifocal lens for practical use. This is explained later by using the radiation pattern. Individual C, also pareto optimal, was designed for enhanced gain. These characteristics are listed in Table 2.

1) *Individual A* : With regard to individual A, the lens shape and the radiation pattern are demonstrated. The lens shape and feed positions are shown in Fig. 11. The lens shape was almost plano-convex. The radiation patterns in the scanning plane, the transverse plane and 45deg-cut plane are shown in Fig. 12, respectively. Solid lines are the characteristics of the proposed lens. Broken lines are for the bifocal lens. In figures for the transverse plane and 45deg-cut plane, each feed was offset by 10 degrees, and the original peak occurs at  $\Phi=0$ deg. Note that the patterns of each feed are not on the same plane.  $\theta$  of each feed is rotated as shown in Fig. 8. The radiation pattern on the 45deg-cut plane had characteristics

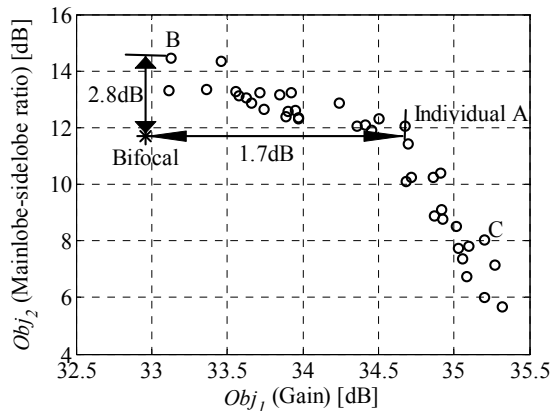


Fig. 10. Two objective functions at final generation

Individual	$Obj_1$	$Obj_2$
A	<b>34.7</b>	12.1
B	33.1	<b>14.5</b>
C	35.2	8.0
(Bifocal)	33.0	11.7

Table. 2. Characteristics of three individuals and bifocal lens

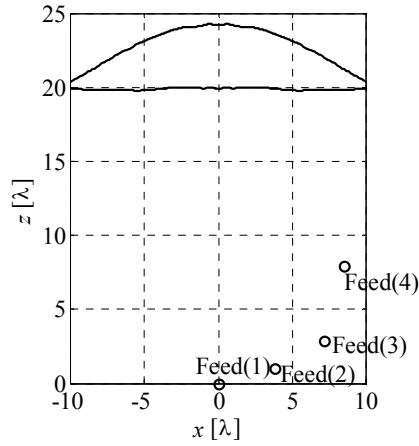


Fig. 11. Lens shape and feed position of individual A

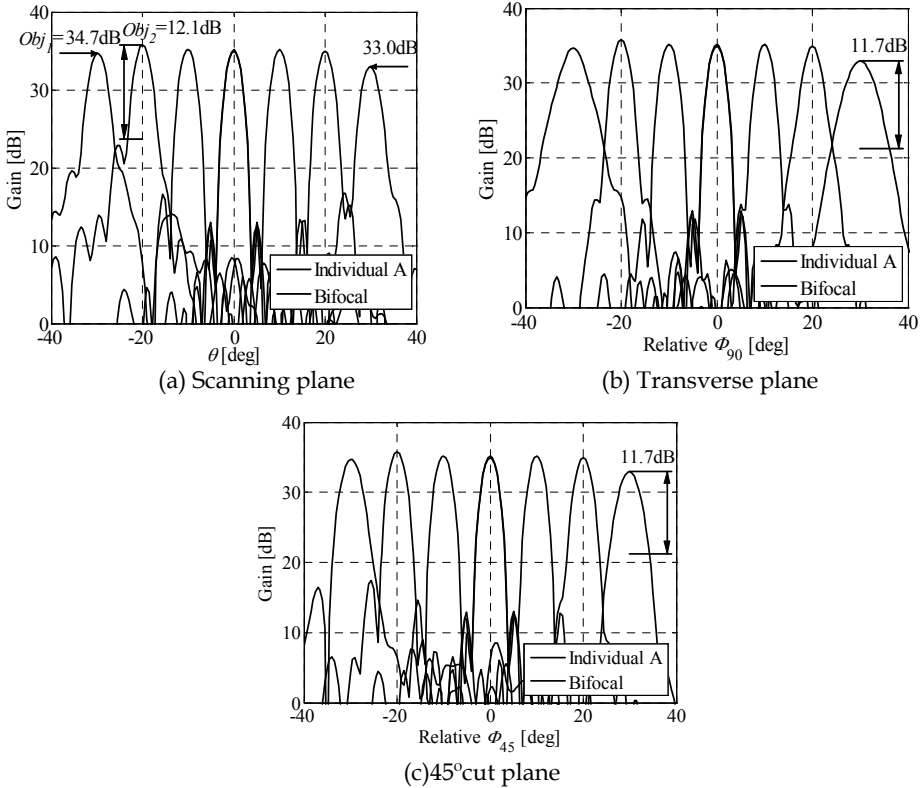


Fig. 12. Radiation pattern of individual A

intermediate between those on the scanning plane and those on the transverse plane.  $Obj_2$  for individual A appeared in the radiation pattern of feed(3) on the scanning plane. On the other hand, that of the bifocal lens appeared in the radiation pattern of feed(4) on the transverse plane. In both cases, the small shoulder of the mainlobe was detected as the sidelobe. While the sidelobe level is almost the same, the gain of the proposed lens is significantly improved.

2) *Individual B* : With regard to individual B, the lens shape and the feeds position and the radiation pattern are shown in Fig. 13 to 14, respectively. The pattern on the 45deg-cut plane was omitted because  $Obj_2$  did not appear on the plane. Individual B was designed for improved sidelobe level.  $Obj_2$  appeared in the radiation pattern of feed (4) on the transverse plane. Compared to the bifocal lens, it seems to have almost the same gain and improved sidelobe level. The worst sidelobe level in the case of bifocal lens is always identified as a shoulder in the main lobe. The shoulder is very difficult to identify by visual inspection

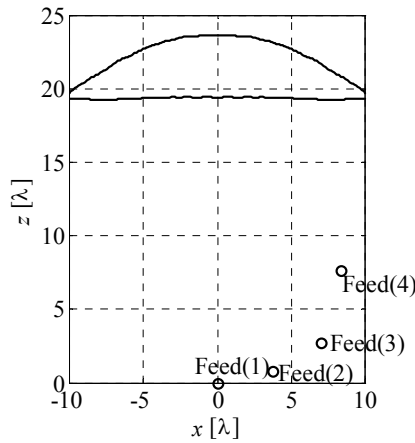


Fig. 13. Lens shape and feed position of individual B

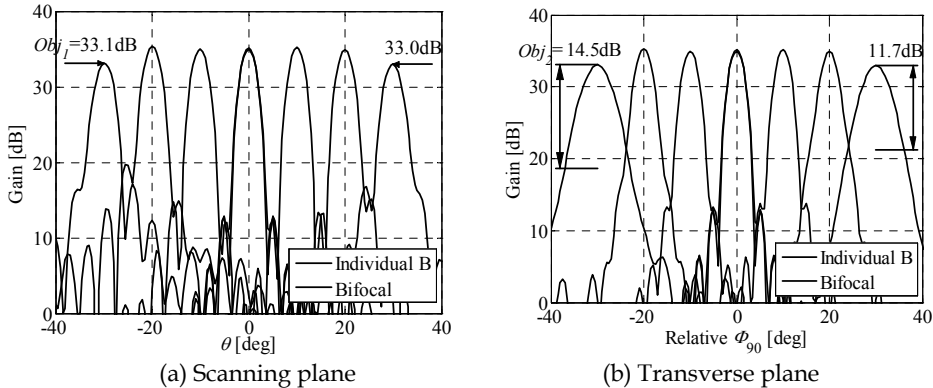


Fig. 14. Radiation pattern of individual B

since it is associated to a 2nd order polarity change for directivity. Such a sidelobe on that beam is not very dangerous for practical use.

3) *Individual C* : With regard to individual C, the lens shape and the radiation pattern are shown in Fig. 15 to 16, respectively. In exchange for a rise of the sidelobe level in feed(4), the gain of feed(4) is improved up to the same extent as the other feeds.

### 3.3 Design for the collision avoidance radar antenna

In this section, we examine the collision avoidance radar. In order to avoid detecting miss due to the road inclination, it is necessary to form vertical fan beam. Also, in order to detecting miss in the azimuth plane, it is necessary to overlap adjacent 2 beams. That is, we should reduce the pattern loss. Fig. 17 shows the requirements in this case. Each feed is placed at interval of  $10^\circ$ . The negative side display is symmetrical and so is omitted.

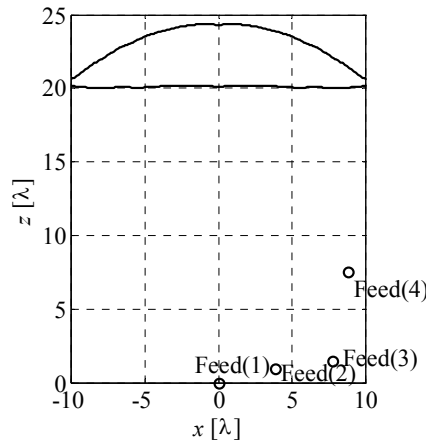


Fig. 15. Lens shape and feed position of individual C

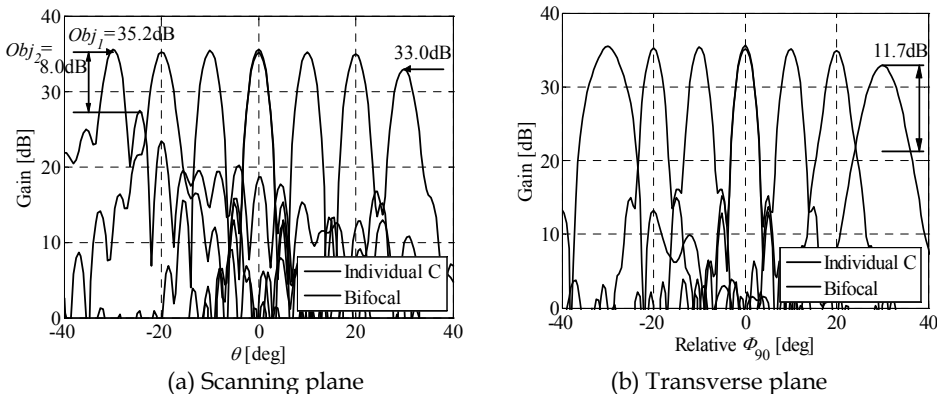


Fig. 16. Radiation of individual C

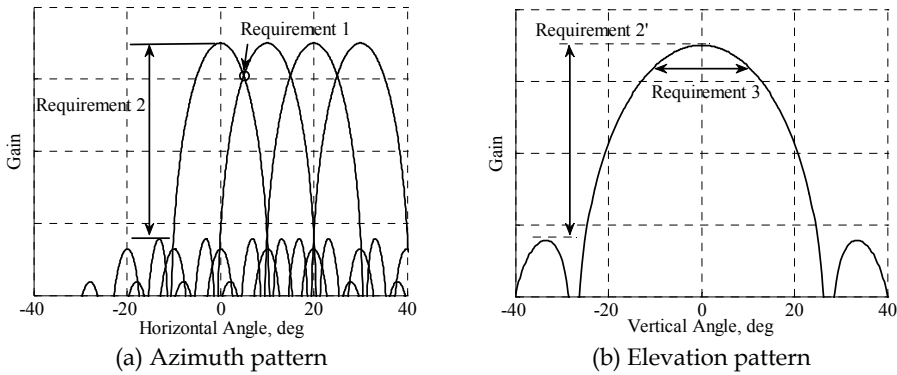


Fig. 17. Requirements of the radiation pattern

First requirement is high gain including pattern loss; the gain should be as large as possible. This can be achieved by using a large aperture but this narrows the beamwidth. If the beamwidth was smaller than that shown in Fig. 17(a), deep nulls may appear at intermediate angles between the peaks;  $5^\circ$ ,  $15^\circ$  and  $25^\circ$ . This must be avoided because it could lead to the failure to detect targets. Accordingly, it is preferable that the mainlobes created by adjacent feeds overlap. Because the minimum detection sensitivity is determined by the gain at the overlap point rather than maximum gain, we aim to maximize the gain at the overlap angle. This is shown in Fig. 17(a), Requirement 1. This value is determined by the aperture size, focal length and radiation pattern of the feed. The second requirement is the suppression of the sidelobe level, see Fig. 17(a), Requirement 2. This requirement can be satisfied by tapering the electric field of the aperture, which reduces the edge taper level. This technique can be realized by moving the feed array closer to the lens or narrowing the beam of each feed. However, the gain and/or radiation efficiency should be considered. The requirement in the elevation plane is similar to that in the azimuth plane, see Fig. 17(b), Requirement 2'. The beamwidth in the elevation plane is the third requirement, see Fig. 17(b), Requirement 3. A certain value is required to ensure adequate coverage in the vertical plane. Because the beamwidth and the gain conflict, these requirements should be balanced.

### (1) Design procedures

Basic procedure is the same as preceding section. However, in order to form the vertical fan beam, the aperture is cut off elliptically. Therefore, the minor and major axis are added to chromosomes as new gene. The chromosome structure, calculation procedure and lens configuration are shown in Fig. 18.

In this case,  $P_1(1)$  is also defined by chromosome. Because it is considered that the optimum focal length exists on the midpoint between the optimum for the circular aperture with major axis and that with the minor axis.

$$P_1(1) = [0 \ z_1(1) + \Delta z_1(1)]^T \quad (20)$$

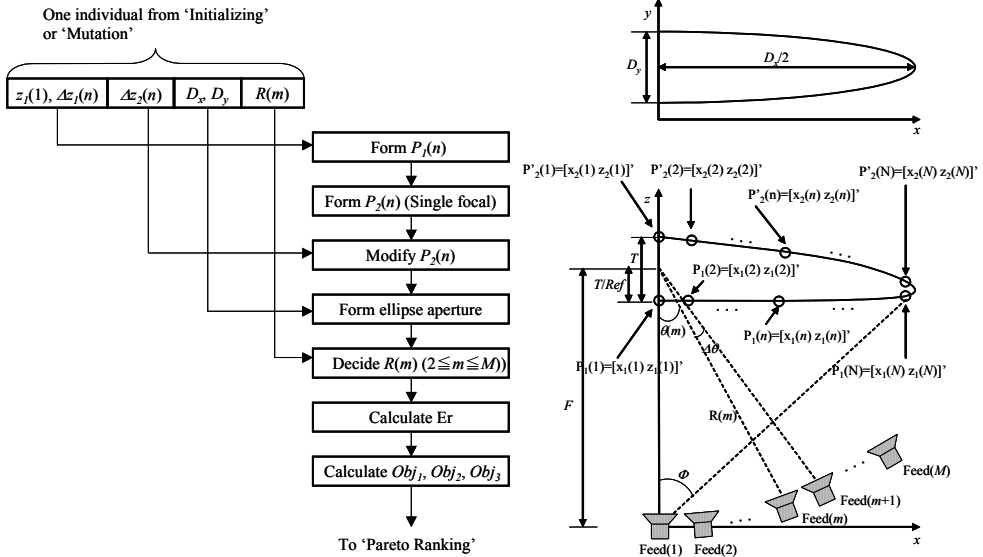


Fig. 18. Calculation procedure and lens configuration

$\Delta z_1(1)$  is the correction value derived from the individuals. Applying  $\Delta z_1(1)$  can yield superior results in multibeam antenna design. The coordinates of the first plane that starts from  $P_1(1)$  are determined. The interval, in the  $x$ -direction, of each  $P_1(n)$  is constant,  $\Delta x_1$ . The difference, in the  $z$ -direction, from the previous point is defined as  $\Delta z_1(n)$ . Accordingly,  $P_1(n)$  is expressed by the following recursion.

$$P_1(n) = [x_1(n-1) + \Delta x_1 \quad z_1(n-1) + \Delta z_1(n)]^T \quad (2 \leq n \leq N) \quad (21)$$

$\Delta z_1(n)$  are derived from the individuals. Referring to  $P_1(n)$ , the coordinates of the second plane  $P_2(n)$  are determined so that a single focal lens can be formed. The result is a single focal lens with modified first plane. Next,  $P_2(n)$  are modified to  $P'_2(n)$  to obtain the desired multibeam characteristics. Similar to  $P_1(n)$ ,  $x_2(n)$  in  $P_2(n)$  are left and  $z_2(n)$  are modified to  $z'_2(n)$ .

$$P'_2(N) = [x_2(N) \quad z_2(N) + \Delta z_2(N)]^T \quad (22)$$

$$P'_2(n) = [x_2(n) \quad z_2(n) + \Delta z_2(n) + z'_2(n+1) - z_2(n+1)]^T \quad (N-1 \geq n \geq 1) \quad (23)$$

$\Delta z_2(n)$  are also derived from the individuals. By rotating the cross section made by  $P_1(n)$  and  $P_2(n)$  around  $z$  axis, form of lens is achieved.

Feed (2), (3), (4) are placed on the line formed by  $\theta(2) = 10^\circ, 20^\circ$  and  $30^\circ$ , respectively. Each feed is directed to  $P_1(1)$  to reduce the spillover. The focal lengths are also derived from the individuals to obtain better performance.



To investigate the beam width in the elevation plane and the pattern loss in the azimuth plane, the major axis  $D_x$ , and the minor axis  $D_y$  of the lens are incorporated into the chromosome as the gene.

To evaluate the modified lens performance, the radiation patterns of the designed shapes  $E_{rm}(\theta, \phi)$  are calculated. The patterns from  $E_{r1}(\theta, \phi)$  to  $E_{r4}(\theta, \phi)$  correspond to each feed. Here three objective functions are defined. The first object is the minimum gain where two beams intersect.

$$Obj_1 = \min[E_{rm}(\theta_{cross}(m), 0)] \quad (m = 1 \cdots 3) \quad (24)$$

$\theta_{cross}(m)$  is an angle intersecting  $m$ th beam with  $m+1$ th beam. The second object is the minimum value of the ratio between the gain and the sidelobe level.

$$Obj_2 = \min[E_{rm}(\theta(m), 0)/SLL(E_{rm}(\theta, 0)) \quad E_{rm}(\theta(m), 0)/SLL(E_{rm}(\theta(m), \phi))] \quad (m = 1 \cdots 4) \quad (25)$$

$SLL(\cdot)$  represents the calculated value of the maximum sidelobe level. The first half of Equ.(25) represents the multibeam pattern in the azimuth plane. The second half of Equ.(25) represents the fan beam pattern in the elevation plane. Here, evaluation on  $45^\circ$  cut-plane described in the preceding section is omitted, since the maximum sidelobe must not appear on  $45^\circ$  cut-plane. The third object is formation of sector beam in the elevation plane. Here, it is assumed to form beamwidth of  $20^\circ$ .

$$Obj_3 = \min[ -|\phi_{3dB}(m) - 20| ] \quad (m = 1 \cdots 4) \quad (26)$$

$\phi_{3dB}(m)$  is beamwidth of vertical pattern of  $m$ th beam. Equ. (24), (25) and (26) are evaluated for all individuals.

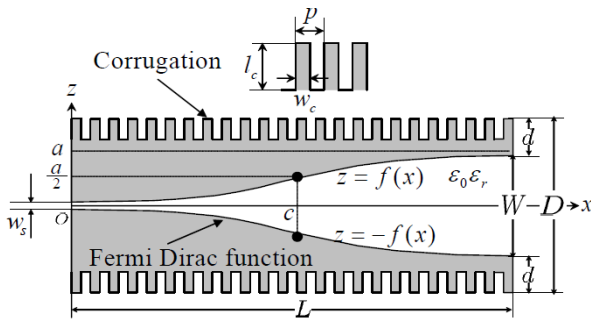
## (2) Feed design

In the past, we used the Vivaldi slot line (Yun & Chang, 2001) antenna as the feeds. However, there were some drawbacks as sidelobe, beamwidth, and pattern symmetry. We have tried to use the Fermi antenna with corrugation (Sugawara et al., 1998) as the feeds. It is featured by low sidelobe, good symmetric radiation pattern and wide frequency range. Configuration of the antenna is shown in Fig. 19. The antenna has taper slot represented by Fermi function and corrugation at both sides. Fermi function is expressed by

$$f(x) = \frac{a}{1 + e^{-b(x-c)}} \quad (27)$$

Where,  $a$ ,  $b$  and  $c$  are parameters that determine the taper.

We have examined design parameters, that is, Fermi function, aperture width, antenna length, corrugation pitch, and corrugation depth by FDTD. The design policies are large difference between beamwidth of the elevation and azimuth plane, low sidelobe, good symmetric radiation pattern and impedance. We have used Duclad 522 which thickness is 0.8mm and the dielectric constant is 2.6 as the substrate. The designed configuration is shown in Fig. 20. Parameters in Equ.(27) are  $a=4[\text{mm}]$ ,  $b=0.048$ ,  $c=25[\text{mm}]$ . The radiation pattern is shown in Fig. 21. The VSWR was lower than 2.7 from 20 to 27GHz. Beamwidth of the azimuth and elevation plane is  $36^\circ$  and  $30^\circ$ , respectively. Sidelobe level of the azimuth and elevation plane is -13 and -19dB, respectively.



Index	value
a	12.75
b	50
c	5.25
d	8.25
e	1
f	0.25
lc	2
g	3
h	3.5
i	1
j	6.5

Fig. 19. Fermi antenna with corrugation

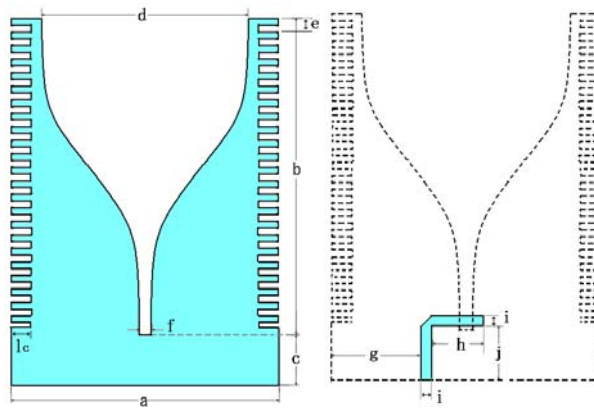


Fig. 20. Design results

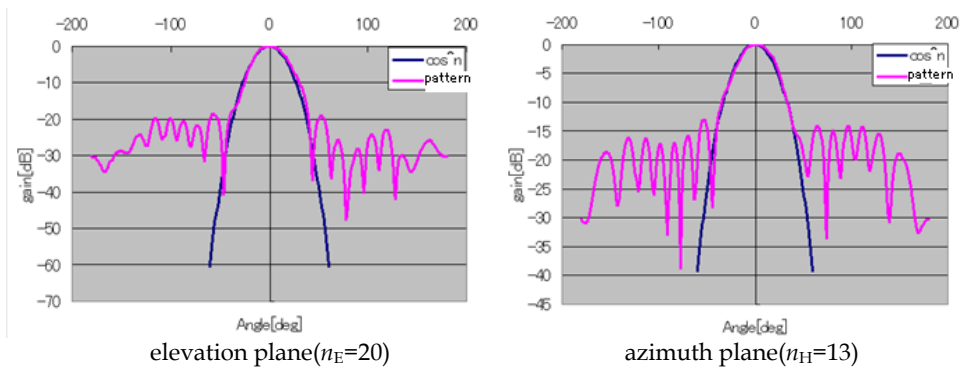


Fig. 21. Radiation pattern and  $\cos^n \theta$  approximation

### (3) Numerical simulation

#### A. Simulation model

A design obtained by the proposed method is demonstrated in this section. The calculation conditions are shown in Table 3. We assumed the feed pattern as power of cosine function as shown in Fig. 21. The power index in Equ.(9) are  $n_E=20$  or  $n_H=13$ . The radiation pattern of the feed is modified.

$$D_0(\theta_E, \theta_H) = 2\sqrt{(n_E + 1)(n_H + 1)} \cos^{n_E} \theta_E \cos^{n_H} \theta_H \quad (28)$$

In order to calculate the refraction at the lens edge accurately, the lens was formed up to  $+0.5\lambda$  from  $D_x$  and  $D_y$  and ray tracing was carried out up to  $D_x$  and  $D_y$ . Mutation probability is gradually reduced by the convergence of the results. Crossover probability is set at a relatively low value because mutation with elitist preserving selection yielded better performance rather than crossover. Calculation of all possible combinations of the chromosomes is impractical since  $2^{392}$  combinations (about  $10^{118}$ ) would have to be assessed. Considering calculation loads, our procedure with GA is far more practical.

Elements	Values
Direction interval of feeds, $\Delta\theta$	$10^\circ$
Power index of the feed, $n$	$n_E=20, n_H=13$
Range of aperture diameter, $D_x, D_y$	1.5 to $9\lambda$
Range of lens offset against feed(1), $z_1(1)$	1 to $12\lambda$
Interval of $x_1(n)$ ( $=\Delta x_1$ )	$0.5\lambda$
Range of $\Delta z_1(n)$ and $\Delta z_2(n)$	$\pm 0.05\lambda$
Distance between lens and feed $R(m)$	$F\cos(\theta(m))$ to $F$
Refractive index, $Ref$	1.6
Number of individual	50
	49
Number of elements composing one individual	$(D_x, D_y, z_1(1), \Delta z_1(n) \times 21, \Delta z_2(n) \times 22, R(m) \times 3)$
Number of bits for each element	8 (256 levels)
Number of generations	100
Mutation probability	Start : 0.2 End : 0.1
Crossover probability	0.01

Table 3. Simulation conditions

#### B. Results

A calculation result is shown below. The values of objective functions Equ.(24), (25) and (26) at the final generation are shown in Fig. 22. The increasing extent of each axis represents superior performance. The circles in this figure represent each individual's performance. We can see that pareto-optimal solutions with various characteristics were obtained. The design specialized for one object yielded relatively decreased values in other objective functions. On the other hand, when the restriction of  $Obj_1$  was reduced, design parameters yielding improvements in  $Obj_2$  and  $Obj_3$  were obtained. Considering balance between objective functions, we have selected the filling individual in Fig. 22. The lens shape and feed positions are shown in Fig. 23. The radiation patterns in the azimuth and elevation planes are shown in Fig. 24.

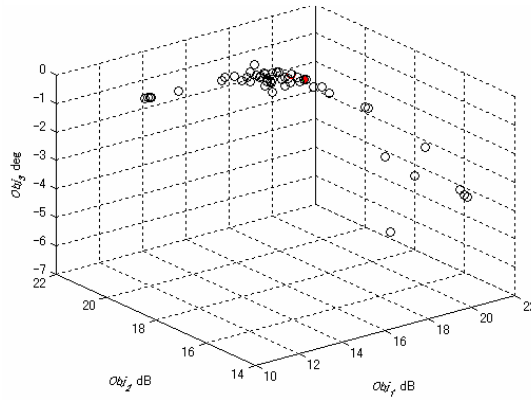


Fig. 22. distribution of the results

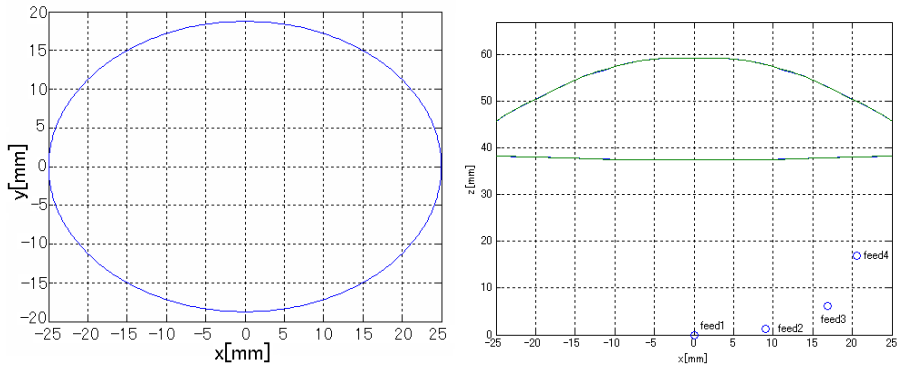
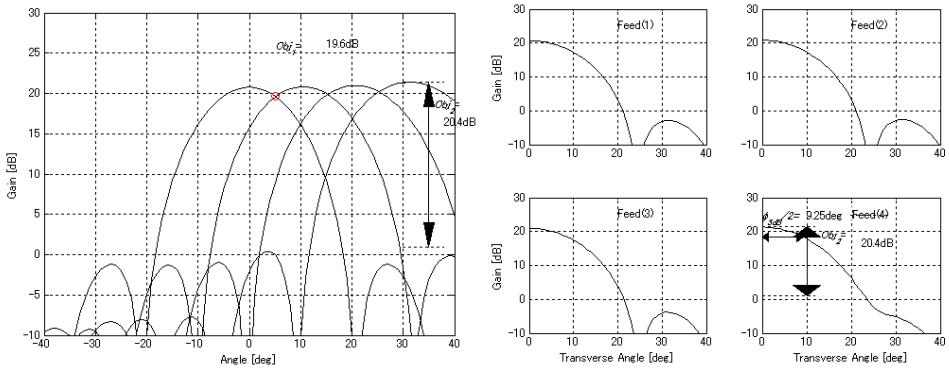


Fig. 23. Antenna configuration (f=24GHz)



(a) azimuth plane

(b) elevation plane

Fig. 24. Radiation patterns in the

#### 4. Trial model and evaluation

We have manufactured a trial model based on the feed shown in Fig.20 and antenna configuration shown in Fig.23.

##### 4.1 Feed

We have manufactured the trial model and have evaluated the performance. The trial model and the measured VSWR are shown in Fig.25. The VSWR is lower than 2.4 from 20 to 27GHz. The radiation patterns are shown in Fig.26. Beamwidth of the horizontal and vertical plane is  $35^\circ$  and  $29^\circ$ , respectively. Sidelobe level of the horizontal and vertical plane is  $-12$  and  $-15$ dB, respectively. These values are almost same as the numerical simulation results.

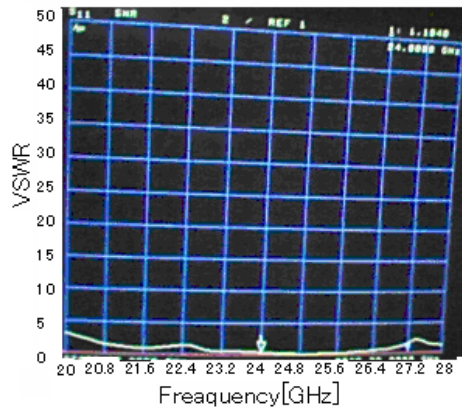
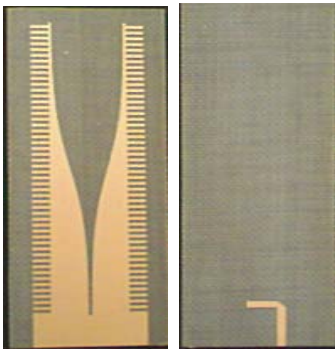


Fig. 25. Trial model

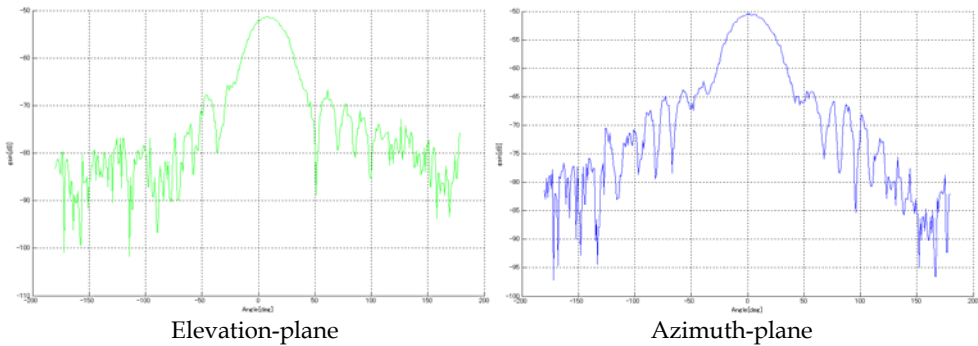


Fig. 26. Measured Radiation Pattern

##### 4.2 Multibeam lens antenna

We have manufactured a trial model. Lens shape is shown in Fig.27. 3 arms are used for installation. The top view of whole structure is shown in Fig.28. Since we have confirmed that the aperture center of Fermi antenna is on the tips by phase pattern measurements, the tips are placed on the focal positions.

The measured radiation patterns are shown in Fig.29. The peak gain is 18 to 21dB, and inequality between multibeams is observed. The inequality is because of manufacturing error of the feed. The sidelobe level is -10 to -14dB. It is considered that the sidelobe rises up by interference between the feeds. The shoulders along the mainbeam are also observed. The shoulders are appeared by interference between the feeds and reflection of the antenna structure. The vertical beamwidth is 18°. It is almost the same value of the design. We were not able to measure the sidelobe in the vertical plane due to limitations of measuring system.

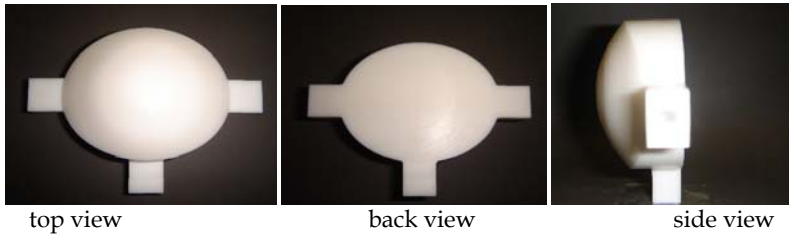


Fig. 27. dielectric lens

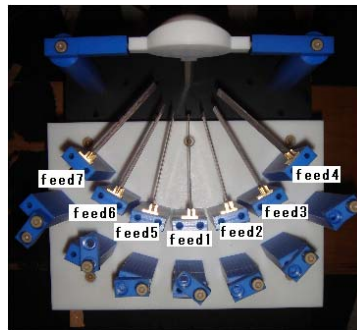


Fig. 28. Whole structure (Top view)

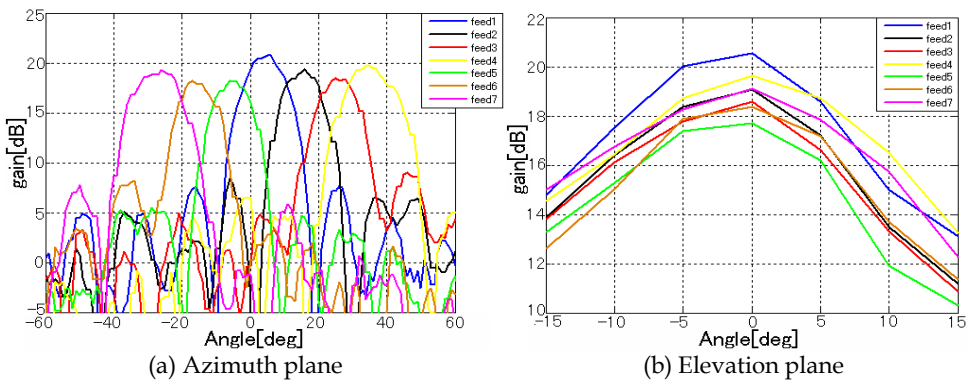


Fig. 29. measured pattern

## 5. Conclusions

We have proposed the design scheme for multibeam dielectric lens antennas that well balances the conflicting aims of high gain and low sidelobe level. The scheme is based on pareto-GA and lens shape is associated with GA chromosomes.

In the first, two objective functions are defined: the gain and the sidelobe level. Individuals are renewed yielding pareto optimal solutions that identify various lens shape. Some examples of lens shape and their radiation patterns were demonstrated by numerical simulation. Our design scheme provides various forms that offer well balanced performance including the gain-tuned lens and the sidelobe level tuned lens.

Second, as an example of 3 objectives, multibeam dielectric lens antennas with the fan beam has examined. To optimize the lens antennas balancing the gain including pattern loss of multibeam and sidelobe level of the scanning and transverse patterns taking into account of beamwidth of the vertical pattern, the pareto-genetic algorithm is successfully introduced. The validities have been confirmed by numerical simulation.

Then, Fermi antenna with corrugation has been examined for feed. We have confirmed the good performances of Fermi antennas with corrugation for the feed at 24GHz band through trial manufacturing and evaluation tests. And, trial model has been manufactured and evaluated. Although we were able to confirm certain degrees of performance, the evaluation results were not satisfied with our goals. The main problem is interference between feeds. We confirmed that the performance were dramatically improved when feeds separated away. Therefore, we are to design with constrain of focal length. Of course, the feed pattern must be examined.

## 6. References

- Y. Kuwahara, M. Hamai, and T. Maruyama, "Multi-beam antenna with vertical fan beam of the dielectric lens and Fermi antennas with corrugation," in *Proc. 2009 IEEE int. symposium on antennas and propagation*, 426.6, June 2009.
- T. Maruyama, K. Yamamori, and Y. Kuwahara, "Design of multibeam dielectric Lens antennas by multi-objective optimization," *IEEE Trans. Antennas and Propagat.*, Vol.57 No.1, pp.57-63, Jun. 2009.
- Y. Kuwahara, "Design of multibeam dielectric Lens antennas with the fan beam by multi-objective optimization," *Proc. of ISAP 2008*, 1645103, Oct. 2008.
- B. L. J. Rao, "Bifocal dual reflector antenna," *IEEE Trans. Antennas Propagat.*, Vol. 22, No. 5, pp. 711-714, Sept. 1974.
- R. M. Brown, "Dielectric bifocal lenses," *IRE International Conv. Rec.*, pp.180-187, Mar. 1956.
- A. L. Peebles, "A dielectric bifocal lens for multibeam antenna applications," *IEEE Trans. Antennas Propagat.*, Vol.36, No. 5, pp. 599-606, May. 1988.
- R. K. Luneburg, *Mathematical Theory of Optics*, Univ. of California Press, 1964.
- E. E. Altshuler and D. S. Linden, "Wire-antenna designs using genetic algorithms," *IEEE Antennas Propagat. Mag.*, Vol. 39, No. 2, pp. 33-43, Apr. 1997.
- E. A. Jones and W. T. Joines, "Design of Yagi-Uda antennas using genetic algorithms," *IEEE Trans. Antennas Propagat.*, Vol. 45, No. 9, pp. 1386-1392, Sept. 1997.
- Y. Kuwahara, "Multiobjective optimization design of Yagi-Uda antenna," *IEEE Trans. Antennas Propagat.*, Vol. 53, No. 6, pp. 1984-1992, June. 2005.

- C. M. Fonseca and P. J. Fleming, "Genetic algorithms for multiobjective optimization: Formulation, discussion and generalization," in *Proc. 5th Int. Conf. Genetic Algorithm*, 1993, pp. 416-423.
- R. L. Haupt and S. E. Haupt, "Practical Genetic Algorithms," Wiley-Interscience, New York, ISBN 0-471-18873-5, 1998.
- Y. Rahmat-Samii and E. Michielessen, "Electromagnetic Optimization by Genetic Algorithms," Wiley-Interscience, New York, ISBN 0-471-29454-0, 1999.
- D. H. Werner and R. Mittra, "Frontiers in Electromagnetics," IEEE Press, New York, ISBN 0-7803-4701-3, 2000.
- E. E. Alshuler and D. S. Linden, "Wire-Antenna Designs Using Genetic Algorithms," *IEEE Antennas and Propagat. Magazine*, Vol. 39, No. 2, pp.33-43, Apr. 1997.
- D. S. Weile, E. Michielssen, and D. E. Goldberg, "Genetic Algorithm Design of Pareto Optimal Broadband Microwave Absorbers," *IEEE Trans. on Electromagnetic Compatibility*, Vol. 38, No. 3, pp.518-525, Aug. 1996.
- D. S. Weile and E. Michielssen, "Genetic Algorithm Optimization Applied to Electromagnetics: A Review," *IEEE Trans. Antennas Propagat.*, Vol. AP-45, No. 3, pp.343-353, Mar. 1997.
- D. S. Weile and E. Michielssen, "Integer coded Pareto genetic algorithm design of constrained antenna arrays," *Electronics Letters*, Vol. 32, No. 19, pp.1744-1745, 1996.
- S. E. Fisher, D. S. Weile, and E. Michielssen, "Pareto Genetic Algorithm Based Optimization of Log Periodic Monopole Arrays Mounted on Realistic Platforms," *Journal of Electromagnetic Waves and Applications*, Vol. 13, pp.571-598, 1999.
- H. Choo and H. Ling, "Design of electrically small planar antennas using inductively coupled feed," *Electronics Letters*, Vol. 39, No. 22, pp.1563-1565, 2003.
- J. Horn, N. Nafpliotis, and D. E. Goldberg, "A Niche Pareto Genetic Algorithm for Multiple Objective Optimization," *Proc. of the 1<sup>st</sup> IEEE Conf. Computation*, pp.82-87, 1994.
- K. A. D. Jong, "An Analysis of the Behavior of a Class of Genetic Adaptive Systems," Doctoral dissertation, University of Michigan, 1975.
- J. D. Saffer, "Multiple objective optimization with vector evaluated genetic algorithm," *Proc. of the 1st International Conference on Genetic Algorithm and their Applications*, pp.160-168, 1985.
- Y. Tajima, Y. Yamada, S. Sasaki, A. Kezuka, "Calculation of Wide Angle Radiation Patterns and Caustics of a Dielectric Lens Antenna by a Ray Tracing Method," *IEICE Trans. Elec.*, vol. E87-C, No.9, pp. 1432-1440, Sept. 2004.
- J.J.Lee, *Handbook of Antenna Theory and Design*, Chapter. 16, Van Nostrand Reinhold Co, New York, 1988.
- Y. Kuwahara, T. Ishita, Y. Matsuzawa, and Y. Kadowaki, "An X-band phased array antenna with a large elliptical aperture," *IEICE Trans. Commun.*, vol. E76-B, no. 10, pp. 1249-1257, Oct. 1993.
- T. Yun and K. Chang, "A Low Cost 8 to 26.5GHz Phased Array Antenna Using a Piezoelectric Transducer Controlled Phase Shifter," *IEEE Trans. on Antennas and Propagation*, vol49, no.5, pp.1290-1298, Sep. 2001.
- S. Sugawara, Y. Maita, K.Adachi, K. Mori and K. Mizuno, "Characteristics of a MM-wave Tapered Slot Antenna with Corrugated Edges," *1998 MTT-S Digest*, pp.533-536, 1998.



# Modelling and Design of Photonic Bandgap Devices: a Microwave Accelerating Cavity for Cancer Hadrontherapy

Roberto Marani and Anna Gina Perri

*Politecnico di Bari, Dipartimento di Elettrotecnica ed Elettronica  
Bari, Italy*

## 1. Introduction

In recent years hadrontherapy became one of the most important way to fight against deep-sided cancer. This technique had been theoretically studied and now it seems to be the main method able to replace radiosurgery, which is not always incisive and sometimes leads up to side effects. These results can be obtained by exploiting the capability of accelerated hadrons (heavy particles) to hit ill tissue with high accuracy, without any damage to neighbour tissues. Nevertheless the high dimensions and costs of the present structures, implemented to accelerate hadrons, forbid the actual use of hadrontherapy in oncology. The research aim is concerned with the definition of new techniques able to develop integrated systems that can accelerate and control particle beams to improve performance and that can decrease the cost of classical medical accelerators.

By analysing the energy transmission profile of accelerated protons and ions through water, which is the main component of a biological tissue of the human body, it is possible to understand that hadrons can easily reach a penetration depth between 25 and 30 *cm*, discharging the maximum value of energy in a small volume at the travel ending. This maximum is also called *Bragg peak*. The protons beam energy can be modulated in order to get the exact depth where the cancer tissue is localized. If the cancer thickness is higher than the Bragg peak extension, a SOBPs (Spread-Out Bragg Peak) could be realized by adding an appropriate number of power peaks of a decreasing intensity. In this case it is possible to create a peak of the desired depth, equal to that of the cancer mass.

This fundamental quality, together with the low lateral diffusion that happens when a hadron beam flows inside a biological tissue, allows a millimeter accuracy and consequently the possibility to realize an actual radiotherapy with a deep continuous scanning by varying the particles energy and the beam localization along the lateral directions, by a translation of the incident beam.

The high selectivity of these treatments, comparable to a surgical intervention (radiosurgery), allows to attack cancer cells without damages of near healthy tissues. Moreover this characteristic is fundamental if the cancer mass is localized near a vital organ or in a critical area.

In this chapter, after a review about the principal characteristics and applications of PBG devices, we carefully describe the design of a microwave PBG-based accelerating cavity for cancer hadrontherapy. The prototype has been fabricated and experimentally characterized obtaining confirmation of expected theoretical results.

## 2. PBG-based accelerating cavity for medical applications

One of the most important issue in hadrontherapy is related to the choice of the particle accelerator, that are typically classified in cyclotrons and synchrotrons. A hospital accelerator should obey some specifications different from the conventional rules of a research system. All beam parameters, such as energy variation and current intensity, have to be optimized for clinical applications. The main specification for a correct design of the accelerating system are reliability, flexibility and, finally, low fabrication and maintenance costs. The control system plays a fundamental role in meeting the quality requirements: it has to be user-friendly and full integrated in the security system of the whole apparatus.

Typical energy values for protons beam are estimated to be in a range between 60 and 250 MeV (Coutrakon et al., 1999), which implies a path inside the biological tissue that spans from  $3.1 \text{ g/cm}^2$  to  $38.3 \text{ g/cm}^2$ . It is thus necessary to get high acceleration gradient and energy values whatever particle accelerator is used.

Traditional particle accelerators can be considered as metallic waveguides which carry  $\text{TM}_{01}$  mode, thus producing the highest acceleration for a given working power, but suffering from the excitation of higher order modes (HOM) at high frequencies. Moreover, metallic walls produce absorption losses that increase with the frequency (Shapiro et al., 2001).

The PBG-based resonant cavities are used in particle accelerator applications, with a drastic improvement of performances. In fact:

- PBG materials can substitute the metallic walls to achieve perfectly reflective surfaces, without absorption losses;
- PBG structures allow the suppression of higher order modes in the resonant cavity of the accelerator;
- Since the field in a PBG-based cavity is strongly confined in a very small region, wider tolerances become acceptable for the material quality, which has to be very high in the centre of the cavity – where the field is confined – but can be lower in the external region. This aspect is very important when a superconductor material is used, since semiconductors have not a uniform high quality on large surfaces;
- Straight structures can be realized and high accelerations obtained;
- It is possible to optimize the coupling between the resonant cavity and the input waveguide, thus reducing the resonance frequency shift which is a typical problem of a standard pillbox cavities.

Moreover the presence of a defective region, in which the periodicity is not regular because one or more rods are removed, produces a strong electromagnetic field localization at a given frequency, which depends on the characteristics of the defect. The presence of the defect allows resonant effects with high value of quality factor and high suppression of higher order modes.

The main design parameters are: height, diameter and rods number, distance among the rods centres, geometry and thickness of plates. Anyway, the design statements are related to the application of these accelerant cavities.

To explain carefully the design procedure of the proposed microwave PBG-based accelerating cavity for cancer hadrontherapy, it is necessary a brief review about the principal characteristics of PBG crystals and their applications to the PBG devices design.

### 3. Principal Characteristics of Photonic Crystals

Photonic crystals are materials able to influence the light propagation analogously it occurs for the propagation of the electrons in semiconductors (Perri, 2007).

In fact, in a semiconductor the crystal lattice causes the formation of a periodic potential for an electron which propagates through it. This periodicity determines the formation of energy bandgaps for the electronic states, where the propagation of electrons is forbidden.

In photonic crystals a principle similar to what seen for the semiconductor crystals is exploited for the propagation of some light quanta (or photons). In this case the crystal periodicity is artificially realized by means of an alternation of dielectric macroscopic materials.

According to their geometrical characteristics, photonic crystals inhibit the light propagation in one or more directions, depending on the working frequency. This leads to the existence of a bandgap, i.e. a frequency range in which the wave can not propagate. The bandgap is complete if the propagation is prevented in all possible directions at those frequencies.

Fig.1 shows different PBG based structures, characterized by one-dimensional (1D), two-dimensional (2D) or three-dimensional (3D) periodicity, each of them infinitely extended and then so-called "bulk". On the contrary, Fig. 2 shows waveguiding periodic structures, characterized by a finished thickness and a 1D, 2D or 3D periodicity.

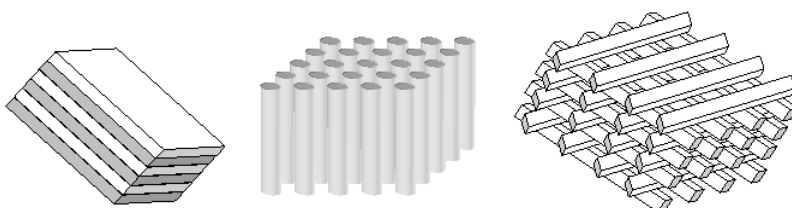


Fig. 1. Bulk 1D, 2D and 3D photonic crystals.

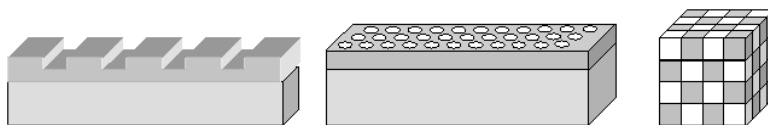


Fig. 2. Waveguiding 1D, 2D and 3D structures.

A wave that impinges on a dielectric discontinuity is partially reflected, partially transmitted and partially diffracted. We can then distinguish between two waves, one propagating in a positive direction and the other in a negative direction. If the wave is incident on a periodic structure, the produced waves can - in particular conditions - destructively interfere and propagation is then inhibited, so a bandgap appears.

The characterization of a photonic crystal is carried out through the so called *Brillouin diagrams*, where the frequency of the allowed electromagnetic modes is plotted as a function of the normalized propagation constant in all directions of the irreducible Brillouin zone.

Fig. 3 shows a frequency range (i.e. bandgap), between the dashed lines, in which no propagation can occur.

The frequency range in which the wave is particularly concentrated in the high refractive index medium is called *dielectric band*, while the other one is called *air band*.

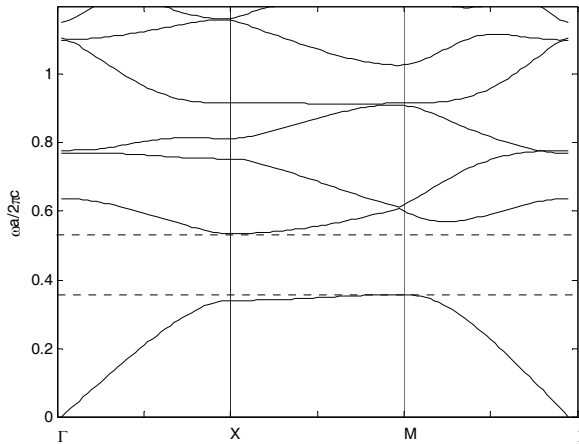


Fig. 3. Photonic band of a PBG structure having lattice constant  $a$  and with different thickness layers. The thickness of the layers at high index is  $0.2 a$  and that of the layers at low index is  $0.8 a$ .

Moreover, a lattice of circular rods is shown in Fig.4.

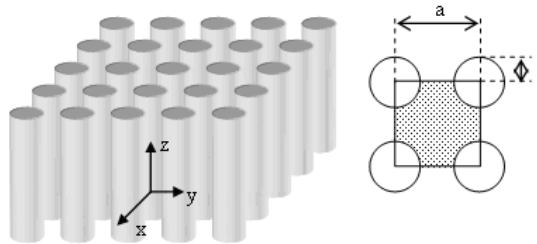


Fig. 4. 2D PBG structure.

The material is homogeneous in the  $z$  direction and periodic in the  $xy$ -plane, being  $a$  the lattice constant. The grating is arranged accordingly with a square cell array, as shown in the inset of the same Fig. 4.

The physical characteristics of the described structure are determined by its design parameters: the lattice constant, the *filling factor* or *ratio*, the rod radius, the geometry of the unit cell, the refractive index contrast.

The filling factor gives a measure of the electromagnetic energy located inside the high index dielectric regions in comparison with the energy distributed in the whole volume, being large in the dielectric band and small in the air band.

The photonic investigation of the described structure, having rod radius equal to  $0.2 a$ , shows a different behaviour for TE and TM modes, as depicted in Fig. 5. In particular, there is a complete bandgap for TM modes, while TE modes can always propagate for each frequency.

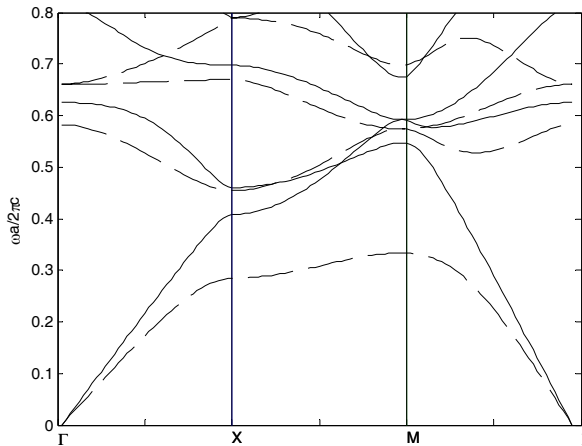


Fig. 5. Brillouin diagram for a squared array of dielectric columns having  $r = 0.2 a$  for: TE modes (solid line) and TM modes (dashed line).

The structure, composed by a square array of high dielectric columns, has a complete bandgap for the TM modes but not for the TE ones for the following reasons:

- the mode mainly localized in the high refractive index medium has a frequency lower than that of the mode concentrated in the low refractive index medium: this explains the bandgap formation (separation in  $\omega$ );
- TM modes have the Maxwell displacement vector  $D$  orthogonal to the periodicity plane and, then, localized in the high refractive index regions;
- for the TE modes the Maxwell displacement vector  $D$  is oriented in the periodicity plane and must necessarily enter into the low index regions (for both the air and dielectric bands), thus resulting in a smaller separation among the bands in comparison with the TM ones.

The wave behaviour changes if the type of used structures varies.

For example a structure with square section rods at low index has characteristics, in terms of bandgap, opposite to those of a structure with circular section rods. In fact:

- the squared structure offers a continuous path among the high index regions: the field, orthogonal to the periodicity plane in the TM modes, is concentrated in the crossings among the high index bars (dielectric band) or inside the high index bars (air band). It follows that the field configuration is similar for both the bands and, so, the separation between them is small;

- for the TE modes the  $D$  field is contained in the periodicity plane and localizes inside the high index regions in the dielectric band, while, presenting nodes in the high index bars, it must necessarily penetrate into the low index regions to place itself in the air band structure, with a consequent greater bandgap in comparison to the TM case.

According to the investigated structures, design rules, useful to establish the necessary conditions for a complete bandgap, can be determined:

- not connected regions of high refractive index materials improve the bandgap for TM modes;
- connected regions of high refractive index material improve the bandgap for TE modes;
- an hexagonal cell of air columns carries out both the previous characteristics, thus providing a complete bandgap for both polarizations;
- for strong index contrasts even a square cell of air columns presents a complete bandgap.

The following photonic band diagram (Fig. 6), calculated for a structure having a triangular cell of air columns drilled in a semiconductor substrate, shows a complete bandgap for both TE and TM modes.

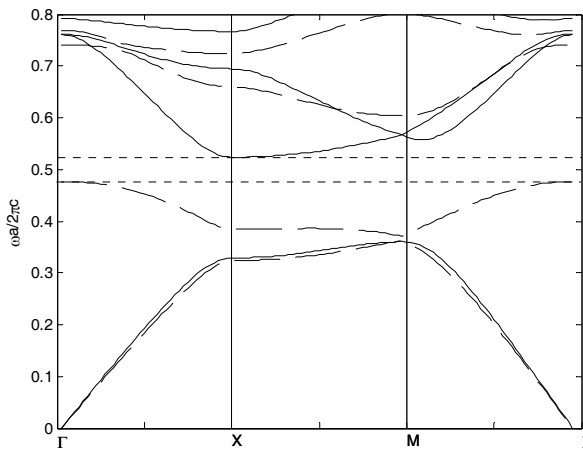


Fig. 6. Photonic diagram for a structure having a triangular cell of air columns drilled in a semiconductor substrate. A bandgap for both polarizations is shown.

A 3D crystal has an almost infinite numbers of geometries, but only few of them having a complete bandgap. A typical 3D structure is the opal (Fig. 7), constituted by high index spheres in a low index background or vice versa (inverted opal). The spheres can be arranged in a suitable manner, thus reproducing a general crystal structure.

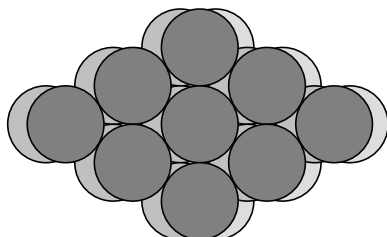


Fig. 7. 3D PBG opal.

#### 4. Defects and devices on PBG

The introduction of defects in a photonic crystal determines the forming of photonic states located in the gap. Such characteristic is exploited to carry out devices with high capabilities, for example optical microresonators (where a column is removed) or low losses waveguides, based on the presence of a bandgap instead of the total internal reflection.

The behaviour of a defective photonic crystal is analogous to that of a doped semiconductor, which is characterized by the presence of allowed states for the electrons inside the forbidden band near the conduction or the valence bands, depending on the kind of impurities embedded in the semiconductor.

The presence of the defects in 1D, 2D and 3D structures is analyzed in following subsections.

##### 4.a Defects in 1D structures

The defect is constituted by a missing layer or a layer having a width different from the others. This situation is depicted in Fig.8.

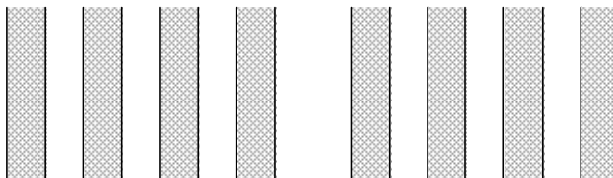


Fig. 8. Defect in a 1D photonic crystal.

If the defect has a suitable width, an allowed state is provided within the bandgap, thus resulting in a strong localization of the mode, which exponentially vanishes into the surrounding periodical regions.

The presence the 1D defect provides a phase shift of an odd multiple of  $\pi$  for a complete oscillation (backwards and forwards).

It follows that the allowed states exist only at discrete energies and the corresponding resonance frequencies decrease with an increasing defect size.

The transmission curve is also modified at the allowed state wavelength ( $\lambda$ ) showing a maximum, as depicted in Fig. 9.

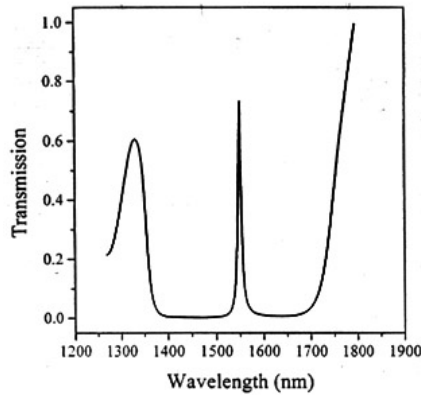


Fig. 9. Transmission coefficient in presence of a defect to  $\lambda/4$ .

Fabry-Perot passband filters can be also designed by using defective 1D PBG based structures.

**4.b Defects in 2D structures**

In two-dimensional photonic crystals a single defect is achieved by removing a rod from the lattice (Fig. 10) or replacing it with another one of different refractive index material (Fig. 11).

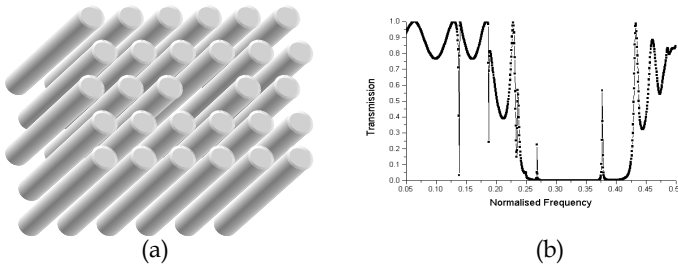


Fig. 10. (a) 2D photonic crystal with defect obtained by removing a dielectric rod; (b) Transmission spectrum.

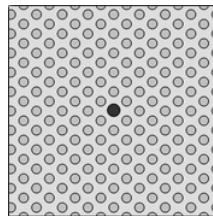


Fig. 11. 2D defect obtained by using an high refractive index rod.



The presence of a defect determines a transmission peak inside the forbidden band and produces a concentration of field in the defective region, thus creating a two-dimensional cavity surrounded by reflecting walls supporting an allowed state inside the bandgap.

In a 2D PBG, unlike a one-dimensional crystal, line defects can be realized by removing one or more sets of rods.

A waveguide is realized by making a defective path, where the light can be confined since no propagation in the surrounding crystal can occur, thus decreasing propagation losses. This feature can be advantageously used to realize strongly curved waveguides.

Fig. 12 shows the architecture of several PBG-based optical devices.

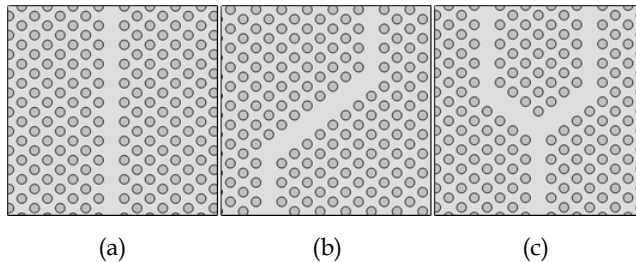


Fig. 12. Different structures realized with line defects: (a) straight; (b) curved waveguide; (c) Y-branch.

#### 4.c Defects in 3D structures

It is possible to introduce some irregularities in the grating of a 3D crystal:

- by adding a material with different dielectric constant in the unitary cell (dielectric defect);
- by removing part of the dielectric material from the unitary cell (air defect).

In the first case the defect behaves analogously to a donor atom in a semiconductor crystal, thus producing an allowed state (*donor mode*) near the lower edge of the air band.

Likewise, an air defect is similar to an acceptor atom, and localizes the field distribution (*acceptor mode*) near the upper edge of the dielectric band. These defects are particularly interesting for realizing resonant microcavities with high quality factor  $Q$ .

Some theoretical investigations (Yablonovich, 1994) show that the frequency of the acceptor mode increases with an increasing volume of removed material, while a small amount of volume results in an acceptor level near the edge of the dielectric band. Moreover, a too small amount of removed material pushes localized states within a continuum of levels below the top of the dielectric band.

Similarly, a donor level requires a minimum removed volume for creating an allowed level below the air band edge. In this case, the frequency of the donor level diminishes with increasing the defect volume.

In a 3D crystal it is possible to localize the light in a single region introducing a point defect. This behaves as an entirely reflecting walls resonant cavity, where the electromagnetic field is confined. Outwardly the defect, the field will vanish along the three crystal dimensions.

Besides point defects, linear type defects can also be realized by creating a defective region in the crystal. This approach allows to fabricate high quality waveguides, able to confine the light and to make negligible losses also at optical frequencies.

## 5. Applications of Photonic Bandgap Crystals

The first PBG crystal was fabricated by Yablonovitch in 1989 at Bell Communications Research in New Jersey, characterized by a bandgap only at microwave frequencies because of technological limitations (to work with smaller wavelengths a smaller rod size is required). The 2D bulk crystal was obtained by drilling the silicon according a face centred cubic (FCC) arrangement, being this architecture the simplest and most suitable for achieving a complete bandgap (in all directions and for all polarizations), as suggested by theoretical studies.

Currently, 2D structures are most investigated at optical frequencies to realize waveguides and monolithic integrated optical circuits.

The most important applications are:

- waveguides, power splitters and switches with low losses over long distances and in presence of strong bends;
- optical fibres, monomodal in a wide range of wavelength, with a low core refractive index. Only the mode that satisfies the Bragg condition can propagate;
- perfectly reflective mirrors, in particular for laser cavity walls;
- LED diodes having very high external efficiency (4% without PBG) because only the emission of the transmittable modes occurs. All the emitted energy is then transmitted;
- laser diodes having low threshold ( $<100 \mu A$ ): since the spontaneous emission is suppressed, because photons having energy inside the band-gap are not emitted, the related loss decreases, the efficiency increases, the dissipated power decreases;
- narrow band filters for DWDM (Dense Wavelength Division Multiplexing) systems;
- resonant cavities with very high  $Q$ -factor;
- biomedical sensing applications based on porous silicon;
- particle physics applications to realize high spectral purity accelerators;
- photonic integrated circuits: PBG allow to reduce photonic circuits sizes (up to a few hundred of squared  $\mu m$ ) because:
  - laser beam can propagate through strongly bent guides with very low losses;
  - LED and laser high efficiency allows a low power consumption and, then, the integration in very small areas;
  - the power coupling among adjacent waveguides is strongly reduced;
  - superprism effects can be used.

In particular, in the following sub-sections, we examine the PBG applications related to resonant cavities and particle accelerators.

### 5.a Resonant cavities

Conventional microwave resonant cavities are boxes enclosed by conductive walls containing oscillating electromagnetic fields. Conductive walls act as perfect screens, therefore avoiding any radiation of energy away from the box. Because of the large extension of inner walls, current density and losses are reduced.

Optical resonators are rather different from the microwave typical ones for the smaller operative wavelength, which yields a large number of allowed modes. Although there are

several and important differences between optical and microwave resonators, some parameters, as quality factor  $Q$ , are very useful for both kind of cavities. The quality factor  $Q$  is defined as:

$$Q = \omega_0 U / W \quad (1)$$

where  $\omega_0$  is the resonance frequency,  $U$  the electromagnetic energy stored in the cavity and  $W$  the lost power. Losses in the dielectric material and radiations from small apertures can cause the lowering of  $Q$ . The  $Q$  factor allows to evaluate also the filter bandwidth, defined as:

$$\Delta\omega / \omega_0 \cong 1/Q \quad (2)$$

where  $\Delta\omega$  is the range between two frequencies at which the signal power is 3 dB lower than the maximum value. It can be shown that, at a given frequency, the  $Q$ -factor increases with an increasing order of mode.

As seen in the previous paragraph, a resonant cavity can be obtained by introducing a defect in a photonic crystal in order to modify its physical properties. In the case of a defectless structure, electromagnetic waves can not propagate when the operative frequency is inside the bandgap, in which a narrow band of allowed frequencies can be achieved breaking the crystal periodicity through a suitable defect.

Light localization is used in the PBG based microcavity design to optimize the  $Q$ -factor, which depends on the geometrical and physical properties of the defect. Lattice defects are constituted by dielectric regions of different shapes, sizes or refractive index values. By changing one of these parameters in the defective region we can modify the mode number of the resonance frequency inside the cavity. Moreover, the spectral width of the defect mode is demonstrated to decrease rapidly with an increasing number of repetitions of the periodic structure around the cavity region, so improving the selectivity of the resonance frequency inside the bandgap.

The excellent performances of PBG structures have been used to develop resonators characterized by high values of  $Q$ -factor working at microwave frequencies, by introducing defects in 3D and particularly in 2D structures. Microwave resonant cavities are constituted by dielectric materials and metals, thus keeping the same fundamental properties of the PBG structures. Metallic structures are easier and less expensive to realize and can be used for accelerator-based applications. Most interesting 2D and 3D devices have a geometrical structure that allows a large bandgap, achieved by using a triangular cell for 2D or woodpile cell for 3D structures, with an efficient wake-field suppression at higher frequencies, without interfering with the working mode.

In microwave applications the use of carbon based low losses materials (Duroid, Teflon), aluminium oxide or highly resistive silicon is already described in literature. In particular highly resistive silicon has been demonstrated to be most suitable at frequencies near 100 GHz (Kiriakidis & Katsarakis, 2000). Moreover, both dielectric and metallic-dielectric gratings have been investigated, thus achieving an improvement in terms of  $Q$ -factor.

The final architecture is constituted by a 2D triangular lattice, in which a rod at the centre has been removed (defect), thus producing a resonant cavity (Fig. 13). To localize the mode,

three rows of rods have been used, and all the rods are confined inside a metallic cylinder closed on both ends.

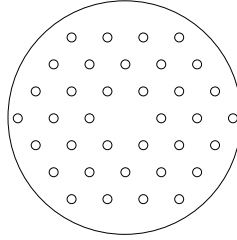


Fig. 13. Architecture of the PBG cavity.

The main difference with traditional cavities is the absence of coupling holes, at the opening of waveguide, which produce a down-shift frequency of 2%. PBG-based cavities are not affected by this problem because of the distributed cavity coupling. In fact, fields are confined by the rods nearest to the defect, and these rods are not perturbed in order to obtain the coupling.

The main steps required to design a resonant cavity are:

- design of the periodic structure to obtain a suitable bandgap around the required working frequency;
- creation of a defect in the grating to establish a defect mode;
- analysis of higher order modes that have to be not confined, being in the crystal passband, and thus can be absorbed by coatings at the edge of the structure;
- design of a suitable hole in the central region of the plates to allow the propagation of the accelerated beam outside the device.

### 5.b Particle accelerators

Traditional particle accelerators can be considered as metallic waveguides that carry  $TM_{01}$  mode, thus producing the highest acceleration for a given working power, but even suffering from the excitation of higher order modes (HOM) at high frequencies. Moreover, metallic walls produce absorption losses that increase with the frequency (Shapiro et al., 2001).

PBG-based resonant cavities are used in particle accelerator applications, with drastic improvement of performances. (Fig. 14).

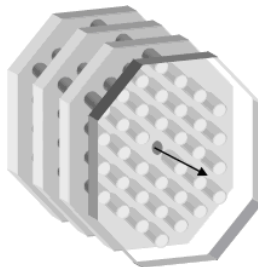


Fig. 14. PBG based particle accelerator architecture.

The structure is formed by three triangular cell gratings, separated by superconductor layers. Each grating has a defect, obtained by removing a rod. The hole at the centre of conductor layers allows the particle beam emission.

In fact:

- PBG can substitute the metallic walls, obtaining perfectly reflective surfaces without absorption losses;
- PBG allows the suppression of higher order modes in the resonant cavity of the accelerator;
- since the field in a PBG based cavity is strongly confined in a very small region, wider tolerances become acceptable on the material quality, which has to be very high in the centre of the cavity – where the field is confined – but can be lower in the outer regions. This aspect is very important when a superconductor material is used, since semiconductors have not a uniform high quality on large surfaces;
- straight structures can be realized and high accelerations obtained;
- it is possible to optimize the coupling between the resonant cavity and the input waveguide, thus reducing the resonance frequency shift which is a typical problem of a standard pillbox cavities.

The presence of a defective region, in which the periodicity is not regular because one or more rods are missing, produces a strong electromagnetic field localization at a given frequency, which depends on the characteristics of the defect. The bandwidth of the defect is related to the  $Q$ -factor, so it is possible to make resonators with high  $Q$ -value and high suppression of the higher order modes.

The main design parameters are: height, diameter and rods number, distance between rods centres, geometry and thickness of plates. In any case, the design statements are related to the application of these accelerant cavities.

## 6. Design of PBG-based Accelerating Cavity

In order to take into account all effects due to the shape of the accelerating cavity, we consider two different architectures both constituted by either dielectric or metallic rods arranged according a 2D periodic triangular lattice, embedded in air and sandwiched between two ideal metal layers. In this way only TM modes are excited. The investigated structures are shown in Fig. 15.

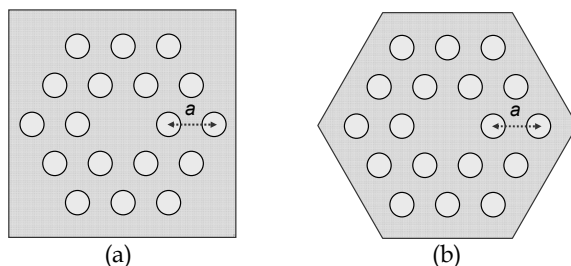


Fig 15. Accelerator with squared external wall (a) and hexagonal external wall (b).

The aim of the analysis is to find the optimal geometrical parameters for placing the operating resonance frequency close to the centre of the bandgap. Once the lattice

parameters have been determined, the central rod must be removed to create the resonance condition, thus providing a localized state inside the bandgap.

The analysis makes use of a rigorous formulation of the Quality Factor according to the Floquet-Bloch formalism, to investigate the photonic behaviour of the resonant cavity.

We assume rod radius  $R$ , lattice constant  $a$  (see Fig. 15) and rod height  $t_g$ .

To evaluate the Q-factor, defined according to Eqn. (1), it is necessary to calculate the energy  $U$  stored by the electromagnetic field and the lost power  $W$ .

The electromagnetic field energy is given by:

$$U = \frac{\mu_0}{2} \int_V H^2 dv \quad (3)$$

where  $H$  is the magnetic field amplitude,  $\mu_0$  is the vacuum permeability and the integral is extended over the cavity volume. Since the periodic structure is sandwiched between two ideal metal layers, only TM modes can be excited, being the electric field perpendicular to the periodicity plane and all the field components constant with respect to the cavity height. In this case the relationship (3) can be rearranged as:

$$U = l \frac{\mu_0}{2} \int_S H^2 ds \quad (4)$$

where  $l$  is the height of the cavity and  $S$  is the cavity cross section.

The lost power  $W$  can be written as follows:

$$W = l \frac{1}{2} R_s \int_{l_i} H^2 dl + 2 \frac{1}{2} R_s \int_{S_s} H^2 ds \quad (5)$$

where  $R_s$  is the metal surface resistance. In the previous relationship the first term takes into account the lost power due to the currents on the rods, while the second term evaluates the losses due to currents on the metal layers. By putting:

$$\delta = \frac{2R_s}{\omega\mu_0} \quad (6)$$

$$R_{\text{eff}} = 2 \frac{\int_{S_s} H^2 ds}{\int_{l_i} H^2 dl} \quad (7)$$

we obtain:

$$Q = \frac{1}{\delta \left( \frac{1}{R_{\text{eff}}} + \frac{1}{l} \right)} \quad (8)$$

This relationship can be used also for superior order modes supported by the structure, if all fields are constant along the rod height.

The Q factor can be written as:

$$\frac{1}{Q} = \frac{1}{Q_\delta} + \frac{1}{Q_{met}} \tag{9}$$

where  $Q_\delta$  is the quality factor taking into account losses in the dielectric medium, while  $Q_{met}$  accounts for the ohmic losses due to the currents on metallic walls. Moreover:

$$Q_\delta = \frac{1}{k \times \tan\delta} \tag{10}$$

where  $k$  is the fraction of the energy stored in dielectric rods, while  $\tan\delta$  is the loss tangent due to the dielectric medium. For our calculations we have assumed  $\tan\delta$  is equal to  $10^{-4}$ .

$Q_{met}$  can be calculated by using Eqn. (8), where  $R_{eff}$  is defined in a different way, since the integral at the denominator of Eqn. (7) has to be extended only on the external edge.

### 7. Numerical results

As first step we have investigated the physical properties of a microwave 2D periodic structure in terms of forbidden frequencies.

The designed parameters values are:  $a = 8.58 \text{ mm}$ ,  $R = 1.5 \text{ mm}$ ,  $t_g = 4.6 \text{ mm}$ ,  $\epsilon_a = 9$ ,  $\epsilon_b = 1$ .

The photonic band diagram shows the first bandgap extending from 12.7 GHz to 20.15 GHz.

In order to take into account the defect presence, constituted by a rod missing (see Fig. 15), several simulation have been performed by using a FEM (Finite Element Method) based approach (Dwoyer et al., 1988), thus computing both field distributions and Q-factors for different configurations.

Fig. 16 shows the first three modes for the electric field  $E_z$  component.

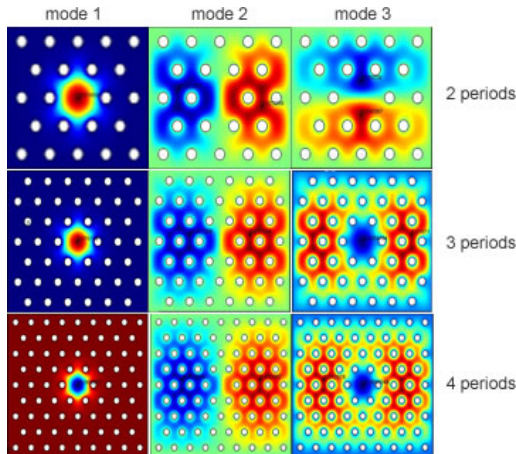


Fig. 16. Electric field component  $E_z$  for 2, 3 and 4 grating periods.

Modes have been computed for two, three and four grating periods, not showing any difference in the first mode which is well confined in the defect space also for two grating periods. Of course the increase of grating periods does not change the distribution of the first mode, but becomes very significant for high order modes which are distributed externally with respect to the defect space and suffer from losses due to the third grating period.

This aspect can also be noticed from Table 1, in which two different accelerators are compared, the first one with external squared wall (Fig. 15a), the second one with external hexagonal wall (Fig. 15b). Both accelerators have the same periodic structure with metallic rods. In the first column of the Table I the number of grating periods is reported. The change of both the first mode resonant frequency and quality factor with increasing the period number is negligible. On the contrary, high order modes are external to the defect and suffer from any further grating period thus producing an additional loss and a consequent decrease in the  $Q$ -factor.

N	mode	Squared wall		Hexagonal wall	
		Frequency (GHz)	Q	Frequency (GHz)	Q
2	1	14.1594	4434.3	14.1598	4439.0
	2	20.5393	3721.5	21.0130	4091.0
	3	20.8323	3893.7	21.0130	4091.7
3	1	14.1592	4436.2	14.1592	4432.1
	2	20.2662	3445.6	20.5412	3592.5
	3	20.3322	3427.0	20.5412	3592.4
4	1	14.1592	4430.9	14.1592	4431.7
	2	20.1152	3335.0	20.2944	3342.8
	3	20.1177	3314.5	20.2959	3403.3

Table 1. Comparison between two accelerators.

In Table 2 a comparison between particle accelerators, based on a triangular cell array and an external hexagonal wall, is shown.

N	mode	Dielectric rods		Metallic rods	
		Frequency (GHz)	Q	Frequency (GHz)	Q
2	1	14.9091	7018.3	14.1598	4439.0
	2	18.8251	6877.4	21.0130	4091.0
	3	19.1886	7128.9	21.0130	4091.7
3	1	14.8314	7142.2	14.1592	4432.1
	2	18.4442	7020.8	20.5412	3592.5
	3	18.5926	7068.8	20.5412	3592.4
4	1	14.8216	7163.0	14.1592	4431.7
	2	18.2596	7056.2	20.2944	3342.8
	3	18.3614	7096.1	20.2959	3403.3

Table 2. Comparison between two accelerators, based on a triangular cell array and an external hexagonal wall.



The two structures have been designed with dielectric and metallic rods, respectively. Of course, only two grating periods are required for localizing the first mode, thus reducing every further loss. The structure characterized by dielectric rods does not suffer from any reduction of performances due to the increase of the number of grating periods, both for the first mode and high order modes. In fact, the dielectric rods improve the quality factor with respect to the same structure with metallic rods, which are characterized by strong resistive losses.

Fig. 17 shows the  $E_z$  field component distribution in the hexagonal cavity.

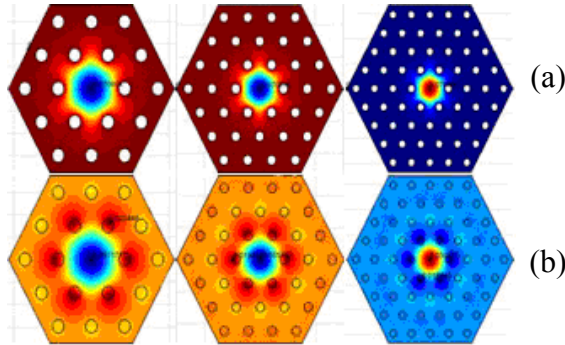


Fig. 17. First mode for metallic rods (a) and dielectric rods (b).

In Fig. 17 the first mode is shown in case of metallic rods (first row) for two, three and four grating periods. The same mode is sketched for dielectric rods (second row), thus showing a different field distribution. The same situation is depicted in Fig. 18, where the second order mode is shown. Because of field penetration inside columns, also losses due to dielectric medium have to be considered, according to Eqns. (9) and (10). However the losses due to the dielectric medium can be lower than the metallic ones, with improvement of the  $Q$ -factor, as demonstrated in Table 2.

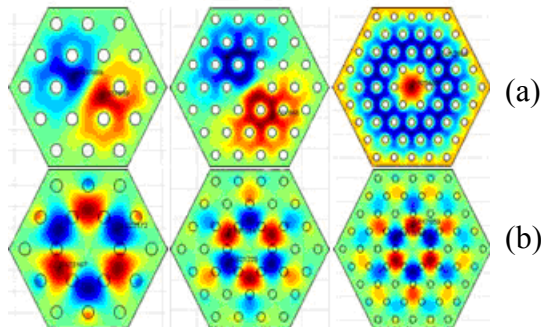


Fig. 18. Second mode for metallic rods (a) and dielectric rods (b).

## 8. Prototype realization and experimental measurements

The copper prototype, shown in Fig. 19, has been realized by the Electronic Device Laboratory research group of Politecnico di Bari (Italy).

The difference between the theoretical results and those obtained by measures are related to the actual realization tolerances that, in this case, are limited to  $0.1\text{ mm}$ , and the inaccuracy of the experimental characterization. This implies that cylinders are placed in different position, not vertically aligned, with rough surfaces, etc.



Fig.19. Prototype images. Dimensions are compared with a pen and a PC-mouse.

Secondly, the cavity is made of 36 cylinders enclosed between two copper plates. Thus the contact resistance between elements is added to the copper resistivity with an increasing value of losses with respect to the preliminary theoretical investigation and a consequent decrease of the  $Q$ -factor.

Finally, a  $5\text{ mm}$  diameter hole has to be placed on each plate near the central defect region, in order to get the correct measures.

As shown in Fig. 20, the network analyzer HP 8720ES has been implemented to measure the  $s$ -parameters for the experimental characterization of the prototype.



Fig. 20. Network Analyzer HP 8720ES with excitation and measure probes.

By setting the spectrum analyzer (Agilent Technologies, 2004) in a frequency range between  $12$  and  $20\text{ GHz}$  and a bandwidth at intermediate frequency (IF bandwidth) of  $10\text{ Hz}$  (minimum value that allows to remove noise), the  $s_{11}$  and  $s_{21}$  parameters are measured, as shown in Fig.21. In this way the quality factor  $Q$  of the first resonant mode (fundamental mode) is estimated as  $\omega_{ris}/\Delta\omega_{.3dB}$ , where  $\omega_{ris}$  is the angular frequency under resonant conditions and  $\Delta\omega_{.3dB}$  is the difference between the angular frequencies at the right and the

left of the resonant frequency at which  $s_{21}$  decreases of 3 dB with respect to the peak value. Thus the measured  $Q$ -factor is 352.98.

The second resonant peak at 19.7 GHz, is smaller and wider than the first, placed at about 5 GHz of distance. The quality factor  $Q$  of this peak is about 109.44 and, consequently, lower than that obtained for the first mode, as expected.

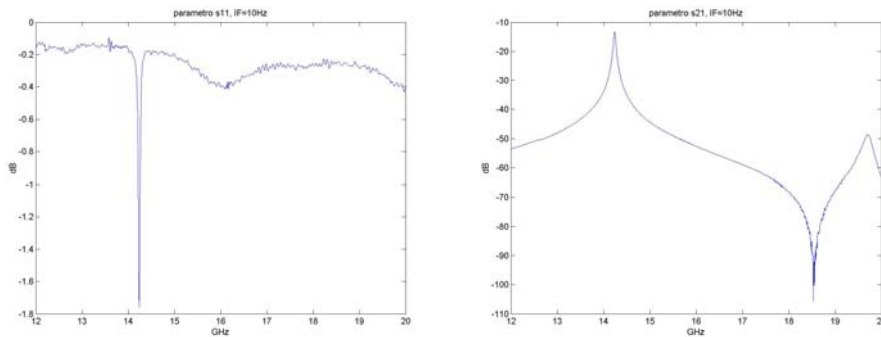


Fig. 21. Measured values of  $s_{11}$  and  $s_{21}$  between 12 GHz and 20 GHz with IF = 10 Hz.

## 9. Conclusions

We have investigated several structures in order to find the main geometrical parameters able to improve performances of a PBG based particle accelerator. All the simulations reveal good performances for a structure based on dielectric rods and a suitable number of grating periods.

A PBG-based resonant cavity has been designed, realized and measured for the first time in Europe. This cavity is able to accelerate hadrons in order to define the elementary unit cell of a high-efficiency and low-cost accelerator, whose sizes are smaller than the classical cyclotron, which is now used to accelerate hadrons with a lot of limitations.

The designed PBG accelerator will allow the attainment of important results in terms of therapy efficiency and feasibility, reaching a higher number of patients because of the reliability of the accelerator, which is the system kernel, and the falling implementation cost.

## 10. References

- Agilent Technologies (2004). Exploring the architectures of Network Analyzers.
- Coutrakon, G.; Slater, J. M.; Ghebremedhin, A. (1999). Design consideration for medical proton accelerators. *Proceedings of the 1999 Particle Accelerator Conference*, 1999, New York.
- Dwoyer, D.L.; Hussaini, M.Y.; Voigt, R.G. (1988). *Finite Elements - Theory and Application*. Ed. Springer-Verlag, ISBN 0-387-96610-2, New York.
- Kiriakidis, G. & Katsarakis, N. (2000). Fabrication of 2D and 3D Photonic Bandgap Crystals in the GHz and THz regions. *Mater. Phys. Mech.*, Vol. 1, pp. 20-26.
- Perri, A. G. (2007). *Introduzione ai dispositivi micro e nanoelettronici*. Ed. Biblios, Vol. 1 - 2, ISBN 978-88-6225-000-9, Bari, Italy.

- Shapiro, M. A.; Brown, W. J.; Mastovsky, I.; Sirigiri, J. R.; Temkin, R. J. (2001). 17 GHz photonic band gap cavity with improved input coupling. *Physical Review Special Topics-Accelerators and beams*, Vol. 4, 2001, pp. 1-6.
- Yablonovitch, E. (1994). Photonic crystals. *Journal of Modern Optics*, Vol. 41, n. 2, 1994, pp. 173-194.

# Specific Millimeter-Wave Features of Fabry-Perot Resonator for Spectroscopic Measurements

Petr Píkša, Stanislav Zvánovec and, Petr Černý  
*Czech Technical University in Prague  
 Czech Republic*

## 1. Introduction

The spectral resolution and intensity sensitivity represent crucial quality parameters for millimeter-wave spectroscopic measurements. A Fabry-Perot resonator (see Fig. 1) can, very efficiently, enhance the sensitivity of the absorption as well as of emission measurements in the millimeter-wave spectroscopy (Zvanovec et al., 2009) (Grabow, 2009). For the monochromatic radiation, the resonator can be tuned to a resonance at which the constructive interference of the multiple-reflected electromagnetic waves enables to accumulate the radiated energy. The higher sensitivity to weak absorptions (resulting from the apparent lengthening of the optical path length by means of multiple reflections) stands for the main advantage of the Fabry-Perot resonator.

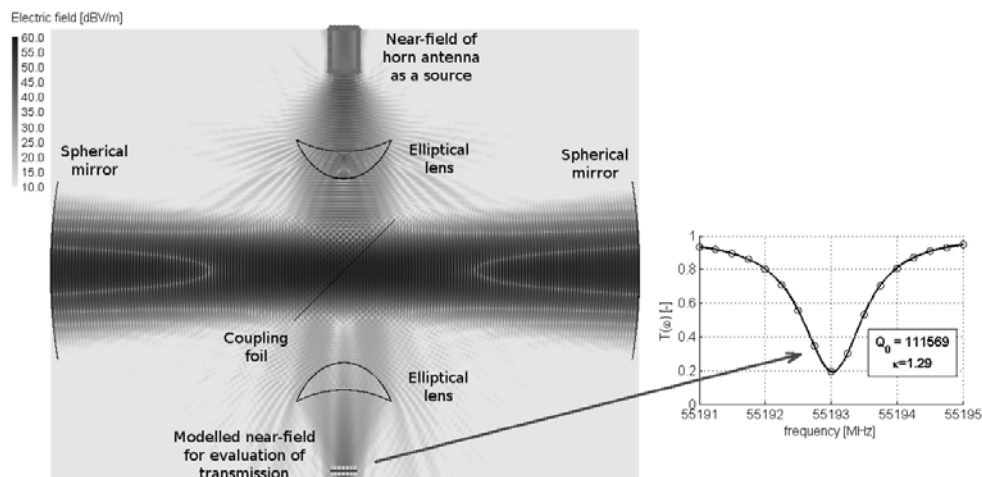


Fig. 1. Model of Fabry-Perot resonator with electric field distribution and enumerated quality factor from resonance curve

This chapter deals with the millimeter-wave features of the Fabry-Perot resonator as a tool for spectroscopic measurements. These features derived from the theoretical knowledge were investigated by means of the results of full-wave numerical modeling in connection with Multi Level Fast Multipole Method (MLFMM) (Chew et al., 2001) and Uniform Theory of Diffraction (UTD) approximation of Method of Moments (MoM). Firstly, the theoretical solution is introduced and then the development and comparison of several models of Fabry-Perot resonator (see an example in Fig. 1) are subject to in-depth analysis and discussion. A simplified model able to solve the resonator performance up to 110 GHz (the radius of the mirrors equals 55 times the wavelength) is introduced. Simulation aspects of specific parts of measuring system are investigated as well. Based on the aforementioned investigations, the full model is proposed.

Last but not least, the attention is paid to the description of the unified technique for obtaining a spectrum of absorption coefficient from the measured resonance curves of the gas-filled as well as evacuated resonators.

## 2. Fabry-Perot resonator

The majority of Fabry-Perot resonators, when applied to the millimeter-wave spectrum, provide a suited tool to making sensitive and accurate medium loss and dispersal measurements.

Types of Fabry-Perot arrangements, which are usually used, range with respect to the excitation and coupling of the resonator. Either axial or radial excitations of resonator cavity are possible. The resonator can be connected either for measurement of transmission through the resonator or for measurement of reflection by the resonator with the corresponding coupling. The radial excitation utilizes a coupling through a thin dielectric foil (French & Arnold, 1967), where it is possible to excite the dominant mode  $TEM_{00}$  without any additional higher-order modes. On the other hand, the dielectric coupling foil decreases a quality factor of the resonator. The axial excitation is realized either by waveguides and coupling holes (Zimmerer, 1963) (Hirvonen et al., 1996), or by coaxial lines and inductive coupling or an L-shaped antenna (Montgomery, 1947, p. 318) (Grabow, 2009, p. 423).

The investigated Fabry-Perot resonator comprises a radial excitation and comprises two spherical mirrors, dielectric coupling foil placed between these mirrors and dielectric lenses necessary for the establishment of the plane wave into/out of the resonator via the coupling foil; see Fig. 1. The radiated energy is coupled into/out of the resonator cavity by means of the special elliptical dielectric lenses (Milligan, 2005, p. 448) (Johnson, 1993, p. 16-4) that are placed in the windows. Moreover, the above-mentioned energy is coupled also via the dielectric polyethylene coupling foil from/to the perpendicularly placed feeder and detector (horn antennas). The lenses focus the required radiated energy on/from the coupling foil and thus form the diverging waveforms in the near field region onto the flat uniform field. The optimization of lenses parameters was accomplished in order to optimize the waveform inside the resonator. It was necessary to avoid additional undesirable resonances inside the resonator that are caused by inner surfaces of lenses, for these resonances evoke a dummy increase of the quality factor. The optimal field distribution on the coupling foil together with the position of the feeding antenna in front of the lens were also carefully sought (Zvanovec et al., 2009).

It is essential to note that the polarization of incident wave in case of the radial excitation affects the coupling into the resonator. The parallel polarization proves a low reflection from the dielectric foil, therefore, the resonator is coupled to a very low extent. Hence solely the perpendicular polarization was utilized.

**2.1 Resonance condition**

The resonator has to fulfill the following resonance condition:

$$\frac{2d}{\lambda} = q + (2p + l + 1) \frac{1}{\pi} \arccos \left( \sqrt{\left(1 - \frac{d}{R_1}\right) \left(1 - \frac{d}{R_2}\right)} \right) - \frac{1.655t \left(\sqrt{\varepsilon_r} - 1\right)}{\lambda_0 / 2}, \tag{1}$$

where  $p, l, q$  are indexes of TEM modes,  $q$  means the number of half-wavelengths on the distance  $d$  between the mirrors,  $R_{1,2}$  stand for the radii of the curvature of mirrors,  $t$  is thickness and  $\varepsilon_r$  is relative permittivity of the dielectric coupling foil. The second part on the right side of (1) introduces the correction from the plane to the spherical wave and the last part of (1) counts for an approximate correction of the dielectric foil.

**2.2 Equivalent circuit, coupling coefficient and quality factor**

As it has been already mentioned, the investigated resonator is straight-through and the coupling is realized with the thin dielectric foil. The level of the transmitted power therefore depends on the value of the coupling coefficient, quality factor and relative frequency misalignment of the resonator. In the resonance, the transmitted power shows minimum value. Out of the resonance and under the low coupling, the transmitted power is not influenced by the resonator. Thus, the resonator can be described by an equivalent circuit such as the one depicted in Fig. 2b).

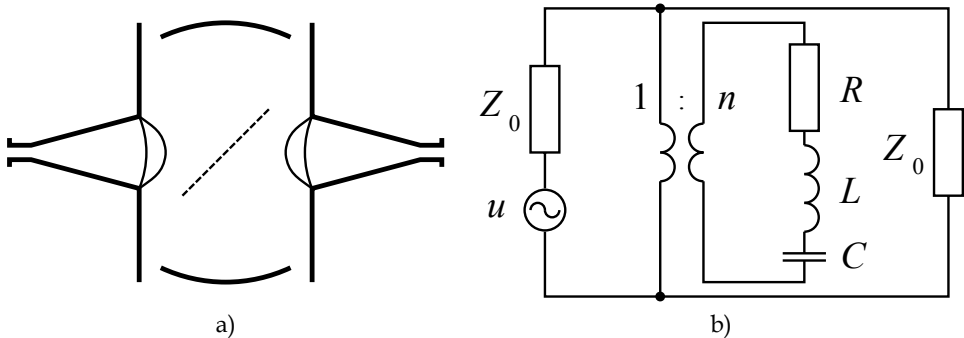


Fig. 2. a) Fabry-Perot resonator scheme and b) equivalent circuit

The theoretical solution of the equivalent circuits is based upon the techniques such as (Montgomery, 1947, p. 314). As a result, we can specify the most important parameters of this resonator.

The unloaded quality factor can be defined by equation that follows

$$Q_0 = \frac{\omega_0 L}{R}, \quad (2)$$

where  $\omega_0$  is the angular frequency equal to  $2\pi f_0$  ( $f_0$  represents the resonant frequency), while the parameters  $L, R$  are obvious from Fig. 2b).

The external quality factor, which considers the losses in external feeding lines, can be expressed as

$$Q_v = \frac{\omega_0 L}{\frac{n^2 Z_0}{2}}. \quad (3)$$

The loaded quality factor involving the external and internal losses, can be determined from

$$Q_z = \frac{\omega_0 L}{R + \frac{n^2 Z_0}{2}}. \quad (4)$$

The relation between the unloaded and loaded quality factor is given by

$$Q_z = \frac{Q_0}{1 + \kappa}, \quad (5)$$

where  $\kappa$  stands for the coupling coefficient defined as

$$\kappa = \frac{Q_0}{Q_v} = \frac{n^2 Z_0}{2R}. \quad (6)$$

Since  $1/LC = \omega_0^2$ , the impedance of resonance circuit  $Z_r$  is modified into the following form

$$Z_r = R \left( 1 + j \frac{\omega_0 L}{R} \left( \frac{\omega}{\omega_0} - \frac{\omega_0}{\omega} \right) \right), \quad (7)$$

where the form in inner brackets equals a double relative frequency misalignment  $\delta$  within the condition of  $\omega \approx \omega_0$ ; see below

$$\frac{\omega}{\omega_0} - \frac{\omega_0}{\omega} \approx 2 \frac{\omega - \omega_0}{\omega_0} = 2\delta. \quad (8)$$

The impedance of the resonance circuit transformed through the transformer (1:n) is under consideration of equations (2), (6) and (8). Thus it can be stated

$$Z_m = \frac{R}{n^2} (1 + j2Q_0\delta) = \frac{Z_0}{2\kappa} (1 + j2Q_0\delta). \quad (9)$$

Output power  $P_z$  on the load  $Z_0$  is determined as

$$P_z = \frac{1}{8} \frac{|u|^2}{Z_0} \frac{1 + (2Q_0\delta)^2}{(\kappa + 1)^2 + (2Q_0\delta)^2}. \quad (10)$$

With respect to the equations listed above, the transmission coefficient  $T(\omega)$ , given by the output power divided by the maximum output power (at  $\kappa=0$  and  $\delta=0$ ), is defined as



$$T(\omega) = \frac{1 + (2Q_0\delta)^2}{(\kappa + 1)^2 + (2Q_0\delta)^2} \tag{11}$$

At the resonant frequency ( $\delta=0$ ), the coupling coefficient can be defined as

$$\kappa = \frac{1}{\sqrt{T(\omega_0)}} - 1 \tag{12}$$

In regard of the values of the relative frequency misalignment  $\delta_{1,2}$  fulfilling the condition:

$$2Q_0\delta_{1,2} = \pm 1 \tag{13}$$

the unloaded quality factor is determined in the way listed below

$$Q_0 = \frac{1}{\delta_1 - \delta_2} = \frac{f_0}{f_1 - f_2} \tag{14}$$

where frequencies  $f_1$  and  $f_2$  correspond to the relative frequency misalignments  $\delta_{1,2}$  from the resonance frequency  $f_0$  and the transmission coefficient at the frequencies  $f_{1,2}$  is equal to

$$T(\omega_{1,2}) = \frac{2}{(\kappa + 1)^2 + 1} \tag{15}$$

From the above-explained procedure, we can obtain the resonance curve described as a frequency dependence of the transmission coefficient. Owing to the equation (12), we can obtain the coupling coefficient. Equation (15) serves as a tool for obtaining the values of the tracing transmission coefficient  $T(\omega_{1,2})$ , whereby we can indicate the frequencies  $f_{1,2}$  on the resonance curve. The unloaded quality factor can also be evaluated with the help of the equation (14).

### 2.3 Losses in Fabry-Perot resonator

It is apparent that there are several types of unwanted losses within the Fabry-Perot resonator that influence the unloaded quality factor. Indeed they call for a very careful attention and treatment. Except for the measured attenuation of an inserted medium, we can distinguish among the diffraction and reflection losses at the mirrors and the coupling losses caused by the dielectric foil.

The diffraction losses  $\alpha_D$  are interpolated by the approximation (Zimmerer, 1963) (Engstova, 1973) given by

$$\alpha_D = 29 \cdot 10^{-4.83 N'} \tag{16}$$

where

$$N' = \frac{a^2}{\lambda d} \sqrt{1 - g} = N \sqrt{1 - g} \tag{17}$$

$a$  is the radius of mirrors,  $N$  stands for the Fresnel number and  $g=1-d/R_i$ , where parameter  $d$  represents the distance between the mirrors and  $R_i$  radius of curvature of mirrors ( $R_i=R_1=R_2$ ).

Although simplified expressions of diffraction losses have been published in (Arora and Mongia, 1992), they are inconsistent with the numerical results given by (Fox and Li, 1961). The numerical results and approximation curves of diffraction losses  $\alpha_D$  are depicted in Fig. 3.

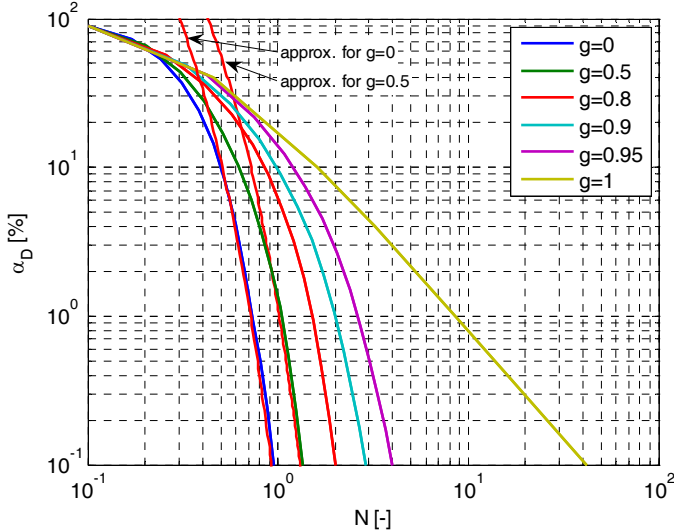


Fig. 3. Coefficient of diffraction losses  $\alpha_D$  in dependence on Fresnel number  $N$  with approximations given by equation (16)

Reflection losses can be expressed by

$$\alpha_R = 1 - |\rho|^2 \cong 2 \sqrt{\frac{2 \omega \varepsilon_0 \varepsilon_r}{\sigma}} \quad (18)$$

where  $\rho$  is a reflection coefficient of the mirror,  $\varepsilon_r$  stands for the relative permittivity of medium and  $\sigma$  represents the conductivity of mirrors.

Coupling losses  $\alpha_c$  can be enumerated from the reflection on the dielectric foil in the following way:

$$\alpha_c = |\rho|^2 = \left[ \frac{t}{\lambda} \pi \sqrt{2} (\varepsilon_r - 1) \right]^2 \quad (19)$$

Unfortunately, when taking into account the real condition, the theoretical equation of the coupling losses (19) (Engstova, 1973) does not correspond to the results gained from the simulations (more details are discussed in Chapter 2.4.3).

The quality factors for particular losses can be approximated by

$$Q_x = \frac{2 \pi d}{\lambda \alpha_x} \quad (20)$$

The total unloaded quality factor can be derived from particular loss components as

$$\frac{1}{Q_0} = \frac{1}{Q_D} + \frac{1}{Q_R} + \frac{1}{Q_c} = \frac{\lambda}{2\pi d} (\alpha_D + \alpha_R + \alpha_c) . \quad (21)$$

## 2.4 Numerical modeling

Various models of Fabry-Perot resonator, with different feeding and coupling components, have been investigated (see the example in Fig. 1). Series of numerical principles with respect to the used approximation of the Method of Moments (MLFMM or hybrid technique of MLFMM and UTD) were applied in order to find a workable and efficient model in the numerical simulator FEKO (FEKO website). The differences of applied principles are based on the surface or the volume definition of dielectric parts. The completely workable model (without using any limitations) is based on the surface equivalence principle in line with the used Multi Level Fast Multipole Method.

There are several possibilities how to model the dielectric structures in FEKO. If the surface current method is employed, the surface of the dielectric solid is subdivided into triangles. On the contrary, in case that the volume current method is utilized, the dielectric solid is subdivided into cuboids.

In the first approach, the surface of dielectric parts is subdivided into a surface mesh using triangular elements. Merely the MLFMM method is applied here. In case of the second class of models, the dielectric volume is subdivided into cuboidal elements. The MLFMM+UDT hybrid technique is used here. In fact, the MLFMM method is required due to the electrically large metallic mirrors.

### 2.4.1 Surface equivalence principle

In general, the Method of Moments utilizes the surface equivalence principle for modeling of dielectric bodies. In this method, the interfaces between different homogeneous regions are subdivided into a surface mesh using the triangular elements. Basic functions are applied to these elements for the equivalent electric and the equivalent magnetic surface currents. Boundary conditions result from the use of equivalent sources.

The dielectric parts of the Fabry-Perot resonator subdivided into the surface mesh using the triangular elements are depicted in Fig. 4a).

The FEKO simulator provides a possibility of simplification of the thin dielectric coupling foil by the employment of the skin effect, where the body of the foil is defined only in one face.

### 2.4.2 Volume equivalence principle

The Method of Moments can also be applied with the volume equivalence principle. In this case, the volume is subdivided into cuboidal elements. In principle, the polarization current inside the volume element is unknown. Nevertheless, the volume element has usually more unknowns than a surface mesh, which represents one of drawbacks of this approach. However, this technique is highly suitable for thin sheets and proves to be very stable for low frequencies. Therefore the coupling dielectric foil as a thin structure was modeled by utilization of this technique.

The subdivision of the dielectric parts of the Fabry-Perot resonator into cuboidal elements can be seen in Fig. 4b). Unfortunately, it was observed that particularly at higher frequencies

the lens consisting of cuboidal elements results in an unstable process of the MLFMM+UTD hybrid method. The MLFMM+UDT method introduces a suitable tool for thin structures (equal or less than the wavelength), but not for thick structures (such as the dielectric lens).

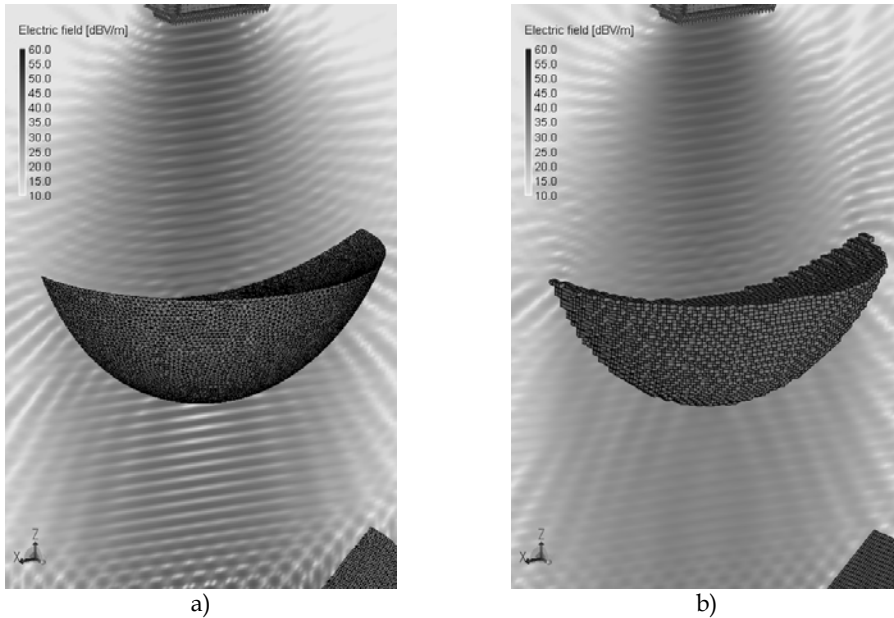


Fig. 4. Dielectric parts subdivided by a) surface equivalence principle into triangular elements or by b) volume equivalence principle into cuboidal elements

As a result, the simplified model consisting of the spherical mirrors and dielectric coupling foil was created. The dielectric lens was not considered and the volume equivalence principle was used on the dielectric coupling foil. As for the source, the ideal point source with  $\cos^{24}$  radiation pattern (corresponding to the antenna gain of 20 dBi) was used here instead of the actual source of the horn antenna. The main virtue of the proposed approach is the fact that this model can be used particularly at higher frequencies (up to 110 GHz), with respect to computational requirements.

### 2.4.3 Influence of dielectric coupling foil

The influence of the polyethylene coupling foil ( $\epsilon_r = 2.26$ ) was investigated from the numerical simulations via the simplified model described above. Frequency dependences of the quality factor under effect of coupling losses and the coupling coefficient are indicated for three different thicknesses of the polyethylene coupling foil; see Fig. 5.

It is necessary to point out that the impact of the dielectric foil on the measurement sensitivity (with regards to the quality factor) is considerably frequency-dependent. The influence of the dielectric foil on the coupling loss can be explained by a smaller depth of penetration at a lower working frequency. This causes low coupling, where reflection

aspects only cannot be involved in the coupling enumeration at lower frequencies. Indeed, also other phenomena have to be taken into account.

The quality factor  $Q_c$ , derived from simulation results ( $Q_0$ ), decreases at lower frequencies due to the low coupling; see Fig. 5a). The values of  $Q_c$  were evaluated from (21). The increased reflection of electromagnetic waves can be observed at higher frequencies; therefore losses rise in accordance with (19). It is necessary to emphasize that the obtained effect of the dielectric coupling foil approaches the theoretical definition (19) only at higher frequencies of the coupling foil usability.

The thickness of the coupling foil has to be carefully selected, i.e. it is necessary to take into account the low coupling losses and optimal coupling coefficient ( $\kappa$  within the interval from 0.5 to 2) and set it in harmony with the above-mentioned factors. In our particular case (Fig. 5) the optimal thickness of the foil equals 0.1 mm.

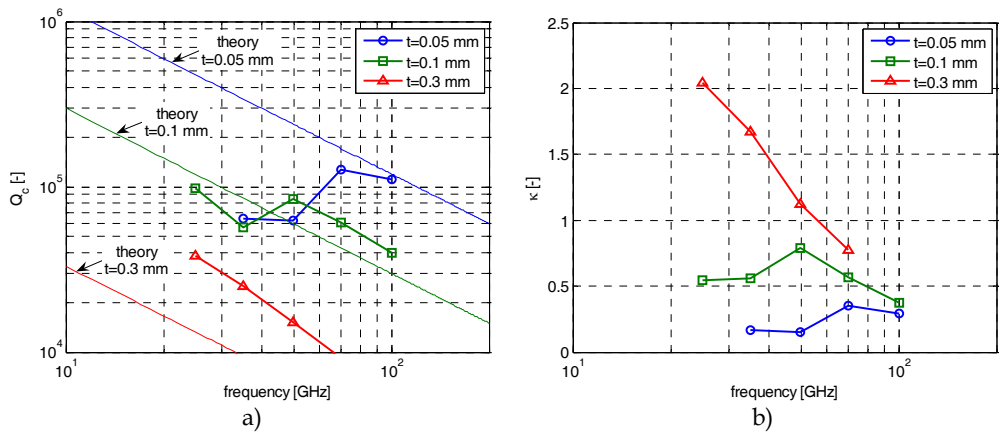


Fig. 5. Frequency dependence of a) quality factor under effect of coupling losses and b) coupling coefficient for three different thicknesses of polyethylene coupling foil

### 2.4.4 Higher-order modes

Since it is necessary to develop a resonator for a wide frequency band, i.e. the Fresnel number  $N$  ranges from 1 to higher numbers (note  $N=1$  at the lowest frequency usability of the stable resonator), the emergence of higher-order modes is inevitable. Simulations were performed in order to validate the higher-order modes of the resonator. It was determined that in case of the mirror distance higher than radii of the curvature of mirrors, the higher even modes  $TEM_{10,20}$  of the Fabry-Perot resonator are shifted towards higher frequencies. Fig. 6 depicts the particular analyzed frequency distribution of modes for the non-confocal resonator deployment (the distance between mirrors is of 0.493 m, radii of curvatures equals 0.455 m and radii of mirrors amounts to 0.075 m) around the frequency of 110 GHz (corresponds to  $q=361$  and  $N=4.18$ ). As in our practice case, the source input power of 10 dBm was chosen.

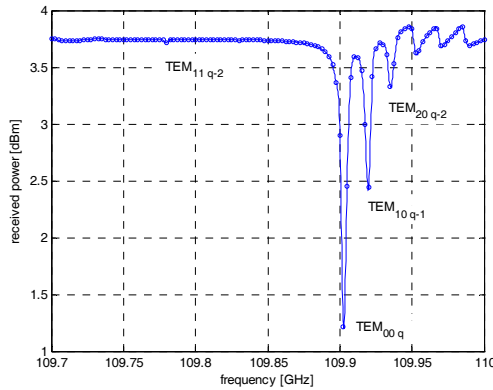


Fig. 6. Higher-order modes around frequency of 110 GHz

The principle of the electric field distribution in transverse plane is demonstrated for instance in (Grabow, 1996) and (Kogelnik, 1966). A longitudinal distribution of the electric field intensity of distinguishable TEM modes inside the resonator is shown in Fig. 7. The maximum energy of the dominant mode  $TEM_{00}$  is accumulated in the axis of the resonator. Since the majority of measurements are performed at the dominant mode, it is essential to properly adjust the Gaussian mode shape so that as much active molecules of measured gas as possible are affected by the homogeneous electromagnetic field.

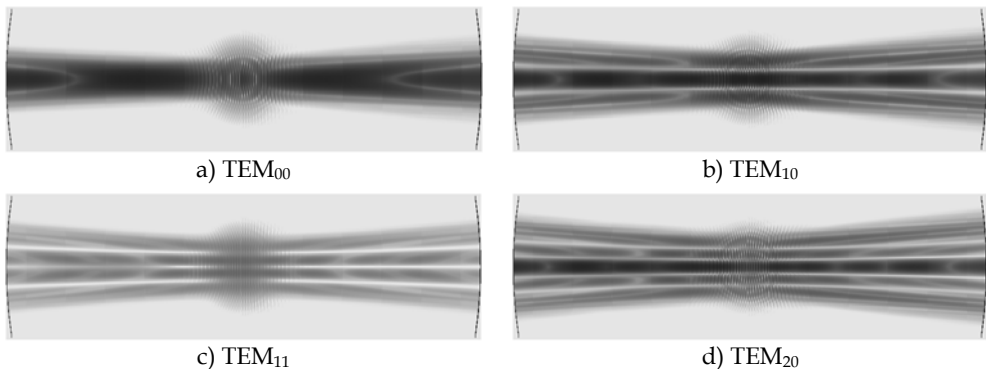


Fig. 7. Electric field distribution along resonator at resonant frequencies of particular  $TEM_{plq}$  modes

It was derived from the measurements and simulations that the turn of the coupling foil essentially influences the odd transverse mode  $TEM_{11}$ . This phenomenon could be almost neglected by a proper setting of the foil and mirrors. On the contrary, an improper setting of the coupling foil could result even in the attenuation at this mode (which would be comparable with the dominant mode). This phenomenon would worsen the identification of operating frequencies. It could be stressed that the mode  $TEM_{11}$  lies approximately in the middle of two dominant modes.

#### 2.4.4 Full model

In order to comprehend the other influences (caused by an actual source and by the reflections) in analyses, the full model was developed. The latter comprises the whole system including two spherical mirrors, dielectric coupling foil, two dielectric lenses and actual source of horn antenna. The horn antenna was substituted by its simulated near-field in order to utilize the MLFMM method. The arrangement of particular parts of the resonator was indicated in Fig. 1. The model employs the surface equivalence principle.

In the above-mentioned simplified model with the ideal point sources, the resonator was excited by a spherical wave. Contrary to that, in the full model with dielectric lenses, the resonator is excited by a plane wave. This approach enables a better excitation of the dominant  $TEM_{00}$  mode inside the resonator. A better insight into the quality factor of the resonator can be then obtained from simulations - without the degradation of results by an imperfect source.

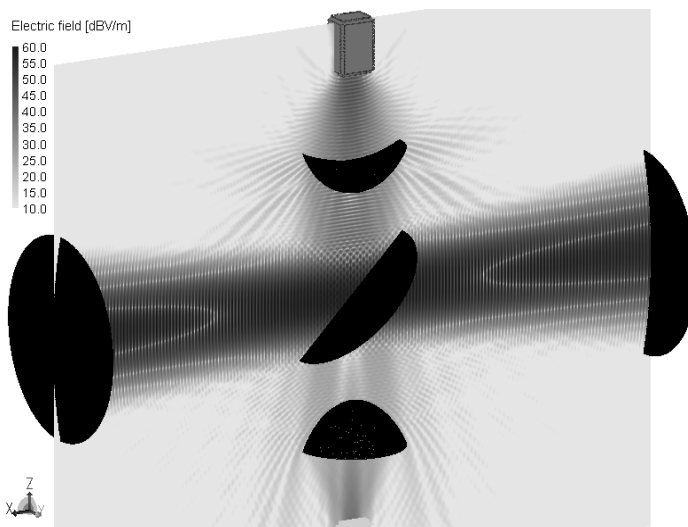


Fig. 8. The full model of Fabry-Perot resonator

The quality factors of  $0.8 \cdot 10^5$  and  $1.1 \cdot 10^5$  can be determined from simulations performed for both the simplified model and the full model (see Fig. 8), respectively. A particular resonator configuration in this case equaled  $R=0.455$  m,  $d=0.495$ - $0.510$  m,  $a=0.075$  m and frequency usability 26-80 GHz - it corresponds to  $N$  within the interval ranging from 1 to 3. The response of the modeled resonator is described by the frequency dependence of the transmission coefficient. This resonance curve is demonstrated in Fig. 9. From the resonance curve, the unloaded quality factor as well as the coupling coefficient was enumerated in accordance with the process mentioned at the end of Chapter 2.2.

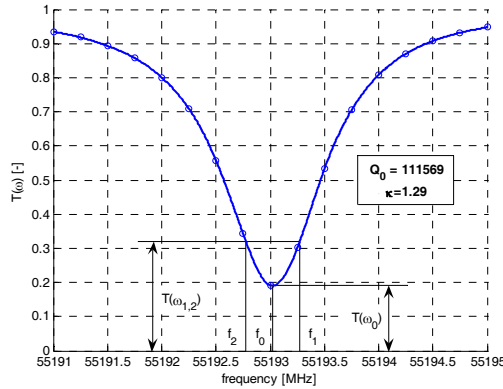


Fig. 9. Resonance curve of modeled resonator

**2.5 Methodology of resonator design**

From the solution of ABCD matrix of the resonator (indeed under the condition of keeping the beam inside the resonator) the resonator dimensions have to fulfill the following stability condition, which constitutes the first limitation:

$$0 < g_1 g_2 < 1 \quad . \quad (22)$$

This can be expressed graphically as stable and unstable areas; see Fig. 10.

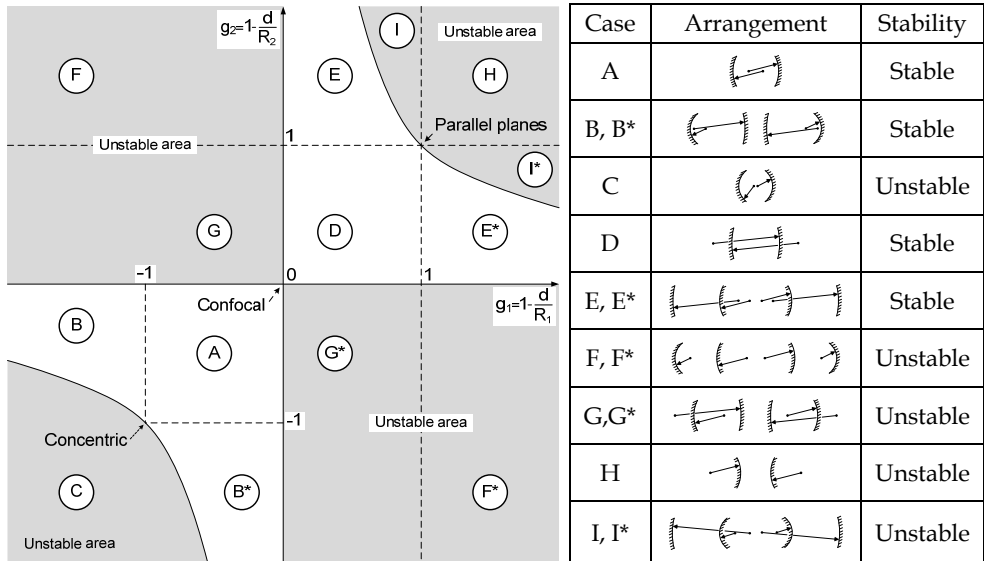


Fig. 10. Stability diagram of open resonators



The second limitation takes into account the diffraction losses. In principle, the diffraction losses of the dominant mode TEM<sub>00</sub> can be neglected by using the curved reflectors and the correct plate separation  $d$  (when Fresnel number  $N=1$ ).  $N$  is given by

$$N = \frac{a_1 a_2}{\lambda d} . \tag{23}$$

The arrangement of mirrors is usually set as a near-confocal in order to avoid an overlap of modes TEM<sub>00</sub> and TEM<sub>10</sub>. Higher-order modes are the cause of the high Fresnel number, where these higher-order modes show lower diffraction losses.

The excitation of the resonator has a crucial impact on the rise in higher-order modes as well. The ideal source (as a plane wave that incidents perpendicularly to the resonator cavity) creates a pure excitation of the dominant TEM<sub>00</sub> mode.

### 3. Millimeter-wave gas absorption measurement

The main advantage of gas absorption laboratory measurements is represented by the fact that the measured medium can be accurately adjusted in terms of the homogeneity of a particular gas composition and distribution, which cannot be truly described in case of open measurements. The high sensitivity of the Fabry-Perot resonant cavity results from its very high quality factor.

#### 3.1 Attenuation constant

The propagation constant  $\gamma$  is defined by

$$\gamma = \alpha + j\beta = \pm\sqrt{\Gamma^2 - \omega^2 \mu \varepsilon} , \tag{24}$$

where  $\alpha$  is the attenuation constant in Np·m<sup>-1</sup>, and  $\beta$  stands for the phase constant stated in radians per meter,  $\Gamma$  represents the transverse propagation constant,  $\omega$  describes the angular frequency,  $\mu$  is the permeability, while  $\varepsilon$  stands for the complex permittivity of the medium given by

$$\varepsilon = \varepsilon' (1 - j \operatorname{tg} \delta) . \tag{25}$$

By taken equation (25) into (24), as well as by the separation of real and imaginary parts and, furthermore, by solving these equations we get the complex relations for  $\alpha$  and  $\beta$  (Tysl & Ruzicka, 1989, p. 67).

In case of the low-loss medium (loss factor  $\operatorname{tg} \delta \ll 1$ ) and neglecting of  $\Gamma$ , the attenuation constant can be determined as

$$\alpha = \frac{\pi}{\lambda} \operatorname{tg} \delta . \tag{26}$$

The medium influences the quality factor in accordance with

$$\frac{1}{Q_0'} = \frac{1}{Q_0} + \operatorname{tg} \delta . \tag{27}$$

The quality factor  $Q_0$  and the coupling coefficient  $\kappa$  can be obtained from the measurement without gas by means of the approach described in Chapter 2.2.

Very narrow spectral lines can deform the resonance curve of the resonator and also the resulting gas-filled quality factor  $Q_0'$ . Therefore, the loss factor can be expressed more accurately with the help of the relation to the coupling coefficient fulfilling (6), which can be obtained from the measurement of the transmission coefficient merely at the resonant frequency by (12). The loss factor can be then expressed from the coupling coefficients without ( $\kappa$ ) and with the sample gas ( $\kappa'$ ) as follows.

$$\text{tg } \delta = \frac{1}{Q_0} \left( \frac{\kappa}{\kappa'} - 1 \right). \tag{28}$$

By taken equation (28) into (26), the attenuation constant can be given by

$$\alpha = \frac{\pi}{\lambda Q_0} \left( \frac{\kappa}{\kappa'} - 1 \right) \quad (\text{Np/m}) \tag{29}$$

or

$$\alpha = \frac{27.288}{\lambda Q_0} \left( \frac{\kappa}{\kappa'} - 1 \right) \quad (\text{dB/m}). \tag{30}$$

We can find these final equations e.g. in (Valkenburg & Derr, 1966).

Parameters of the theoretical equation (11) of resonance curve were optimized by means of the measured data of  $\text{CH}_3\text{CN}$ . The example of the fitting around the resonant frequency of 55193 MHz is depicted in Fig. 11.

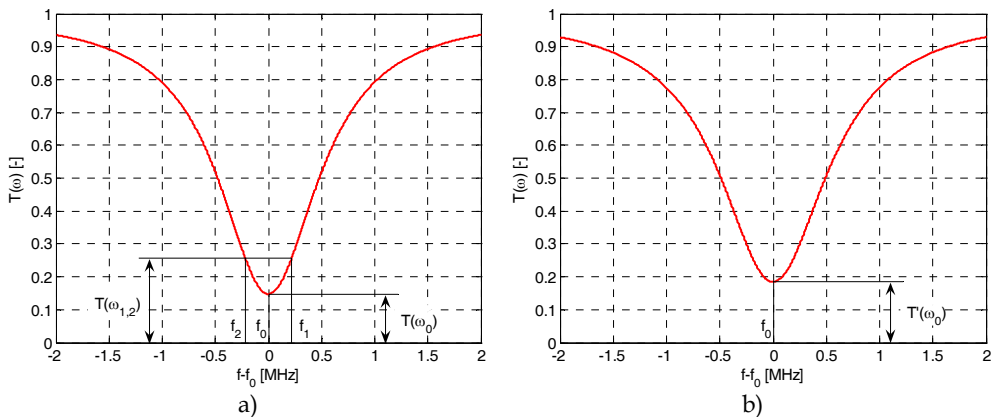


Fig. 11. Fitted measured resonance curves of a) empty and b) gas ( $\text{CH}_3\text{CN}$ )- filled resonator

### 3.2 Measurement

The measuring system fully controlled by the computer was developed in the Department of electromagnetic field, Czech Technical University in Prague (see setup illustrated in Fig. 12). It involves mixers and multipliers working within the band ranging from 50 to 110 GHz.

By means of the automated step-motor the adjustment of the cavity length from 0.495 to 0.510 m with a 0.05  $\mu\text{m}$  step can be accomplished.

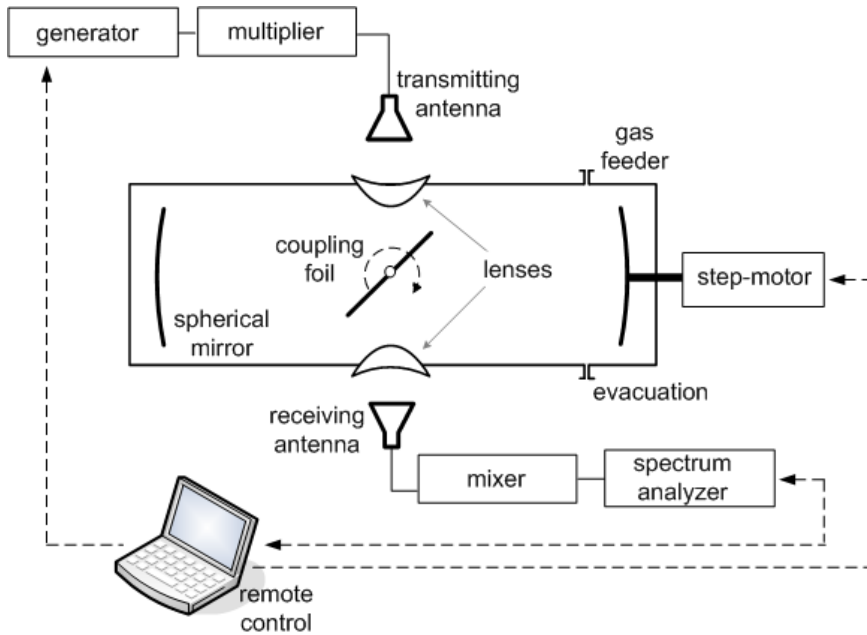


Fig. 12. Fabry-Perot resonator setup for gas absorption measurements (Zvanovec et al., 2009)

First, the received power was measured when the resonator was not coupled. Second, by turning of the coupling foil the resonator was coupled to the minimum received power at the resonance frequency. The transmission coefficient was determined by the received power with the coupling divided by the received power without coupling. The frequency dependence of the transmission coefficient describes the resonance curve. In next step, the resonator was retuned with the adjusting of mirrors distance by a step-motor and the resonance curve was measured again. The process of measurement of resonance curves was repeated also for the case of the gas-filled resonator. From the measured resonance curves, the unloaded quality factor and the coupling coefficient of the empty as well as gas-filled resonator were enumerated in accordance with the process mentioned at the end of Chapter 2.2.

In order to clearly demonstrate the measurement approach, the examples of measured results for the gas of acetonitrile  $\text{CH}_3\text{CN}$  are shown in Fig. 13 and Fig. 14. The curves in Fig. 13 illustrate frequency dependences of the unloaded quality factor and coupling coefficients of the empty and gas-filled resonator. It is obvious that the unloaded quality factor remains stable around the value of 128 000.

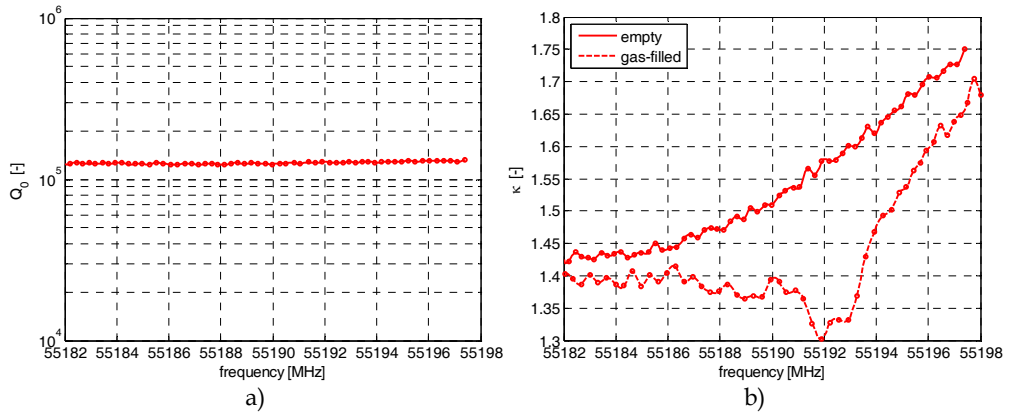


Fig. 13. Measured a) unloaded quality factor and b) coupling coefficient with and without gas

The gas absorption loss (attenuation constant) was enumerated from the unloaded quality factor and the coupling coefficients with the help of (30). The frequency dependence of the gas absorption loss is depicted in Fig. 14.

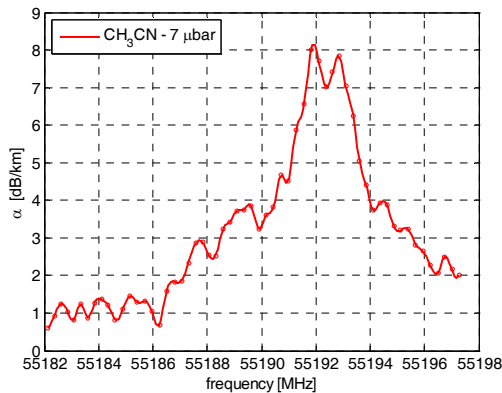


Fig. 14. Gas absorption loss of acetonitrile CH<sub>3</sub>CN under pressure of 7  $\mu$ bar

#### 4. Conclusions

In this chapter, specific millimeter-wave features of the Fabry-Perot resonator were discussed. The main contents include the proposal for fundamental steps (based on the theoretical knowledge and simulations analyses) crucial for the design of the resonator for spectroscopic measurements. The electrically large structures are very complicated to be simulated because of the computational requirement. Hence, the approximation methods were selected. The Multi Level Fast Multipole Method and the Uniform Theory of Diffraction approximation of Method of Moments were tested. As a result, the full model was proposed.

Owing to the simulation in FEKO and the analysis in MATLAB, the electromagnetic field going through the resonator and its analyzed frequency dependence of power (which represents the simulated resonance curve) were obtained. Firstly, parameters of the Fabry-Perot resonator, such as the unloaded quality factor and the coupling coefficient, were evaluated from the simulated resonance curve. Secondly, the theoretical resonance curve is solved by application of latter parameters into the theoretical equation (11). Finally, it is necessary to point out that there is a very good agreement between the theoretical and simulated resonance curves.

The high sensitivity of the Fabry-Perot resonant cavity results from its very high quality factor. The quality factor is reduced with the losses inside the resonator, where the coupling losses caused by the dielectric coupling foil are crucial. Hence, the numerical simulations of the influence of the coupling foil were performed. In our practical case, we qualified the frequency usability of the resonator.

The Fabry-Perot resonator represents a tool for millimeter-wave spectroscopic measurements and fine measurement of medium loss for a propagation purpose. In case that the gas  $\text{CH}_3\text{CN}$  was measured, the measuring procedure was verified. A satisfactory agreement of the unloaded quality factor of the empty resonator between the simulation ( $Q_0=1.1 \cdot 10^5$ ) and the measurement ( $Q_0=1.3 \cdot 10^5$ ) was achieved. The coupling coefficient turned out to be more sensitive, which is obvious from the comparison of the results for the simulation ( $\kappa=1.29$ ) with those relating to the measurement ( $\kappa=1.6$ ).

The entire approach concerning the theoretical simulation and practical analyses considerably extends the comprehension of particular millimeter-wave phenomena.

It is necessary to sum up the following important results. The overall resonator was modeled using approximation of the Method of Moments. The thickness of the dielectric coupling foil can be determined for the optimal coupling in advance in order to perform the measurement in the requested frequency band. On the other hand, the dielectric foil shows a considerable, highly frequency-dependent, influence on the resonator parameters, such as quality factor and coupling coefficient. Moreover, the coupling coefficient of the resonator varies with the resonator retuning. The aforementioned effect increases the system measurement error. As a goal for our future research work, we plan to strive to decrease these negative effects and increase the system sensitivity.

## 5. Acknowledgments

We would like to express our gratitude to Professor Václav Tysl for his experienced advice in the field of the theoretical background on the Fabry-Perot resonator. The work was supported through grants obtained from the Czech Science Foundation (GACR 102/08/P346) and from the Ministry of Education, Youth and Sports of the Czech Republic (research programs LC06071 and MSM 6840770014).

## 6. References

- Montgomery, C. G. (1947). *Technique of Microwave Measurements*, McGraw-Hill
- French, I. P., Arnold, T. E. (1967). High-Q Fabry-Perot Resonator for Nitric Oxide Absorption Measurements at 150 GHz. *Review of Scientific Instruments*, Vol. 38, 1967, pp. 1604-1607

- Zimmerer, R. W. (1963). Spherical Mirror Fabry-Perot Resonators. *IEEE MTT*, Vol. 11, No. 5, Sept. 1963, pp. 371-379, ISSN 0018-9480
- Hirvonen, T. M., Vainikainen, P., Lozowski, A., Räsänen, V. (1996). Measurement of Dielectrics at 100 GHz with an Open Resonator Connected to a Network Analyzer. *IEEE MTT*, Vol. 45, No. 4, Aug. 1996, pp. 780-786
- Grabow, J.-U. (2009). *Frontiers of Molecular Spectroscopy*, chap. 14: Microwave Spectroscopy: Experimental Techniques. Elsevier, p. 383-454, ISBN 978-0-444-53175-9
- Grabow, J.-U. (1996). A multioctave coaxially oriented beam-resonator arrangement Fourier-transform microwave spectrometer. *Review of Scientific Instruments*, Vol. 67, Dec. 1996, pp. 4072-4084
- Chew, W. C., Jin, J.-M., Michielssen, E., Song, J. (2001). *Fast and Efficient Algorithms in Computational Electromagnetics*. Artech, ISBN 1-58053-152-0.
- Milligan, T. A. (2005). *Modern Antenna Design*, 2<sup>nd</sup> ed. Wiley, ISBN 978-0-471-45776-3
- Johnson, R. C. (1993). *Antenna Engineering Handbook*, third ed. McGraw-Hill, ISBN 0-07-032381-X
- Fox, A. G., Li, T. (1961). Resonant modes in a maser interferometer. *Bell Sys. Tech. J.*, Vol. 40, March 1961, pp. 453-488
- Kogelnik, H., Li T. (1966). Laser Beams and Resonators. *Proceedings of the IEEE*, Vol. 54, No. 10, Oct. 1966, pp. 1312-1329
- Tysl, V., Ruzicka, V. (1989). *Teoretické základy mikrovlnné techniky*. SNTL, Prague, ISBN 80-03-00141-2 (in czech)
- Engstova, R. (1973). *Fabry-Perotův rezonátor pro mikrovlnnou spektroskopii plynu*. Dissertation thesis, CTU FEE, Prague, Dec. 1973 (in czech)
- Valkenburg, E. P., Derr, V. E. (1966). A High-Q Fabry-Perot Interferometer for Water Vapor Absorption Measurements in the 100 Gc/s to 300 Gc/s Frequency Range. *Proceedings of the IEEE*, Vol. 54, No. 4, April 1966, pp. 493-498
- Arora, R. K., Mongia, R. K. (1992). Simple expressions for diffraction loss in open resonators. *Microwave Opt. Tech. Lett.*, vol. 5, August 1992, pp. 401-403
- Zvanovec, S., Cerny, P., Piksa, P., Korinek, T., Pechac, P., Mazanek, M., Varga, J., Koubek, J., Urban, S. (2009). The use of the Fabry-Perot interferometer for high resolution microwave spectroscopy. *J. Mol. Spectrosc.*, Vol. 256, No. 1, July 2009, pp. 141-145, ISSN 0022-2852
- Feko website. Available: <http://www.feko.info>